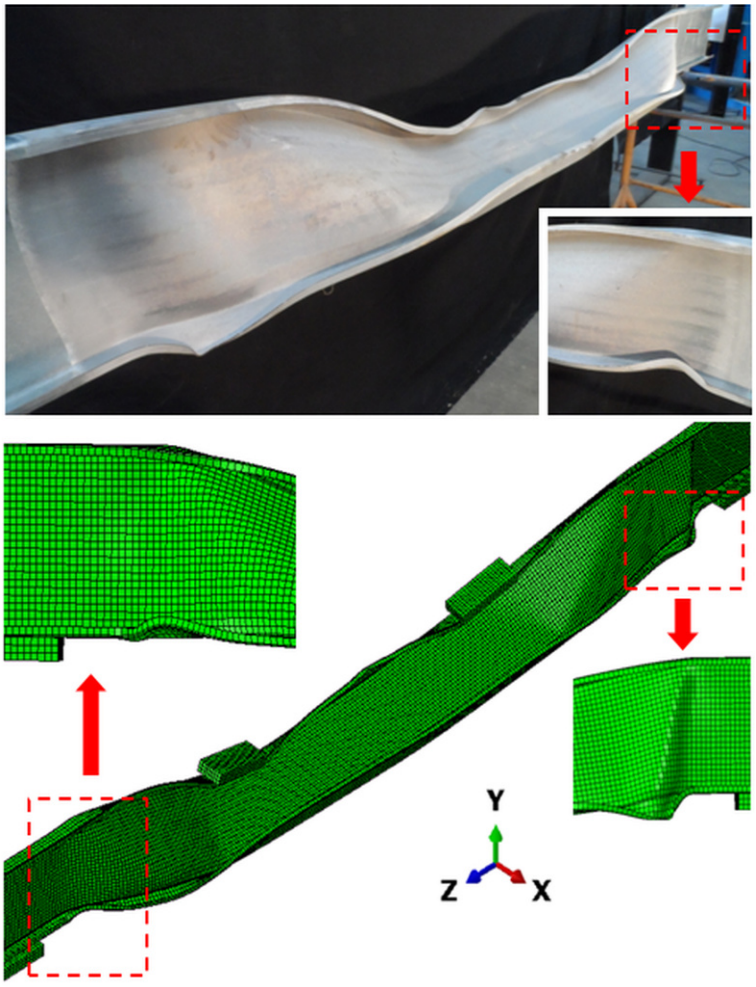

Luís Miguel dos Santos Laím

EXPERIMENTAL AND NUMERICAL ANALYSIS ON THE STRUCTURAL BEHAVIOUR OF COLD-FORMED STEEL BEAMS SUBJECTED TO FIRE

Tese de Doutoramento em Engenharia de Segurança ao Incêndio, orientada por João Paulo Correia Rodrigues e apresentada à Faculdade de Ciências e Tecnologia da Universidade de Coimbra

August 2013

· U C ·

UNIVERSIDADE DE COIMBRA

FCTUC DEPARTAMENTO DE ENGENHARIA CIVIL
FACULDADE DE CIÊNCIAS E TECNOLOGIA
UNIVERSIDADE DE COIMBRA

EXPERIMENTAL AND NUMERICAL ANALYSIS ON THE STRUCTURAL BEHAVIOUR OF COLD-FORMED STEEL BEAMS SUBJECTED TO FIRE

Thesis presented in fulfilment of the requirements for the degree of Doctor of Philosophy in ”Engenharia de Segurança ao Incêndio”

Author

Luís Miguel dos Santos Laím

Supervisor

Prof. Doutor João Paulo Correia Rodrigues

Coimbra, August, 2013

ACKNOWLEDGEMENTS

First of all, I am sincerely grateful to my supervisor Professor João Paulo Correia Rodrigues for his expertise, guidance and constructive suggestions over the last few years and the valuable assistance in many ways.

I would like to thank the Portuguese Foundation for Science and Technology (www.fct.mctes.pt), FCT, for providing financial support under the framework of research project PTDC/ECM/116859/2010 and for the Ph.D. scholarship SFRH/BD/47334/2008. Thanks also to the Portuguese cold-formed steel profile maker PERFISA S.A. (www.perfisa.net) for their support.

I would also like to thank the University of Coimbra for providing the necessary facilities and technical support.

Many wonderful people have still supported me on this journey. Without their help, I would not be able to finish my thesis successfully. First and foremost I would like to express my deep and sincere appreciation to my wife, Célia Antunes. She made great part of this adventure possible and showed me with love and optimism all the way to the end. To the Laboratory staff members (Fernando Rodrigues, Francisco Sousa, Luís Gaspar, Rafael Campos, Rui Ferreira) I thank their support for assistance with fabricating, preparing and testing the cold-formed steel specimens. It was truly a pleasure to work in the Laboratory where everyone was so caring, thoughtful, and willing to maintain a comfortable atmosphere for all. To all my colleagues that investigate in the Fire area at University of Coimbra (António Correia, Cristina Calmeiro, Hélder Craveiro, Hugo Caetano, Pedro Barata, Tiago Pires) my gratitude for their measureless help in this work. Finally, a special word of appreciation to my parents (Corália Laím, Jaime Laím) and relatives (Ana Laím, Benilde Antunes, Bruno Ribeiro, Elisabete Antunes, Jaíme Antunes, João Costa Afonso) and also to my friends (Maria Adélia Coelho, Natália Maurício, Tiago Orfão, Vasco Vasconcelos), for their endless support, encouragement and patience throughout the duration of this project.

RESUMO

A construção metálica é uma tecnologia cada vez mais corrente na construção civil que se baseia essencialmente na utilização de perfis pré-fabricados de aço estrutural. Estes, por sua vez, encontram-se em três formas distintas, nomeadamente, em perfis laminados a quente, em perfis soldados ou em perfis enformados a frio. Estes últimos, relativamente aos outros, têm fundamentalmente a vantagem de facilidade de produção, montagem e transporte, devido ao baixo peso dos perfis, conferido pelas espessuras reduzidas dos mesmos. No entanto, o facto de estes apresentarem estas espessuras pode originar a ocorrência de fenómenos de instabilidade local e distorcional. Neste sentido, diversos autores estudam experimental e numericamente estes fenómenos à temperatura ambiente.

Outro fenómeno também problemático é quando os elementos de aço enformados a frio estão sujeitos ao fogo, existindo neste caso muito poucos estudos. Deste modo, este trabalho de investigação teve como objectivo estudar o comportamento de vigas em aço galvanizado enformadas a frio em situação de incêndio, com base num vasto programa de ensaios experimentais. Ensaios de flexão de quatro pontos foram assim realizados com o intuito de avaliar a influência (i) do tipo de secção transversal das vigas (secções C, I-enrijecido, R e 2R), (ii) da restrição axial à elongação térmica (0 e 15 kN/mm) e (iii) da restrição rotacional nos apoios (0 e 150 kN.m/rad). Por outro lado, como referência, ainda foram efectuados ensaios à temperatura ambiente para a determinação da carga de instabilidade das respectivas vigas, assim como, dos seus modos de instabilidade que foram responsáveis pela perda de capacidade de carga da mesma, a fim de comparar com os ensaios a altas temperaturas. Estas vigas, normalmente utilizadas nos edifícios com perfis aço enformados a frio, tinham 3000 mm de vão e eram compostas por um ou mais perfis de aço enformados (perfis C e U) aparafusados entre si, os quais tinham 2.5 mm de espessura, 43 mm de banzo e 250 mm de altura para os perfis C e 255 mm para os perfis U.

O estudo experimental foi também complementado por uma intensiva análise numérica através do programa de elementos finitos ABAQUS. Neste domínio foi realizado um estudo paramétrico de modo a avaliar ainda o efeito da altura (entre 200 e 300 mm) e da espessura (entre 1,5 e 2,5 mm) das secções transversais das vigas, do comprimento do vão das mesmas (entre 2000 e 5000 mm) e, ainda, de outros valores de rigidezes de restrição axial (entre 0 e infinita) e rotacional (entre 0 e 1200 kN.m/rad) no desempenho estrutural deste tipo de vigas quando submetidas ao fogo.

Finalmente, com recurso a esta base de dados procurou-se comparar os resultados com as disposições estabelecidas no Eurocódigo 3, para o aço laminado a quente, e propor possíveis novas equações simplificadas de cálculo para o dimensionamento de vigas em aço enformadas a frio, em situação de incêndio.

As principais conclusões deste trabalho de investigação foram essencialmente que as vigas de aço enformadas a frio correntemente utilizadas neste tipo de edifícios apresentam uma resistência ao fogo baixa (inferior que 30 minutos), mas temperaturas críticas elevadas (maiores que 350 ºC, isto é, temperaturas superiores ao limite recomendado pelo Eurocódigo 3, Parte 1.2, para elementos de classe 4), na maioria das situações. Por outro lado, verificou-se que as temperaturas críticas das vigas podem reduzir substancialmente (30% em alguns casos) quando são restringidas à elongação térmica. Contudo, esta diminuição pode ser atenuada quando a restrição à rotação dos apoios da viga é significativa, comparativamente com a restrição rotacional da respectiva viga.

Palavras chave: Fogo, Vigas, Aço, Perfis enformado a frio, Capacidade de carga, Encurvadura, Experimental, Numérico, Equações simplificadas de cálculo.

ABSTRACT

The steel construction is increasingly an important technology for civil building. Actually, the steel industry is constantly in search of more and better uses for steel. The uses of hot-rolled, welded and cold-formed steel elements in the construction of buildings are ones of the solutions that can easily replace the traditional technology of construction. Indeed, cold-formed steel is one of which are becoming a very popular material in construction because they provide a high strength to weight ratio, are easy to produce, transport and assembly when compared to thicker hot-rolled steel members. Another advantage is the great variety of profiles available on the market which allow the building of different member cross-sections.

However, they may behave poorly under fire conditions, especially when they are unprotected in fire case, due to the combination of the high thermal conductivity of steel and section factor of these structural members (small wall thickness), both of which lead to a rapid rise of temperature in steel in fire situation. In addition, cold-formed steel members usually have complex buckling behaviour, involving local, distortional, global buckling and their interactions.

Studies on fire performance of cold-formed steel members are still fairly rare, are mostly of a numerical nature and are based on the structural behaviour of single and short elements at elevated temperatures. Hence, this research work intended to study the behaviour of cold-formed galvanized steel beams under fire conditions, basing on the results of a large programme of experimental tests. Four-point bending tests on cold-formed steel C-, lipped I-, R- and 2R-section beams were performed, both under fire conditions, under flexural loading conditions and under simply supported boundary conditions (roller and pinned supports) with different restraining conditions, including no restraints, partial axial restraint to the thermal elongation of the beam (15 kN/mm) and partial rotational restraint at the beam supports (150 kN.m/rad). In other words, it was investigated the influence of the cross-sections, the axial restraining to the thermal elongation of the beam and the rotational stiffness of the beam supports. These beams, commonly used in CFS buildings, had a span of 3000 mm and were made of one or more cold-formed steel profiles (channel, U, and lipped channel, C, profiles), which were 2.5 mm thick, 43 mm wide and 250 mm tall for C sections and 255 mm for the U sections. On the other hand, as reference, four-point bending tests on the same type of beams at room temperature and under simply supported boundary conditions were also carried out to assess their ultimate bending strength and to compare with the failure modes.

A numerical study was still performed by the finite element program ABAQUS. So a great number of numerical simulations aimed to carry out a parametric study outside the bounds of the original experimental tests, in other words, to find out the effect of thickness (from 1.5mm to 3.5mm) and height (from 200mm to 300mm) of the beam cross-sections, of the beam spans (from 2000mm to 5000mm) and of other values of axial (from zero to infinite) and rotational stiffness (from zero to 1200kN.m/rad) of the surrounding structure to the beam.

Finally, the results of the experimental tests and the numerical simulations were the basis of an analytical study for the development of simplified calculation equations for fire design of cold-formed steel beams.

The main conclusions of this research study were that the cold-formed steel beams commonly used in this kind of buildings may have a quite low fire resistance (less than 30 minutes), but high critical temperatures (higher than 350 ºC - limitation enforced by Eurocode 3, Part 1.2) in most of the cases. On the other hand, the critical temperature may drop significantly (30% in some cases) with the axial restraint to thermal elongation of the beam. This decreasing is however minimized when the rotational restraint at beam supports is relevant comparing with rotational stiffness of the beam.

Keywords: Fire, Cold-formed steel, Beam, Load-bearing capacity, Buckling, Experimental, Numerical, Simplified calculation equations.

TABLE OF CONTENTES

LIST OF FIGURES

LIST OF TABLES

NOTATION

Roman upper case letters

A	cross-sectional area
A_{eff}	effective cross-sectional area
A_s	effective cross-sectional area of the edge stiffener
$A_{s,red}$	reduced effective cross-sectional area of the edge stiffener
C_b	buckling factor depending on the moment distribution
D	coiling diameter
E , E_{normal} , E_{20}	modulus of elasticity at ambient temperature
E_T	modulus of elasticity at temperature T
F_y	yield stress
G	shear modulus
I	second moment about the strong axis of a cross-section
I_s	second moment of effective area of the edge stiffener
I_T	torsional constant
I_W	warping constant
$I_{eff,x}$	second moment of effective area with respect to x-axis
I_x	second moment of area with respect to x-axis
$I_{eff,xy}$	product moment of effective area with respect to x- and y-axis
I_{xy}	product moment of area with respect to x- and y-axis
K	spring stiffness of the edge stiffener per unit length
L	beam span
L_e	effective length
M	bending moment
M_a	flexural allowable strength
M_b	nominal member moment capacity
$M_{b,fi,\theta,Rd}$	design buckling resistance moment at elevated temperature θ
$M_{b,Rd}$	design buckling resistance moment
M_{cr} , M_{cre} , M_o	critical elastic moment for lateral-torsional buckling
M_{crd}	critical elastic distortional buckling moment
M_{crl}	critical elastic local buckling moment
M_d	flexural design strength
M_n	nominal flexural strength

M_{nd}	nominal flexural strength for distortional buckling
M_{ne}	nominal flexural strength for lateral-torsional buckling
M_{nl}	nominal flexural strength for local buckling
M_R	restraining moment at beam support
M_{Rd}	resistant moment of the gross or effective cross-section
M_{sx}	section moment capacity about the strong axis
M_u	ultimate failure moment
$M_{xx'}$ - *S.M.*	measured bending moment about the xx' axis
$M_{xx'}$ - *C.B.T.*	calculated bending moment about the xx' axis
M_y	yield moment
$M_{yy'}$ - *S.M.*	measured bending moment about the yy' axis
$M_{yy'}$ - *C.B.T.*	calculated bending moment about the yy' axis
N_A	axial restraining forces generated in the beam
P	applied load on the beams
P_{FEA}	maximum numerical load-carrying capacity of the beam
P_{max}	maximum load-carrying capacity of the beam
P_{TEST}	maximum experimental load-carrying capacity of the beam
P_0	initial applied load on the beam
PW	maximum load-bearing capacity of the beam including its self-weight
S_f	gross section modulus referenced to the extreme fibre in the first yield
SW	self-weight of the beam
S_x	first moment of area with respect to x-axis
T	mean furnace temperature
U_{SC}	shear centre co-ordinate with respect to u-axis
W_{eff}	effective section modulus of the beam
W_y	section modulus of a cross-section
$X_{eff,GC}$	effective gravity centre co-ordinate with respect to x-axis
X_{GC}	gravity centre co-ordinate with respect to x-axis

Roman lower case letters

b	width of the flange or width of the plate
b_1	distance from the web-to-flange junction to the centre of the effective area of the edge stiffener (including effective part b_{eff} of the flange)

b_{eff}	effective flange width
b_p	width of the flange taken into account the influence of rounded corners
c	width of the edge stiffener
c_{eff}	effective width of the edge stiffener
c_p	width of the edge stiffener taken into account the influence of rounded corners
d	vertical displacement of the specimen
d_1	maximum local imperfection in a stiffened element
d_2	maximum deviation from straightness for a lip stiffened or unstiffened flange
d_{S1}	vertical displacement of the specimen at mid-span (section S1)
$f_{0.2p}$, $f_{0.2,20ºC}$	0.2% yield strength at ambient temperature
$f_{0.2,\theta}$	0.2% yield strength at temperature θ
$f_{0.5}$	0.5% yield strength
f_p	proportional stress limit
f_u	ultimate strength
f_y , $f_{y,normal}$, $f_{y,20}$	yield strength at ambient temperature
$f_{y,T}$	yield strength at temperature T
f_{yb}	nominal yield strength
h	height of the section
h_{eff}	effective web width
h_p	width of the web taken into account the influence of rounded corners
i_u	radius of gyration with respect to u-axis
i_0	polar radius of gyration about shear centre
k_a	axial restraint to the thermal elongation of the beam
$k_{a,b}$	axial stiffness of the beam
$k_{E,\theta}$	reduction factor for the slope of the linear elastic range of steel at the steel temperature θ_a reached at time t
k_r	rotational stiffness of the beam supports
$k_{r,b}$	rotational stiffness of the beam
k_v , k_y	effective length factor
k_W	warping effective length factor
$k_{y,\theta}$	reduction factor for the yield strength of steel at the steel temperature θ_a reached at time t
k_σ	plate local buckling factor
r_0	outer radius of a bend
t	thickness

t_{cr}	critical time of the beam
t_n	nominal thickness
t_{N_max}	time when the maximum restraining force in the beam is reached
t_{req}	reduced thickness
v_i	maximum co-ordinate of the plate with respect to v-axis
v_j	minimum co-ordinate of the plate with respect to v-axis
v_{max}	maximum co-ordinate of the section with respect to v-axis
v_{min}	minimum co-ordinate of the section with respect to v-axis

Greek upper case letters

ΔX_{GC}	Distance in x-direction from gravity centre to effective gravity centre of the cross-sectional area
Φ_{LT}	capacity reduction factor for bending
Ω	safety factor

Greek lower case letters

α_{LT}	imperfection factor of the beam
β	angle between x-axis (local axis) and u-axis (principal axis)
β_{S1}	lateral rotation of the beam at mid-span (section S1)
γ_{M0}	partial factor for resistance of cross-sections
γ_{M1}	partial factor for resistance of members
γ_{S1}	lateral rotation of the specimen at mid-span (section S1)
ε	longitudinal strain or elastic strain
ε_{eng}	engineering (nominal) strain
$\varepsilon_{f,T}$	total elongation at temperature T ºC
ε_{S1}	measured strain in the beam at mid-span (section S1)
ε_{true}	true (logarithmic) strain
η	rotation of the beam supports
η_{PS}	rotation of the pinned support
η_{RS}	rotation of the roller support

θ	rotation of the beam supports
$\overline{\theta}_B$	mean outer beam temperature
θ_{cr}	critical temperature of the beam
θ_{N_max}	beam temperature when the maximum restraining force is reached
θ_S	steel temperature
$\overline{\theta}_S$	mean outer steel temperature
$\overline{\lambda}_d$	edge stiffener slenderness for the distortional buckling
$\overline{\lambda}_{LT}$	non-dimensional beam slenderness for lateral-torsional buckling at ambient temperature
$\overline{\lambda}_p$	plate slenderness
$\overline{\lambda}_{p,red}$	reduced plate slenderness
μ	mean value
ν	poisson ratio
ρ	reduction factor for plate buckling
σ	stress or standard deviation
$\sigma_{com,Ed}$	maximum design compressive stress in the plate or reduced compression stress
$\sigma_{cr,s}$	elastic critical buckling stress of the edge stiffener
σ_{eng}	engineering (nominal) stress
σ_{max}	maximum stress in the plate
σ_{min}	minimum stress in the plate
σ_{true}	true stress
σ_x	normal stress in *X* direction
ϕ	resistance factor
χ_d	reduction factor for the distortional buckling resistance of the edge stiffener
χ_{LT}	reduction factor for lateral-torsional buckling
ψ	stress ratio in the plate

ABREVIATIONS

ASD	Allowable Stress Design
CBT	Classical Beam Theory
CFS	Cold-Formed Steel
cFSM	constrained Finite Strip Method
CV	Coefficient of Variation
DEC	Department of Civil Engineering
DOF	Degrees of Freedom
DSM	Direct Strength Method
EAM	Effective Area Method
EC3	Eurocode 3
ECBL	Erosion of Critical Bifurcation Load
ECCS	European Convention for Constructional Steelwork
ESM	Effective Section Method
EWM	Effective Width Method
FCT	Portuguese Foundation for Science and Technology
FCTUC	Faculty of Sciences and Technology of the University of Coimbra
FEA	Finite Element Analyses
FEM	Finite Element Method
FSM	Finite Strip Method
GBT	Generalized Beam Theory
GMNIA	Geometrically and Materially Nonlinear Analysis with Imperfections Included
LEME	Laboratory of Testing Materials and Structures
LL	Load Level
LRFD	Load and Resistance Factor Design
LVDT	Linear Variable Displacement Transducer
SM	Strain Measurements
UC	University of Coimbra

1 INTRODUCTION

1.1 Overview

The use of cold-formed steel profiles in construction started in the 19th century, in the USA and England, where it was used to a limited extent and without appropriate technical information about the structural behaviour of these elements. Given the population growth in the USA, it was necessary to use faster and more productive methods to build houses, using readily available local materials, like wood. At the end of World War II, however, steel was an abundant resource and the metallurgical companies had gained great experience in the use of this metal during the war. Hot-rolled steel was used first, in large buildings like sky-scrapers, and later cold-formed steel (CFS) members came to be used in residential buildings, replacing wood (fig. 1.1).

a)

b)

Figure 1.1 – General construction of wood (a) and CFS (b) buildings (Steel Framing Alliance@, 2009)

Concerning the Europe, its construction mainly uses concrete elements associated with brick walls, since Europe was partially destroyed after the Second World War, and the buildings were restored using these materials. Building had to be quick and cheap, without taking into account any requirements of comfort or well-being. So in the past few decades new solutions have been sought to replace the traditional technology of construction, and the steel industry has prompted the finding of those solutions. Cold-formed steel elements are one example, since this type of steel elements present several advantages, particularly ease of production, transport and assembly, when compared to thicker hot-rolled steel members. Another benefit is the great variety of profiles available on the market which allow the building of different member cross-sections, involving single open sections, open built-up sections and closed built-up sections (fig. 1.2). They are manufactured from sheet steel (fig. 1.3) essentially by cold rolling or brake pressing and have normally a thickness between 0.8 and 3 mm. Roll forming is a process in which a strip or sheet of metal, such as steel, is passed through a continual set of stands (rolls), until a desired cross-section profile is achieved. The sheet or strip is plastically deformed along a linear axis in a room temperature environment. Each stand in the roll forming process has a specific job in the fabrication of the piece, and every stage involves minor changes in the configuration of the metal, shown in Figure 1.4. In this example, a Ω section is formed. The size of the stands used depends on the metal's type, thickness, formability. Roll forming is usually used to produce sections where very large quantities of a given shape are required. The initial tooling costs are high but the subsequent labour content is low. Brake pressing is normally used for low volume production where a variety of shapes are required and the roll forming tooling costs cannot be justified. Here a section is formed from a length of strip by pressing the strip between shaped dies to form the profile shape (fig. 1.5).

Structures with this kind of steel elements are also known as light steel framing because of the fact that these elements are light (high strength to weight ratio) and so fewer foundations are needed and, as well as the thicker hot-rolled steel elements they still allow to provide flexible structures, less material wastage and an significant reduction in dead loads. On the other hand, since in most cases beams and columns are not necessary, all the external walls can be considered as the building structure, which thus increases the seismic resistance of these buildings. In addition, thanks to the flexibility of the construction solutions and the materials used, such as expanded polystyrene panels, OSB, rock wool and plaster boards, the thermal and acoustic parameters can be easily controlled. Given these great advantages CFS sections began to be used in a lot of countries and this emergent use made the knowledge of its structural behaviour vital.

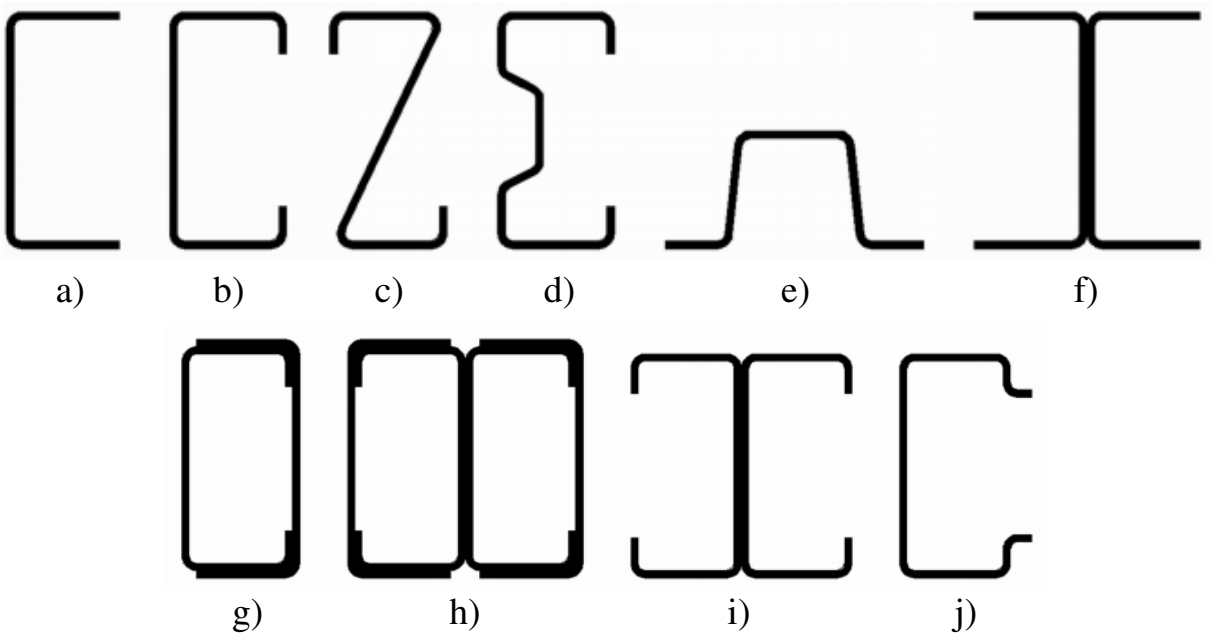

Figure 1.2 – Typical forms of sections for cold-formed steel structural members: a) U (channel) section; b) C (lipped channel) section; c) Z (zed) section; d) Σ (sigma) section; e) Ω (omega) section; f) built-up I (double-U) section; g) built-up R section; h) built-up 2R section; i) built-up lipped I (double-C) section; j) double lipped U (channel) section (Tichelmann *et al.*, 2005; EN 1993-1-3, 2004)

Figure 1.3 – Galvanized steel coils (Perfisa@, 2008)

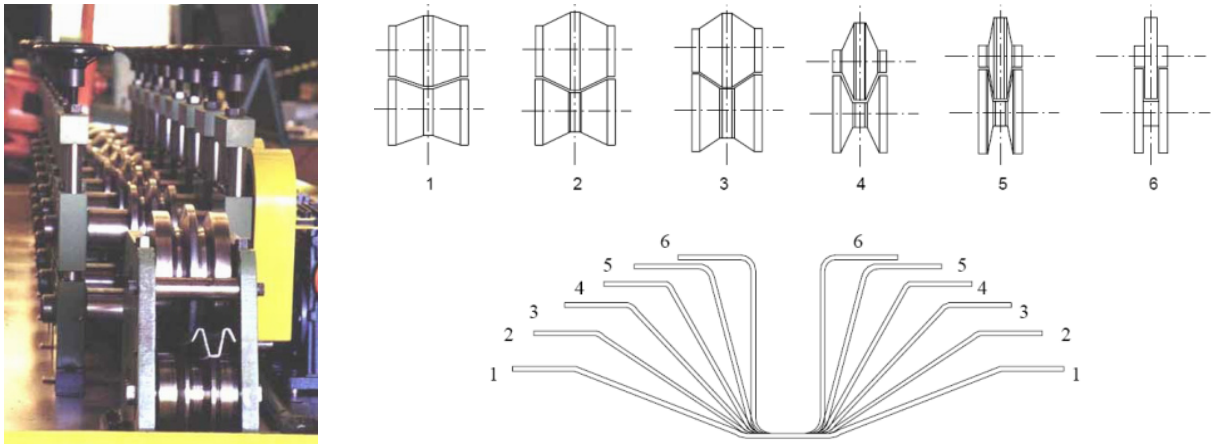

Figure 1.4 – Stages in roll forming a single section (Rezende, 2005, and Rhodes, 1991)

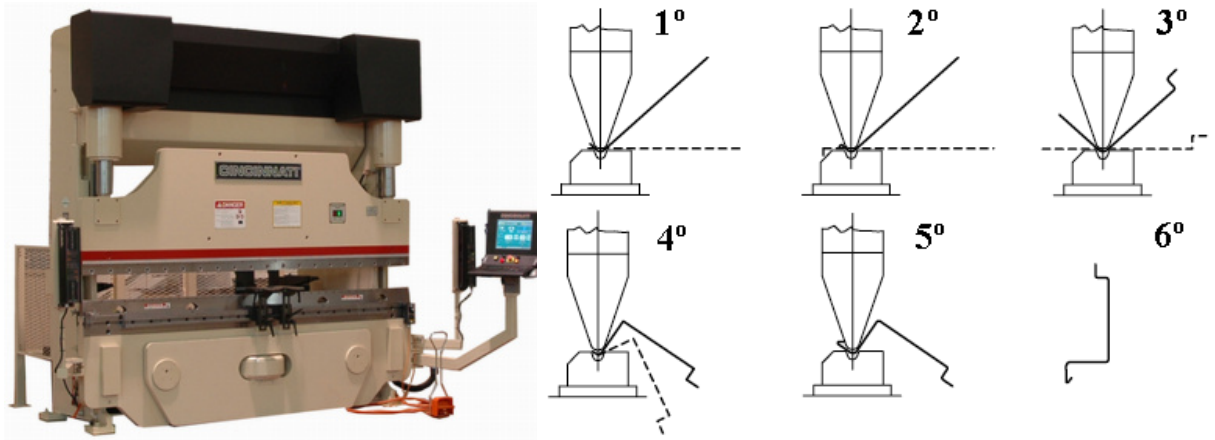

Figure 1.5 – Forming steps in press braking process (Futureng@, 2010, and Veríssimo, 2008)

CFS structures are a versatile and fast building system manufactured from lightweight cold-formed pre-galvanised steel sections with a standard (Z275) zinc coating thickness of 0.04 mm (275 g/m^2), at least in Europe and North of America. It is well known that steel rusts when left unprotected in almost any environment. Applying a thin coating of zinc to steel is an effective and economical way to protect steel from corrosion. Zinc coatings protect steel by providing a physical barrier as well as cathodic protection to the underlying steel. So, in the end, the construction time, cost and zinc coating are the main reasons why CFS sections are screwed on site and not welded. These connections are generally materialized by means of carbon steel self-drilling screws and usually an extensive number of them is used in CFS structures (fig. 1.6).

Figure 1.6 – A view of the amount of screws used in connections of CFS structures (Steel Framing Alliance@, 2009)

In 1939, on the initiative of and funded by the American Iron and Steel Institute (AISI), a series of research programs started, that lead to the publication, in 1946, of the first technical specification for the design of structural elements of cold-formed steel sections. In 1984 the Canadian Standards Association (CSA), published the CAN3-S136-1984 standard (cold-formed steel structural members), and this was replaced in 2001 by the North American Cold-Formed Steel Specification (2001) from the AISI, which was developed by the partnership of the United States and Mexico. Australia and New Zealand also researched into the use of cold-formed steel elements, and in 1996, they published the AS/NZS4600:1996 standard (cold-formed steel structures). In Brazil the use of these profiles started in the late 1960s, and NB 143 (calculation of steel structures constituted by lightweight profiles) was published. It has recently been replaced by NBR 14762 (design of cold-formed steel structures) published by ABNT (Brazilian Association of Technical Standards). Lastly, the technical document that currently guides the design of CFS structures in Europe is the EN 1993-1-3 (2004) (Eurocode 3 - Design of steel structures: part 1.3 – general rules: supplementary rules for cold-formed members and sheeting). But there are still no regulations for the fire design of these elements, and so the designer is left at the mercy of his/her experience and good sense. The design of this type of structures is not always on the safe side, and all too often the solutions are not economical. The structures are sometimes under-designed and sometimes over-designed, due to the fact that there are no fire design methods that are straightforward enough to be used by designers. The design of CFS elements is even more complex than hot rolled steel elements, because of the high slenderness of the cross-sections. In addition to the phenomena of overall instability by torsion and bending-torsion, commonly observed in the hot-rolled steel elements, the local and distortional buckling also have to be considered in the design of CFS members.

Finally, given the lack of regulations in the area of fire design of CFS elements and the small number of scientific works in this area, and the emerging use of this type of construction in Europe, this research intends to contribute to the development of knowledge in the area as a way to create conditions for the better use of structures of this type.

1.2 Motivation

During the last several decades an important tendency of the civil engineering industry is the application of more slender elements and structures. A characteristic of this tendency is the wider application of cold-formed steel members, which is supported by developments in the production technology as well as improvements in design methods, design standards, and, in general, computational techniques. In addition, CFS members have a major advantage over hot-rolled steel shapes. The former can be easily shaped and sized to meet any particular design requirement. As such, they provide a much larger variety of choices for steel designers. The result often is a lighter and more economical section compared with hot-rolled steel beams for low-rise building structures when the beam spans are not long. The price to be paid for this versatility is however the complicated iterative design process. And finding the optimum or minimum weight beam is a challenging problem considering the complex and highly nonlinear constraints that govern their design. It is hereby important to stress that the application of slender elements requires first of all an appropriate handling of buckling phenomena.

Cold-formed steel members are very different from hot-rolled steel members, since the latter are mostly found in class 1 or 2 cross-sections, while in general the former are class 4, according to Eurocode 3, part 1-1. In thin-walled members usually three basic types of instability phenomena are distinguished: global buckling (for example flexural, flexural-torsional or lateral-torsional buckling), distortional buckling, local (or local plate) buckling and interactive buckling between or among the above buckling modes, due to their plate width-to-thickness ratio. These buckling modes are mostly responsible for the ultimate strength of the compression members and nevertheless these ones may occur even before parts of the cross-section yield. Local buckling is characterized by the relatively short wavelength buckling of individual plate elements. Distortional buckling involves both translation and rotation at the compression flange/lip fold line of the member. And the global buckling is a buckling mode where the member deforms with no deformation in its cross-sectional shape, consistent with classical beam theory. Another factor which causes complexity in CFS members arises from the fact that these members are in most cases open and/or asymmetric sections leading to low levels of torsional stiffness, since there is generally

no coincidence between the shear centre and the centroid of the section and its thickness is too low as well. This means that they also may be extremely flexible and weak in resistance to torsion. It is also important to stress that the geometric imperfections of this kind of members are normally of the same order or higher than the thickness of the respective cross-sections.

In addition, the fire resistance of this kind of elements is quite compromised due to the combination of the high thermal conductivity of steel and the high section factor of these structural members (small wall thickness) both of which lead to a rapid rise in steel temperature in a fire. Another important issue is that the deterioration of steel mechanical properties with increasing the temperature can induce serious deformation of structural members or even the premature failure of a building. It is noticed that this deterioration is still more severe for CFS profiles than for hot-rolled steel profiles.

The parts of Eurocodes related to fire design does not have consistent methods for fire design of cold-formed steel elements. Only Eurocode 3 part 1.2 (EN1993-1.2, 2004) states that "The methods given are also applicable to cold-formed steel members and sheeting within the scope of EN 1993-1-3". The Eurocode 3 part 1.3, relates to the design at room temperature, nothing presents in case of fire. The proposal of EN1993-1.2 is away from the reality of the behaviour of cold formed steel elements in fire which may be absolutely different from hot-rolled ones. So there is an urgent and absolute need of finding new design methods for cold formed steel elements, beams, columns and joints subjected to fire. Furthermore, it appears that more research has been conducted into the structural behaviour of compression members than of flexural members, as well as on the structural performance of joints. From the author's point of view, it is however better to design overly the joints than the structural members, due to economic reasons. Hence, it is quite important to study the flexural behaviour of CFS beams under many and different conditions, including loading, boundary and fire conditions.

The advantages which can be gained by the use of CFS structural applications are bought at the expense of the requirement to use increased sophistication in the design analysis. This thesis attempts therefore to address a special and detail study in depth on the structural behaviour of CFS beams under fire conditions so that a good and accurate fire design of CFS structures are made for the scientific and engineering communities. It is the hope of the author that this document contributes toward some standardization of educational and technical material and to expand and disseminate existing and new knowledge within the area of fire safety engineering in buildings based on scientific and practical research.

1.3 Research Objectives and Scope

The overall purpose of this research was to investigate the structural behaviour of cold-formed steel beams under fire conditions so as to develop adequate simplified calculation methods for the safe and economical fire design rules of CFS beams, similar to those that exist for hot-rolled steel. This goal is intended to achieve with the aid of both experimental tests and advanced numerical analyses. Therefore, the research plan was implemented in two great phases which were accomplished in the Department of Civil Engineering (DEC) of the University of Coimbra (UC). The main objectives of the experimental research were obviously to assess the true fire behaviour (critical time and temperature) of the beams, characterize their failure modes and to provide reliable experimental data for the numerical studies, in order to develop and validate a suitable finite element model capable of obtaining reliable results from a parametric study outside the bounds of the original experimental tests. It is noticed that after the numerical models are calibrated, they may be very useful for extrapolations, saving time and money. So, at the end, basing on the experimental and numerical results, it was intended to undertake an analytical study for the development of simplified calculation methods for fire design of CFS beams.

In the experimental phase, a great number of tests on CFS beams were performed in the Laboratory of Testing Materials and Structures (LEME) of UC, intending to study several parameters that have influence on the structural response of these members in fire, such as, the axial and rotational restraint to the thermal elongation of the beam. The LEME was very well equipped with fire furnaces for vertical and horizontal elements. These furnaces were acquired in the extent of the research project of re-equipment of the laboratories REEQ/499/2001, financed by the Portuguese Foundation for Science and Technology (FCT). Instead of this equipment, the laboratory was equipped with dozens of load cells, ranging between 10kN and 3 MN, displacement transducers ranging between 5 and 200 mm, wire displacement transducers for displacement measurements up to 1000 mm, a lot of static hydraulic actuators with load capacity between 10 kN and 3 MN, central hydraulic units, restraining frames of different stiffness, heat blankets and data acquisition systems. The experimental models were thereby instrumented and mounted in the LEME, however the CFS profiles were fabricated by the company PERFISA S.A. – Portugal, which it was its specialty.

This experimental phase was followed by a numerical phase that included a huge amount of numerical simulations using a commercially available finite element software package, in other words, the program ABAQUS/CAE 6.10-1 (Abaqus Analysis – User's Manual, 2010). These analyses made possible to verify the results of the experimental tests and to enlarge the

research to other situations not tested experimentally. A lot of different parameters that have influence on the behaviour of CFS members in case of fire were simulated.

Thus, the specific objectives of this study are:

- To explore the instability phenomena of cold-formed steel beams (local, distortional, lateral-torsional buckling and their interactions) both at ambient temperature and under fire conditions.
- To investigate the failure loads and the failure modes of industry standard CFS beams (namely C, lipped I, R and 2R beams) commonly used in any CFS buildings, but especially in warehouses and industrial buildings where the fire risk may be higher; performing several flexural member tests at ambient temperature.
- To study the influence of the stiffness of the surrounding structure to the beams, when just these ones are subject to fire. So, a large number of fire tests on bare CFS beams with and without axial restraint to the thermal elongation of the beam and with combined axial and rotational restraint were undertaken. These restraints intended to reproduce as faithful as possible the actual boundary conditions of a beam when is inserted in a real CFS building structure, making it possible to understand how the surrounding structure effects a CFS beam when is subjected to fire. Stiffness values as realistic as possible were considered on these tests.
- To compare experimentally the structural response of different kinds of beams (beams with a single profile and built-up beams with two and four profiles) both at ambient temperature and under fire conditions.
- To develop accurate finite element models that are capable of simulating the local, the distortional and the global buckling behaviour of CFS flexural members and above all their interactions both at ambient temperature and under fire conditions.
- To validate the developed finite element models by comparison with experimental results.
- To carry out an extensive parametric study, trying to find out the effect of the initial geometric imperfections, of the initial load level applied on the beams, of the finite element mesh size, of the thickness and height of the beam cross-sections, of the beam spans and of other values of axial and rotational stiffness which were not used in the experimental tests, on the structural performance of the respective CFS beams.
- To compare the obtained results with the predictions from the currently available design rules both at ambient temperature and under fire conditions.
- To develop new simplified calculation methods for fire design of CFS members under both pure bending and composed bending (pure bending plus axial load).

- To contribute to a future revision of EN1993-1-2 document (Eurocode 3 - part 1-2), relative to the fire design of these members.
- To develop new shapes of CFS profiles or of built-up CFS structural members with enhanced fire behaviour.
- To propose issues for good practice for the CFS building construction looking for a better way to improve its fire performance.

1.4 Contents of the Thesis

This dissertation consists of a total of six chapters and the contents of each chapter except for this chapter are briefly described as follows.

Chapter 2, Literature Review, presents the state-of-the-art describing the findings pertinent to this research project based on experimental, numerical and analytical investigations conducted by previous researchers. It describes the different design methods of CFS members made available by international standards and past research both at ambient and elevated temperatures. It also focuses particularly on the buckling behaviour of CFS flexural members at ambient and elevated temperatures as well as under fire situations, including the local, distortional, lateral-torsional buckling and their interactions. Fire test methods (for example, steady-state and transient-state tests), advanced methods (such as, finite element and finite strip analyses) and also the effects of temperature increase on the mechanical properties of the flat and corner parts of CFS profiles are reported in this chapter.

Chapter 3, Experimental Analysis of Cold-Formed Steel Flexural Members, presents a series of flexural tests at ambient temperature and under fire conditions focused on simply supported CFS beams made of one and more CFS profiles, namely, channel and lipped channel profiles also known as U and C profiles, respectively. These profiles were combined in different manner in order to build lipped I-, R- and 2R-shaped cross-sections. The built-up lipped I beams consisted of two C profiles connected back to back, the built-up R beams consisted of one C profile inside one U profile, generating a closed built-up beam, and finally the built-up 2R beams consisted of two C profiles connected back to back which were then connected over by two U profiles (fig. 2). It is described in detail the experimental programme, the testing procedures and the test set-up for bending tests performed in the DEC of UC. The load applied on the beams, the bending moments, the vertical and horizontal displacements of the beams, as well as, their lateral rotation, the rotation of their supports and still some longitudinal strains are shown as results of these experimental tests at ambient temperature so as to characterize the structural behaviour of the CFS beams at ambient temperature in the

best possible way. The main purpose of these tests was to assess the failure loads and the failure modes of the studied beams and also to compare the structural response of these different kinds of beams at ambient temperature. It is noticed that these tests were carried out to provide a reference for the fire tests.

When it comes to fire, three sets of experimental tests were conducted in order to evaluate the influence of the stiffness of the surrounding structure to the beams, in other words, the first set of the experimental tests was carried out on simply supported CFS beams without any kind of restraining to the thermal elongation of the beam, whereas the second and third sets were undertaken on the same type of beams, but with axial restraint and with combined axial and rotational restraint at the beam supports, respectively. The load applied on the beams, the bending moments, the restraining forces, the vertical and horizontal displacements of the beams, as well as, the temperatures in the furnace and at several points of the beams are shown as results of these experimental tests so as to characterize the structural behaviour of the CFS beams subjected to fire in the best possible way. The main goal of these tests was to assess the critical time and the critical temperature of the studied beams with the different boundary conditions mentioned before. This means that the fire tests conducted at DEC of UC tried to reproduce as faithful as possible standard fire resistance tests, i.e. fire curves identical to the standard fire curve and thermal action given by flame action. It is noticed that the standard fire exposure curve is defined by a temperature-time relationship and increases monotonically during the rating period and is the same for almost all building occupancies. Before the heating rate starts the structural member to be tested is firstly loaded. This loading is normally a percentage (30, 50 or 70%) of the design value of buckling load of the member at ambient temperature, calculated in accordance with the methods proposed in the currently available design rules (EN 1993-1-1, EN 1993-1-3, EN 1993-1-5). So, the load intended to simulate the serviceability load of the member when this one is inserted in a real building structure. During the period of heating, the load is kept constant until member reaches its failure (transient-state tests). This period, in other words, the time between the beginning of the heating and the failure of the member, corresponds to the fire resistance of the member and its temperature at the ending of the test to the critical temperature (for cross-sections with uniform temperatures). Most fire design formulas for members (beams, columns, slabs) are derived from both experimental and numerical results of standard fire resistance tests (transient-state tests), whereas fire design formulas for joints (such as connectors that assures the shear transfer between the steel profile and the concrete deck, and connections between other members) are derived from steady-state tests, since the design resistance of these last ones should only be verified for the critical temperature of the respective member, that is, if failure occurs, this one should be responsible for the loss of strength of the members.

Therefore, this research work of this thesis was based as faithful as possible on fire resistance tests.

Chapter 4, Finite Element Modelling of Cold-Formed Steel Flexural Members, reports on a numerical investigation concerning the distortional and lateral-torsional buckling behaviour of simply supported CFS beams subjected to major axis bending at ambient temperature and subjected to combined bending and fire. A suitable finite element model was first developed to compare with the experimental results. The numerical results presented and discussed were obtained through shell finite element analyses performed using the ABAQUS program, as it has already been stated. It was intended to describe in detail all parameters, considerations and assumptions took into account in a three-dimensional nonlinear finite element model to predict the behaviour of CFS beams in fire, such as, the beams previously tested in Laboratory by the author. The numerical results were thereby compared with those given by the experimental tests in order to validate the developed finite element model. The effect of some parameters such as mesh density, eccentricity of the applied load on the beams and diameter of the screws used in the connection of the profiles in order to obtain the built-up CFS beams were also taken into account in this numerical research work of this thesis. This made it possible to understand which parameters or assumptions have more influence on the analysis of this kind of numerical models.

Chapter 5, Parametric Studies and Development of Simplified Design Rules, reports on a numerical investigation regarding the structural behaviour of CFS beams outside the bounds of the original experimental tests. After validating the developed finite element model, it was performed a parametric study concentrating on variation in thickness, height and length of the respective beams and influence of the bending moments on failure at ambient temperature and under fire conditions. Furthermore, the effect of some parameters such as the level of initial applied load on the beam, the initial geometric imperfections of the beams and the stiffness of the surrounding structure, including the axial stiffness, rotational stiffness and their interactions were also target of this numerical study.

Finally, the results of the experimental tests and the numerical simulations were thereby the basis of an analytical study for the elaboration of simplified calculation equations for fire design of cold formed steel beams. Firstly, the results presented in the previous chapters of this thesis are compared with those given by the predictions from the currently available design rules both at ambient temperature and under fire conditions, involving the EN1993-1.1, -1.2 and -1.3, for instance. Then, simplified calculation equations are described in this

chapter. Finally, these methods are expected to be a useful tool for the designers and constitute a first step for a future part for Eurocode 3 related to fire design of CFS beams.

Chapter 6, Conclusions and Recommendations, provides an overview of the developed work and a summary of the most significant findings of this research and also presents recommendations for possible future research on the buckling behaviour and fire design of cold-formed steel structures. Some considerations related to the use of CFS beams and rules of conduct and good practice for the CFS building construction are still addressed in this chapter, looking for a better way to improve the fire performance of this type of structures.

2 LITERATURE REVIEW

2.1 Mechanical Properties of Cold-Formed Steel

2.1.1 Behaviour at ambient temperature

There are two general types of stress–strain curves of steel (Figures 2.1 and 2.2). One is of sharp-yielding type (fig. 2.1) and the other is of gradual yielding type (fig. 2.2). Steels produced by hot rolling are usually sharp yielding. For this type of steel, the yield point is defined by the level at which the stress–strain curve becomes horizontal. Steels that are cold-worked, such as the ones produced by cold rolling or brake pressing, often show gradual yielding. For gradual-yielding steel, the stress–strain curve is rounded out between the proportional stress limit and the strain-hardening of steel. It can be seen in this figure that the yield strength is not well-defined comparing with steels produced by hot rolling. Therefore, in these cases, the yield strength widely accepted is the stress at strain levels of 0.2% or 0.5%. The 0.2% yield strength is the intersection point of stress-strain curve and the proportional line offset by 0.2% strain (offset method), whereas the 0.5% yield strength is the intersection point of the same curve and the non-proportional vertical line specified at 0.5% strain (strain-underload method). In this method, the yield strength is the stress corresponding to a specified elongation or extension under load and other strain levels can be used, namely 1.5% and 2%. In many cases, the yield point determined by these two methods is similar. The ultimate tensile strength of steel sheets or strip used for cold-formed steel (CFS) sections has little direct relationship to the design of such members. The load-carrying capacities of CFS flexural and compression members are usually limited by yield point or buckling stresses that are less than the yield point of steel, particularly for those compression elements having relatively large width-thickness ratios and for compression members having relatively large slenderness ratios. The exceptions are screwed, bolted and welded connections, where the strength of which depends not only on the yield point but also on the ultimate tensile strength of the material (Yu, 2000 and Hancock *et al.*, 2001).

A large proportion of the steel used for CFS structures is thereby of this type. These steels are high tensile and often have limited ductility as a result of the manufacturing processes. The induced deformations at flat parts of the section may be elastic deformations; however, the deformations expected at corners of the section are essentially plastic deformations. The changes in the mechanical properties due to cold work are caused mainly by three

phenomena: strain hardening, strain aging and the Bauschinger effect (Chajes *et al.*, 1963). As a mild steel specimen is strained beyond the yield plateau, an increasing stress is required to produce further deformation. The region of the stress-strain curve representative of this type of yielding, that is, increasing stress with increasing plastic deformation, lies between the yield plateau and the ultimate strength and is known as the strain hardening range. Additionally, if a mild steel specimen is plastically stretched and a period of time is allowed to elapse before reloading, a further increase in the tensile yield strength occurs, beyond that which results from strain hardening. This is known as strain aging. Finally, the phenomenon that results in an increase in the proportional limit and yield strength by reloading a plastically deformed specimen in the same direction, (tension after pre-stretching), or in a decrease by reloading it in the opposite direction (compression after pre-stretching), is known as the Bauschinger effect. As illustrated in Figure 2.3, curve C represents the stress-strain curve of a coupon specimen taken from a CFS profile, in other words, the stress-strain curve of a coupon specimen taken from a steel sheet after coiling, uncoiling and flattening. If this curve is compared with curve A for the virgin material, it is evident that both strain hardening and strain aging increase the proportional limit and decrease the ductility of the material. As it can be noticed a bit further ahead on this thesis, the effects of cold work on the mechanical properties of CFS profiles, especially at corners, also depend on the type of steel, the inside-radius-to-thickness ratio, the thickness of the steel sheet, the coil radius, among other parameters. It is important to stress that both residual stresses and increase of yield strength are results of manufacturing process and tend to compensate one another (Dubina and Ungureanu, 2002). This way, the increase of yield strength might not be much relevant and, therefore, when this is taken in account in numerical simulations the residual stresses should be considered as well.

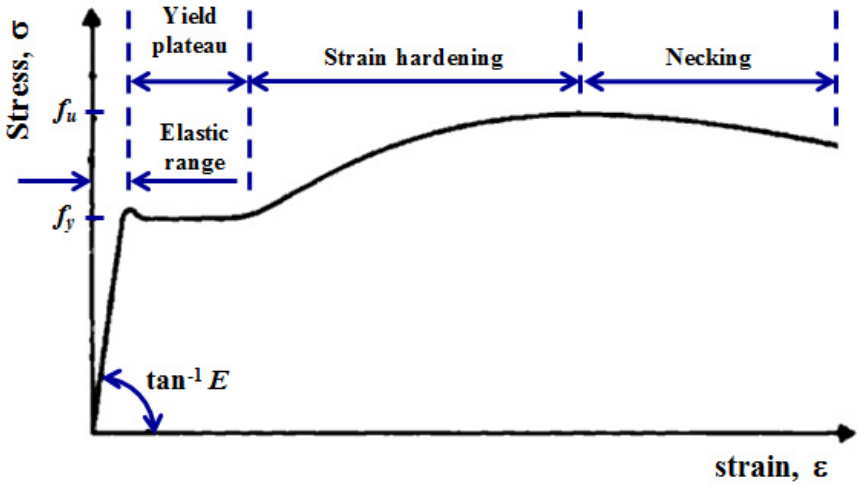

Figure 2.1 – Stress-strain curve of steel elements usually produced by hot rolling (Yu, 2000)

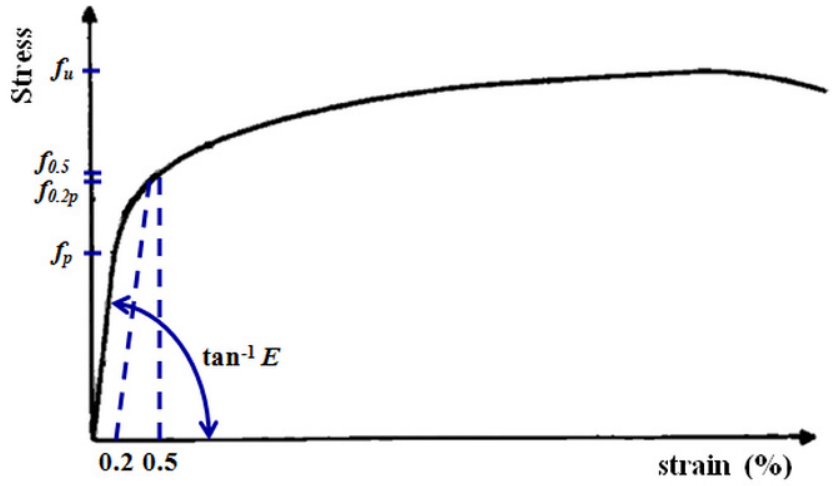

Figure 2.2 – Stress-strain curve of steel elements usually produced by cold-worked (Yu, 2000)

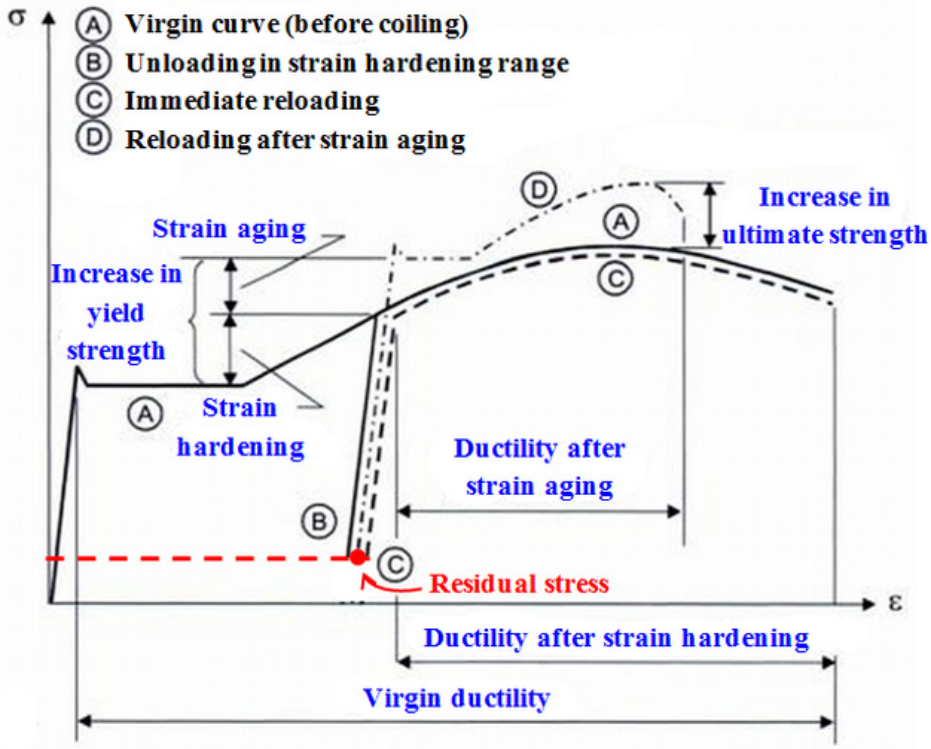

Figure 2.3 – Effects of strain hardening and strain aging on stress-strain characteristics of structural steel (Chajes *et al.*, 1963; Rondal e Dubina, 2005; Moen *et al.*, 2008)

2.1.2 Behaviour at elevated temperature

In 2000, Outinen *et al.* (Outinen *et al.*, 2000) published some results of an extensive experimental research programme carried out in the Laboratory of Steel Structures at Helsinki University of Technology for investigating the mechanical properties of various structural steels at elevated temperatures. Among these steels, the structural sheet steel with yield strength of 350 N/mm^2 was of particular interest (S350GD+Z). So, the test pieces were cut from a CFS sheet with nominal thickness of 2 mm, longitudinally to rolling direction. The purpose of this research was to study the behaviour of this material for fire temperatures using both transient state and steady state tensile test methods. It is noticed that the transient state tests are more reliable because they may also take into account the creep effects. These authors compared their results with the EN 1993-1-2 (2004) material model for the hot-rolled steel members and concluded that there were significant differences (figs. 2.4 and 2.5). For instance, in the EN 1993-1-2 (2004) the nominal yield strength is assumed to be constant until 400 ºC, whereas actually the behaviour of the studied steel started to decrease earlier. It is also showed that the difference between steady state and transient state test results was negligible, except for the modulus of elasticity at 400 and 500 ºC (fig. 2.5). However, some authors draw attention to the fact that both the steady state and transient state tests are usually completed within an hour, and thus they include only a limited amount of creep behaviour (Ranawaka and Mahendran, 2009). This means that there may be little difference between the two types of tests in relation to creep effects.

Continuing with these studies, Outinen (Outinen, 2006 and 2007) observed that the yield strength of coupon specimens taken from steel compression members that was in fire (until 950 ºC) decreased almost back to the nominal yield strength level of the material (fig. 2.6). As the author stated, this finding supports the advice given in BS5950 (1990), that for cold finished steel the strength can be assumed to be 90 % of the original strength if the distortions are within the shape and the straightness tolerances of the structure.

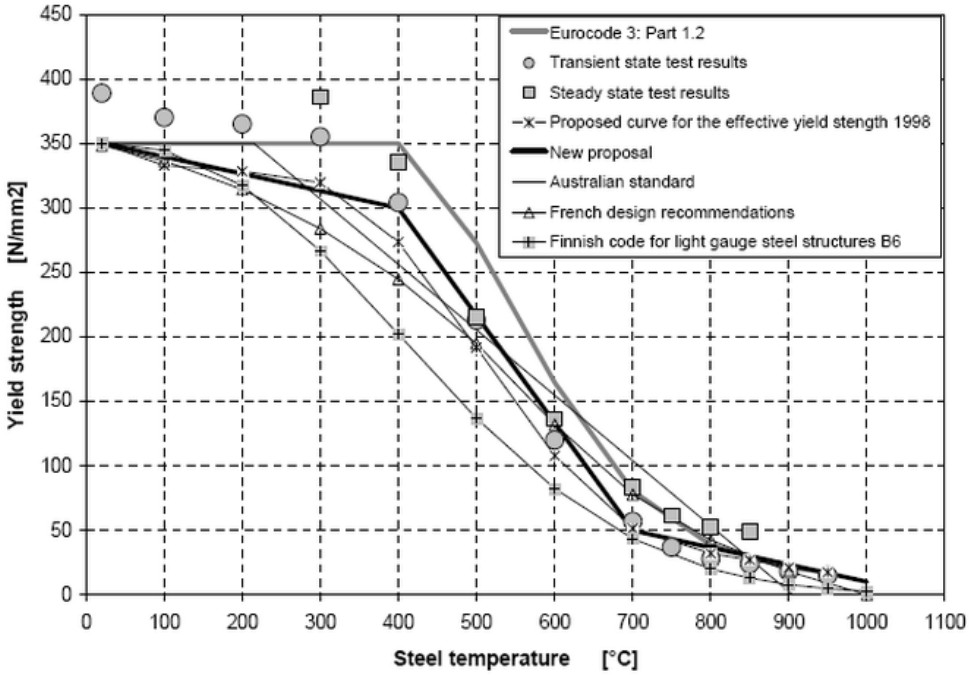

Figure 2.4 – Yield strength of structural steel S350GD+Z determined from test results compared with yield strength given in different design codes (Outinen *et al.*, 2000)

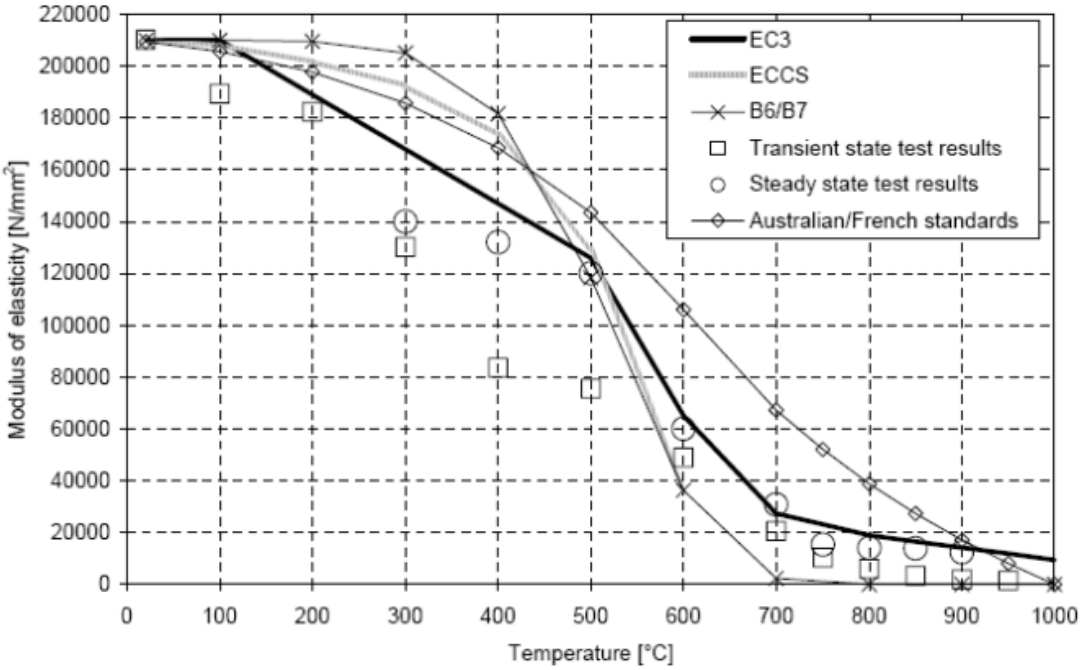

Figure 2.5 – Modulus of elasticity of structural steel S350GD+Z determined from test results compared with those given in different design codes (Outinen *et al.*, 2000)

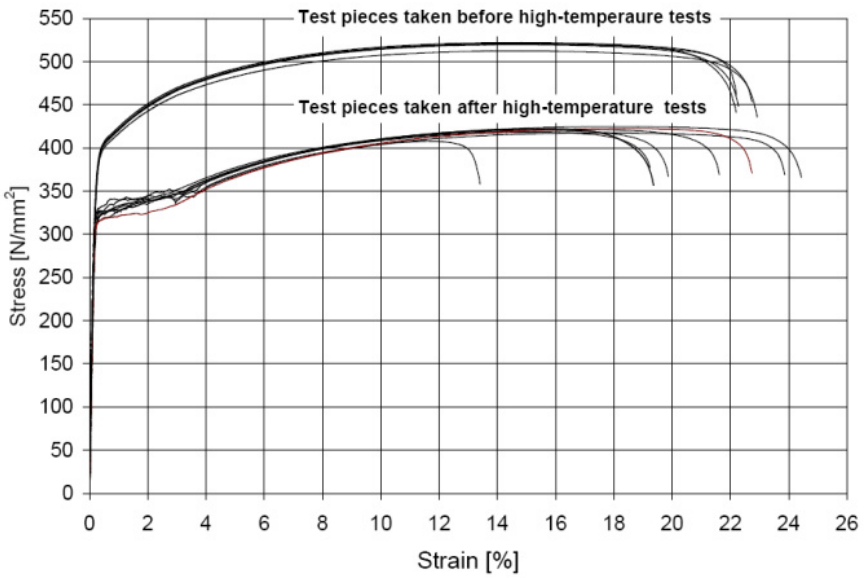

Figure 2.6 – Tensile test results for structural steel S350GD+Z obtained before and after high-temperature compression tests (Outinen and Mäkeläinen, 2002)

Cheng and Young also conducted both steady and transient tensile coupon tests at different temperatures ranged approximately from 20 to 1000 ºC for obtaining essentially the deterioration of the mechanical properties of yield strength (0.2% proof stress) and modulus of elasticity (Cheng and Young, 2007a). This study included CFS grades G550 and G450 with plate thickness of 1.0 and 1.9 mm, respectively. The reduction factor of 0.2% yield strength obtained from the tests were compared with the EN 1993-1-2 (2004) prediction and also compared with the test results conducted by Lee *et al.* (2003), as shown in Figure 2.7. The comparison showed that the EN 1993-1-2 (2004) provided conservative predictions for G450, 1.9mm, from 20 to 550 ºC and for G550, 1.0mm, from 20 to 400 ºC. The test results obtained in this study were far below than the EN 1993-1-2 (2004) prediction for G450, 1.9mm at 660 ºC and for G550, 1.0mm from 450 to 800 ºC. It is interesting to note that the test results obtained in this study were significant different from the ones conducted by Lee *et al.* (2003) for temperatures ranged from 450 to 700 ºC.

The reduction factor of modulus of elasticity determined from the transient state tests was compared with the steady state test results for G450 1.9mm specimens, as shown in Figure 2.8. The transient state test results were also compared with the AS 4100 (1998) and EN 1993-1-2 (2001) prediction as well as compared with the transient state tests conducted by Outinen *et al.* (2001). It can been seen that the reduction factor of modulus of elasticity obtained from the transient state tests in this study agree well with the EN 1993-1-2 (2001) prediction and the test results obtained by Outinen *et al.* (2001) for temperatures ranged from

320 to 450 ºC. For temperatures ranged from 80 to 320 ºC and from 550 to 660 ºC, the values of the reduction factor of modulus of elasticity obtained from the transient state tests were smaller than those predicted by EN 1993-1-2 (2001) and the tests conducted by Outinen *et al.* (2001). The AS 4100 (1998) predictions of the modulus of elasticity were un-conservative compared with the transient state test results. It should be noted that the reduction factor of modulus of elasticity obtained from the transient state tests was quite different from the steady state tests.

Cheng and Young (Cheng and Young, 2007a) still assessed the thermal elongation of the specimens at a tensile stress level of 2MPa that is close to free thermal expansion and compared with the thermal elongation calculated according to BS 5950-8 (1998), EN 1993-1-2 (2001) and Outinen (1999). The comparison indicated that the thermal elongation of G450 1.9mm steel was generally less than the values predicted by BS 5950-8 (1998) and EN 1993-1-2 (2001) for temperatures ranged from 140 to 550 ºC and by Outinen (1999) for temperatures ranged from 320 to 550 ºC (fig. 2.9).

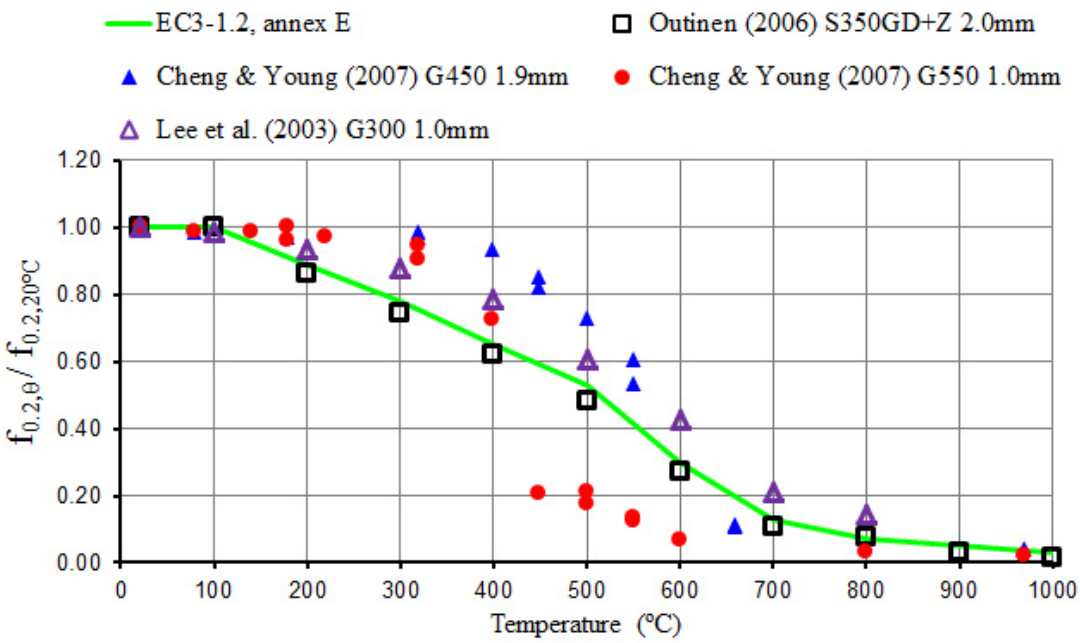

Figure 2.7 – Comparison of reduction factor of 0.2% strength predicted by EN 1993-1-2 (2004) with test results obtained by Cheng and Young (2007a), Lee *et al.* (2003) and Outinen (2006)

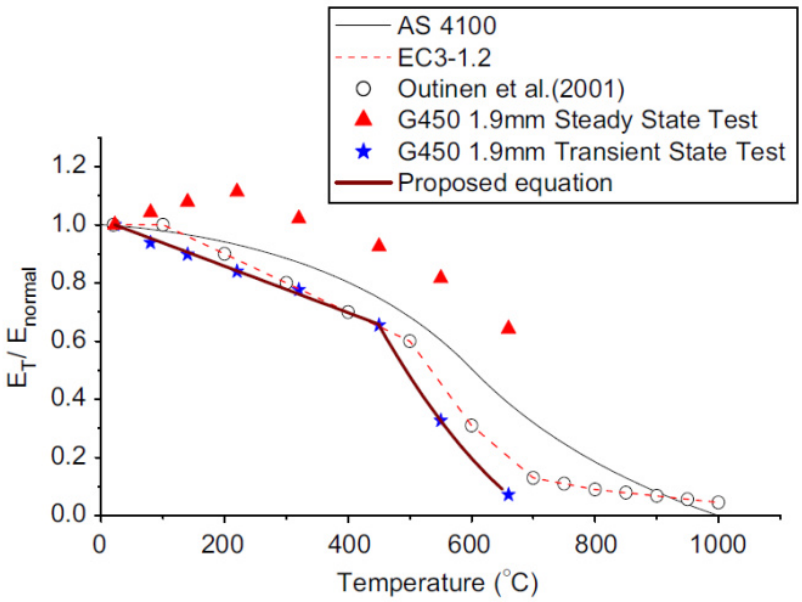

Figure 2.8 – Comparison of modulus of elasticity predicted by AS 4100 (1998), EN 1993-1-2 (2001) and proposed equation by Cheng and Young (2007a) with test results for transient and steady state tests

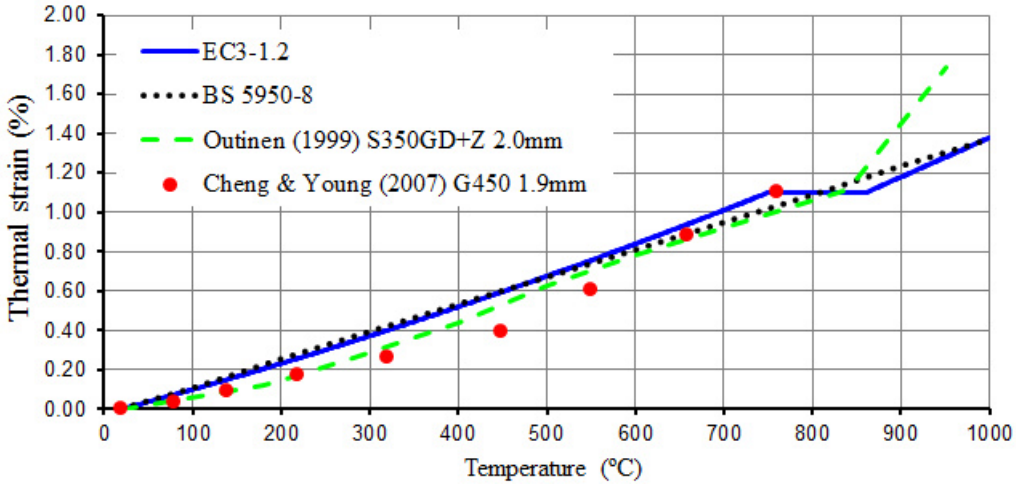

Figure 2.9 – Comparison of thermal elongation predicted by BS 5950-8 (1998), EN 1993-1-2 (2001) and Outinen (1999) with test results obtained by Cheng and Young (2007a)

Cheng and Young (Cheng and Young, 2006) also presented a test program on the material properties of the corner parts of CFS profiles at elevated temperatures. This test program included the inner and outer corner coupon specimens (fig. 2.10) of grade G500 with the nominal plate thickness of 1.9 mm. The yield strength, modulus of elasticity, ultimate strength, ultimate strain and total elongation obtained from their tests were compared with

those of the flat coupon specimens of the cold-formed steel. A yield strength of 524 MPa for the flat coupon specimens, of 545 MPa for the inner corner coupon specimens and of 573 MPa for the outer coupon specimens were obtained from those tests at ambient temperature. It can clearly be seen the great influence of the cold-work due to forming on the mechanical properties of the steel. Summarizing, the yield strength of the outer corner coupon specimens (a 90º bend) increased by 9 % comparing to the yield strength of the flat coupon specimens. On the other hand, the main experimental results of this research work showed that generally the reduction factors of yield strength, modulus of elasticity and ultimate strength of the corner coupon specimens were similar to those of the flat coupon specimens (figs. 2.11 and 2.12). It could still be seen from that comparison and Figure 2.13 that the effect of the cold-forming operation on the ductility of corner parts of CFS profiles was obvious for temperatures below 180 ºC and less obvious for temperatures greater than or equal to 180 ºC.

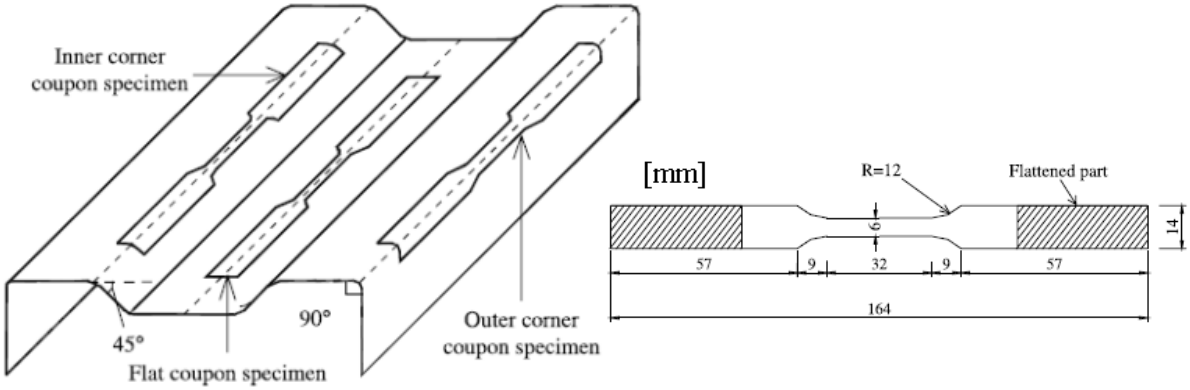

Figure 2.10 – Coupon specimens (Cheng and Young, 2006)

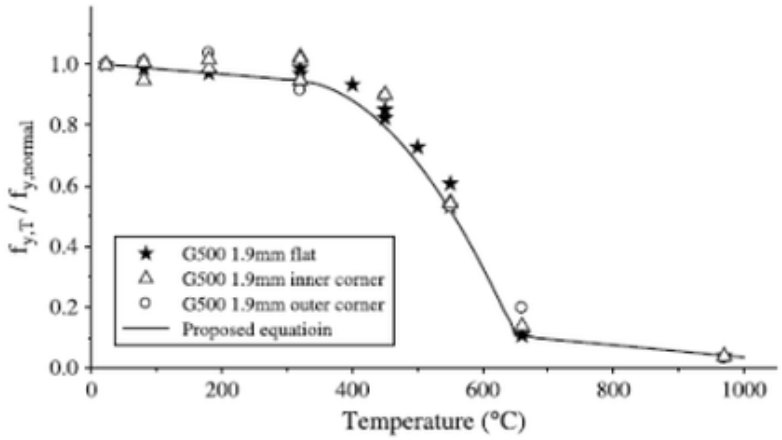

Figure 2.11 – Reduction factors of yield strength of the different coupon specimens (Cheng and Young, 2006)

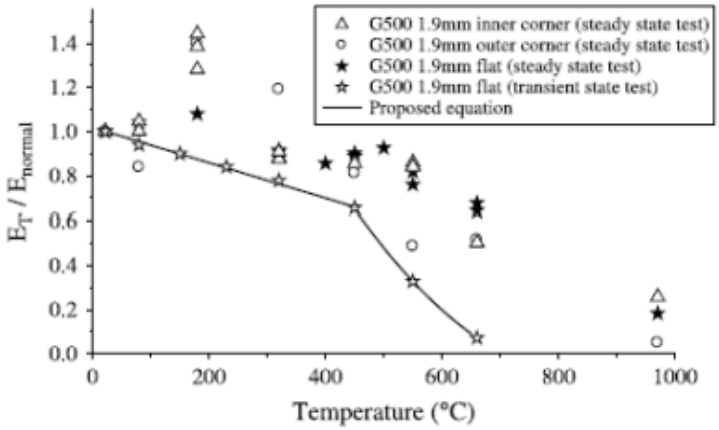

Figure 2.12 – Reduction factors of modulus of elasticity of the different coupon specimens (Cheng and Young, 2006)

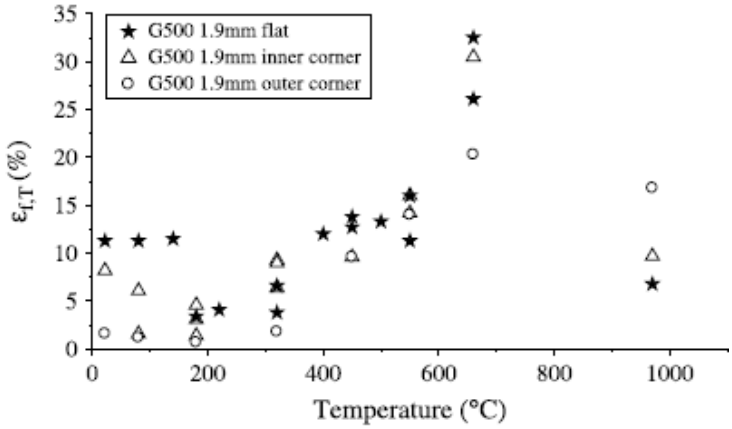

Figure 2.13 – Comparison of test results of total elongation (Cheng and Young, 2006)

Ranawaka and Mahendran (Ranawaka and Mahendran, 2009) described a detailed experimental study into the mechanical properties of light gauge cold-formed steels made of low- (G250) and high-strength (G550) steels with thickness in the range of 0.6-1 mm at elevated temperatures. Their results showed that the steel grade had an influence on the yield strength of steel. As seen in Figure 2.14, low-strength steels lost their strength more rapidly at lower temperatures than high-strength steels. There was a considerable difference in the degradation of yield strength between low- and high-strength steels in the range of 200-500 ºC. However, when the temperature increased beyond 400 ºC, high-strength steels lost their strength more rapidly than low-strength steels. This may mean that higher level of cold-working used in high-strength steels is the reason for the difference in the rates of strength degradation between these steels. The steel thickness did not appear to have a significant influence on the reduction factors. On the other hand, there was also no clear relationship

between the modulus of elasticity and the steel grade or the thickness of steel (fig. 2.15). Unlike for yield strength, the reduction factors were similar for low- and high-strength steels, with the difference being less than 10 %.

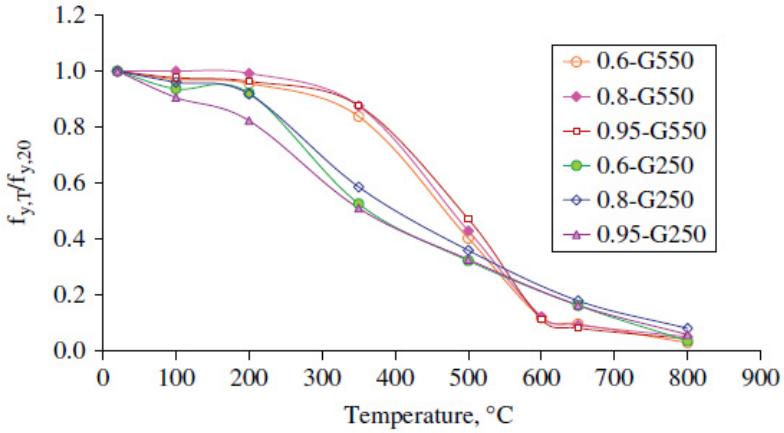

Figure 2.14 – Yield strength reduction factors based on 0.2% proof stress (Ranawaka and Mahendran, 2009)

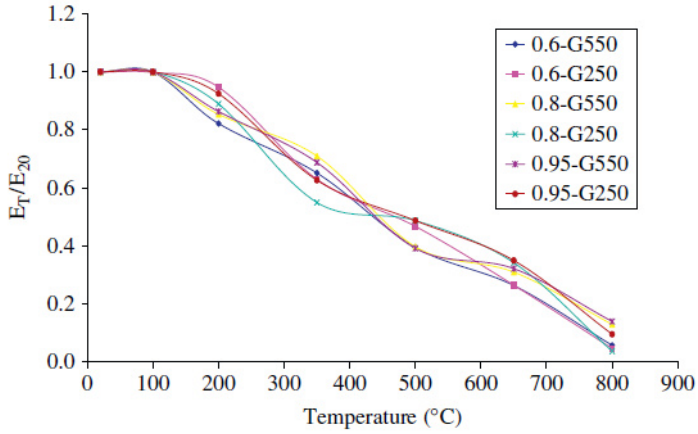

Figure 2.15 – Reduction factors of modulus of elasticity (Ranawaka and Mahendran, 2009)

Kankanamge and Mahendran (Kankanamge and Mahendran, 2011) also performed an experimental study of the mechanical properties of cold-formed steels with different thicknesses and steel grades at elevated temperatures. Their conclusions were similar to the ones of Ranawaka and Mahendran (Ranawaka and Mahendran, 2009). Nevertheless, Kankanamge and Mahendran (Kankanamge and Mahendran, 2011) highlighted the lack of reliable predictive equations for the mechanical properties of cold-formed steels. For instance, Figures 2.16 and 2.17 present respectively a comparison of the reduction factors of yield strength and modulus of elasticity predicted by them with those given by other researchers.

They concluded that there is a great difference between these results, which may introduce considerable doubts about the viability of these reduction factors for the mechanical properties of cold-formed steels, especially the reduction factors established in EN 1993-1-2 (2004), because these are very close to the ones obtained by Outinen (Outinen , 1999) (Figs. 2.7 and 2.17), who was the first one to present some results. Kankanamge and Mahendran (Kankanamge and Mahendran, 2011) stated that the differences in results may result from the variation between cold-formed steels and the test methods used.

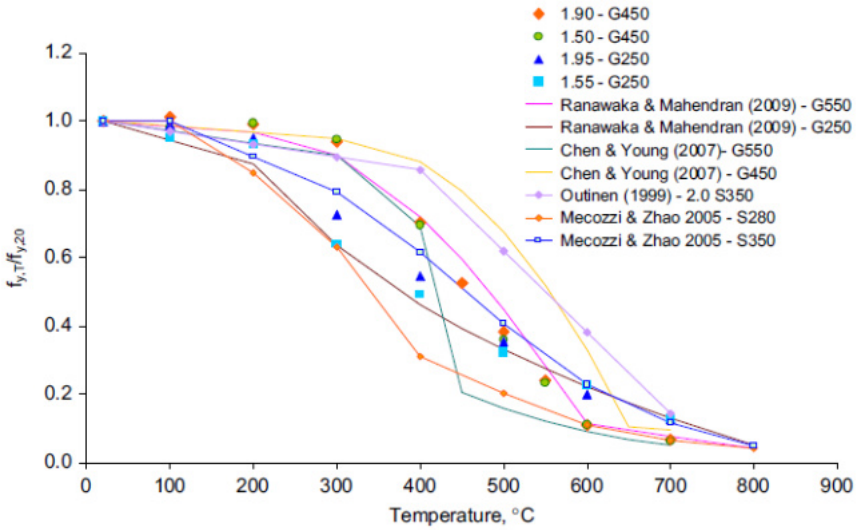

Figure 2.16 – Comparison of yield strength reduction factors with those obtained by other researchers (Kankanamge and Mahendran, 2011)

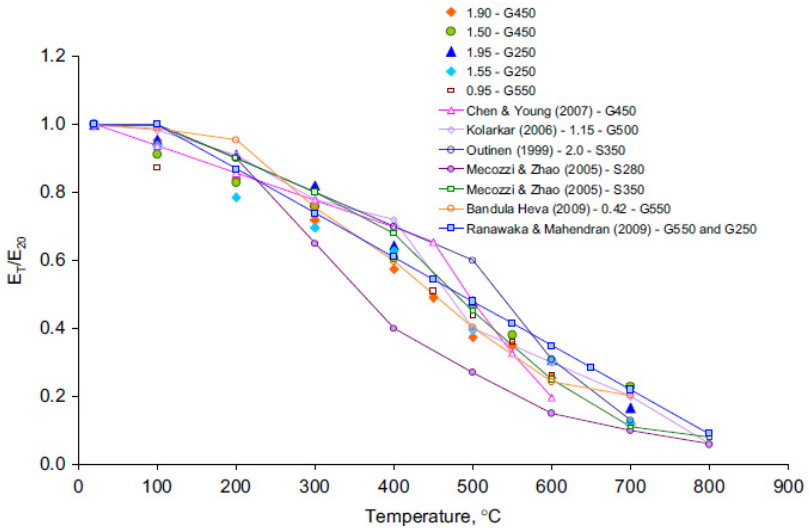

Figure 2.17 – Comparison of the reduction factors of modulus of elasticity with those obtained by other researchers (Kankanamge and Mahendran, 2011)

2.2 Residual Stresses in Cold-Formed Steel Members

The stresses in structural steels in their unload state are known as residual stresses. For example, in hot-rolled steel members the residual stresses are the result of cooling of the member after hot-rolling. These stresses are mostly of membrane type and depend on the shape of the cross-sections (Almeida, 2006). On the other hand, residual stresses in CFS sections are in general due to both the cold-forming process (press-braking or cold rolling) and the prior coiling-uncoiling process. In both processes, residual stressses are induced as a result of plastic bending. Shafer and Pekoz (Shafer and Pekoz, 1998) were the first researchers to recommend a flexural residual stress distribution for CFS channel sections (fig. 2.18). From their experimental results, it could be concluded that membrane residual stresses are reasonably small when compared with the flexural residual stresses and can be ignored, especially in press-braked sections, since membrane residual stresses are still more prevalent in rolled-formed members than in press-braked ones (Tables 2.1 and 2.2). It can be also seen in Table 2.2 that the residual stresses in the corners of rolled-formed sections are lower than in the corners of press-braked sections, in contrast to the residual stresses in the flat portions.

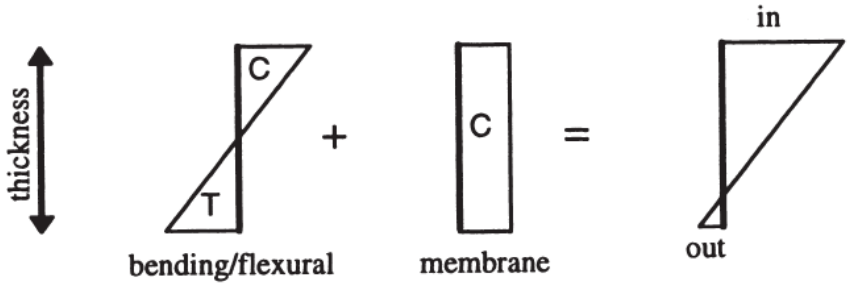

Figure 2.18 – Definition of flexural and membrane residual stress (Shafer and Pekoz, 1998)

Table 2.1 – Membrane residual stress as % f_y (Shafer and Pekoz, 1998)

	Roll-formed		Press-braked	
Element	Mean	Variance	Mean	Variance
Corners	6.8	1.1	5.2	0.4
Edge stiffened	3.9	1.0	0.9	1.0
Lip	7.9	1.5	0.2	0.3
Stiffened	−1.7	1.2	0.9	0.1

Table 2.2 – Flexural residual stress as % f_y (Shafer and Pekoz, 1998)

	Roll-formed		Press-braked	
Element	Mean	Variance	Mean	Variance
Corners	26.8	5.0	32.7	3.3
Edge stiffened	23.5	1.0	8.0	2.5
Lip	6.7	6.4	56.0*	11.6
Stiffened	38.9	6.2	16.9	4.5

* Some lips are flame-cut, thus distorting this value.

In spite of this, as Shafer and Pekoz (Shafer and Pekoz, 1998) stated, the experimental measurements of residual stresses through thickness is very difficult or infeasible and so usually only surface residual stresses are measured, with the variations across the plate thickness being assumed to be linear. Analytical and numerical models (Quach *et al*., 2004) and also residual stresses measured on thicker plates (Weng and White, 1990) have shown more complex variation through the thickness.

In 2006, Quach *et al*. (Quach *et al*., 2006) developed a finite element method for the prediction of residual stresses in CFS sections produced by press-brake operations. In order to validate the numerical model, two sets of existing experiments (Weng and Peköz, 1990; Weng and White, 1990) were shown to agree closely with the finite element results. Then, the finite element code ABAQUS was employed to simulate cold bending in press-brake operations from a CFS sheet with nominal thickness of 1.8 mm. At the end, the authors stated very clearly in this work that the maximum residual stresses in a press-braked section generally occur in the corner region and away from the surfaces (fig. 2.19). This means that the conventional method of measuring the surface residual stresses in the laboratory and assuming a linear variation across the plate thickness may greatly underestimate the real residual stresses. They also showed that the distributions of residual stresses in the flat portions are highly dependent on the initial coil diameter (fig. 2.20). It is noticed that different residual stresses can arise in the flat portions of otherwise identical cold-formed sections as a result of different initial coil diameters, which are unknown to designers and users of these sections. So, the authors considered that this may be responsible for the significant scatter in the test load capacity of CFS members.

Concerning the above, Quach (Quach, 2005) also studied the cold work effect of the manufacturing process on the structural behaviour of the press-braked members. A commonly used mono-symmetric lipped channel section was selected for this study. Section dimensions of 76.23 mm web depth, 41.45 mm flange width and 15.37 mm lip were used. This section was 1.8 mm thick and the yield stress of the steel was 250 MPa. The numerical simulations showed that the column strength was more sensitive to the cold work in the flat portions than the cold work in the corner regions (fig. 2.21). The enhancement of the column strength due to cold work in the corners decreased as the column length increased and become negligible for longer columns ($L_e \geq 1500$ mm). Like Ranawaka and Mahendran said (Ranawaka and Mahendran, 2010), the cold work in the corner regions may be ignored because the corners are usually just a small proportion of the overall cross-sectional area. In addition, it was observed that the cold work in the flat portions enhanced the strength of short columns, but reduced the column strength when the column was long enough ($L_e \geq 1000$ mm). Hence, it is clear that while the cold work in the corner regions may cause positive effect, the cold work in the flat portions might not always induce positive effect on the column strength. Furthermore, Quach's results (Quach , 2005) also show that cold work in the corner regions may have a negligible effect on the member stiffness, but in the flat portions may reduce the member stiffness (fig. 2.22).

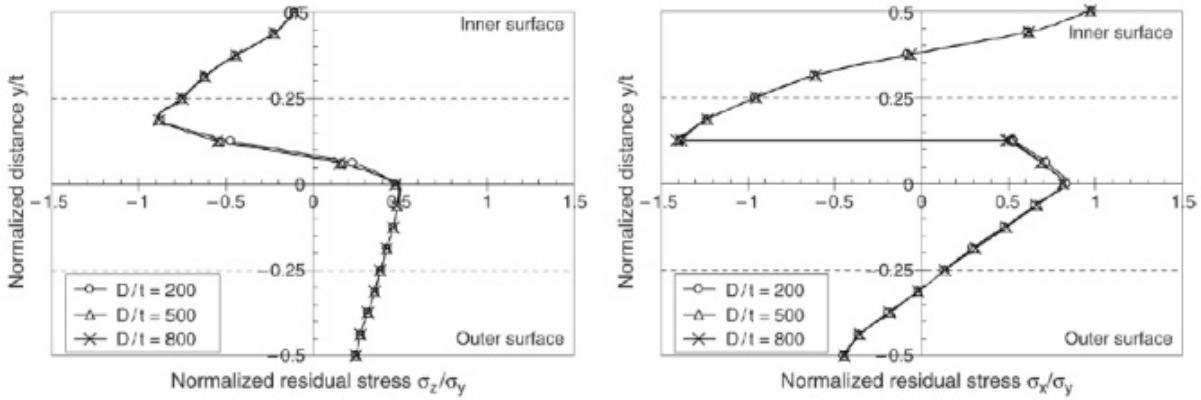

(a) Longitudinal residual stress at the centre of the lip-flange corner (b) Transverse residual stress at the centre of the lip-flange corner

Figure 2.19 – Through-thickness variations of residual stresses in the corner region (Quach *et al.*, 2006)

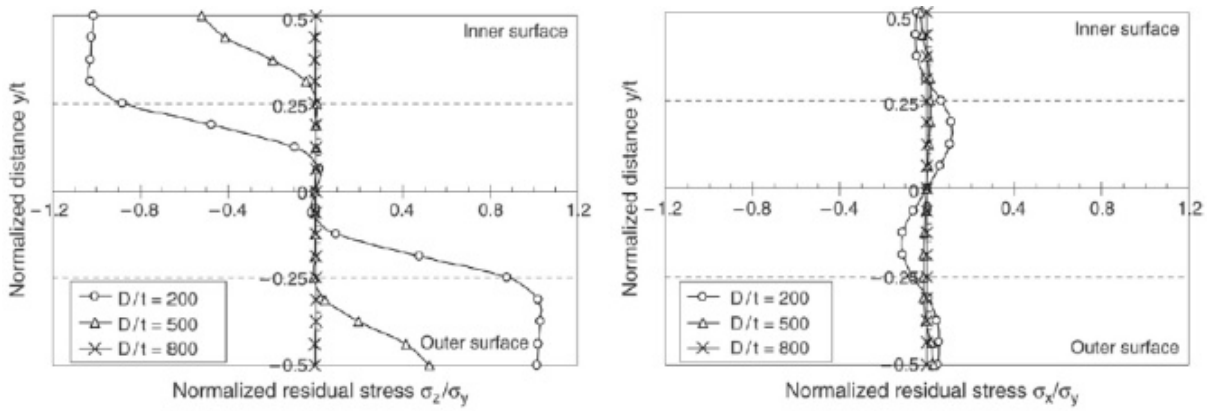

(a) Longitudinal residual stress at the mid-web section. (b) Transverse residual stress at the mid-web section.

Figure 2.20 – Through-thickness variations of residual stresses at the mid-web section (Quach *et al*., 2006)

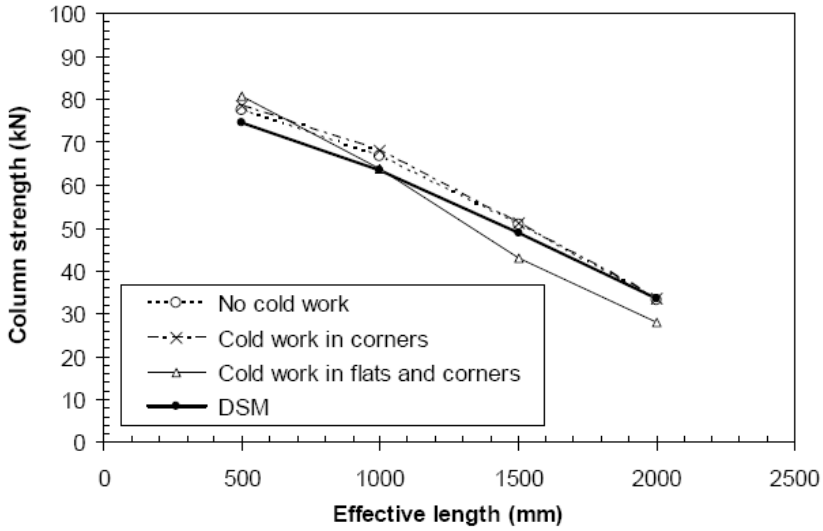

Figure 2.21 – Cold work effect on the strength of pin-ended press-braked columns (Quach, 2005)

In 2008, Moen *et al*. (Moen *et al*., 2008) provided a general mechanics-based prediction method for residual stresses and effective plastic strains in CFS members produced by cold-rolling processes. It was also shown that both transverse and longitudinal residual stress distributions and the shapes of these distributions are nonlinear through the thickness. Taking advantage of this method, Figure 2.23 presents, for instance, the predicted longitudinal residual stress distribution from coiling, uncoiling and flattening of a steel sheet with nominal thickness of 2.5 mm, a steel grade of S280GD+Z and with a mean coil radius of 400 mm; and, Figure 2.24, the predicted longitudinal residual stress distribution from cold-rolling in the corner regions and at the flat parts of the sections. It can be seen that the residual stresses are

nonlinear through the thickness and have different shapes for flats and corners. Furthermore, the stress magnitudes at the inner fibres in the corners of rolled-formed sections are thereby lower than in the corners of press-braked sections. On the other hand, the stress magnitudes at the outer fibres increase for thicker sheets and lower yield stresses (fig. 2.25). However, additional work is needed to experimentally and numerically evaluate the residual stresses of rolled-formed sections, especially their interaction between the corners and flats.

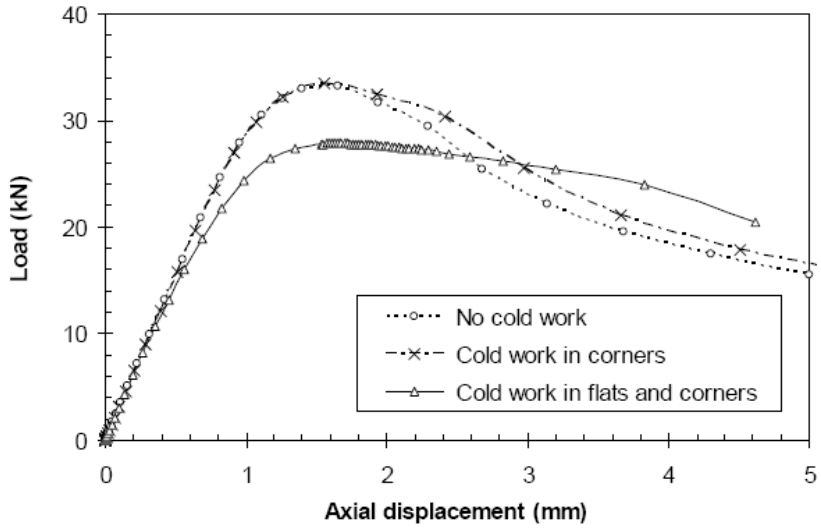

Figure 2.22 – Cold work effect on the stiffness of a pin-ended press-braked column (Quach, 2005)

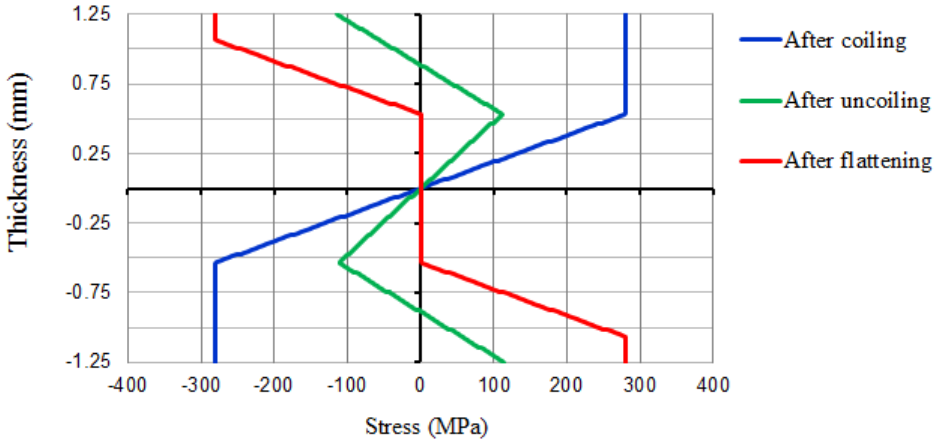

Figure 2.23 – Predicted longitudinal residual stress distribution from coiling, uncoiling, and flattening of a steel sheet

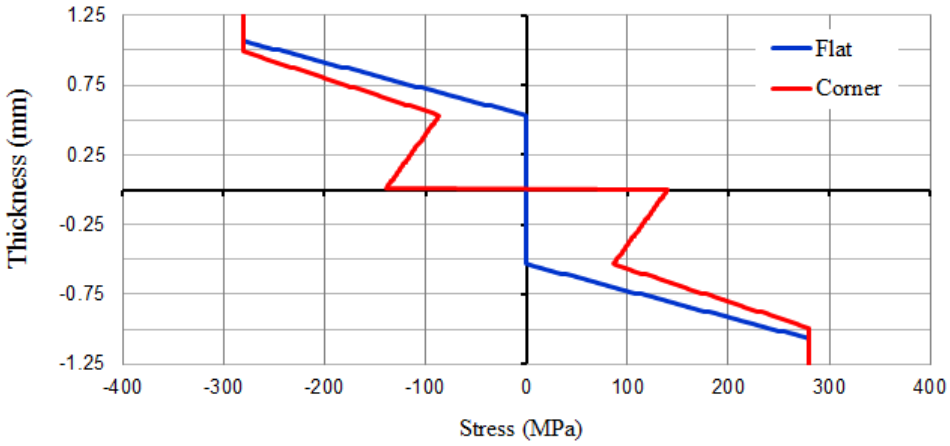

Figure 2.24 – Predicted longitudinal residual stress distribution from cold-rolling

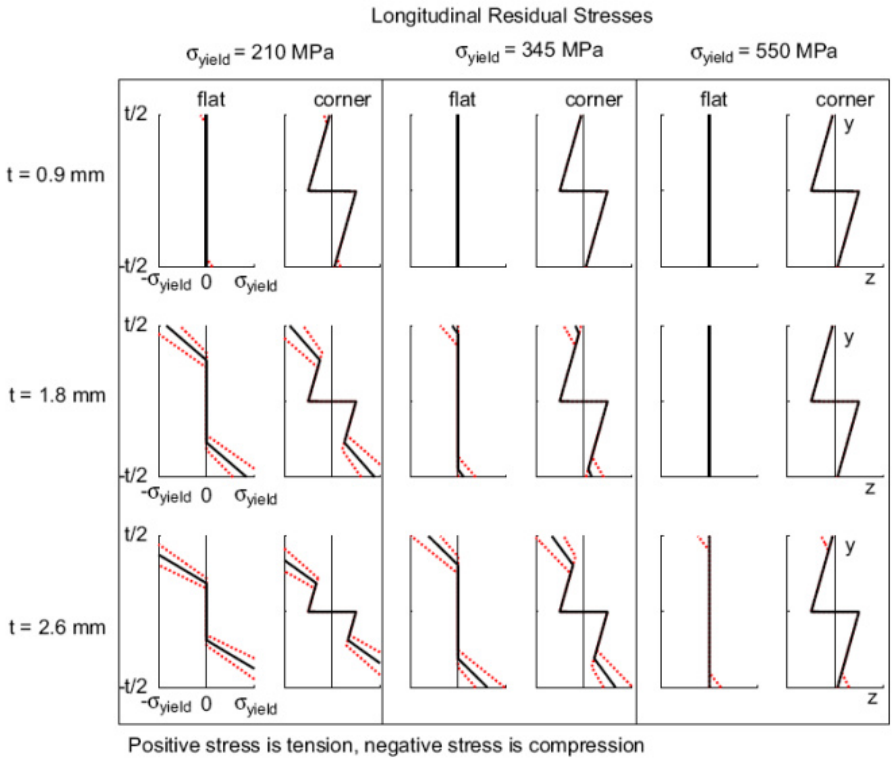

Figure 2.25 – Influence of sheet thickness and yield stress on through-thickness longitudinal residual stresses (Moen *et al.*, 2008)

Other parameters that may influence the residual stress magnitude, especially in press-braked sections, are the outer radius of bend to thickness of plate ratio (r_0/t) and the bent angles. Regarding to this matter, Anis *et al.* (Anis *et al.*, 2012) published a study on the effect of residual stress in cold formed corners of S355 and S650 structural steels. During the analyses, r_o/t ratio of 4, 5, 6 and 7 for 5 mm plate thickness and r_o/t ratio of 6, 7 and 8 for 10 mm plate

thickness with bent angle of 110º, 100º, 90º, 80º and 70º have been evaluated using two-dimensional nonlinear finite element analyses (FEA), in order to achieve magnitude of residual stresses inside corners of cold bent sections. The authors concluded that the tension residual stresses obtained in the middle of the thickness of the bend ranged from 60% to 92% of the yield strength of the material. It is clear from Figure 2.26 that smaller corners have higher values of residual stress than larger corners. Similarly, corners with small bent angles have higher magnitudes of residual stress than the ones with larger bent angles but this variation is not much significant.

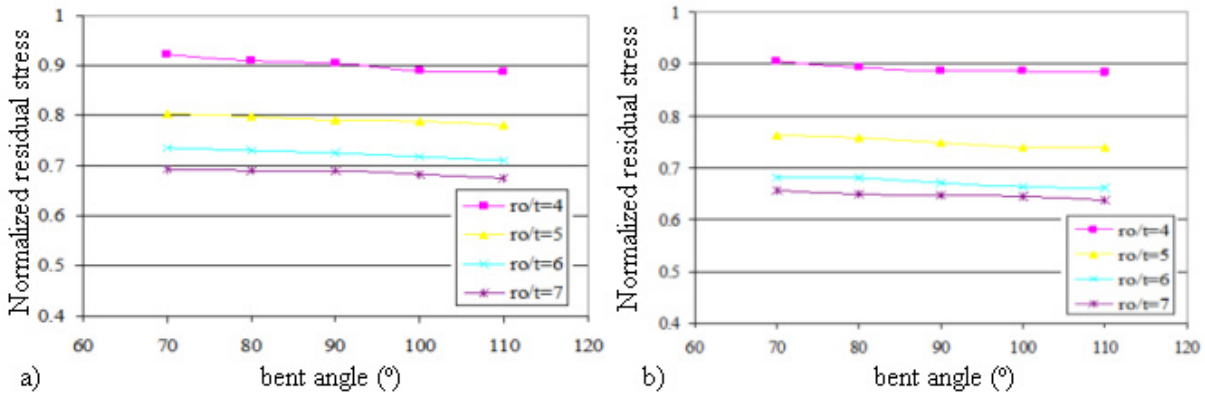

Figure 2.26 – Comparison of residual stress magnitudes between different r_o/t ratios and bent angles for (a) S355 and (b) S650 steels (Anis *et al*., 2012)

Keeping in mind Ranawaka and Mahendran' s work again (Ranawaka and Mahendran, 2010), their brief analysis of the influence of flexural residual stress in a press-braked C-section allowed to conclude that these residual stresses are also irrelevant (< 1%). This may have occurred because the members may buckle at a stress level lower than the yield point of steel, as it has already been stated here. Hence, members with high values of steel yield strength and / or low values of the steel sheet thickness are little susceptible to residual stresses and, on the other hand, in those cases, the residual stresses also have the tendency to be low (Moen *et al*., 2008). Lastly, the residual stresses are not often considered at elevated temperatures since they decrease with increasing temperatures (Vila Real *et al.*, 2004).

2.3 Imperfections in Cold-Formed Steel Members

The thickness of CFS sections is usually thin and the ultimate strength and post-buckling mechanisms of them are both sensitive to their initial geometric imperfections (Schafer and Peköz, 1999; Dubina and Ungureanu, 2002 and Dinis and Camotim, 2010). None member has a perfect geometry. Bowing, warping, twisting and local deviations are some examples of

geometric imperfections of a member. In order to provide information about the above, Schafer and Peköz (Schafer and Peköz, 1998a) analysed the amplitude of two types of sectional geometrical imperfections: type 1 (d_1), maximum local imperfection in a stiffened element (as representative of local buckling) and type 2 (d_2), maximum deviation from straightness for a lip stiffened or unstiffened flange (as representative of distortional buckling) (fig. 2.27). These ones were based on probabilistic analysis of measured imperfections from actual cross-sections. From their statistical results, it can be observed that a 0.95% value of the cumulative distribution function corresponds to a d_1/t of 1.35 and a d_2/t of 3.44. As alternative, they suggested codified values for the maximum amplitude of geometrical imperfections: $d_1=6te^{-2t}$ or $d_1=0.006h$ for the local buckling mode and $d_2=0.014b+0.5t$ or $d_2=t$ for the distortional buckling mode. These values should be applied for height to thickness ratios less than 200, width to thickness ratios less than 100 and the thickness less than 3 mm. Concerning to overall sinusoidal imperfection, the magnitude of 1/1000 times member length (L) can be used, as proposed by Eurocode 3, Part 1.1 (EN 1993-1-1, 2004).

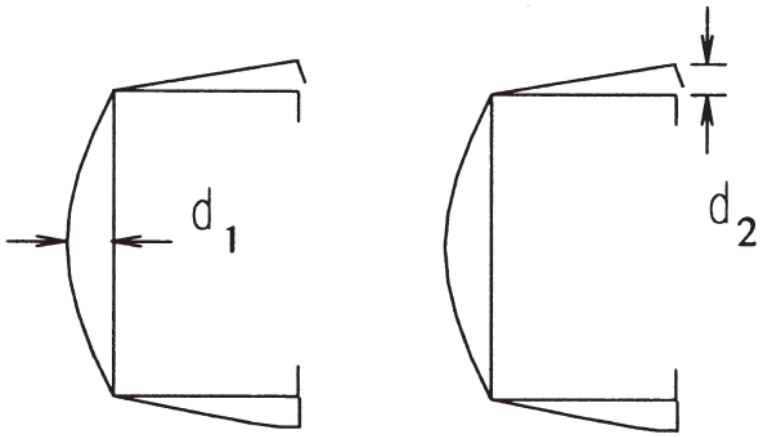

Figure 2.27 – Sectional geometrical imperfections (Schafer and Peköz, 1998a)

In 2002, Kaitila (Kaitila, 2002a) carried out an imperfection sensitivity analysis on CFS lipped channel columns. It was concluded that the increase of the magnitude of the local imperfections may lead to a relatively straightforward decrease of initial stiffness of the member and that, on the other hand, the magnitude of global imperfections may have more influence on the ultimate load of the member. For instance, it was observed that the compressive ultimate load of a C column may be reduced by 5.1% when the global imperfection magnitude increases from L/1000 to L/500 and may also be reduced by 3.9% when the local imperfection magnitude increases from h/200 to h/100 at 600 ºC. Kaitila still suggested that L/500 and h/200 are suitable values for global and local imperfections, respectively. Nevertheless, the failure by distortional buckling may still be further affected by

the initial geometric imperfections. Ranawaka and Mahendran (Ranawaka and Mahendran, 2010) noted that the maximum load capacity of a C column may be reduced by 20 and 30% when the distortional imperfection magnitude increases from zero to $2t_n$ at 20ºC and 500ºC, respectively. Moreover, it was noted that the effect of imperfection direction on the ultimate load was very small, less than 3% (fig. 2.28). Another important thing is that the peak load is in general sensitive to the imperfection magnitude in contrast to the failure mechanism, in other words, the response in the post-peak range seems to be nearly identical (Yu and Schafer, 2007).

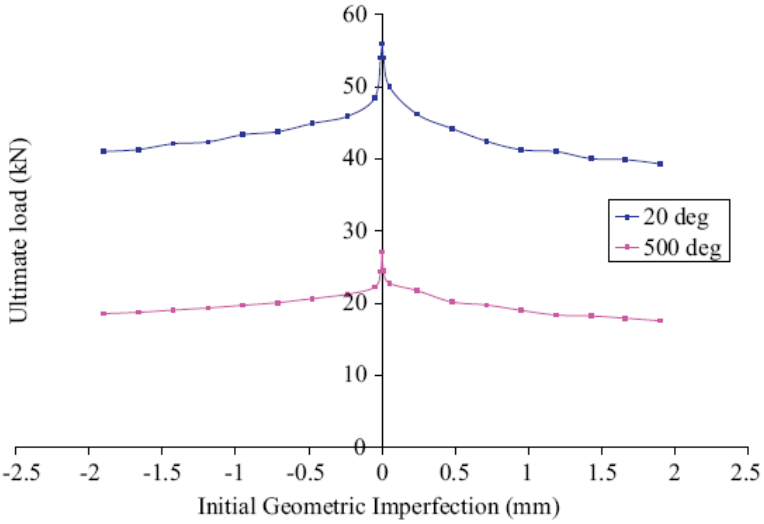

Figure 2.28 – Effect of initial geometric imperfections on failure loads (Ranawaka and Mahendran, 2010)

2.4 Research on Cold-Formed Steel Structural Beams

2.4.1 Behaviour at ambient temperature

Investigations on the structural behaviour of cold-formed steel beams extend over the last decades. These studies were generally concentrated on the instability of CFS beams of individual sections, including channel (U) sections (Ren *et al.*, 2006), lipped channel (C) sections (Wang and Zhang, 2009), channel sections with double-box flanges (fig. 2.29) (Magnucka-Blandzi, 2011), channel sections with drop flanges (fig. 2.30) (Magnucki and Paczos, 2009), zed sections (Chu *et al.*, 2006), omega sections (Karim and Adeli, 1999) and sigma sections (Li, 2009). It is noticed that these cross-sections are opened and/or asymmetric where the centroid and shear centre do not coincide. If a transverse load is applied away from the shear centre it causes torque. To make matters worse, in general, this torque is non-

uniform, that is, torsion combined with warping. The magnitude of the warping stresses can be as high as the bending stresses in some cases. However, depending on the type of the section the serviceability limit state may be more critical than the strength limit state (Gotluru *et al.*, 2000). Some beams, like U and C beams, may undergo large rotation before failure.

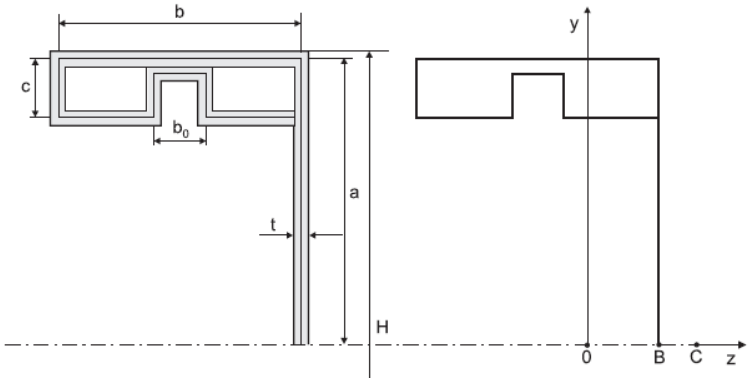

Figure 2.29 – Cross-section of a beam with double-box flanges (Magnucka-Blandzi, 2011)

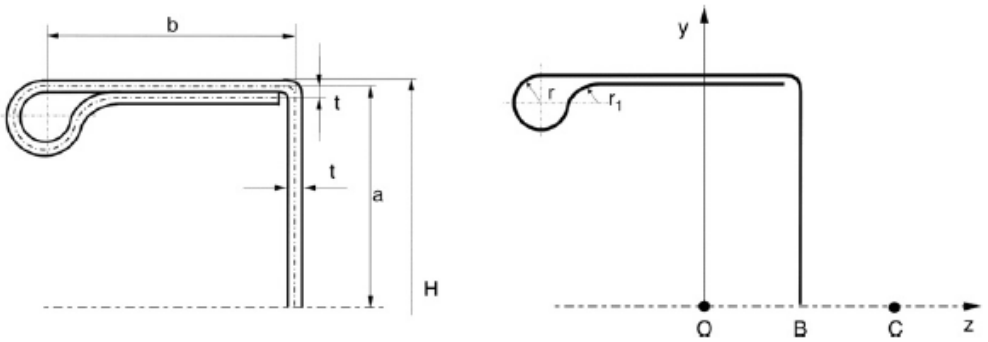

Figure 2.30 – Cross-section of a beam with drop flanges (Magnucki and Paczos, 2009)

Among other parameters, the low torsional stiffness (low torsional constant, I_T), the high slenderness (high width-to-thickness ratio, *b/t*) and the geometric imperfections (normally of the same order of magnitude or higher than the thickness of the steel plates) are some of the main causes for their high susceptibility to buckling phenomena (Yu, 2000). It is well known that beams made of CFS sections and subjected to bending moment may exhibit local (wall transverse bending only), distortional (both wall transverse bending and cross-section distortion) and global (lateral-torsional) buckling (fig. 2.31). Local buckling is particularly prevalent and is characterized by the relatively short wavelength buckling of individual plate elements. Distortional buckling involves both translation and rotation at the compression flange/lip fold line of the member (Yu and Schafer, 2002). These special buckling modes are the most interesting and complex subjects within this research field. Beyond them, interactive

buckling modes between or among the above ones are the most frequently in the CFS flexural members. Buckling modes without this kind of interaction are referred to as pure buckling modes. Thus, the terms global, distortional and local buckling have the exact meaning of pure global, pure distortional and pure local buckling mode, respectively (Ádány and Schafer, 2006a).Understanding and dealing with these phenomena has been the central focus of recent research efforts (Wang and Zhang, 2009; Dinis and Camotim, 2010). These buckling modes are mostly responsible for the ultimate strength of the compression members as they may occur even before parts of the cross-section yield. There are also other types of bucking which may still occur in beams. Shear buckling and web crushing are some examples of that. Whereas the primary function of the top and bottom flange plates of the beam is to resist the axial compressive and tensile forces arising from the applied bending moment, the primary function of the web plate is to resist the applied shear force. So, when the web is very thin and deep, the web may therefore be prone to shear buckling at relatively low values of applied shear. Web crushing is other problem which often arises with CFS beams under the action of concentrated loads, which can arise at points of load transfer from other parts of the structure or at support points. This type of behaviour is also called web buckling or web crippling (Macdonald *et al.*, 2008).

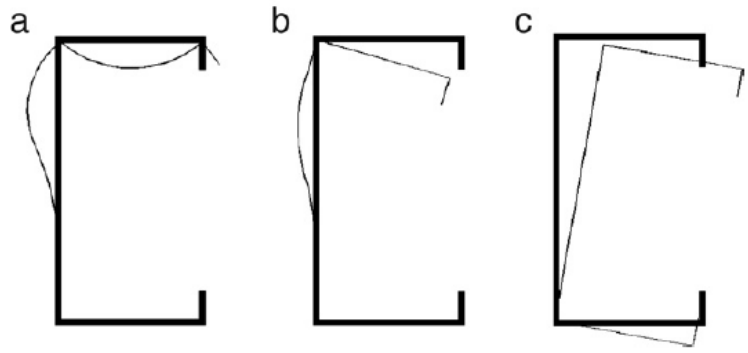

Figure 2.31 – Buckling modes of a cold-formed steel C-section flexural member: (a) Local buckling, (b) Distortional buckling and (c) Lateral-torsional buckling (Wang and Zhang, 2009)

The strength calculations of CFS members are carried out at several levels of complexity depending on the purpose of its use. For the standardised design of flexural members the Effective Width Method (EWM) and the recently developed Direct Strength Method (DSM) (Schafer, 2008) may be applied. The EWM is formally available in the Eurocode 3, Parts 1.3 and 1.5 (EN 1993-1-3, 2004 and EN 1993-1-5, 2006) and in the North American Specification (AISI S100-1996), whereas the DSM is available in the Appendix 1 of the North American Specification (AISI S100-2004 - Appendix 1). The EWM, introduced by

Von Kármán *et al.* in 1932 (Von Karman *et al.*, 1932), performs a reduction of the plates that comprise a cross-section based on the stability of the individual plates for the prediction of the local buckling strength. It is noticed that this method is a semi-empirical calibrated formulation which takes into account the local buckling effects for thin-walled sections, but does not have sufficient procedures for predicting the distortional buckling failure. However, the Eurocode 3, Part 1.3 (EN 1993-1-3, 2004) provides specific provisions for the distortional buckling strength of CFS flexural members. This method adopted in the Eurocode considers the distortional buckling by using a reduced thickness in the calculation of the effective area of the edge stiffener and the distorted part of the compression flange. The reduction factor of thickness for distortional buckling depends, among other parameters, on the elastic buckling stress of the edge stiffener and the material yield strength. In the end, the beam strength can still be calculated in an optional iteration procedure, both for the calculation of the effective area of the edge stiffener and the distorted part of the compression flange and for the calculation of the effective area of the cross-section since the stress distribution over the new effective cross-section may be different from the effective cross-section previously calculated, especially for flexural members. To sum up, a great amount of time and labour involved in carrying out subsequent effective width calculations for multiple plate elements is always associated to the EWM.

On the other hand, the direct strength method was initially proposed by Schafer and Peköz in 1998 (Schafer and Peköz, 1998b) and it is based on the member elastic stability in contrast to the EWM. The essential difference between these two methods is therefore the replacement of plate stability with member stability. First, all elastic instability loads (or moments) for the gross cross-section should be determined (local, distortional and global buckling mode) as well as the load (or moment) that causes the section to yield. Then the member strength can be directly determined by predicting the load (or moment) capacities separately for global, local, and distortional buckling, in the same way of Eurocode 3, Part 1.1 (EN 1993-1-1, 2004) predicts the design buckling resistance of a hot-rolled steel column (or beam), in other words, basing on reduction factors for the corresponding buckling curves and taking also into account the post-buckling reserve and the interaction between these modes. Here, the designers should have computational tools for the calculation of the elastic buckling loads (or moments) of the members, which can be determined either by a FEA software such as ABAQUS or, in a speedier way, using CUFSM program, developed by Schafer (Schafer, 1997). As numerical techniques for finding approximate solutions to partial differential equations and their systems, as well as integral equations, the programs ABAQUS and CUFSM use respectively the finite element method (FEM) (Schafer *et al.*, 2010) and the semi-analytical finite strip method (FSM) (Ádány and Schafer, 2006b). In CFS members design the FSM and the

recently developed constrained finite strip method (cFSM) (Schafer and Ádány, 2006) are the most commonly used tool for elastic buckling prediction. Other design approaches include: the generalized beam theory (GBT) (Silvestre and Camotim, 2002a,b), the effective area method (EAM) (Batista, 2009), the effective section method (ESM) (Batista, 2010) and the erosion of critical bifurcation load (ECBL) approach championed by Dubina (Ungureanu and Dubina, 2004 and Szabo *et al.*, 2004). It is noticed that the GBT solution can be obtained with GBTUL program, developed by the research group of the IST – Instituto Superior Técnico from Lisbon (Bebiano *et al.*, 2008), and that the EWM and the DSM are the design methods commonly used by designers, although their application is not so easy. As well as the EWM, the EAM is a direct method, which was originally proposed to cover local-global buckling interaction for CFS columns (Batista, 1989) and did not contemplate distortional buckling and flexural behaviour of beams. The ESM is an extension of the EAM for the design of CFS members (columns and beams) under local-global buckling interaction. In this field, this method represents an advantage over the traditional EWM, because it is much more understandable, accurate and simpler to be applied.

The conventional FSM provides the most widely used approach to examining instabilities in a thin-walled member under longitudinal stress (axial, bending, and/or warping torsion), in terms of buckling half-wavelength vs. buckling load (or moment) (fig. 2.32), as popularized by Hancock (Hancock, 1978). Figure 2.32 shows a typical buckling load - half-wavelength curve for a lipped channel section with a straight-line model and under axial compression. Traditionally, the first minimum is local buckling, the second distortional buckling, and global buckling is identified in the descending branch of the curve at a longer half-wavelength equal to the global unbraced length of the member (Li and Schafer, 2010). In particular, the FSM is used in members with pinned boundary conditions and in members that have regular geometry along their length. The GBT method on the other hand is able to perform buckling analysis with any kind of end conditions by combining free and fixed supports for global and local plate buckling modes (Batista, 2010). Basically, the semi-analytical FSM is a variant of the common finite element method. A thin-walled cross-section is discretized into a series of longitudinal strips (or elements) opposite to finite element discretization, as shown in Figure 2.33. Each strip is based on the plane stress assumption and Kirchhoff thin plate theory (Li and Schafer, 2010).

While determination of the elastic buckling loads (or moments) is more straightforward than traditional effective width calculation, it is not always trivial. Even for common member geometry elastic buckling calculations can sometimes lead to ambiguous predictions, which is particularly true for distortional buckling (Beregszászi and Ádány, 2011). The cFSM is

presented as a potential solution to this problem, as it provides methods for definitively separating the buckling modes from one another (fig. 2.34). Alternatively, the GBT can also be used for the same purpose, since cFSM and GBT lead to very similar results (Ádány *et al.*, 2009), as shown in Figure 2.35.

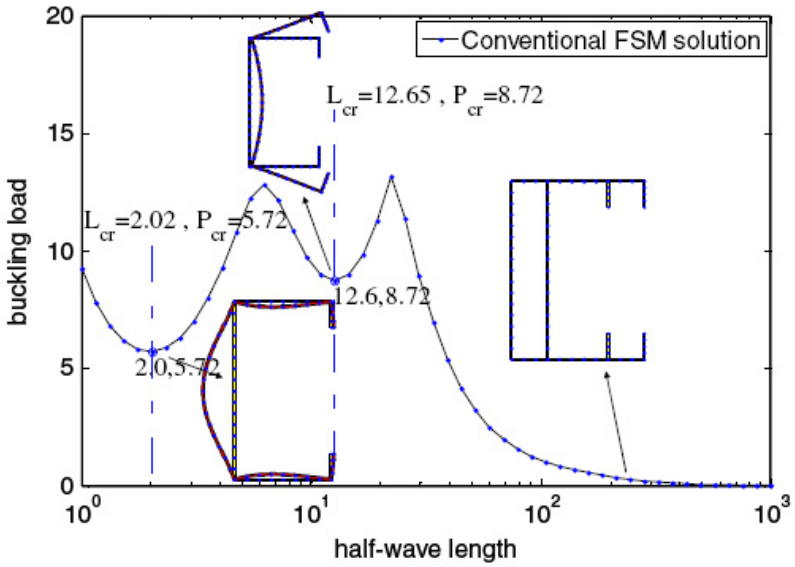

Figure 2.32 – Buckling load as a function of the buckling half-wavelength from an FSM solution (Li and Schafer, 2010)

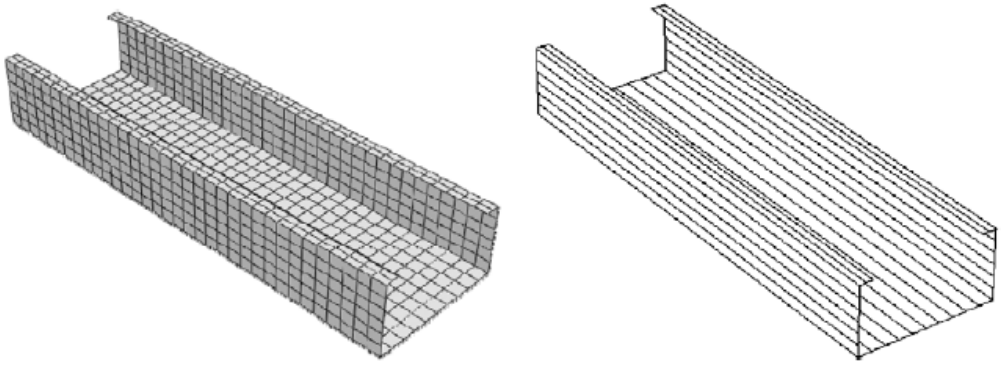

(a) FE mesh (e.g. ABAQUS S4 shell element), 5670 D.O.F.

(b) Finite strip mesh, 108 D.O.F.

Figure 2.33 – Mesh configuration using the FEM (a) and the FSM (b) (Li and Schafer, 2010)

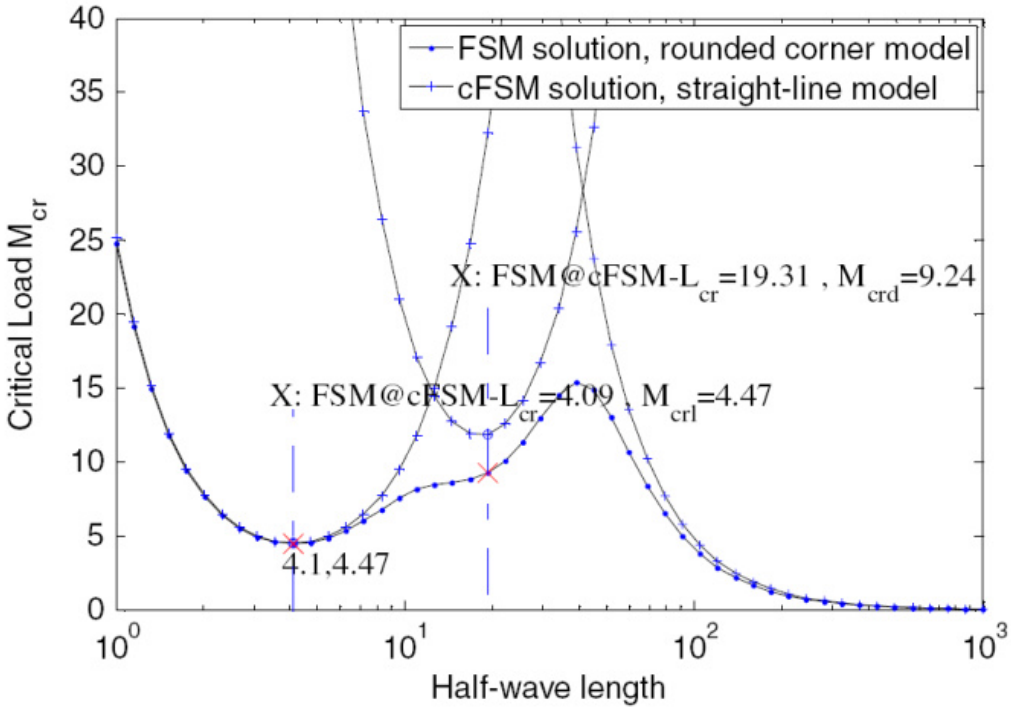

Figure 2.34 – Buckling moment as a function of the buckling half-wavelength from an FSM and a cFSM solution (Li and Schafer, 2010)

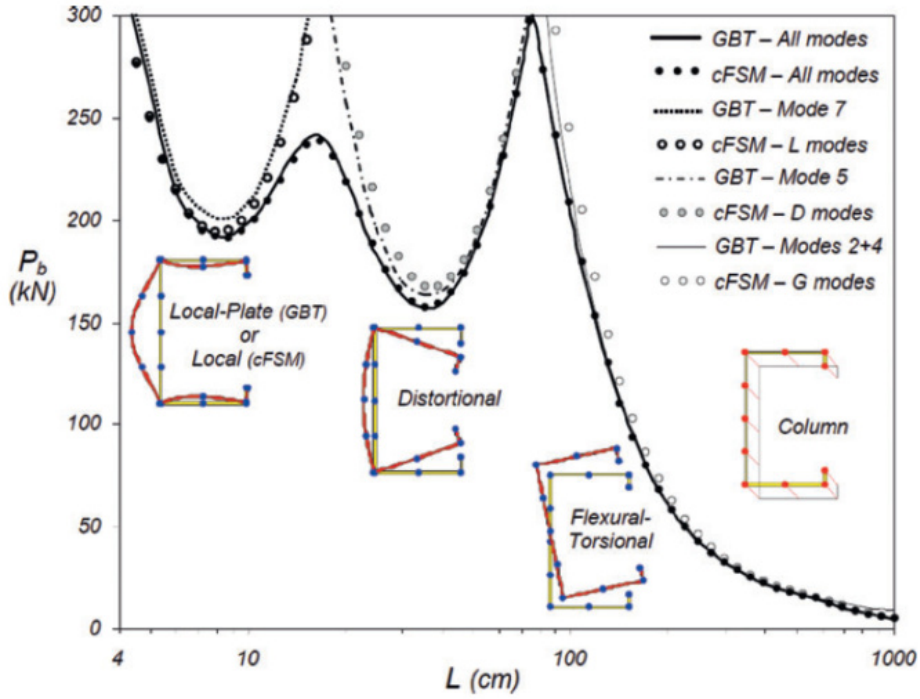

Figure 2.35 – Comparison of member stability analysis by GBT and cFSM (Ádány *et al.*, 2009)

After all, the most complete analysis, however at the same time also the most computer time consuming and deep involvement requiring, is the use of analysis by the FEM. Particularly, this relates to the geometrically and materially non-linear FEM analysis of the strength of CFS members with imperfections (GMNIA). As a consequence, its application is mainly aimed at strength calculations of important structural members or parts (Sadovský *et al.*, 2012). In addition, the finite element approach provides many advantages over physical experiments, especially when a parametric study of cross-section geometry is involved. However, the FEM should always be verified against experimental results to ensure an accurate and reliable model. The FEA should therefore be capable to directly predict the ultimate loads and failure modes of steel structural members (Zhu and Young, 2012). FEM is not typically used because of the overhead in initiating the model and the fact that it cannot uniquely identify the buckling modes. The elastic buckling loads (or moments) of the members can also be obtained by the FEM using the ABAQUS program for instance. However, the buckling curves given by ABAQUS and CUFSM are not totally identical, because the ABAQUS buckling curve exhibits the local (or distortional) critical loads (or moments) associated with one (two, three, and so on) half-wave buckling modes, as shown in Figure 2.36.

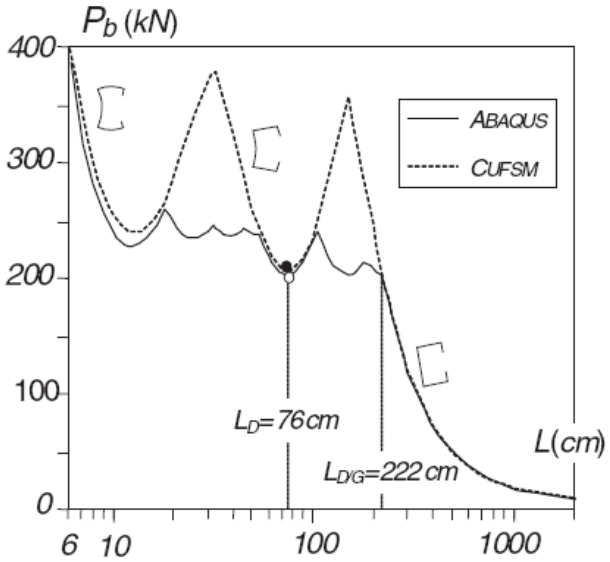

Figure 2.36 – Comparison of buckling curves of a member provided by ABAQUS and CUFSM (Dinis and Camotim, 2011)

It is worth pointing out, for example, that simulations, previously verified against experimental tests, performed with ABAQUS program allowed to conclude that the DSM yields overly conservative predictions if the moment gradient effect on CFS beams under

moment gradient is ignored in distortional buckling (Yu and Schafer, 2007). On the other hand, with the goal of maximizing the load capacity of CFS members, many research works have been dealing with the problems of optimal design of CFS beams. For instance, Magnucki and Magnucka-Blandzi (Magnucki and Magnucka-Blandzi, 1999) formulated and solved the variational and parametric optimization of arbitrary mono-symmetrical open cross sections of thin-walled beams in pure bending, Karim and Adeli (Karim and Adeli, 1999) reported the use of the neural network model to global optimum design of CFS thin-walled beams with omega sections, Tian and Lu (Tian and Lu, 2004) optimized the steel C-channel with or without lipped flanges, and Lee *et al.* (Lee e*t al.*, 2005) described the micro Genetic Algorithm and calculate the optimization problem of the CFS channel beam section.

Additionally, an important parameter normally to take into account in the numerical analysis is the mesh density. For example, an approximately 40 mm mesh size may yield a 9% higher load capacity than an approximately 10 mm mesh size in case of the S4 element. Note that this element is double-curved, a four-node (4), quadrilateral and stress/displacement shell (S) element. It is also essential to stress that, for distortional buckling, the lip itself of C sections undergoes bending and at least four linear elements or two quadratic elements are required to provide reasonable accuracy (Schafer *et al*., 2010). The lips are thereby small additional elements provided to a section to improve its efficiency to stiffen outstands under compressive loads.

Finally, it is clear that the majority of studies in this field emphasize further the structural behaviour of these members by means of analytical approximations and numerical methods. Hence, it is intended to publish in this thesis good experimental data on the structural response of CFS beams which is at the same time the hot point of this thesis.

2.4.1.1 Design of cold-formed steel beams according the DSM established in the Appendix 1 of AISI S100 (2004)

According to DSM, if all the elastic instabilities for the gross section, including local, distortional, and global buckling moments, have been determined (by CUFSM, for instance) and also the yield moment, then the strength can be directly determined by predicting the moment capacities separately for global, local, and distortional buckling. The relevant DSM formulae for beams are presented here in condensed form. A practical example is also shown in Appendix D of this thesis.

Prior to 1996, the American Iron and Steel Institute issued two separate specifications for the design of CFS structural members, connections, and structural assemblies. One was for the

allowable stress design (ASD) method, and the other was for the load and resistance factor design (LRFD). These two design specifications were combined into a single standard in 1996. Both methods are now equally acceptable for the design of CFS structures, even though they may or may not produce identical designs. However, the two methods should not be mixed in designing the various CFS components of a structure. To sum up, when the strength is calculated according the ASD method, the load combinations have to be calculated according the ASD method as well. Hence, for the ASD method, the flexural allowable strength, M_a, is determined by:

$$M_a = \frac{M_n}{\Omega} \tag{2.1}$$

where, M_n is the nominal flexural strength and Ω is the safety factor. For the LRFD method, the flexural design strength, M_d, is calculated by:

$$M_d = \phi \cdot M_n \tag{2.2}$$

where, ϕ is the resistance factor. For beams meeting the geometrical and material criteria of Section 1.1.1.2 of the AISI Specification (AISI S100-1996), Ω and ϕ are equal to 1.67 and 0.90, respectively. The nominal flexural strength, M_n, is the minimum of the nominal flexural strength for global buckling (lateral-torsional buckling), M_{ne}, for local buckling, M_{nl}, and for distortional buckling, M_{nd}, as given below.

$$M_{ne} = \begin{cases} M_{cre} & \text{if } M_{cre} < 0.56M_y \\ \frac{10}{9} M_y \left(1 - \left(\frac{10M_y}{36M_{cre}}\right)\right) & \text{if } 2.78M_y \geq M_{cre} \geq 0.56M_y \\ M_y & \text{if } M_{cre} > 2.78M_y \end{cases} \tag{2.3}$$

$$M_{nl} = \begin{cases} M_{ne} & \text{if } \lambda_l \leq 0.776 \\ \left(1 - 0.15\left(\frac{M_{crl}}{M_{ne}}\right)^{0.4}\right)\left(\frac{M_{crl}}{M_{ne}}\right)^{0.4} M_{ne} & \text{if } \lambda_l > 0.776 \end{cases} \tag{2.4}$$

$$M_{nd} = \begin{cases} M_y & \text{if } \lambda_d \leq 0.673 \\ \left(1 - 0.22\left(\frac{M_{crd}}{M_y}\right)^{0.5}\right)\left(\frac{M_{crd}}{M_y}\right)^{0.5} M_y & \text{if } \lambda_d > 0.673 \end{cases} \quad (2.5)$$

where,

$$\lambda_l = \sqrt{M_{ne}/M_{crl}} \quad (2.6)$$

$$\lambda_d = \sqrt{M_y/M_{crd}} \quad (2.7)$$

$$M_y = S_f \cdot F_y \quad (2.8)$$

M_{cre} is the critical elastic lateral-torsional buckling moment, M_{crl} is the critical elastic local buckling moment, M_{crd} is the critical elastic distortional buckling moment, M_y is the yield moment, F_y is the yield stress, and S_f is the gross section modulus referenced to the extreme fibre in the first yield. It is noticed that these critical elastic moments can be provided by CUFSM program, for instance.

2.4.1.2 Design of cold-formed steel beams according the EWM established in EN 1993-1-3 (2004)

The Eurocode 3 (EN 1993-1-1, 2004; EN 1993-1-3, 2004 and EN 1993-1-5, 2006) provides also specific provisions against local, distortional and lateral-torsional buckling strength for CFS beams. The method adopted in EN 1993-1-3 (2004) is essentially based on effective width concept. The methodology established in EN 1993-1-3 (2004) for the design of CFS beams is presented here in condensed form and practical examples are still shown in the Appendix C of this thesis.

If the cross-section class of a beam is Class 4 means that the local buckling limits the moment resistance. It is worth mentioning that for members with Class 4 sections the effect of local buckling on global behaviour at the ultimate limit state is such that the elastic resistance, calculated on the assumption of yielding of the extreme fibres of the gross section (criteria for Class 3 sections), cannot be achieved (EN 1993-1-1, 2004). The reason for the reduction in strength is that local buckling occurs at an early stage in parts of the compression elements of the member; the stiffness of these parts in compression is thereby reduced and the stresses are

distributed to the stiffer edges. So, the actual nonlinear distribution of stress is taken into account by a linear distribution of stress only acting on a reduced effective plate width leaving the remaining plate with no stress, where the buckle occurs (fig. 2.37). In other words, the local buckling strength is considered by using a reduced (effective) width in all compressed walls of the member. These effective widths of compression elements are calculated by using a reduction factor, ρ, which depends on the plate slenderness, $\bar{\lambda}_p$ (which in turn depends on the stress distribution, k_σ (Tables 2.3 and 2.4), the material yield strength, ε, the plate width, b, and the thickness, t, of the steel plate) and it is different between outstand and internal elements, as follows:

- For internal compression elements:

$$\rho = \begin{cases} 1.0 & \text{if } \bar{\lambda}_p \leq 0.5 + \sqrt{0.085 - 0.055\psi} \\ \frac{\bar{\lambda}_p - 0.055(3+\psi)}{\bar{\lambda}_p^2} \leq 1.0 & \text{if } \bar{\lambda}_p > 0.5 + \sqrt{0.085 - 0.055\psi} \end{cases} \quad (2.9)$$

- For outstand compression elements:

$$\rho = \begin{cases} 1.0 & \text{if } \bar{\lambda}_p \leq 0.748 \\ \frac{\bar{\lambda}_p - 0.188}{\bar{\lambda}_p^2} \leq 1.0 & \text{if } \bar{\lambda}_p > 0.748 \end{cases} \quad (2.10)$$

where, ψ is the stress ratio determined in accordance with Tables 2.3 and 2.4, and $\bar{\lambda}_p$ is taken as:

$$\bar{\lambda}_p = \frac{b/t}{28.4\ \varepsilon\sqrt{k_\sigma}} \quad (2.11)$$

However, when the maximum stress in a plate, $\sigma_{com,Ed}$, is lower than the yield strength, f_y, the above equations can be replaced by the followings:

- For internal compression elements:

$$\rho = \begin{cases} 1.0 & \text{if } \bar{\lambda}_p \leq 0.5 + \sqrt{0.085 - 0.055\psi} \\ \frac{1 - 0.055(3+\psi)/\bar{\lambda}_{p,red}}{\bar{\lambda}_{p,red}} + 0.18\frac{(\bar{\lambda}_p - \bar{\lambda}_{p,red})}{(\bar{\lambda}_p - 0.6)} \leq 1.0 & \text{if } \bar{\lambda}_p > 0.5 + \sqrt{0.085 - 0.055\psi} \end{cases} \quad (2.12)$$

- For outstand compression elements:

$$\rho = \begin{cases} 1.0 & \text{if } \bar{\lambda}_p \leq 0.748 \\ \frac{1-0.188/\bar{\lambda}_{p,red}}{\bar{\lambda}_{p,red}} + 0.18\frac{(\bar{\lambda}_p - \bar{\lambda}_{p,red})}{(\bar{\lambda}_p - 0.6)} \leq 1.0 & \text{if } \bar{\lambda}_p > 0.748 \end{cases} \quad (2.13)$$

where,

$$\bar{\lambda}_{p,red} = \bar{\lambda}_p \sqrt{\frac{\sigma_{com,Ed}}{f_{yb}/\gamma_{M0}}} \quad (2.14)$$

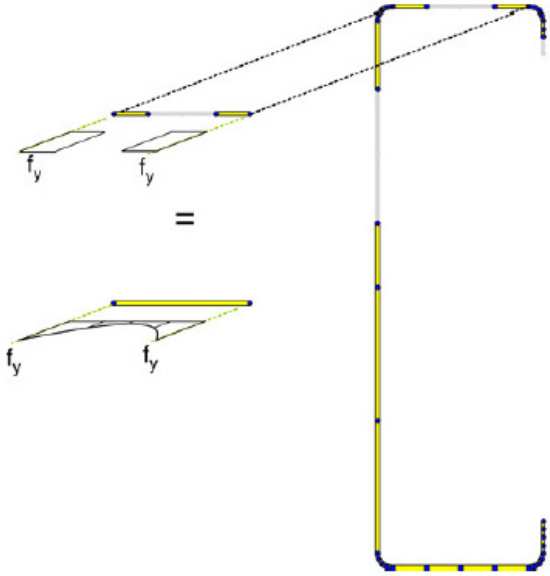

Figure 2.37 – An effective C beam determined as a composition of effective plates (Schafer, 2008)

On the other hand, for an edge stiffener the buckling factor, k_σ, must not be obtained from Table 2.4, but from the following:

$$k_\sigma = \begin{cases} 0.5 & \text{if } b_{p,c}/b_p \leq 0.35 \\ 0.5 + 0.83\sqrt[3]{\left(b_{p,c}/b_p - 0.35\right)^2} & \text{if } 0.35 < b_{p,c}/b_p \leq 0.6 \end{cases} \quad (2.15)$$

where, $b_{p,c}$ is the width of the edge stiffener and b_p is the flange width for a C section, as indicated in Figure 2.38. It is noticed that this procedure requires an iterative calculation in

which the stress ratio, ψ, is determined at each step from the stresses calculated on the effective cross-section defined at the end of the previous step. In order to account the influence of distortional buckling, EN 1993-1-3 (2004) stipulates a reduced thickness in the calculation of the effective area of the edge stiffener and the distorted part of the compression flange. The reduction factor of thickness for distortional buckling depends on the elastic buckling stress, $\sigma_{cr,s}$, of the edge stiffener and the material yield strength, f_y; the factor can be refined by an optional iteration procedure. The equations to calculate the reduction factor, χ_d, are as follows:

$$\chi_d = \begin{cases} 1.0 & \text{if } \bar{\lambda}_d \leq 0.65 \\ 1.47 - 0.723\bar{\lambda}_d & \text{if } 0.65 < \bar{\lambda}_d < 1.38 \\ 0.66/\bar{\lambda}_d & \text{if } \bar{\lambda}_d \geq 1.38 \end{cases} \tag{2.16}$$

where,

$$\bar{\lambda}_d = \sqrt{f_{yb}/\sigma_{cr,s}} \tag{2.17}$$

EN 1993-1-3 (2004) assumes that the edge stiffener behaves as a compression member with continuous partial restraint, with a spring stiffness that depends on the boundary conditions and the flexural stiffness of the adjacent plane elements. Figure 2.38 shows the analysis model in EN 1993-1-3 (2004) to determine the rotational spring stiffness of the stiffener C sections. In the case of the edge stiffeners of a C beam in bending about the strong axis, the spring stiffness, K, and the elastic buckling stress, $\sigma_{cr,s}$, can be obtained from:

$$K = \frac{Et^3}{4(1-\nu^2)} \cdot \frac{1}{b_1^2 h_p + b_1^3} \tag{2.18}$$

$$\sigma_{cr,s} = \frac{2\sqrt{K \cdot E \cdot I_s}}{A_s} \tag{2.19}$$

where, A_s is the effective cross-sectional area of the edge stiffener, I_s is the second moment about a-axis (fig. 2.38) of effective area of the edge stiffener, E is the modulus of elasticity, ν is the poisson ratio, h_p is the web width, and b_1 is the distance from the web-to-flange junction

to the centre of the effective area of the edge stiffener (including effective part b_{e2} of the flange).

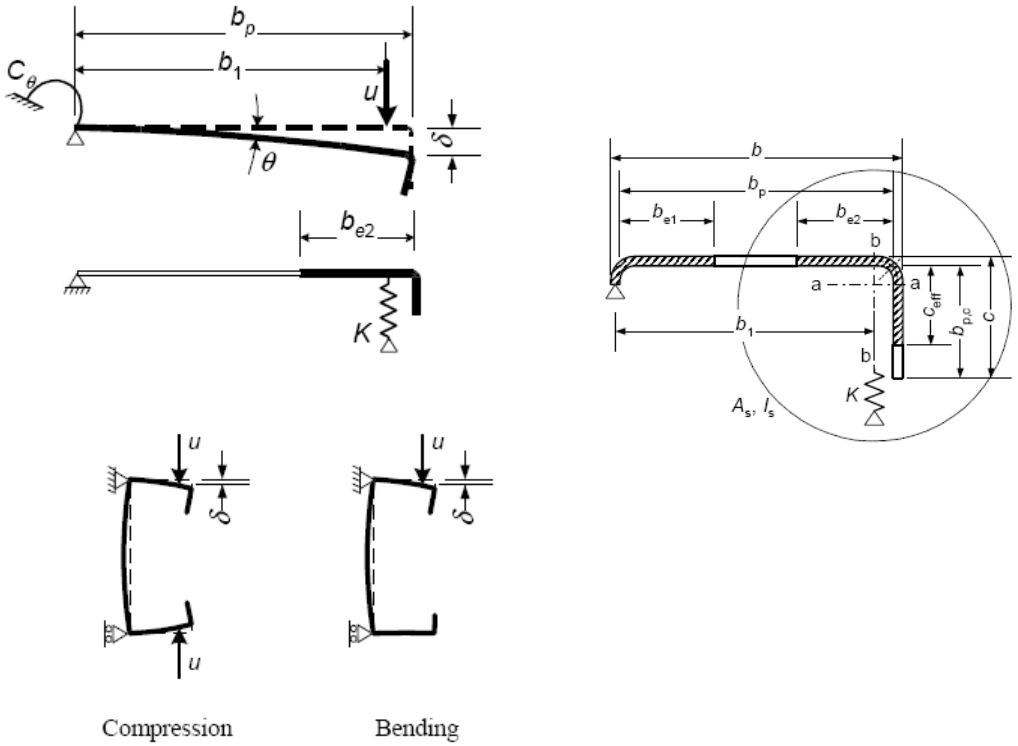

Figure 2.38 – Edge stiffener of a C section (EN 1993-1-3, 2004)

Table 2.3 – Effective widths of internal compression elements (EN 1993-1-5, 2003)

Stress distribution (compression positive)	Effective[p] width b_{eff}
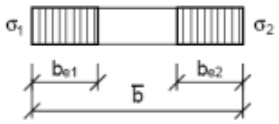	$\psi = 1$: $b_{eff} = \rho\ \bar{b}$ $b_{e1} = 0,5\ b_{eff}$ $b_{e2} = 0,5\ b_{eff}$
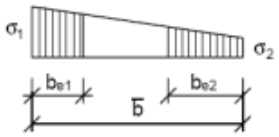	$1 > \psi \geq 0$: $b_{eff} = \rho\ \bar{b}$ $b_{e1} = \frac{2}{5-\psi} b_{eff}$ $b_{e2} = b_{eff} - b_{e1}$
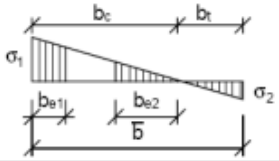	$\psi < 0$: $b_{eff} = \rho\ b_c = \rho\ \bar{b} / (1-\psi)$ $b_{e1} = 0,4\ b_{eff}$ $b_{e2} = 0,6\ b_{eff}$

$\psi = \sigma_2/\sigma_1$	1	$1 > \psi > 0$	0	$0 > \psi > -1$	-1	$-1 > \psi > -2$
Buckling factor k_σ	4,0	$8,2 / (1,05 + \psi)$	7,81	$7,81 - 6,29\psi + 9,78\psi^2$	23,9	$5,98\ (1 - \psi)^2$

Table 2.4 – Effective widths of outstand compression elements (EN 1993-1-5, 2003)

Stress distribution (compression positive)	Effective[P] width b_{eff}
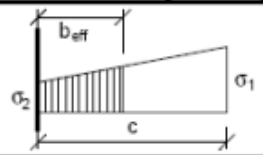	$1 > \psi \geq 0$: $b_{eff} = \rho\, c$
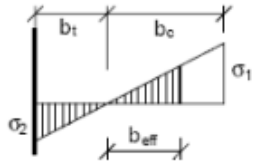	$\psi < 0$: $b_{eff} = \rho\, b_c = \rho\, c / (1-\psi)$

$\psi = \sigma_2/\sigma_1$	1	0	-1	$1 \geq \psi \geq -3$
Buckling factor k_σ	0,43	0,57	0,85	$0,57 - 0,21\psi + 0,07\psi^2$

Stress distribution (compression positive)	Effective[P] width b_{eff}
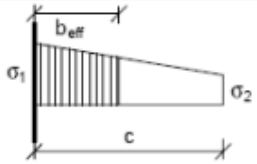	$1 > \psi \geq 0$: $b_{eff} = \rho\, c$
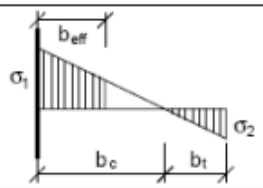	$\psi < 0$: $b_{eff} = \rho\, b_c = \rho\, c / (1-\psi)$

$\psi = \sigma_2/\sigma_1$	1	$1 > \psi > 0$	0	$0 > \psi > -1$	-1
Buckling factor k_σ	0,43	$0,578 / (\psi + 0,34)$	1,70	$1,7 - 5\psi + 17,1\psi^2$	23,8

Finally, global buckling is considered by replacing the cross-sections with class 4 elements by an effective cross-section and then designed in a similar manner to class 3 sections using elastic cross-sectional resistance limited by yielding in the extreme fibres. Thus, according the EN1993-1.1 (2004), the design buckling resistance moment of a member susceptible to lateral-torsional buckling is given as follows:

$$M_{b,Rd} = \chi_{LT} \cdot W_y \cdot \frac{f_y}{\gamma_{M1}} \tag{2.20}$$

in which χ_{LT} is defined as follows:

$$\chi_{LT} = 1.0 \quad \text{if } \bar{\lambda}_{LT} \leq 0.4$$
$$\chi_{LT} = \frac{1}{\Phi_{LT} + \sqrt{\Phi_{LT}^2 - \bar{\lambda}_{LT}^2}} \quad \text{if } \bar{\lambda}_{LT} > 0.4 \tag{2.21}$$

where,

$$\Phi_{LT} = 0.5\left[1 + \alpha_{LT}\left(\bar{\lambda}_{LT} - 0.2\right) + \bar{\lambda}_{LT}^2\right] \tag{2.22}$$

$$\bar{\lambda}_{LT} = \sqrt{\frac{W_y f_y}{M_{cr}}} \tag{2.23}$$

W_y in Equations 2.20 and 2.23 are the appropriate section modulus of the cross-section depending on its class (for example, elastic section modulus, W_{el}, for class 3, and effective section modulus, W_{eff}, for class 4 cross-sections), f_y is the yield strength of steel, and α_{LT} is the imperfection factor of the beam. The elastic critical moment for lateral-torsional buckling, M_{cr}, can be calculated (for doubly symmetric sections or mono-symmetric sections which are subjected to bending about the symmetry axis (AS/NZS 4600, 1996)) by:

$$M_{cr} = C_b \sqrt{\frac{\pi^2 EI}{\left(k_y L\right)^2}\left[GI_T + \frac{\pi^2 EI_W}{(k_W L)^2}\right]} \tag{2.24}$$

in which EI, EI_w and GI_T are the minor axis flexural rigidity, warping rigidity and torsional rigidity, respectively. k_y represents the effective lateral buckling length factor and k_w the factor which accounts for the beam end warping. Lastly, C_b is a coefficient depending on the moment distribution along the length of the beams (Trahair, 1993).

2.4.2 Behaviour at elevated temperatures or under fire conditions

As can be seen from the foregoing, studies in this area at ambient temperature are not too much, and are mostly of a numerical nature or give importance to the numerical analysis more than the experimental analysis. However, they address the most important phenomena related to these elements, including post-buckling resistance (local and distortional buckling) (Camotim and Dinis, 2011), global flexural, torsional and flexural-torsional buckling (Narayanan and Mahendran, 2003), shear resistance of stud walls (Pan and Shan, 2011),

bending resistance (Wang and Zhang, 2009) and resistance of some type of screwed connections (Zaharia and Dubina, 2006).

But when it comes to fire, there are even fewer studies related to the behaviour of CFS elements subjected to high temperatures. Fire is still other phenomenon which deteriorates its structural behave. The high thermal conductivity of steel and the high section factor of these structural members (small wall thickness) can lead to a rapid rise in steel temperature in a fire and together with the deterioration of its mechanical properties as a function of temperature can cause serious deformation of structural elements and the premature failure of the building. As it is an emerging technology and as a great variety of profiles with different geometric shapes can be easily produced, it is of the utmost importance that studies within this area of research should be undertaken.

There are only a few studies related to numerical studies on the behaviour of CFS beams subjected to elevated temperatures. From the view of the author of this thesis, the best study on CFS beams is the research work performed by Kankanamge and Mahendran. For instance, it seems from their results that the design method given in EN 1993-1-2 (2004) is over-conservative for all the temperatures excepted for CFS beams with very high slenderness values (fig. 2.39) (Kankanamge and Mahendran, 2012). These authors also concluded from a parametric study that the EN 1993-1-3 (2004) design methods with buckling curve b are unsafe or over-conservative for some temperatures, especially in the intermediate slenderness region. Therefore, they proposed the use of other buckling curves for different temperature ranges for the fire design of CFS lipped channel beams. It is noticed that the methods established in EN 1993-1-2 (2004) were investigated by the authors in fire design by using the CFS mechanical properties at elevated temperatures. With regard to the maximum temperature in CFS members, EN 1993-1-2 (2004) has enforced a limit of 350 ºC, which seems to be overly conservative for some researchers (Kankanamge, 2010), especially, on the fire behaviour of beams. For example, it was also found out by Laím and Rodrigues (Laím and Rodrigues, 2011) and Lu *et al.* (Lu *et al.*, 2008) that CFS beams under certain boundary conditions can have load-carrying capacity until 700 ºC. Hence, it is clear evidence that experimental tests on CFS beams are needed, especially on beams consisting on compound CFS profiles, as well as more numerical simulations based obviously on experimental tests so that simplified calculation methods for fire design of CFS beams can be developed. This thesis therefore intends to fill the knowledge gap in this almost unexplored area and bring a better understanding about these issues.

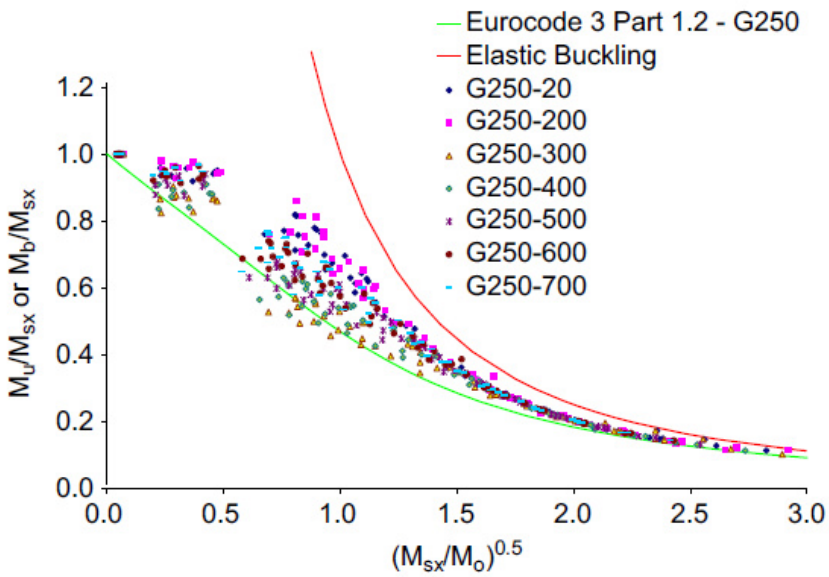

Figure 2.39 – Comparison of FEA results with Eurocode 3 Part 1.2 (Kankanamge and Mahendran, 2012)

3 EXPERIMENTAL ANALYSIS OF COLD-FORMED STEEL BEAMS

3.1 Introduction

This chapter presents a series of flexural tests at ambient temperature and under fire conditions focused on simply supported cold-formed steel (CFS) beams made of one and more CFS profiles. It is described in detail the experimental programme, the testing procedures and the test set-up for bending tests performed in the Department of Civil Engineering (DEC) of the University of Coimbra (UC). The main purpose of the tests at ambient temperature was to assess the failure loads and the failure modes of the studied beams and also to compare the structural response of the different kinds of beams. These tests were carried out to provide a reference for the fire tests. On the other hand, three sets of fire tests were conducted in order to evaluate the influence of the stiffness of the surrounding structure to the beams, in other words, the first set of the experimental tests was carried out on simply supported CFS beams without any kind of restraining to the thermal elongation of the beam, whereas the second and third sets were undertaken on the same type of beams, but with axial restraint and with combined axial and rotational restraint at the beam supports, respectively. Other important goal of this research was to provide experimental data for numerical studies, in order to carry out a parametric study outside the bounds of the original experimental tests. To sum up, the experimental and numerical results was the basis of an analytical study for the development of simplified calculation methods for fire design of CFS beams.

3.2 Test Specimens

The specimens consisted of beams made of one or more CFS profiles, namely, channel and lipped channel profiles, also known as U and C profiles, respectively (fig. 3.1). All these cross-sections were 2.5 mm thick and 43 mm wide. The inside bend radius and the length of the edge stiffeners of the C profiles measured respectively 2 and 15 mm. The C sections were 250 mm tall, whereas the U sections were 255 mm tall, so that the C profiles could be placed between the flanges of the U profiles (R beams), as illustrated in Figure 3.1. Therefore, as it can also be seen in this figure, the compound lipped I beams consisted of two C connected in the web, whereas the compound R beams consisted of one C profile and one U profile connected in the flanges. The compound 2R beams were made of two R beams connected together by the C profiles' web. The total beam length was 3.6 m for all specimens, but the

span, *L*, was only 3 m in such a way that the beams and their supports could be accommodated by the horizontal electric furnace available in the laboratory.

In addition, the profiles were screwed together as indicated in Figure 3.1 by means of Hilti S-MD03Z 6.3x19 carbon steel self-drilling screws in S235 steel, at sections 0.05 m and 1.15 m away from the ends of the beams so that the spacing of the screws along the beam was about 1 m (*L*/3) (fig. 3.2). All the profiles were made of S280GD+Z structural steel, which is a continuous carbon steel sheet with a zinc coating thickness of 0.04 mm (275 g/m2) and with a yield strength of 280 MPa and an ultimate tensile strength of 360 MPa, according to NP-EN 10147 (2002). These profiles were manufactured by the company PERFISA S.A., which is specialized in the fabrication of CFS profiles in Portugal, and the choice of the cross-sections and the distance between the screws was based on the observation of CFS structures and design projects for this kind of buildings, representing commonly used details in several countries.

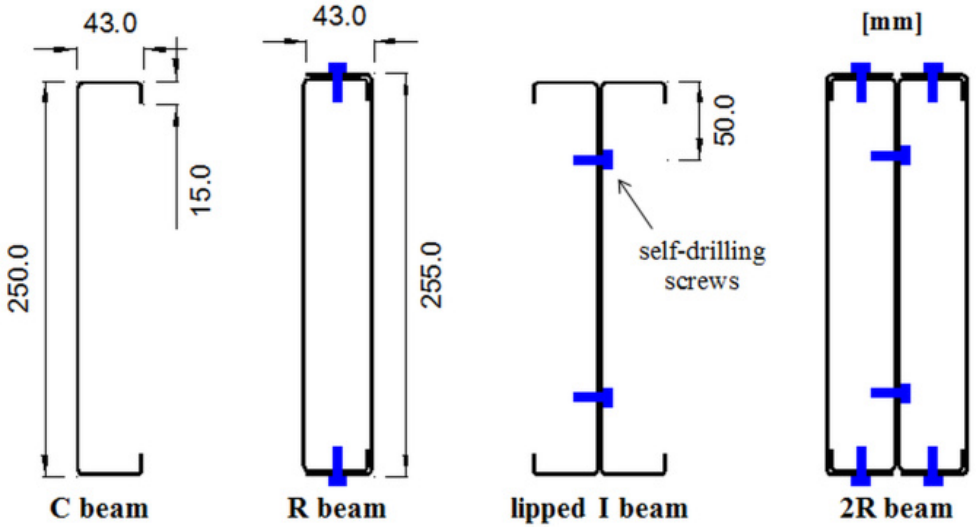

Figure 3.1 – Scheme of the cross-sections of the tested beams

3.3 Test Set-up

Schematic and overall views of the experimental system used in the fire tests of the beams are shown in Figures 3.2, 3.3, 3.4, 3.5 and 3.6. Figure 3.3 shows many views of the test set-up which essentially consisted of a reaction frame (no. 1 in fig. 3.3), a hydraulic jack (no. 2 in fig. 3.3) to impose loading, a modular electric furnace (no. 3 in fig. 3.3) to simulate fire conditions, a roller and pinned support (no. 4 in fig. 3.3) to provide a simply supported beam. As it can be seen in Figure 3.2, the test specimens (no. 5 in fig. 3.3) were loaded at two points

1.0 m (one-third of the beam span) away from the beam supports in such a way that between the two loading points the beam was under pure bending state (four point bending test). The loading was applied by an ENERPAC hydraulic jack, model RR 3014 (no. 2 in fig. 3.3), which was hung on a two-dimensional reaction frame (no. 1 in fig. 3.3) that consisted of two HEB300 columns and a HEB300 beam of class S355 steel. This hydraulic jack had a maximum loading capacity in compression of 295 kN and a maximum stroke length of 360 mm and was controlled by a servo hydraulic central unit W+B NSPA700/DIG2000. Additionally, beneath the hydraulic jack a Novatech F204 load cell of 250 kN capacity (no. 6 in fig. 3.3) was mounted in order to monitor the applied load during the fire tests. This loading was transferred from the hydraulic jack to the specimen by a HEA160 column (no. 7 in fig. 3.3) and applied at two points on the specimen by means of a HEB140 beam (no. 8 in fig. 3.3), both filled up with fire-protection mortar between the profile flanges to prevent their destruction by the high temperatures developed during the fire tests. It can be seen in this figure that the whole test specimen and the HEB140 beam and consequently a piece of the HEA160 column were inside the furnace.

The specimens were heated with a horizontal modular electric furnace (no. 3 in fig. 3.3). This furnace was 4500 mm x 1000 mm x 1000 mm in internal dimensions and capable to heat up to 1200 ºC and to follow fire curves with different heating rates. Only about 2.5 m in length of the specimens were directly heated, because the beams supports were protected by 50 mm layer of ceramic wool to prevent its destruction during all tests as well. A spherical plain bearing and a spherical hinge (respectively no. 9 and 10 in fig. 3.3) were also assembled in the loading system in such a way that the load applied on the beams could easily follow the local, distortional and global deformations of the beams during the tests, especially, the lateral buckling. Although the spherical hinge was not completely free to rotate due to the threaded rods which allowed to make the connection between the HEA160 column and HEB140 beam, the spherical plain bearing could rotate 90º to both sides about an axis passing through its own centre and it was perpendicular to a plane formed by the longitudinal axes of the HEA160 column and the HEB140 beam. In addition, the spherical plain bearing could still rotate about 10º to both sides around an axis that passed through its own centre and it was perpendicular to a plane composed of the reaction frame.

The tested beams were statically determinate over a roller and pinned support as also shown respectively in Figures 3.4a and 3.4b. These supports were made of refractory stainless steel, typically used for elevated temperature applications. They prevented the vertical displacement, the lateral displacement and the lateral rotation of the beams. In addition, the

roller support allowed the horizontal displacement of the beams in contrast to the pinned support as it can clearly be seen in this figure.

Furthermore, the experimental system still comprised four restraining steel beams, two of them to simulate the axial restraint to the thermal elongation of the beam (fig. 3.5) and the other two with the purpose of simulating the rotational stiffness of the beam supports (fig. 3.6). Hence, the axial restraining system was composed of two simply supported beams, one with high flexural rigidity (near the pinned support) (no. 1 in fig. 3.5) and the other with low flexural rigidity (near the roller support) (no. 2 in fig. 3.5). On the other hand, the rotational restraining system was composed of two cantilever beams (no. 1 in fig. 3.6), both with identical flexural rigidity. It is noticed that these beams were placed in the basement floor of the Laboratory, below the testing floor (fig. 3.6). Also note that the specimen was connected to the rotational restraining beams by means of pin-ended steel smooth rods (they passed through the holes of the slab) (no. 2 in fig. 3.6), whereas the specimen was connected to the axial restraining beams by means of a HEB220 profile (near the pinned support) (no. 3 in fig. 3.5) and a threaded rod system (near the roller support) (no. 4 in fig. 3.5) which allowed to eliminate the clearances between the specimen and those beams. At the end of this HEB220 profile and this threaded rod system, a steel semi-sphere was placed (no. 5 in fig. 3.5), covered with a thin layer of Teflon (PTFE) sheet, so that the vertical displacement was possible without friction.

It is worth mentioning that this kind of test set-up allowed studying separately the effects of axial and rotational restraint on the failure times and temperatures of CFS beams. Also, a Novatech F204 load cell of 500 kN capacity was mounted in order to monitor the axial restraining forces generated in the test specimen (no. 6 in fig. 3.5) during the fire tests, as well as two Novatech F202 load cells of 100 kN capacity (no. 3 in fig. 3.6) so as to measure the restraining forces due to the rotational restraint imposed by the cantilever beams. The actual axial, k_a, and rotational, k_r, stiffnesses were, respectively, about 15 kN/mm and 150 kN.m/rad, which were taken indirectly from the experimental results. These restraining systems intended to reproduce as faithful as possible the actual boundary conditions of a beam when is inserted in a real CFS building structure, making it possible to understand how the surrounding structure effects a CFS beam when is subject to fire. Stiffness values as realistic as possible were considered in this type of tests. It is worth mentioning that it was built a 3D model of a general CFS building (two floors with nine identical rooms on each floor) using beam elements in ABAQUS program, in order to predict realistic values of axial and rotational stiffness (Appendix I).

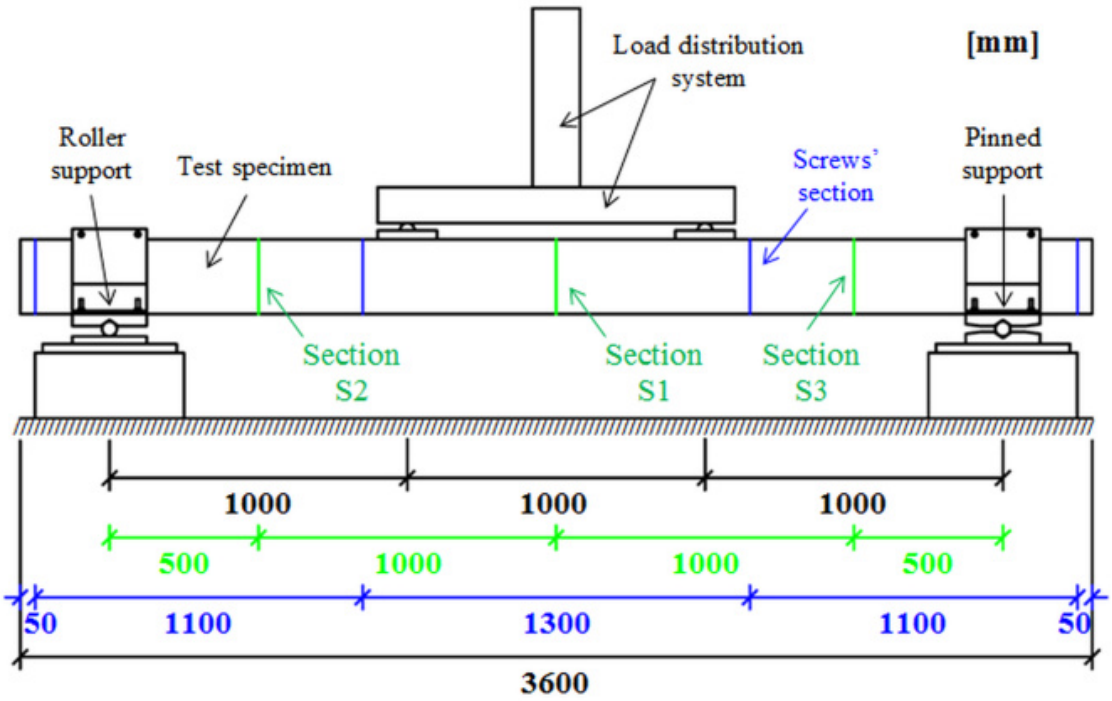

Figure 3.2 – Schematic view of the experimental set-up for flexural tests of beams

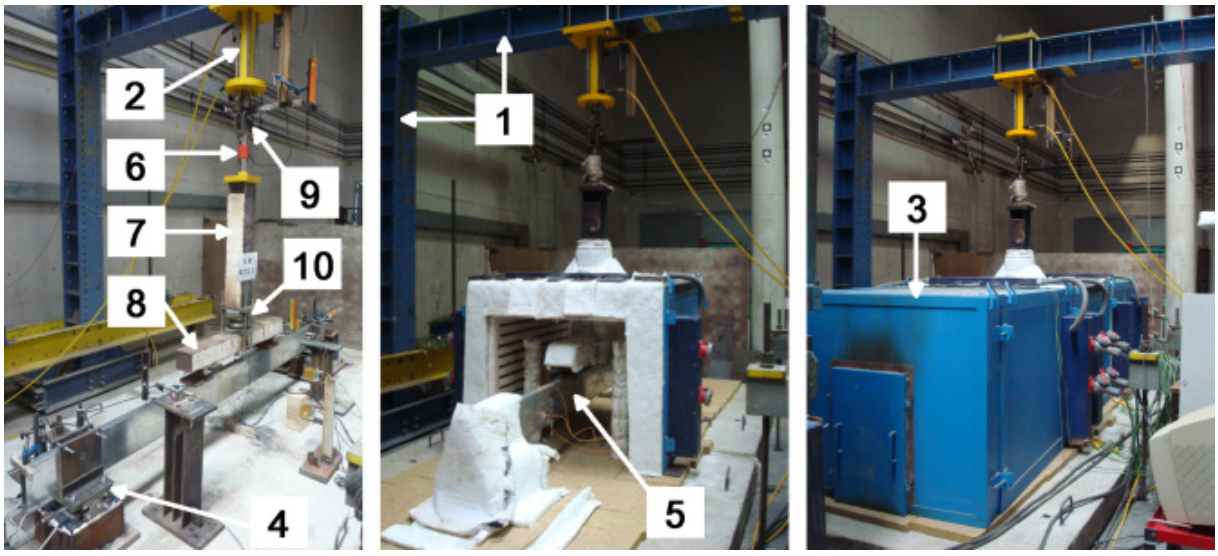

Figure 3.3 – Test set-up for structural fire tests of CFS beams

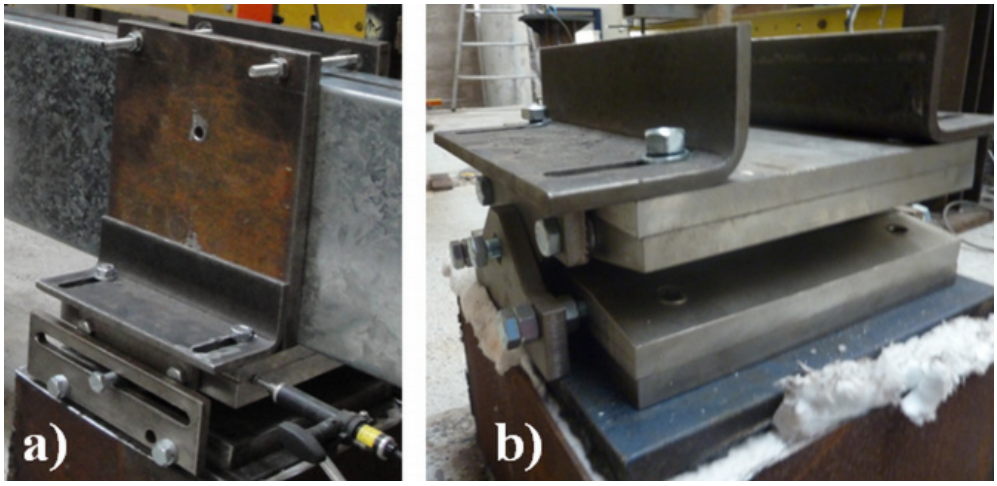

Figure 3.4 – Detail of the beam support system: (a) roller and (b) pinned supports

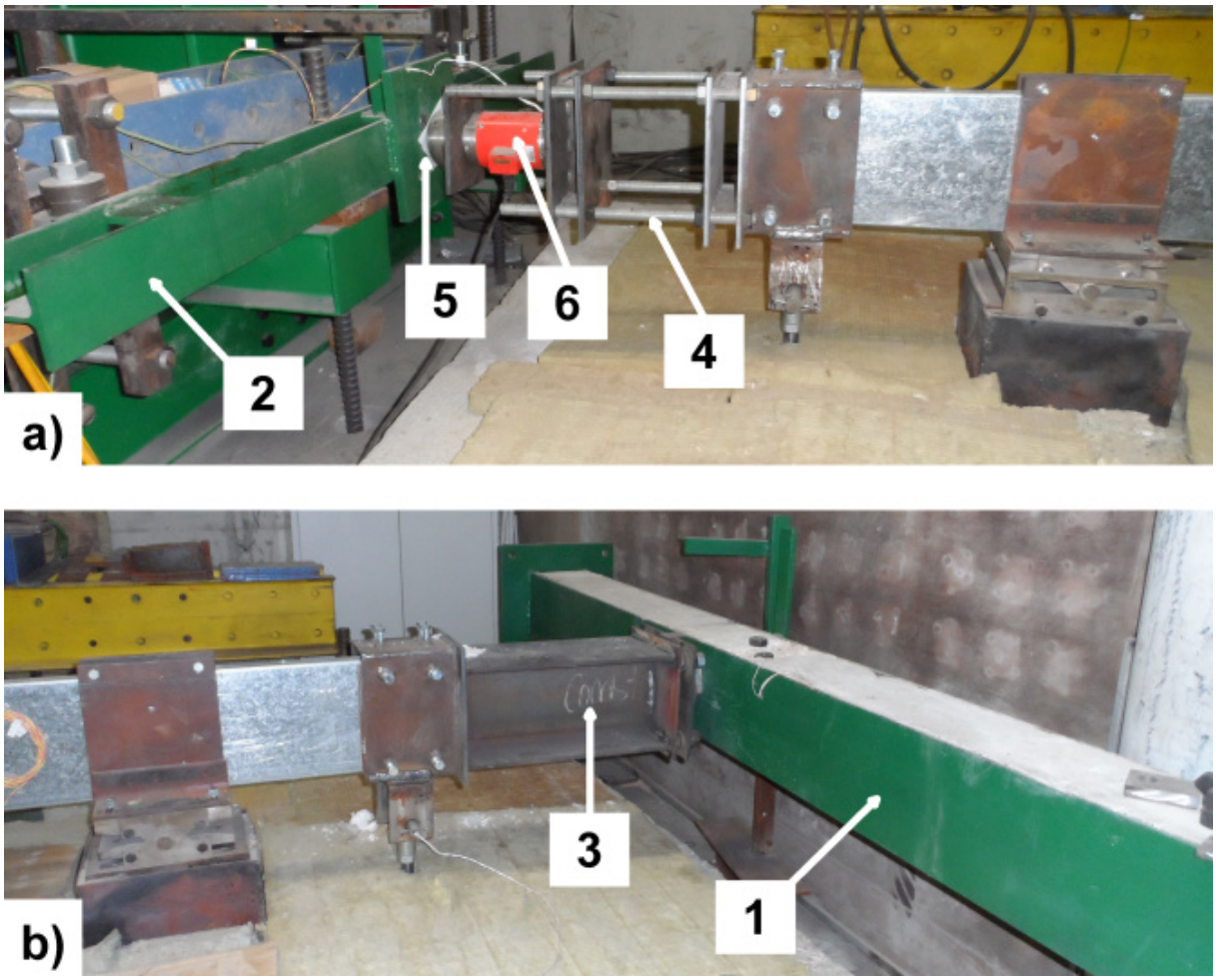

Figure 3.5 – Detail of the axial restraining beams with low (a) and high (b) flexural stiffness

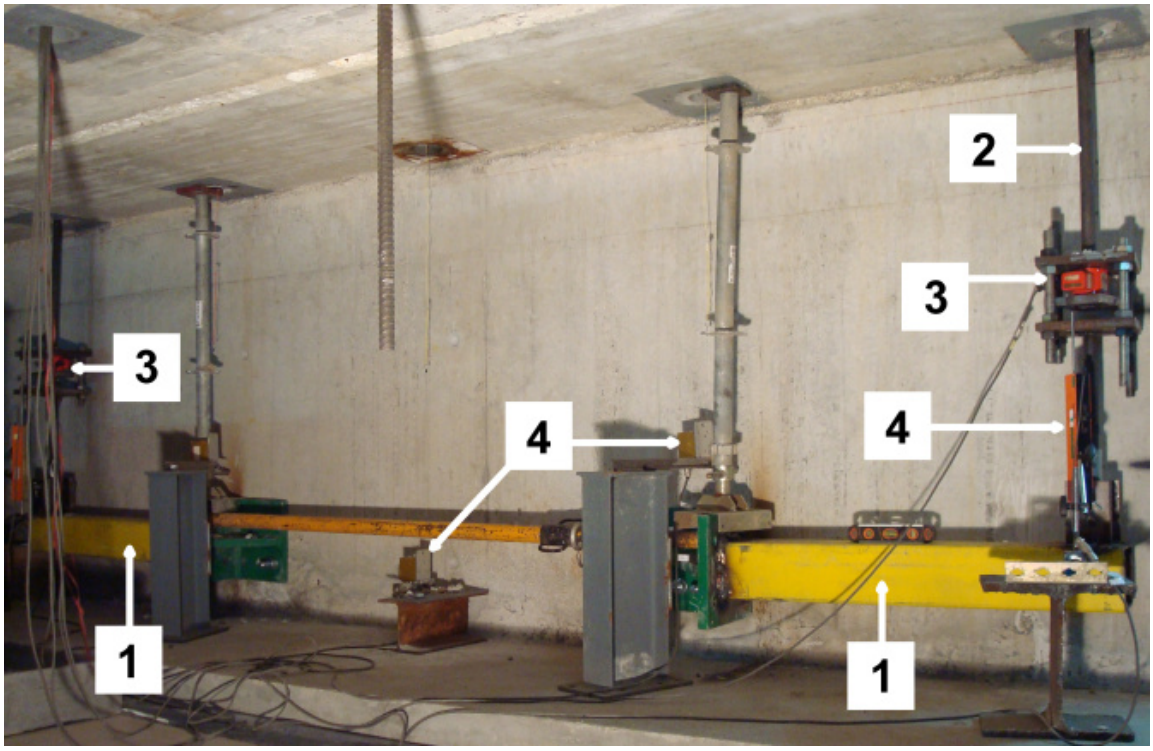

Figure 3.6 – Detail of the rotational restraining system

3.4 Test Plan

3.4.1 Ambient temperature tests

The experimental tests on CFS beams at ambient temperature were conducted in the Laboratory of Testing Materials and Structures (LEME) of the University of Coimbra (UC), in Portugal. The experimental programme consisted of 12 quasi-static bending tests, allowing the study of the flexural behaviour of 4 type of beams with different cross-sections. For each type of beam-specimen, 3 tests were carried out (B-C_*i*, B-I_*i*, B-R_*i* and B-2R_*i*, where *i* stands for the test number, *i* = 1-3), in order to obtain a better correlation of the results. The main objective of this series of tests was to investigate the effects of the section shape (open, closed, single and compound section) on the failure moments and the failure modes of the different beams.

3.4.2 Fire tests

The experimental tests on CFS beams under fire conditions were also conducted in the LEME of the UC, in Portugal. The experimental programme consisted of 36 fire tests, 12 of which

were just simply supported beams, 12 others were the same beams but with restrained thermal elongation, and the others were beams with axial and rotational restraint. So, for each series of 12 fire tests, 3 tests for each type of beam were carried out, in order to obtain a better correlation of the results, as well as at ambient temperature. Note that it was intended to test the same type of specimens that were used for ambient temperature tests, but under high temperatures. This experimental programme is summarized in Table 3.1. For example, the reference B_ka+kr-C_3 indicates the third test (3) of the C (C) beam (B) with axial (ka) and rotational (kr) restraint. The main goal of these series of tests was also to investigate the effects of the section shape and still the influence of the axial and rotational restraint of the surrounding structure to the beam on the critical temperature of the different beams.

Table 3.1 – Test plan for the fire tests

Test reference	$\bar{\lambda}_{LT}$	M_{Rd} (kN.m)	M_{cr} (kN.m)	$M_{b,Rd}$ (kN.m)	$k_{a,b}$ (kN/mm)	$k_{r,b}$ (kN.m/rad)	P_0 (kN)	k_a (kN/mm)	k_r (kN.m/rad)
B-C_1 **B-C_2** **B-C_3**	1.61	15.87	6.09	3.93	61	1984	3.93	0	0
B-I_1 **B-I_2** **B-I_3**	1.22	32.15	21.71	11.88	124	4018	11.88	0	0
B-R_1 **B-R_2** **B-R_3**	0.81	28.93	43.63	16.52	120	3888	16.52	0	0
B-2R_1 **B-2R_2** **B-2R_3**	0.58	57.89	173.10	41.96	241	7814	41.96	0	0
B_ka-C_1 **B_ka-C_2** **B_ka-C_3**	1.61	15.87	6.09	3.93	61	1984	3.93	15	0
B_ka-I_1 **B_ka-I_2** **B_ka-I_3**	1.22	32.15	21.71	11.88	124	4018	11.88	15	0
B_ka-R_1 **B_ka-R_2** **B_ka-R_3**	0.81	28.93	43.63	16.52	120	3888	16.52	15	0
B_ka-2R_1 **B_ka-2R_2** **B_ka-2R_3**	0.58	57.89	173.10	41.96	241	7814	41.96	15	0

B_ka+kr-C_1 **B_ka+kr-C_2** **B_ka+kr-C_3**	1.61	15.87	6.09	3.93	61	1984	3.93	15	150
B_ ka+kr-I_1 **B_ ka+kr-I_2** **B_ ka+kr-I_3**	1.22	32.15	21.71	11.88	124	4018	11.88	15	150
B_ ka+kr-R_1 **B_ ka+kr-R_2** **B_ ka+kr-R_3**	0.81	28.93	43.63	16.52	120	3888	16.52	15	150
B_ ka+kr-2R_1 **B_ ka+kr-2R_2** **B_ ka+kr-2R_3**	0.58	57.89	173.10	41.96	241	7814	41.96	15	150

3.5 Test Procedure

3.5.1 Ambient temperature tests

Four-point bending tests were used to assess the ultimate bending strength of the CFS beams at ambient temperature as well as to check the failure modes responsible for their failure, including local, distortional, global and their interactions. These experiments provided useful results for detailed numerical studies. The load was applied under displacement control, which was controlled by a TML SDP-200D linear variable displacement transducer (LVDT) at a rate of 0.01 mm/s until the specimen failed and reached its unloading stage, where the beam deformation or the lateral rotation of the beam was too large, or the maximum stroke of hydraulic jack was reached. During these tests, the load applied on the beams, the displacements of the beams and supports, as well as, some strains in the beams were measured. Therefore, the instrumentation of the beams included LVDTs for displacement measurements (fig. 3.7) and also TML FLA-6-11 strain gauges for strain measurements (fig. 3.8). Three LVDTs were used to measure the vertical displacements of the beams (no. 2 in fig. 3.7) at three sections (S1, S2 and S3 – fig. 3.2) and two LVDTs to evaluate the lateral rotation of the beam at section S1 (mid-span), as shown in Figure 3.8. A number of strains gauges were also placed around sections S1 and S2 (figs. 3.8 and 3.9) to measure the longitudinal strains and consequently to assess the bending moment in the beams. Lastly, two LVDTs were positioned in each beam support to allow the determination of their rotations (no. 1 in fig. 3.7). The data acquisition was done by a TML data logger, model TDS-530.

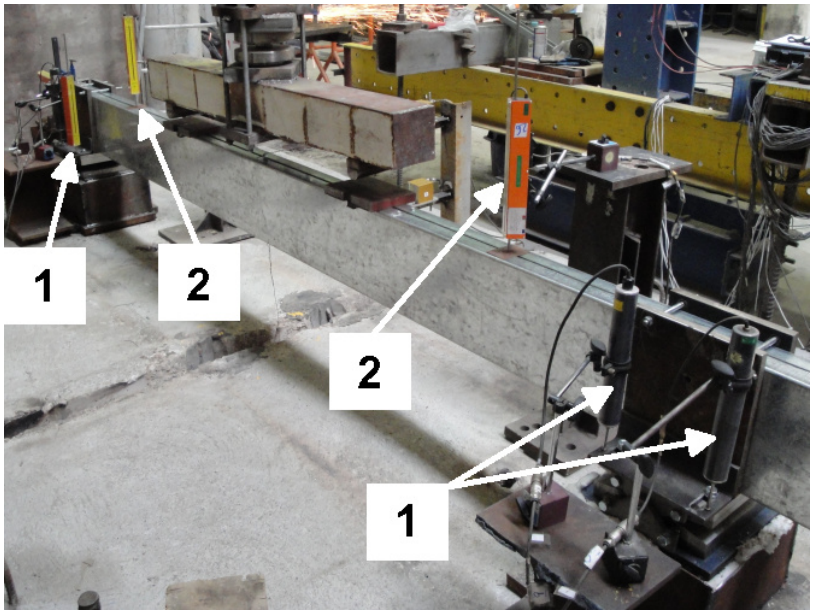

Figure 3.7 – Detail of the beam instrumentation for the displacement measurements at ambient temperature

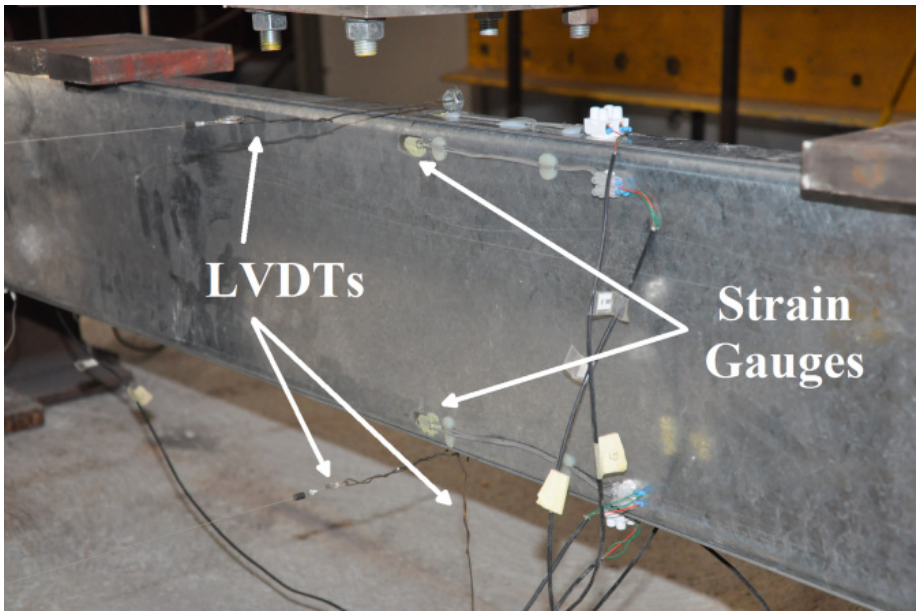

Figure 3.8 – Detail of the beam instrumentation for the strain and displacement measurements at mid-span and at ambient temperature

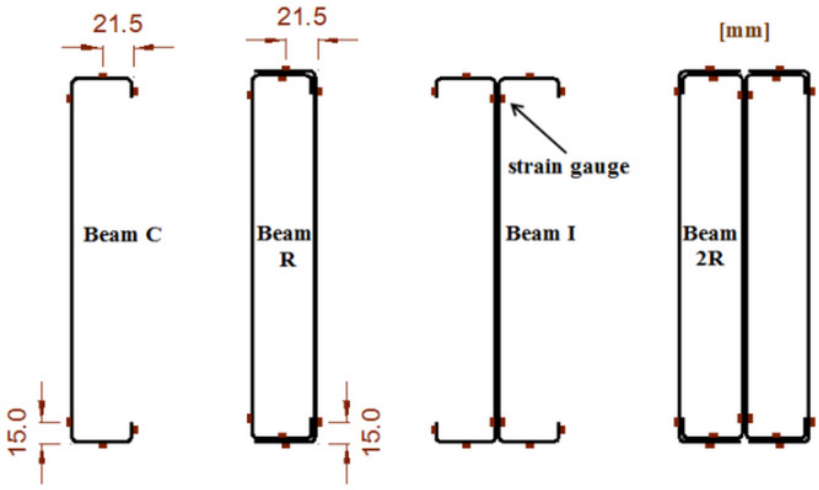

Figure 3.9 – Strain gauge locations in the CFS beams for flexural tests at ambient temperature

3.5.2 Fire tests

To achieve the goals of this investigation, these experimental tests were performed in two stages: loading and heating stage. First, the specimens were loaded up to the target force under load control at a rate of 0.1 kN/s. The load level applied on the beams, P_0, was 50 % of the design value of the load-bearing capacity of the beams at ambient temperature (Table 3.1), and calculated in accordance with the methods proposed in EN 1993-1-1 (2004), EN 1993-1-3 (2004) and EN 1993-1-5 (2006). The reason for the use of this load level lay in the fact that the load level on the structural members of most buildings in accidental situations ranged from approximately 20 to 50 %, and it is supposed that a 50 % load level is on safe side. Hence, the loading intended to simulate the serviceability load of a beam inserted in a real building structure. Finally, the heating stage was started after the desired load was reached. Thus, the specimens were heated up according to a fire curve as near as possible to the standard fire curve ISO 834 (1999), since an electric furnace was used and the initial heating rate of this curve is very difficult for this type of furnace to reproduce. During the heating period, the load was kept constant until the specimen buckled, where the beam deformation was too large or the maximum stroke of hydraulic jack was reached. Although these fire tests did not follow exactly a standard fire resistance test, the failure criteria specified in ISO 834-1 (1999) were adopted, but only for the fire tests of beams without axial restraint to the thermal elongation. This standard says that the resistance of elements subjected to flexural loading depends on the amount of deformation and the rate of deformation (failure criteria in terms of deformation). According to this standard, a flexural member is considered to have failed if the beam deflection is greater than $L^2/(400h)$ mm or the rate of deflection reaches $L^2/(9000h)$ mm/min when the maximum deflection exceeds $L/30$ mm (L and h in mm). Regarding the fire

tests of beams with restrained thermal elongation, the member was considered to have failed when the restraining forces on it returned to the value of the initial applied axial load (which corresponds approximately to zero), in other words, when the deterioration of mechanical properties of steel is so high that the member no longer has any load carrying capacity against the restraining forces (failure criteria in terms of strength). Thus the load applied on the beams, the axial restraining forces, the restraining moments at beam supports, the horizontal and vertical displacements of the beams, as well as, the temperatures in the furnace and at several points of the beams were measured during the tests. The instrumentation of the beams thereby included LVDTs for vertical displacement measurements at sections S1 (mid-span), S2 and S3 (no. 4 in fig. 3.6), and thermocouples for thermal measurements in the furnace and at different points of the specimen's cross-section (fig. 3.10) and at sections S1, S2 and S3 as well. It is noticed that the LVDTs were placed in the basement floor of the Laboratory, below the testing floor, in order to protect them from the high temperatures. The data acquisition was also done by a TML data logger, model TDS-530.

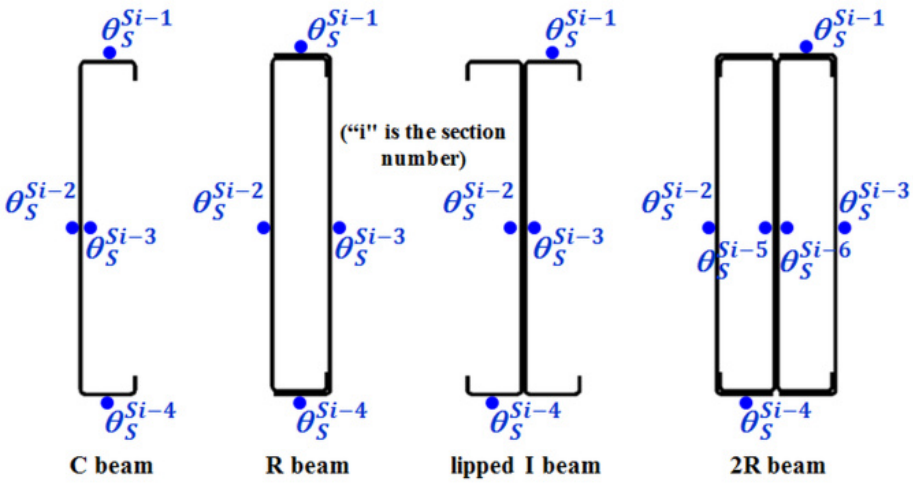

Figure 3.10 – Location of thermocouples in the different cross-sections

3.6 Results and Discussion

3.6.1 Ambient temperature tests

Figure 3.11 shows the load-displacement curves for the tested CFS beams as a function of the vertical displacement at section S1, d_{S1}. It shows the results of the three tests carried out for each type of beam. The quasi-static structural behaviour of the beams (i.e., loading stage, failure load and unloading stage) was identical for all tests of each type of beam. The small differences detected between the load-displacement curves for the same type of beams were

essentially due to the eccentricity of the load applied on the beams and, but slightly less significant, to the geometric and material imperfections in the specimens. An important conclusion to be drawn was that the 2R beams presented a mean ultimate load capacity of 132.32 kN (fig. 3.11d) that is much higher than for the other types of beams tested. In contrast, the mean ultimate load capacity of the C beams was only 11.72 kN (fig. 3.11a). Finally, the lipped I and R beams showed a mean ultimate load capacity of 41.68 and 60.14 kN (figs. 3.11b and 3.11c), respectively. Hence, the maximum load capacity of the lipped I, R and 2R beams was over 3.5, 5 and 10 times higher than the one of the C beam, respectively. From these results it may also be concluded that the use of closed built-up sections (R beams) can increase by 1.45 times the load-carrying capacity of beams comparing to the open sections (lipped I beams). On the other hand, at failure a sharp decay in the load was observed in all compound beams (there was no plastic plateau). One reason for that may be the local or distortional buckling in one profile close to the peak load. Beyond that, the resistance of the beams depended essentially on the remaining resistance of the other beams' profiles. Furthermore but not so relevant in this case, during the unloading stage, some screws in the compressed part of the beams failed in shear, as it can be seen by the discontinuities in some curves in Figures 3.11b and 3.11c.

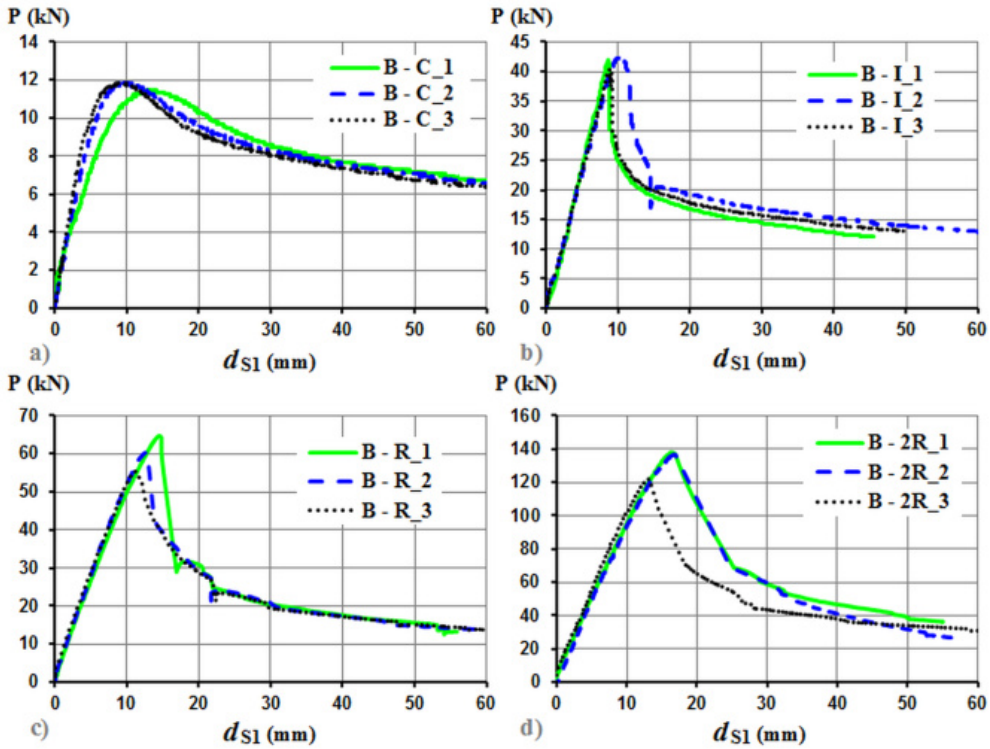

Figure 3.11 – Load-displacement diagrams for the four-point bending tests for the C (a), lipped I (b), R (c) and 2R (d) beams

In what concerns the lateral buckling behaviour of the beams, it can be seen in Figure 3.12 that this one depended on the shape of the beam cross-sections as expected. The relative load (P / P_{max}) applied on the beams is plotted in the vertical axis of the graph and the horizontal axis is plotted against different values of lateral rotation of the respective beam at mid-span. It can be observed that from the beginning of the tests, all the beams except the 2R beams showed immediately lateral rotation at mid-span of the beams (section S1), the C beams being the most affected. For instance, when the load on the beam B-C_2 reached its maximum capacity the lateral rotation at section S1 was already about 12º, whereas for beams B-I_2 and B-R_2 was only 2.5 and 1º (fig. 3.12), respectively. This improved behaviour resulted from the coincidence of the shear centre with the centroid, secondly, from the torsional stiffness of the compound cross-sections and lastly from of the increased thickness of the beam cross-section. It is also important to emphasize that the 2R beams exhibited lateral-torsional buckling, but only after one of their U profiles failed by distortional buckling, as it will be seen later in this thesis.

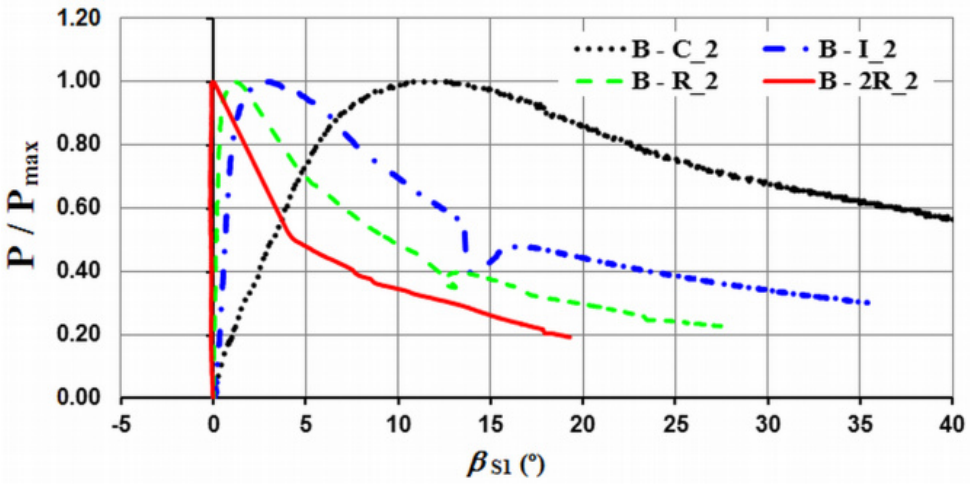

Figure 3.12 – Evolution of the relative loads (P / P_{max}) applied on the beams as a function of the lateral rotation of the beam at mid-span

Figure 3.13 presents, as an example, the rotations of the beam supports during the tests for the B-C_2 and B-R_2 beams (figs. 3.13a and 3.13b, respectively). The rotations of the roller support for test B-C_2 coincided with the rotations of the pinned support, whereas for test B-R_2 the rotations of the two supports only coincided until its maximum load-carrying capacity was reached. This was due to the fact that there has been neither local nor distortional buckling in Beam B-C_2 up to its maximum load-carrying capacity in contrast to the Beam B-R_2 that exhibited local and distortional buckling near the mid-span, closer to the roller support than the pinned support. So, the rotations of the roller support were higher than

the rotations of the pinned support beyond its ultimate capacity (fig. 3.13b). The same conclusions were observed for all lipped I, R and 2R beams (Appendix A) since they all had a complex buckling behaviour, including local, distortional, global buckling and their interactions. Finally, it can also be seen in Figure 3.13 that the rotations of both beam supports were about 0.5º for the beam B-C_2 and 0.6º for the beam B-R_2 at the level of the maximum load.

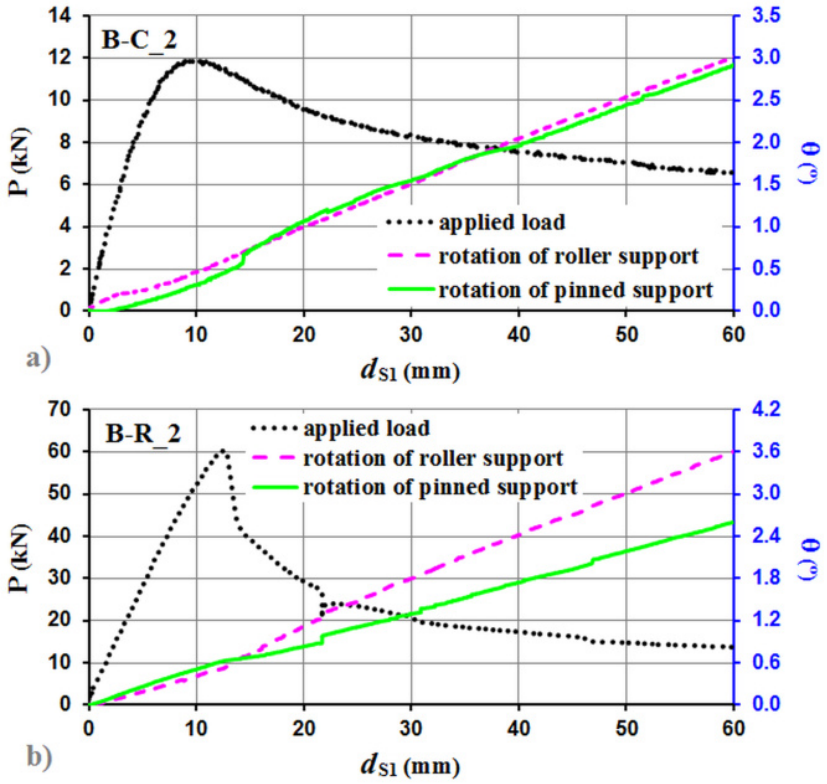

Figure 3.13 – Rotation of the beam supports throughout the tests B-C_2 (a) and B-R_2 (b)

Another important parameter taken into account in this study was the strain evolution in the different cross-sections of the tested beams as a function of the loading applied on them (figs. 3.14 – 3.17). The main conclusion to be drawn was that the compressive and tensile behaviour of the flanges of the closed built-up beams (R and 2 R beams, Figures 3.16 and 3.17) was similar up to the maximum load, in contrast to the open section beams (C and lipped I beams, figs. 3.14 and 3.15). All the readings of the strain gauges placed in the tensile flanges of all beams followed nearly the same tendency during the loading stage, whereas the strain gauges placed in the compressive flanges of the C and lipped I beams showed a non-uniform increase in the strains (figs. 3.14a and 3.15a). While the lateral rotation of the beam at mid-span increased, the compressive strains recorded by the stain gauges placed further apart from the

vertical plane that passed through the geometric centre of the cross-section increased less than the ones recorded by the strain gauges nearer to that plane. Moreover, during the unloading stage some of the strain gauges located further apart from that plane inverted the sign of the strains. Figures 3.14b, 3.15b, 3.16b and 3.17b show that the maximum measured value of tensile strain was 0.067 (ε_5), 0.106 (ε_11), 0.159 (ε_8) and 0.237 % (ε_14) for, respectively, the C, lipped I, R and 2R beams at mid-span and at the maximum load level. On the other hand, the maximum measured value of compressive strain in the same conditions was respectively of -0.113 (ε_1), -0.152 (ε_1), -0.179 (ε_1) and -0.323 % (ε_2) (figs. 3.14a, 3.15a, 3.16a and 3.17a). From these results, it can be observed that the maximum strains varied a lot between the different cross-sections and the respective flanges of the beams. Furthermore, those maximum compressive strains occurred in the flanges for the closed built-up section beams and near the end of the web and in the lip for the C and lipped I beams (open section beams), respectively. On the other hand, all the tensile strains occurred in the flanges of the beams, as expected. It can still be seen clearly by Figure 3.17a that the top surface of one flange of the 2R beam (ε_2) exhibited an elastic-plastic behaviour with a corresponding elastic strain limit of 0.3 %. All this confirms that CFS profiles can be used in a better way, in other words, compound sections can lead to a better use of the material's structural properties and to a delay of the failure modes including local and / or distortional buckling.

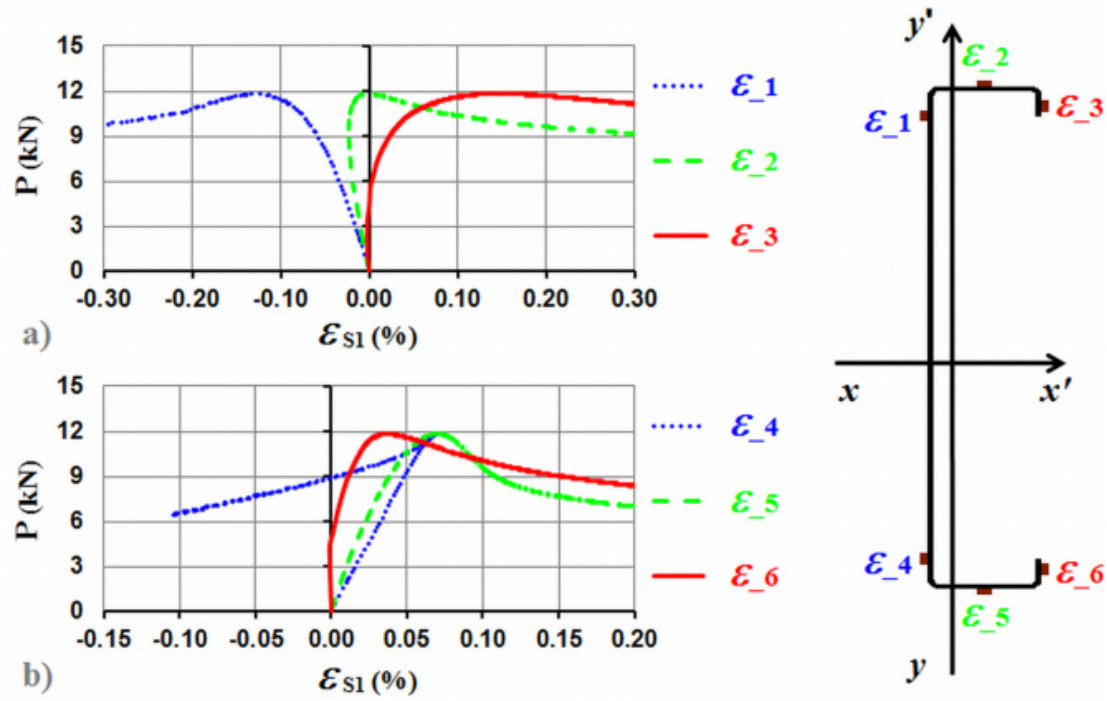

Figure 3.14 – Load-strain curves obtained from the strain gauges which were placed in the compressive (a) and tensile (b) flange of the beam B-C_2 at section S1

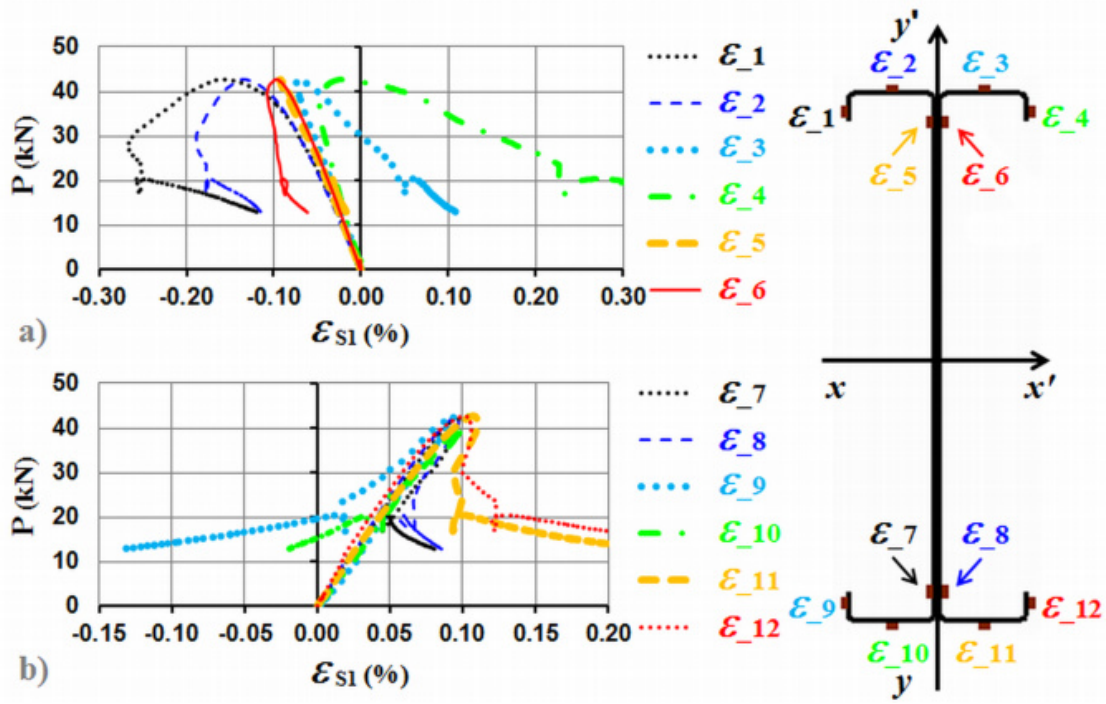

Figure 3.15 – Load-strain curves obtained from the strain gauges which were placed in the compressive (a) and tensile (b) flange of the beam B-I_2 at section S1

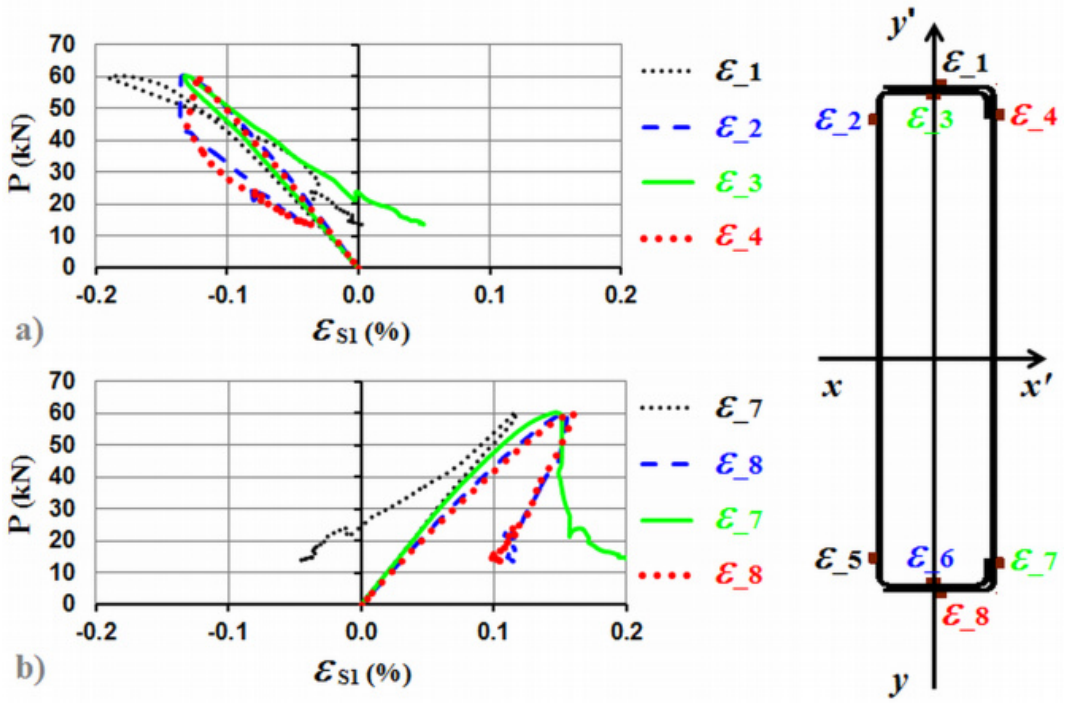

Figure 3.16 – Load-strain curves obtained from the strain gauges which were placed in the compressive (a) and tensile (b) flange of the beam B-R_2 at section S1

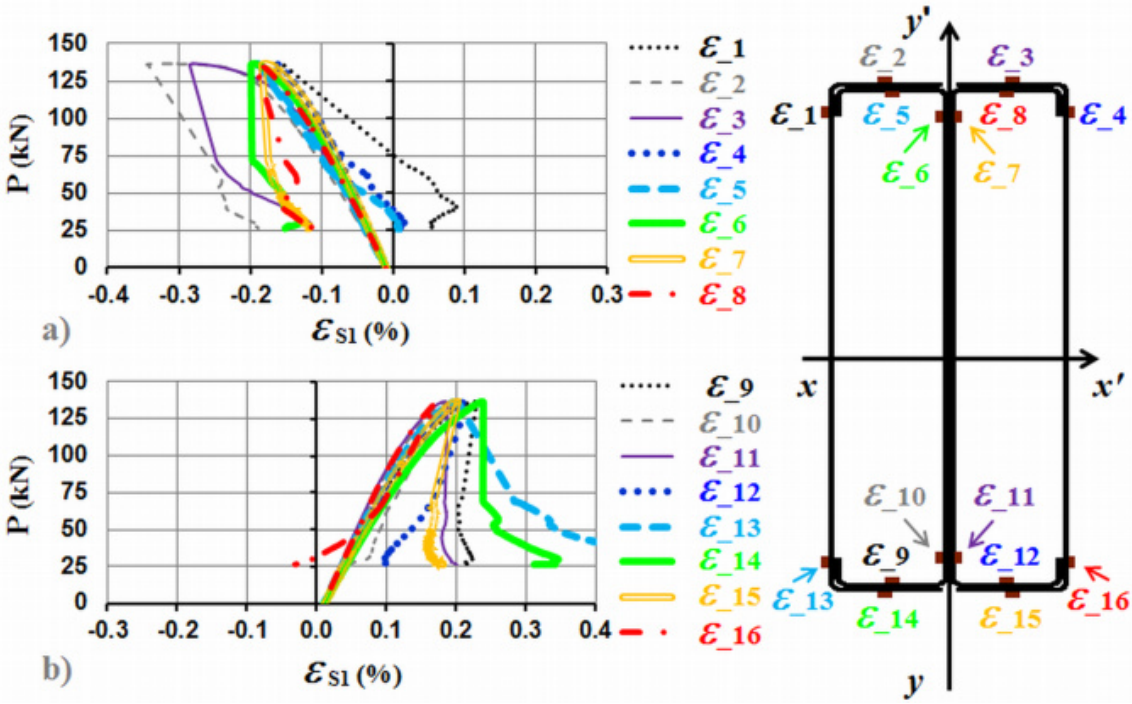

Figure 3.17 – Load-strain curves obtained from the strain gauges which were placed in the compressive (a) and tensile (b) flange of the beam B-2R_2 at section S1

From these strain measurements (S.M.) and assuming that the cold-formed steel of the tested beams reached the yield plateau (fig. 3.18), the bending moments about both the xx' axis and the yy' axis could be calculated. Thus similar moments were also calculated based on classical beam theory (C.B.T.) for comparison (fig. 3.19). Good agreement is noted for both calculations (i.e. between $M_{xx'}$ -S.M. and $M_{xx'}$ - C.B.T. and also between $M_{yy'}$ - S.M. and $M_{yy'}$ - C.B.T.). The C beam was subject to biaxial bending around xx' axis and bending around yy' axis throughout the test while the other beams (I, R and 2R) were approximately under pure bending until their ultimate load-carrying capacity was reached. The reason was that the C beam was the only one in which there was no coincidence between the shear and geometric centres of the cross-section. It is still noticed that the signal change relative to strains (from compression to tension and vice-versa) recorded by some strain gauges (figs. 3.14, 3.15, 3.16 and 3.17) was due to the appearance of this bending moment around the yy' axis ("weak" axis).

All other load-displacement diagrams, load-rotation diagrams, rotations of beam supports and load-strain curves, not presented here but which are also in agreement with the above results, can be seen in Appendix A.

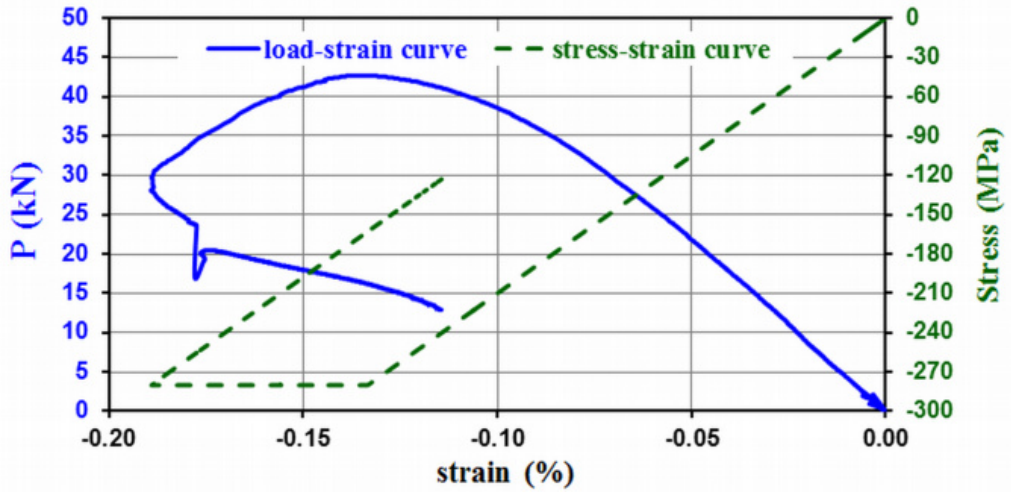

Figure 3.18 – Load-strain and stress-strain curves obtained from the strain gauge ε_2 which was placed in the beam B-I_2 at mid-span

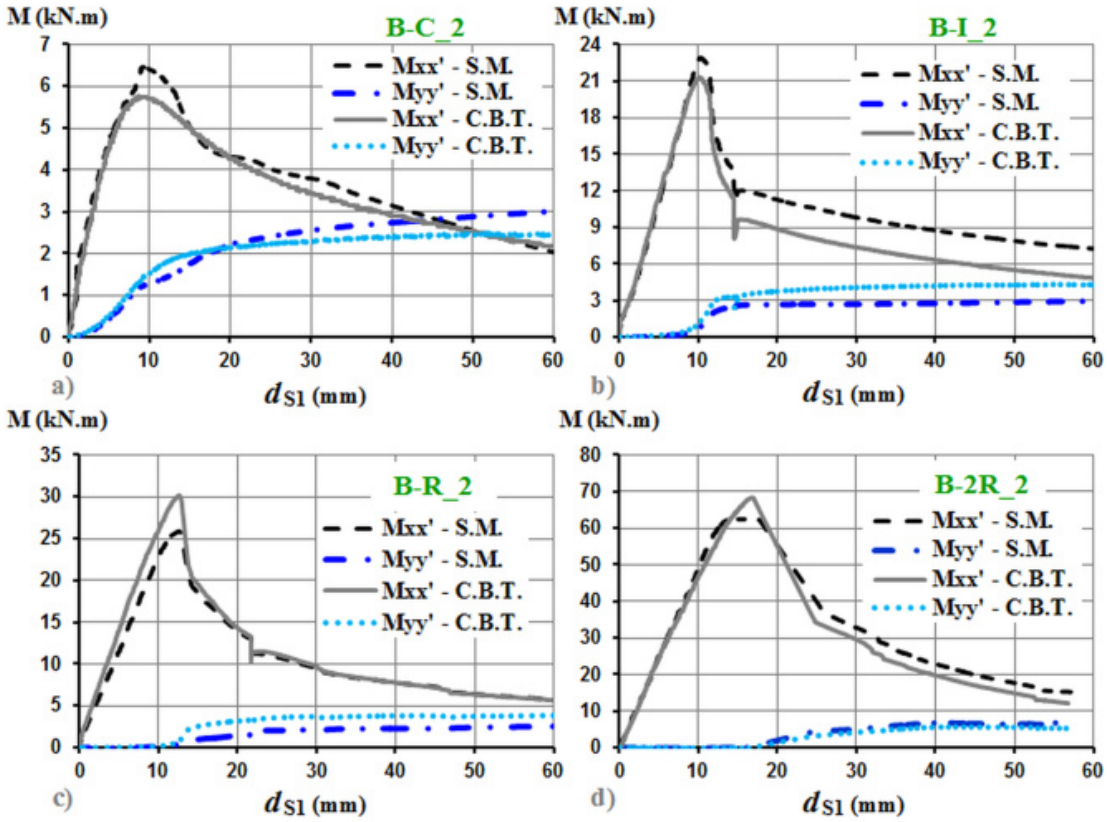

Figure 3.19 – Moment-displacement diagrams recorded during the four-point bending tests for the C (a), lipped I (b), R (c) and 2R (d) beams at ambient temperature

3.6.2 Fire tests

3.6.2.1 Temperature distribution

Figure 3.20 presents the furnace temperatures as a function of time of some fire tests of simply supported beams (fig. 3.20a), of axially restrained beams (fig. 3.20b), of axially and rotationally restrained beams (fig. 3.20c), and of both these cases (fig. 3.20d). The temperatures exhibited a small delay in the initial minutes in relation to the ISO 834 fire curve because this part of the curve is very difficult for an electric furnace to reproduce and this becomes worse for larger furnaces (high initial thermal inertia). However, nine minutes after the beginning of the heating, the furnace temperatures followed the programmed ISO 834 fire curve quite well. Also, the evolution of temperatures inside the furnace over time was very uniform in all fire tests, meaning that the tests are comparable.

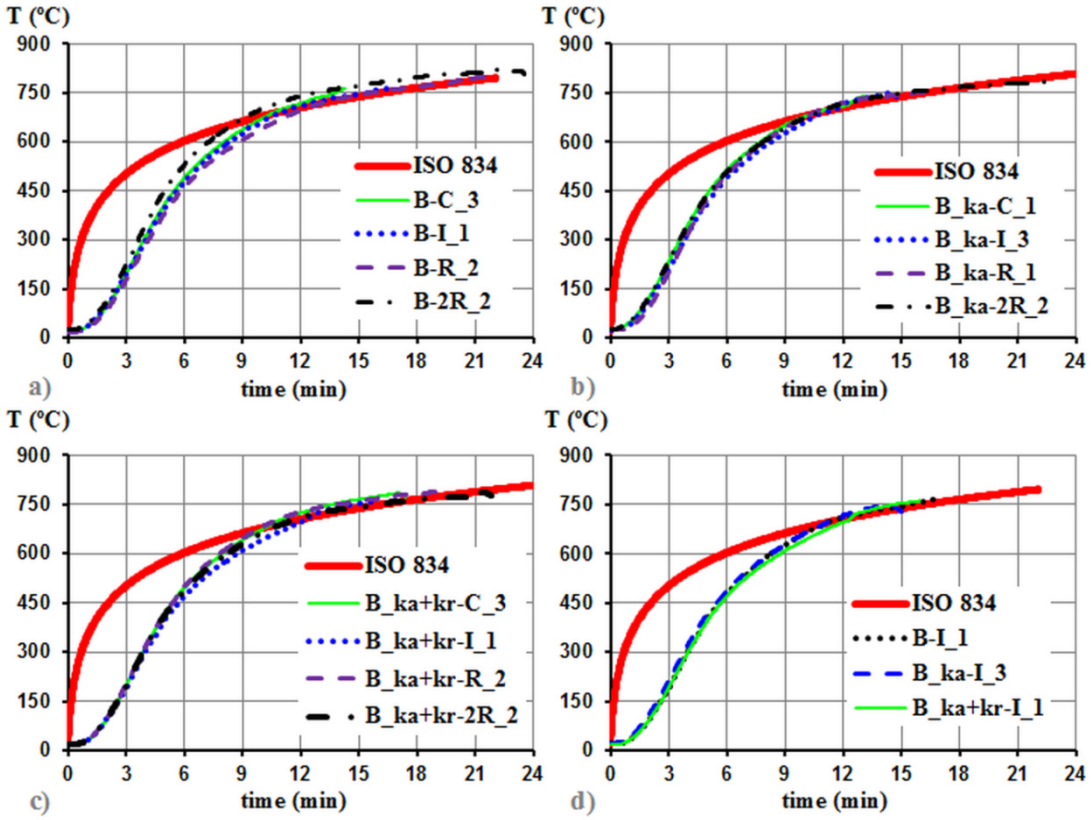

Figure 3.20 – Furnace temperatures in tests on (a) simply supported beams, (b) axially restrained beams, (c) axially and rotationally restrained beams and on lipped I beams with different boundary conditions

Figures 3.21, 3.22, 3.23 and 3.24 show, as an example, the evolution of the temperatures in a cross-section of each type of test beam as well as the furnace temperature and the standard fire curve ISO 834. Each measuring point in the cross-sections was used for assessing an average temperature ($\bar{\theta}_S$), taking into account the influence areas defined by the thermocouples welded to the steel. The temperature in the flanges was considered uniform and in the web it was assumed a linear variation from the centre to the flanges. As a result of this average temperature in each studied cross-section, it was possible to establish the temperature distribution along the beams for different time instants (fig. 3.25) and, consequently, to calculate the mean temperature of the steel beam, $\bar{\theta}_B$, which is the integral of the mean temperatures calculated in each cross-section (fig. 3.26).

The thermocouples seem to show good results: thermocouples θ_S^{Si-1}, θ_S^{Si-4} (which were welded to the flange), θ_S^{Si-2} and θ_S^{Si-3} (which were welded to the web) recorded in general similar temperatures (figs. 3.21, 3.23 and 3.24), as well as the thermocouples θ_S^{Si-5} and θ_S^{Si-6} (which were welded to the inner web) (fig. 3.24). Only small differences were noted, for example, thermocouples θ_S^{S3-1} and θ_S^{S3-4} in the test beam B_ka+kr-I_1 at section S3 measured temperatures higher than thermocouples θ_S^{S3-2} and θ_S^{S3-3} (fig. 3.22), since the web was thicker than the flanges. In addition, the temperatures in the upper flanges of the beams were slightly higher than the ones in the lower flanges (figs. 3.22 and 3.24), because the temperatures inside the furnace slightly increased along the height of the furnace, as it was expected. Note that this was only observed at sections S2 and S3, at section S1 (mid-span) the temperatures in the upper flanges of the beams were slightly lower (fig. 3.23) than it was supposed to be, as a result of the shadow projected by the HEB140 beam (which was above the test beam and allowed to apply the load at two points) onto the upper flanges of the tested beams.

On the other hand, a large thermal gradient was observed from the inner web to the outer webs of the test beam B_ka+kr-2R_3, where the difference between the thermocouples θ_S^{S2-2}, θ_S^{S2-3} and the thermocouples θ_S^{S2-5}, θ_S^{S2-6} was about 250 ºC at the ending of test (fig. 3.24).

It is also important to emphasize that the evolution of temperature depended on the cross-section shape. It is clear that the rate of temperature rise was higher in the open beams than in the closed built-up beams, due to the confined air in the beams which has quite low thermal conductivity and to the fact that only the external sections (U sections in the 2R cross-sections) were directly exposed to radiation. For instance, it took the beams B_ka+kr-C_3, B_ka+kr-I_1, B_ka+kr-R_1 and B_ka+kr-2R_3, 15 minutes to reach about 740, 590, 520 and

450 ºC, respectively (fig. 3.25). When the temperatures in the beams were higher than 150 ºC, the rates of temperature rise in the C, lipped I, R and 2R beams were respectively about 67, 48, 43 and 33 ºC/min (fig. 3.26).

When analysing the graphs in Figure 3.25 it should be pointed out that the temperatures of the steel profile at beam supports was considered uniform and equal to 20 ºC and also that the specimen temperature along its length was assumed to vary linearly between the chosen cross-sections. It is worth remembering that the beams supports were protected by 50 mm layer of ceramic wool to prevent its destruction during all fire tests. However, the temperature of the steel profile between the beam supports and section S2 or S3 may have a minor influence on the beam behaviour at high temperatures since the buckling modes responsible for the collapse of the beams occurred in their central part, including local, distortional and lateral-torsional buckling, as discussed further ahead in this thesis. This led to the fact that the structural performance of the studied beams has been characterized as a function of the mean beam temperature between the sections S2 and S3. For this reason and due to the fact that the thermocouples θ_S^{Si-5} and θ_S^{Si-6} have not been placed in all identical 2R beams, the temperatures recorded by these thermocouples were not taken into account neither in the mean steel temperature, $\bar{\theta}_S$, nor in the mean beam temperature, $\bar{\theta}_B$, also called mean outer steel temperature and mean outer beam temperature, respectively.

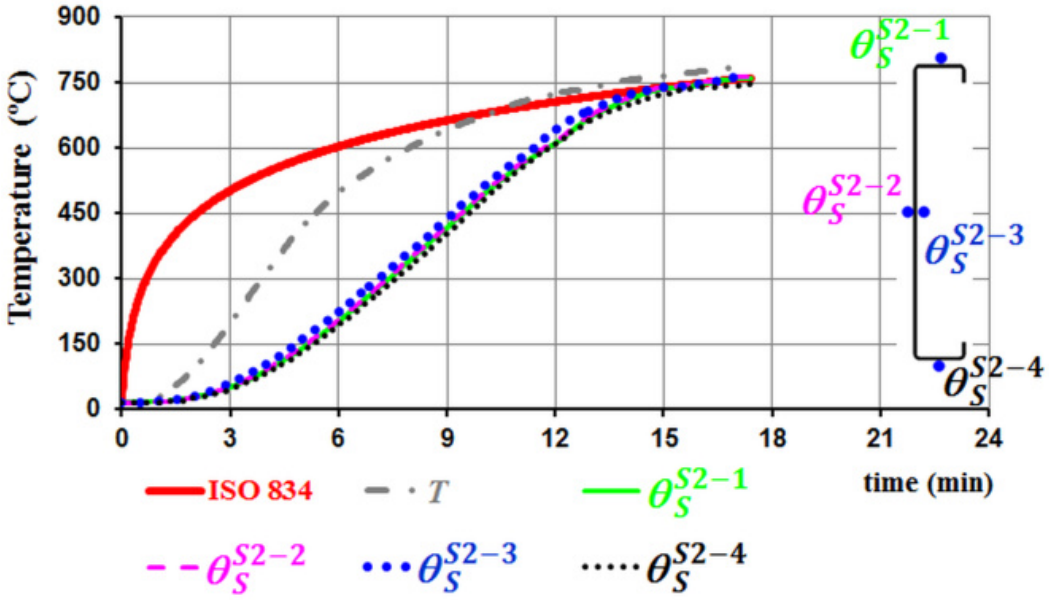

Figure 3.21 – Evolution of temperature in cross-section S2 of the test beam B_ka+kr-C_3 as a function of time

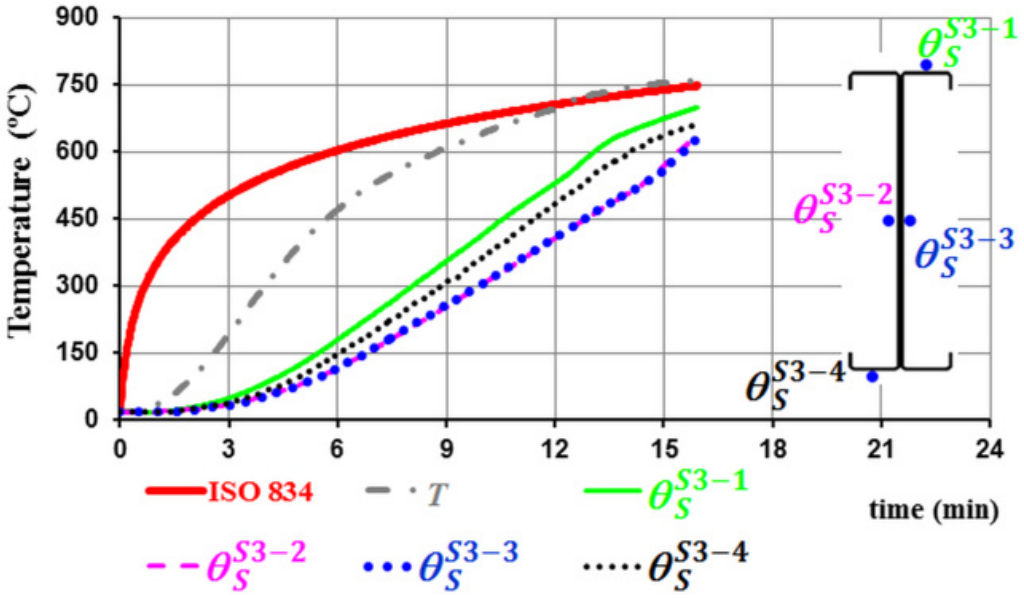

Figure 3.22 – Evolution of temperature in cross-section S3 of the test beam B_ka+kr-I_1 as a function of time

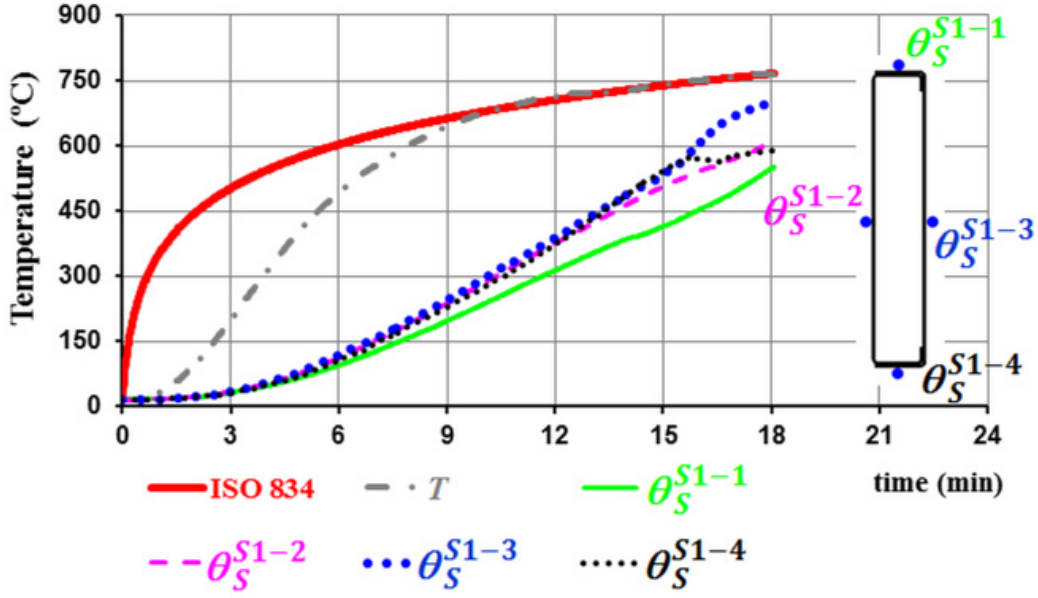

Figure 3.23 – Evolution of temperature in cross-section S1 of the test beam B_ka+kr-R_1 as a function of time

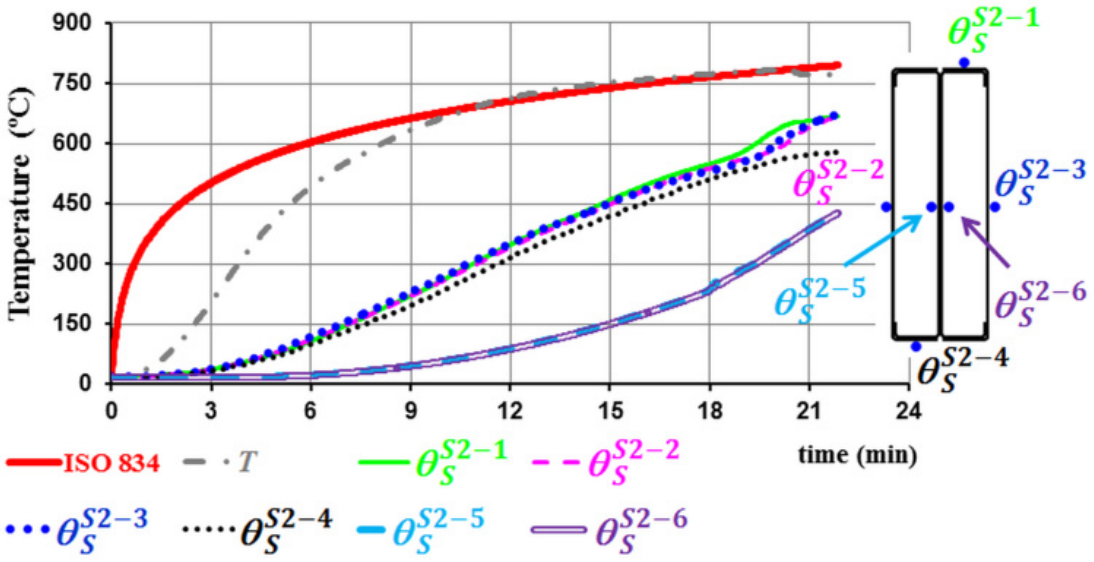

Figure 3.24 – Evolution of temperature in cross-section S2 of the test beam B_ka+kr-2R_3 as a function of time

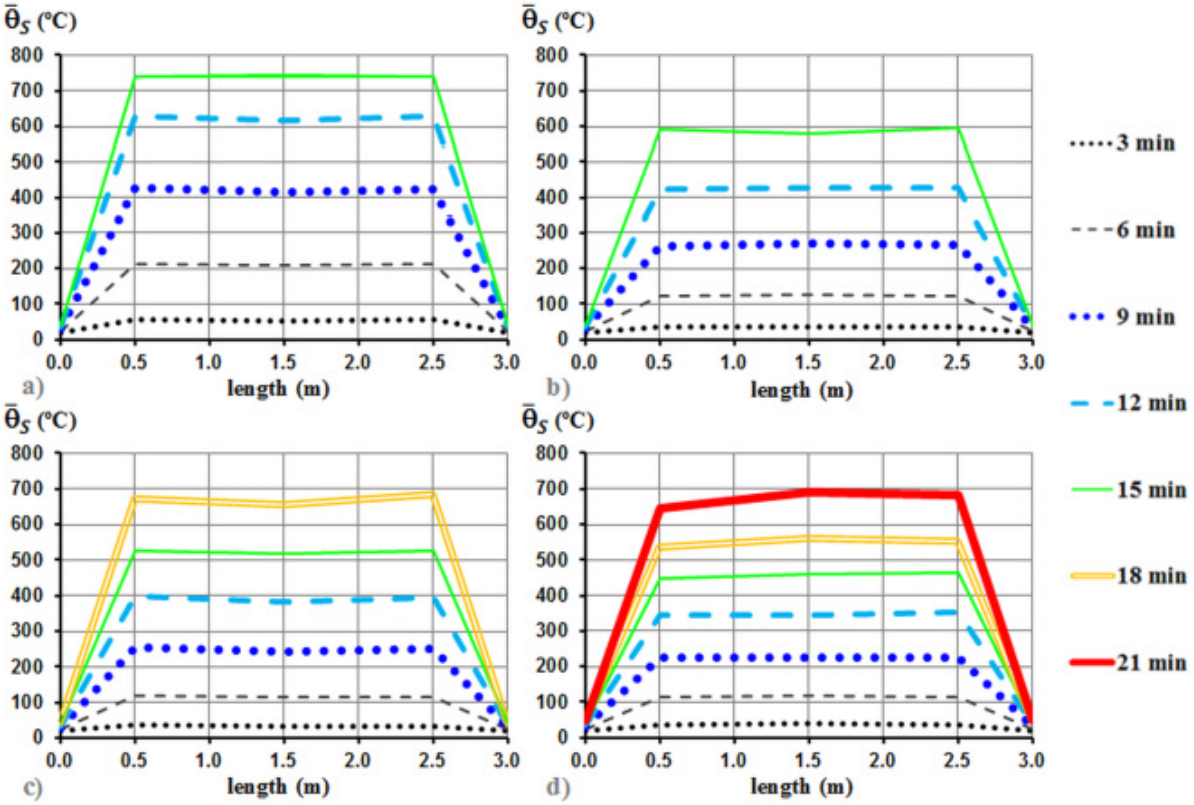

Figure 3.25 – Evolution of temperature in steel along the length of the test beams: (a) B_ka+kr-C_3, (b) B_ka+kr-I_1, (c) B_ka+kr-R_1 and (d) B_ka+kr-2R_3 at different time instants of the fire test

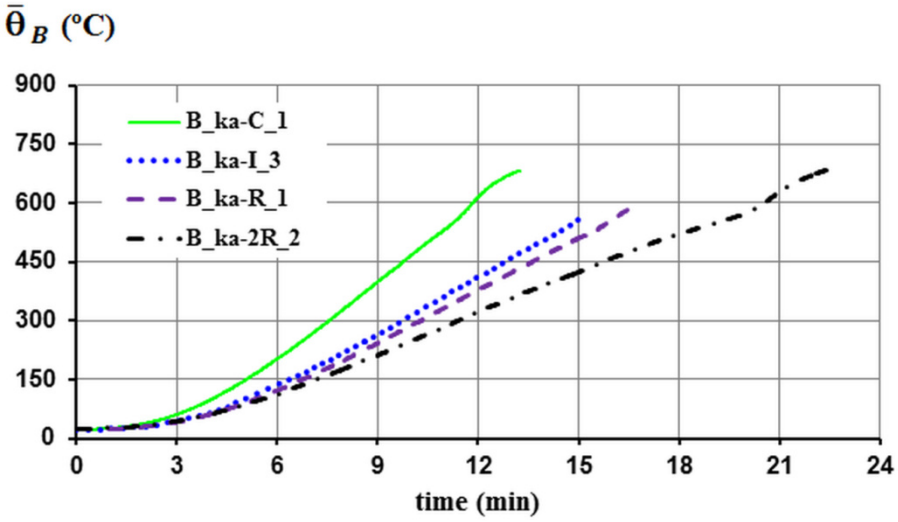

Figure 3.26 – Evolution of temperature in axially restrained beam as a function of time

3.6.2.2 Vertical deflections

Figure 3.27 provides a general idea of how the different kind of beams with different boundary conditions (simply supported, axially restrained and rotationally restrained) might behave as a function of its temperature and in terms of deformation, under fire conditions. It seems that all these simply supported beams under a load level of 50 % of the design value of buckling load of the respective beams at ambient temperature (black dotted line in the graphs) present a critical temperature of about 700 ºC. However, when the beams were axially restrained, the critical temperature of the beams already depended on the cross-section shape. It is obvious that the critical temperature of a beam increases with increasing axial stiffness of the respective beam, $k_{a,b}$, for the same axial stiffness of the surrounding structure, k_a. This can be confirmed in this figure, where it can be seen that the structural resistance of the C, lipped I, R and 2R beams reached its limit for temperatures of about 300, 400, 500 and 650 ºC, respectively (blue dashed line in the graphs). Finally, as it was expected, the rotational restraint (green continuous line in the graphs) slightly improved the fire behaviour of the beams comparing to the beams with just restrained thermal elongation, except for the 2R beams. Once again, similarly to the axial stiffness, the benefits of the rotational restraint to the fire performance of beams are a question of balance between the rotational stiffness of the beam supports, k_r, and the rotational stiffness of the beam, $k_{r,b}$. So, it is interesting to observe that, when a CFS beam is engulfed by a fire (under high uniform temperatures), the axial restraint to the thermal elongation of the beam may significantly reduce its critical temperature, whereas the rotational restraint may be beneficial to the fire resistance of beams. This is further discussed below.

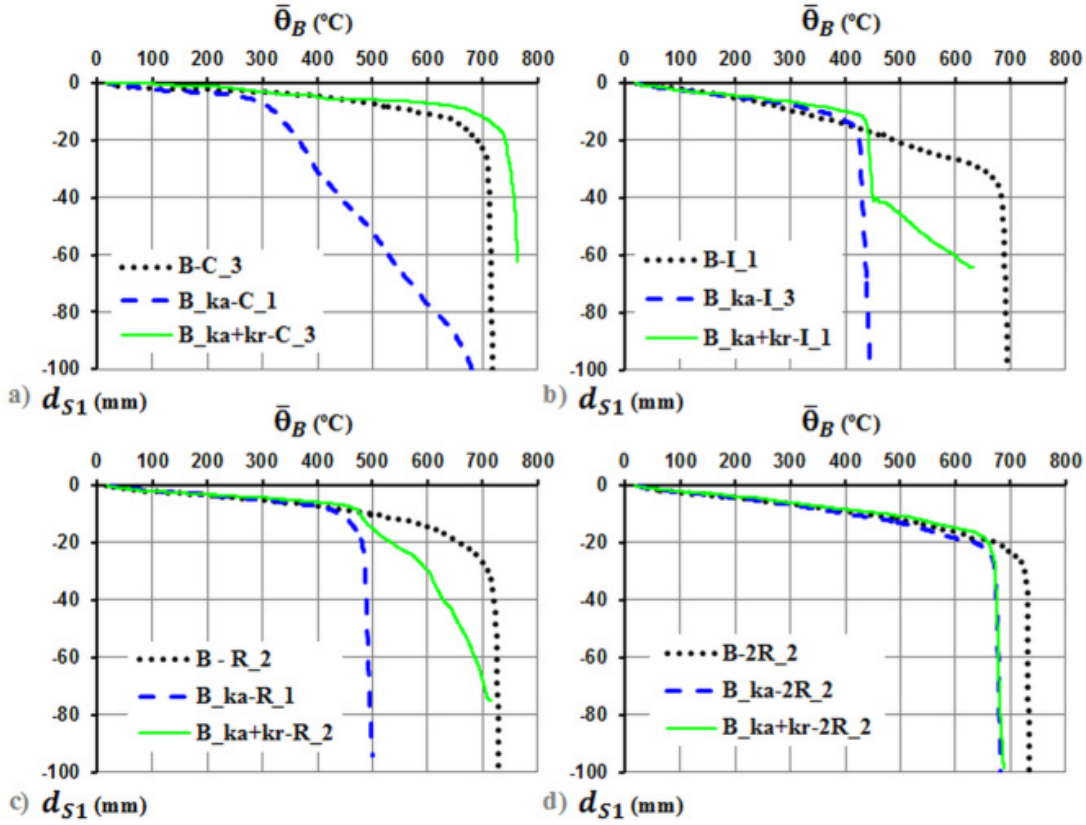

Figure 3.27 – Evolution of vertical deflections at mid-span of the (a) C, (b) lipped I, (c) R and (d) 2R beams as a function of temperature

3.6.2.3 Restraining forces

The evolution of the axial restraining forces generated in beams as a function of temperature for the different cross-sections is depicted in Figure 3.28. These graphs represent the typical behaviour of a real beam under high uniform temperatures and inserted in a building structure, in which it is submitted to restraint to thermal elongation. Due to the effect of the thermal action, the axial force on the beam begins to increase until it reaches a maximum value. After this maximum it begins to decrease due to deterioration of mechanical properties of steel with temperature. The critical temperature is defined in these tests as that at the time when the restraining forces on it returned to the value of the initial applied axial load (failure criteria in terms of strength), as mentioned before. From this figure, it can be again concluded that the critical temperature is affected by the rotational restraint, i.e. it increases with increasing rotational restraint. For instance, a stiffness of the beam supports of 150 kN.m/rad induced an increase in the critical temperature from 513 ºC to 646 ºC for the C beam (fig. 3.28a), from 443 ºC to 567 ºC for the lipped I beam (fig. 3.28b), from 516 ºC to 628 ºC for the R beam (fig.

3.28c) and from 676 ºC to 677 ºC for the 2R beam (fig. 3.28d). It is also important to stress that those differences between the mean temperatures of the respective beams, $\bar{\theta}_B$, were not so high when the maximum restraining force in the beams was reached (i.e., when the maximum flexural and compressive loading was reached). In this particular case, the mean beam temperature, $\bar{\theta}_B$, just increase from 304 ºC to 363 ºC for the C beam (fig. 3.28a), from 411 ºC to 428 ºC for the lipped I beam (fig. 3.28b), from 414 ºC to 446 ºC for the R beam (fig. 3.28c) and from 573 ºC to 597 ºC for the 2R beam (fig. 3.28d).

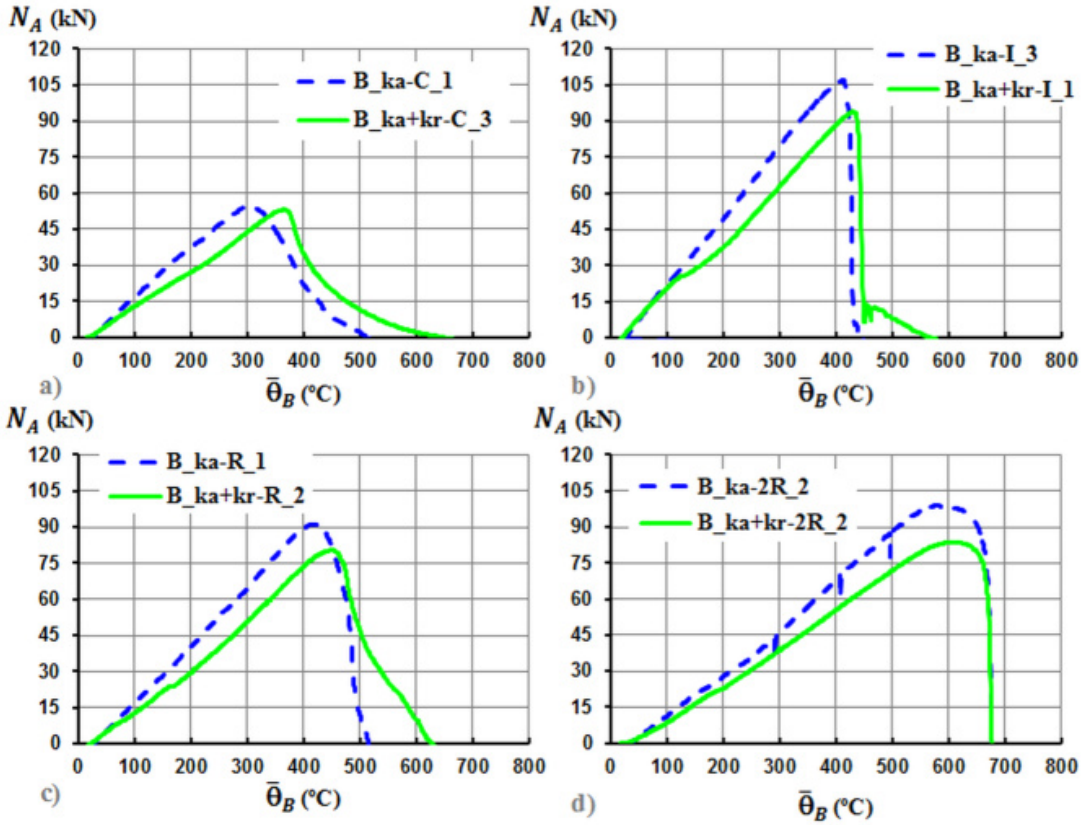

Figure 3.28 – Evolution of axial restraining forces in the (a) C, (b) lipped I, (c) R and (d) 2R beams as a function of temperature

Tables 3.2, 3.3, 3.4 and 3.5 summarize the main results obtained from all fire tests especially the critical time and temperature in terms of deformation and strength. These results can also be seen in Appendix E. First of all, it is worth mentioning that there is an acceptable agreement between the mean temperatures of identical beams with the same boundary conditions, since in most of the cases the coefficient of variation (CV) was less than 10%, except for the lipped I beams with rotational restraint at the beam supports, but only regarding to the temperature in the beam at the time when the maximum restraining force was reached.

One reason for that may be due to the fact that these beams are probably the most sensitive to geometric imperfections, from the universe of tested beams, as it can be seen further ahead in this thesis. Secondly, it is clear that CFS beams exhibited low critical times, less than 30 minutes. However, the simply supported beams showed the best results, as expected, 13.7 minutes for the C beams, 15.9 minutes for the lipped I beams, 20.5 minutes for the R beams and 23.2 minutes for the 2R beams, corresponding to the following critical temperatures of 718, 691, 735 and 731 ºC. Hence, closed built-up beams presented enhanced fire behaviour in relation to the open beams, with no restraint. On the other hand, when 15 kN/mm of axial restraint to the thermal elongation was imposed on beams, their critical temperature dropped significantly in some cases, for instance, from 718 ºC to 529 ºC for the C beams (Table 3.2), from 691 ºC to 443 ºC for the lipped I beams (Table 3.3), from 735 ºC to 504 ºC for the R beams (Table 3.4) and from 731 ºC to 664ºC (Table 3.5), corresponding to a decrease of 26%, 36%, 31% and 9%, respectively. However, when compared with the mean beam temperature corresponding to its maximum restraining force, the temperatures dropped drastically, from 718 ºC to 302 ºC for the C beams (Table 3.2), from 691 ºC to 411 ºC for the lipped I beams (Table 3.3), from 735 ºC to 413 ºC for the R beams (Table 3.4) and from 731 ºC to 595 ºC for the 2R beams (Table 3.5), corresponding to a decrease of 58%, 41%, 44% and 19%, respectively.

In practice, most civil engineering projects using CFS structures do not take into account the rotational stiffness at the ends of beams. However, the findings of this study show that even a small value of rotational stiffness (150 kNm/rad) could increase the critical temperature of the beams, from 529 ºC to 641 ºC for the C beams (Table 3.2), from 433 ºC to 567 ºC for the lipped I beams (Table 3.3), from 504 ºC to 626 ºC for the R beams (Table 3.4), and from 664 ºC to 670 ºC for the 2R beams (Table 3.5) corresponding to an increase of 21%, 28%, 24% and 1%, respectively. Only the critical temperature of the 2R beams seemed not to be affected by the rotational restraining (Table 3.5). One reason for that may be due to the low value of the rotational restraining used for the case of the 2R beams. Another interesting point to note when comparing the critical temperature between all beams in terms of deformations is that the difference between the critical temperatures of the beams with axial and rotational restraining and the simply supported beams would be small; in other words, the critical temperature of the C beams increased just by 7% whereas the critical temperature of the lipped I, R and 2R beams decreased just by 14%, 10% and 7%, respectively. It is worth mentioning that these differences might have been higher if the effect of catenary action had been considered in the test set-up (Liu *et al.*, 2002). It is noticed that the test beams were not connected to the restraining beams, only in contact. Finally, other important thing to conclude from Table 3.3 is that the critical temperature of a beam might be strongly affected by the

axial restraint to the thermal elongation of that beam, even when the axial restraint is very low. For instance, the critical temperature of the lipped I beams dropped from 691 ºC to 544 ºC (21 %) and from 544 ºC to 443 ºC (19 %) when the axial restraining increased respectively from 0 to 3 kN/mm and from 3 kN/mm to 15 kN/mm (Table 3.3).

Figure 3.29 shows the evolution of the axial restraining forces (fig. 3.29a) and the restraining moments (fig. 3.29b) in the test beam B_ka+kr-I_1, for instance. So, it can be confirmed that the axial restraining was about 15 kN/mm and the rotational restraining about 150 kNm/rad. The difference in the axial restraining forces during the increasing and the decreasing of its axial displacement may have been due to the hysteresis phenomenon of the restraining beams, as it was expected.

All other furnace temperatures, mean temperatures in beams, vertical displacements and axial restraining forces in beams as a function of both time and mean temperature of the respective beams, not presented here but which are also in agreement with the above results, can be seen in Appendix E.

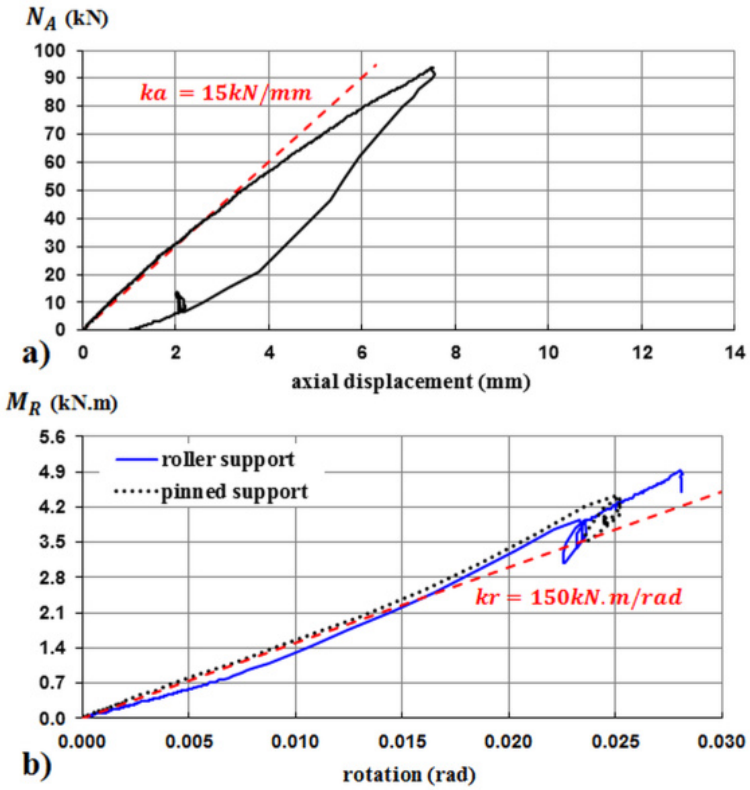

Figure 3.29 – Evolution of the axial restraining forces (a) and the restraining moments (b) in the test beam B_ka+kr-I_1

Table 3.2 – Critical times and temperatures of the C beams

Test reference	Failure criteria in terms of strength				Failure criteria in terms of deformation	
	t_{N_max} (min)	θ_{N_max} (ºC)	t_{cr} (min)	θ_{cr} (ºC)	t_{cr} (min)	θ_{cr} (ºC)
B-C_1	- - -	- - -	- - -	- - -	13.9	710
B-C_2	- - -	- - -	- - -	- - -	13.8	729
B-C_3	- - -	- - -	- - -	- - -	13.5	716
μ	- - -	- - -	- - -	- - -	13.7	718
σ	- - -	- - -	- - -	- - -	0.21	9.7
CV (%)	- - -	- - -	- - -	- - -	1.54	1.34
B_ka-C_1	7.6	304	10.7	513	12.6	656
B_ka-C_2	7.1	281	10.6	519	12.4	661
B_ka-C_3	7.8	323	11.0	554	11.9	604
μ	7.5	302	10.8	529	12.3	640
σ	0.33	20.6	0.17	22.2	0.36	31.6
CV (%)	4.38	6.81	1.61	4.21	2.92	4.94
B_ka+kr-C_1	8.6	365	12.2	629	16.0	763
B_ka+kr-C_2	7.9	324	12.3	647	16.7	775
B_ka+kr-C_3	8.2	363	12.4	646	16.5	766
μ	8.2	351	12.3	641	16.4	768
σ	0.34	23.5	0.06	10.2	0.35	6.4
CV (%)	4.16	6.69	0.49	1.59	2.16	0.83

Table 3.3 – Critical times and temperatures of the lipped I beams

Test reference	Failure criteria in terms of strength				Failure criteria in terms of deformation	
	t_{N_max} (min)	θ_{N_max} (ºC)	t_{cr} (min)	θ_{cr} (ºC)	t_{cr} (min)	θ_{cr} (ºC)
B-I_1	- - -	- - -	- - -	- - -	15.9	693
B-I_2	- - -	- - -	- - -	- - -	16.3	709
B-I_3	- - -	- - -	- - -	- - -	15.5	672
μ	- - -	- - -	- - -	- - -	15.9	691
σ	- - -	- - -	- - -	- - -	0.40	18.5
CV (%)	- - -	- - -	- - -	- - -	2.51	2.67
B_ka-I_1*	13.2	458	14.9	544	15.2	559
B_ka-I_2*	11.3	487	12.2	544	12.4	556
μ	12.3	473	13.6	544	13.8	557
σ	1.38	20.6	1.94	0.5	1.98	2.0
CV (%)	11.25	4.35	14.34	0.09	14.35	0.36
B_ka-I_3	12.0	411	12.7	443	12.7	443
B_ka+kr-I_1	12.0	428	14.7	567	15.1	597
B_ka+kr-I_2	11.1	365	15.1	567	15.4	590
μ	11.5	396	14.9	567	15.3	594
σ	0.70	44.0	0.24	0.2	0.20	5.2
CV (%)	6.02	11.10	1.58	0.04	1.31	0.88

* Tests where the actual axial stiffness was of about 3 kN/mm, instead of 15 kN/mm

Table 3.4 – Critical times and temperatures of the R beams

Test reference	Failure criteria in terms of strength				Failure criteria in terms of deformation	
	t_{N_max} (min)	θ_{N_max} (ºC)	t_{cr} (min)	θ_{cr} (ºC)	t_{cr} (min)	θ_{cr} (ºC)
B-R_1	- - -	- - -	- - -	- - -	20.4	728
B-R_2	- - -	- - -	- - -	- - -	21.2	732
B-R_3	- - -	- - -	- - -	- - -	19.8	745
μ	- - -	- - -	- - -	- - -	20.5	735
σ	- - -	- - -	- - -	- - -	0.71	8.5
CV (%)	- - -	- - -	- - -	- - -	3.48	1.16
B_ka-R_1	12.8	414	15.2	516	14.7	498
B_ka-R_2	13.5	411	15.4	489	15.0	472
B_ka-R_3	12.3	414	13.9	506	13.9	510
μ	12.9	413	14.8	504	14.5	493
σ	0.61	1.9	0.83	13.7	0.54	19.5
CV (%)	4.75	0.46	5.60	2.71	3.69	3.95
B_ka+kr-R_1	13.5	459	16.4	595	17.1	630
B_ka+kr-R_2	13.6	446	17.5	628	18.6	673
B_ka+kr-R_3	13.3	450	17.5	656	18.2	690
μ	13.5	452	17.1	626	18.0	664
σ	0.19	6.8	0.61	30.5	0.78	31.0
CV (%)	1.39	1.51	3.55	4.86	4.33	4.66

Table 3.5 – Critical times and temperatures of the 2R beams

Test reference	Failure criteria in terms of strength				Failure criteria in terms of deformation	
	t_{N_max} (min)	θ_{N_max} (ºC)	t_{cr} (min)	θ_{cr} (ºC)	t_{cr} (min)	θ_{cr} (ºC)
B-2R_1	- - -	- - -	- - -	- - -	22.4	715
B-2R_2	- - -	- - -	- - -	- - -	22.7	732
B-2R_3	- - -	- - -	- - -	- - -	24.3	744
μ	- - -	- - -	- - -	- - -	23.2	731
σ	- - -	- - -	- - -	- - -	1.02	14.6
CV (%)	- - -	- - -	- - -	- - -	4.41	2.00
B_ka-2R_1	21.1	622	23.0	696	23.1	699
B_ka-2R_2	20.0	573	22.1	676	22.3	681
B_ka-2R_3	17.6	591	18.5	620	18.6	622
μ	19.6	595	21.2	664	21.3	667
σ	1.80	24.5	2.38	39.1	2.42	40.2
CV (%)	9.20	4.11	11.21	5.89	11.35	6.02
B_ka+kr-2R_1	19.3	615	20.7	675	20.9	682
B_ka+kr-2R_2	19.4	597	21.0	677	21.3	684
B_ka+kr-2R_3	18.8	579	20.5	659	21.0	674
μ	19.2	597	20.7	670	21.1	680
σ	0.35	18.3	0.29	9.8	0.23	5.2
CV (%)	1.81	3.06	1.42	1.46	1.11	0.77

3.7 Failure Mode Analysis

3.7.1 Ambient temperature tests

Figures 3.30, 3.31, 3.32 and 3.33 illustrate respectively the experimental failure modes of the test beams B-C_3, B-I_3, B-R_2 and B-2R_1 under flexural loading conditions. Figures of identical failure modes of the other tested beams are presented in Appendix B. The local, distortional and lateral-torsional buckling modes that were responsible for collapse of the beams are clearly identified.

It was possible to observe that distortional buckling was the main failure mode responsible for the collapse of the compound beams. It was noticed that the 2R beams started to slightly rotate laterally in one direction, reversing its rotation as distortional buckling occurred on the most affected U profile (fig. 3.33). In addition, failure of the web of the R beam only occurred after the distortional buckling of the U profile, as well as in the 2R beams (Appendix B). Increase of the lateral rotation of the beam further increased the local buckling of the web (fig. 3.32). It cannot be forgotten that the maximum load of the R beams was about half load of the 2R beams and if the local buckling was the main failure mode responsible for the collapse of the beam, that difference would be higher. The distortional buckling always occurred nearer to the roller support of the beams rather than in mid-length of the specimens since the other beam support (pinned support) could not move. Finally, the lateral-torsional buckling was the main failure mode responsible for the collapse of the C and lipped I beams (figs. 3.30 and 3.31). The distortional buckling of the compression flange of the lipped I beams occurred due to the loading conditions which avoided the free rotation of the flanges during the tests.

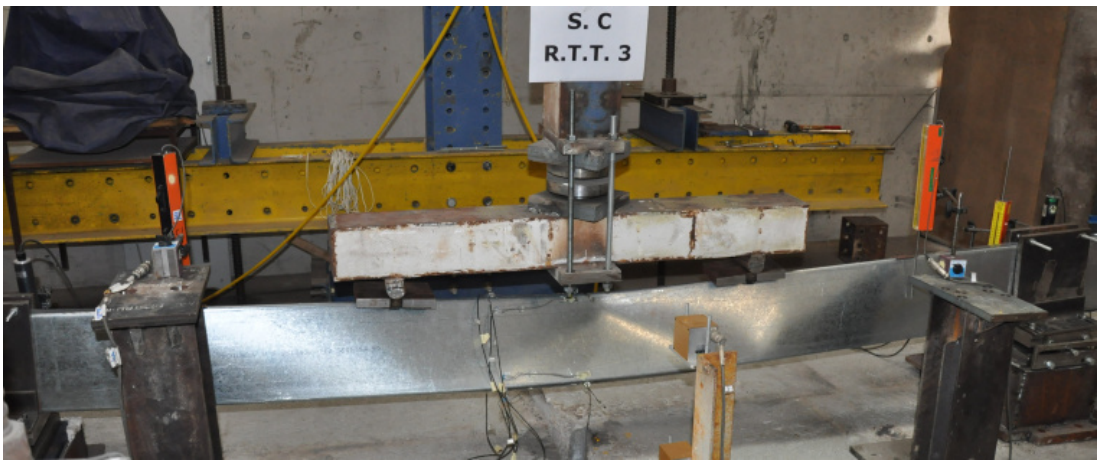

Figure 3.30 – Failure modes of the test beam B-C_3 at ambient temperature

Figure 3.31 – Failure modes of the test beam B-I_3 at ambient temperature

Figure 3.32 – Failure modes of the test beam B-R_2 at ambient temperature

Figure 3.33 – Failure modes of the test beam B-2R_1 at ambient temperature

3.7.2 Fire tests

The main observation made after the fire tests of simply supported beams was that their failure modes (figs. 3.34, 3.35, 3.36 and 3.37) were similar to the ones observed in the identical test series at ambient temperature. As example, Figures 3.34, 3.35, 3.36 and 3.37 illustrate respectively the failure modes of the test beams B-C_3, B-I_1, B-R_3 and B-2R_2 under fire conditions. Figures of identical failure modes of the other tested beams are presented in Appendix F.

As well as at ambient temperature, it is understandable that lateral-torsional buckling was the main failure mode responsible for the collapse of the open sections (C and lipped I beams) and the distortional buckling for the collapse of the closed built-up sections (R and 2R beams). It can still be seen that after the lateral-torsional buckling on the test beam B-C_3 (fig. 3.34), in other words, when the deformation of the beam was too high, a local buckling half-wave began to emerge at mid-span and a distortional buckling half-wave appeared on the upper flange of the beam near both beam supports. Regarding the lipped I beam, a distortional buckling half-wave also appeared on the compression flange of the beam and in the middle of its length (fig. 3.35) during the lateral-distortional buckling of the respective beam, since the loading conditions avoided the free rotation of the flange during the lateral rotation of the beam. A local buckling half-wave also occurred on the C section of the R beam in the middle of its length (fig. 3.36) after the distortional buckling on the U section and consequently after the lateral-torsional buckling of the R beam. It is quite interesting to observe that one or two distortional buckling half-waves may appear on the U section of the 2R beam (fig. 3.37).

Afterwards, multiple local buckling half-waves along the beam length occurred on the opposite U section as well as a distortional buckling half-wave near both beam supports, like it happened to the C beam (fig. 3.34). Note that this can be better seen in Figure 3.41. Although only the final shape of the beam could be observed since the fire tests were performed inside the horizontal modular electric furnace, the authors think that the 2R beams started to slightly rotate laterally in one direction, reversing its rotation as distortional buckling occurred on the most affected U profile like it happened at ambient temperature.

Figure 3.34 – Failure modes of the test beam B-C_3 under fire conditions

Figure 3.35 – Failure modes of the test beam B-I_1 under fire conditions

Figure 3.36 – Failure modes of the test beam B-R_3 under fire conditions

Figure 3.37 – Failure modes of the test beam B-2R_2 under fire conditions

The failure modes of the beams with just axial restraint were similar to the simply supported beams, except the R beam which it was similar to the R beam with rotational restraint (fig. 3.40). This is why their final configuration is not presented here, but in Appendix F. On the other hand, in what concerns to the final configuration of the deformed C, lipped I, R and 2R beams with rotational restraint, some differences were observed comparing with the simply supported beams. The effect of the torsion was clearly higher than the effect of the lateral buckling on the beams with rotational restraint at their supports, as expected. This was the reason for the appearance of further local and distortional buckling modes on some beams;

especially on the open section beams (figs. 3.38 and 3.39). Firstly, it is worth pointing out that the C and R beams underwent lateral-torsional buckling, but they rotated on the opposite direction of the same kind of tested beams with no restraint to thermal elongation. This may be due to the axial restraining force generated in beams. As a result, the final shape of the failed C beam displayed a distortional buckling half-wave near the mid-span on the upper flange and near the beam supports on the lower flange with different directions, i.e., with inward and outward flange (fig. 3.38). The same was confirmed in the lipped I beams, but the distortional buckling modes on the lower flanges presented the same direction (outward) (fig. 3.39). Concerning the R beams, after the lateral-torsional buckling, a distortional buckling half-wave began to emerge near the beam supports on both flanges (lower and upper flanges), as it can be seen in Figure 3.40. Finally, there was no difference between the test beams B_ka+kr-2R_2 and B-2R_2 (figs. 3.37 and 3.41), because the rotational restraint of the beam supports may have been too low in relation to the rotational restraint of the beam. To sum up, CFS beams can fail in a variety of buckling modes including local, distortional and global (lateral-torsional) buckling both at ambient temperature and at high temperatures. However, in general it seems that the failure modes become more complicate in CFS members with complex boundary conditions.

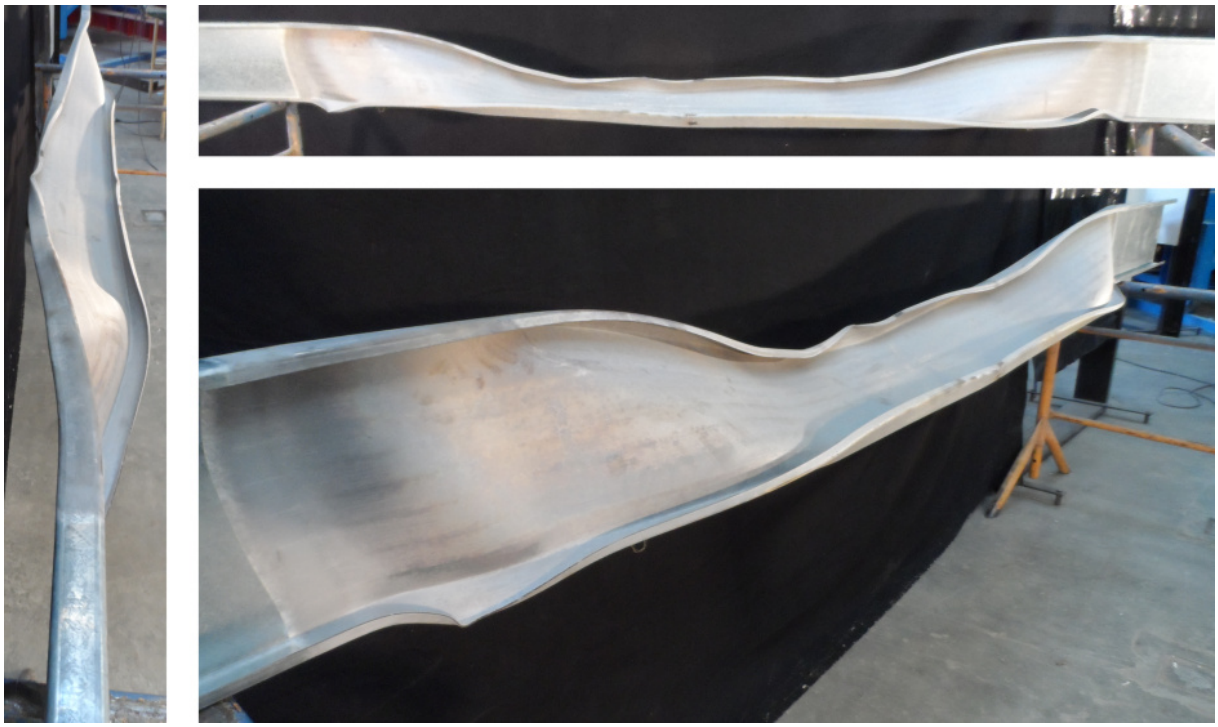

Figure 3.38 – Failure modes of the test beam B_ka+kr-C_3 under fire conditions

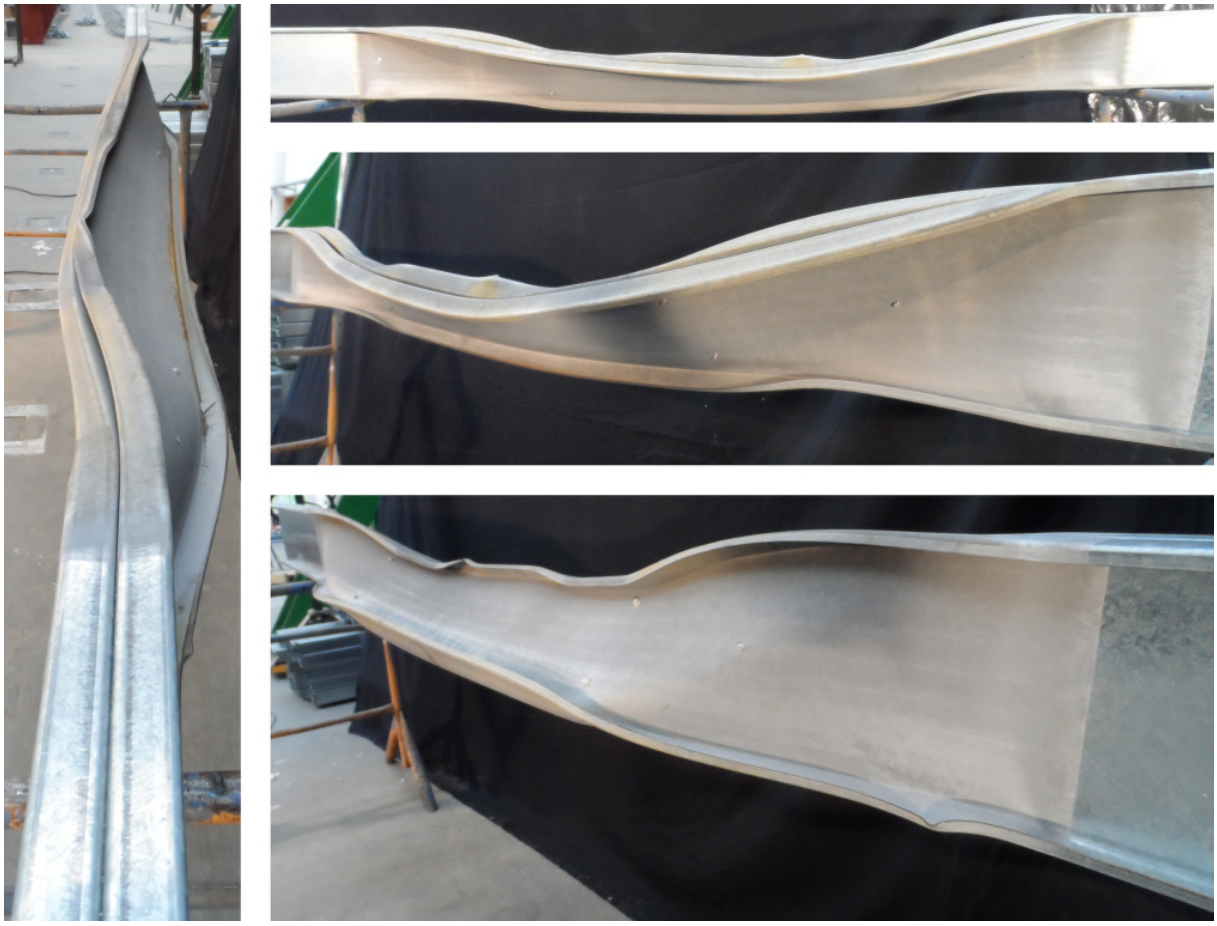

Figure 3.39 – Failure modes of the test beam B_ka+kr-I_2 under fire conditions

Figure 3.40 – Failure modes of the test beam B_ka+kr-R_2 under fire conditions

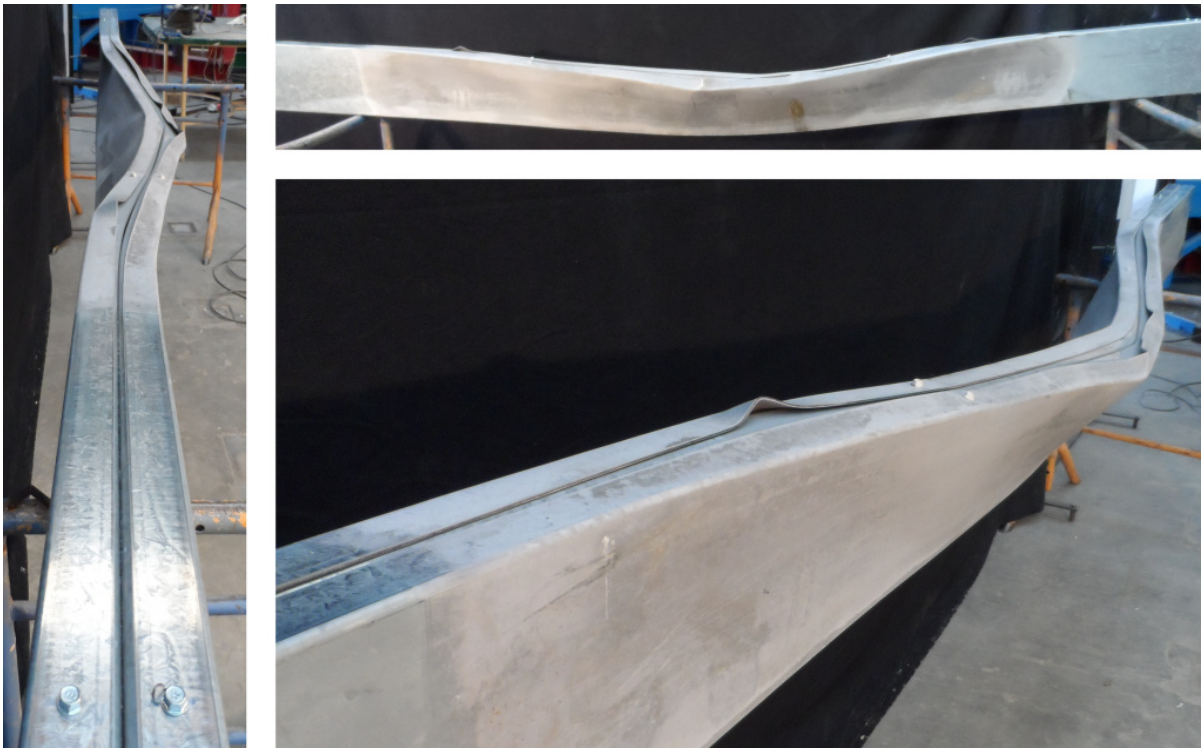

Figure 3.41 – Failure modes of the test beam B_ka+kr-2R_2 under fire conditions

3.8 Final Remarks

This chapter dealt with the experimental modelling of CFS beams at ambient temperature and in case of fire. The experimental research was performed with the main goal of studying the influence of section shape, axial restraint to the thermal elongation of beam and of rotational restraint of beam supports on the fire performance of CFS beams. The buckling modes responsible for the collapse of the beams were also investigated.

The main conclusions of this research study were that the CFS beams commonly used in this kind of buildings may have a quite low fire resistance (less than 30 minutes). However, the built-up hollow sections (R and 2R beams) showed a significantly enhanced fire behaviour than the open sections (C and lipped-I beams). The hollow section beams may have an increase about 50% in the fire resistance, comparing with the open section beams. The use of two or more profiles in a beam can increase its strength-to-weight ratio at ambient temperature, as well.

On the other hand, the critical temperature of beam may drop significantly (30% in some cases) with the axial restraint to thermal elongation of the beam. This decreasing is however

minimized when the rotational restraint at beam supports is relevant comparing with rotational stiffness of the beam (the critical temperature may increase around 20%, comparing with the same beams, but just axially restrained).

It was also possible to observe that the lateral-torsional buckling was also the main failure mode responsible for the collapse of the open beams and the distortional buckling the main failure mode responsible for the collapse of the closed built-up beams. However, in general it seems that the failure modes become more complicate in CFS beams with complex boundary conditions.

4 NUMERICAL MODELLING OF COLD-FORMED STEEL BEAMS

4.1 Introduction

ABAQUS (ABAQUS Analysis – User's Manual, 2010) was developed by "Hibbitt, Karlsson & Sorensen, Inc" of Providence, Rhode Island, USA, founded in 1978, due to its strong capabilities in dealing with nonlinear problems. It seems to be the most widely used software in the academic research of material and geometric nonlinear analysis due to the flexibility that it provides for the users with numerous options for materials models, analysis and solutions techniques. ABAQUS is a suite of powerful engineering simulation programs, based on the finite element method that can solve problems ranging from relatively simple linear analyses to the most challenging nonlinear simulations. ABAQUS contains an extensive library of elements that can model virtually any geometry. It has an equally extensive list of material models that can simulate the behaviour of most typical engineering materials including metals, rubber, polymers, composites, reinforced concrete, crushable and resilient foams, and geotechnical materials such as soils and rock. Designed as a general-purpose simulation tool, ABAQUS can be used to study more than just structural (stress/displacement) problems. It can simulate problems in such diverse areas as heat transfer, mass diffusion, thermal management of electrical components (coupled thermal-electrical analyses), acoustics, soil mechanics (coupled pore fluid-stress analyses), and piezoelectric analysis. ABAQUS offers a wide range of capabilities for simulation of linear and nonlinear applications. In a nonlinear analysis ABAQUS automatically chooses appropriate load increments and convergence tolerances and continually adjusts them during the analysis to ensure that an accurate solution is obtained efficiently. ABAQUS/CAE (Complete ABAQUS Environment) is an interactive, graphical environment for ABAQUS. It allows models to be created quickly and easily by producing or importing the geometry of the structure to be analysed and decomposing the geometry into meshable regions. Physical and material properties can be assigned to the geometry, together with loads and boundary conditions. ABAQUS/CAE contains very powerful options to mesh the geometry and to verify the resulting analysis model. Once the model is complete, ABAQUS/CAE can submit, monitor, and control the analysis jobs. Finally, the Visualization module can then be used to interpret the results.

To sum up, the finite element program ABAQUS is a powerful computational tool for modelling structures with material and geometric nonlinear behaviour. Hence, ABAQUS

version 6.10-1 (ABAQUS Analysis – User's Manual, 2010) was used extensively by the author to simulate the behaviour and strength of cold-formed steel (CFS) beams under flexural loading conditions and under combined bending and fire conditions. The numerical results were thereby compared with those given by the experimental tests in order to validate the developed finite element model and consequently to use it for a parametric study outside the bounds of the original experimental tests. All parameters, considerations and assumptions took into account in the developed three-dimensional nonlinear finite element model to predict the behaviour of CFS beams at ambient temperature and in fire are also described here.

4.2 Finite Element Type

All CFS beams were modelled by using shell elements (S4R) for the profiles and solid elements (C3D8R) for the screws. The S4R element (fig. 4.1) was chosen because it is one of the general-purposes from the ABAQUS program library for elements of type shell, which also take transverse shear deformation into account as well as the thick shell elements. Thick shell elements use a theory similar to the one of Mindlin (1951), whereas the formulation of thin shell elements is similar to the one of the discrete Kirchhoff-Love theory (1888). However, S4R element uses a mixed finite element formulation as it can be seen in detail in the ABAQUS Theory Manual (2010). Moreover many researchers in this area often use this type of element in their numerical analyses (Yu and Schafer, 2007; Narayanan and Mahendran, 2003; Dinis and Camotim, 2011; Feng *et al.*, 2003b).

The S4R element is a four-node (4), quadrilateral and stress/displacement shell element (S) with reduced integration (R), a large-strain formulation, hourglass control and a first-order (linear) interpolation. The selected element type uses a reduced (lower-order) integration to form the element stiffness with only one integration location per element. The reduced integration reduces the amount of CPU time necessary for analysis of the model and avoids shear locking. Shear locking may occur in elements under pure bending and without reduced integration, because the element edges must remain straight and the angle between the deformed isoparametric lines is not equal to 90º which means that the strain in the thickness direction is not zero (fig. 4.2). So, this can lead to overestimation of the load capacity in bending dominated problems. These elements can be used in parts of the structure where local stress concentration is high but no large bending is expected.

The only disadvantage of using S4R is its susceptibility to hourglass distortions. Reduced integration elements tend to be too flexible and create a zero-energy mode distortion with no

strain energy related to the distortions (fig. 4.3), so they may introduce non-physical deformation. Fully integrated elements are not affected by this behaviour. To avoid hourglassing ABAQUS implements an artificial controlling force on the element which can lead to over stiff response of the structure if the control coefficients are set too high. The default value for these control coefficients, as advised by ABAQUS, is 1.0 and eliminates the hourglassing modes completely, but influences the deformation behaviour excessively, with the artificial work done exceeding 10 % of the overall internal energy. However, hourglassing is not a problem if multiple elements across the thickness are used, allowing to capture either compressive or tensile axial strains but not both (fig. 4.3). Each node has three displacement and three rotation degrees of freedom. Lastly, each of the six degrees of freedom uses an independent bilinear interpolation function.

The C3D8R element (fig. 4.4) is defined as a three-dimensional (3D), continuum (C), hexahedral and an eight-node brick element with reduced integration (R), hourglass control and first-order (linear) interpolation. These finite elements have three degrees of freedom per node, referring to translations in the three directions X, Y and Z (global coordinates).

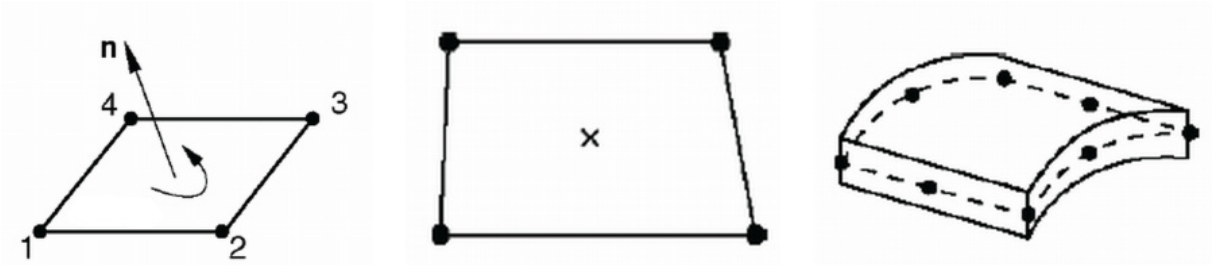

Figure 4.1 – Scheme of the S4R element (ABAQUS Analysis – User's Manual, 2010)

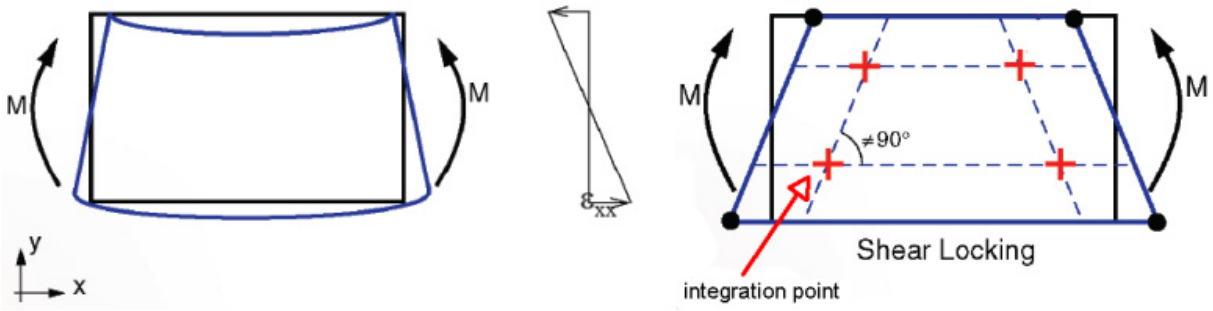

Figure 4.2 – Shear locking in elements without reduced integration points (ABAQUS Analysis – User's Manual, 2010)

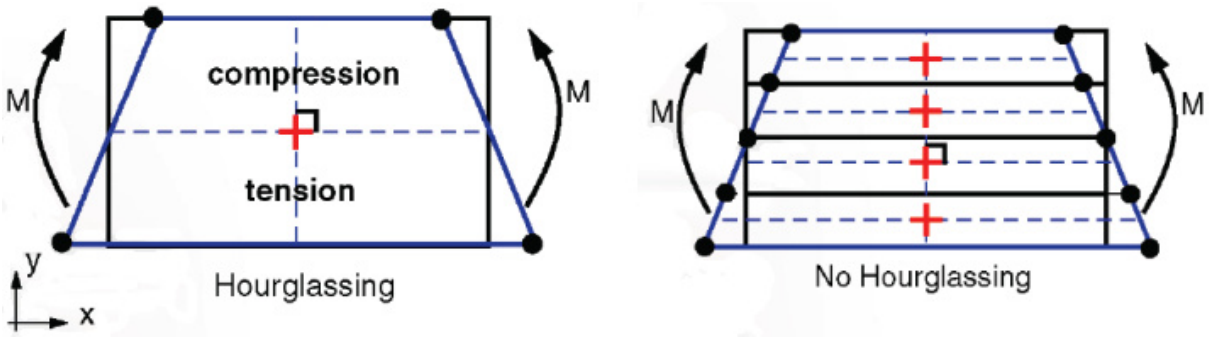

Figure 4.3 – Hourglassing in elements with reduced integration points (ABAQUS Analysis – User's Manual, 2010)

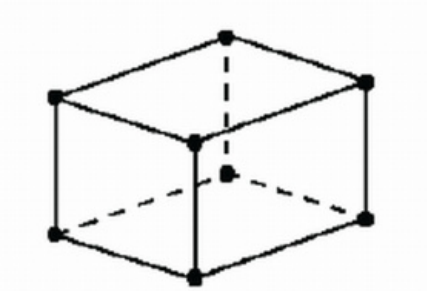

Figure 4.4 – Scheme of the C3D8R element (ABAQUS Analysis – User's Manual, 2010)

4.3 Material Modelling

Material non-linearity in the specimens was modelled with von Mises criteria and isotropic hardening. The material behaviour provided by ABAQUS allows for a multi-linear stress–strain curve to be used. Stress-strain relationship of CFS profiles was described by a gradual yielding behaviour followed by a considerable period of strain hardening, whereas an elastic-perfectly plastic behaviour was assumed for the steel screws. Figure 4.5 shows the stress-strain curve used in the finite element analysis (FEA) for the CFS profiles based on tensile coupon test results and at the same time on other studies of literature (Feng *et al.*, 2003b). So, it was tried to reproduce as faithful as possible the stress-strain relationship of the steel coupon specimens taken from the web of the tested beams. A yield strength of 295 MPa, a tensile strength of 412 MPa and a modulus of elasticity of 208 GPa were obtained from those tests at ambient temperature, as it can be seen in Table 4.1 and Appendix G. The initial slope of the stress-strain curve was taken as the elastic modulus, E, of the material. The second, third and fourth slope (E_1, E_2 and E_3) of the curve were defined by tangent modulus which were respectively 38, 10 and 0.5 % of the elastic modulus. Therefore, a gradual yielding behaviour was idealized by using a bilinear representation with tangent modulus E_1 and E_2

between 70 and 100 % of the yield strength, f_y, with an intermediate point at a stress of 0.875 f_y. All other components were modelled as elastic, i.e. the elastic modulus was equal to 210 GPa and the Poisson's ratio to 0.3 at ambient temperature. However, this last value was assumed to remain unchanged with increasing temperature (Kaitila, 2002b).

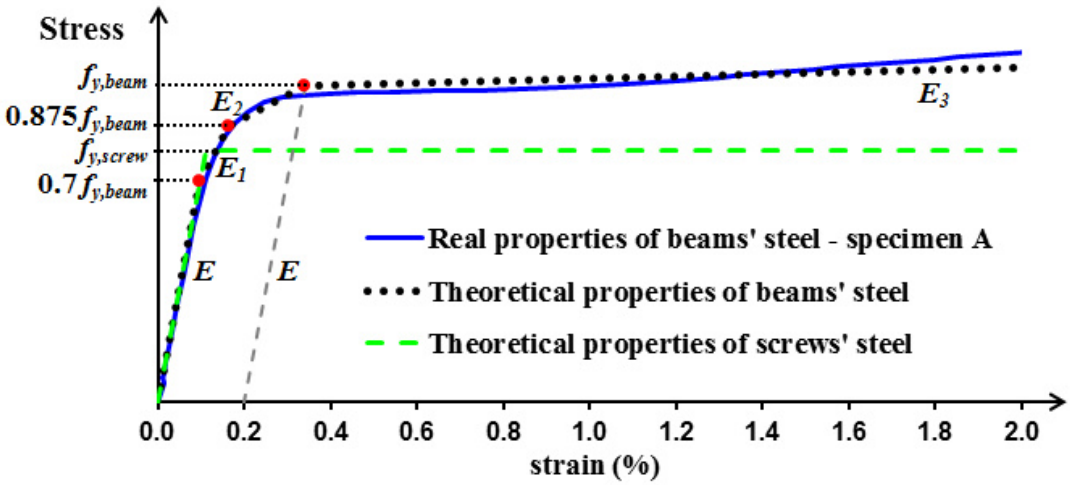

Figure 4.5 – Stress-strain relationship of the beam's and screw's steel

The cold work of manufacturing process may cause a positive effect (i.e. the strength enhancement) and a negative effect (i.e. the reduction of the load-carrying capacity) on a cold-formed member, as a result of the combined effect of the residual stresses and equivalent plastic strains in the member. These (longitudinal and transverse) residual stresses caused by cold forming do not exist alone and are always accompanied by corresponding equivalent plastic strains which are responsible for the definition of the work hardened state. Also, as described in Chapter 2 of this thesis, they depend on many parameters, which make it difficult to predict these stresses properly. So, residual stresses and cold-work of forming (where the apparent yield stress in the corners is increased) were ignored in these analyses.

Table 4.1 – Mechanical properties of structural steel S280GD at ambient temperature

Specimen	E (GPa)	f_p (MPa)	$f_{0.2p}$ (MPa)	$f_{0.5}$ (MPa)	f_y (MPa)	f_u (MPa)
A	202	187	284	290	290	411
B	213	199	295	297	298	414
C	209	189	294	297	297	411
μ	208	192	291	295	295	412
σ	5.5	6.7	6.1	4.3	4.4	1.8
CV	2.66	3.47	2.09	1.47	1.49	0.44

The thermal properties of the CFS sections at elevated temperatures considered in the model (mass density, thermal conductivity and specific heat) were those given in EN 1993-1-2 (2004), whereas the expansion was taken from Cheng and Young (2007) (fig. 2.9). The reduction factors for the yield strength of steel at elevated temperatures were still obtained from the EN 1993-1-2, annex E (2004), whereas the reduction factors for the modulus of elasticity were taken from Ranawaka (2006) (fig. 4.6). Since the analysis of post-buckling may involve large in-elastic strains, the nominal (engineering) static stress–strain curve was converted to a true stress and logarithmic plastic strain curve (Chen and Young, 2007b). EN 1993-1-2 (2004) steel properties are given as engineering stress-strain input, which should be converted to true stress and true (logarithmic) strain using Equations 4.1 and 4.2 where ε_{eng} and σ_{eng} are the engineering (nominal) strain and stress, respectively whereas ε_{true} and σ_{true} are the true strain and stress, respectively. Further information about the true stress and plastic true strain is available in ABAQUS User's Manual (2010).

$$\varepsilon_{true} = \ln(1 + \varepsilon_{eng}) \tag{4.1}$$

$$\sigma_{true} = \sigma_{eng}(1 + \varepsilon_{eng}) \tag{4.2}$$

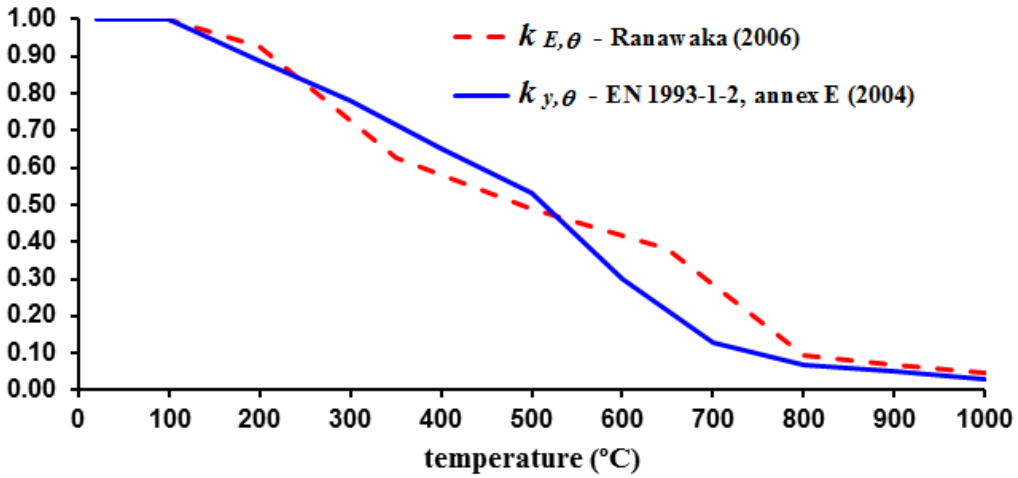

Figure 4.6 – Reduction factors for the stress-strain relationship of CFS sections at elevated temperatures

4.4 Finite Element Mesh

The influence of the finite element size on the behaviour of CFS beams was first studied. To demonstrate the mesh sensitivity three mesh densities for the closed built-up sections (fig. 4.7) and four for the open sections (fig. 4.8) were examined. The mesh density has a

significant impact on the peak load, especially in closed built-up sections (fig. 4.7). For example, the fine mesh yielded a 13% higher capacity than the coarse mesh in the case of the S4R element. It was also observed that the increase of the mesh size led to a relatively straightforward decrease of initial stiffness of the beam. Finally, it was found that good simulation results could be obtained by using finite element meshes of 5 x 5 mm, 10 x 10 mm or 20 x 20 mm. To save computational time, finite element meshes of 10 x 10 mm for C, lipped I and R beams and of 15 x 15 mm for 2R beams (fig. 4.9) were generated automatically by the ABAQUS program and used in all simulations. In relation to the screws, an approximately 2 mm mesh size was used (fig. 4.10).

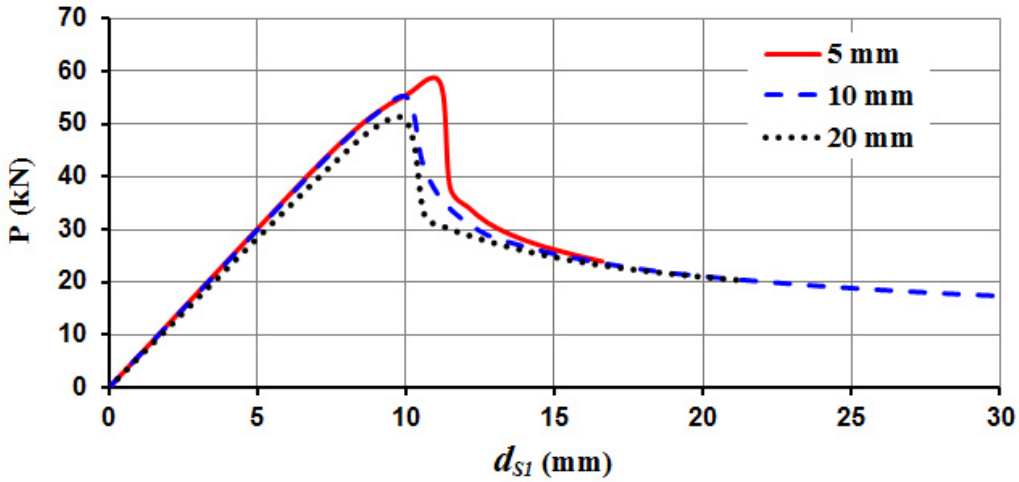

Figure 4.7 – Predicted load for the R beam using FEA at ambient temperature

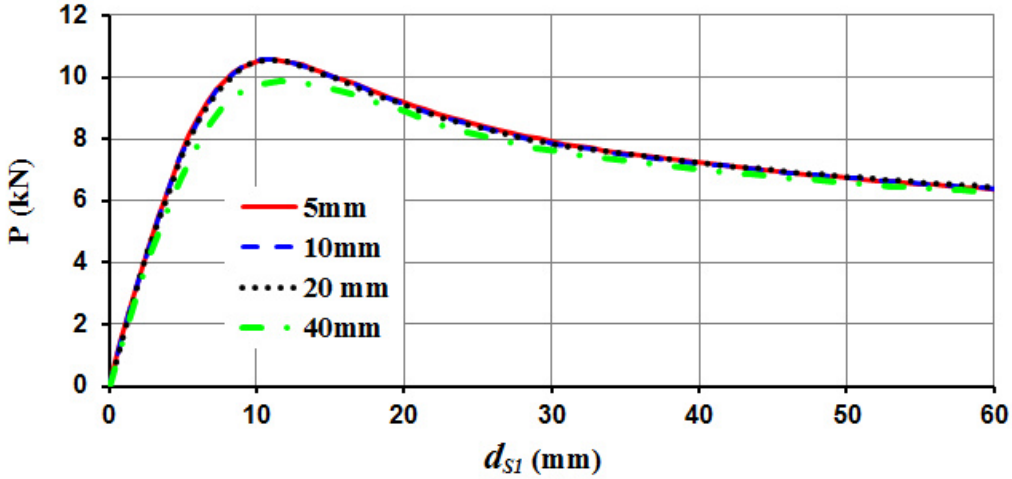

Figure 4.8 – Predicted load for the C beam using FEA at ambient temperature

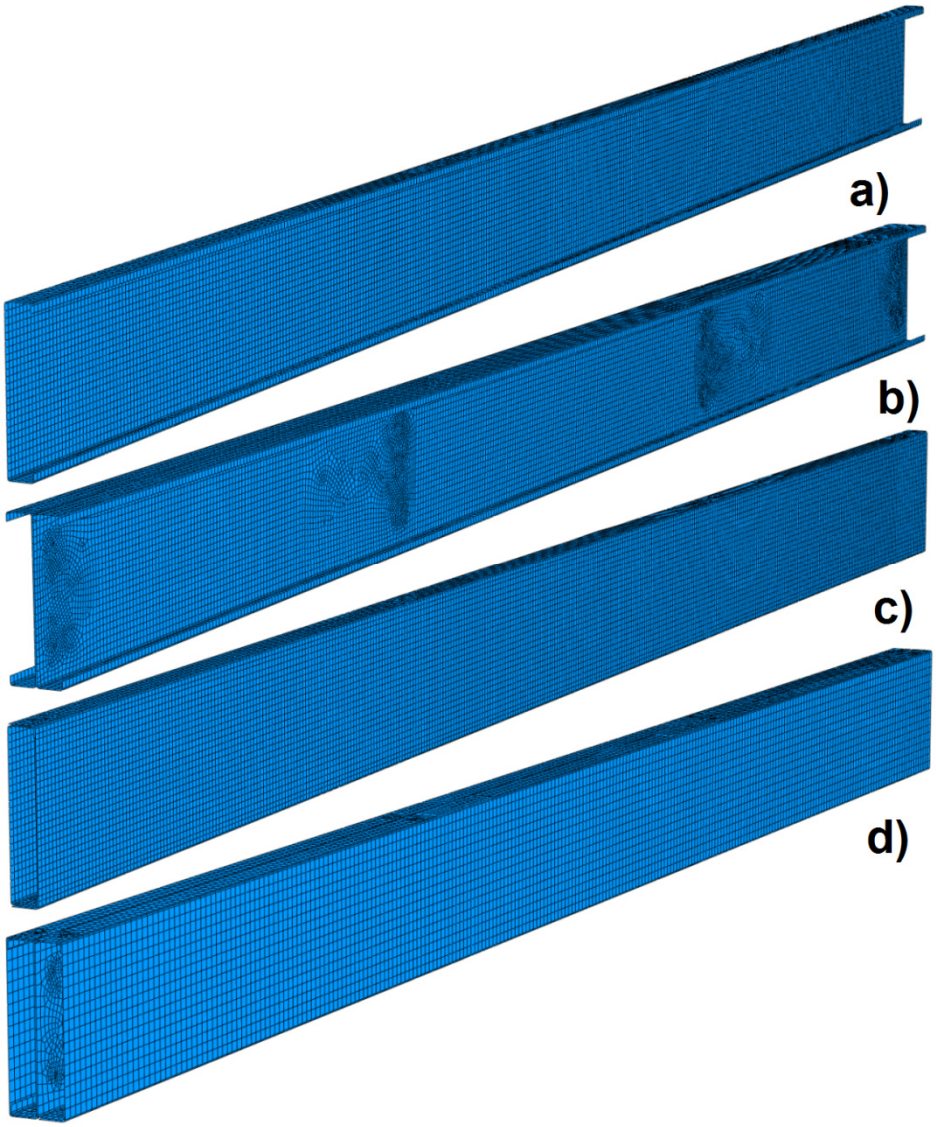

Figure 4.9 – Finite element mesh used for the C (a), lipped I (b), R (c) and 2R (d) beams

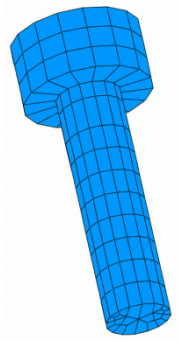

Figure 4.10 – Finite element mesh used for the screws

4.5 Boundary, Loading and Contact Conditions

A three-dimensional numerical model was used to describe all buckling modes observed in the experimental tests. The cross-sections of the different beams, the screws, the beam support system, the axial and rotational restraining system and the beam loading system were tried to reproduce with great accuracy in the numerical simulations. As it can be seen in Figure 4.11, the axis system of the model is such that Z axis lies in the longitudinal direction of the beam while X and Y axes lie in the major and minor axes of the beam's cross-section, respectively. Such as observed in the real test set-up, the beam supports and the loading were also applied on rigid plates attached to beams so as to distribute possible concentrated forces on them. Therefore, with regard to the loading on the beams, concentrated forces with the direction -Y were applied at the centre of those plates and each one was at a distance of 1 m from the nearest beam support, i.e., the forces were applied at one-third of the beam span.

On other hand, to simulate the pinned support all degrees of freedom of the nodes located on the bottom surface and at the middle of the respective rigid plate were constrained, whereas for the roller support only the translations in the directions X and Y were constrained. Finally, the translations in the direction X of all nodes located at each end of both supports were constrained in order to prevent their lateral deformation. All simulated beams were still modelled using the centre line dimensions, as it can be seen in Figure 4.11b. Furthermore, two assumptions were introduced in these analyses for modelling the contact behaviour between the profiles and also between these ones and the screws. Thus, it was assumed a tangential friction coefficient of 0.2 for the contact behaviour in tangential direction and a hard contact (full transmission of compressive forces and no transmission of tensile forces) for the contact behaviour in normal direction between the profile surfaces.

The surface-to-surface contact method was used, because this one gives a good convergence rate and it is much less sensitive to the choice of master and slave surfaces. For surface-to-surface contact, contact conditions are enforced in an average sense, rather than at discrete points such as node-to-node discretization. Such averaging technique provides more accurate and smooth contact state transition (Selamet and Garlock, 2010). As well as that the penalty method was defined as the contact property (both tangential and normal contact) between the steel profile surfaces. Finite sliding was also used in the contact tracking algorithm, which takes account for large relative movements between contact pairs compared to their element sizes and updates their contact tracking state for each contact iteration. So, it is well suited for models under fire conditions with large plastic deformations. A rough and hard contact between the profiles and the screws was also employed.

For the modelling of the axial and rotational restraining system, a linear spring model was used (fig. 4.12). ABAQUS allows the user to define axial spring elements, connected to a node of the member and a support that have the appropriate stiffness coefficients. The springs were connected to the beams at the centre of the cross-section by means of the *Coupling Constraints option in ABAQUS. The kinematic coupling constraint was employed in order to constrain the motion of the end surfaces of the beams to the motion of a single point, in this case the centre point of the beam cross-section. This method can also be used (i) to apply loads or boundary conditions to a model, (ii) to model end conditions and (iii) to model interactions with other constraints, such as connector elements (like it happens in this particular model).

Finally, the beam temperatures registered in the experimental tests were considered as an input in the numerical simulations, since the temperature distribution along the beam presented some irregularities, in other words the distribution was not perfect, as mentioned in chapter 3. Hence, it was assumed that the temperatures in the web and flanges were uniform and equal to the respective thermocouples (fig. 4.13), meaning that the temperatures recorded by the thermocouples welded in section S1 were uniform in the longitudinal direction of the beam between the sections S7 and S8, that the temperatures recorded by the thermocouples welded in section S2 were uniform in the longitudinal direction of the beam between the sections S5 and S6 and that the temperatures recorded by the thermocouples welded in section S3 were uniform in the longitudinal direction of the beam between the sections S9 and S10. Between these sections a linear variation was assumed and that the temperature was uniform and equal to 20 ºC at beam supports. On the other hand, the ISO 834 standard fire curve and an uniform temperature distribution (in the longitudinal direction) along all beam were considered for the parametric study. Therefore, in these simulations the fire action was defined in ABAQUS program by two types of surface, namely, “film condition” and “radiation to ambient”, corresponding respectively to heat transfer by convection and radiation. It is worth mentioning that before using the ISO 834 standard fire curve the numerical heat transfer analyses were performed with the furnace temperatures registered in the experimental tests in order to validate the model. In these simulations, a 4-node linear heat transfer quadrilateral element (DC2D4) was chosen and a two-dimensional numerical model was developed to estimate the temperature distribution in the cross-sections of the beams. The resultant emissivity was taken as 0.2 (considering the emissivity of the furnace’s electric resistance and the profiles equal to 0.7 and 0.3, respectively), due to the mirror surface of the zinc coating on the profiles used. In addition, a coefficient of heat transfer by convection equal to 15 W/(m^2K) was adopted when the furnace temperatures were an input data and 25 W/(m^2K) when the ISO 834 standard fire curve was an input data.

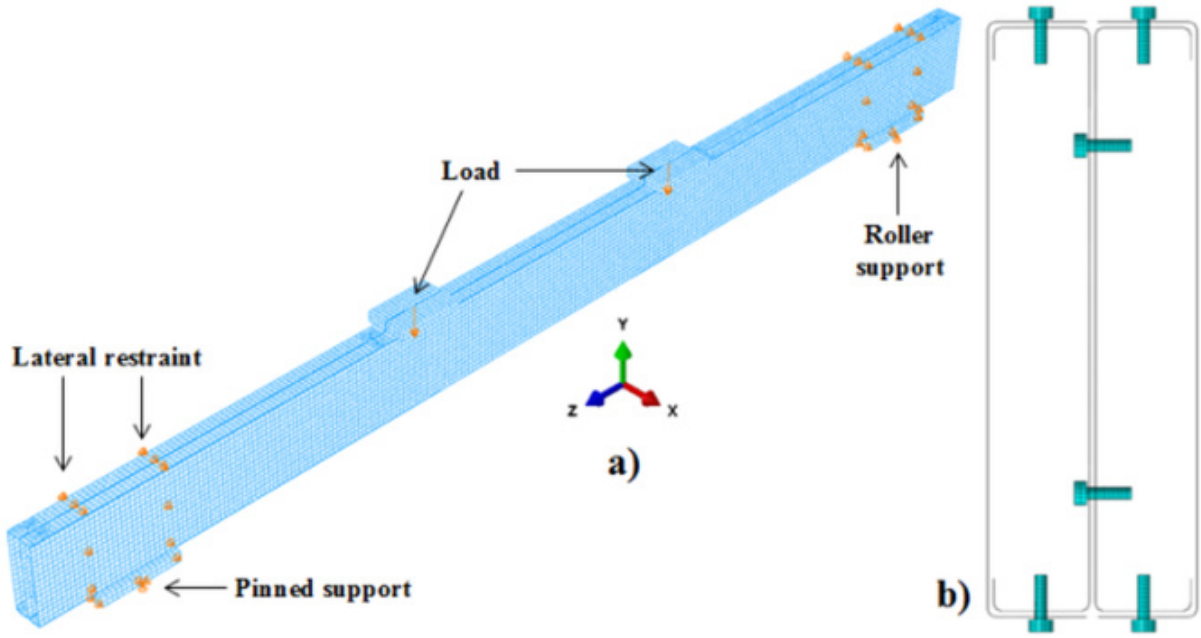

Figure 4.11 – Numerical model used in the finite element analysis: (a) perspective and (b) cross-sectional view

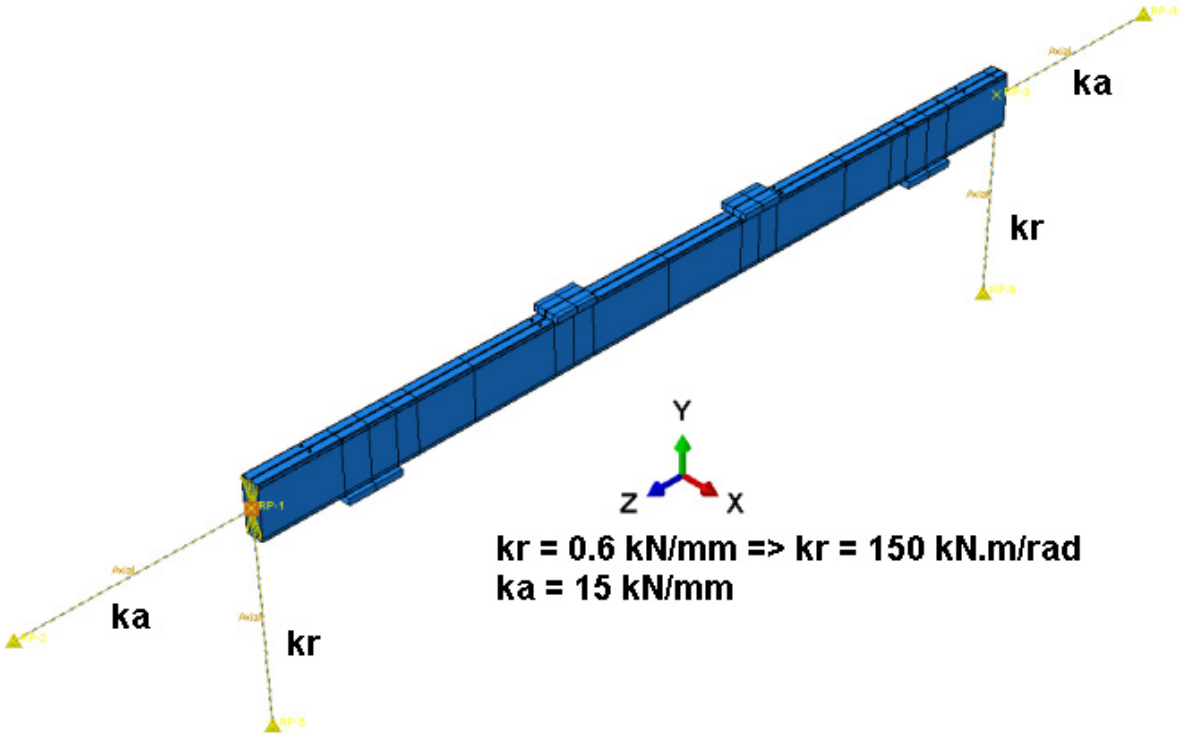

Figure 4.12 – Axial and rotational restraining system introduced in the numerical model using linear axial springs

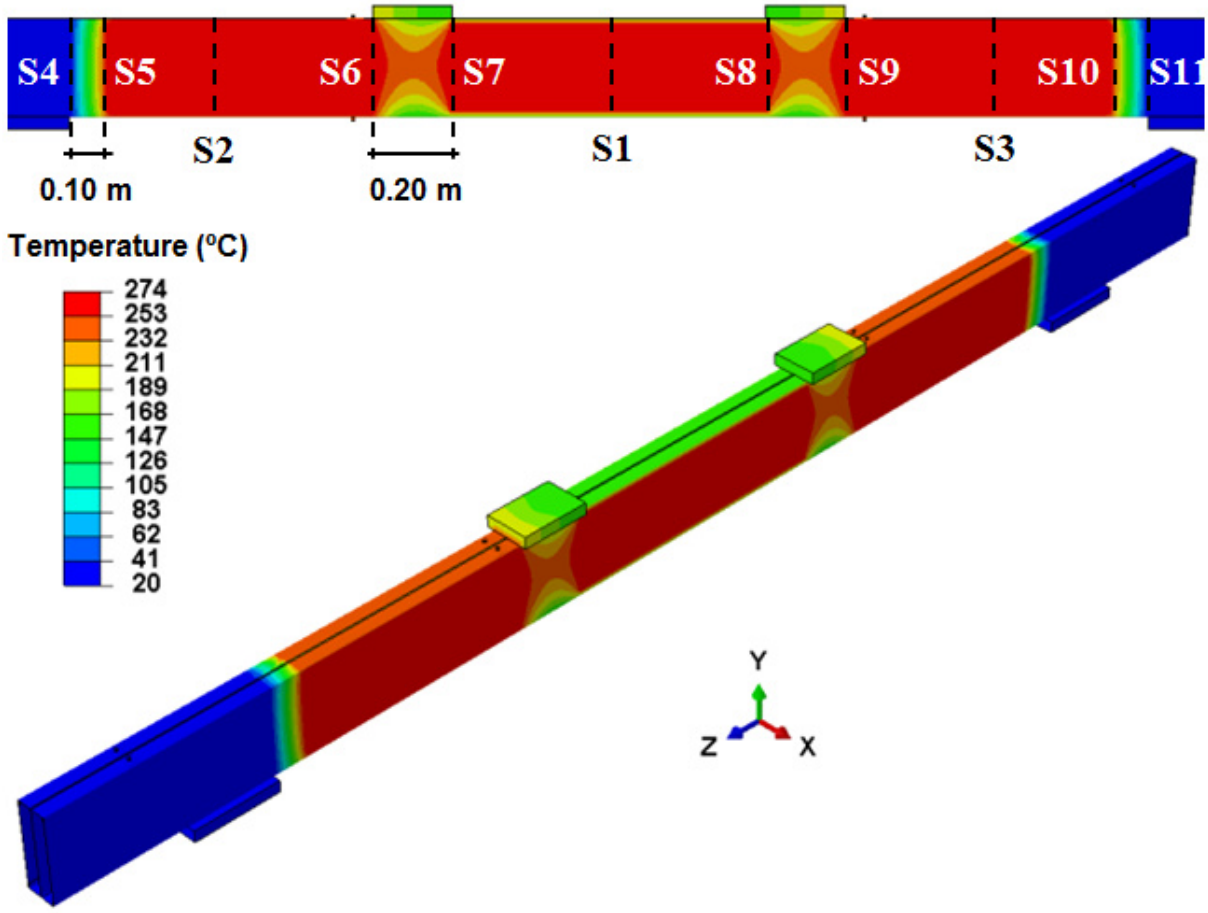

Figure 4.13 – Temperature distribution introduced in ABAQUS of test beam B-2R_1 at 580 seconds of test run

4.6 Analysis Method

Two types of analysis were employed by using the developed finite element model: elastic buckling and nonlinear static analyses. Elastic buckling (eingenvalue) analysis was performed to establish the buckling modes which were observed in the experimental tests, thus using them to input the geometric imperfections in the nonlinear analysis. In contrast to the adopted procedure, only the lowest buckling mode predicted from the eigenvalue analysis is used for practical applications. It is worth noting that the magnitude of the imperfections was the main parameter used to calibrate the models. After knowing their effects on structural response of this kind of beams and comparing with the results of the experimental tests, it was observed that a suitable maximum value for global imperfections was found to be approximately $L/1000$, for distortional imperfections t and for local imperfections $h/200$. Finally, a structural analysis was undertaken with the purpose of simulating the performance of CFS beams under

fire conditions until failure. The nonlinear geometric parameter (*NLGEOM=ON) was set to deal with the geometric nonlinear analysis, namely, with the large displacement analysis.

4.7 Validation of Finite Element Model

4.7.1 Structural performance at ambient temperature

Figure 4.14 shows a comparison of the load-vertical displacement curves of CFS beams obtained from the experimental tests and FEA used for the calibration of the model. All curves from FEA fit closely with the experimental curves, especially with the ones that presented the lowest maximum load. Also note that the maximum numerical load of the C, lipped I, R and 2R beams was, respectively, 10.58, 39.86, 54.97 and 120.78 kN, i.e., the mean values of the FEA-to-experimental loading capacity ratios (P_{FEA} / P_{TEST}) for these beams were 0.90, 0.96, 0.91 and 0.91, respectively. However, concerning the minimum value of the maximum load-carrying capacity of beam obtained from the three experimental tests for each type of beam, those ratios were already 0.92 for the C beam and 0.99 for the other beams (Table 4.2). This good agreement and accuracy between the experimental and numerical results ensures a strong validity of the developed finite element model and may also ensure reliable and safe results obtained from the parametric study.

The developed numerical model reproduced both the loading stage and the failure load of all types of beams with great accuracy so that the numerical results were always on the safe side. The differences were higher in the failure load of the C beams than in the other beams because of the change of the action line of the force during the tests. The numerical post-collapse response of the R and 2R beams were less accurate with regard to the C and lipped I beams, but the same happened in the experimental tests, in other words, the unloading stage of the three R and 2R beams was not so identical in what concerns to the C and lipped I beams. The reason for the differences between the numerical and experimental results and between the experimental results of identical test series (figs. 18c and 18d) may result from differences in the residual stresses of the members, the straightness of the plates, the yield strength on the member cross-section due to cold-forming and the assembly process of these beams. The discontinuities in some curves corresponding to the failure of screws were not observed in the FEA due to the elastic-plastic behaviour modelled for the mechanical properties of these screws.

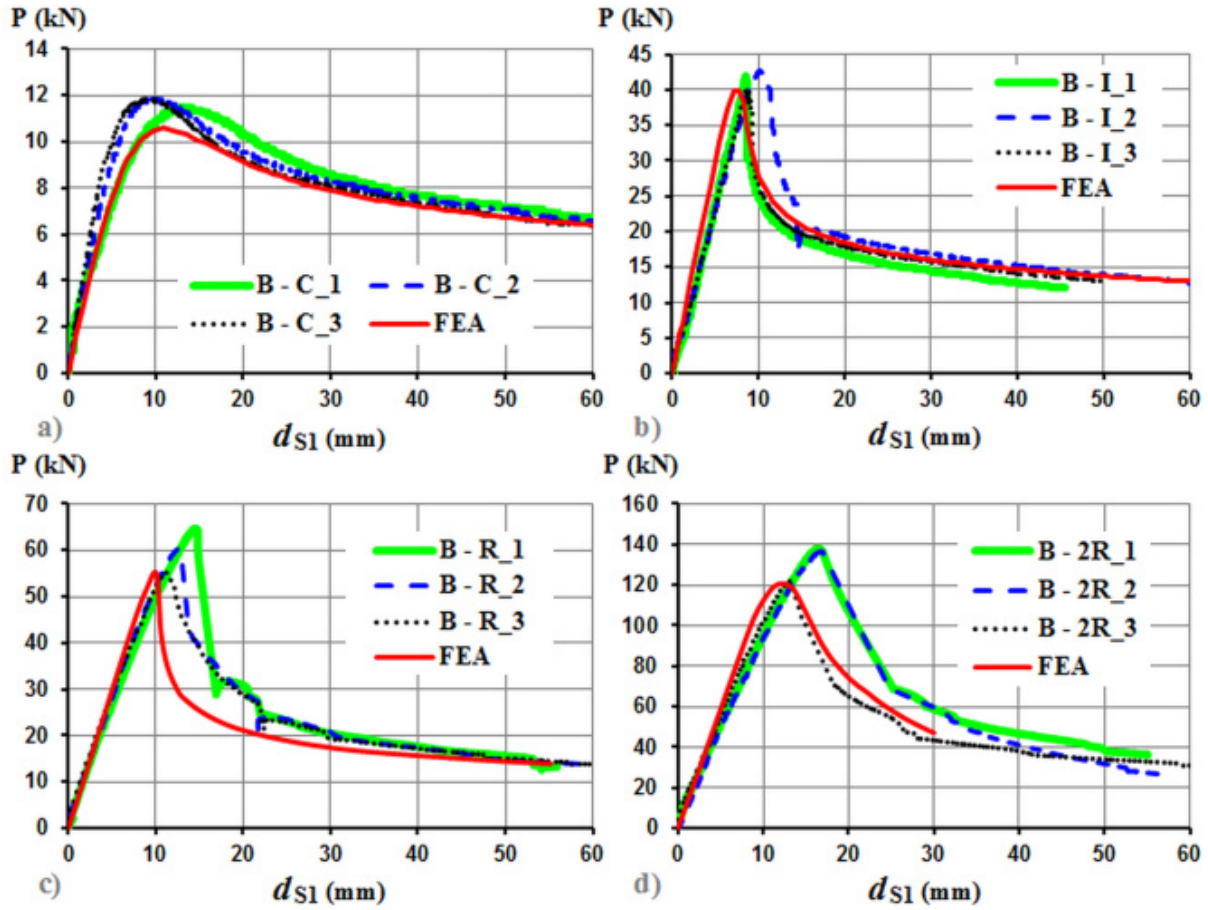

Figure 4.14 – Comparison of the FEA and experimental load-displacement curves for the C (a), lipped I (b), R (c) and 2R (d) beams

Table 4.2 – Experimental and numerical load-carrying capacity of the CFS beams

Test reference	**Experimental** P_{TEST} (kN)	**Numerical** P_{FEA} (kN)	P_{FEA} / P_{TEST}
B-C_1	11.48	10.58	0.92
B-C_2	11.84		0.89
B-C_3	11.84		0.89
μ	11.72	10.58	0.90
B-I_1	41.95	39.86	0.95
B-I_2	42.68		0.93
B-I_3	40.42		0.99
μ	41.68	39.86	0.96

B-R_1	64.68	54.97	0.85
B-R_2	60.38		0.91
B-R_3	55.36		0.99
μ	60.14	54.97	0.91
B-2R_1	138.09	120.78	0.87
B-2R_2	136.70		0.88
B-2R_3	122.32		0.99
μ	132.19	120.78	0.91

4.7.2 Structural performance under fire conditions

Figure 4.15 shows respectively the comparison of the displacement-temperature curves of the simply supported beams obtained from the experimental tests and FEA used for the calibration of the model, whereas Figures 4.16 and 4.17 present the comparison of the axial restraining force-temperature curves of the axially and rotationally restrained beams, respectively. All curves from FEA fit closely with the experimental curves, especially in what concerns to the critical temperature of the respective beams, as it can be seen in Tables 4.3, 4.4 4.5 and 4.6. The results show that the mean differences between experimental and numerical critical temperatures were less than 10 %, except for the rotationally restrained C beams. Although this difference has been higher than 10 %, the numerical temperature was higher than the experimental one, indicating that the respective estimated data is unsafe. The highly complex post-buckling reserve of the rotationally restrained C beam and the change of the action line of the force during these tests may be two of the main reasons for that difference. However, concerning the maximum axial restraining force, the difference was almost zero (fig. 4.17a).

From the tables below, it can be seen that the critical temperatures predicted by the numerical model was respectively of 666, 647, 652 and 706 ºC for the simply supported C, lipped I, R and 2R beams, of 522, 401, 436 and 596 ºC for the axially restrained C, lipped I, R and 2R beams and of 768, 558, 586 and 687 ºC for the axially and rotationally restrained C, lipped I, R and 2R beams. It is noticed that those values for the simply supported beams were respectively 7.3, 6.4, 11.3 and 3.3 % lower than the experimentally measured results by an average and 6.2, 3.7, 10.5 and 1.2 % regarding to the best and safe prediction. The numerical critical temperatures for the axially restrained C, lipped I, R and 2R beams were respectively 1.4, 9.5, 13.4 and 10.2 % lower than the experimentally measured results by an average and 5.9, 9.5, 10.7 and 3.9 % regarding to the best and safe prediction. Finally, the numerical

critical temperatures for the axially and rotationally restrained lipped I and R beams were respectively 1.7 and 6.5 % lower than the experimentally measured results by an average. On the other hand, the numerical critical temperatures for the axially and rotationally restrained C and 2R beams were respectively 19.9 and 2.5 % higher than the experimentally measured results by an average. All these results indicate that the estimated data are generally on the safe side but not too conservative either. The general good agreement and accuracy between the experimental and numerical results ensures a strong validity of the developed finite element model and may also ensure reliable results obtained from the parametric study, especially the results needed for the development of simplified calculation methods for fire design of simply supported and of axially restrained CFS beams. It is clear that predicting the structural behaviour of the CFS beams at ambient temperature is easier than under fire conditions. The number of variables which affect the structural response of the beams at high temperatures is much higher than at ambient temperature.

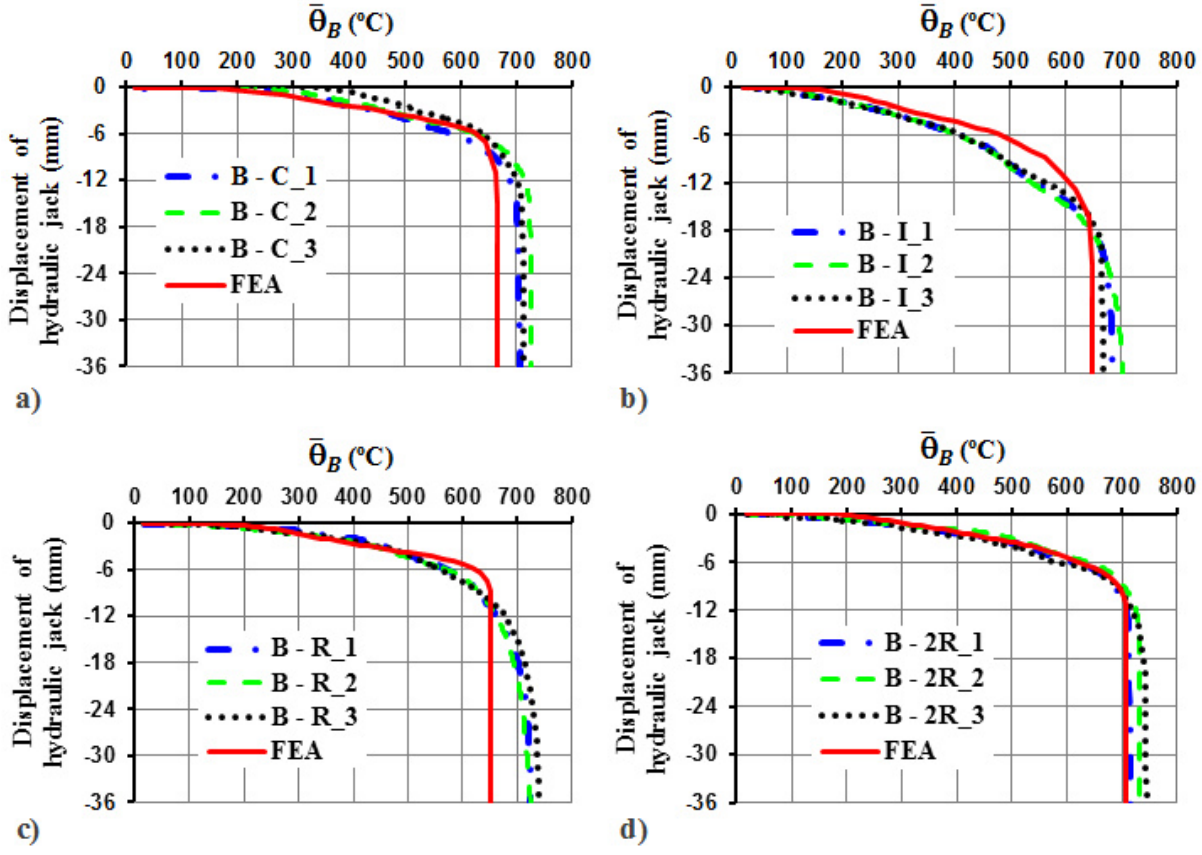

Figure 4.15 – Comparison of the FEA and experimental displacement-temperature curves for the simply supported C (a), lipped I (b), R (c) and 2R (d) beams

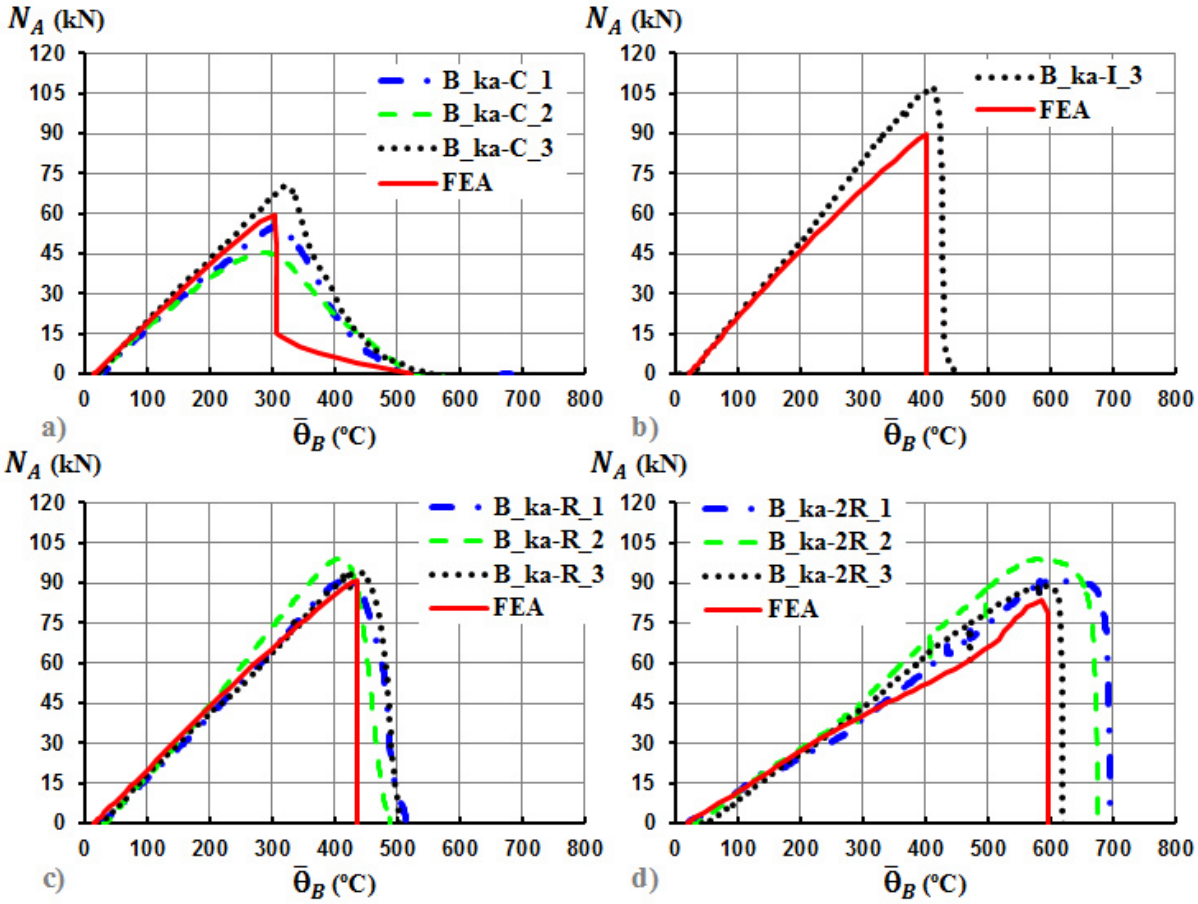

Figure 4.16 – Comparison of the FEA and experimental axial restraining forces in the axially restrained C (a), lipped I (b), R (c) and 2R (d) beams

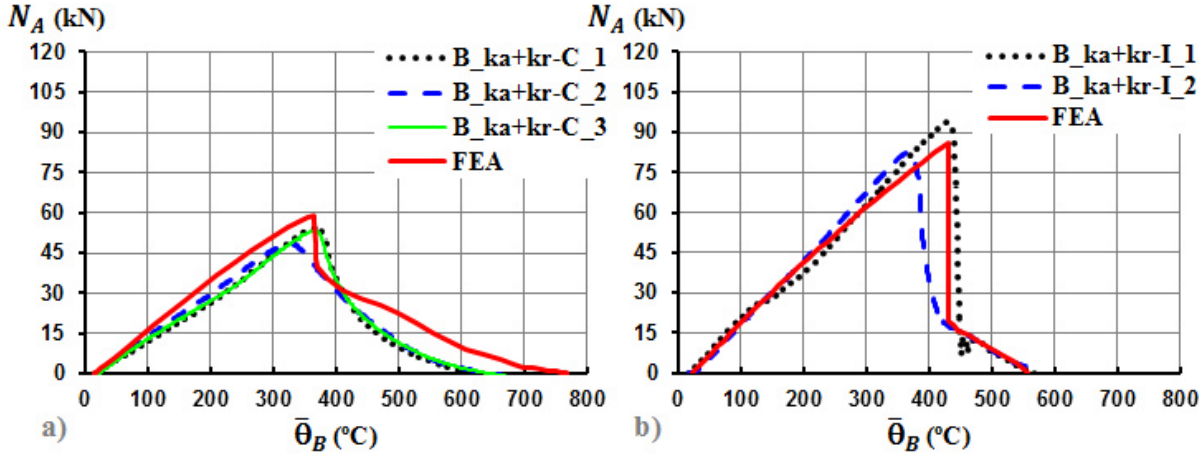

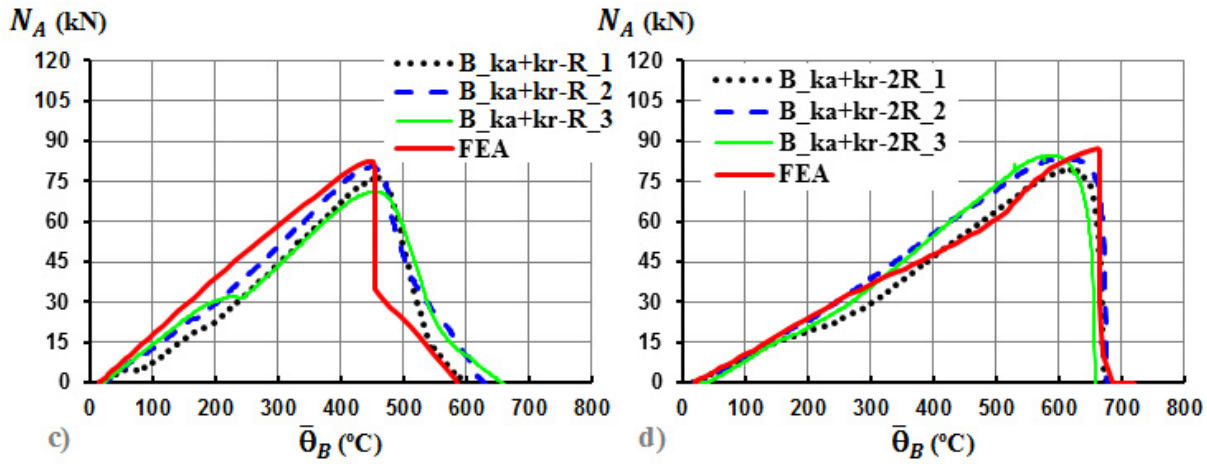

Figure 4.17 – Comparison of the FEA and experimental axial restraining forces in the axially and rotationally restrained C (a), lipped I (b), R(c) and 2R (d) beams

Table 4.3 – Experimental and numerical critical temperatures of the C beams

Test reference	**Experimental** θ_{cr} (ºC)	**Numerical** θ_{cr} (ºC)	**Difference** (%)
B-C_1	710	666	-6.2
B-C_2	729		-8.6
B-C_3	716		-7.0
μ	718	666	-7.3
B_ka-C_1	513	522	1.7
B_ka-C_2	519		0.5
B_ka-C_3	554		-5.9
μ	529	522	-1.4
B_ka+kr-C_1	629	768	22.1
B_ka+kr-C_2	647		18.7
B_ka+kr-C_3	646		18.9
μ	641	768	19.9

Table 4.4 – Experimental and numerical critical temperatures of the lipped I beams

Test reference	**Experimental θ_{cr}** (ºC)	**Numerical θ_{cr}** (ºC)	**Difference** (%)
B-I_1	693	647	-6.6
B-I_2	709		-8.7
B-I_3	672		-3.7
μ	691	647	-6.4
B_ka-I_1*	544	504	-7.3
B_ka-I_2*	544		-7.4
μ	544	504	-7.3
B_ka-I_3	443	401	-9.5
B_ka+kr-I_1	567	558	-1.7
B_ka+kr-I_2	567		-1.7
μ	567	558	-1.7

* Tests where the actual axial stiffness was of about 3 kN/mm, instead of 15 kN/mm

Table 4.5 – Experimental and numerical critical temperatures of the R beams

Test reference	**Experimental θ_{cr}** (ºC)	**Numerical θ_{cr}** (ºC)	**Difference** (%)
B-R_1	728	652	-10.5
B-R_2	732		-11.0
B-R_3	745		-12.4
μ	735	652	-11.3
B_ka-R_1	516	436	-15.4
B_ka-R_2	489		-10.7
B_ka-R_3	506		-13.8
μ	504	436	-13.4

B_ka+kr-R_1	595	586	-1.6
B_ka+kr-R_2	628		-6.7
B_ka+kr-R_3	656		-10.7
μ	626	586	-6.5

Table 4.6 – Experimental and numerical critical temperatures of the 2R beams

Test reference	Experimental θ_{cr} (ºC)	Numerical θ_{cr} (ºC)	Difference (%)
B-2R_1	715	706	-1.2
B-2R_2	732		-3.6
B-2R_3	744		-5.1
μ	731	706	-3.3
B_ka-2R_1	696	596	-14.3
B_ka-2R_2	676		-11.8
B_ka-2R_3	620		-3.9
μ	664	596	-10.2
B_ka+kr-2R_1	675	687	1.8
B_ka+kr-2R_2	677		1.5
B_ka+kr-2R_3	659		4.3
μ	670	687	2.5

4.7.3 Failure mode analysis at ambient temperature

Figures 4.18a, 4.19a, 4.20a and 4.21a illustrate the numerical failure modes of the tested specimens under bending and they can be compared to the experimental failure modes as shown in Figures 4.18b, 4.19b, 4.20b and 4.21b. The local, distortional and lateral-torsional buckling modes that were responsible for collapse of the beams were also clearly identified in the numerical modes. This confirms that the finite element model predicted the failure modes

of CFS beams with an acceptable precision. The figures also present the finite element results in the form of von Mises or minimum principal stresses to help understanding the behaviour of the beams. It was also confirmed that distortional buckling was the main failure mode responsible for the collapse of the closed built-up beams (R and 2R beams) (figs. 4.20a and 4.21a), and the lateral-torsional buckling the main failure mode responsible for the collapse of the open beams (C and lipped I beams) (figs. 4.18a and 4.19a).

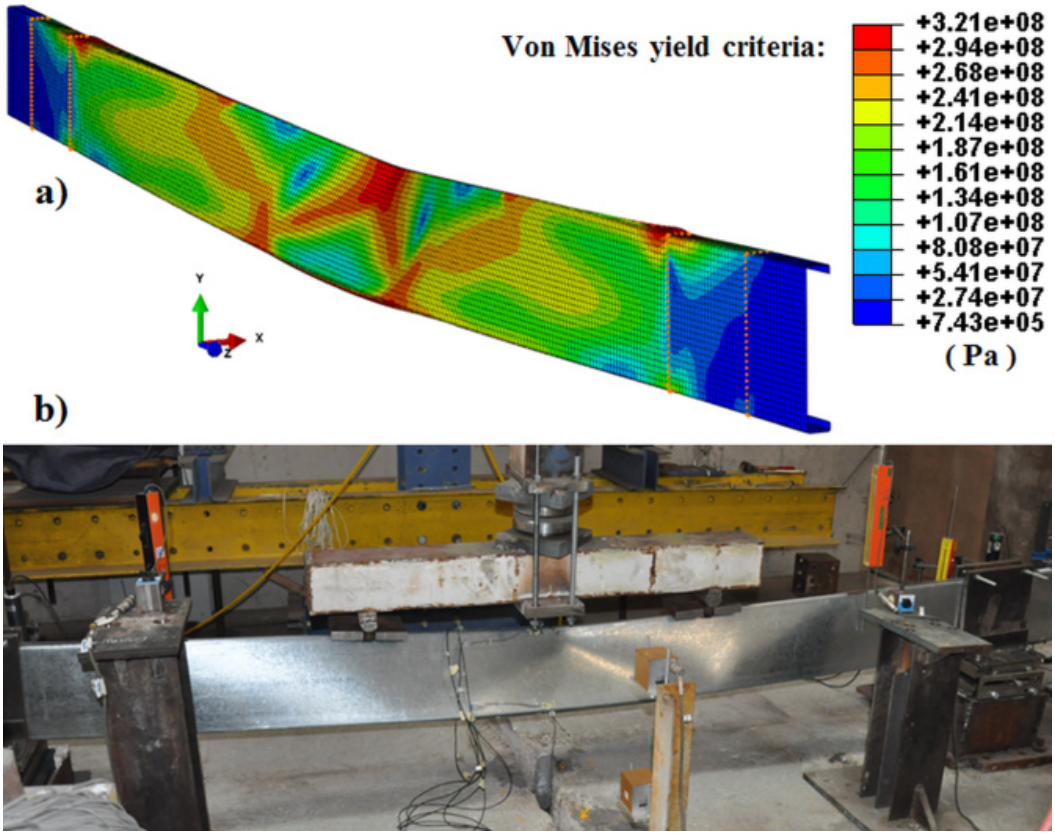

Figure 4.18 – Numerical (a) and experimental (b) failure modes for the C beam

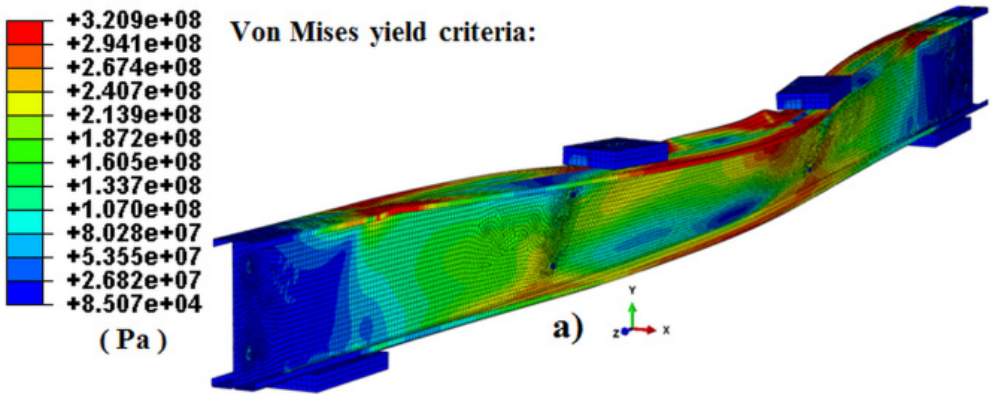

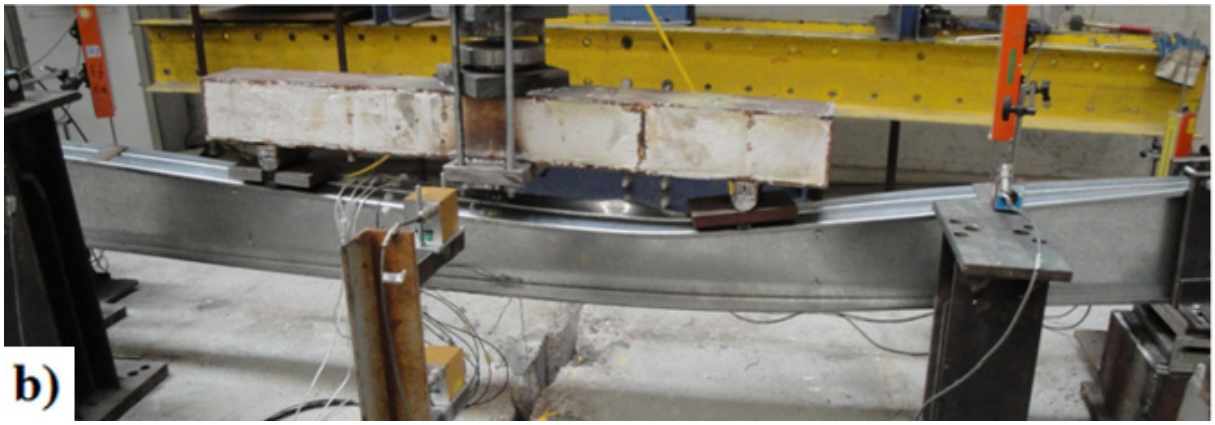

Figure 4.19 – Numerical (a) and experimental (b) failure modes for the lipped I beam

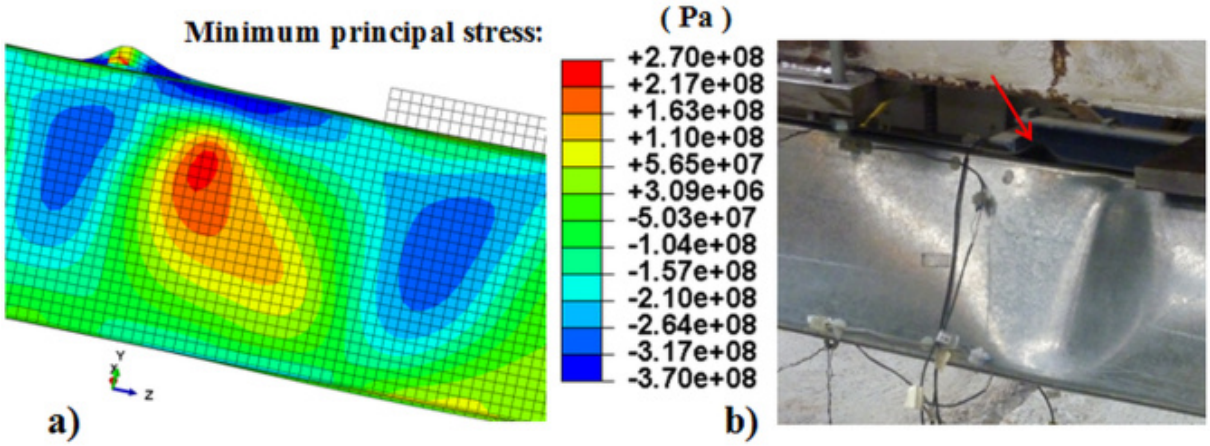

Figure 4.20 – Numerical (a) and experimental (b) failure modes for the R beam

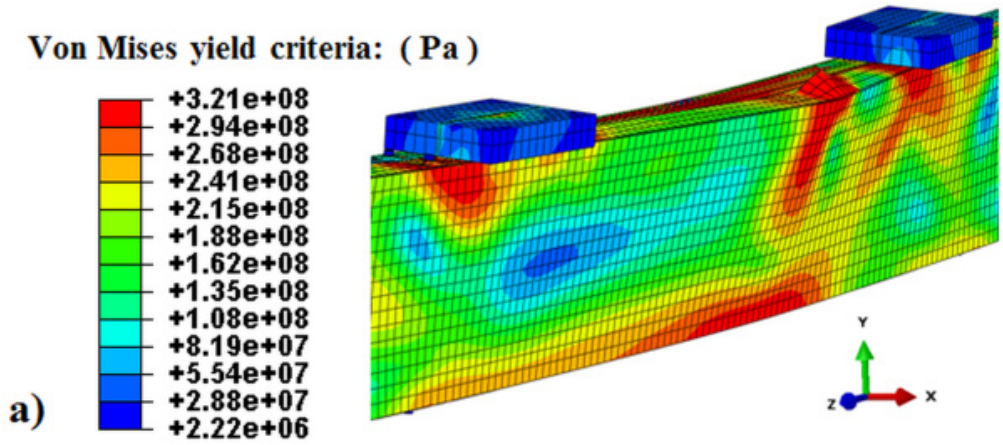

b)

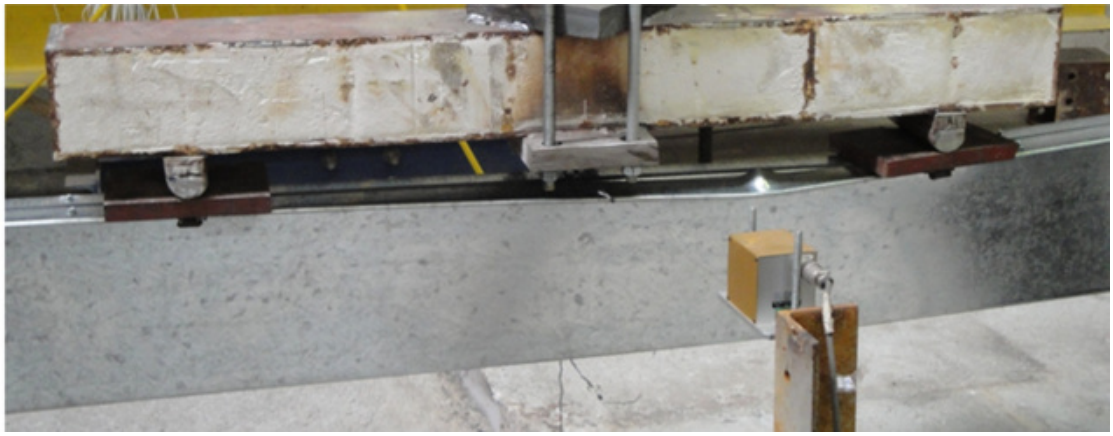

Figure 4.21 – Numerical (a) and experimental (b) failure modes for the 2R beam

4.7.4 Failure mode analysis under fire conditions

The figures below present the main features of the failure modes of the tested beams under fire conditions, in order to validate the performance of developed finite element model for fire tests in terms of deformations, especially the final configuration of the beams. Figures 4.22b, 4.23b, 4.24b and 4.25b illustrate the FEA failure modes of the simply supported C, lipped I, R and 2R beams under fire conditions and they can be contrasted to the experimental failure modes, as shown in Figures 4.22a, 4.23a, 4.24a and 4.25a, as well as the Figures 4.26, 4.27 and 4.28 which show different buckling modes and more complex (interaction of buckling modes). It can be seen clearly by both kinds of figures that the distortional and lateral-torsional buckling modes were respectively responsible for collapse of the closed built-up beams (figs. 4.24 and 4.25) (except for the axially restrained R beam, as shown Figure 4.28) and open beams (figs. 4.22 and 4.23), similarly to the tested beams at ambient temperature. To sum up, it was still noticed that the web collapse of the simply supported R beams only occurred after the distortional buckling of the U profile. The effect of the rotational restraint at beam supports on the buckling modes of the open beams was also evident in the numerical failure modes (figs. 4.26b and 4.27b). Once again, it can be conclude that the developed finite element model predicted the behaviour of CFS beams with an acceptable precision. However, some little differences between the experimental and numerical modes can be seen, such as: (i) the numerical distortional buckling appeared nearer either the mid-span (figs. 4.23, 4.26 and 4.27) or the beam support (figs. 4.25 and 4.28) than the experimental one, (ii) no distortional buckling in the numerical failure mode was observed on the lower flange of the rotationally restrained R beam (fig. 4.28), (iii) distortional buckling modes with opposite directions (fig. 4.26) and (iv) only one distortional buckling half-wave in the numerical failure mode emerged on the U section of the 2R beam near the mid-span (fig. 4.25).

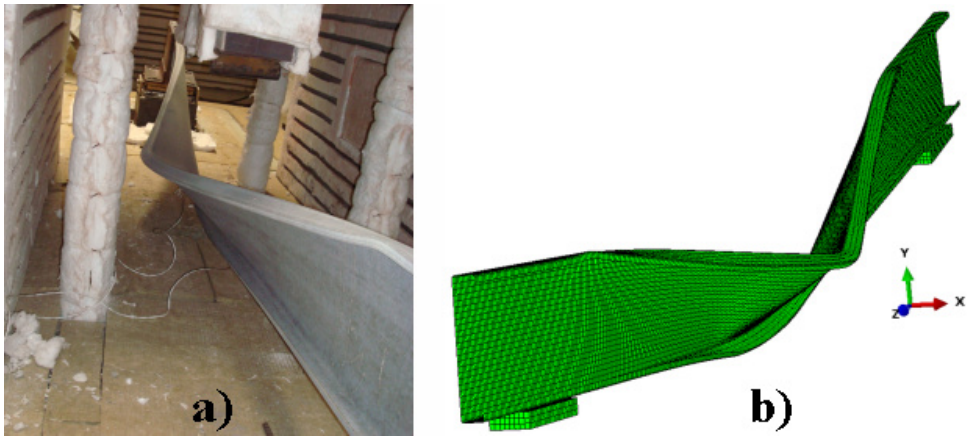

Figure 4.22 – Experimental (a) and numerical (b) configuration of the deformed C beam with no restraints after fire test

Figure 4.23 – Experimental (a) and numerical (b) configuration of the deformed lipped I beam with no restraints after fire test

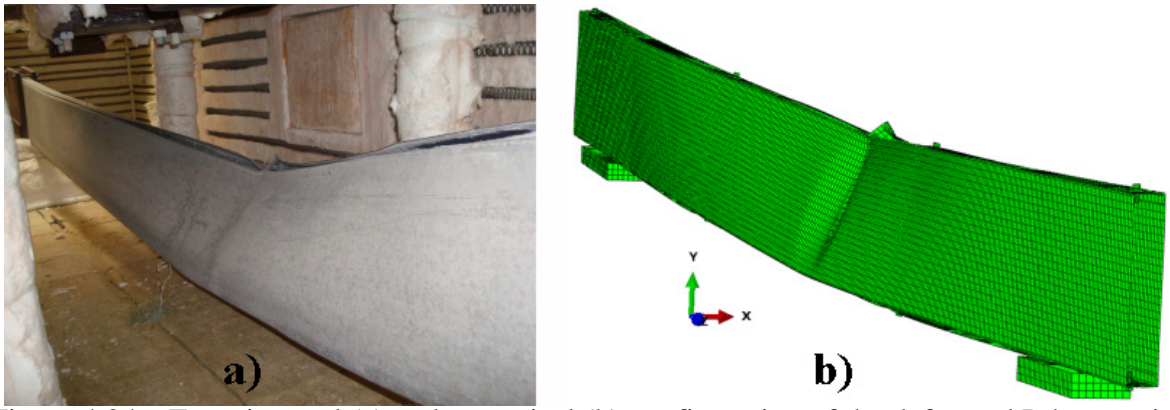

Figure 4.24 – Experimental (a) and numerical (b) configuration of the deformed R beam with no restraints after fire test

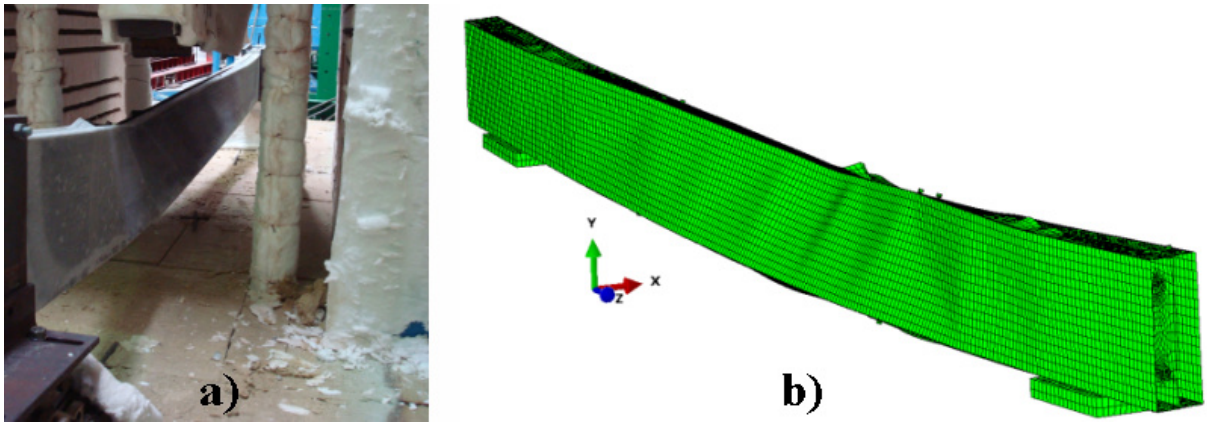

Figure 4.25 – Experimental (a) and numerical (b) configuration of the deformed 2R beam with no restraints after fire test

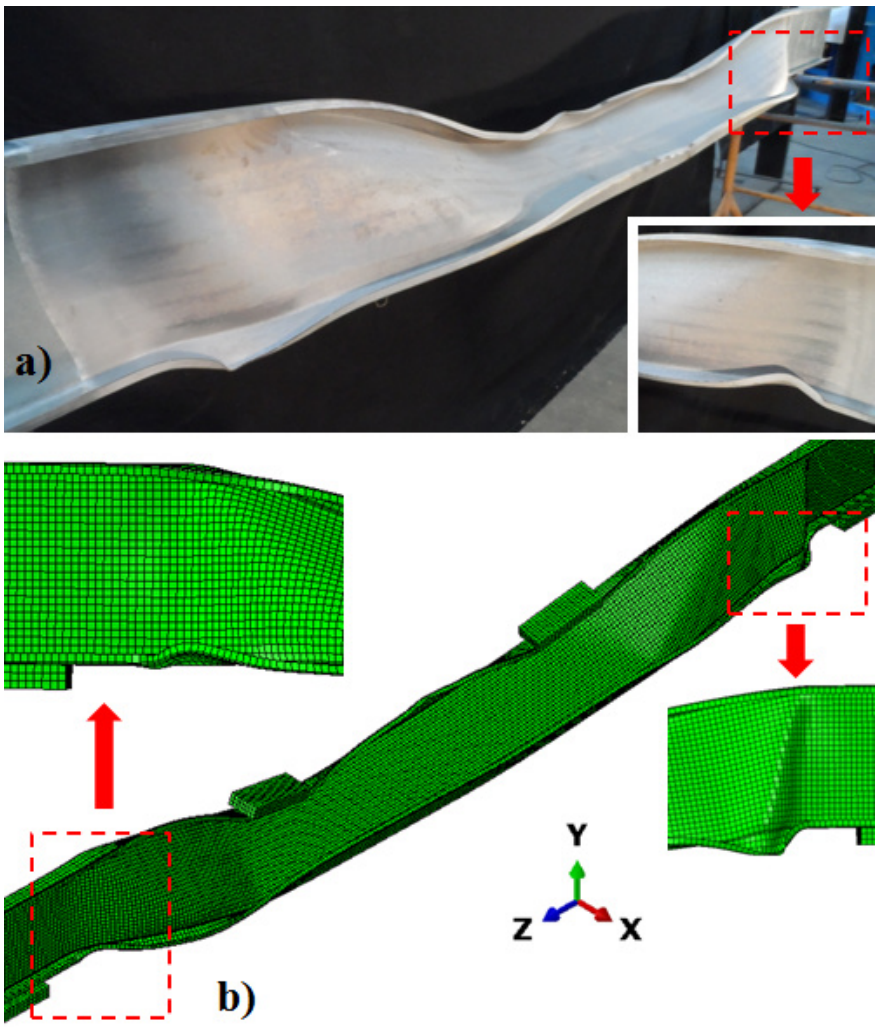

Figure 4.26 – Experimental (a) and numerical (b) configuration of the deformed C beam with axial and rotational restraint after fire test

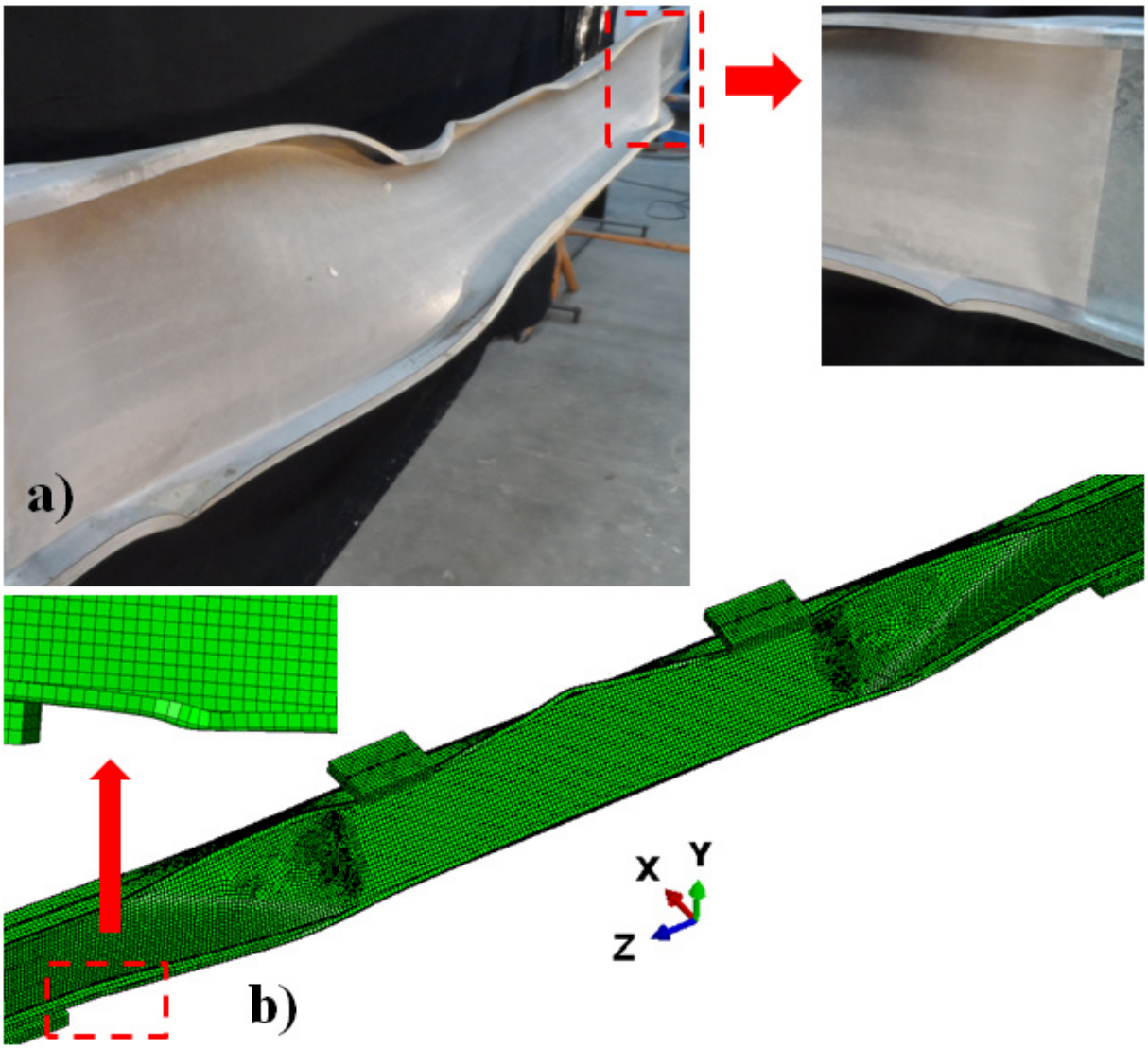

Figure 4.27 – Experimental (a) and numerical (b) configuration of the deformed lipped I beam with axial and rotational restraint after fire test

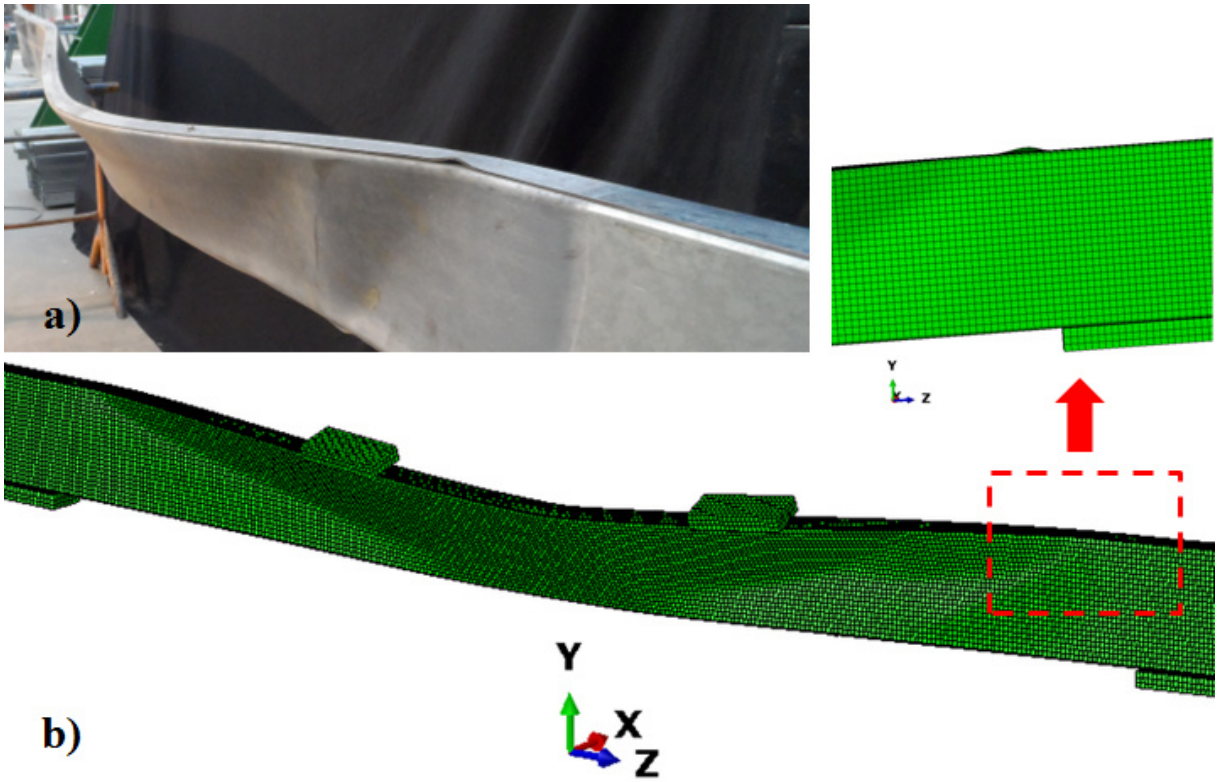

Figure 4.28 – Experimental (a) and numerical (b) configuration of the deformed R beam with axial and rotational restraint after fire test

4.7.5 Heat transfer analysis

The purpose of this section is to check the suitability of a thermal model using the heat transfer option available in ABAQUS, and to determine the appropriate modelling parameters, in particular, the input thermal boundary conditions and material thermal properties, so that standard fire resistances tests of CFS beams can be simulated. It is also worth remembering again that an uniform temperature distribution along all beam length was intended for the parametric study, in contrast to the tested beams in the Laboratory. In addition, in order to provide data for the development of simplified calculation methods for fire design of CFS beam, the ISO 834 standard fire curve must be used.

To achieve this goal, the temperatures used in the numerical simulations for calibration of the numerical model were the gas temperatures registered in the experimental tests. As mentioned before, the thermal action was defined by two types of surface, namely, “film condition” and “radiation to ambient”, corresponding respectively to heat transfer by convection and radiation. The radiative heat flux was calculated using a steel emissivity value of 0.3 and 0.7

for fire, and the Stefan-Boltzmann constant was 5.67×10^{-8} W/m^{2}K^4. On the other hand, convection was considered with heat transfer coefficient equal to 15 W/(m^{2}K) for the fire test curves and 25 W/(m^{2}K) for the ISO 834 fire curve, as recommended by EN 1991-1-2 (2002).

The heat transfer analysis of the R and 2R beams has an additional challenge because of the voids between the profiles. This problem can be solved in a simplified way by three different technical approaches. One is to simply neglect the cavity, the other is to use the assumption of isothermal and iso-emissive cavity facets (Feng *et al.*, 2003a) and the last one is to consider the air as a solid material, i.e., the heat transfer by convection in the cavity is neglected. As the beams are generally horizontal elements in the buildings and the cavities were very small, the last technique was chosen. Therefore, a two-dimensional model was developed on the basis of the CFS cross-sections (figs. 4.30, 4.31, 4.32 and 4.33) and the thermal resistances to heat conduction developed at steel-steel and steel-fresh air interfaces were respectively considered with thermal contact conductance coefficients equals to 200 and 10 W/(m^{2}K). Note that the emissivity coefficients, the heat transfer coefficients and the thermal contact conductance coefficients remained unchanged with increasing temperature.

The thermal properties (thermal conductivity and specific heat) of the air inside the closed built-up sections at high temperatures were those presented in Figure 4.29 (taken from tables of technical properties). The specific weight was assumed constant and equal to 1.16 Kg/m^3.

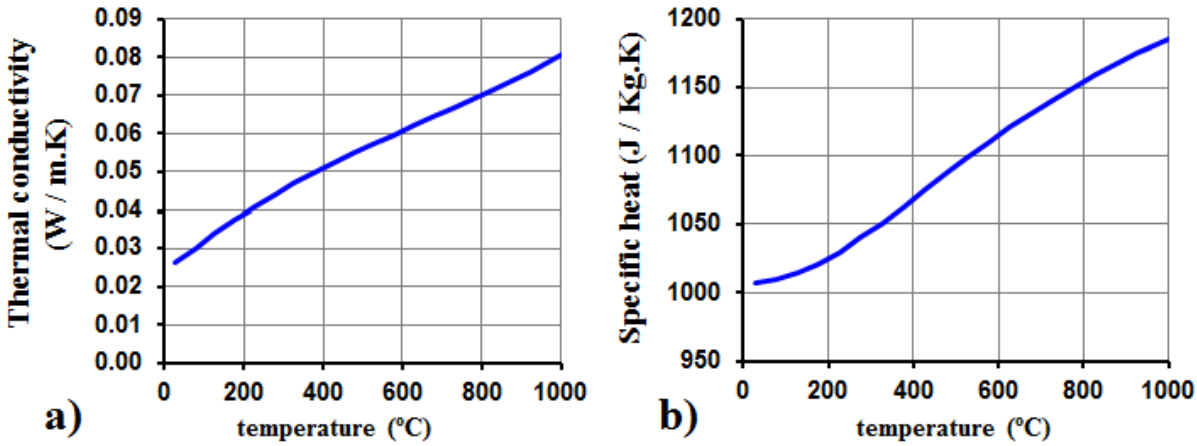

Figure 4.29 – Thermal properties (a – thermal conductivity, b – specific heat) of air at one atmospheric pressure as a function of temperature

Figures 4.30, 4.31, 4.32 and 4.33 show respectively the temperature distribution in the C, lipped I, R and 2R sections at 9 minutes of test run. Once again, it can be seen that the temperature gradients were very small (the temperature was almost uniform in the cross-sections), especially for the C and R sections and except for the 2R section. Nine minutes after the beginning of the tests, the temperature gradient was of 7 ºC in the C section (fig. 4.30), 112 ºC in the lipped I section (fig. 4.31), 60 ºC in the R section (fig. 4.32) and 195 ºC in the 2R section (fig. 4.33). Although some sections can present significant temperature gradients, the temperatures in the flanges were almost uniform. Another important thing to point out is that symmetric temperature distributions were obtained from ABAQUS, since the thermal action was assumed constant with height of the cross-section. Hence, the numerical results were also compared with the experimental temperatures recorded by the thermocouples which presented the best correlation, as it can be seen in Figures 4.34, 4.35, 4.36 and 4.37.

A good agreement was generally observed between the experimental and numerical temperatures. The agreement in the C and R sections was almost perfect (figs. 4.34 and 4.36), where the differences were around 5 %. The numerical temperatures in the web of the lipped I beams were slightly higher (about 10%) than the experimental temperatures (fig. 4.35), especially between the 12 and 15 minutes of test run. Although this difference is a bit high, between other identical tests the difference is smaller. In contrast to these sections, the differences in the 2R sections were not so good, especially in the inner web (fig. 4.37). In the middle of the test period, the experimental and numerical temperatures started to diverge. This may be due to the fact that the spacing between the flanges of both profiles (C and U) starts to increase in some places (even though too small) and so allowing the hot air to enter the voids between the profiles. This may introduce some differences in the numerical deformations comparing to the experimental ones of the beams but not in their strength, because they failed in distortional buckling. However, the differences between the other numerical temperatures (outer web and flange) and the respective experimental ones were about 10 %. To sum up, the tools of ABAQUS program for the application of thermal actions allow simulating the phenomenon of heat transfer between hot air and structural CFS elements with satisfactory results.

Figure 4.30 – Numerical analysis of the temperature distribution in the C section

Figure 4.31 – Numerical analysis of the temperature distribution in the lipped I section

Figure 4.32 – Numerical analysis of the temperature distribution in the R section

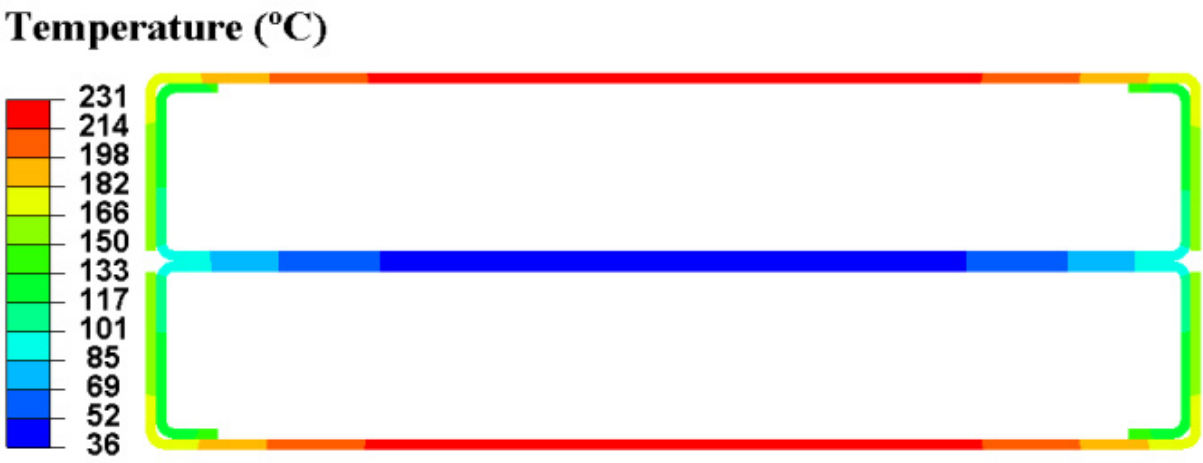

Figure 4.33 – Numerical analysis of the temperature distribution in the 2R section

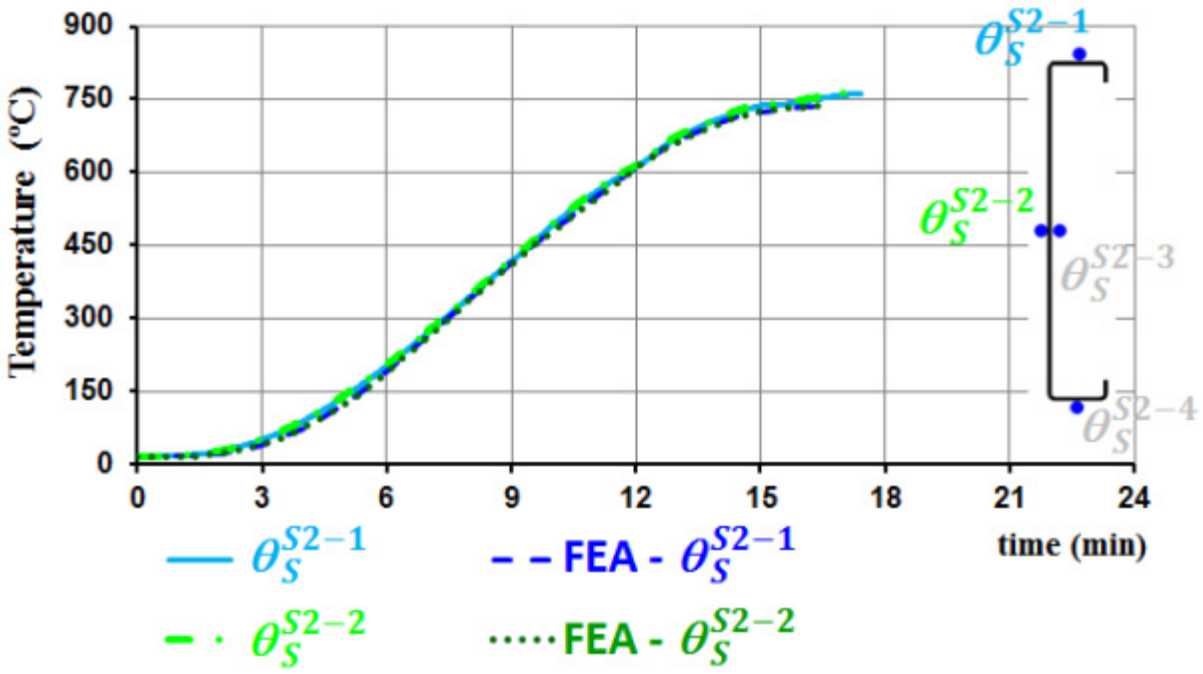

Figure 4.34 – Comparison of the FEA and experimental temperature distribution in the cross-section S2 of the test beam B_ka+kr-C_3

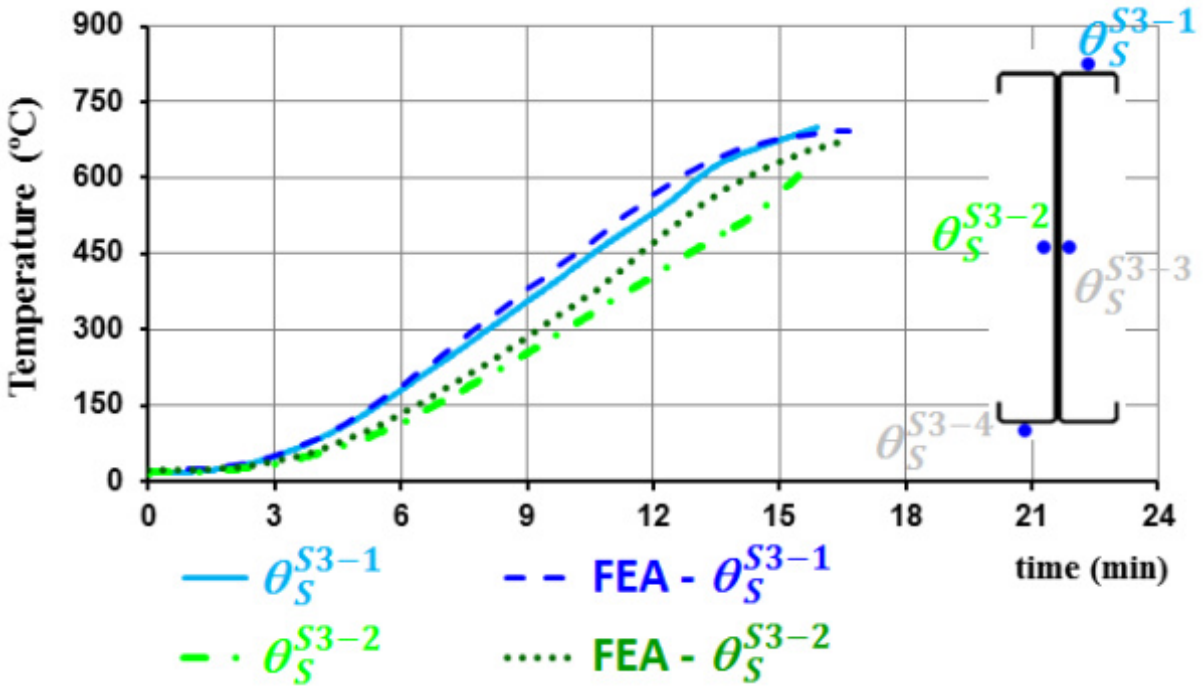

Figure 4.35 – Comparison of the FEA and experimental temperature distribution in the cross-section S3 of the test beam B_ka+kr-I_1

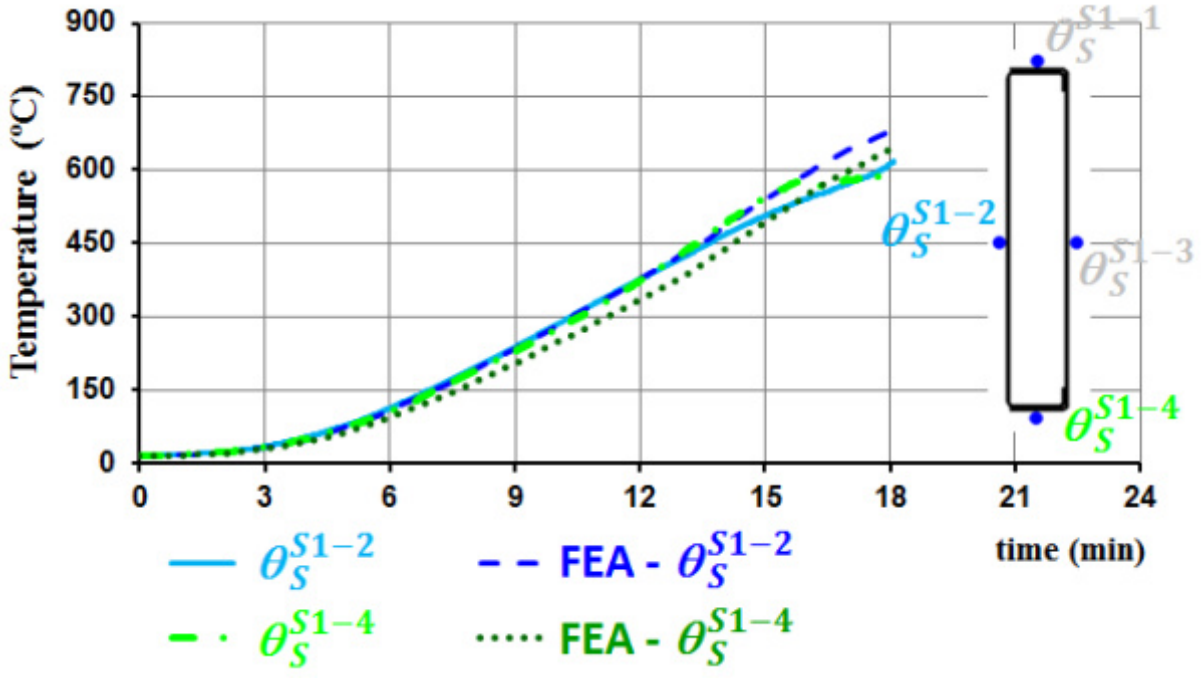

Figure 4.36 – Comparison of the FEA and experimental temperature distribution in the cross-section S1 of the test beam B_ka+kr-R_1

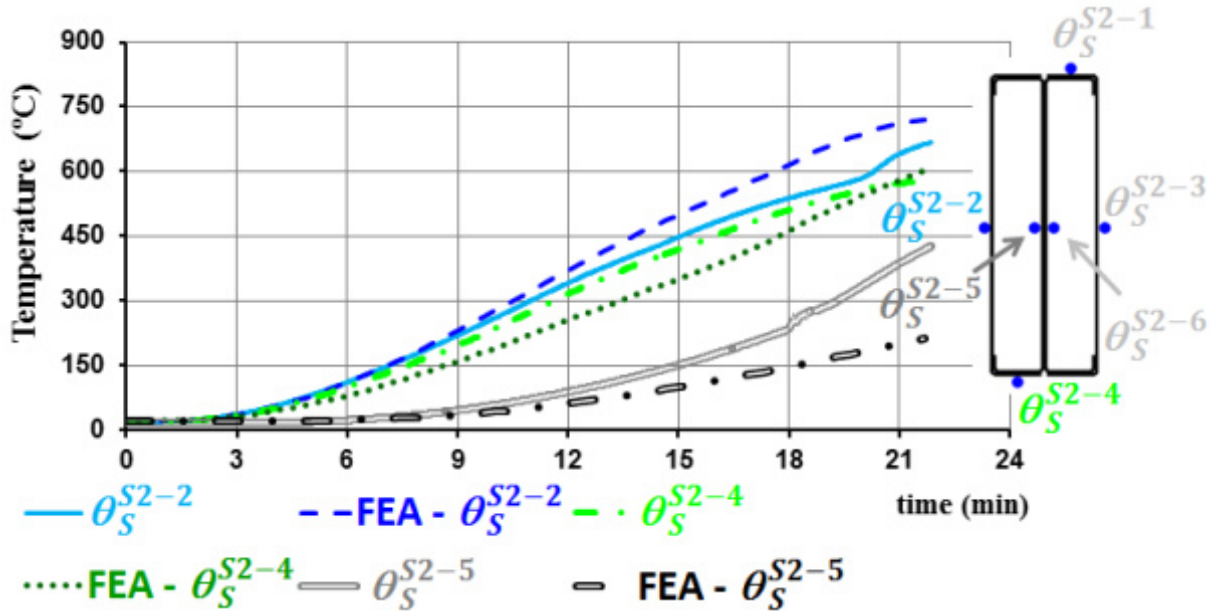

Figure 4.37 – Comparison of the FEA and experimental temperature distribution in the cross-section S2 of the test beam B_ka+kr-2R_3

4.8 Final Remarks

This chapter has described the finite element models developed for the investigation into the structural behaviour of CFS beams subjected to major axis bending at ambient temperature and subjected to combined bending and fire. The numerical modelling was mainly intended to simulate as faithful as possible the structural response (maximum load-carrying capacity and critical time and temperature of the beams) and the buckling modes of these type of beams such as the ones observed in the beams previously tested in Laboratory by the author.

The good agreement between the experimental and numerical results and between the respective failure buckling modes, presented in this chapter, proved that the developed finite element models may be a reliable tool to get quite accurate results. Therefore, the model developed in this study has the potential to be used in parametric studies to obtain simplified calculation methods for fire design of CFS beams under both bending and composed bending (bending plus axial load).

The tools of ABAQUS program for the application of thermal actions also allow simulating the phenomenon of heat transfer between air and structural elements with satisfactory results.

It is also understandable that the use of material and geometric nonlinear finite element analysis is required for solving such highly nonlinear problems involving thin-walled structures, high temperatures and contact. The behaviour of such members or structures may be very complex, especially in case of fire and under particular boundary conditions. The computational modelling has thereby a strong role to play in the research and design of such structures.

Finally, a suitable maximum value for global imperfections was found to be approximately $L/1000$, for distortional imperfections t and for local imperfections $h/200$. The use of shell elements with finite element mesh of 10 x 10 mm seems to give very accurate results, as well.

5 PARAMETRIC STUDY AND PROPOSAL OF SIMPLIFIED DESIGN EQUATIONS

5.1 Cold-Formed Steel Beams at Ambient Temperature

5.1.1 Parametric study

After validating the finite element model at ambient temperature a parametric study has been performed, with about fifty numerical simulations, considering several combinations of thickness, height and length of the beams so that the influence of these parameters on the flexural structural response of beams at ambient temperature could be identified, as well as the evolution of strength-to-weight ratio (*PW / SW*) as a function of those parameters (fig. 5.1).

It is noticed that the first, second, third and last letter of the reference C-h-t-L corresponds respectively to the type of simulated beam (for this case corresponds to the C beam), the height (h), the thickness (t) and the length (L) of the beam in millimetres. Therefore, five different thicknesses (1.5, 2.0, 2.5, 3.0 and 3.5 mm), heights (200, 225, 250, 275 and 300 mm) and lengths (3000, 3500, 4000, 4500 and 5000 mm) for each kind of beam (C, lipped I, R and 2R) were used in this particular parametric study.

Figure 5.1 summarizes all numerical results showing that an increase of the number of profiles per compound cross-section leads to an increase in the *PW / SW* ratio. However, it is expected that this ratio stops to increase since the difference between the R and 2R beams was already small. The same tendency was found for this ratio in what concerns to the increase of thickness and height of beams. Finally, the average *PW/ SW* ratio of the lipped I, R and 2R beams was 1.80, 2.59 and 2.91 times higher than the one of the C beams, respectively. From the studied beams, the maximum ratio obtained was of 55.6 for the C beams, 99.3 for the lipped I beams, 140.0 for the R beams and 152.6 for the 2R beams, corresponding respectively to the beams C-250-3.5-3000, I-250-3.5-3000, R-300-2.5-3000 and 2R-300-2.5-3000. It should also be pointed out that the *PW / SW* ratio had a strong reduction when the span of the beams changed from 3000 to 4000 mm, especially for the R and 2R beams.

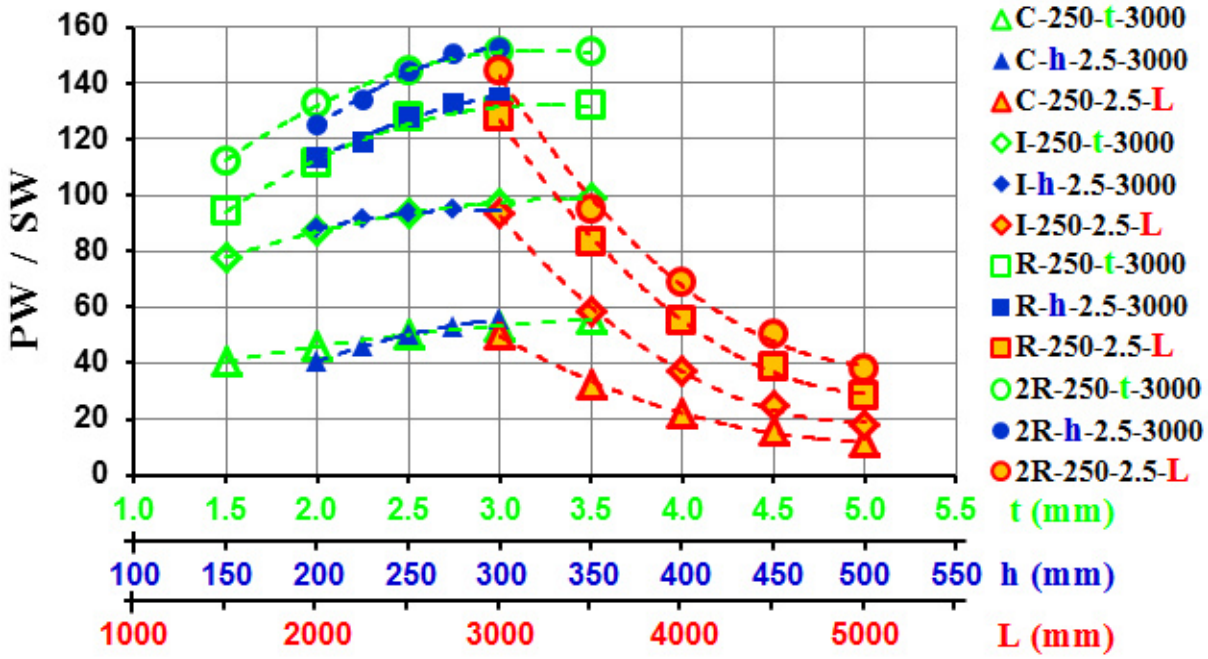

Figure 5.1 – Evolution of strength-to-weight ratio of beams as a function of their thickness, height and length

5.1.2 Proposal of simplified calculation equations

According to EN1993-1.1 (2004) the design buckling resistance moment of a member susceptible to lateral-torsional buckling is given as follows:

$$M_{b,Rd} = \chi_{LT} \frac{M_{Rd}}{\gamma_{M1}} = \chi_{LT} \cdot W_y \cdot \frac{f_y}{\gamma_{M1}} \tag{5.1}$$

in which χ_{LT} is defined as follows:

$$\begin{aligned} \chi_{LT} &= 1.0 && \text{if } \bar{\lambda}_{LT} \leq 0.4 \\ \chi_{LT} &= \frac{1}{\Phi_{LT} + \sqrt{\Phi_{LT}^2 - \bar{\lambda}_{LT}^2}} && \text{if } \bar{\lambda}_{LT} > 0.4 \end{aligned} \tag{5.2}$$

where,

$$\Phi_{LT} = 0.5\left[1 + \alpha_{LT}\left(\bar{\lambda}_{LT} - 0.2\right) + \bar{\lambda}_{LT}^2\right] \tag{5.3}$$

$$\bar{\lambda}_{LT} = \sqrt{\frac{W_y f_y}{M_{cr}}} \tag{5.4}$$

W_y in Equations 5.1 and 5.4 are the appropriate section modulus of the cross-section depending on its class (elastic section modulus, W_{el}, for class 3 and effective section modulus, W_{eff}, for class 4 cross-sections) and f_y is the yield strength of steel. It is noticed that α_{LT} in Equation 5.3 was equal to 0.76 (buckling curve d) for calculating the resistant moment of these beams according to EN1993-1.1 (2004) (Tables 5.1, 5.2, 5.3 and 5.4), since the beam profiles were connected to each other by screws (Tables 6.3 and 6.4 of the EN1993-1.1, 2004). In addition, the effective section modulus was calculated considering the individual contribution of each profile and, consequently, the effective geometrical properties of class 4 cross-sections were still determined based on the Clause 5.5 of EN1993-1.3 (2004) and Clause 4.4 of EN1993-1.5 (2006). Finally, the elastic critical moment for lateral-torsional buckling, M_{cr}, can be calculated (for doubly symmetric sections or mono-symmetric sections which are subjected to bending about the symmetry axis (AS/NZS 4600, 1996)) by:

$$M_{cr} = C_b \sqrt{\frac{\pi^2 EI}{(k_y L)^2}\left[GI_T + \frac{\pi^2 EI_W}{(k_W L)^2}\right]} \tag{5.5}$$

in which EI_y, EI_w and GJ are the minor axis flexural rigidity, warping rigidity and torsional rigidity, respectively. k_y represents the effective lateral buckling length factor and k_w the factor which accounts for the beam end warping. Regarding the lateral deformed shape of the beams obtained from the FEA, the value of k_y = 0.8 has been used and the value of k_w = 1.0 representing the free end warping condition. On the other hand, C_b is a coefficient depending on the moment distribution along the length of the beams (Trahair, 1993). In this specific study, C_b was equal to 1.0.

Tables 5.1, 5.2, 5.3 and 5.4 summarise the results obtained from all numerical simulations carried out respectively for C, lipped I, R and 2R beams and the corresponding results given by the currently available design rules. It should be pointed out that most of the numerical results were higher than the corresponding design results. The opposite was only valid for the I-250-2.5-5000, 2R-250-2.5-4500 and 2R-250-2.5-5000 beams, which means that the design methods, as presented here, may be on the safe side for CFS beams in the same conditions as the ones studied in this work and at least for spans lower than 4500 mm. It is thereby noticed that, when the values of non-dimensional slenderness are low, they do not have to correspond exactly to safe design values.

Another important conclusion to be drawn was that EN1993-1.1 (2004) predicted the buckling moment capacity accurately for the simulated C beams (fig. 5.2). However, EN1993-1.3 (2004) suggests using the lateral buckling curve a (with α_{LT} = 0.21) instead of the lateral buckling curve d for this kind of beams. If it had been shown the difference between the FEA results and the design results using the lateral buckling curve a, it would have been seen that some numerical results would be lower than the respective design results. Nevertheless, it is very important do not forget that the loading applied on the C beams was made at the middle of the flange and not at the centroid of the section, which means that the FEA results for the C-beams could still be a little bit higher. This is not presented in this paper since it was intended to model the worst structural response of the beams which were observed in the experimental tests as already mentioned.

From Figure 5.2, it appears that different buckling curves could be adopted for each kind of beam in such a way that more accurate and safe predictions can be made, as the ones presented in Figure 5.3. So, the author recommends the use of Equations 5.2 and 5.3 with α_{LT} = 0.76 for the design of cold-formed steel C beams at ambient temperature and, instead of these equations, Equations 5.6 and 5.7 should be used for the design of cold-formed steel lipped I beams, Equations 5.8 and 5.9 for the R beams and Equations 5.10 and 5.11 for the 2R beams. However, further experimental tests on cold-formed steel beams should still be performed, especially on compound beams, in order to validate experimentally these equations for different section geometries, loading types and boundary conditions.

New equations for the design of cold-formed steel lipped I beams at ambient temperature:

$$\chi_{LT} = 1.0 \quad \text{if } \bar{\lambda}_{LT} \leq 0.6$$
$$\chi_{LT} = \frac{1}{\Phi_{LT\_I} + \sqrt{\Phi_{LT\_I}^2 - \bar{\lambda}_{LT}^2}} \quad \text{if } \bar{\lambda}_{LT} > 0.6 \tag{5.6}$$

$$\Phi_{LT\_I} = 0.59\left[1 + 0.80\left(\bar{\lambda}_{LT} - 0.85\right) + \bar{\lambda}_{LT}^2\right] \tag{5.7}$$

New equations for the design of cold-formed steel R beams at ambient temperature:

$$\chi_{LT} = 1.0 \quad \text{if } \bar{\lambda}_{LT} \leq 0.5$$
$$\chi_{LT} = \frac{1}{\Phi_{LT\_R} + \sqrt{\Phi_{LT\_R}^2 - \bar{\lambda}_{LT}^2}} \quad \text{if } \bar{\lambda}_{LT} > 0.5 \tag{5.8}$$

$$\Phi_{LT\_R} = 0.70\left[1 + 0.70\left(\bar{\lambda}_{LT} - 1.00\right) + \bar{\lambda}_{LT}^2\right] \tag{5.9}$$

New equations for the design of cold-formed steel 2R beams at ambient temperature:

$$\begin{aligned} \chi_{LT} &= 1.0 && \text{if } \bar{\lambda}_{LT} \le 0.5 \\ \chi_{LT} &= \frac{1}{\Phi_{LT\_2R} + \sqrt{\Phi_{LT\_R2}^2 - \bar{\lambda}_{LT}^2}} && \text{if } \bar{\lambda}_{LT} > 0.5 \end{aligned} \tag{5.10}$$

$$\Phi_{LT\_2R} = 0.70\left[1 + 1.00\left(\bar{\lambda}_{LT} - 0.73\right) + \bar{\lambda}_{LT}^2\right] \tag{5.11}$$

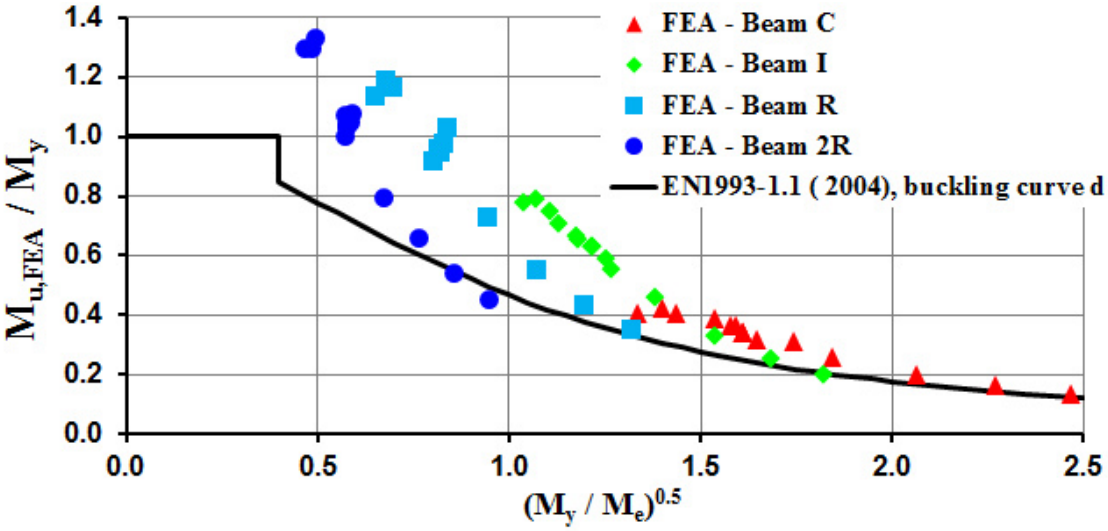

Figure 5.2 – Comparison of FEA results with EN1993-1.1 (2004) formulation

Table 5.1 – Comparison of FEA results with EN1993-1.1 (2004) for C-section beams

Beam reference	$\bar{\lambda}_{LT}$	M_{Rd} **(kN.m)**	M_{cr} **(kN.m)**	$M_{b,Rd}$ **(kN.m)**	M_{FEA} **(kN.m)**
C-250-**1.5**-3000	1.34	6.41	3.59	2.09	2.61
C-250-**2.0**-3000	1.40	9.46	4.81	2.88	3.99
C-250-**2.5**-3000	1.61	15.87	6.09	3.93	5.40
C-250-**3.0**-3000	1.59	18.86	7.45	4.78	6.87
C-250-**3.5**-3000	1.75	27.14	8.90	5.96	8.39

C-200-2.5-3000	1.54	11.47	4.84	3.05	4.41
C-225-2.5-3000	1.58	13.60	5.46	3.49	4.92
C-250-2.5-3000	1.61	15.87	6.09	3.93	5.40
C-275-2.5-3000	1.65	18.29	6.74	4.40	5.82
C-300-2.5-3000	1.44	15.32	7.41	4.50	6.19
C-250-2.5-**3000**	1.61	15.87	6.09	3.93	5.40
C-250-2.5-**3500**	1.85	15.87	4.66	3.19	4.09
C-250-2.5-**4000**	2.06	15.87	3.72	2.66	3.19
C-250-2.5-**4500**	2.27	15.87	3.08	2.27	2.55
C-250-2.5-**5000**	2.47	15.87	2.61	1.97	2.10

Table 5.2 – Comparison of FEA results with EN1993-1.1 (2004) for lipped I-section beams

Beam reference	$\overline{\lambda}_{LT}$	M_{Rd} **(kN.m)**	M_{cr} **(kN.m)**	$M_{b,Rd}$ **(kN.m)**	M_{FEA} **(kN.m)**
I-250-**1.5-**3000	1.04	12.91	11.96	5.78	10.03
I-250-**2.0-**3000	1.07	19.10	16.59	8.24	15.05
I-250-**2.5-**3000	1.22	32.15	21.71	11.88	20.15
I-250-**3.0-**3000	1.18	38.30	27.41	14.69	25.08
I-250-**3.5-**3000	1.27	54.42	33.75	19.01	29.97
I-200-2.5-3000	1.13	23.25	18.13	9.40	16.37
I-225-2.5-3000	1.18	27.55	19.93	10.64	18.33
I-250-2.5-3000	1.22	32.15	21.71	11.88	20.15
I-275-2.5-3000	1.26	37.03	23.50	13.14	21.81
I-300-2.5-3000	1.11	30.93	25.27	12.87	23.15
I-250-2.5-**3000**	1.22	32.15	21.71	11.88	20.15
I-250-2.5-**3500**	1.38	32.15	16.80	9.99	14.66
I-250-2.5-**4000**	1.54	32.15	13.57	8.56	10.60
I-250-2.5-**4500**	1.68	32.15	11.32	7.46	8.12
I-250-2.5-**5000**	1.82	32.15	9.69	6.60	6.44

Table 5.3 – Comparison of FEA results with EN1993-1.1 (2004) for R-section beams

Beam reference	$\overline{\lambda}_{LT}$	M_{Rd} **(kN.m)**	M_{cr} **(kN.m)**	$M_{b,Rd}$ **(kN.m)**	M_{FEA} **(kN.m)**
R-250-**1.5-**3000	0.65	10.75	25.36	7.26	12.24
R-250-**2.0-**3000	0.69	16.57	34.36	10.72	19.31
R-250-**2.5-**3000	0.81	28.93	43.63	16.52	27.69
R-250-**3.0-**3000	0.81	35.17	53.25	20.12	33.85
R-250-**3.5-**3000	0.82	42.38	63.26	24.09	40.15
R-200-2.5-3000	0.84	20.71	29.40	11.51	21.31
R-225-2.5-3000	0.83	24.68	36.13	13.91	24.12
R-250-2.5-3000	0.81	28.93	43.63	16.52	27.69
R-275-2.5-3000	0.80	33.48	51.91	19.35	30.80
R-300-2.5-3000	0.68	28.00	60.95	18.42	33.26
R-250-2.5-**3000**	0.81	28.93	43.63	16.52	27.69
R-250-2.5-**3500**	0.94	28.93	32.45	14.36	21.14
R-250-2.5-**4000**	1.07	28.93	25.19	12.50	15.92
R-250-2.5-**4500**	1.20	28.93	20.20	10.92	12.59
R-250-2.5-**5000**	1.32	28.93	16.64	9.61	10.20

Table 5.4 – Comparison of FEA results with EN1993-1.1 (2004) for 2R-section beams

Beam reference	$\overline{\lambda}_{LT}$	M_{Rd} **(kN.m)**	M_{cr} **(kN.m)**	$M_{b,Rd}$ **(kN.m)**	M_{FEA} **(kN.m)**
2R-250-**1.5-**3000	0.47	21.53	98.06	17.25	27.93
2R-250-**2.0-**3000	0.50	33.17	134.65	25.94	44.12
2R-250-**2.5-**3000	0.58	57.89	173.10	41.96	60.15
2R-250-**3.0-**3000	0.57	70.36	213.59	51.21	75.54
2R-250-**3.5-**3000	0.58	85.38	256.29	61.96	88.31
2R-200-2.5-3000	0.59	41.46	117.97	29.64	44.72
2R-225-2.5-3000	0.59	49.38	144.18	35.56	51.77
2R-250-2.5-3000	0.58	57.89	173.10	41.96	60.15
2R-275-2.5-3000	0.57	66.98	204.73	48.85	66.97
2R-300-2.5-3000	0.48	56.02	239.06	44.28	72.52

2R-250-2.5-**3000**	0.58	57.89	173.10	41.96	60.15
2R-250-2.5-**3500**	0.67	57.89	128.08	38.29	46.11
2R-250-2.5-**4000**	0.77	57.89	98.85	34.81	38.15
2R-250-2.5-**4500**	0.86	57.89	78.80	31.58	31.45
2R-250-2.5-**5000**	0.95	57.89	64.46	28.63	26.19

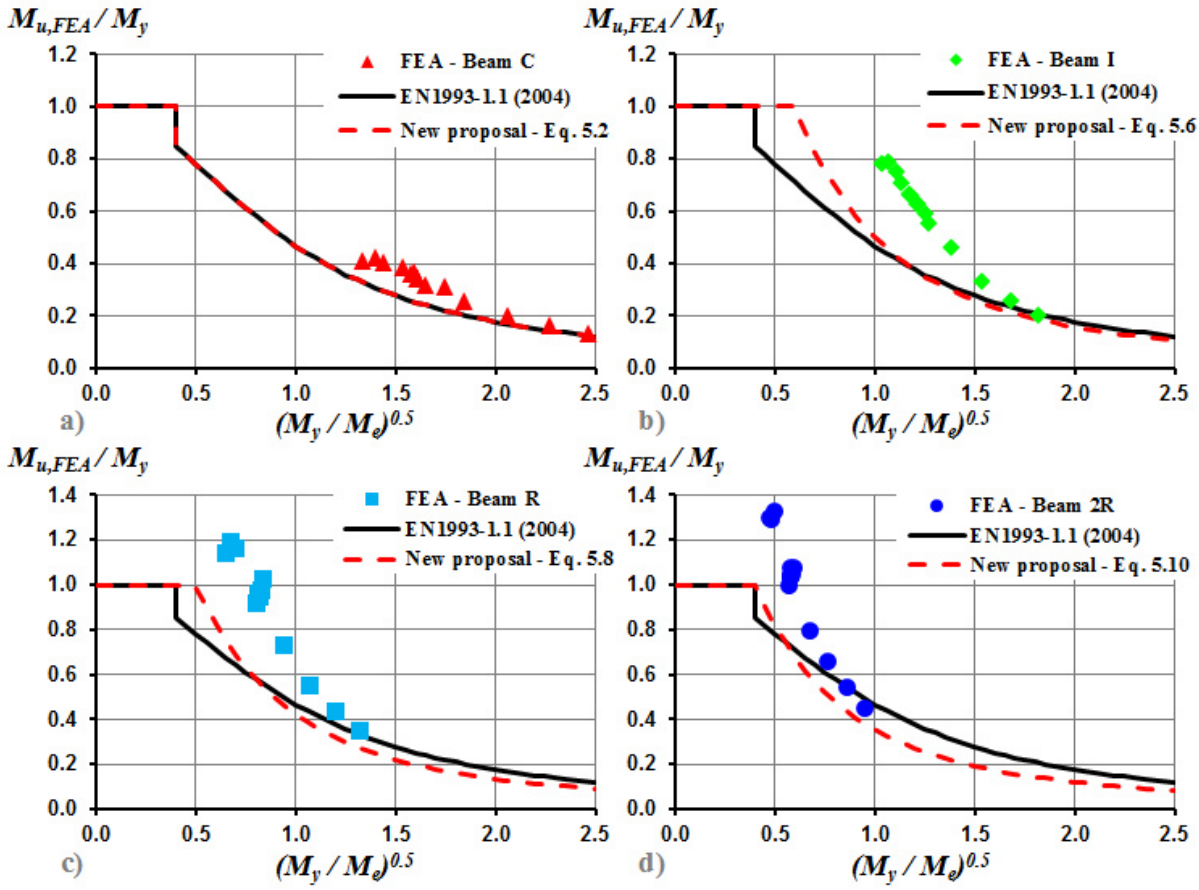

Figure 5.3 – Comparison of FEA results with the alternative approach proposed by the author for the design of cold-formed steel C (a), lipped I (b), R (c) and 2R (d) beams

5.2 Cold-Formed Steel Beams at High Temperatures

5.2.1 Parametric study

After validating the finite element model at high temperatures a parametric study has also been performed, with about one hundred and fifty numerical simulations, so as to investigate the thermal performance of different CFS beams (C, lipped I, R and 2R beams) with different initial load levels (LL = $M_{b,fi,\theta,Rd}$ / $M_{b,Rd}$), span lengths (slenderness, $\overline{\lambda}_{LT}$), initial geometric imperfections, axial restraint to the thermal elongation of the beam and rotational stiffness of the beam supports. The C-250-43-15-2.5, I-250-43-15-2.5, R-250-43-15-2.5 and 2R-250-43-15-2.5 sections were chosen for this study. It is noticed that the first, second, third and fourth value in the name of these sections correspond to the geometric dimensions of the cross-section of a C profile which makes part the respective section. Hence, the C profile cross-section used in these numerical simulations was 250 mm tall, 43 mm wide and 2.5 mm thick, and finally its edge stiffener was 15 mm long.

Therefore, the load levels selected in this study were 30, 50 and 70% of the design value of buckling load of the beams at ambient temperature, the span lengths selected ranged from 2000 to 5000 mm at the interval of 1000 mm, the axial restraints selected were 0, 7.5 kN/mm, 15 kN/mm, 30 kN/mm and ∞ and finally the rotational restraints were 0, 150, 300 and 1200 kN.m/rad for a constant axial restraint equal to 15 kN/mm.

These load levels were chosen, because the tabular methods established in available design rules define, in general, the critical time and/or temperature of a structural member as a function of these values of identical ones. These beam lengths were also selected since the residential and office buildings usually have spans of this order of magnitude. On the other hand, it was investigated the effect of the axial and rotational restraint on the beams, obviously with different values of the ones tested in Laboratory, namely, half, double and their minimum and maximum limits. However, the maximum rotational restraint chosen for the simulations was only equal to 1200 kN.m/rad (eight times the value used in the experimental tests) since the rotational restraint at beam supports is often affected by fire. Note that the beam supports are normally exposed directly to fire, whereas the structural members which comprise the axial restraint to thermal elongation of beams may not be exposed to fire (high temperatures).

Furthermore, the values L/5000, L/1000 and L/200 were employed as the maximum magnitudes of global geometric imperfections for the open sections (C and lipped I beams)

and the values $0.25t_n$, t_n and $2t_n$ as the maximum magnitudes of distortional geometric imperfections for the closed built-up sections (R and 2R beams), with the purpose to evaluate their influence on the fire behaviour of these beams, in other words, to understand how the critical temperature of the CFS beams is affected by varying those parameters. Note that the effect of the geometric imperfections was studied considering that the beams were 4000 mm in length and could deform with no restraints to the thermal action (*ka*=*kr*=0).

5.2.1.1 Effect of slenderness

Figure 5.4 presents the critical temperature of the C (a), lipped I (b), R (c) and 2R (d) beams with no restraints to thermal elongation as a function of their slenderness for different load levels. It can be seen for all beams that as the slenderness of the beams increases the critical temperature decreases. As expected, the higher the load level, the lower the critical temperature. When the span of the C beam increased from 2000 mm (1.11 of slenderness) to 5000 mm (2.47 of slenderness), the critical temperature decreased by 10% (from 745 ºC to 670 ºC) for 30% of load level and 43% (from 617 ºC to 352 ºC) for 70% of load level (fig. 5.4a). Regarding the lipped I, R and 2R beams, the critical temperature decreased respectively by 20% (from 751 ºC to 601 ºC), 11% (from 711 ºC to 630 ºC) and 39% (from 811 ºC to 491 ºC) for 30% of load level and by 67% (from 618 ºC to 204 ºC), 70% (from 585 ºC to 176 ºC) and 71% (from 672 ºC to 192 ºC) for 70% of load level. An interesting point to note is that the critical temperature was always higher than 350ºC, only for 30% and 50% of load level and except for the 2R beam with 5000 mm in length.

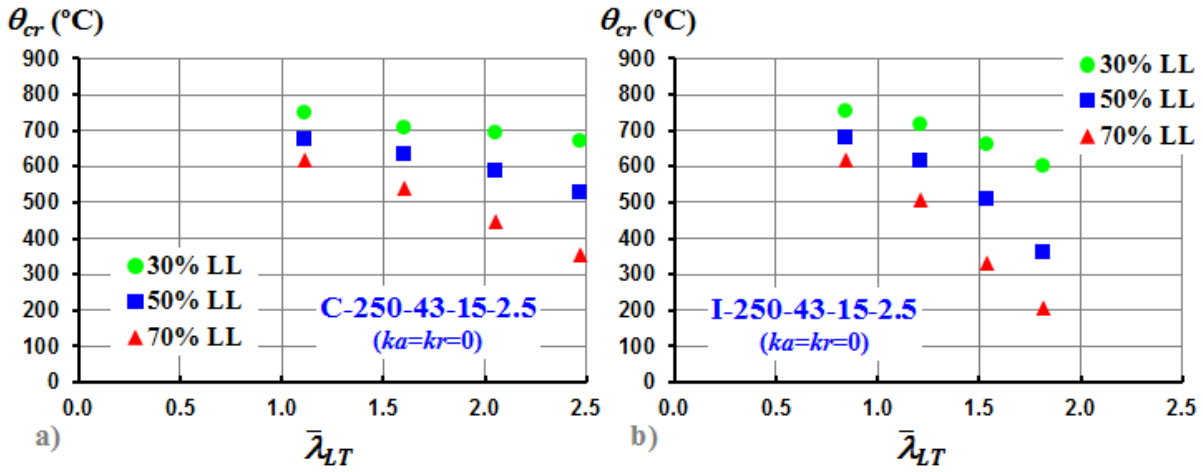

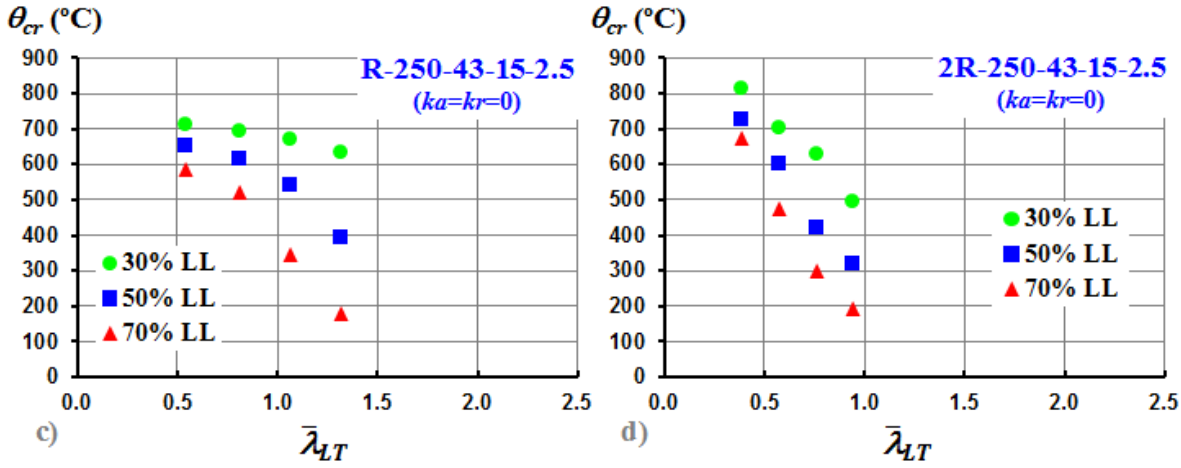

Figure 5.4 – Effects of slenderness on the critical temperature of the C (a), lipped I (b), R (c) and 2R (d) beams

5.2.1.2 Effect of initial geometric imperfections

Figure 5.5 shows the relative flexural strength ($M_{b,fi,\theta,Rd}$ / $M_{b,Rd}$) of the C (a), lipped I (b), R (c) and 2R (d) beams with no restraints to thermal elongation as a function of the critical temperature and for different magnitudes of geometric imperfections. It is observed a reduction on the critical temperatures with the increasing of imperfections. However, as before, the reduction was more relevant for beams with higher load level ($M_{b,fi,\theta,Rd}$ / $M_{b,Rd}$ = 0.70). When the maximum global geometric imperfection increased from L/5000 to L/200, the critical temperature of the C beam decreased by 5% (from 690ºC to 656ºC) for 30% of load level and 20% (from 445ºC to 358ºC) for 70% of load level (fig. 5.5a). On the other hand, the critical temperature of the lipped I beam decreased respectively by 20% (from 705ºC to 562ºC) and 59% (from 463ºC to 192ºC) for the same conditions of the C beam (fig. 5.5b). Still in this context, the critical temperature of the R and 2R beams decreased respectively by 4% (from 668ºC to 639ºC) and 1% (from 627ºC to 619ºC) for 30% of load level and by 23% (from 348ºC to 267ºC) and 4% (from 299ºC to 288ºC) for 70% of load level, when the maximum distortional geometric imperfection increased from 0.25 t_n to 2 t_n (figs. 5.5c and 5.5d). It is quite interesting to observe that the lipped I beams may be very sensitive to the initial global geometric imperfections and by contrast the 2R beams may just be a little sensitive to the initial distortional geometric imperfections. The critical temperature of the 2R beam only decreased by 12% (from 327ºC to 288ºC) for 70% of load level, when the maximum distortional geometric imperfection increased from 0 to 2 t_n (fig. 5.5d).

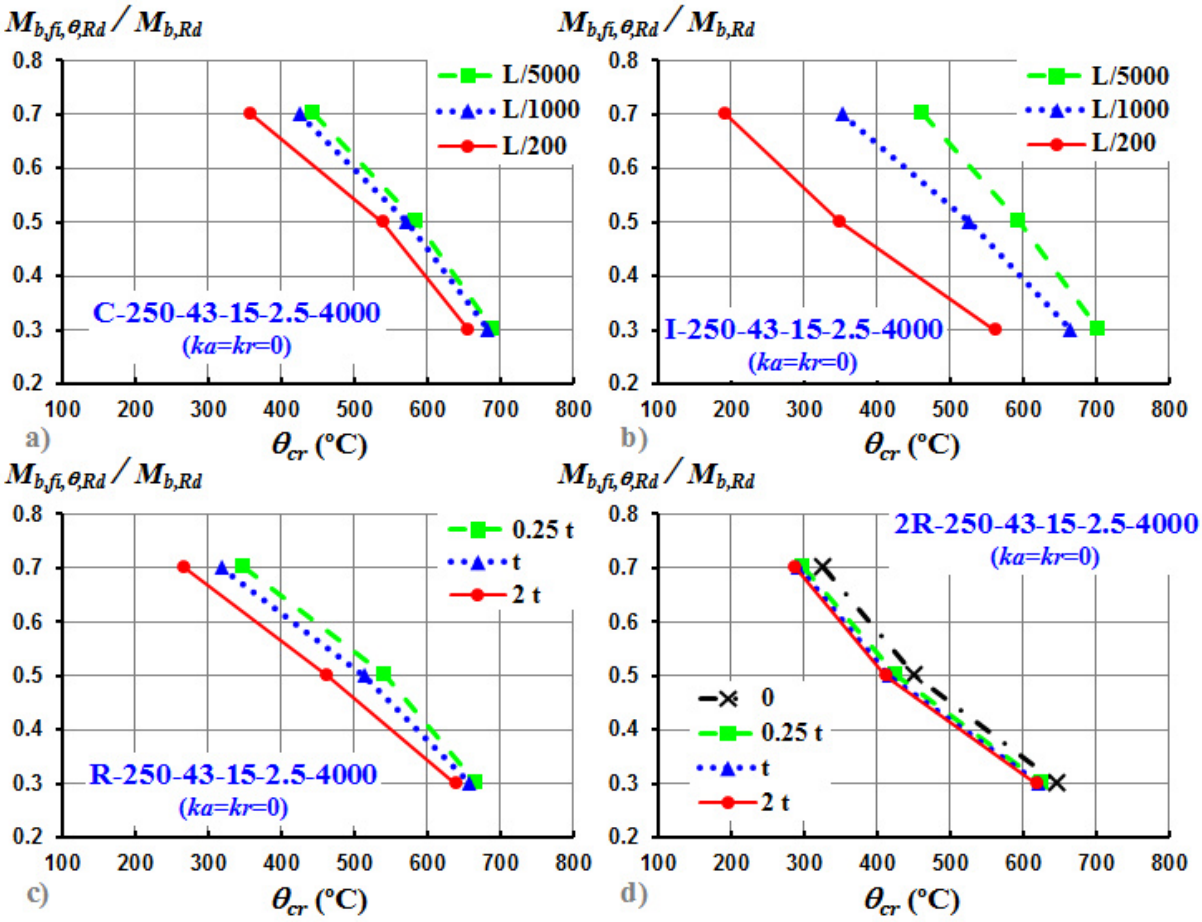

Figure 5.5 – Effects of initial geometric imperfections on the critical temperature of the C (a), lipped I (b), R (c) and 2R (d) beams

5.2.1.3 Effect of axial restraint

Figure 5.6 presents the critical temperature of the C (a), lipped I (b), R (c) and 2R (d) beams as a function of their slenderness for 50% of load level and for different axial restraints. Once again, it can be seen for all beams that as the slenderness of the beams increases the critical temperature decreases and it is clear that the critical temperature of the beams is affected by the axial restraint level, i.e. it decreases with increasing axial restraint. It is worth pointing out that the effect of axial restraint depended strongly on the shape of the beam cross-section. The R section showed a much better behaviour against the axial restraint to the thermal elongation than the open sections. In addition, the critical temperature of the open beams dropped drastically even for low values of axial restraint. Beyond 7.5 kN/mm of axial restraint the critical temperature of the C beams is almost the same for any value of non-dimensional slenderness between 1.11 and 2.47. When the axial restraint level increased from 0 to infinite,

the critical temperature of the C beam decreased by 38% (from 675ºC to 420ºC) for 2000 mm of span (1.11 of non-dimensional slenderness) and 15% (from 526ºC to 448ºC) for 5000 mm of span (2.47 of non-dimensional slenderness) (fig. 5.6a). Regarding the lipped I, R and 2R beams, the critical temperature decreased respectively by 52% (from 677 ºC to 328 ºC), 6% (from 648 ºC to 608 ºC) and 20% (from 724 ºC to 319 ºC) for 2000 mm of span and by 58% (from 357 ºC to 151 ºC), 5% (from 392 ºC to 374 ºC) and 43% (from 319 ºC to 182 ºC) for 5000 mm of span. It is also important to emphasize that the critical temperature of the C and R beams was always higher than 350ºC for load level below 50% and for any value of axial restraint and of span between 2000 and 5000 mm (figs. 5.6a and 5.6c). From Figures 5.4 and 5.7, it can be concluded that the effect of load level is slightly worse for higher axial restraints, except for the 2R beams. The critical temperatures of the C, lipped I and R beams decreased respectively by an average 47%, 52% and 47% for 15 kN/mm of axial restraint and by 31%, 41% and 40% for zero of axial restraint, when the load level increased from 30% to 70%. Anyway, the critical temperature was always higher than 350ºC for 30% of load level and 15 kN/mm of axial restraint to the thermal elongation (fig. 5.7).

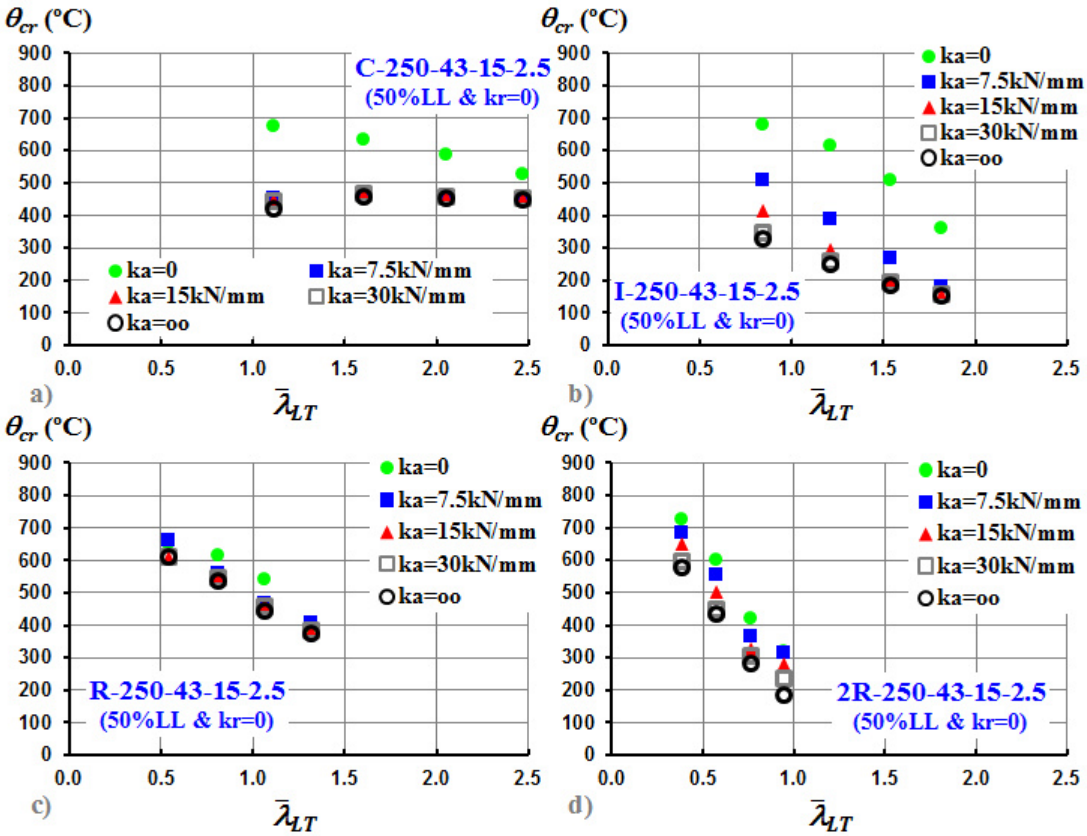

Figure 5.6 – Effects of axial restraint on the critical temperature of the C (a), lipped I (b), R (c) and 2R (d) beams

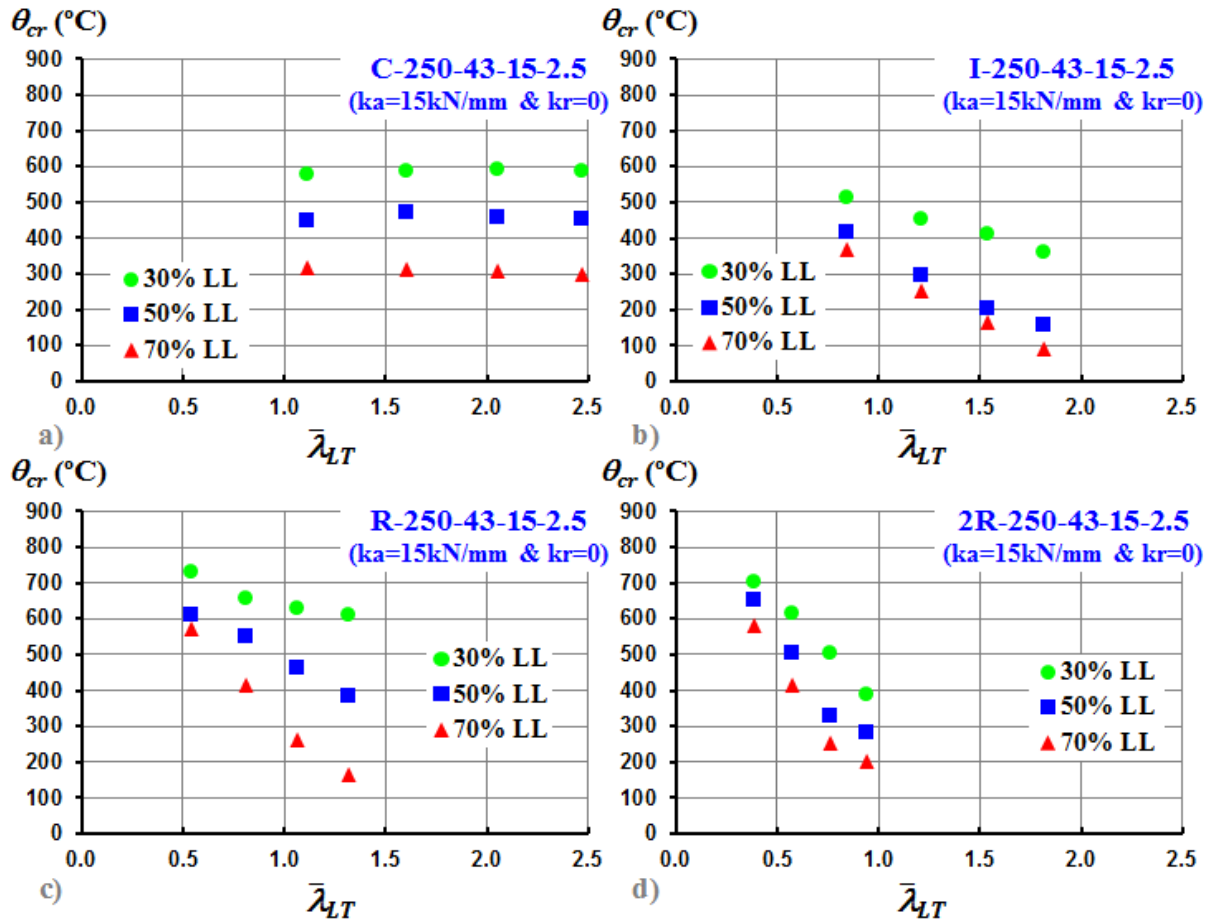

Figure 5.7 – Effects of slenderness on the critical temperature of the C (a), lipped I (b), R (c) and 2R (d) beams when the axial restraint to thermal elongation is equal to 15 kN/mm

5.2.1.4 Effect of rotational restraint

In what concerns to the effects of rotational restraint at beam supports on the critical temperature of the beams, only the results relative to the C beams are here presented. In contrast to the axial restraint, the rotational restraint improved the fire behaviour of the beam. Form Figure 5.8, it can be observed that the critical temperature of the C beam with 15 kN/mm of axial restraint increased from about 450 ºC to 700 ºC for any value of non-dimensional slenderness between 1.11 and 2.47, when the rotational restraint increased from 0 to 150 kN.m/rad or to higher values. However, it seems that the critical temperature depended on the rotational restraint for non-dimensional slenderness below 1.11, as it can be clearly seen in Figure 5.9. This figure also shows that the critical temperature of the C beam may reach 800 ºC, when the load level is equal to 30% and the axial and rotational restraints are respectively of 15 kN/mm and 300 kN.m/rad.

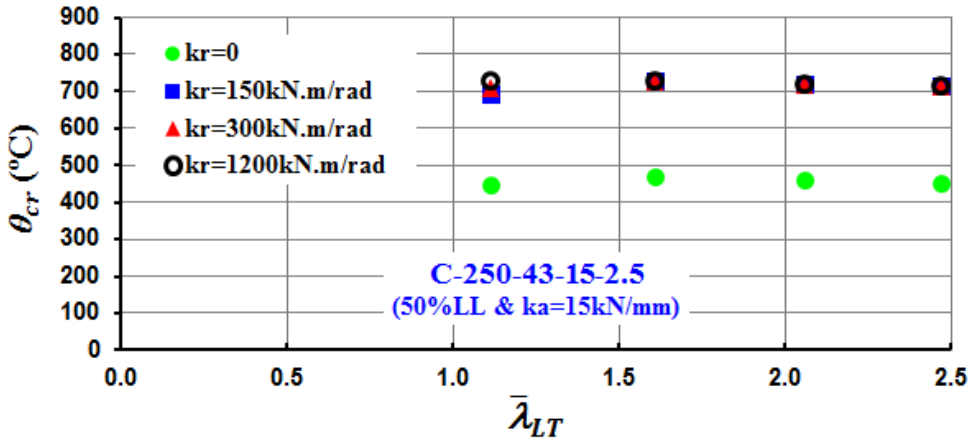

Figure 5.8 – Effects of rotational restraint on the critical temperature of the C beam

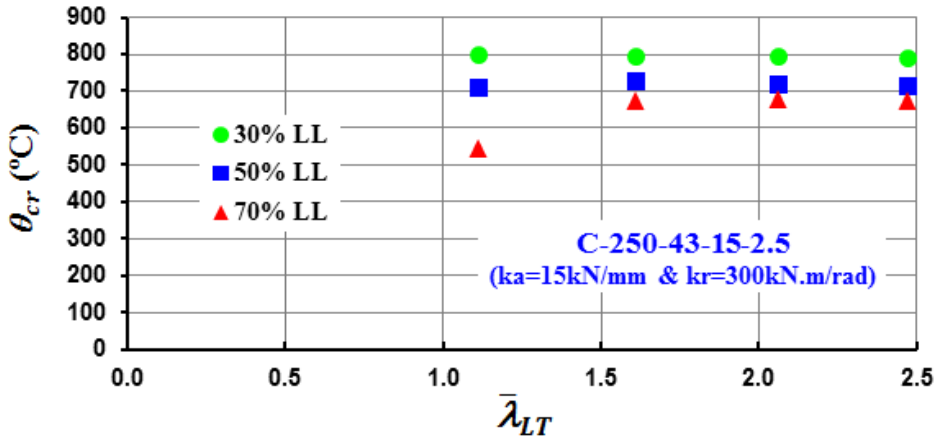

Figure 5.9 – Effects of slenderness on the critical temperature of the C beam when the axial and rotational restraints are respectively of 15 kN/mm and 300 kN.m/rad

5.2.2 Proposal of simplified calculation equations

The analysis of some graphs presented above allowed the derivation of analytical formulae for the assessment of the critical temperatures and times of CFS beams for a wide range of slenderness (changing the beam length between 2000 mm and 5000 mm) and axial restraint levels, depending obviously on the shape of its cross-sections. However, it is worth mentioning that the following equations (Equations 5.12 - 5.23) are still useful for cross-sections identical to the ones studied experimentally and for a load level equal to 50%. Critical temperatures corresponding to 30% and 70% of load level can also be obtained conservatively, in most cases, by multiplying the critical temperature obtained for 50% of load level by 1.15 and 0.60, respectively. For example, from Equation 5.12 it can be obtained critical temperatures of 580 and 448 ºC for the C-250-43-2.5-15-4000 beam ($\bar{\lambda}_{LT} = 2.06$)

with 50 % of load level, when the axial restrains to the thermal elongation of the beam were respectively zero and 15 kN/mm. So, the critical temperatures corresponding to 30% and 70% of load level would be respectively of 667 (580 x 1.15) and 348 ºC (580 x 0.60) for that C beam without axial restraint and of 515 (448 x 1.15) and 269 ºC (448 x 0.60) for that C beam with an axial restraint equal to 15 kN/mm. Comparing these temperatures with the ones obtained from the numerical study (figs. 5.4a and 5.7a), differences between 3 % and 22 % can be observed. Therefore, critical temperatures for 30% and 70% of load levels can be predicted in a trivial way, but sometimes they can be far away of the reality.

On the other hand, it is noticed that these equations did not take the effect of the rotational restraint into account in the critical temperature and time of this kind of beams, i.e., the rotational restraint effect was ignored in these equations. Further numerical simulations must still be done.

Finally, the proposed formulae were obtained for the best fit of the numerical data (Appendix H), using just linear or quadratic functions (Equations 5.12 - 5.23). The author also recommends that the critical times and temperatures of CFS beams with axial restraints between the values used in the parametric study should be determined by a linear interpolation between those values. It is also clear that these equations can be used in rotationally restrained beams, but the results might be over-conservative. However, a maximum difference of approximately 8% was observed between the critical temperatures given by the Equations 5.12, 5.14, 5.18 and 5.20 and the ones presented in Figure 5.6, i.e. a strong correlation between the numerical results and the ones obtained from the new proposed simplified design equations was achieved.

➢ New equations for the fire design of cold-formed steel C-250-43-15-2.5 beams with 50% of load level:

$$\begin{aligned} \theta_{cr} &= -0.0492 \cdot L + 776.88 \qquad \text{if } ka = 0 \\ \theta_{cr} &= 8.24 \times 10^{-3} \cdot L + 415 \qquad \text{if } ka \geq 7.5 \end{aligned} \tag{5.12}$$

$$\begin{aligned} t_{cr} &= -1.89 \times 10^{-3} \cdot L + 16 \qquad \text{if } ka = 0 \\ t_{cr} &= 1.34 \times 10^{-4} \cdot L + 4.62 \qquad \text{if } ka \geq 7.5 \end{aligned} \tag{5.13}$$

where, θ_{cr} is the critical temperature of the beam in Celsius degree, t_{cr} is the critical time of the beam in minutes, L is the beam span in millimetres and ka is the axial restraint to the

thermal elongation of the beam in kN/mm. These last equations (Equations 5.12 and 5.13) shall not be applied to non-dimensional slenderness, $\bar{\lambda}_{LT}$, outside the range of 1.11 to 2.47, as well.

➢ New equations for the fire design of cold-formed steel I-250-43-15-2.5 beams with 50% of load level:

$$\begin{aligned} \theta_{cr} &= \beta 1_I(ka) \cdot L^2 + \beta 2_I(ka) \cdot L + \beta 3_I(ka) && \text{if } ka \leq 15 \\ \theta_{cr} &= 1.2 \times 10^{-5} \cdot L^2 - 1.44 \times 10^{-1} \cdot L + 570 && \text{if } ka \geq 30 \end{aligned} \tag{5.14}$$

$$\begin{aligned} \beta 1_I(ka) &= -1.71 \times 10^{-7} \cdot ka^2 + 5.19 \times 10^{-6} \cdot ka - 2.17 \times 10^{-5} \\ \beta 2_I(ka) &= 1.44 \times 10^{-3} \cdot ka^2 - 3.86 \times 10^{-2} \cdot ka + 4.57 \times 10^{-2} \\ \beta 3_I(ka) &= -1.51 \cdot ka^2 + 2.87 \times 10^{1} \cdot ka + 6.72 \times 10^{2} \end{aligned} \tag{5.15}$$

$$\begin{aligned} t_{cr} &= \upsilon 1_I(ka) \cdot L^2 + \upsilon 2_I(ka) \cdot L + \upsilon 3_I(ka) && \text{if } ka \leq 15 \\ t_{cr} &= 1.97 \times 10^{-7} \cdot L^2 - 2.26 \times 10^{-3} \cdot L + 8.58 && \text{if } ka \geq 30 \end{aligned} \tag{5.16}$$

$$\begin{aligned} \upsilon 1_I(ka) &= -2.63 \times 10^{-9} \cdot ka^2 + 6.20 \times 10^{-8} \cdot ka \\ \upsilon 2_I(ka) &= 1.13 \times 10^{-5} \cdot ka^2 - 1.98 \times 10^{-4} \cdot ka - 3.29 \times 10^{-3} \\ \upsilon 3_I(ka) &= 2.93 \times 10^{-2} \cdot ka^2 - 1.06 \cdot ka + 21.7 \end{aligned} \tag{5.17}$$

where, θ_{cr} is the critical temperature of the beam in Celsius degree, t_{cr} is the critical time of the beam in minutes, L is the beam span in millimetres and ka is the axial restraint to the thermal elongation of the beam in kN/mm. These last equations (Equations 5.14 and 5.16) shall not be applied to non-dimensional slenderness, $\bar{\lambda}_{LT}$, outside the range of 0.85 to 1.82, as well.

➢ New equations for the fire design of cold-formed steel R-250-43-15-2.5 beams with 50% of load level:

$$\begin{aligned} \theta_{cr} &= -2.80 \times 10^{-5} \cdot L^2 + 1.12 \times 10^{-1} \cdot L + 534 && \text{if } ka = 0 \\ \theta_{cr} &= -0.0793 \cdot L + 766.66 && \text{if } ka \geq 7.5 \end{aligned} \tag{5.18}$$

$$\begin{aligned} t_{cr} &= -5.08 \times 10^{-7} \cdot L^2 + 8.73 \times 10^{-4} \cdot L + 15.1 \quad \text{if } ka = 0 \\ t_{cr} &= -2.21 \times 10^{-3} \cdot L + 17.1 \quad \text{if } ka \geq 7.5 \end{aligned} \tag{5.19}$$

where, θ_{cr} is the critical temperature of the beam in Celsius degree, t_{cr} is the critical time of the beam in minutes, L is the beam span in millimetres and ka is the axial restraint to the thermal elongation of the beam in kN/mm. These last equations (Equations 5.18 and 5.19) shall not be applied to non-dimensional slenderness, $\bar{\lambda}_{LT}$, outside the range of 0.55 to 1.32, as well.

➢ New equations for the fire design of cold-formed steel 2R-250-43-15-2.5 beams with 50% of load level:

$$\begin{aligned} \theta_{cr} &= \beta 1_{2R}(ka) \cdot L^2 + \beta 2_{2R}(ka) \cdot L + \beta 3_{2R}(ka) \quad \text{if } ka \leq 15 \\ \theta_{cr} &= 1.21 \times 10^{-5} \cdot L^2 - 2.18 \times 10^{-1} \cdot L + 968 \quad \text{if } ka \geq 30 \end{aligned} \tag{5.20}$$

$$\begin{aligned} \beta 1_{2R}(ka) &= -1.42 \times 10^{-7} \cdot ka^2 + 3.77 \times 10^{-6} \cdot ka \\ \beta 2_{2R}(ka) &= 9.16 \times 10^{-4} \cdot ka^2 - 2.45 \times 10^{-2} \cdot ka - 1.39 \times 10^{-1} \\ \beta 3_{2R}(ka) &= -1.24 \cdot ka^2 + 2.93 \times 10^{1} \cdot ka + 1000 \end{aligned} \tag{5.21}$$

$$\begin{aligned} t_{cr} &= \upsilon 1_{2R}(ka) \cdot L^2 + \upsilon 2_{2R}(ka) \cdot L + \upsilon 3_{2R}(ka) \quad \text{if } ka \leq 15 \\ t_{cr} &= 7.54 \times 10^{-7} \cdot L^2 - 8.53 \times 10^{-3} \cdot L + 26.8 \quad \text{if } ka \geq 30 \end{aligned} \tag{5.22}$$

$$\begin{aligned} \upsilon 1_{2R}(ka) &= 3.47 \times 10^{-9} \cdot ka^2 - 9.13 \times 10^{-8} \cdot ka + 1.93 \times 10^{-6} \\ \upsilon 2_{2R}(ka) &= -3.20 \times 10^{-5} \cdot ka^2 + 8.93 \times 10^{-4} \cdot ka - 1.95 \times 10^{-2} \\ \upsilon 3_{2R}(ka) &= 7.64 \times 10^{-2} \cdot ka^2 - 2.31 \cdot ka + 55 \end{aligned} \tag{5.23}$$

where, θ_{cr} is the critical temperature of the beam in Celsius degree, t_{cr} is the critical time of the beam in minutes, L is the beam span in millimetres and ka is the axial restraint to the thermal elongation of the beam in kN/mm. These last equations (Equations 5.20 and 5.22) shall not be applied to non-dimensional slenderness, $\bar{\lambda}_{LT}$, outside the range of 0.39 to 0.95, as well.

5.3 Final Remarks

This chapter was based on a detailed parametric study of CFS beams at ambient temperature and both under fire conditions, under flexural loading conditions and under simply supported boundary conditions (roller and pinned supports) with different restraining conditions, including no restraints, partial axial restraint to the thermal elongation of the beam and partial rotational restraint at the beam supports. Hence, extensive parametric studies were undertaken using an advanced finite element tool ABAQUS by changing various factors: slenderness, level of initial applied load on the beam, initial geometric imperfections of the beam and stiffness of the surrounding structure, including the axial and rotational stiffness. The obtained results from the FEA at ambient temperature were also compared with the available design rules (EN1993-1.1, 2004; EN1993-1.3, 2004 and EN1993-1.5, 2006).

The results at ambient temperatures show mainly that EN1993-1.3 predictions may be conservative for beams comprised of two or more CFS profiles or even over-conservative as it was observed in some studied cases. However, these design guidelines may give unsafe results for beams with spans longer than 4.5 m.

Regarding the numerical simulations on beam under fire conditions, the results demonstrated the importance of using initial geometric imperfections and serviceability loads as close to the reality as possible, because the imperfections may affect the critical temperature of the flexural members by 20%, or even 60% depending on the shape of the cross-section, and the serviceability load by 70 % when the load level increased from 30% to 70%.

Results from these investigations also indicated that the critical temperature decreases with increasing slenderness (span length), load level, axial restraint or geometric imperfections, as it was expected. However, it was possible to see that the load level was by far the parameter which most affected the fire behaviour of the studied beams. In contrast to this, the rotational restraint may increase the fire behaviour of the beams.

Finally, comparisons with the numerical results demonstrated that the new developed equations might be accurate and even useful for designers due to the lack of simplified calculation methods for fire design of CFS structures. However, this method depends just on the shape of the cross-section, the beam length and the axial restraint. Further numerical simulations should still be done so that the new simplified design methods could also be taken into account the beam slenderness (length, thickness and height of the cross-section), the load level and the rotational restraint at the beam supports.

6 CONCLUSIONS AND FUTURE WORK

6.1 Experimental Analysis on Cold-Formed Steel Beams

6.1.1 Ambient temperature

An experimental investigation into the behaviour of cold-formed steel C-, lipped I-, R- and 2R-section beams under flexural conditions at ambient temperature have been presented in this thesis. A total of twelve four-point bending tests at ambient temperature were carried out. As it was expected, cold-formed steel beams are very sensitive to local, distortional and global buckling and also their interactions. It was observed that the failure loads of the beams with C- and lipped I-shaped cross-sections (open beams) corresponded to the lateral-torsional buckling modes, whereas the distortional buckling was the responsible buckling mode for the failure loads of the R and 2R beams (closed built-up beams). In order to improve the structural behaviour of these two types of beams, the author suggested, for instance, that (i) the U profiles of these beams are replaced by lipped U profiles like the C profiles, but with the lips towards the exterior side of the profile. In other words, the U profiles should be replaced by hat (omega) profiles, or that (ii) the C profiles are placed over the U profiles, as presented respectively in Figures 6.1 and 6.2. The advantage of the first one over the second one is that is easier to assembly, but its application in buildings is more complicate. As well as that, the use of sigma profiles (fig. 1.2d) instead of C profiles might improve the behaviour of cold-formed steel beams against the lateral-torsional buckling. All beams should also be reinforced with extra screws, maybe of a larger diameter or improved steel class. Another important conclusion to be drawn was that the use of two or more profiles in a beam can increase its strength-to-weight ratio. From the tested beams, the 2R beams showed the best ratio. However, it seems that this ratio tends to be constant for beams comprised of more than four profiles.

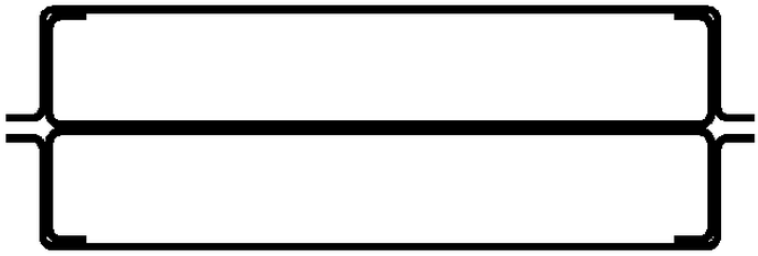

Figure 6.1 – New 2R section with omega profiles

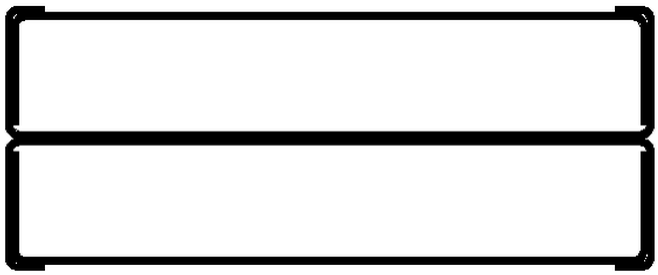

Figure 6.2 – New 2R section with the C profiles over the U profiles

6.1.2 Fire situation

This thesis also reported and discussed in detail the results of an experimental investigation into the behaviour of CFS C-, lipped I-, R- and 2R-section beams both under fire conditions, under flexural loading conditions and under simply supported boundary conditions (roller and pinned supports) with different restraining conditions, including no restraints, partial axial restraint to the thermal elongation of the beam and partial rotational restraint at the beam supports. A total of thirty-six fire tests were made.

The main conclusion of this research work was that critical temperature of a CFS beam might be strongly affected by the axial restraint to the thermal elongation of the beam, even for low values of axial restraint. This study showed that the critical temperature of all studied simply supported beams was about 700 ºC, whereas the critical temperature of these beams with restrained thermal elongation depended on the cross-section shape. In some cases, the critical temperature decreased approximately by 30 % for 15 kN/mm of axial restraining and by 20 % for 3 kN/mm of axial restraining, comparing with the critical temperature of the respective beams without restraints. As it was expected, all these members had low critical times (less than 30 minutes). However, it was observed that the closed built-up sections (R and 2R beams) presented an enhanced fire behaviour (higher failure times) than the open sections (C and lipped I beams). The closed built-up section beams may have an increase of about 50% in the critical time, comparing with the open section beams.

On the other hand, in relation to beams with just axial restraint, the results of this experimental research still allowed concluding that when the rotation is also partially restrained at the beam supports, the critical temperature of the studied CFS beams might significantly increase, depending on the relation between the rotational stiffness of the beam supports and the rotational stiffness of the beam. In this particular case of study, there was an increase of around 20 % in the critical temperature, when the rotational restraint increased from zero to 150 kNm/rad, with the 2R beams being the only exception.

Finally, CFS beams can also fail in a variety of buckling modes including local, distortional and global (lateral-torsional) buckling at high temperatures. It was possible to observe that the lateral-torsional buckling was also the main failure mode responsible for the collapse of the open beams and the distortional buckling the main failure mode responsible for the collapse of the closed built-up beams. However, in general it seems that the failure modes become more complicate in CFS beams with complex boundary conditions.

The new sections, mentioned above, should also improve the fire performance of CFS structures in relation to the studied beams.

6.2 Parametric Study and Development of Simplified Design Equations

6.2.1 Ambient temperature

A numerical investigation into the behaviour of cold-formed steel C-, lipped I-, R- and 2R-section beams under bending conditions at ambient temperature have still been presented here. About fifty numerical simulations performed with the finite element program ABAQUS were made. Lastly, the suitability of design methods established by EN1993-1.1 (2004) for the buckling moment capacity was also investigated using the developed finite element model.

The good agreement between the experimental and numerical results and between the respective failure buckling modes proves that the finite element analysis is a reliable tool to get quite accurate results. The finite element results showed that the strength-to-weight ratio of the simulated beams decreases a lot when their span increases, especially, from 3.0 to 4.0 m. It is also shown that EN1993-1.3 (2004) predictions may be conservative for beams comprised of two or more CFS profiles or even over-conservative as it was observed in some studied cases. However, these design guidelines may give unsafe results for these beams with spans longer than 4.5 m.

In an attempt to improve the EN1993-1.1 (2004) predictions, new different buckling curves have been provided taking into account the shape of the cross-section. It was also clear to observe that the use of the buckling curve ‘a’ proposed in EN1993-1.3 (2004) for the design buckling resistance moment of a CFS member that is susceptible to lateral-torsional buckling may be unsafe. However, it is recommended that further experimental and numerical research is needed to confirm the proposed design equations or developed new design guidelines for

lateral-torsional buckling of cold-formed steel beams comprised of more than one profile and connected by screws.

6.2.2 Fire situation

Finally, this thesis has described the development of a finite element model capable of simulating the distortional buckling and lateral-torsional buckling behaviour of CFS flexural members both under fire conditions and under simply supported boundary conditions with different restraining conditions, including no restraints, axial and rotational restraint and also their interactions. About one hundred and fifty numerical simulations were performed with the program ABAQUS.

The good agreement between the experimental and numerical results and between the respective failure buckling modes proved that the finite element analysis is a reliable tool to get quite accurate results. As expected, it was observed that the hollow sections (R and 2R beams) show an enhanced fire behaviour than the open sections (C and lipped-I beams), but, in some cases, the former may present critical temperatures rather lower than the latter.

The results also demonstrated the importance of using initial geometric imperfections and serviceability loads as close to the reality as possible, because the imperfections may affect the critical temperature of the flexural members by 20%, or even 60% depending on the shape of the cross-section, and the serviceability load by 70 %, i.e, the critical temperature of some studied beams decreased by 70% when the load level increased from 30% to 70%. So, results from these investigations indicate that the critical temperature decreases with increasing slenderness (span length), load level, axial restraint or geometric imperfections, as it was expected. However, it was possible to see that the load level was by far the parameter which most affected the fire behaviour of the studied beams. In contrast to this, the rotational restraint may increase the fire behaviour of the beams. For instance, the fire resistance of the studied C beam with 15 kN/mm of axial restraint increased 3 times and the critical temperature 1.5 times (at least), when the rotational restraint increased from 0 to 150 kN.m/rad.

An important consequence resulting from this research work was that the limitation enforced by EN1993-1-2 (2004), on the maximum temperatures to 350ºC for cold-formed steel beams may be over-conservative, especially when the serviceability load of the beams is too low, less than 30% of the design value of buckling load of the respective beam at ambient temperature. Otherwise, when the load level is higher than 70% the critical temperature may

be lower than 350 ºC. In addition, the author recommends that the critical temperature method presented in this Eurocode for hot rolled steel members should not be used for CFS members since in this method the critical temperature almost does not change when the non-dimensional slenderness changes and that is far away from the truth as it could be observed in this thesis. So, it is understandable that design methods for critical temperature and fire resistance of CFS beams as a function of their slenderness and the load level are established in a future revision of EN1993-1-2 document. In this thesis a set of simplified equations for assessing the critical temperature and the fire resistance of CFS beams with C-, I-, R- and 2R-shaped cross-sections has been proposed. The new equations also show that they depend on the section shape in contrast to the design methods established in EN1993-1-2 (2004). Another important point to be emphasized in relation to the EN1993-1-2 (2004) is that there is nothing concerning the effect of rotational restraint on the fire performance of beams. Finally, it can still be stated that this research has developed accurate strength equations for axially restrained CFS beams that can be used to provide safe structural designs and economical CFS structures in fire situations.

6.3 Future Work

Compound cross-section profiles more and more complex, the interaction between buckling and yielding, and the strength sensitivity to imperfections make the full understating of buckling behaviour of cold-formed steel structures a great challenge to researchers. However, many problems remain unaddressed, especially in the field of fire design of cold-formed steel structures. This thesis is a step in the right direction but there is still too much to be done and discover. Regarding the CFS beam under fire conditions, further experimental and numerical studies are needed. So, extensive numerical simulations have been carrying out by the author of this thesis with the goal of achieving such new simplified calculation methods for CFS beam, especially for beams with C-, I-, R- and 2R-shaped cross-sections. Further experimental and numerical research is also needed to investigate the behaviour of other section geometries (with sigma and zed profiles, for instance) and other loading types (concentrated load at mid-span of the beam, uniform distributed load along the beam and uniform bending along the beam, for example).

It is still worth remembering that this work research was limited to CFS beams subjected to a uniform temperature distribution throughout the beam. But in practice the beams may be subjected to non-uniform temperature distribution in a fire situation. Hence, studies of structural behaviour of CFS floors under fire conditions are recommended. It is also important not to forget that in real structures the effect of catenary action is very relevant. With the

presence of axial constraints, the beam will behave in catenary action at large deflection stage. The catenary action is a load carrying mechanism where the bending moment capacity of the beam may be negligible but the beam would still be able to resist the applied transversal load with the tension force developed in the beam via further deflection even with reduced material strength. If large deflection may be acceptable in a fire situation, the fire protection might be unnecessary. So, further research is recommended in this area. However, before this it should still be looked into the fire performance of CFS connections subjected to fire. The fire behaviour of beam-to-column connections is almost unknown and there are a lot of fastening types in CFS structures, with the screw attachment, the welding and the bolting being the most common fastening types.

As well as that an experimental and numerical investigation into the structural behaviour of CFS slender columns with different types of compound cross-sections, end-support conditions (pin-ended and semi-rigid support conditions), load levels and axial restraints to the thermal elongation of the column should be undertaken, as it has already started at the Laboratory of the University of Coimbra. In addition, similarly to the beams, CFS stud walls under both compression and fire conditions should be analysed. And, therefore, these experimental and numerical results would be the basis of an analytical study for the development of simplified calculation methods for fire design of cold-formed steel columns. Fire resistance tests on composite steel and concrete columns, made with CFS profiles (R and 2R sections, for instance) and micro-concrete, should also be carried out, in order to compare the behaviour with the bare steel columns.

Finally, all these studies might contribute to a future revision of EN1993-1-2 document, relative to the fire design of these members, or to a new document associated with Eurocode 3 and/or with the technical notes of the European Convention for Constructional Steelwork (ECCS), fulfilling a gap in the structural steel engineering.

REFERENCES

Ádány, S., Schafer, B.W. (2006a), Buckling mode decomposition of single-branched open cross-section members via finite strip method: Derivation, Thin-Walled Structures, Vol. 44, pp. 563-584.

Ádány, S., Schafer, B.W. (2006b), Buckling mode decomposition of single-branched open cross-section members via finite strip method: Application and examples, Thin-walled Structures, Vol. 44, pp. 585-600.

Ádány, S., Silvestre, N., Schafer, B.W., Camotim, D. (2009), GBT and cFSM: two modal approaches to the buckling analysis of unbranched thin-walled members, International Journal of Advanced Steel Construction, Vol. 5, Issue 2, pp. 195-223.

AISI S100-1996: AISI specification for the design of cold-formed steel structures members. American Iron and Steel Institute, Washington (DC), USA; 1996.

AISI S100-2001: North American Specification for the design of cold-formed steel structural members. American Iron and Steel Institute, Washington (DC), USA; 2001.

AISI S100-2004 - Appendix 1: Design of cold-formed steel structural members using the Direct Strength Method. In: 2004 supplement to the North American Specification for the design of cold-formed steel structures. American Iron and Steel Institute, Washington (DC), USA; 2004.

Almeida, A.C.B. (2006), Análise inelástica de pórticos planos considerando a plasticidade distribuída e o efeito das tensões residuais nos perfis estruturais de aço, MSc Thesis, Department of Structural Engineering, School of Engineering of the Federal University of Minas Gerais, Belo Horizonte, Brazil.

ANIS, A., BJORK, T., HEINILLA, S. (2012), Prediction of residual stresses in cold formed corners, Journal of Advanced Science and Engineering Research, Vol. 2, Issue 4, pp. 252-264.

AS 4100 (1998): Steel structures. Australia standard, Sydney, Australia.

AS/NZS 4600 (1996): Cold formed steel structures. New Zealand standard, Australia.

Bandula, H. (2009), Behaviour and design of cold-formed steel compression members at elevated temperatures, PhD thesis, Queensland University of Technology, Brisbane, Australia.

Batista, E.M. (1989), Étude de la stabilité des profils à paróis minces et section ouverte de types U et C, Collection des publications de la Faculté des Sciences Appliquées, no.119, University of Liege.

Batista, E.M. (2009), Local-global buckling interaction procedures for the design of cold-formed columns: Effective width and direct method integrated approach, Thin-Walled Structures, Vol. 47, pp. 1218-1231.

Batista, E.M. (2010), Effective section method: A general direct method for the design of steel cold-formed members under local-global buckling interaction, Thin-Walled Structures, Vol. 48, pp. 345-356.

Bebiano, R., Pina, P., Silvestre, N., Camotim, D. (2008), http://www.civil.ist.utl.pt/gbt, GBTUL 1.0β — Buckling and vibration analysis of thin-walled members, DECivil/IST, Technical University of Lisbon.

Beregszászi, Z., Ádány, S. (2011), Application of the constrained finite strip method for the buckling design of cold-formed steel columns and beams via the direct strength method, Computers and Structures, Vol. 89, pp. 2020-2027.

BS 5950-8 (1990), Structural Use of Steelwork in Building - Part 8: Code of Practice for Fire Resistance Design. British Standards Institution (BSI), London, UK.

Camotim, D., Dinis, B. (2011), Coupled instabilities with distortional buckling in cold-formed steel lipped channel columns, Thin-Walled Structures, Vol. 49, pp. 562-575.

Chajes, A., Britvec, S.J., Winter, G. (1963), Effect of cold-straining on structural sheet steels, Journal of the Structural Division, Proceedings of the American Society of Civil Engineers, Vol. 89, n. ST2, pp. 1-32.

Chen, J., Young, B. (2006), Corner properties of cold-formed steel sections at elevated temperatures, Thin-Walled Structures, Vol. 44, pp. 216-223.

Chen, J., Young, B. (2007a), Experimental investigation of cold-formed steel material at elevated temperatures, Thin-Walled Structures, Vol. 45, pp. 96-110.

Chen, J., Young, B. (2007b), Cold-formed steel lipped channel columns at elevated temperatures, Engineering Structures, Vol. 29, pp. 2445-2456.

Chu, X.-t., Ye, Z.-m., Li, L.-y., Kettle, R. (2006), Local and distortional buckling of cold-formed zed-section beams under uniformly distributed transverse loads, International Journal of Mechanical Sciences, Vol. 48, pp. 378-388.

Dassault Systèmes Simulia Corp., 2010, http://www.3ds.com/products/simulia/overview/, Abaqus Analysis – User's Manual, version 6.10-1, USA.

Dinis, P.B., Camotim, D. (2010), Local/distortional mode interaction in cold-formed steel lipped channel beams, Thin-Walled Structures, Vol. 48, pp. 771-785.

Dinis, P.B., Camotim, D. (2011), Post-buckling behaviour and strength of cold-formed steel lipped channel columns experiencing distortional/global interaction, Computers and Structures, Vol. 89, pp. 422-434.

Dubina, D., Ungureanu, V. (2002), Effect of imperfections on numerical simulation of instability behaviour of cold-formed steel members, Thin-Walled Structures, Vol. 40, pp. 239-262.

EN 1991-1-2 (2002), Eurocode 1: Actions on structures, Part 1-2: General actions – Actions on structures exposed to fire, European Committee for Standardisation, Brussels, Belgium, 60 p.

EN 1993-1-1 (2004), Eurocode 3: Design of steel structures, Part 1-1: General rules and rules for buildings, European Committee for Standardisation, Brussels, Belgium, 91 p.

EN 1993-1-2 (2004), Eurocode 3: Design of steel structures, Part 1-2: General rules, Structural fire design, European Committee for Standardisation, Brussels, Belgium, 78 p.

EN 1993-1-3 (2004), Eurocode 3: Design of steel structures, Part 1-3: General rules, Supplementary rules for cold-formed members and sheeting, European Committee for Standardisation, Brussels, Belgium, 125 p.

EN 1993-1-5 (2006), Eurocode 3: Design of steel structures, Part 1-5: Plated structural elements, European Committee for Standardisation, Brussels, Belgium, 55 p.

Feng, M., Wang, Y.C., Davies, J.M. (2003a), Thermal performance of cold-formed thin-walled steel panel systems in fire, Fire Safety Journal, Vol. 38, pp. 365-394.

Feng, M., Wang, Y.C., Davies, J.M. (2003b), Structural behaviour of cold-formed thin-walled short steel channel columns at elevated temperatures. Part 2: Design calculations and numerical analysis, Thin-Walled Structures, Vol. 41, pp. 571-594.

Futureng@ (2010), http://www.futureng.com, Engineering and consulting company, specialized in steel framing, with the purpose of facilitating the transition from the traditional to the lightweight galvanized steel construction, providing comprehensive and specific technical assistance at various stages of the process, São João da Talha, Lisbon, Portugal.

Gotluru, B.P., Schafer, B.W., Peköz, T. (2000), Torsion in thin-walled cold-formed steel beams, Thin-Walled Structures, Vol. 37, pp. 127-145.

Hancock, G.J. (1978), Local, distortional and lateral buckling of I beams, Journal of the Structural Division, ASCE, Vol. 104, Issue 11, pp. 1787-1798.

Hancock, G.J., Murray, T.M., Ellifritt D.S. (2001), Cold-Formed Steel Structures to the AISI Specification, Marcel Dekker, Inc., USA, 606 p.

ISO 834-1 (1999): Fire resistance tests – elements of building construction, Part 1: general requirements, International Organization for Standardization ISO 834, Geneva, Switzerland.

Kaitila, O. (2002a), Imperfection sensitivity analysis of lipped channel columns at high temperatures, Journal of Constructional Steel Research, Vol. 58, pp. 333-351.

Kaitila O. (2002b), Finite element modeling of cold-formed steel members at high temperatures, Licentiate thesis, Helsinki University, Finland.

Kankanamge, N.D. (2010), Structural behaviour and design of cold-formed steel beams at elevated temperatures, Ph.D. thesis, Queensland University of Technology, Brisbane, Australia.

Kankanamge, N.D., Mahendran, M. (2011), Mechanical properties of cold-formed steels at elevated temperatures, Thin-Walled Structures, Vol. 49, pp. 26-44.

Kankanamge, N.D., Mahendran, M. (2012), Behaviour and design of cold-formed steel beams subject to lateral-torsional buckling at elevated temperatures, Thin-Walled Structures, Vol. 61, pp. 213-228.

Karim, A., Adeli, H. (1999), Global optimum design of cold-formed steel hat-shape beams, Thin-Walled Structures, Vol. 35, pp. 275-288.

Kolarkar, P. (2010), Structural and fire behavior of a new steel stud wall system using composite panels, PhD thesis, Queensland University of Technology, Brisbane, Australia.

Laím, L., Rodrigues, J.P.C. (2011), Fire behaviour of cold-formed steel beams for industrial buildings, In: Proceedings of the 1st Ibero-Latin-American congress on fire safety, Natal, Brazil, Vol. 1, pp. 53-62 (in Portuguese).

Lee, J., Kim, S.-m., Park, H.-s., Woo, B.-h. (2005), Optimum design of cold-formed steel channel beams using micro Genetic Algorithm, Engineering Structures, Vol. 27, pp. 17-24.

Lee, J.H., Mahendran, M., Mäkeläinen, P. (2003), Prediction of mechanical properties of light gauge steels at elevated temperatures, Journal of Constructional Steel Research, Vol. 59, Issue 12, pp. 1517-1532.

Li, L.-y. (2009), Analyses of distortional buckling of cold-formed sigma purlins using EN1993-1-3, Journal of Constructional Steel Research, Vol. 65, Issue 12, pp. 2099-2102.

Li, Z., Schafer B.W. (2010), Application of the finite strip method in cold-formed steel member design, Journal of Constructional Steel Research, Vol. 66, pp. 971-980.

Liu, T.C.H., Fahad, M.K., Davies, J.M. (2002), Experimental investigation of behaviour of axially restrained steel beams in fire, Journal of Constructional Steel Research, Vol. 58, pp. 1211-1230.

Love, A.E.H. (1888), The small free vibrations and deformations of a thin elastic shell, Philosophical Transactions of the Royal Society (London), Vol. 179, pp. 491-546.

Lu, W., Mäkeläinen, P., Outinen, J. (2008), Numerical simulation of catenary action in cold-formed steel sheeting in fire, In: Proceedings of the fifth international conference on thin-walled structures, Brisbane, Australia, pp. 713–720.

Macdonald, M., Heiyantuduwa, M.A., Rhodes, J. (2008), Recent developments in the design of cold-formed steel members and structures, Thin-Walled Structures, Vol. 46, pp. 1047-1053.

Magnucka-blandzi, E. (2011), Effective shaping of cold-formed thin-walled channel beams with double-box flanges in pure bending, Thin-Walled Structures, Vol. 49, pp. 121-128.

Magnucki, K. AND Magnucka-blandzi, E. (1999), Variational design of open cross section thin-walled beam under stability constraints, Thin-Walled Structures, Vol. 35, pp. 185–191.

Magnucki, K., Paczos, P. (2009), Theoretical shape optimization of cold-formed thin-walled channel beams with drop flanges in pure bending, Journal of Constructional Steel Research, Vol. 65, pp. 1731-1737.

Mecozzi, E., Zhao, B. (2005), Development of stress-strain relationships of cold-formed lightweight steel at elevated temperatures, Proceedings of Eurosteel 2005 – 4th European Conference on Steel and Composite Structures, Maastricht, Netherlands, pp. 5.1-41 - 5.1-49.

Mindlin, R.D. (1951), Influence of rotatory inertia and shear on flexural motions of isotropic, elastic plates, ASME Journal of Applied Mechanics, Vol. 18, pp. 31-38.

Moen, C.D., Igusa, T., Schafer, B.W. (2008), Prediction of residual stresses and strains in cold-formed steel members, Thin-Walled Structures, Vol. 46, pp. 1274-1289.

Narayanan, S., Mahendran, M. (2003), Ultimate capacity of innovative cold-formed steel columns, Journal of Constructional Steel Research, Vol. 59, pp. 489-508.

NBR 14762 (2001), Dimensionamento de estruturas de aço constituídas por perfis formados a frio. Associação Brasileira de Normas Técnicas, Rio de Janeiro, Brazil.

NP-EN 10147 (2002), Specification for continuously hot-dip zinc coated structural steel sheet - Technical delivery conditions, European Committee for Standardisation (Portuguese version), CEN.

Outinen, J (1999), Mechanical properties of structural steels at elevated temperatures, Licentiate thesis, Helsinki University of Technology, Finland.

Outinen, J. (2006), Mechanical properties of structural steels at elevated temperatures and after cooling down, Proceedings of the Fire and Materials Conference, San Francisco, USA, 15 p.

Outinen, J. (2007), Mechanical properties of structural steels at high temperatures and after cooling down, Dissertation for the degree of Doctor of Science in Technology, Department of Civil and Environmental Engineering, Helsinki University, Helsinki, Finland, 37 p.

Outinen, J., Kaitila, O., Mäkeläinen, P. (2000), A study for the development of the design of steel structures in fire conditions, Proceedings of the 1st International Workshop of Structures in Fire, Copenhagen, Denmark, pp. 267-281.

Outinen, J., Kaitila, O., Mäkeläinen, P. (2001), High-temperature testing of structural steel and modelling of structures at fire temperatures, Research report TKK-TER-23, Helsinki University of Technology, Laboratory of Steel Structures, Helsinki, Finland.

Outinen, J., Mäkeläinen, P. (2002), Mechanical properties of structural steel at elevated temperatures and after cooling down, Proceedings of the 2nd International Workshop of Structures in Fire, Christchurch, New Zealand, pp. 273- 290.

Pan, C.-l., Shan, M.-y. (2011), Monotonic shear tests of cold-formed steel wall frames with sheathing, Thin-Walled Structures, Vol. 49, pp. 363-370.

Perfisa@ (2012), http://www.perfisa.net/, Enterprise in the development and manufacturing of cold-formed steel profiles, Carvalhais, São Pedro do Sul, Portugal.

Quach, W.M. (2005), Residual stresses in cold-formed steel sections and their effect on column behaviour, PhD thesis, Polytechnic University, Hong Kong, China, 479 p.

Quach, W.M., Teng, J.G., Chung, K.F. (2004), Residual stresses in steel sheets due to coiling and uncoiling: a closed-form analytical solution, Engineering Structures, Vol. 26, pp. 1249-1259.

Quach, W.M., Teng, J.G., Chung, K.F. (2006), Finite element predictions of residual stresses in press-braked thin-walled steel sections, Engineering Structures, Vol. 28, pp. 1609-1619.

Ranawaka, T. (2006), Distortional buckling behaviour of cold-formed steel compression members at elevated temperatures, Ph.D. thesis, Queensland University of Technology, Brisbane, Australia.

Ranawaka, T., Mahendran, M. (2009), Experimental study of the mechanical properties of light gauge cold-formed steels at elevated temperatures, Fire Safety Journal, Vol. 44, pp. 219-229.

Ranawaka, T., Mahendran, M. (2010), Numerical modeling of light gauge cold-formed steel compression members subjected to distortional buckling at elevated temperatures, Thin-Walled Structures, Vol. 48, pp. 334-344.

Ren, W.-x., Fang, S.-e., Young, B. (2006), Analysis and design of cold-formed steel channels subjected to combined bending and web crippling, Thin-Walled Structures, Vol. 44, Issue 3, pp. 314-320.

Rezende, P.G. (2005), Análise da resposta numérica de ligações parafusadas em chapas finas e perfis formados a frio, MSc thesis in Structural Engineering, Escola de Engenharia de São Carlos da Universidade de São Paulo, São Carlos, Brasil, 133 p.

Rhodes, J. (1991), Design of cold formed steel members, New York: Elsevier Applied Science, 409 p.

Rondal, J., Dubina, D. (2005), Light gauge metal structures: recent advances, International centre for mechanical sciences (CISM), Udine, Italy, 259 p.

Sadovský, Z., Kriváček, J., Ivančo, V., Ďuricová, A. (2012), Computational modelling of geometric imperfections and buckling strength of cold-formed steel, Journal of Constructional Steel Research, Vol. 78, pp. 1-7.

Schafer, B.W. (1997), Cold-formed steel behaviour and design: analytical and numerical modelling of elements and members with longitudinal stiffeners. PhD dissertation, Cornell University, Ithaca, New York, USA.

Schafer; B.W. (2008), Review: The Direct Strength Method of cold-formed steel member design, Journal of Constructional Steel Research, Vol. 64, pp. 766-778.

Schafer, B.W. (2012), http://www.ce.jhu.edu/bschafer/cufsm/, CUFSM: elastic buckling analysis of thin-walled members by finite strip analysis, CUFSM, version 4.04.

Schafer, B.W., Ádány, S. (2006), Buckling analysis of cold-formed steel members using CUFSM: Conventional and constrained finite strip methods, In: Proceedings of the eighteenth international specialty conference on cold-formed steel structures, Orlando, Florida, USA, pp. 39–54.

Schafer, B.W., Li, Z., Moen, C.D. (2010), Computational modelling of cold-formed steel, Thin-Walled Structures, Vol. 48, pp. 752-762.

Schafer, B.W., Peköz, T. (1998a), Computational modeling of cold-formed steel: characterizing geometric imperfections and residual stresses, Journal of Constructional Steel Research, Vol. 47, pp. 193-210.

Schafer, B.W., Peköz, T. (1998b), Direct strength prediction of cold-formed steel members using numerical elastic buckling solutions, In: Proceedings of the 14th international specialty conference on cold-formed steel structures, St. Louis, Missouri, USA, pp. 69–76.

Schafer, B.W., Peköz, T. (1999), Laterally braced cold-formed steel flexural members with edge stiffened flanges, Journal of Structural Engineering, Vol. 125, Issue 2, pp. 118-127.

Selamet, S., Garlock, M. (2010), Guidelines for modelling three dimensional structural connection models using finite element methods, In: Proceedings of the International Symposium on Steel Structures: Culture and Sustainability, Istambul, Turkey, pp. 351-360.

Silvestre, N., Camotim, D. (2002a), First-order generalised beam theory for arbitrary orthotropic materials, Thin-Walled Structures, Vol. 40, Issue 9, pp. 755–789.

Silvestre, N., Camotim, D. (2002b), Second-order generalised beam theory for arbitrary orthotropic materials, Thin-Walled Structures, Vol. 40, Issue 9, pp. 791–820.

Steel Framing Alliance@ (2009), http://www.steelframing.org, The Steel Framing Alliance intends to encourage the widespread, practical and economical use and preference for cold-formed steel framing by identifying, maintaining, and promoting its advantages. Based in Washington, D.C. (United States of America), SFA's national network of members represents the full spectrum of trades and professions within the construction industry.

Szabo, I.F., Ungureanu, V., Dubina, D. (2004), Recent research advances on ECBL approach. Part II: Interactive buckling of perforated sections, Thin-Walled Structures, Vol. 42, Issue 2, pp. 195–210.

Tichelmann, K.U., Volkwein, J., Lange, L., Naujoks, B. (2005), European Lightweight Steel-framed Construction, Arcelor, Luxemburg, 88 p.

Tian, Y.S., Lu, T.J. (2004), Minimum weight of cold formed steel sections under compression, Thin-Walled Structures, Vol. 42, pp. 515–532.

Trahair, N.S. (1993), Flexural-torsional buckling of structures, E&FN SPON-Chapman and Hall, London, England.

Ungureanu, V., Dubina, D. (2004), Recent research advances on ECBL approach. Part I: Plastic–elastic interactive buckling of cold-formed steel sections, Thin-Walled Structures, Vol. 42, Issue 2, pp. 177–194.

Veríssimo, H. (2008), Dimensionamento de elementos estruturais de aço enformados a frio de acordo com o eurocódigo 3, MSc thesis in Structural Engineering, Instituto Superior Técnico, Universidade Técnica de Lisboa, Lisboa, Portugal, 252 p.

Vila Real, P.M.M., Cazeli, R., Simões DA Silva, L., Santiago, A., Piloto, P. (2004), The effect of residual stresses in the lateral-torsional buckling of steel I-beams at elevated temperature, Journal of Constructional Steel Research, Vol. 60, pp. 783-793.

Von Kármán, T., Sechler, E.E., Donnel, L.H. (1932), The strength of thin plates in compression, Transactions of the American Society of Mechanical Engineers, Vol. 54, pp. 53-57.

Wang, H., Zhang, Y. (2009), Experimental and numerical investigation on cold-formed steel C-section flexural members, Journal of Constructional Steel Research, Vol. 65, pp. 1225-1235.

Weng, C.C., Peköz, T. (1990), Residual stresses in cold-formed steel members, Journal of Structural Engineering, American Society of Civil Engineers (ASCE), Vol. 116, Issue 6, pp. 1611-1625.

Weng, C.C., White, R.N. (1990), Residual stresses in cold-bent thick steel plates, Journal of Structural Engineering, American Society of Civil Engineers (ASCE), Vol. 116, Issue 1, pp. 24-39.

Yu, C., Schafer, B.W. (2002), Local buckling tests on cold-formed steel beams, In: Proceedings of the 16th International Specialty Conference on Cold-Formed Steel Structures, Orlando, Florida, USA, 18 p.

Yu, C., Schafer, B.W. (2007), Simulation of cold-formed steel beams in local and distortional buckling with applications to the direct strength method, Journal of Constructional Steel Research, Vol. 63, pp. 581-590.

Yu, W.-w. (2000), Cold-Formed Steel Design – Third Edition, John Wiley & Sons, Inc., USA, 767 p.

Zaharia, R., Dubina, D. (2006), Stiffness of joints in bolted connected cold-formed steel trusses, Journal of Constructional Steel Research, Vol. 62, pp. 240-249.

Zhu, J.-H., Young, B. (2012), Design of cold-formed steel oval hollow section columns, Journal of Constructional Steel Research, Vol. 71, pp. 26-37.

APPENDIX A Experimental Data from Tests on Cold-Formed Steel Beams at Ambient Temperature

A1 C beams

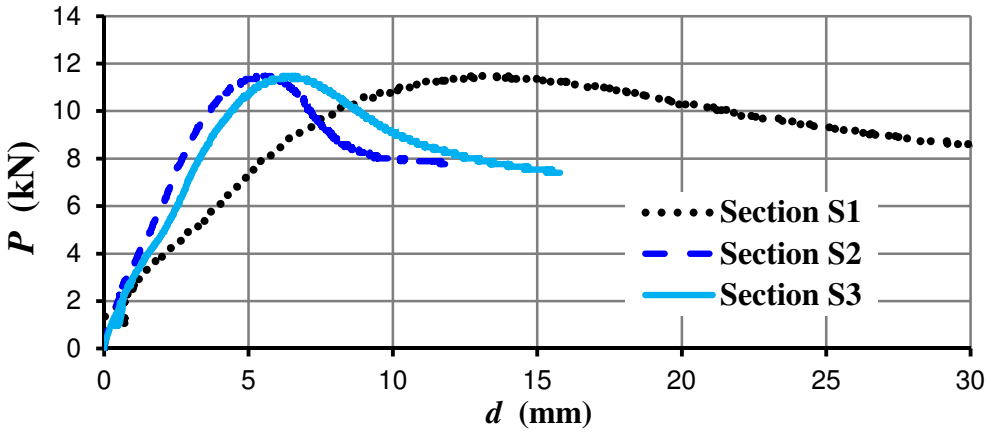

Figure A.1 – Load-displacement diagram at different sections of beam B-C_1

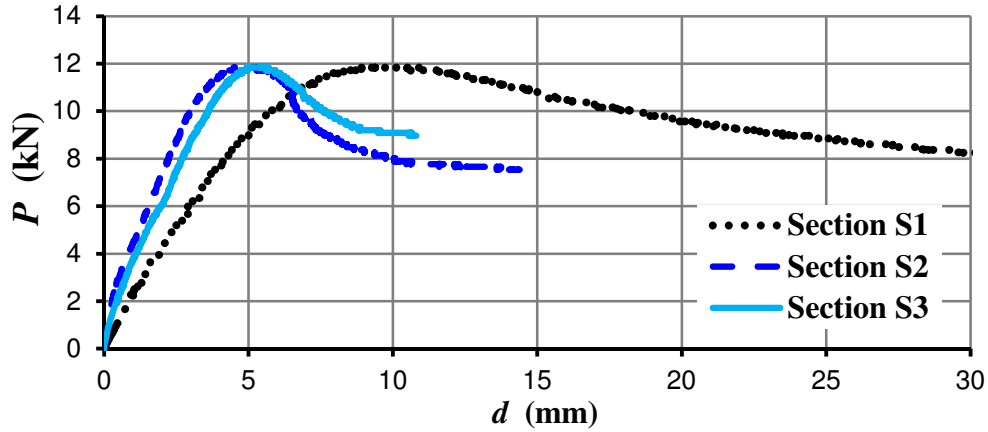

Figure A.2 – Load-displacement diagram at different sections of beam B-C_2

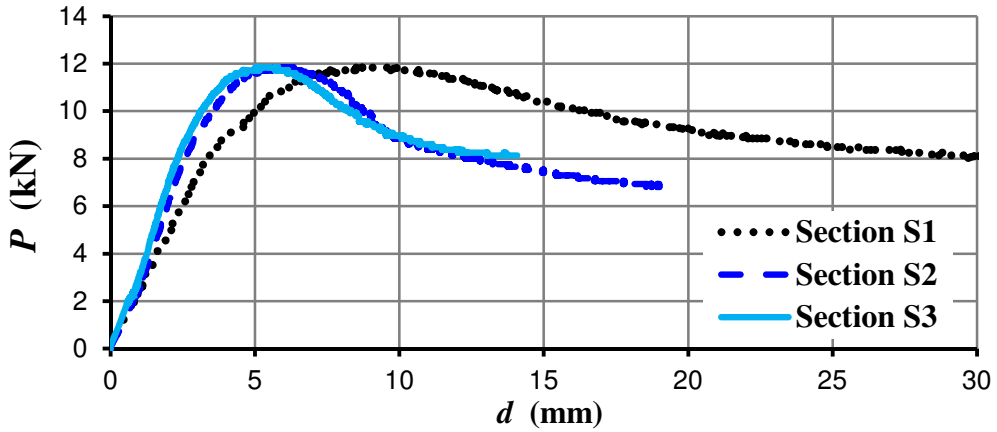

Figure A.3 – Load-displacement diagram at different sections of beam B-C_3

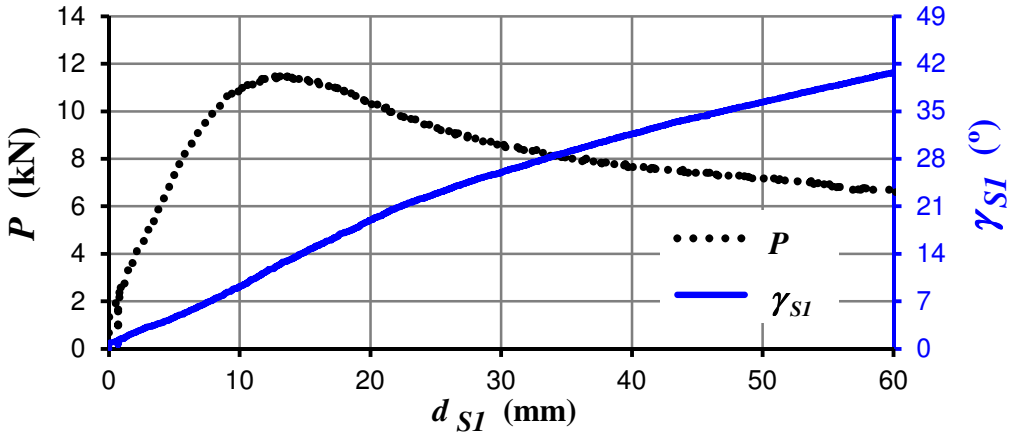

Figure A.4 – Load-rotation diagram at mid-span of beam B-C_1

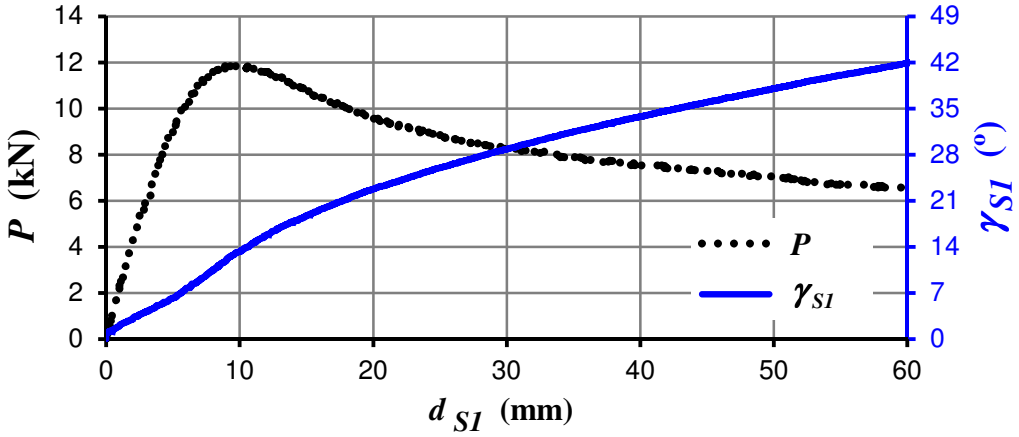

Figure A.5 – Load-rotation diagram at mid-span of beam B-C_2

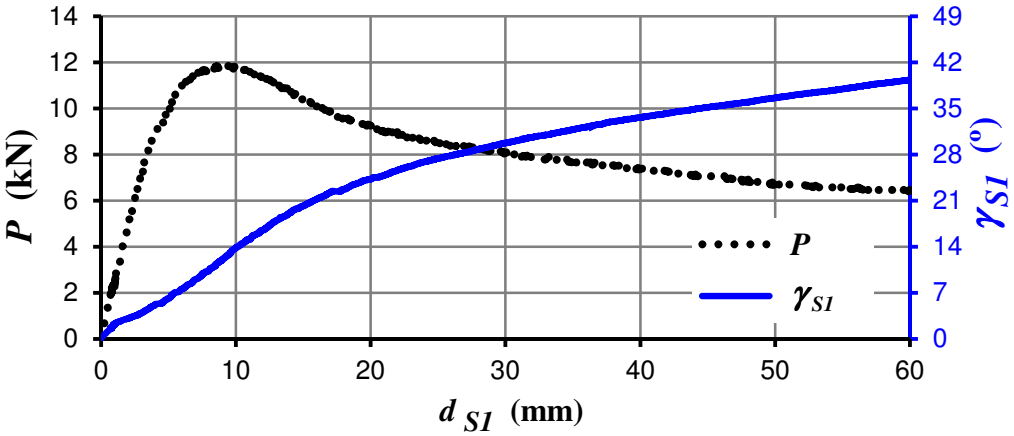

Figure A.6 – Load-rotation diagram at mid-span of beam B-C_3

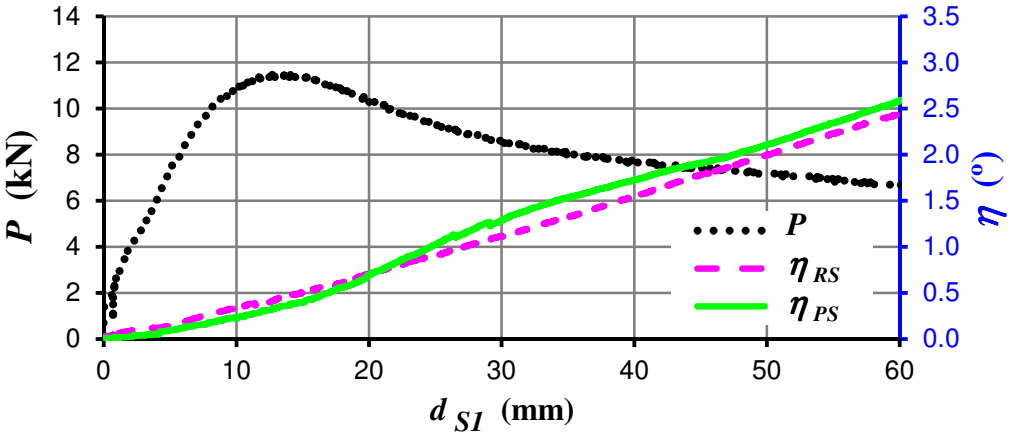

Figure A.7 – Rotation of beam supports in test B-C_1

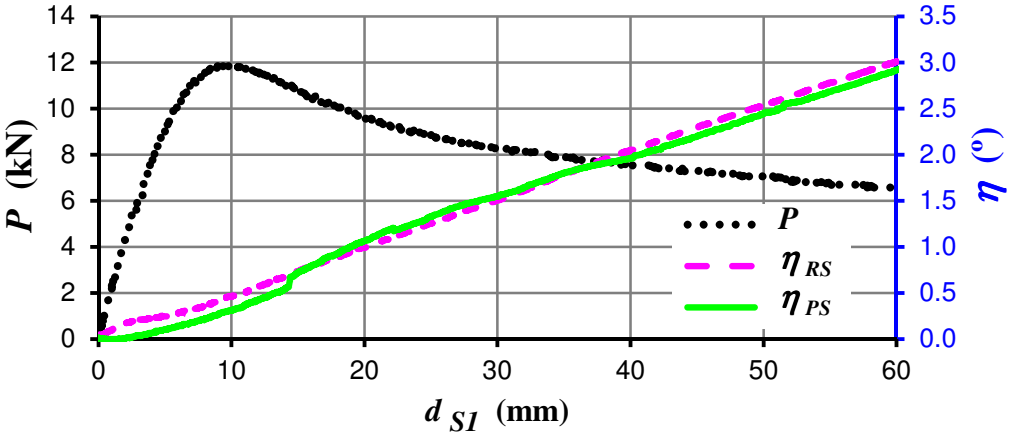

Figure A.8 – Rotation of beam supports in test B-C_2

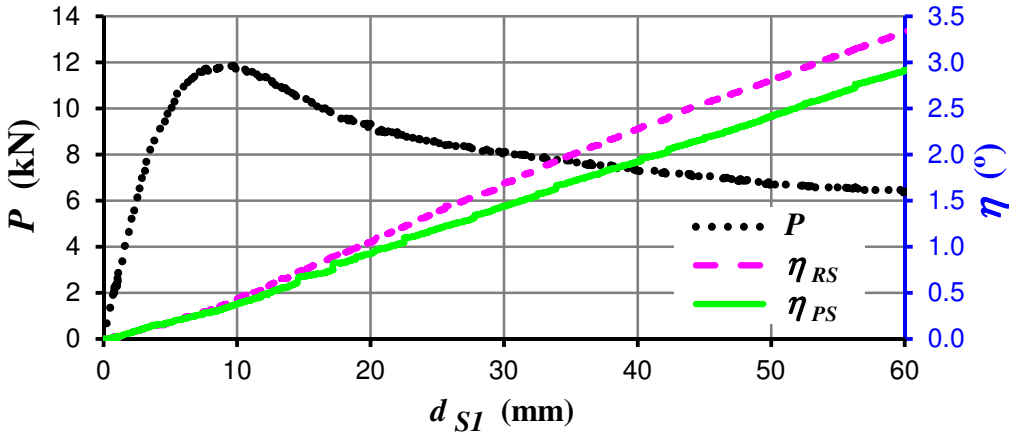

Figure A.9 – Rotation of beam supports in test B-C_3

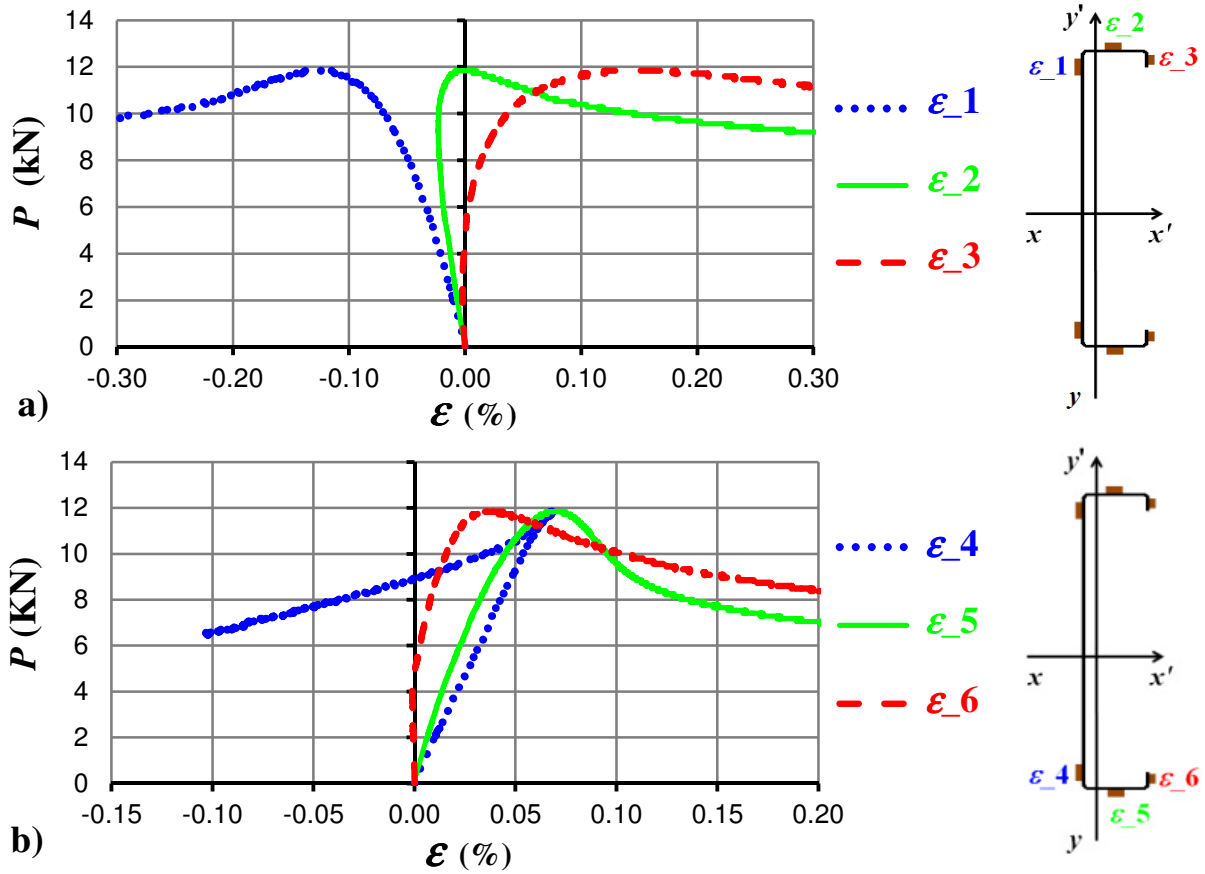

Figure A.10 – Load-strain curves from the strain gauges which were placed in the compressive (a) and tensile (b) flange of beam B-C_2 at section S1

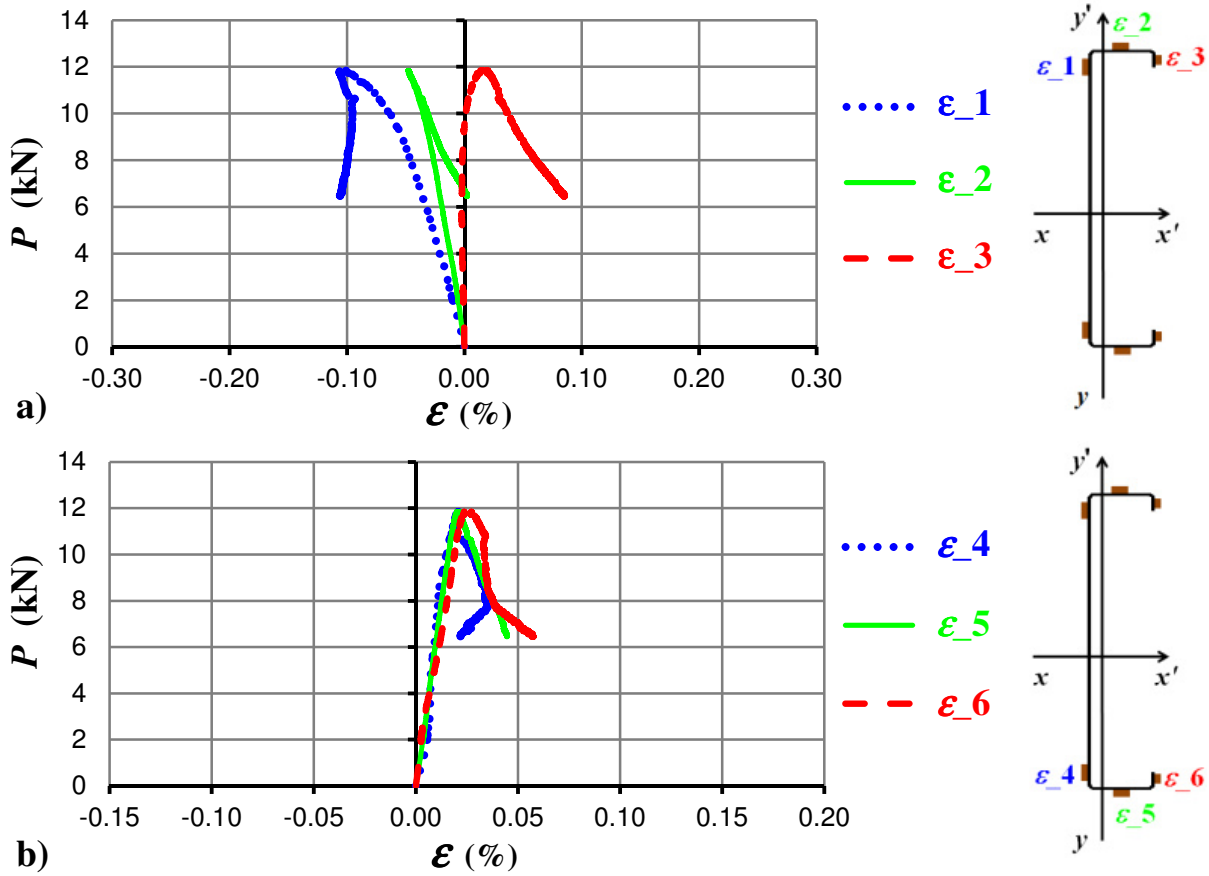

Figure A.11 – Load-strain curves from the strain gauges which were placed in the compressive (a) and tensile (b) flange of beam B-C_2 at section S2

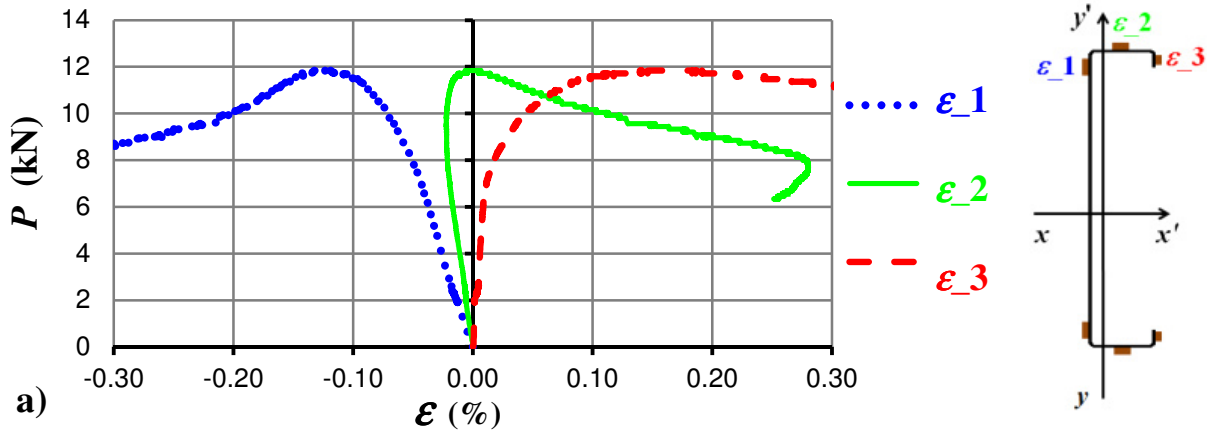

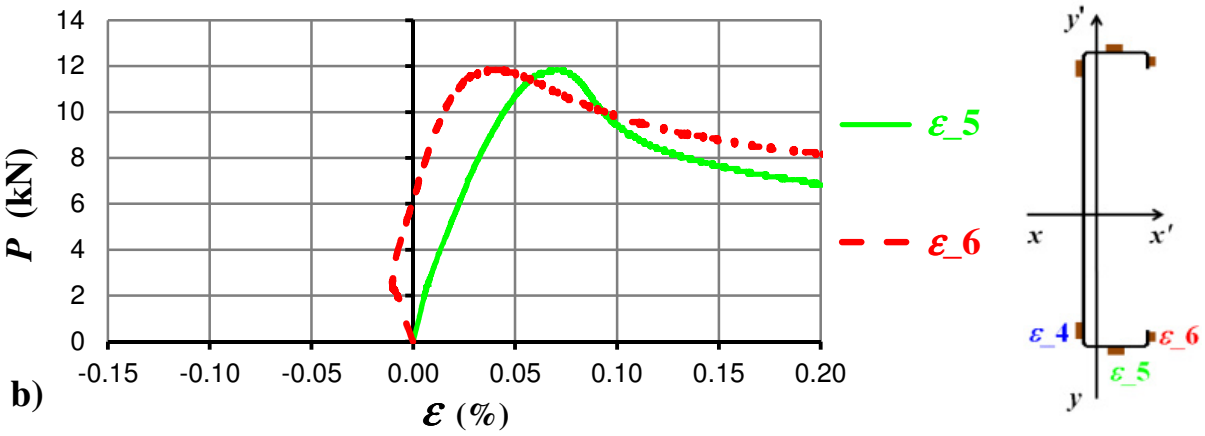

Figure A.12 – Load-strain curves from the strain gauges which were placed in the compressive (a) and tensile (b) flange of beam B-C_3 at section S1

A2 Lipped-I beams

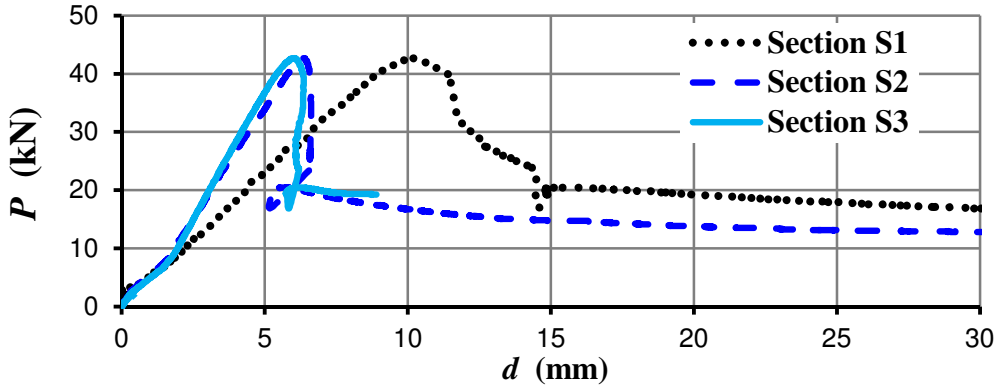

Figure A.13 – Load-displacement diagram at different sections of beam B-I_2

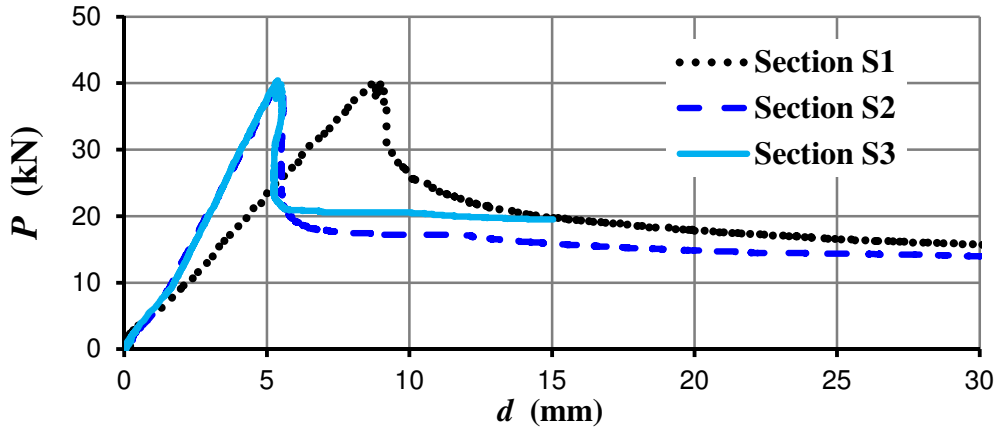

Figure A.14 – Load-displacement diagram at different sections of beam B-I_3

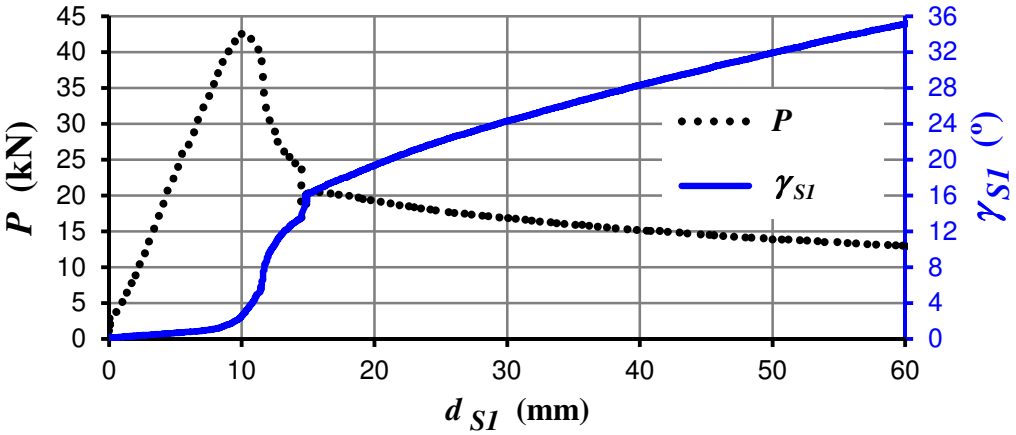

Figure A.15 – Load-rotation diagram at mid-span of beam B-I_2

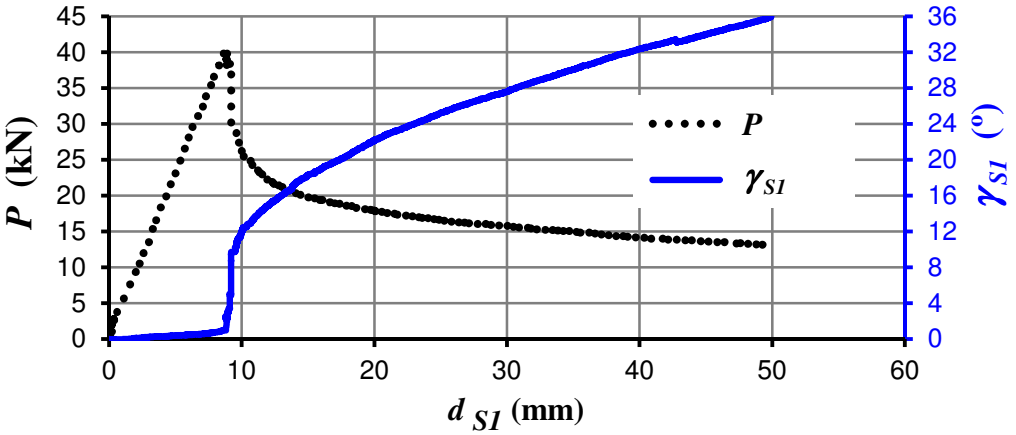

Figure A.16 – Load-rotation diagram at mid-span of beam B-I_3

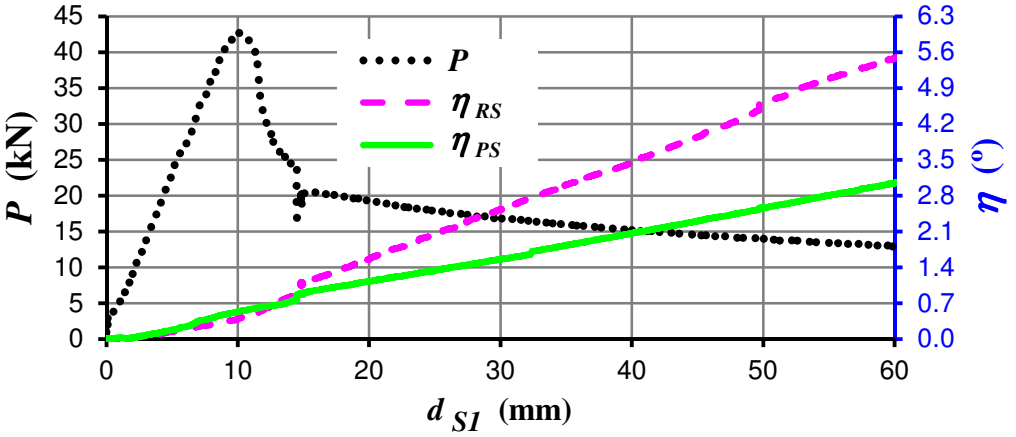

Figure A.17 – Rotation of beam supports in test B-I_2

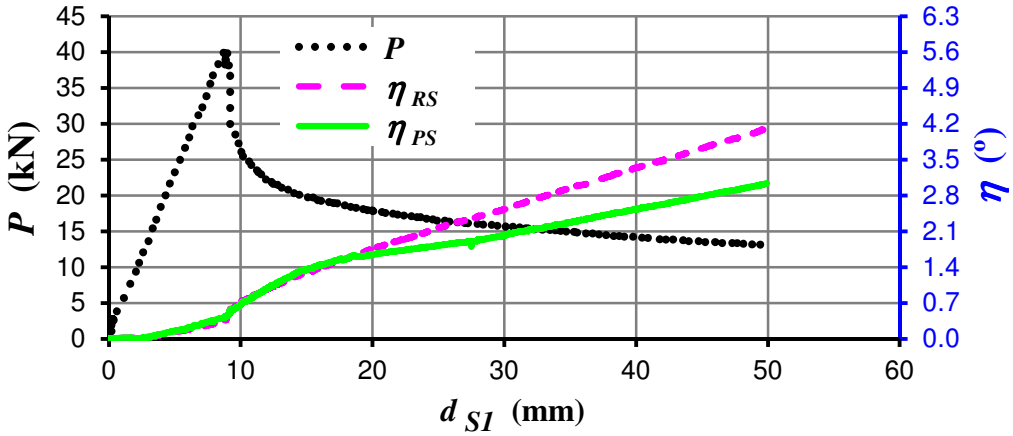

Figure A.18 – Rotation of beam supports in test B-I_3

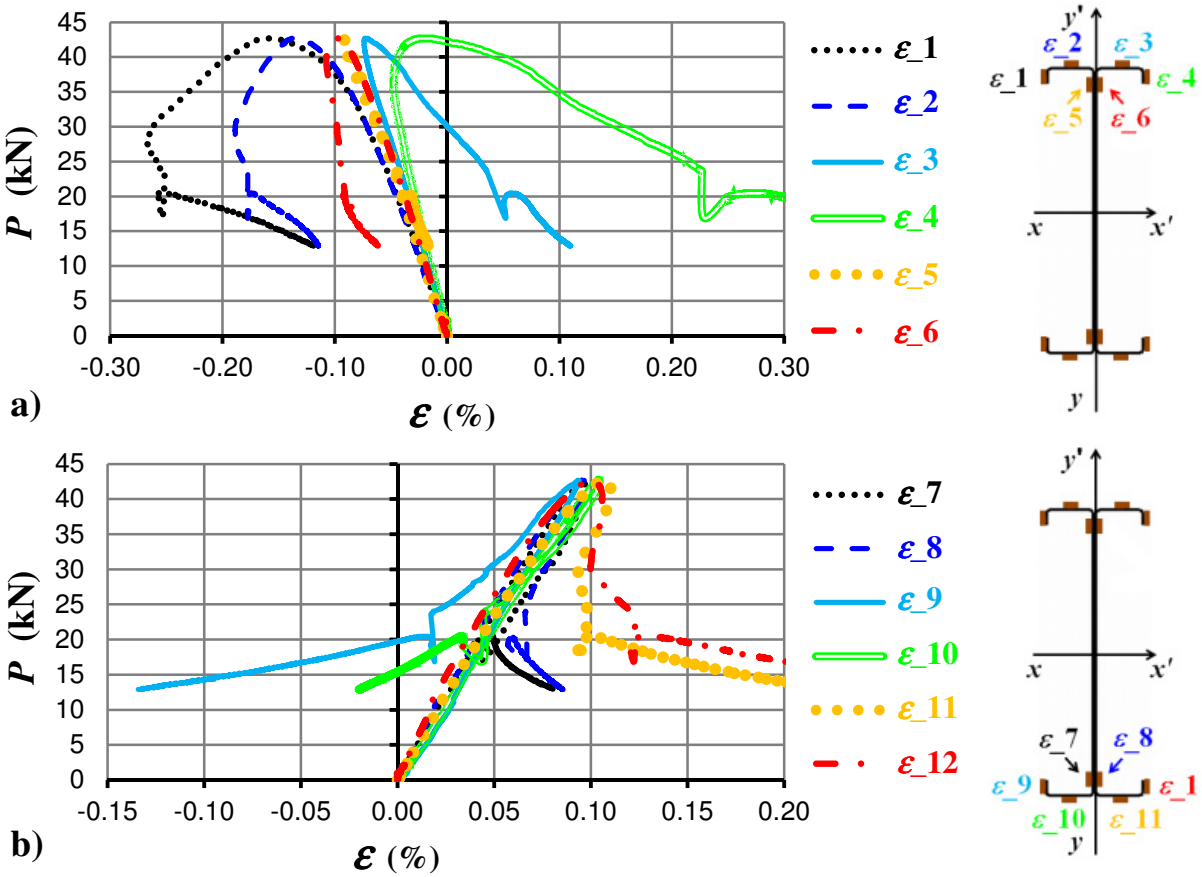

Figure A.19 – Load-strain curves from the strain gauges which were placed in the compressive (a) and tensile (b) flange of beam B-I_2 at section S1

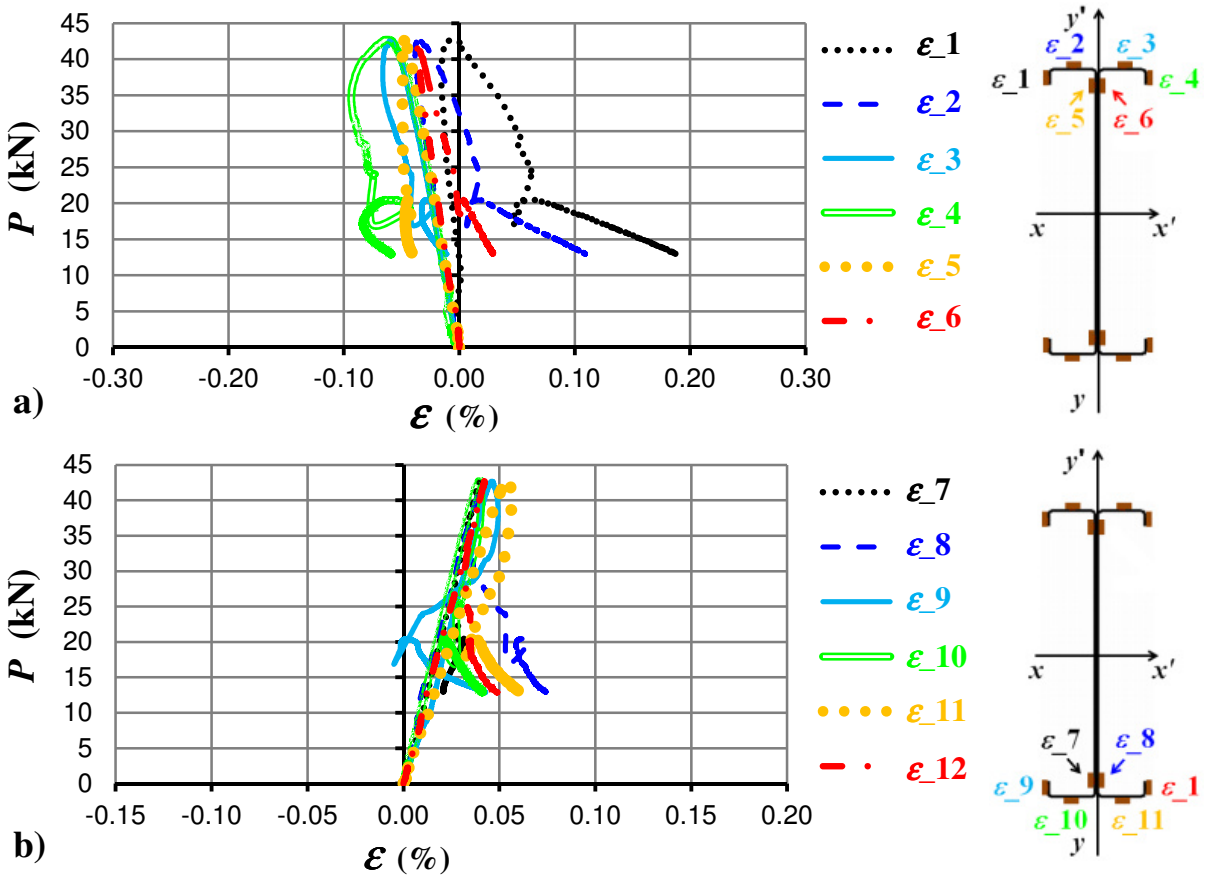

Figure A.20 – Load-strain curves from the strain gauges which were placed in the compressive (a) and tensile (b) flange of beam B-I_2 at section S2

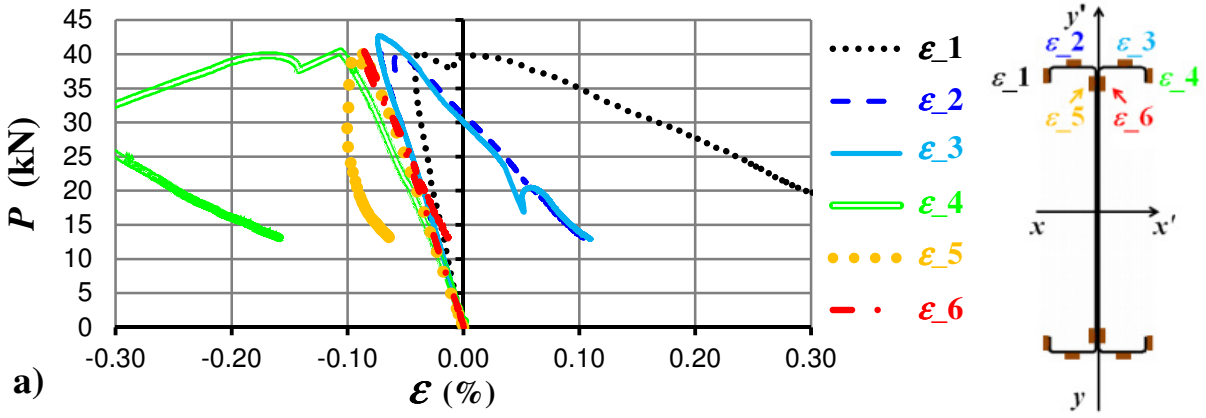

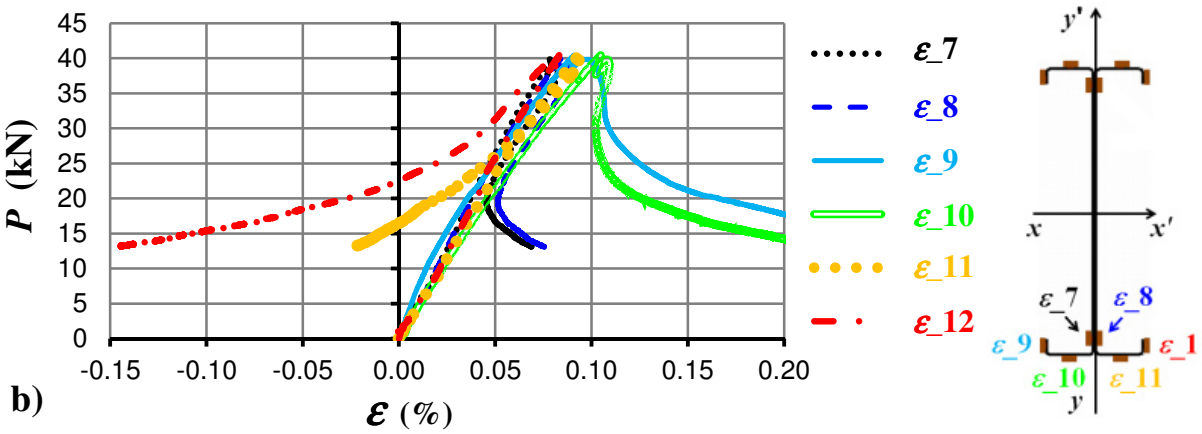

Figure A.21 – Load-strain curves from the strain gauges which were placed in the compressive (a) and tensile (b) flange of beam B-I_3 at section S1

A3 R beams

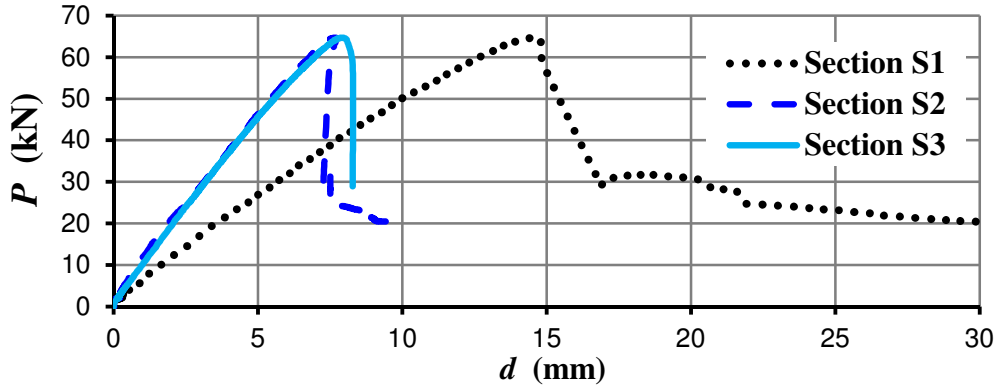

Figure A.22 – Load-displacement diagram at different sections of beam B-R_1

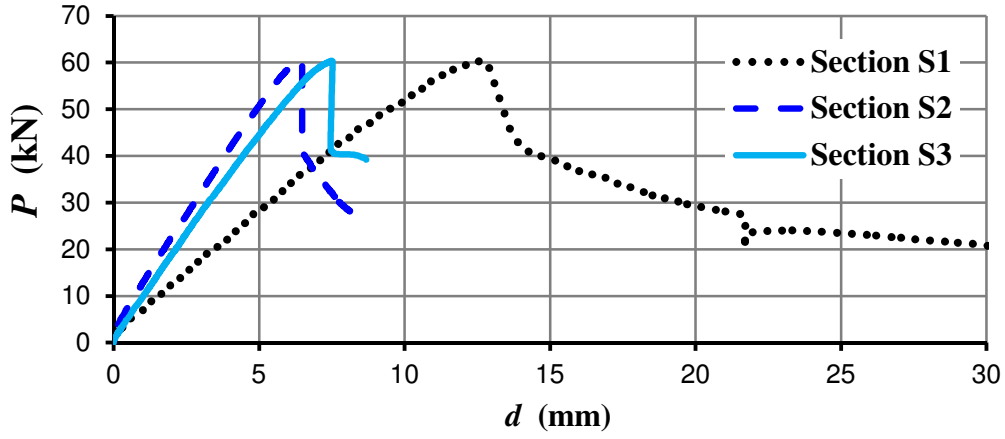

Figure A.23 – Load-displacement diagram at different sections of beam B-R_2

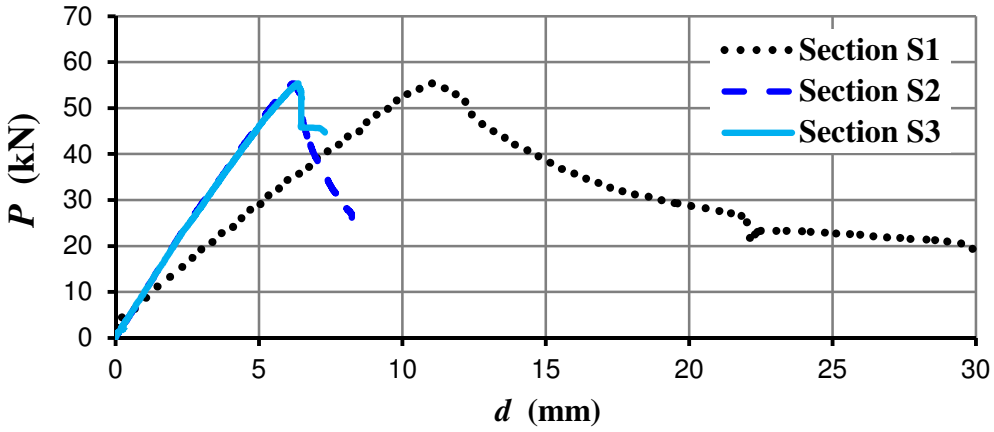

Figure A.24 – Load-displacement diagram at different sections of beam B-R_3

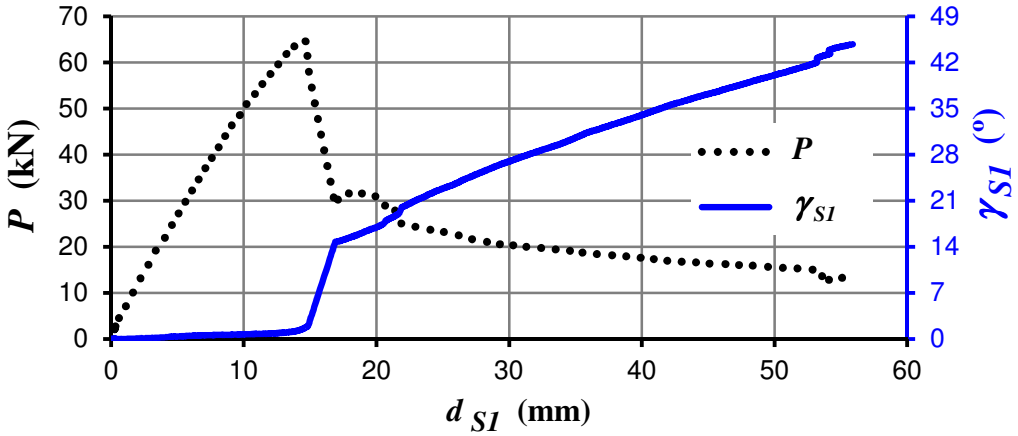

Figure A.25 – Load-rotation diagram at mid-span of beam B-R_1

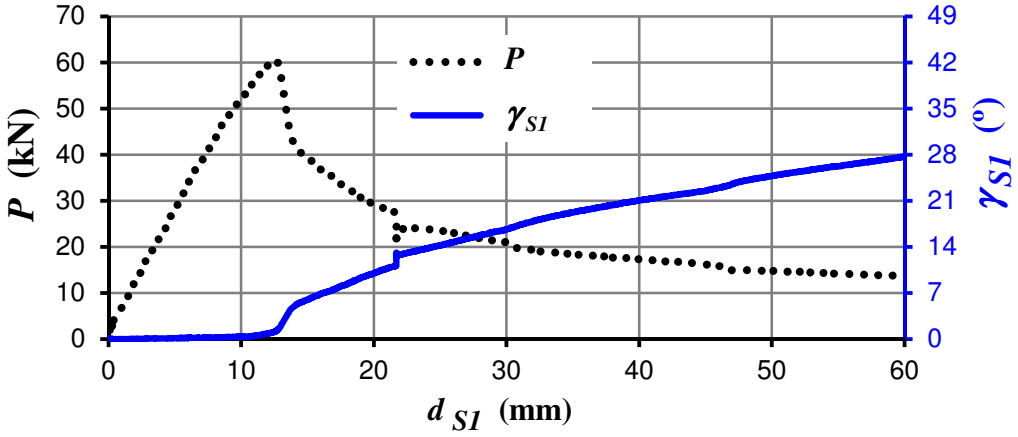

Figure A.26 – Load-rotation diagram at mid-span of beam B-R_2

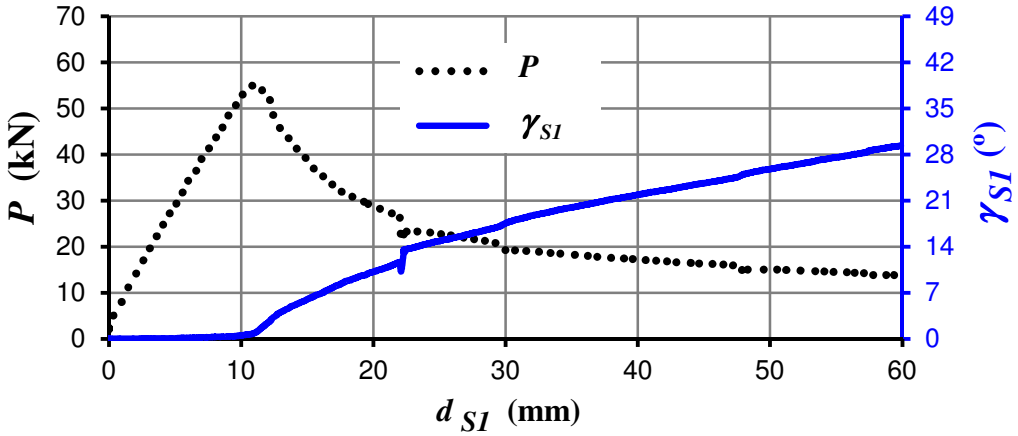

Figure A.27 – Load-rotation diagram at mid-span of beam B-R_3

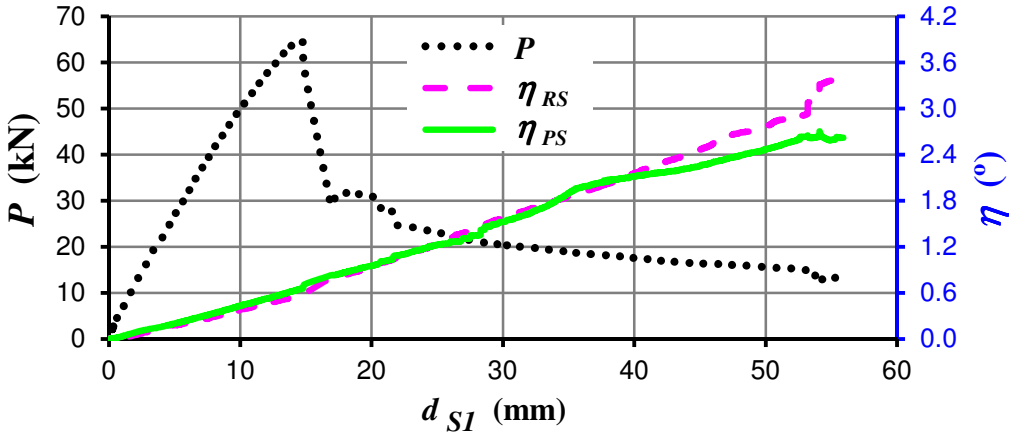

Figure A.28 – Rotation of beam supports in test B-R_1

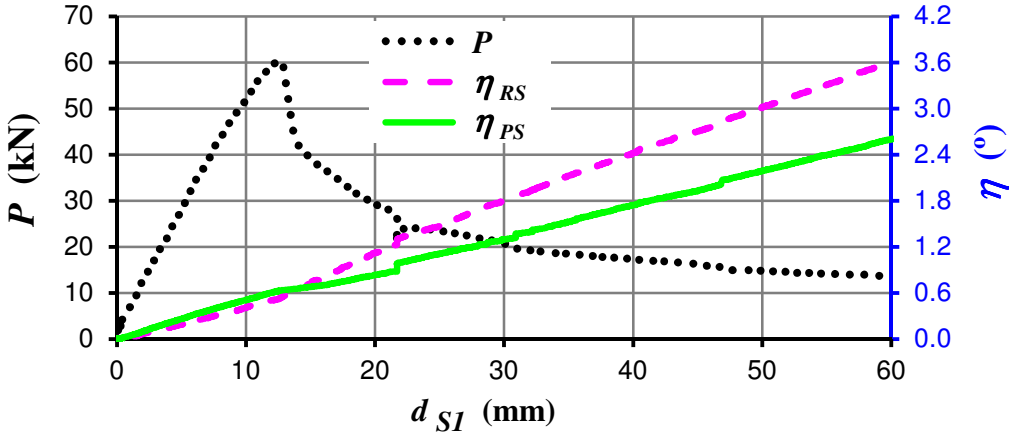

Figure A.29 – Rotation of beam supports in test B-R_2

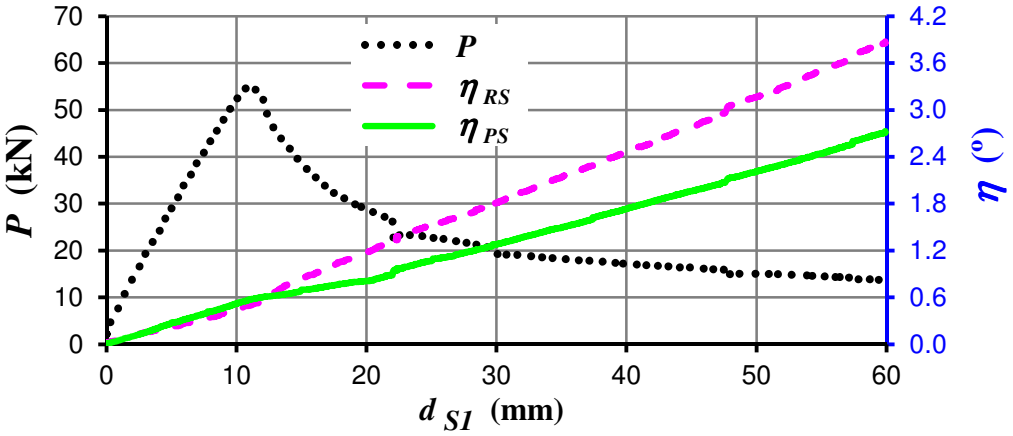

Figure A.30 – Rotation of beam supports in test B-R_3

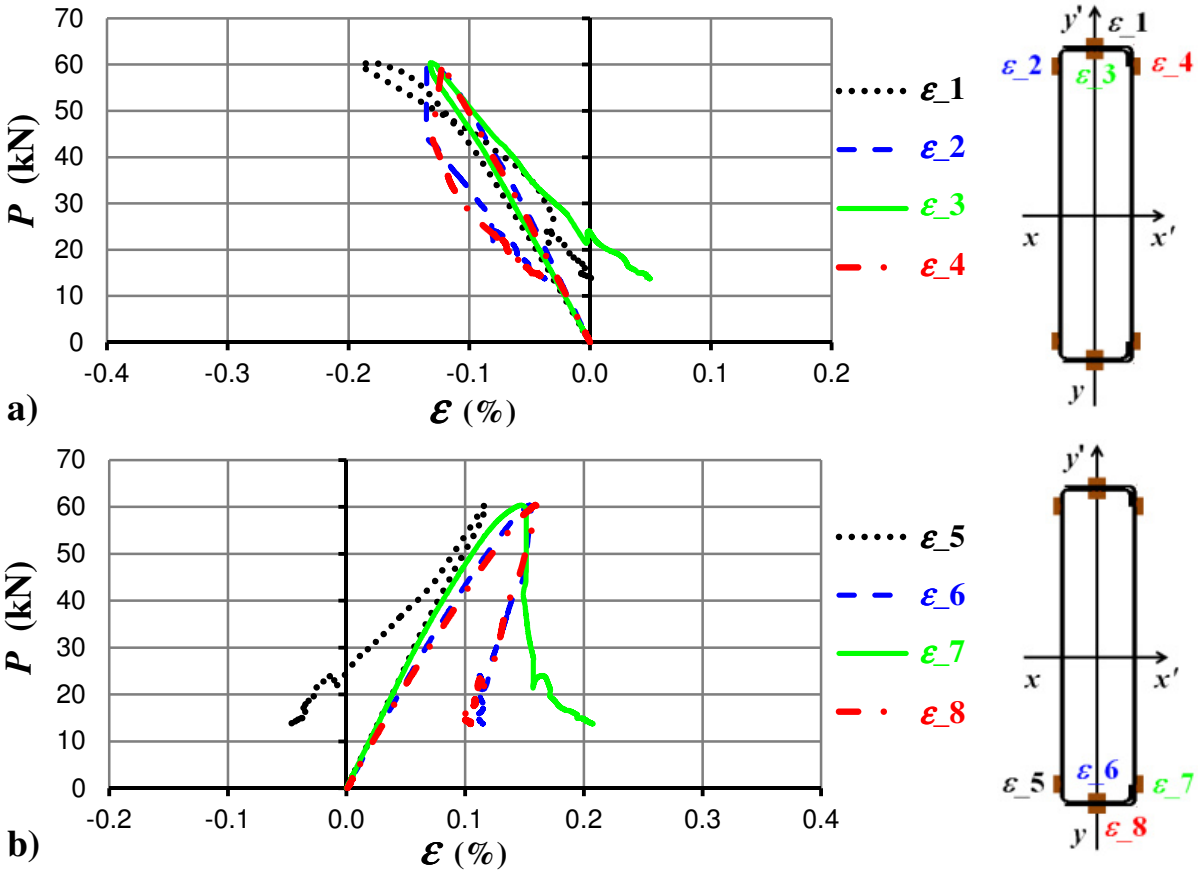

Figure A.31 – Load-strain curves from the strain gauges which were placed in the compressive (a) and tensile (b) flange of beam B-R_2 at section S1

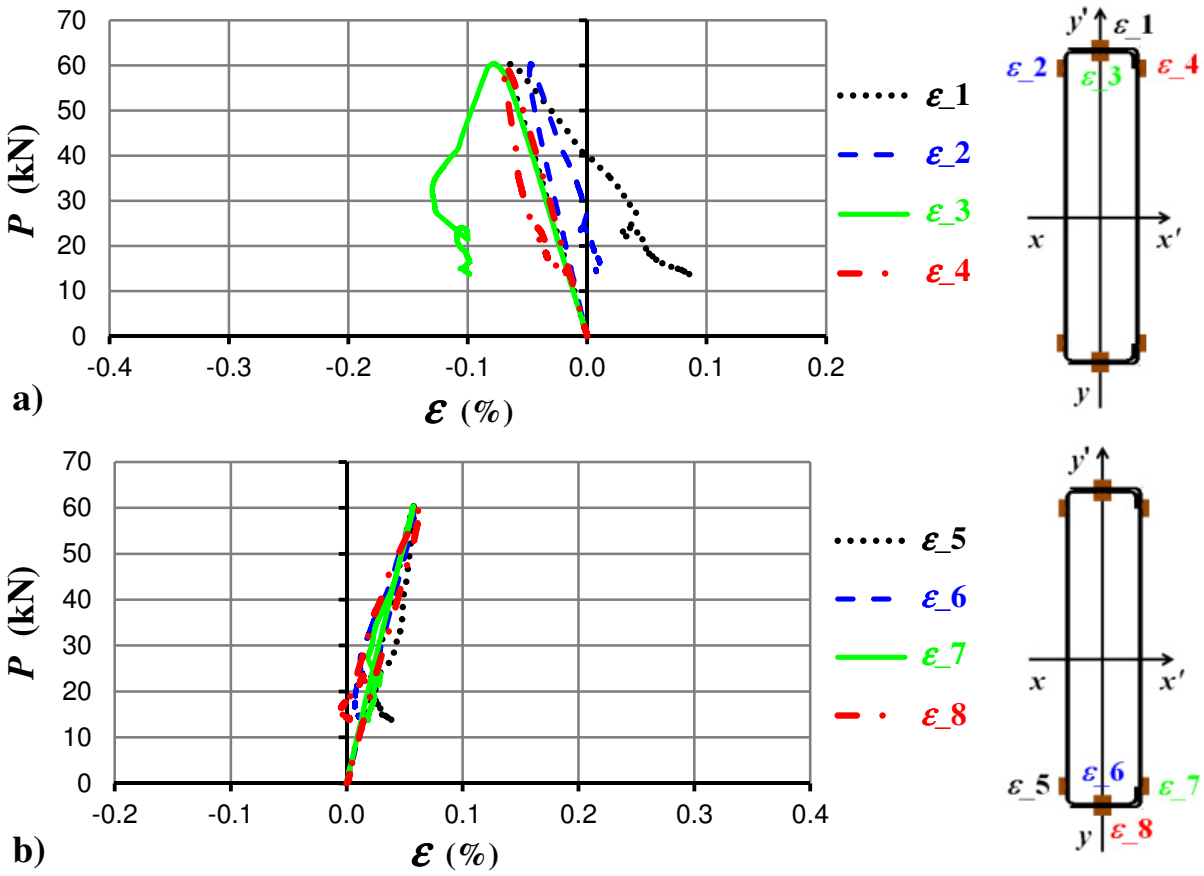

Figure A.32 – Load-strain curves from the strain gauges which were placed in the compressive (a) and tensile (b) flange of beam B-R_2 at section S2

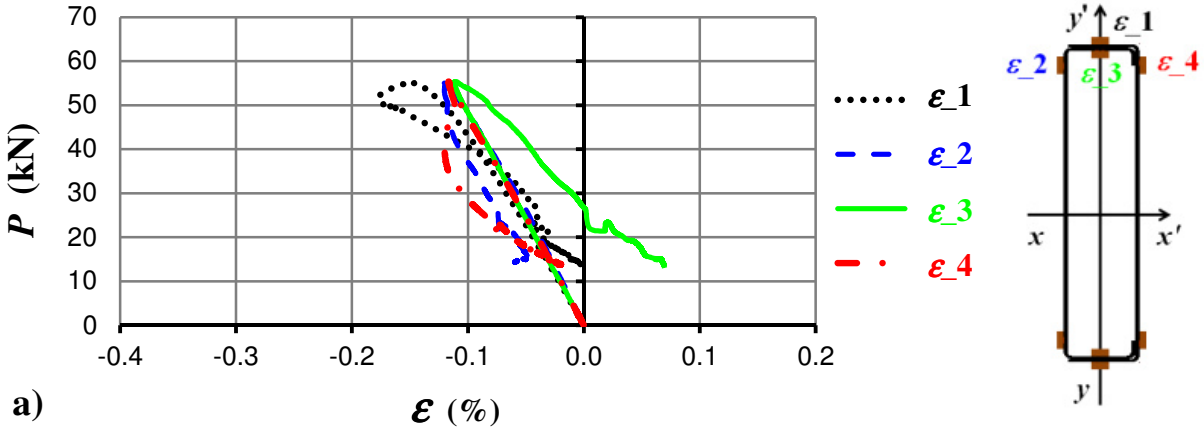

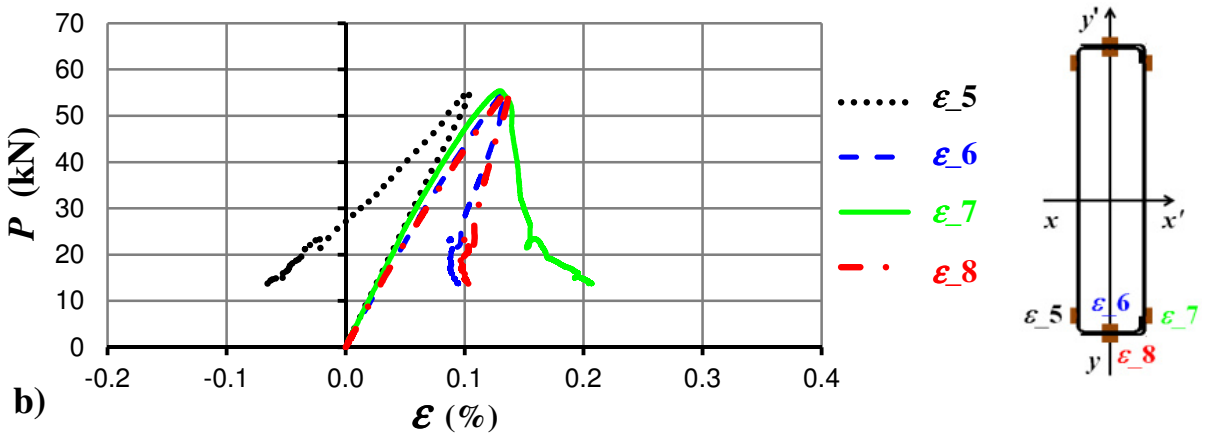

Figure A.33 – Load-strain curves from the strain gauges which were placed in the compressive (a) and tensile (b) flange of beam B-R_3 at section S1

A4 2R beams

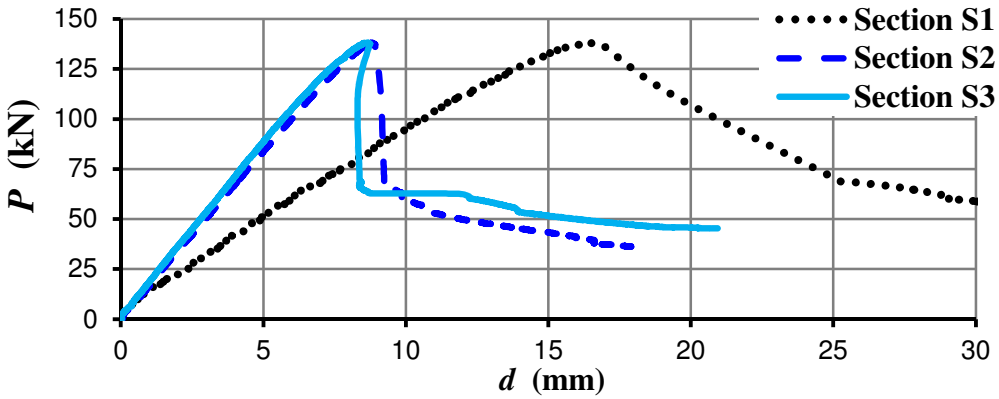

Figure A.34 – Load-displacement diagram at different sections of beam B-2R_1

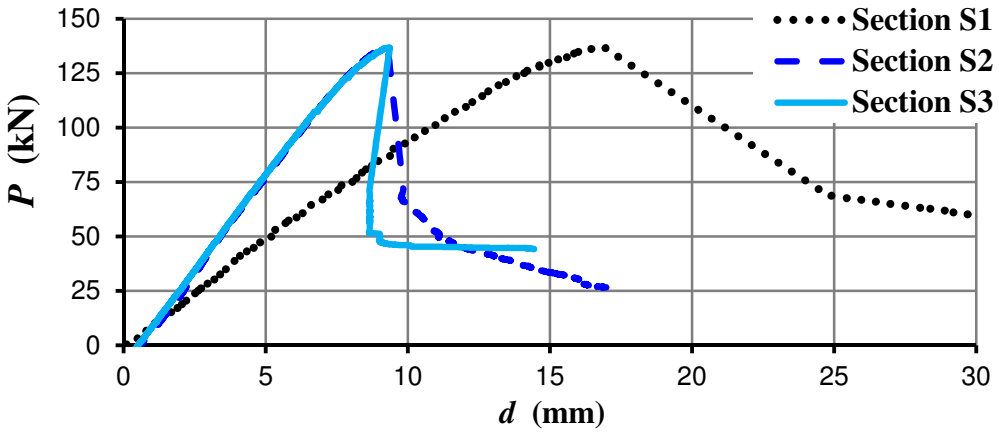

Figure A.35 – Load-displacement diagram at different sections of beam B-2R_2

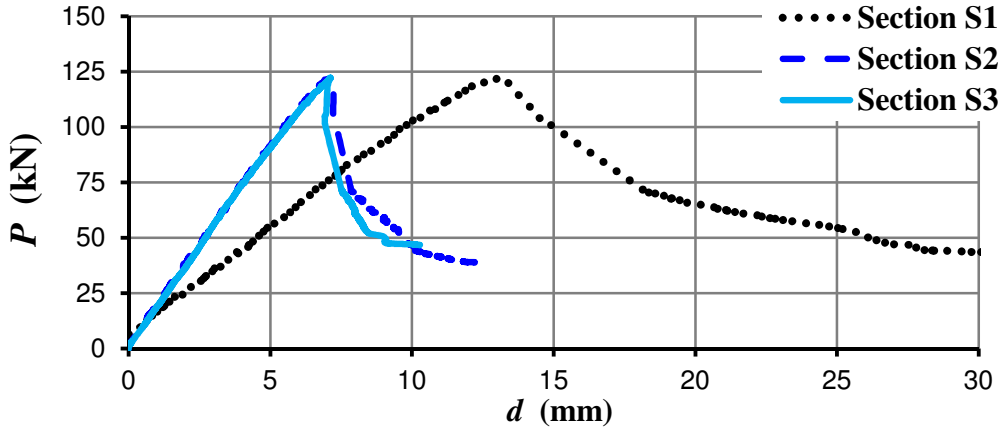

Figure A.36 – Load-displacement diagram at different sections of beam B-2R_3

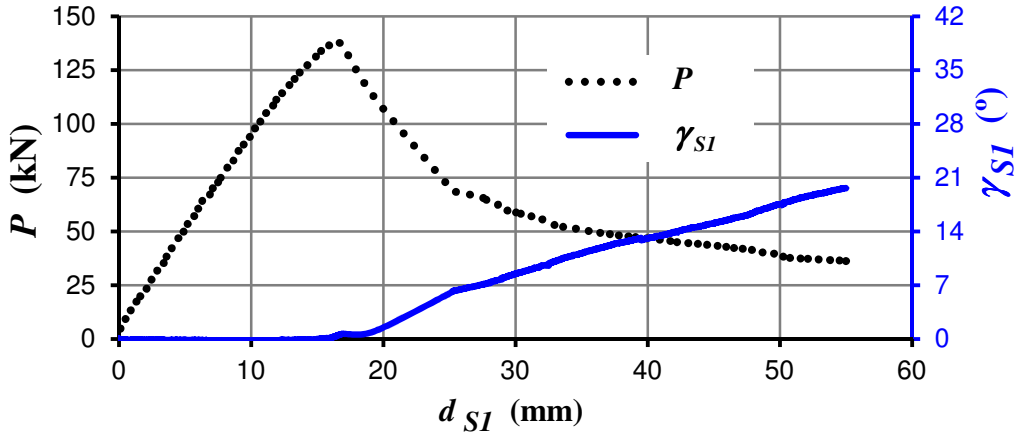

Figure A.37 – Load-rotation diagram at mid-span of beam B-2R_1

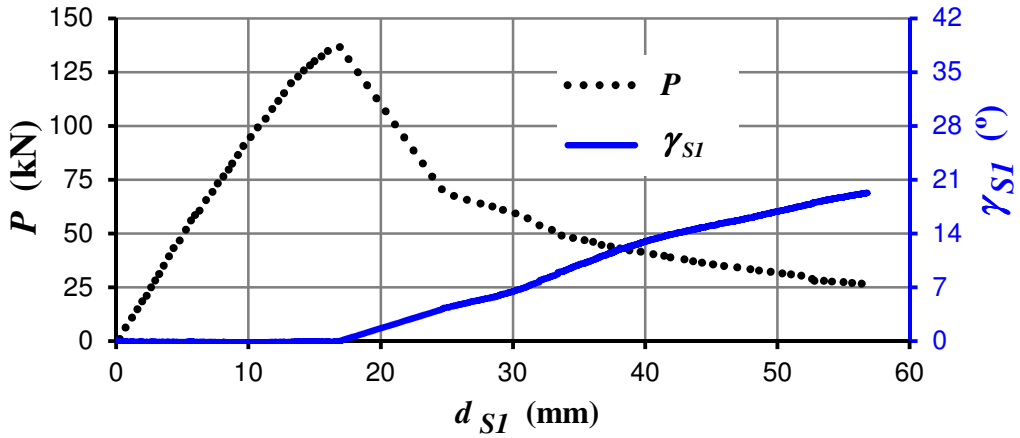

Figure A.38 – Load-rotation diagram at mid-span of beam B-2R_2

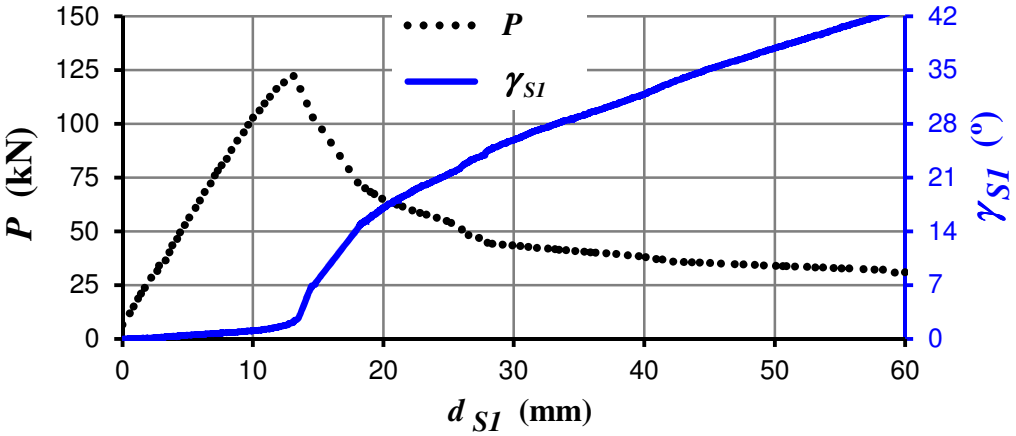

Figure A.39 – Load-rotation diagram at mid-span of beam B-2R_3

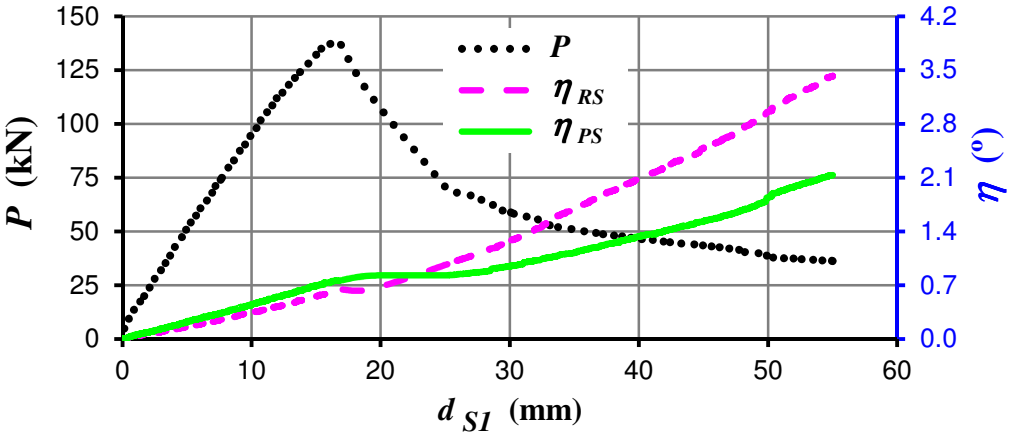

Figure A.40 – Rotation of beam supports in test B-2R_1

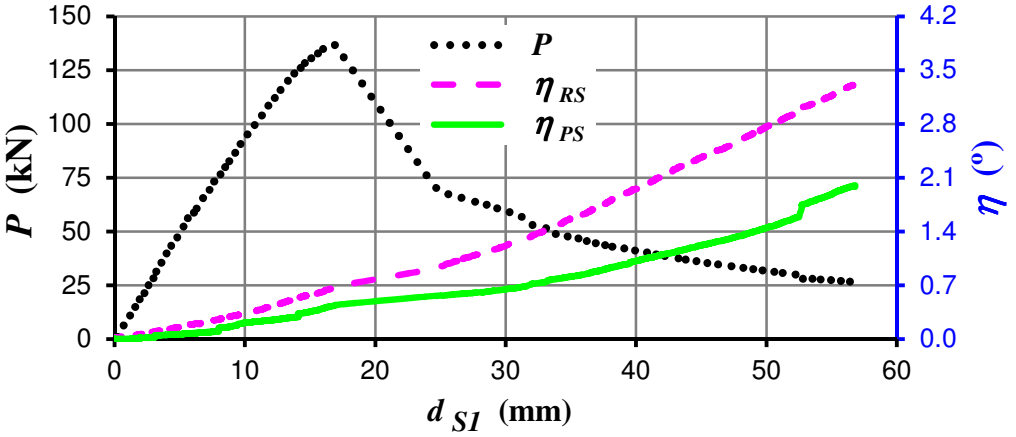

Figure A.41 – Rotation of beam supports in test B-2R_2

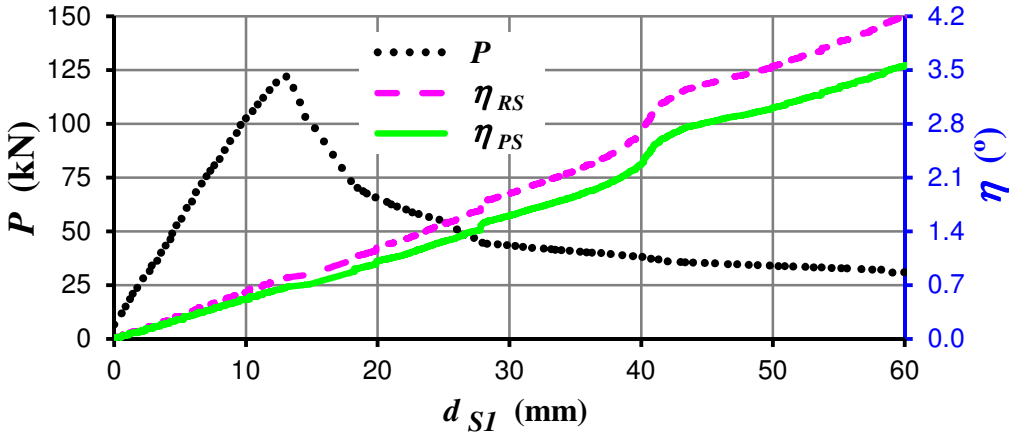

Figure A.42 – Rotation of beam supports in test B-2R_3

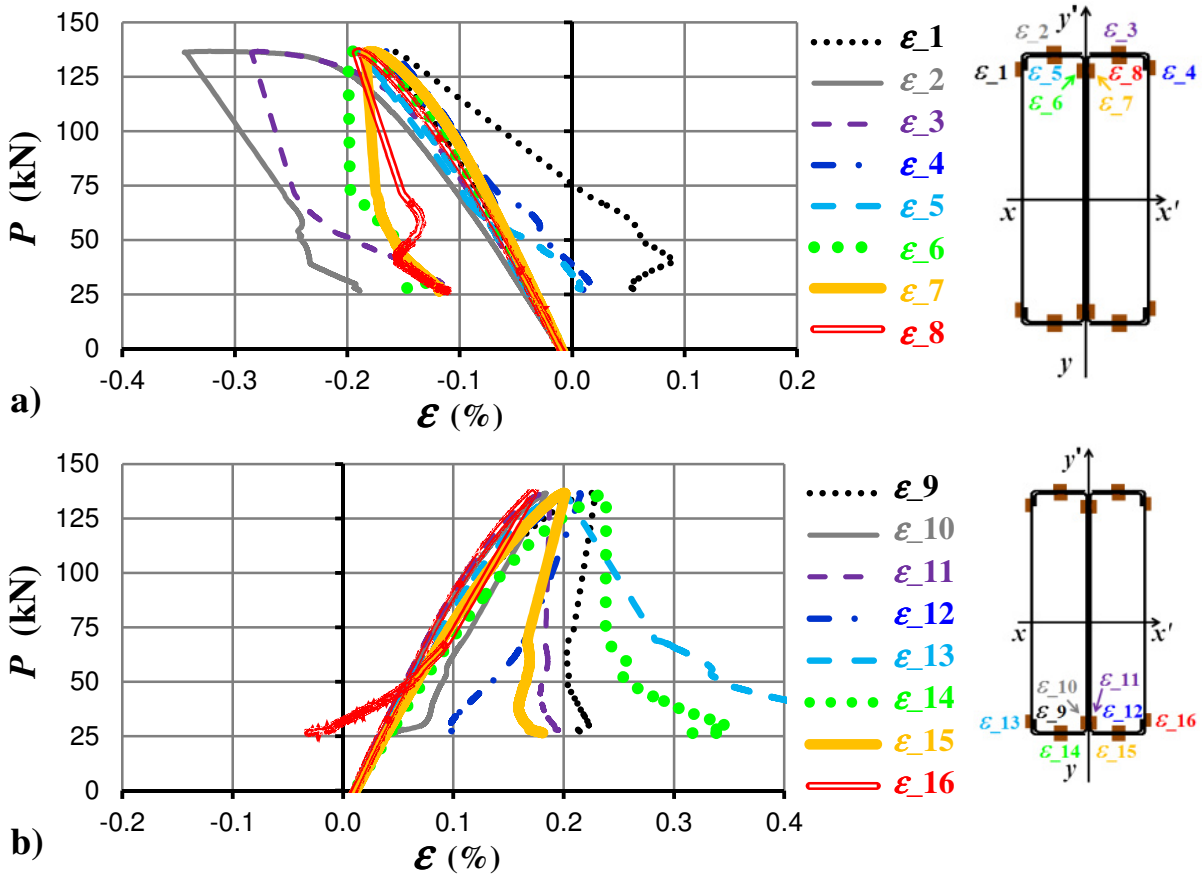

Figure A.43 – Load-strain curves from the strain gauges which were placed in the compressive (a) and tensile (b) flange of beam B-2R_2 at section S1

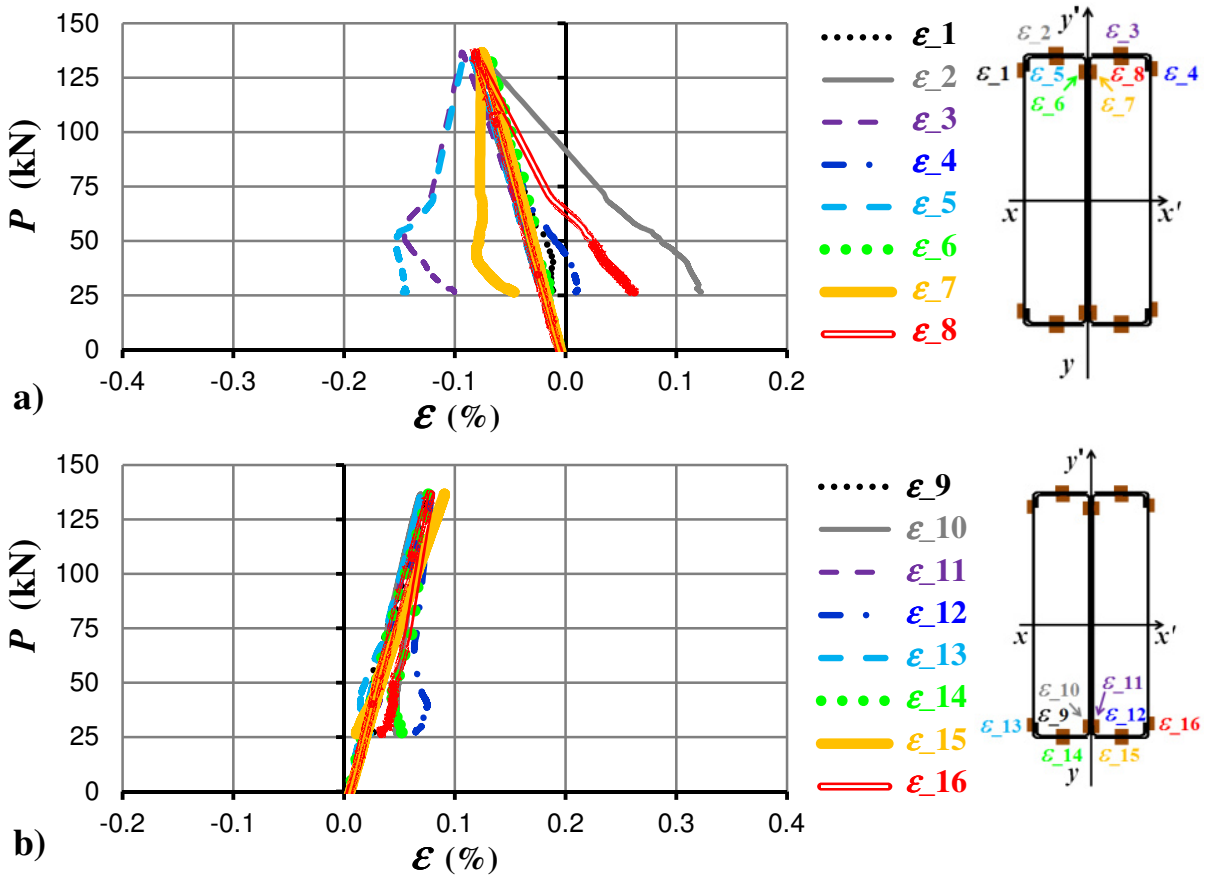

Figure A.44 – Load-strain curves from the strain gauges which were placed in the compressive (a) and tensile (b) flange of beam B-2R_2 at section S2

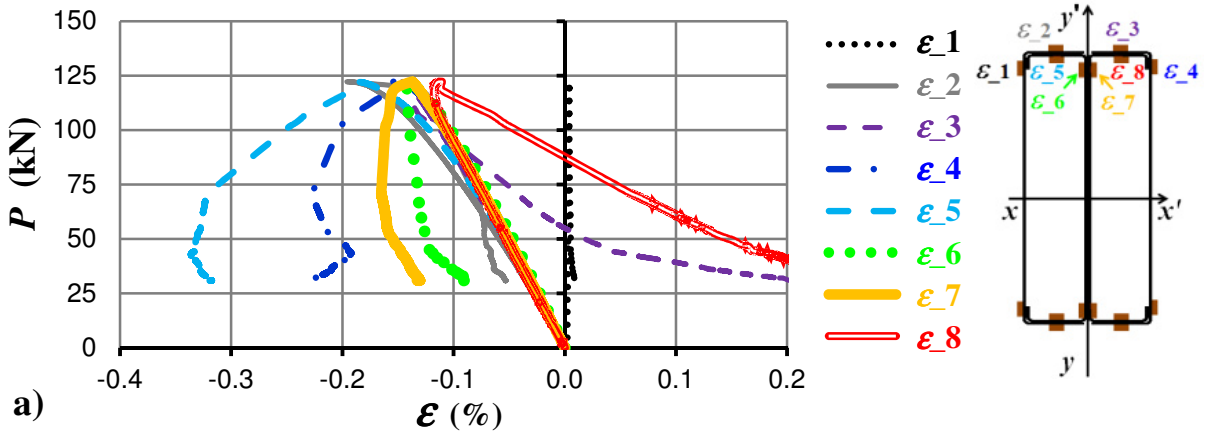

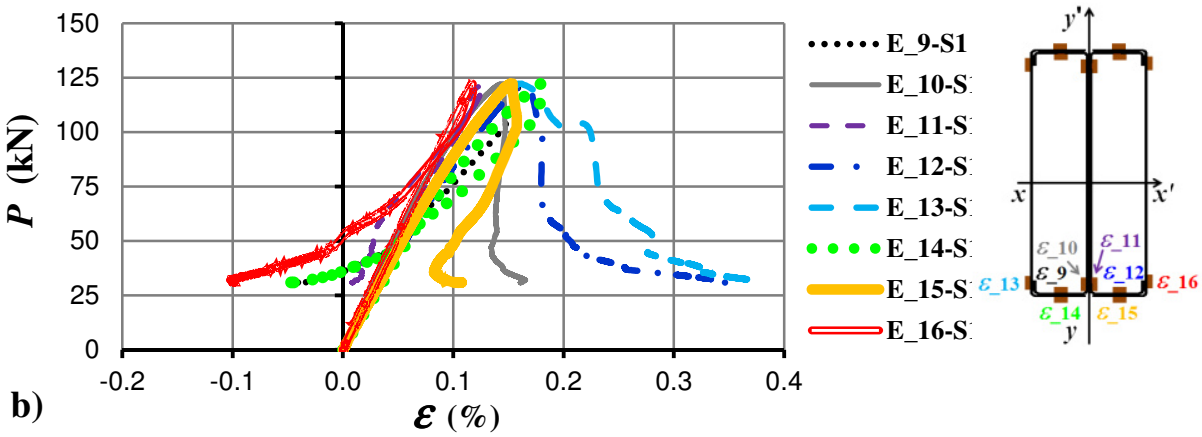

Figure A.45 – Load-strain curves from the strain gauges which were placed in the compressive (a) and tensile (b) flange of beam B-2R_3 at section S1

APPENDIX B Photos of the Experimental Tests on Cold-Formed Steel Beams at Ambient Temperature

B1 C beams

Figure B.1 – Front view of the failure mode of specimen B-C_1

Figure B.2 – Back view of the failure mode of specimen B-C_1

Figure B.3 – Detail view of the failure mode of specimen B-C_1

Figure B.4 – Front view of the failure mode of specimen B-C_2

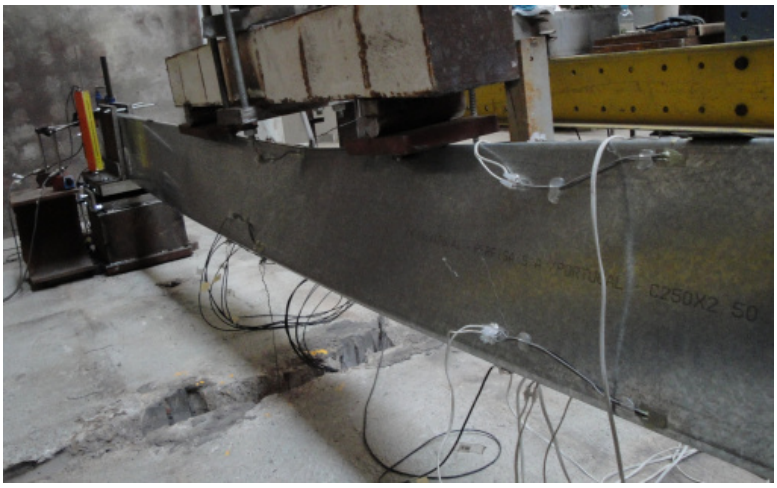

Figure B.5 – Back view of the failure mode of specimen B-C_2

Figure B.6 – Detail view of the failure mode of specimen B-C_2

Figure B.7 – Front view of the failure mode of specimen B-C_3

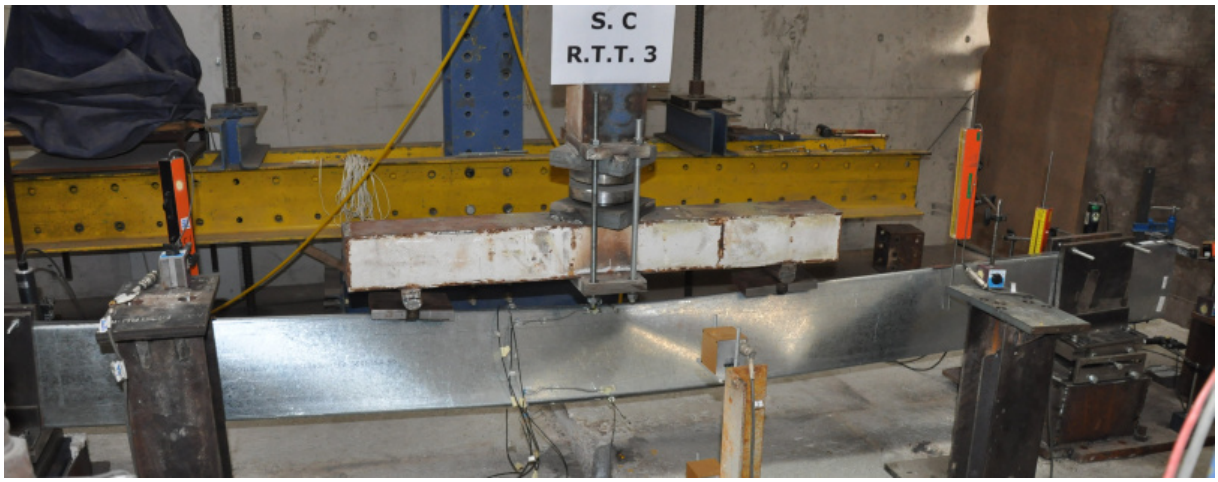

Figure B.8 – Back view of the failure mode of specimen B-C_3

Figure B.9 – Detail view of the failure mode of specimen B-C_3

B2 Lipped-I beams

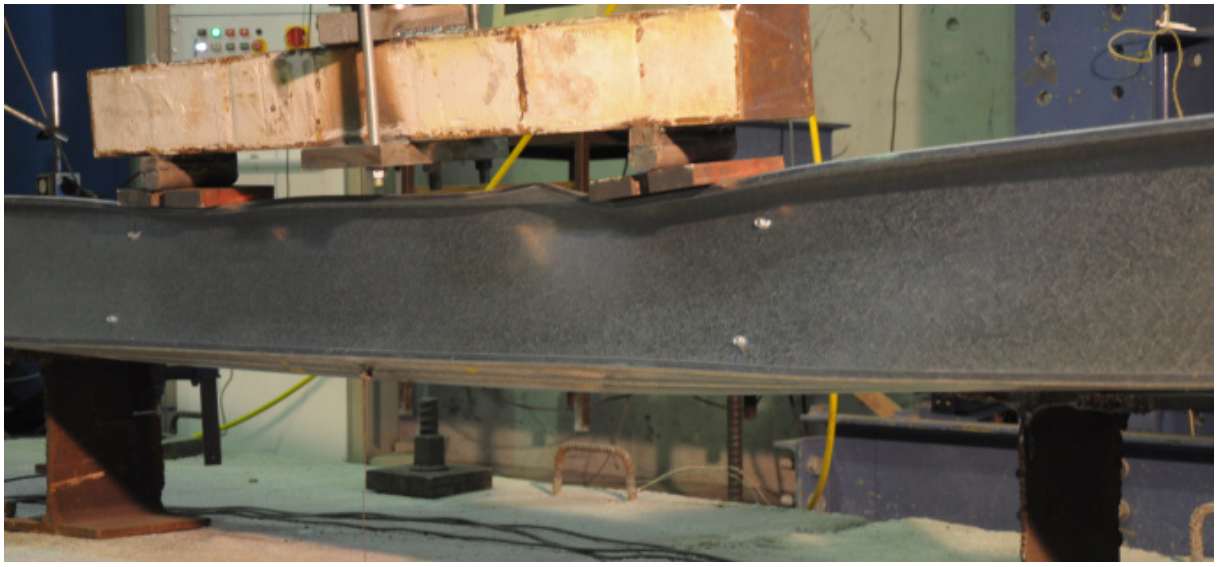

Figure B.10 – Front view of the failure mode of specimen B-I_1

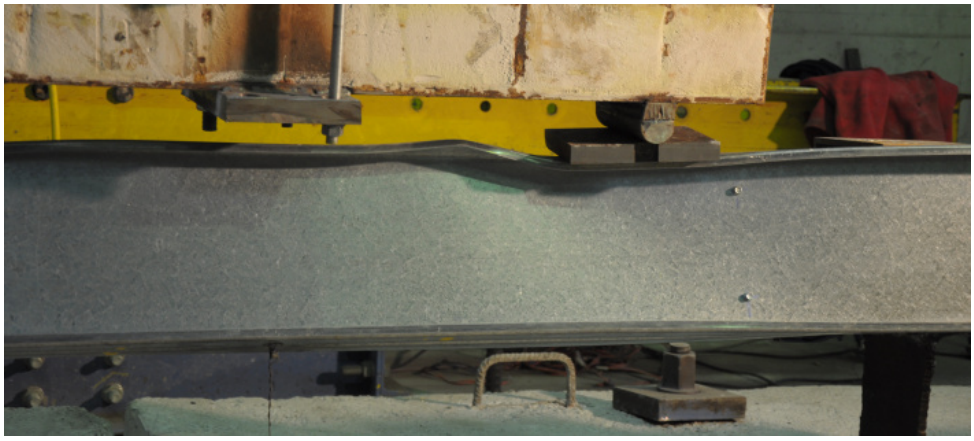

Figure B.11 – Detail view of the failure mode of specimen B-I_1

Figure B.12 – Front view of the failure mode of specimen B-I_2

Figure B.13 – Back view of the failure mode of specimen B-I_2

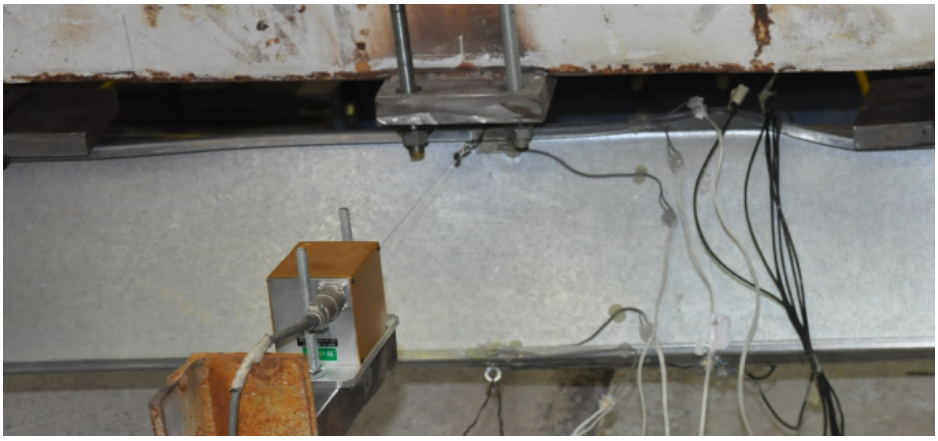

Figure B.14 – Detail view of the failure mode of specimen B-I_2

Figure B.15 – Front view of the failure mode of specimen B-I_3

Figure B.16 – Back view of the failure mode of specimen B-I_3

Figure B.17 – Detail view of the failure mode of specimen B-I_3

B3 R beams

Figure B.18 – Front view of the failure mode of specimen B-R_1

Figure B.19 – Back view of the failure mode of specimen B-R_1

Figure B.20 – Detail view of the failure mode of specimen B-R_1

Figure B.21 – Front view of the failure mode of specimen B-R_2

Figure B.22 – Back view of the failure mode of specimen B-R_2

Figure B.23 – Detail view of the failure mode of specimen B-R_2

Figure B.24 – Front view of the failure mode of specimen B-R_3

Figure B.25 – Back view of the failure mode of specimen B-R_3

Figure B.26 – Detail view of the failure mode of specimen B-R_3

B4 2R beams

Figure B.27 – Front view of the failure mode of specimen B-2R_1

Figure B.28 – Back view of the failure mode of specimen B-2R_1

Figure B.29 – Detail views of the failure mode of specimen B-2R_1

Figure B.30 – Front view of the failure mode of specimen B-2R_2

Figure B.31 – Back view of the failure mode of specimen B-2R_2

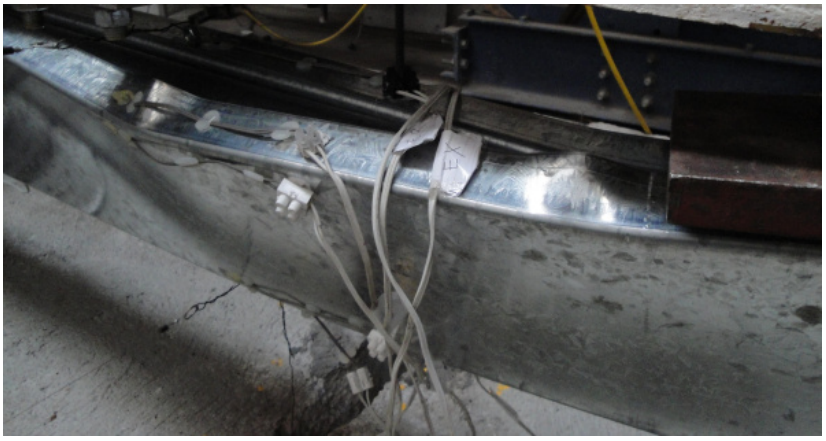

Figure B.32 – Detail view of the failure mode of specimen B-2R_2

Figure B.33 – Front view of the failure mode of specimen B-2R_3

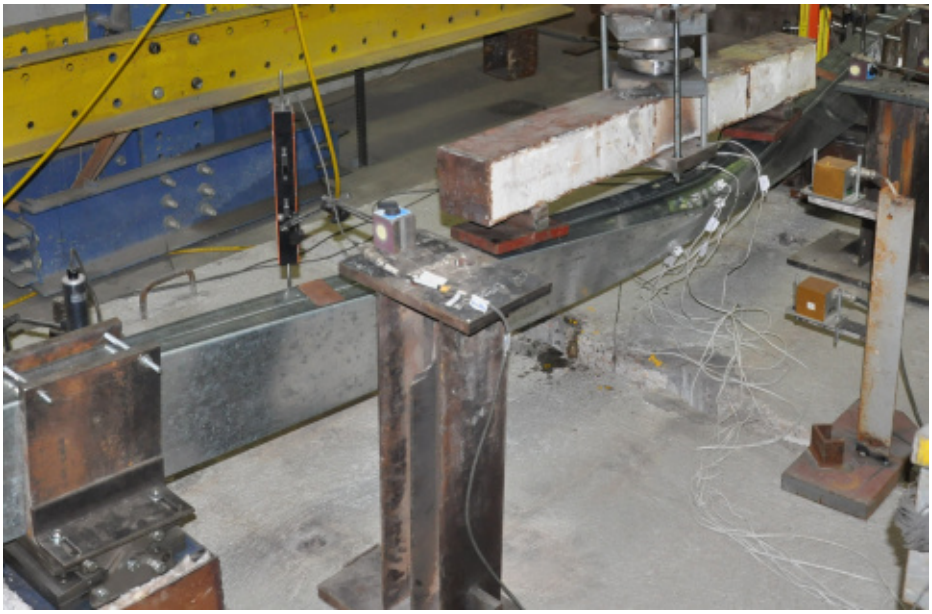

Figure B.34 – Back view of the failure mode of specimen B-2R_3

Figure B.35 – Detail view of the failure mode of specimen B-2R_3

APPENDIX C Calculation of the Design Value of Resistant Buckling Moment According the EN 1993-1-3 (2004)

C1 Cold-formed steel U_4000_203_80_1.5 beam

This example shows how was determined the design buckling resistance moment $M_{b,Rd}$ of a U-shaped section using EN 1993-1-1 (2004), EN 1993-1-3 (2004) and EN 1993-1-5 (2006).

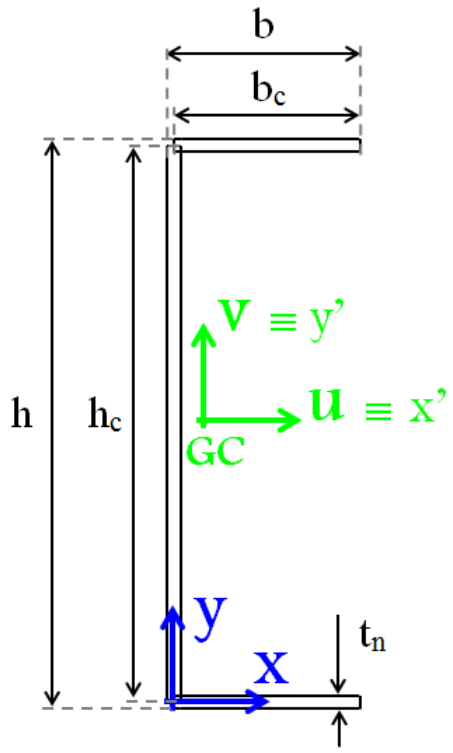

Figure C.1 – Scheme of a U-shaped idealized gross cross-section

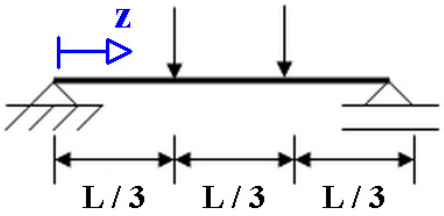

Figure C.2 – Loading system

- **Boundary conditions at beam supports:**
  - no rotation about the longitudinal *z*-*z* axis;
  - no displacements in the plane;
  - no warping restraint.

- **Cross-sectional dimensions:**

Height of the section (overall dimension):		h = 203 mm
Width of the flange (overall dimension):		b = 80 mm
Nominal material thickness:		t_n = 1.5 mm
Material core thickness (clause 3.2.4 of EN 1993-1-3, 2004):	$t_{cor} = t_n - t_{zinc}$ t_{zinc} = 0.04 (Z275)	$t_{cor} = t$ = 1.46 mm
Height of the section (centreline dimension):		h_c = 201.50 mm
Width of the flange (centreline dimension):		b_c = 78.50 mm
Beam span		L = 4000 mm

- **Material properties:**

Modulus of elasticity:		E = 210000 N/mm^2
Poisson ratio:		ν = 0.3
Shear modulus:	$G = E\,[2\,(1 + \nu)]^{-1}$	G = 80769 N/mm^2
Nominal yield strength (S280GD + Z275):		f_{yb} = 280 N/mm^2
Partial factor for resistance of cross-sections (clause 2 of EN 1993-1-3, 2004):		γ_{M0} = 1.00
Partial factor for resistance of members (clause 2 of EN 1993-1-3, 2004):		γ_{M1} = 1.00
Elastic strain:	$\varepsilon = (235 / f_{yb})^{1/2}$	ε = 0.9161

- **Gross cross sectional properties:**

Cross-sectional area:		$A = 525.60$ mm^2
First moment of area with respect to x-axis:		$S_x = 52954$ mm^3
First moment of area with respect to y-axis:		$S_y = 9170$ mm^3
Gravity centre co-ordinate with respect to x-axis:	$X_{GC} = S_y / A$	$X_{GC} = 17.446$ mm
Gravity centre co-ordinate with respect to y-axis:	$Y_{GC} = S_x / A$	$Y_{GC} = 100.75$ mm
Second moment of area with respect to x-axis:		$I_x = 8679516$ mm^4
Second moment of area with respect to y-axis:		$I_y = 484514$ mm^4
Product moment of area with respect to x- and y-axis:		$I_{xy} = 923839$ mm^4
Second moment of area with respect to x'-axis:	$I_{x'} = I_x - A.Y_{CG}^2$	$I_{x'} = 3344381$ mm^4
Second moment of area with respect to y'-axis:	$I_{y'} = I_y - A.X_{CG}^2$	$I_{y'} = 324541$ mm^4
Product moment of area with respect to x'- and y'-axis:	$I_{xy'} = I_{xy} - (S_x \, . \, S_y)/A$	$I_{xy'} = 0$
Angle between x'-axis and u-axis (principal axis):		$\beta = 0$
Second moment of area with respect to u-axis:	$I_u = 0.5[I_{x'} + I_{y'} + \sqrt{((I_{y'} - I_{x'})^2 + 4I_{xy'}^2)}]$	$I_u = 3344381$ mm^4
Second moment of area with respect to v-axis:	$I_v = 0.5[I_{x'} + I_{y'} - \sqrt{((I_{y'} - I_{x'})^2 + 4I_{xy'}^2)}]$	$I_v = 324541$ mm^4
Radius of gyration with respect to u-axis:	$i_u = \sqrt{(I_u / A)}$	$i_u = 79.77$ mm

Radius of gyration with respect to v-axis:	$i_v = \sqrt{(I_v / A)}$	$i_v = 24.85$ mm
Shear centre co-ordinate with respect to u-axis:		$U_{SC} = -45.277$ mm
Shear centre co-ordinate with respect to v-axis:		$V_{SC} = 0$
Polar radius of gyration about shear centre:	$i_0 = \sqrt{(i_u^2 + i_v^2 + U_{SC}^2 + V_{SC}^2)}$	$i_0 = 95.03$ mm
Torsional constant:		$I_T = 373.46$ mm^4
Warping constant:		$I_W = 2327123702$ mm^6
Maximum co-ordinate with respect to u-axis:		$u_{max} = 61.804$ mm
Minimum co-ordinate with respect to u-axis:		$u_{min} = -18.176$ mm
Maximum co-ordinate with respect to v-axis:		$v_{max} = 101.480$ mm
Minimum co-ordinate with respect to v-axis:		$v_{min} = -101.480$ mm

➢ **Effective cross sectional properties:**

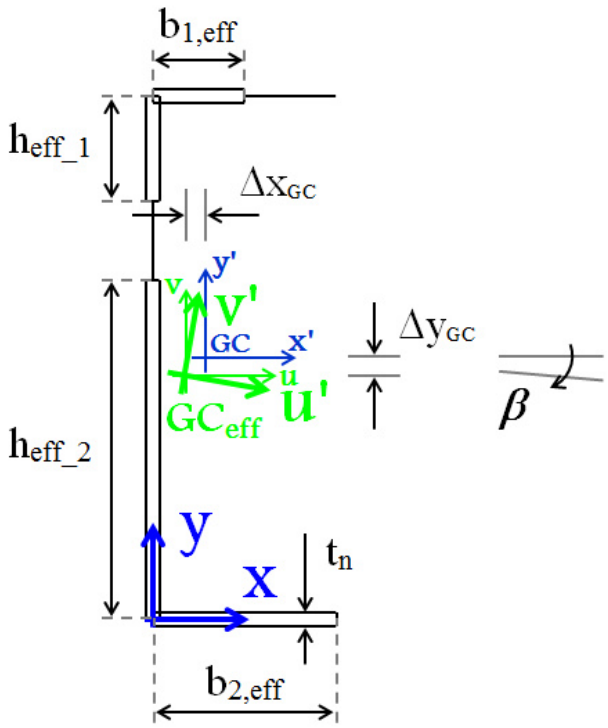

Figure C.3 – Scheme of a U-shaped idealized effective cross-section

1st Iteration:

Flange – outstand compression element:

Maximum stress in the plate (compression positive): $\sigma_{max} = f_{yb} \frac{v_i}{max(|v_{max}|, |v_{min}|)}$ $\sigma_{max} = 278$ N/mm^2

Minimum stress in the plate (compression positive): $\sigma_{min} = f_{yb} \frac{v_j}{max(|v_{max}|, |v_{min}|)}$ $\sigma_{min} = 278$ N/mm^2

Stress ratio in the plate: $\psi = \sigma_{min} / \sigma_{max}$ $\psi = 1$

Plate local buckling factor (Table 4.2 of EN 1993-1-5, 2006): $k_\sigma = 0.43$

Plate slenderness (clause 4.4 of EN 1993-1-5, 2006):	$\bar{\lambda}_p = \frac{b_p/t}{28.4\,\varepsilon\sqrt{k_\sigma}}$	$\bar{\lambda}_p = 3.065 > 0.748$
Maximum design compressive stress in the plate:		$\sigma_{com,Ed} = 280$ N/mm^2
Reduced plate slenderness (clause 4.4 of EN 1993-1-5, 2006):	$\bar{\lambda}_{p,red} = \bar{\lambda}_p \sqrt{\frac{\sigma_{com,Ed}}{f_{yb}/\gamma_{M0}}}$	$\bar{\lambda}_{p,red} = 3.065$
Reduction factor (annex E of EN 1993-1-5, 2006):	$\rho = \frac{1 - 0.188/\bar{\lambda}_{p,red}}{\bar{\lambda}_{p,red}} + +0.18\frac{(\bar{\lambda}_p - \bar{\lambda}_{p,red})}{(\bar{\lambda}_p - 0.6)}$	$\rho = 0.306$
Effective flange width (Table 4.2 of EN 1993-1-5, 2006):	$b_{eff} = \rho\,.\,b_p$	$b_{1,eff} = 24.022$ mm $b_{2,eff} = 78.50$ mm

Initial effective sectional properties:

Cross-sectional area:	$A = 453.54$ mm^2
Gravity centre co-ordinate with respect to x-axis:	$X_{GC} = 11.404$ mm
Gravity centre co-ordinate with respect to y-axis:	$Y_{GC} = 82.617$ mm
Distance in x-direction from gravity centre to effective gravity centre	$\Delta X_{GC} = 6.042$ mm
Distance in y-direction from gravity centre to effective gravity centre	$\Delta Y_{GC} = 18.133$ mm
Second moment of area with respect to u-axis:	$I_u = 2409435$ mm^4
Second moment of area with respect to v-axis:	$I_v = 197610$ mm^4
Product moment of area with respect to u- and v-axis:	$I_{uv} = -334184$ mm^4
Angle between u-axis and u'-axis (principal axis):	$\beta = 8.407°$
Second moment of area with respect to u'-axis:	$I_{u'} = 2458824$ mm^4

Second moment of area with respect to v'-axis: $I_{v'} = 148221$ mm^4

Maximum co-ordinate with respect to u'-axis: $u'_{max} = 79.306$ mm

Minimum co-ordinate with respect to u'-axis: $u'_{min} = -29.286$ mm

Maximum co-ordinate with respect to v'-axis: $v'_{max} = 120.310$ mm

Minimum co-ordinate with respect to v'-axis: $v'_{min} = -84.021$ mm

Web – internal compression element:

Maximum stress in the plate (compression positive): $\sigma_{max} = f_{yb} \frac{v'_i}{max(|v'_{max}|, |v'_{min}|)}$ $\sigma_{max} = 268.0$ N/mm^2

Minimum stress in the plate (compression positive): $\sigma_{min} = f_{yb} \frac{v'_j}{max(|v'_{max}|, |v'_{min}|)}$ $\sigma_{min} = -192.2$ N/mm^2

Stress ratio in the plate: $\psi = \sigma_{min} / \sigma_{max}$ $\psi = -0.72$

Plate local buckling factor (Table 4.1 of EN 1993-1-5, 2006): $k_\sigma = 17.355$

Plate slenderness (clause 4.4 of EN 1993-1-5, 2006): $\bar{\lambda}_p = \frac{h_p/t}{28.4\,\varepsilon\sqrt{k_\sigma}}$ $\bar{\lambda}_p = 1.229 > 0.673$

Maximum design compressive stress in the plate: $\sigma_{com,Ed} = 268$ N/mm^2

Reduced plate slenderness (clause 4.4 of EN 1993-1-5, 2006): $\bar{\lambda}_{p,red} = \bar{\lambda}_p \sqrt{\frac{\sigma_{com,Ed}}{f_{yb}/\gamma_{M0}}}$ $\bar{\lambda}_{p,red} = 1.203$

Reduction factor (annex E of EN 1993-1-5, 2006): $\rho = \frac{1 - 0.055(3 + \psi)/\bar{\lambda}_{p,red}}{\bar{\lambda}_{p,red}} + 0.18 \frac{(\bar{\lambda}_p - \bar{\lambda}_{p,red})}{(\bar{\lambda}_p - 0.6)}$ $\rho = 0.752$

Effective flange width (Table 4.1 of EN 1993-1-5, 2006): $h_{eff} = \rho \,.\, h_p$ $h_{eff\_1} = 20.394$ mm, $h_{eff\_2} = 114.09$ mm

2nd and 3rd Iterations:

Plate	Parameter	Unit	2nd Iteration	3rd Iteration
Flange	σ_{max}	N/mm^2	278.49	278.50
	σ_{min}	N/mm^2	271.61	271.88
	ψ	- - -	0.98	0.98
	k_σ	- - -	0.43	0.43
	$\bar{\lambda}_p$	- - -	3.059	3.059
	$\sigma_{com,Ed}$	N/mm^2	280	280
	$\bar{\lambda}_{p,red}$	- - -	3.059	3.059
	ρ	- - -	0.307	0.307
	$b_{1,eff}$	mm	24.068	24.066
	$b_{2,eff}$	mm	78.500	78.500
Web	σ_{max}	N/mm^2	269.75	270.04
	σ_{min}	N/mm^2	-132.88	-130.59
	ψ	- - -	-0.49	-0.48
	k_σ	- - -	13.282	13.139
	$\bar{\lambda}_p$	- - -	1.405	1.413
	$\sigma_{com,Ed}$	N/mm^2	269.75	270.04
	$\bar{\lambda}_{p,red}$	- - -	1.379	1.388
	ρ	- - -	0.658	0.654
	h_{eff_1}	mm	23.624	23.771
	h_{eff_2}	mm	101.40	100.81

Final effective sectional properties:

Effective cross-sectional area:	A_{eff} = 340.66 mm^2
Effective gravity centre co-ordinate with respect to x-axis:	$X_{eff,GC}$ = 15.187 mm
Effective gravity centre co-ordinate with respect to y-axis:	$Y_{eff,GC}$ = 63.856 mm
Distance in x-direction from gravity centre to effective gravity centre	ΔX_{GC} = 2.259 mm
Distance in y-direction from gravity centre to effective gravity centre	ΔY_{GC} = 36.894 mm
Second moment of effective area with respect to u-axis:	$I_{eff,u}$ = 1874560 mm^4
Second moment of effective area with respect to v-axis:	$I_{eff,v}$ = 178036 mm^4
Product moment of effective area with respect to u- and v-axis:	$I_{eff,uv}$ = -236922 mm^4
Angle between u-axis and u'-axis (principal axis):	β = 7.803º
Second moment of effective area with respect to u'-axis:	$I_{eff,u'}$ = 1907025 mm^4
Second moment of effective area with respect to v'-axis:	$I_{eff,v'}$ = 145570 mm^4
Maximum co-ordinate with respect to u'-axis:	u'_{max} = 72.240 mm
Minimum co-ordinate with respect to u'-axis:	u'_{min} = -34.367 mm
Maximum co-ordinate with respect to v'-axis:	v'_{max} = 138.428 mm
Minimum co-ordinate with respect to v'-axis:	v'_{min} = -65.960 mm

- **Design buckling resistance moment:**

Effective length factor:		$k_v = 1.0$
Warping effective length factor:		$k_w = 1.0$
Buckling factor:		$C_b = 1.0$
Critical elastic moment for lateral-torsional buckling:	$M_{cr} = C_b \sqrt{\frac{\pi^2 E I_v}{(k_v L)^2}\left[G I_T + \frac{\pi^2 E I_W}{(k_W L)^2}\right]}$	$M_{cr} = 3.73$ kN.m
Effective section modulus:	$W_{eff,u'} = \frac{I_{eff,u'}}{v'_{max}}$	$W_{eff,u'} = 13776$ mm^3
Non-dimensional slenderness for lateral-torsional buckling (clause 6.3.2.2 of EN 1993-1-1, 2004):	$\bar{\lambda}_{LT} = \sqrt{\frac{W_{eff,u'} f_{yb}}{M_{cr}}}$	$\bar{\lambda}_{LT} = 1.02$
Imperfection factor (Clause 6.2.4 of EN 1993-1-3, 2004):		$\alpha_{LT} = 0.21$
Capacity reduction factor (clause 6.3.2.2 of EN 1993-1-1, 2004):	$\Phi_{LT} = 0.5\left[1 + \alpha_{LT}\left(\bar{\lambda}_{LT} - 0.2\right) + \bar{\lambda}_{LT}^2\right]$	$\Phi_{LT} = 1.10$
Reduction factor for lateral-torsional buckling (clause 6.3.2.2 of EN 1993-1-1, 2004):	$\chi_{LT} = \frac{1}{\Phi_{LT} + \sqrt{\Phi_{LT}^2 - \bar{\lambda}_{LT}^2}}$	$\chi_{LT} = 0.65$
Design value of the buckling resistance moment:	$M_{b,Rd} = \chi_{LT} \cdot W_{eff,u'} \cdot \frac{f_{yb}}{\gamma_{M1}}$	$\boldsymbol{M_{b,Rd} = 2.52}$ **kN.m**

C2 Cold-formed steel C_4000_200_80_20_1.5 beam

This example shows how was determined the design buckling resistance moment $M_{b,Rd}$ of a C-shaped section using EN 1993-1-1 (2004), EN 1993-1-3 (2004) and EN 1993-1-5 (2006).

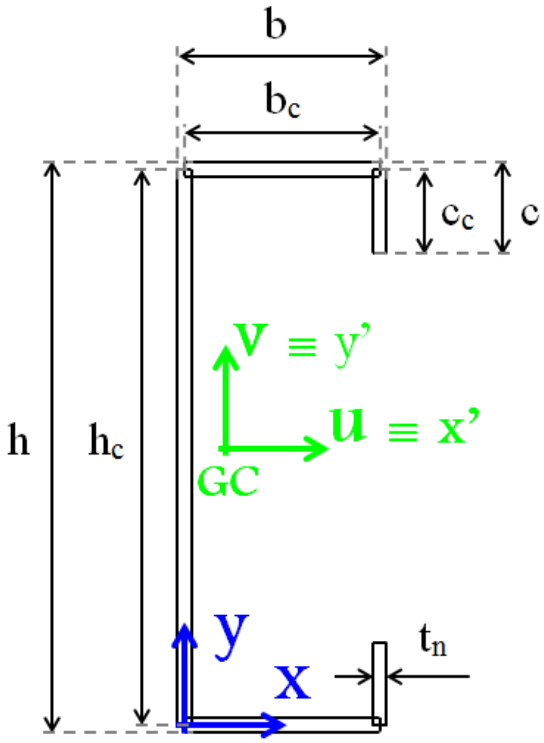

Figure C.4 – Scheme of a C-shaped idealized gross cross-section

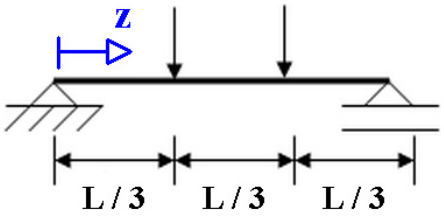

Figure C.5 – Loading system

- **<u>Boundary conditions at beam supports:</u>**
  - no rotation about the longitudinal z-z axis;
  - no displacements in the plane;
  - no warping restraint.

- **<u>Cross-sectional dimensions:</u>**

Height of the section (overall dimension): $h = 200$ mm

Width of the flange (overall dimension): $b = 80$ mm

Width of the edge stiffener (overall dimension):		c = 20 mm
Nominal material thickness:		t_n = 1.5 mm
Material core thickness (clause 3.2.4 of EN 1993-1-3, 2004):	$t_{cor} = t_n - t_{zinc}$ t_{zinc} = 0.04 (Z275)	$t_{cor} = t$ = 1.46 mm
Height of the section (centreline dimension):		h_c = 198.50 mm
Width of the flange (centreline dimension):		b_c = 78.50 mm
Width of the edge stiffener (centreline dimension):		c_c = 19.25 mm
Beam span		L = 4000 mm

- **Material properties:**

Modulus of elasticity:		E = 210000 N/mm^2
Poisson ratio:		ν = 0.3
Shear modulus:	$G = E\,[2\,(1 + \nu)]^{-1}$	G = 80769 N/mm^2
Nominal yield strength (S280GD + Z275):		f_{yb} = 280 N/mm^2
Partial factor for resistance of cross-sections (clause 2 of EN 1993-1-3, 2004):		γ_{M0} = 1.00
Partial factor for resistance of members (clause 2 of EN 1993-1-3, 2004):		γ_{M1} = 1.00
Elastic strain:	$\varepsilon = (235 / f_{yb})^{1/2}$	ε = 0.9161

- **Gross cross sectional properties:**

Cross-sectional area:		$A = 575.24$ mm^2
First moment of area with respect to x-axis:		$S_x = 57093$ mm^3
First moment of area with respect to y-axis:		$S_y = 13409$ mm^3
Gravity centre co-ordinate with respect to x-axis:	$X_{GC} = S_y / A$	$X_{GC} = 23.311$ mm
Gravity centre co-ordinate with respect to y-axis:	$Y_{GC} = S_x / A$	$Y_{GC} = 99.25$ mm
Second moment of area with respect to x-axis:		$I_x = 9329272$ mm^4
Second moment of area with respect to y-axis:		$I_y = 817279$ mm^4
Product moment of area with respect to x- and y-axis:		$I_{xy} = 1330880$ mm^4
Second moment of area with respect to x'-axis:	$I_{x'} = I_x - A.Y_{CG}^2$	$I_{x'} = 3662834$ mm^4
Second moment of area with respect to y'-axis:	$I_{y'} = I_y - A.X_{CG}^2$	$I_{y'} = 504694$ mm^4
Product moment of area with respect to x'- and y'-axis:	$I_{xy'} = I_{xy} - (S_x \, . \, S_y)/A$	$I_{xy'} = 0$
Angle between x'-axis and u-axis (principal axis):		$\beta = 0$
Second moment of area with respect to u-axis:	$I_u = 0.5[I_{x'} + I_{y'} + \sqrt{((I_{y'} - I_{x'})^2 + 4I_{xy'}^2)}]$	$I_u = 3662834$ mm^4
Second moment of area with respect to v-axis:	$I_v = 0.5[I_{x'} + I_{y'} - \sqrt{((I_{y'} - I_{x'})^2 + 4I_{xy'}^2)}]$	$I_v = 504694$ mm^4
Radius of gyration with respect to u-axis:	$i_u = \sqrt{(I_u / A)}$	$i_u = 79.80$ mm

Radius of gyration with respect to v-axis:	$i_v = \sqrt{(I_v / A)}$	$i_v = 29.62$ mm
Shear centre co-ordinate with respect to u-axis:		$U_{SC} = -59.225$ mm
Shear centre co-ordinate with respect to v-axis:		$V_{SC} = 0$
Polar radius of gyration about shear centre:	$i_0 = \sqrt{(i_u^2 + i_v^2 + U_{SC}^2 + V_{SC}^2)}$	$i_0 = 103.69$ mm
Torsional constant:		$I_T = 408.73$ mm^4
Warping constant:		$I_W = 4030341055$ mm^6
Maximum co-ordinate with respect to u-axis:		$u_{max} = 55.919$ mm
Minimum co-ordinate with respect to u-axis:		$u_{min} = -24.041$ mm
Maximum co-ordinate with respect to v-axis:		$v_{max} = 99.980$ mm
Minimum co-ordinate with respect to v-axis:		$v_{min} = -99.980$ mm

➢ **Effective cross sectional properties:**

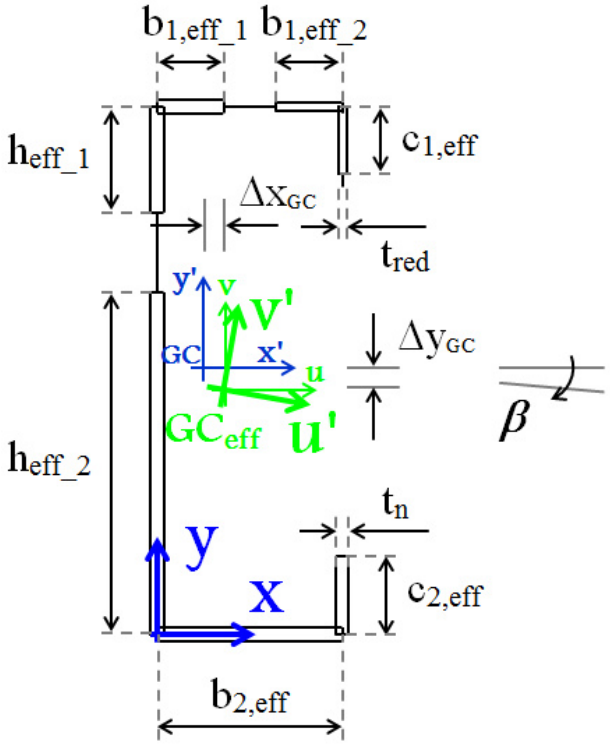

Figure C.6 – Scheme of a C-shaped idealized effective cross-section

1st Iteration:

Flange – internal compression element:

Maximum stress in the plate (compression positive): $\sigma_{max} = f_{yb} \frac{v_i}{max(|v_{max}|, |v_{min}|)}$ $\sigma_{max} = 278$ N/mm^2

Minimum stress in the plate (compression positive): $\sigma_{min} = f_{yb} \frac{v_j}{max(|v_{max}|, |v_{min}|)}$ $\sigma_{min} = 278$ N/mm^2

Stress ratio in the plate: $\psi = \sigma_{min} / \sigma_{max}$ $\psi = 1$

Plate local buckling factor (Table 4.1 of EN 1993-1-5, 2006): $k_\sigma = 4.0$

Plate slenderness (clause 4.4 of EN 1993-1-5, 2006):	$\bar{\lambda}_p = \frac{b_p/t}{28.4\,\varepsilon\sqrt{k_\sigma}}$	$\bar{\lambda}_p = 0.985 > 0.673$
Maximum design compressive stress in the plate:		$\sigma_{com,Ed} = 280$ N/mm^2
Reduced plate slenderness (clause 4.4 of EN 1993-1-5, 2006):	$\bar{\lambda}_{p,red} = \bar{\lambda}_p \sqrt{\frac{\sigma_{com,Ed}}{f_{yb}/\gamma_{M0}}}$	$\bar{\lambda}_{p,red} = 0.985$
Reduction factor (annex E of EN 1993-1-5, 2006):	$\rho = \frac{1 - 0.188/\bar{\lambda}_{p,red}}{\bar{\lambda}_{p,red}} + +0.18\frac{(\bar{\lambda}_p - \bar{\lambda}_{p,red})}{(\bar{\lambda}_p - 0.6)}$	$\rho = 0.788$
Effective flange width (Table 4.1 of EN 1993-1-5, 2006):	$b_{eff} = \rho \,.\, b_p$	$b_{1,eff\_1} = 30.311$ mm $b_{1,eff\_2} = 30.311$ mm $b_{2,eff} = 76.889$ mm

Edge stiffener – outstand compression element:

Maximum stress in the plate (compression positive):	$\sigma_{max} = f_{yb}\frac{v_i}{max(\lvert v_{max}\rvert, \lvert v_{min}\rvert)}$	$\sigma_{max} = 276$ N/mm^2
Minimum stress in the plate (compression positive):	$\sigma_{min} = f_{yb}\frac{v_j}{max(\lvert v_{max}\rvert, \lvert v_{min}\rvert)}$	$\sigma_{min} = 224$ N/mm^2
Stress ratio in the plate:	$\psi = \sigma_{min} / \sigma_{max}$	$\psi = 0.8$
Plate local buckling factor (clause 5.5.3.2 of EN 1993-1-3, 2004):	$k_\sigma = 0.5\,, c_p/b_p \le 0.35$ $k_\sigma = 0.5 + +0.83\sqrt[3]{(c_p/b_p - 0.35)^2}\,,$ $0.35 < c_p/b_p \le 0.6$	$k_\sigma = 0.500$
Plate slenderness (clause 4.4 of EN 1993-1-5, 2006):	$\bar{\lambda}_p = \frac{b_p/t}{28.4\,\varepsilon\sqrt{k_\sigma}}$	$\bar{\lambda}_p = 0.668 < 0.748$
Maximum design compressive		

stress in the plate: $\sigma_{com,Ed} = 280$ N/mm^2

Reduced plate slenderness (clause 4.4 of EN 1993-1-5, 2006): $\bar{\lambda}_{p,red} = \bar{\lambda}_p \sqrt{\frac{\sigma_{com,Ed}}{f_{yb}/\gamma_{M0}}}$ $\bar{\lambda}_{p,red} = 0.668$

Reduction factor (annex E of EN 1993-1-5, 2006): $\rho = \frac{1 - 0.188/\bar{\lambda}_{p,red}}{\bar{\lambda}_{p,red}} + +0.18\frac{(\bar{\lambda}_p - \bar{\lambda}_{p,red})}{(\bar{\lambda}_p - 0.6)}$ $\rho = 1.0$

Effective flange width (Table 4.2 of EN 1993-1-5, 2006): $c_{eff} = \rho \,.\, c_p$ $c_{1,eff} = 18.445$ mm

Reduction factor χ_d for the distortional buckling resistance of the edge stiffener:

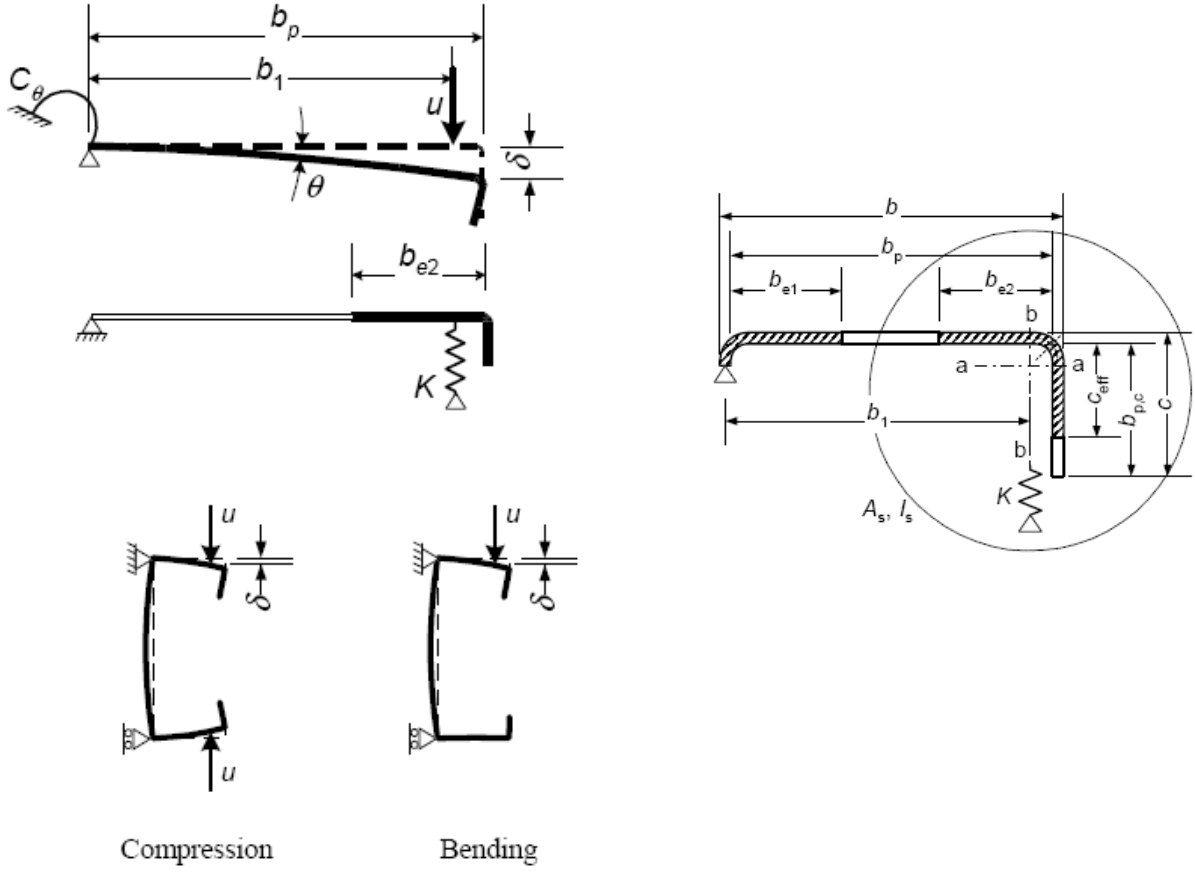

Figure C.7 – Edge stiffener (EN 1993-1-3, 2004)

Distance from the web-to-flange junction to the centre of the effective area of the edge stiffener (including effective part b_{1,eff_2} of the flange):		b_1 = 68.577 mm
Spring stiffness of the edge stiffener per unit length (clause 5.5.3.1 of EN 1993-1-3, 2004):	$K = \frac{Et^3}{4(1-\nu^2)} \cdot \frac{1}{b_1^2 h_p + b_1^3}$ (beam in bending about u-axis)	K = 0.1560 N/mm^2
Second moment of effective area of the edge stiffener with respect to a-axis:		I_s = 2522 mm^4
Effective cross-sectional area of the edge stiffener:		A_s = 73.133 mm^2
Elastic critical buckling stress of the edge stiffener (clause 5.5.3.2 of EN 1993-1-3, 2004):	$\sigma_{cr,s} = \frac{2\sqrt{K \cdot E \cdot I_s}}{A_s}$	$\sigma_{cr,s}$ = 248.57 MPa
Edge stiffener slenderness (clause 5.5.3.1 of EN 1993-1-3, 2004):	$\bar{\lambda}_d = \sqrt{f_{yb}/\sigma_{cr,s}}$	$\bar{\lambda}_d$ = 1.061
Reduction factor for the distortional buckling resistance of the edge stiffener (clause 5.5.3.1 of EN 1993-1-3, 2004):	$\chi_d = \begin{cases} 1.0\,, & \bar{\lambda}_d \le 0.65 \\ 1.47 - 0.723\bar{\lambda}_d, & 0.65 < \bar{\lambda}_d < 1.38 \\ 0.66/\bar{\lambda}_d\,, & \bar{\lambda}_d \ge 1.38 \end{cases}$	χ_d = 0.7027
Reduced thickness:		t_{red} = 1.054 mm
Reduced effective cross-sectional area of the edge stiffener:		$A_{s,red}$ = 51.387 mm
Reduced compression stress:	$\sigma_{com,Ed} = \chi_d \cdot f_{yb}/\gamma_{M0}$	$\sigma_{com,Ed}$ = 196.74 MPa

Iteration to calculate the reduced effective area of the edge stiffener:

Parameter		Unit	Initial calculation	1st Iteration	2nd Iteration	4th Iteration
Edge Stiffener	$\chi_{d,n-1}$	- - -	1.000	0.7027	0.6816	0.6800
Flange	$\bar{\lambda}_p$	- - -	0.985	0.985	0.985	0.985
	$\sigma_{com,Ed}$	N/mm^2	280.00	196.74	190.86	190.39
	$\bar{\lambda}_{p,red}$	- - -	0.985	0.826	0.813	0.812
	ρ	- - -	0.788	0.963	.977	0.978
	b_{1,eff_2}	mm	30.311	37.017	37.571	37.615
Lip	$\bar{\lambda}_p$	- - -	0.668	0.668	0.668	0.668
	$\sigma_{com,Ed}$	N/mm^2	280.00	196.74	190.86	190.39
	$\bar{\lambda}_{p,red}$	- - -	0.668	0.560	0.552	0.551
	ρ	- - -	1.000	1.000	1.000	1.000
	$c_{1,eff}$	mm	18.455	18.445	18.445	18.445
Edge Stiffener	A_s	mm^2	73.133	83.192	84.023	84.089
	b_1	mm	68.577	65.609	65.360	65.340
	I_s	mm^4	2522	2652	2661	2662
	K	N/mm^2	0.1560	0.1723	0.1738	0.1739
	$\sigma_{cr,s}$	N/mm^2	248.57	235.49	234.58	234.50
	$\chi_{d,n}$		0.7027	0.6816	0.6801	0.6800
	$A_{s,red}$	mm^2	51.387	56.707	57.143	57.178

Initial effective sectional properties:

Cross-sectional area:	$A = 540.98$ mm^2
Gravity centre co-ordinate with respect to x-axis:	$X_{GC} = 20.630$ mm
Gravity centre co-ordinate with respect to y-axis:	$Y_{GC} = 92.010$ mm
Distance in x-direction from gravity centre to effective gravity centre	$\Delta X_{GC} = 2.681$ mm
Distance in y-direction from gravity centre to effective gravity centre	$\Delta Y_{GC} = 7.240$ mm
Second moment of area with respect to u-axis:	$I_u = 3258962$ mm^4
Second moment of area with respect to v-axis:	$I_v = 443367$ mm^4
Product moment of area with respect to u- and v-axis:	$I_{uv} = -134250$ mm^4
Angle between u-axis and u'-axis (principal axis):	$\beta = 2.724$º
Second moment of area with respect to u'-axis:	$I_{u'} = 3265348$ mm^4
Second moment of area with respect to v'-axis:	$I_{v'} = 436981$ mm^4
Maximum co-ordinate with respect to u'-axis:	$u'_{max} = 62.888$ mm
Minimum co-ordinate with respect to u'-axis:	$u'_{min} = -26.378$ mm
Maximum co-ordinate with respect to v'-axis:	$v'_{max} = 109.590$ mm
Minimum co-ordinate with respect to v'-axis:	$v'_{min} = -93.598$ mm

Web – internal compression element:

Maximum stress in the plate (compression positive):	$\sigma_{max} = f_{yb}\frac{v'_i}{max(\lvert v'_{max}\rvert, \lvert v'_{min}\rvert)}$	σ_{max} = 267.2 N/mm^2
Minimum stress in the plate (compression positive):	$\sigma_{min} = f_{yb}\frac{v'_j}{max(\lvert v'_{max}\rvert, \lvert v'_{min}\rvert)}$	σ_{min} = -235.3 N/mm^2
Stress ratio in the plate:	$\psi = \sigma_{min} / \sigma_{max}$	ψ = -0.88
Plate local buckling factor (Table 4.1 of EN 1993-1-5, 2006):		k_σ = 20.930
Plate slenderness (clause 4.4 of EN 1993-1-5, 2006):	$\bar{\lambda}_p = \frac{h_p/t}{28.4\,\varepsilon\sqrt{k_\sigma}}$	$\bar{\lambda}_p$ = 1.103 > 0.673
Maximum design compressive stress in the plate:		$\sigma_{com,Ed}$ = 267 N/mm^2
Reduced plate slenderness (clause 4.4 of EN 1993-1-5, 2006):	$\bar{\lambda}_{p,red} = \bar{\lambda}_p\sqrt{\frac{\sigma_{com,Ed}}{f_{yb}/\gamma_{M0}}}$	$\bar{\lambda}_{p,red}$ = 1.077
Reduction factor (annex E of EN 1993-1-5, 2006):	$\rho = \frac{1-0.055(3+\psi)/\bar{\lambda}_{p,red}}{\bar{\lambda}_{p,red}} + 0.18\frac{(\bar{\lambda}_p - \bar{\lambda}_{p,red})}{(\bar{\lambda}_p - 0.6)}$	ρ = 0.837
Effective flange width (Table 4.1 of EN 1993-1-5, 2006):	$h_{eff} = \rho\,.\,h_p$	h_{eff_1} = 18.640 mm h_{eff_2} = 120.15 mm

2nd and 3rd Iterations:

Plate	Parameter	Unit	2nd Iteration	3rd Iteration
Flange	σ_{max}	N/mm^2	278.67	278.39
	σ_{min}	N/mm^2	277.94	278.13
	ψ	- - -	0.997	0.999
	k_σ	- - -	4.006	4.002
	$\bar{\lambda}_p$	- - -	0.984	0.985
	$\sigma_{com,Ed}$	N/mm^2	280	280
	$\bar{\lambda}_{p,red}$	- - -	0.984	0.985
	ρ	- - -	0.789	0.789
	b_{1,eff_1}	mm	30.311	30.311
Edge Stiffener (4th Iteration)	$\chi_{d,n}$		0.6800	0.6800
	$A_{s,red}$	mm^2	57.178	57.178
	b_{1,eff_2}	mm	37.615	37.615
	$c_{1,eff}$	mm	18.445	18.445
	t_{red}	mm	1.020	1.020
Web	σ_{max}	N/mm^2	276.03	276.24
	σ_{min}	N/mm^2	-189.58	-187.18
	ψ	- - -	-0.687	-0.678
	k_σ	- - -	16.744	16.562
	$\bar{\lambda}_p$	- - -	1.233	1.240
	$\sigma_{com,Ed}$	N/mm^2	276.03	276.24
	$\bar{\lambda}_{p,red}$	- - -	1.224	1.231
	ρ	- - -	0.734	0.730
	h_{eff_1}	mm	20.330	20.436
	h_{eff_2}	mm	110.66	110.18

Final effective sectional properties:

Effective cross-sectional area:	$A_{eff} = 441.57$ mm^2
Effective gravity centre co-ordinate with respect to x-axis:	$X_{eff,GC} = 25.274$ mm
Effective gravity centre co-ordinate with respect to y-axis:	$Y_{eff,GC} = 80.279$ mm
Distance in x-direction from gravity centre to effective gravity centre	$\Delta X_{GC} = 1.963$ mm
Distance in y-direction from gravity centre to effective gravity centre	$\Delta Y_{GC} = 18.971$ mm
Second moment of effective area with respect to u-axis:	$I_{eff,u} = 2891862$ mm^4
Second moment of effective area with respect to v-axis:	$I_{eff,v} = 391518$ mm^4
Product moment of effective area with respect to u- and v-axis:	$I_{eff,uv} = -3326$ mm^4
Angle between x-axis and u'-axis (principal axis):	$\beta = 0.076º$
Second moment of effective area with respect to u'-axis:	$I_{eff,u'} = 2891866$ mm^4
Second moment of effective area with respect to v'-axis:	$I_{eff,v'} = 391513$ mm^4
Maximum co-ordinate with respect to u'-axis:	$u'_{max} = 54.081$ mm
Minimum co-ordinate with respect to u'-axis:	$u'_{min} = -26.180$ mm
Maximum co-ordinate with respect to v'-axis:	$v'_{max} = 118.978$ mm
Minimum co-ordinate with respect to v'-axis:	$v'_{min} = -81.062$ mm

- **Design buckling resistance moment:**

Effective length factor:		$k_v = 1.0$
Warping effective length factor:		$k_w = 1.0$
Buckling factor:		$C_b = 1.0$
Critical elastic moment for lateral-torsional buckling:	$M_{cr} = C_b \sqrt{\frac{\pi^2 E I_v}{(k_v L)^2}\left[G I_T + \frac{\pi^2 E I_W}{(k_W L)^2}\right]}$	$M_{cr} = 6.02$ kN.m
Effective section modulus:	$W_{eff,u'} = \frac{I_{eff,u'}}{v'_{max}}$	$W_{eff,u'} = 24306$ mm^3
Non-dimensional slenderness for lateral-torsional buckling (clause 6.3.2.2 of EN 1993-1-1, 2004):	$\bar{\lambda}_{LT} = \sqrt{\frac{W_{eff,u'} f_{yb}}{M_{cr}}}$	$\bar{\lambda}_{LT} = 1.06$
Imperfection factor (Clause 6.2.4 of EN 1993-1-3, 2004):		$\alpha_{LT} = 0.21$
Capacity reduction factor (clause 6.3.2.2 of EN 1993-1-1, 2004):	$\Phi_{LT} = 0.5\left[1 + \alpha_{LT}\left(\bar{\lambda}_{LT} - 0.2\right) + \bar{\lambda}_{LT}^2\right]$	$\Phi_{LT} = 1.16$
Reduction factor for lateral-torsional buckling (clause 6.3.2.2 of EN 1993-1-1, 2004):	$\chi_{LT} = \frac{1}{\Phi_{LT} + \sqrt{\Phi_{LT}^2 - \bar{\lambda}_{LT}^2}}$	$\chi_{LT} = 0.62$
Design value of the buckling resistance moment:	$M_{b,Rd} = \chi_{LT} \cdot W_{eff,u'} \cdot \frac{f_{yb}}{\gamma_{M1}}$	$\boldsymbol{M_{b,Rd} = 4.23}$ **kN.m**

C3 Cold-formed steel lipped I_4000_200_160_20_1.5 beam

This example shows how was determined the design buckling resistance moment $M_{b,Rd}$ of a lipped I-shaped section using EN 1993-1-1 (2004), EN 1993-1-3 (2004) and EN 1993-1-5 (2006).

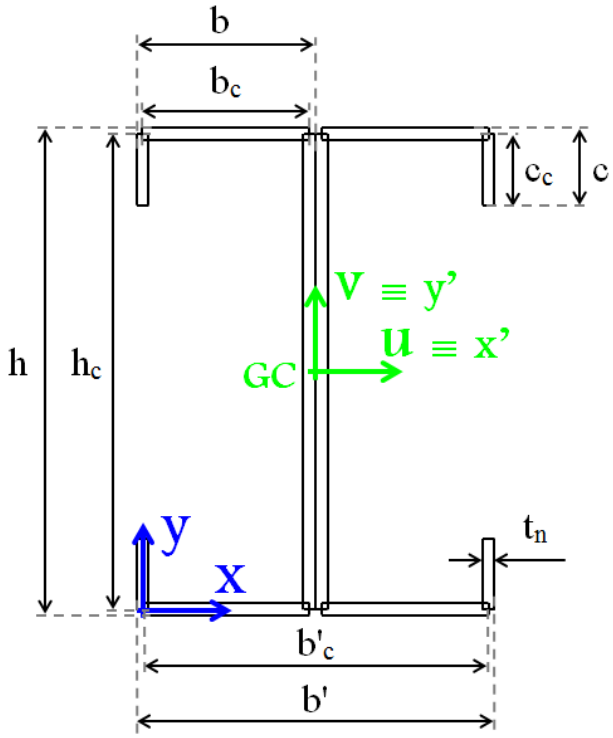

Figure C.8 – Scheme of a lipped I-shaped idealized gross cross-section

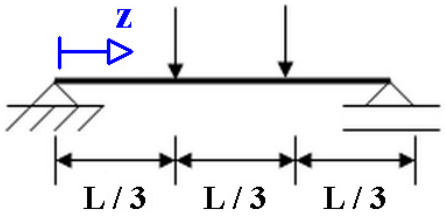

Figure C.9 – Loading system

- **<u>Boundary conditions at beam supports:</u>**
  - no rotation about the longitudinal z-z axis;
  - no displacements in the plane;
  - no warping restraint.

- **<u>Cross-sectional dimensions:</u>**

Height of the section (overall dimension): $h = 200$ mm

Width of the flange (overall dimension): $b = 80$ mm

		b' = 160 mm
Width of the edge stiffener (overall dimension):		c = 20 mm
Nominal material thickness:		t_n = 1.5 mm
Material core thickness (clause 3.2.4 of EN 1993-1-3, 2004):	$t_{cor} = t_n - t_{zinc}$ t_{zinc} = 0.04 (Z275)	$t_{cor} = t$ = 1.46 mm
Height of the section (centreline dimension):		h_c = 198.50 mm
Width of the flange (centreline dimension):		b_c = 78.50 mm b_c' = 158.50 mm
Width of the edge stiffener (centreline dimension):		c_c = 19.25 mm
Beam span		L = 4000 mm

- **Material properties:**

Modulus of elasticity:		E = 210000 N/mm^2
Poisson ratio:		ν = 0.3
Shear modulus:	$G = E\,[2\,(1 + \nu)]^{-1}$	G = 80769 N/mm^2
Nominal yield strength (S280GD + Z275):		f_{yb} = 280 N/mm^2
Partial factor for resistance of cross-sections (clause 2 of EN 1993-1-3, 2004):		γ_{M0} = 1.00
Partial factor for resistance of members (clause 2 of EN 1993-1-3, 2004):		γ_{M1} = 1.00
Elastic strain:	$\varepsilon = (235 / f_{yb})^{1/2}$	ε = 0.9161

- **Gross cross sectional properties:**

Cross-sectional area:		$A = 1155.21$ mm^2
First moment of area with respect to x-axis:		$S_x = 114678$ mm^3
First moment of area with respect to y-axis:		$S_y = 91574$ mm^3
Gravity centre co-ordinate with respect to x-axis:	$X_{GC} = S_y / A$	$X_{GC} = 79.270$ mm
Gravity centre co-ordinate with respect to y-axis:	$Y_{GC} = S_x / A$	$Y_{GC} = 99.270$ mm
Second moment of area with respect to x-axis:		$I_x = 18751109$ mm^4
Second moment of area with respect to y-axis:		$I_y = 8949852$ mm^4
Product moment of area with respect to x- and y-axis:		$I_{xy} = 9090504$ mm^4
Second moment of area with respect to x'-axis:	$I_{x'} = I_x - A.Y_{CG}^2$	$I_{x'} = 7367030$ mm^4
Second moment of area with respect to y'-axis:	$I_{y'} = I_y - A.X_{CG}^2$	$I_{y'} = 1690403$ mm^4
Product moment of area with respect to x'- and y'-axis:	$I_{xy'} = I_{xy} - (S_x \, . \, S_y)/A$	$I_{xy'} = 0$
Angle between x'-axis and u-axis (principal axis):		$\beta = 0$
Second moment of area with respect to u-axis:	$I_u = 0.5[I_{x'} + I_{y'} + \sqrt{((I_{y'} - I_{x'})^2 + 4I_{xy'}^2)}]$	$I_u = 7367030$ mm^4
Second moment of area with respect to v-axis:	$I_v = 0.5[I_{x'} + I_{y'} - \sqrt{((I_{y'} - I_{x'})^2 + 4I_{xy'}^2)}]$	$I_v = 1690403$ mm^4
Radius of gyration with respect to u-axis:	$i_u = \sqrt{(I_u / A)}$	$i_u = 79.86$ mm

Radius of gyration with respect to v-axis:	$i_v = \sqrt{(I_v / A)}$	$i_v = 38.25$ mm
Shear centre co-ordinate with respect to u-axis:		$U_{SC} = 0$ mm
Shear centre co-ordinate with respect to v-axis:		$V_{SC} = 0$
Polar radius of gyration about shear centre:	$i_0 = \sqrt{(i_u^2 + i_v^2 + U_{SC}^2 + V_{SC}^2)}$	$i_0 = 88.55$ mm
Torsional constant:		$I_T = 1744.23$ mm^4
Warping constant:		$I_W = 18567895467$ mm^6
Maximum co-ordinate with respect to u-axis:		$u_{max} = 80.000$ mm
Minimum co-ordinate with respect to u-axis:		$u_{min} = -80.000$ mm
Maximum co-ordinate with respect to v-axis:		$v_{max} = 100.00$ mm
Minimum co-ordinate with respect to v-axis:		$v_{min} = -100.00$ mm

➢ **Effective cross sectional properties:**

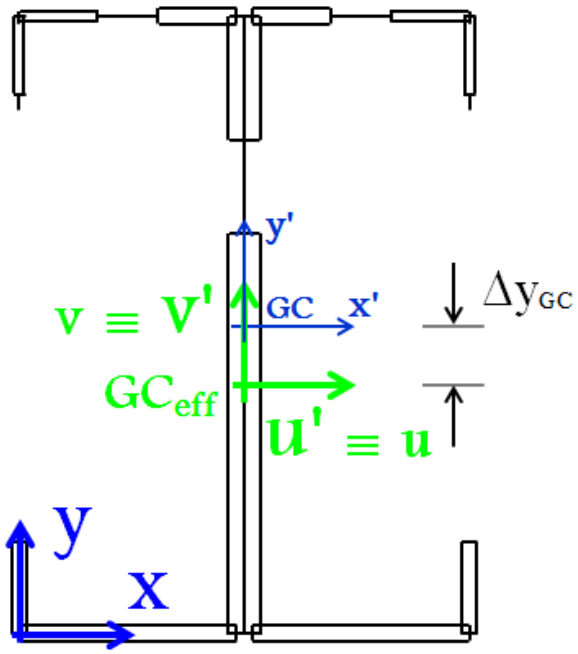

Figure C.10 – Scheme of a lipped I-shaped idealized effective cross-section

Considering the individual contribution of each profile, in other words, the effective geometrical properties of each C section as calculated above, the final effective geometrical properties of the lipped-I section are as follows:

Effective cross-sectional area:	$A_{eff} = 883.16$ mm^2
Effective gravity centre co-ordinate with respect to x-axis:	$X_{eff,GC} = 79.270$ mm
Effective gravity centre co-ordinate with respect to y-axis:	$Y_{eff,GC} = 80.279$ mm
Distance in x-direction from gravity centre to effective gravity centre	$\Delta X_{GC} = 0$ mm
Distance in y-direction from gravity centre to effective gravity centre	$\Delta Y_{GC} = 18.991$ mm
Second moment of effective area with respect to u-axis:	$I_{eff,u} = 5783779$ mm^4
Second moment of effective area with respect to v-axis:	$I_{eff,v} = 1380886$ mm^4
Product moment of effective area with respect to u- and v-axis:	$I_{eff,uv} = 0$ mm^4

Angle between u-axis and u'-axis (principal axis): $\beta = 0º$

Second moment of effective area with respect to u'-axis: $I_{eff,u'} = 5783779$ mm^4

Second moment of effective area with respect to v'-axis: $I_{eff,v'} = 1380886$ mm^4

Maximum co-ordinate with respect to u'-axis: $u'_{max} = 80.000$ mm

Minimum co-ordinate with respect to u'-axis: $u'_{min} = -80.000$ mm

Maximum co-ordinate with respect to v'-axis: $v'_{max} = 118.971$ mm

Minimum co-ordinate with respect to v'-axis: $v'_{min} = -81.029$ mm

- **Design buckling resistance moment:**

Effective length factor: $k_v = 1.0$

Warping effective length factor: $k_w = 1.0$

Buckling factor: $C_b = 1.0$

Critical elastic moment for lateral-torsional buckling:

$$M_{cr} = C_b \sqrt{\frac{\pi^2 E I_v}{(k_v L)^2}\left[G I_T + \frac{\pi^2 E I_W}{(k_W L)^2}\right]}$$

$M_{cr} = 23.61$ kN.m

Effective section modulus:

$$W_{eff,u'} = \frac{I_{eff,u'}}{v'_{max}}$$

$W_{eff,u'} = 48615$ mm^3

Non-dimensional slenderness for lateral-torsional buckling (clause 6.3.2.2 of EN 1993-1-1, 2004):

$$\bar{\lambda}_{LT} = \sqrt{\frac{W_{eff,u'} f_{yb}}{M_{cr}}}$$

$\bar{\lambda}_{LT} = 0.76$

Imperfection factor (Clause 6.3.2 of EN 1993-1-1, 2004): $\alpha_{LT} = 0.76$

Capacity reduction factor (clause 6.3.2.2 of EN 1993-1-1, 2004):

$$\Phi_{LT} = 0.5\left[1 + \alpha_{LT}\left(\bar{\lambda}_{LT} - 0.2\right) + \bar{\lambda}_{LT}^2\right]$$

$\Phi_{LT} = 1.00$

Reduction factor for lateral-torsional buckling (clause 6.3.2.2 of EN 1993-1-1, 2004):

$$\chi_{LT} = \frac{1}{\Phi_{LT} + \sqrt{\Phi_{LT}^2 - \bar{\lambda}_{LT}^2}}$$

$\chi_{LT} = 0.61$

Design value of the buckling resistance moment:

$$M_{b,Rd} = \chi_{LT} \cdot W_{eff,u'} \cdot \frac{f_{yb}}{\gamma_{M1}}$$

$\boldsymbol{M_{b,Rd} = 8.24}$ **kN.m**

C4 Cold-formed steel R_4000_203_81.5_20_1.5 beam

This example shows how was determined the design buckling resistance moment $M_{b,Rd}$ of a R-shaped section using EN 1993-1-1 (2004), EN 1993-1-3 (2004) and EN 1993-1-5 (2006).

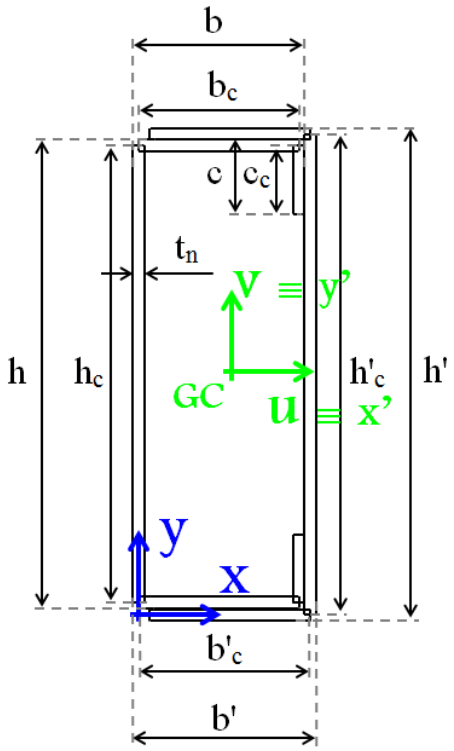

Figure C.11 – Scheme of a R-shaped idealized gross cross-section

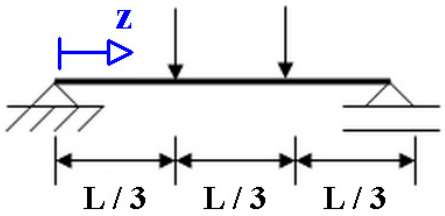

Figure C.12 – Loading system

- **<u>Boundary conditions at beam supports:</u>**
  - no rotation about the longitudinal *z*-*z* axis;
  - no displacements in the plane;
  - no warping restraint.

- **<u>Cross-sectional dimensions:</u>**

Height of the section (overall dimension): $h = 200$ mm

$h' = 203$ mm

Width of the flange (overall dimension): $b = 80$ mm

$b' = 81.5$ mm

Width of the edge stiffener (overall dimension):		c = 20 mm
Nominal material thickness:		t_n = 1.5 mm
Material core thickness (clause 3.2.4 of EN 1993-1-3, 2004):	$t_{cor} = t_n - t_{zinc}$ t_{zinc} = 0.04 (Z275)	$t_{cor} = t$ = 1.46 mm
Height of the section (centreline dimension):		h_c = 198.50 mm h_c' = 201.50 mm
Width of the flange (centreline dimension):		b_c = 78.50 mm b_c' = 80 mm
Width of the edge stiffener (centreline dimension):		c_c = 19.25 mm
Beam span		L = 4000 mm

- **Material properties:**

Modulus of elasticity:		E = 210000 N/mm^2
Poisson ratio:		ν = 0.3
Shear modulus:	$G = E\,[2\,(1 + \nu)]^{-1}$	G = 80769 N/mm^2
Nominal yield strength (S280GD + Z275):		f_{yb} = 280 N/mm^2
Partial factor for resistance of cross-sections (clause 2 of EN 1993-1-3, 2004):		γ_{M0} = 1.00
Partial factor for resistance of members (clause 2 of EN 1993-1-3, 2004):		γ_{M1} = 1.00
Elastic strain:	$\varepsilon = (235 / f_{yb})^{1/2}$	ε = 0.9161

- **Gross cross sectional properties:**

Considering the steel profiles connected to each other by screws at discrete sections, the geometrical properties of the R section were calculated as if it was an open section, as follows:

Cross-sectional area:		$A = 1105.22$ mm^2
First moment of area with respect to x-axis:		$S_x = 111351$ mm^3
First moment of area with respect to y-axis:		$S_y = 46370$ mm^3
Gravity centre co-ordinate with respect to x-axis:	$X_{GC} = S_y / A$	$X_{GC} = 41.955$ mm
Gravity centre co-ordinate with respect to y-axis:	$Y_{GC} = S_x / A$	$Y_{GC} = 100.750$ mm
Second moment of area with respect to x-axis:		$I_x = 18284029$ mm^4
Second moment of area with respect to y-axis:		$I_y = 3211392$ mm^4
Product moment of area with respect to x- and y-axis:		$I_{xy} = 4671737$ mm^4
Second moment of area with respect to x'-axis:	$I_{x'} = I_x - A.Y_{CG}^2$	$I_{x'} = 7065424$ mm^4
Second moment of area with respect to y'-axis:	$I_{y'} = I_y - A.X_{CG}^2$	$I_{y'} = 1265952$ mm^4
Product moment of area with respect to x'- and y'-axis:	$I_{xy'} = I_{xy} - (S_x \,.\, S_y)/A$	$I_{xy'} = 0$
Angle between x'-axis and u-axis (principal axis):		$\beta = 0$
Second moment of area with respect to u-axis:	$I_u = 0.5[I_{x'} + I_{y'} + \sqrt{((I_{y'} - I_{x'})^2 + 4I_{xy'}^2)}]$	$I_u = 7065424$ mm^4
Second moment of area with	$I_v = 0.5[I_{x'} + I_{y'} - \sqrt{((I_{y'} -$	

respect to v-axis:	$I_{x'})^2 + 4I_{xy'}^2)]$	$I_v = 1265952$ mm^4
Radius of gyration with respect to u-axis:	$i_u = \sqrt{(I_u / A)}$	$i_u = 79.95$ mm
Radius of gyration with respect to v-axis:	$i_v = \sqrt{(I_v / A)}$	$i_v = 33.84$ mm
Shear centre co-ordinate with respect to u-axis:		$U_{SC} = -96.496$ mm
Shear centre co-ordinate with respect to v-axis:		$V_{SC} = 0$
Polar radius of gyration about shear centre:	$i_0 = \sqrt{(i_u^2 + i_v^2 + U_{SC}^2 + V_{SC}^2)}$	$i_0 = 129.81$ mm
Torsional constant:		$I_T = 2011.48$ mm^4
Warping constant:		$I_W = 366920006434$ mm^6
Maximum co-ordinate with respect to u-axis:		$u_{max} = 39.505$ mm
Minimum co-ordinate with respect to u-axis:		$u_{min} = -42.685$ mm
Maximum co-ordinate with respect to v-axis:		$v_{max} = 101.46$ mm
Minimum co-ordinate with respect to v-axis:		$v_{min} = -101.46$ mm

- **Effective cross sectional properties:**

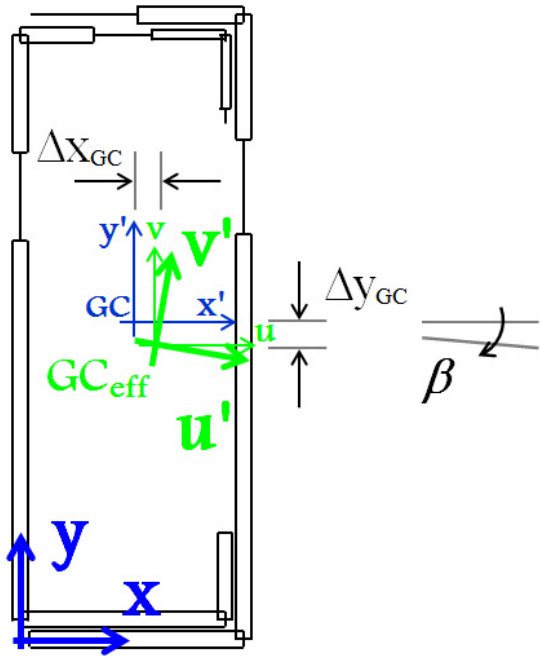

Figure C.13 – Scheme of a R-shaped idealized effective cross-section

Considering the individual contribution of each profile, in other words, the effective geometrical properties of each section (U and C) as calculated above, the final effective geometrical properties of the R section are as follows:

Effective cross-sectional area:	$A_{eff} = 782.25$ mm^2
Effective gravity centre co-ordinate with respect to x-axis:	$X_{eff,GC} = 42.493$ mm
Effective gravity centre co-ordinate with respect to y-axis:	$Y_{eff,GC} = 73.974$ mm
Distance in x-direction from gravity centre to effective gravity centre	$\Delta X_{GC} = 0.538$ mm
Distance in y-direction from gravity centre to effective gravity centre	$\Delta Y_{GC} = 26.776$ mm
Second moment of effective area with respect to u-axis:	$I_{eff,u} = 4828269$ mm^4
Second moment of effective area with respect to v-axis:	$I_{eff,v} = 870186$ mm^4
Product moment of effective area with respect to u- and v-axis:	$I_{eff,uv} = 97339$ mm^4

Angle between x-axis and u'-axis (principal axis): $\beta = 1.408º$

Second moment of effective area with respect to u'-axis: $I_{eff,u'} = 4830599$ mm^4

Second moment of effective area with respect to v'-axis: $I_{eff,v'} = 867715$ mm^4

Maximum co-ordinate with respect to v'-axis: $v'_{max} = 128.39$ mm

Minimum co-ordinate with respect to v'-axis: $v'_{min} = -74.977$ mm

- **<u>Design buckling resistance moment:</u>**

Effective length factor: $k_v = 1.0$

Warping effective length factor: $k_w = 1.0$

Buckling factor: $C_b = 1.0$

Critical elastic moment for lateral-torsional buckling:

$$M_{cr} = C_b \sqrt{\frac{\pi^2 E I_v}{(k_v L)^2}\left[G I_T + \frac{\pi^2 E I_W}{(k_W L)^2}\right]}$$

$M_{cr} = 28.39$ kN.m

Effective section modulus:

$$W_{eff,u'} = \frac{I_{eff,u'}}{v'_{max}}$$

$W_{eff,u'} = 37625$ mm^3

Non-dimensional slenderness for lateral-torsional buckling (clause 6.3.2.2 of EN 1993-1-1, 2004):

$$\bar{\lambda}_{LT} = \sqrt{\frac{W_{eff,u'} f_{yb}}{M_{cr}}}$$

$\bar{\lambda}_{LT} = 0.61$

Imperfection factor (Clause 6.3.2 of EN 1993-1-1, 2004): $\alpha_{LT} = 0.76$

Capacity reduction factor (clause 6.3.2.2 of EN 1993-1-1, 2004):

$$\Phi_{LT} = 0.5\left[1 + \alpha_{LT}\left(\bar{\lambda}_{LT} - 0.2\right) + \bar{\lambda}_{LT}^2\right]$$

$\Phi_{LT} = 0.84$

Reduction factor for lateral-torsional buckling (clause 6.3.2.2 of EN 1993-1-1, 2004):

$$\chi_{LT} = \frac{1}{\Phi_{LT} + \sqrt{\Phi_{LT}^2 - \bar{\lambda}_{LT}^2}}$$

$\chi_{LT} = 0.70$

Design value of the resistant buckling moment:

$$M_{b,Rd} = \chi_{LT} \cdot W_{eff,u'} \cdot \frac{f_{yb}}{\gamma_{M1}}$$

$\boldsymbol{M_{b,Rd} = 7.41}$ **kN.m**

C5 Cold-formed steel 2R_4000_203_163_20_1.5 beam

This example shows how was determined the design buckling resistance moment $M_{b,Rd}$ of a 2R-shaped section using EN 1993-1-1 (2004), EN 1993-1-3 (2004) and EN 1993-1-5 (2006).

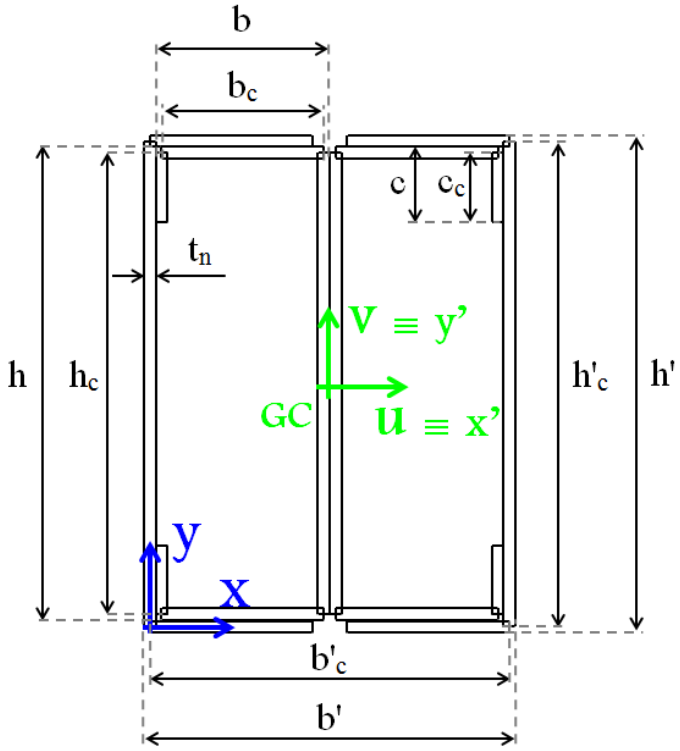

Figure C.14 – Scheme of a 2R-shaped idealized gross cross-section

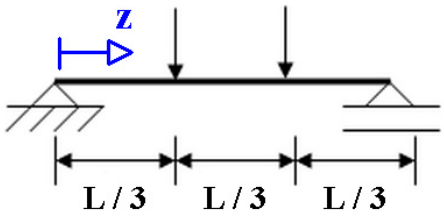

Figure C.15 – Loading system

- **Boundary conditions at beam supports:**
  - no rotation about the longitudinal *z*-*z* axis;
  - no displacements in the plane;
  - no warping restraint.

- **Cross-sectional dimensions:**

Height of the section (overall dimension): $h = 200$ mm

$h' = 203$ mm

Width of the flange (overall dimension): $b = 80$ mm

$b' = 163$ mm

Width of the edge stiffener (overall dimension):		c = 20 mm
Nominal material thickness:		t_n = 1.5 mm
Material core thickness (clause 3.2.4 of EN 1993-1-3, 2004):	$t_{cor} = t_n - t_{zinc}$ t_{zinc} = 0.04 (Z275)	$t_{cor} = t$ = 1.46 mm
Height of the section (centreline dimension):		h_c = 198.50 mm h_c' = 201.50 mm
Width of the flange (centreline dimension):		b_c = 78.50 mm b_c' = 161.5 mm
Width of the edge stiffener (centreline dimension):		c_c = 19.25 mm
Beam span		L = 4000 mm

- **Material properties:**

Modulus of elasticity:		E = 210000 N/mm^2
Poisson ratio:		ν = 0.3
Shear modulus:	$G = E\,[2\,(1 + \nu)]^{-1}$	G = 80769 N/mm^2
Nominal yield strength (S280GD + Z275):		f_{yb} = 280 N/mm^2
Partial factor for resistance of cross-sections (clause 2 of EN 1993-1-3, 2004):		γ_{M0} = 1.00
Partial factor for resistance of members (clause 2 of EN 1993-1-3, 2004):		γ_{M1} = 1.00
Elastic strain:	$\varepsilon = (235 / f_{yb})^{1/2}$	ε = 0.9161

- **Gross cross sectional properties:**

Considering the steel profiles connected to each other by screws at discrete sections, the geometrical properties of the R section were calculated as if it was an open section, as follows:

Cross-sectional area:		$A = 2217.07$ mm^2
First moment of area with respect to x-axis:		$S_x = 223325$ mm^3
First moment of area with respect to y-axis:		$S_y = 178984$ mm^3
Gravity centre co-ordinate with respect to x-axis:	$X_{GC} = S_y / A$	$X_{GC} = 80.730$ mm
Gravity centre co-ordinate with respect to y-axis:	$Y_{GC} = S_x / A$	$Y_{GC} = 100.730$ mm
Second moment of area with respect to x-axis:		$I_x = 36644083$ mm^4
Second moment of area with respect to y-axis:		$I_y = 20999862$ mm^4
Product moment of area with respect to x- and y-axis:		$I_{xy} = 18029051$ mm^4
Second moment of area with respect to x'-axis:	$I_{x'} = I_x - A.Y_{CG}^2$	$I_{x'} = 14148358$ mm^4
Second moment of area with respect to y'-axis:	$I_{y'} = I_y - A.X_{CG}^2$	$I_{y'} = 6550017$ mm^4
Product moment of area with respect to x'- and y'-axis:	$I_{xy'} = I_{xy} - (S_x \,.\, S_y)/A$	$I_{xy'} = 0$
Angle between x'-axis and u-axis (principal axis):		$\beta = 0$
Second moment of area with respect to u-axis:	$I_u = 0.5[I_{x'} + I_{y'} + \sqrt{((I_{y'} - I_{x'})^2 + 4I_{xy'}^2)}]$	$I_u = 14148358$ mm^4
Second moment of area with	$I_v = 0.5[I_{x'} + I_{y'} - \sqrt{((I_{y'} -$	

respect to v-axis:	$I_{x'})^2 + 4I_{xy'}^2)]$	$I_v = 6550017$ mm^4
Radius of gyration with respect to u-axis:	$i_u = \sqrt{(I_u / A)}$	$i_u = 79.88$ mm
Radius of gyration with respect to v-axis:	$i_v = \sqrt{(I_v / A)}$	$i_v = 54.35$ mm
Shear centre co-ordinate with respect to u-axis:		$U_{SC} = 0$
Shear centre co-ordinate with respect to v-axis:		$V_{SC} = 0$
Polar radius of gyration about shear centre:	$i_0 = \sqrt{(i_u^2 + i_v^2 + U_{SC}^2 + V_{SC}^2)}$	$i_0 = 96.62$ mm
Torsional constant:		$I_T = 2556.42$ mm^4
Warping constant:		$I_W = 1.22864 \times 10^{11}$ mm^6
Maximum co-ordinate with respect to u-axis:		$u_{max} = 81.460$ mm
Minimum co-ordinate with respect to u-axis:		$u_{min} = -81.460$ mm
Maximum co-ordinate with respect to v-axis:		$v_{max} = 101.46$ mm
Minimum co-ordinate with respect to v-axis:		$v_{min} = -101.46$ mm

- **Effective cross sectional properties:**

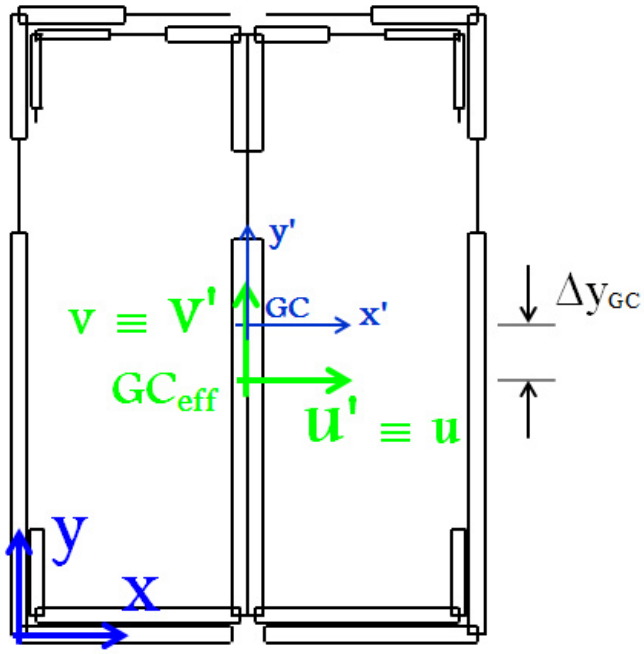

Figure C.16 – Scheme of a 2R-shaped idealized effective cross-section

Considering the individual contribution of each profile, in other words, the effective geometrical properties of each section (U and C) as calculated above, the final effective geometrical properties of the R section are as follows:

Effective cross-sectional area:	$A_{eff} = 1564.52$ mm^2
Effective gravity centre co-ordinate with respect to x-axis:	$X_{eff,GC} = 80.730$ mm
Effective gravity centre co-ordinate with respect to y-axis:	$Y_{eff,GC} = 73.975$ mm
Distance in x-direction from gravity centre to effective gravity centre	$\Delta X_{GC} = 0$
Distance in y-direction from gravity centre to effective gravity centre	$\Delta Y_{GC} = 26.755$ mm
Second moment of effective area with respect to u-axis:	$I_{eff,u} = 9656495$ mm^4
Second moment of effective area with respect to v-axis:	$I_{eff,v} = 4665780$ mm^4
Product moment of effective area with respect to u- and v-axis:	$I_{eff,uv} = -5$ mm^4

Angle between u-axis and u'-axis (principal axis): $\beta = 0$

Second moment of effective area with respect to u'-axis: $I_{eff,u'} = 9656495$ mm^4

Second moment of effective area with respect to v'-axis: $I_{eff,v'} = 4665780$ mm^4

Maximum co-ordinate with respect to v'-axis: $v'_{max} = 127.525$ mm

Minimum co-ordinate with respect to v'-axis: $v'_{min} = -73.975$ mm

- **<u>Design buckling resistance moment:</u>**

Effective length factor: $k_v = 1.0$

Warping effective length factor: $k_w = 1.0$

Buckling factor: $C_b = 1.0$

Critical elastic moment for lateral-torsional buckling:

$$M_{cr} = C_b \sqrt{\frac{\pi^2 E I_v}{(k_v L)^2}\left[G I_T + \frac{\pi^2 E I_W}{(k_W L)^2}\right]}$$

$M_{cr} = 116.96$ kN.m

Effective section modulus:

$$W_{eff,u'} = \frac{I_{eff,u'}}{v'_{max}}$$

$W_{eff,u'} = 75722$ mm^3

Non-dimensional slenderness for lateral-torsional buckling (clause 6.3.2.2 of EN 1993-1-1, 2004):

$$\bar{\lambda}_{LT} = \sqrt{\frac{W_{eff,u'} f_{yb}}{M_{cr}}}$$

$\bar{\lambda}_{LT} = 0.43$

Imperfection factor (Clause 6.3.2 of EN 1993-1-1, 2004): $\alpha_{LT} = 0.76$

Capacity reduction factor (clause 6.3.2.2 of EN 1993-1-1, 2004):

$$\Phi_{LT} = 0.5\left[1 + \alpha_{LT}\left(\bar{\lambda}_{LT} - 0.2\right) + \bar{\lambda}_{LT}^2\right]$$

$\Phi_{LT} = 0.68$

Reduction factor for lateral-torsional buckling (clause 6.3.2.2 of EN 1993-1-1, 2004):

$$\chi_{LT} = \frac{1}{\Phi_{LT} + \sqrt{\Phi_{LT}^2 - \bar{\lambda}_{LT}^2}}$$

$\chi_{LT} = 0.83$

Design value of the buckling resistance moment:

$$M_{b,Rd} = \chi_{LT} \cdot W_{eff,u'} \cdot \frac{f_{yb}}{\gamma_{M1}}$$

$M_{b,Rd} = 17.6$ kN.m

APPENDIX D Calculation of the Flexural Strength According the DSM Established in the Appendix 1 of AISI S100 (2004)

This example shows how was determined the flexural design strength, M_d, and the flexural allowable strength, M_a, of a C-shaped section using the Direct Strength Method (DSM) established in the Appendix 1 of the AISI Specification (AISI S100-2004).

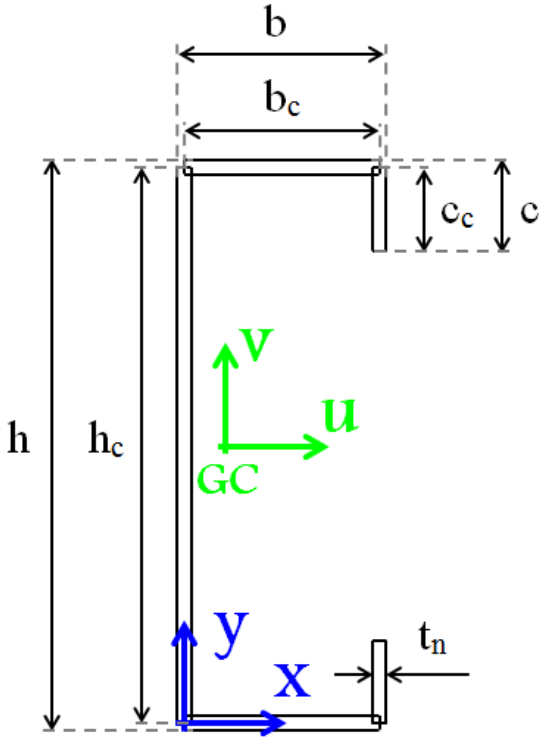

Figure D.1 – Scheme of a C-shaped idealized gross cross-section

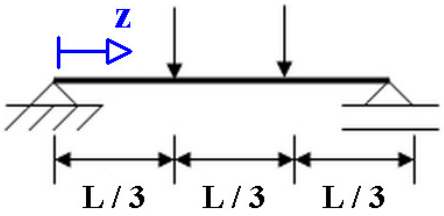

Figure D.2 – Loading system

- **<u>Boundary conditions at beam supports:</u>**
  - no rotation about the longitudinal *z*-*z* axis;
  - no displacements in the plane;
  - no warping restraint.

- **Cross-sectional dimensions:**

Height of the section (overall dimension):		h = 200 mm
Width of the flange (overall dimension):		b = 80 mm
Width of the edge stiffener (overall dimension):		c = 20 mm
Nominal material thickness:		t_n = 1.5 mm
Material core thickness (clause 3.2.4 of EN 1993-1-3, 2004):	$t_{cor} = t_n - t_{zinc}$ t_{zinc} = 0.04 (Z275)	$t_{cor} = t$ = 1.46 mm
Height of the section (centreline dimension):		h_c = 198.50 mm
Width of the flange (centreline dimension):		b_c = 78.50 mm
Width of the edge stiffener (centreline dimension):		c_c = 19.25 mm
Beam span		L = 4000 mm

- **Material properties:**

Modulus of elasticity:		E = 210000 N/mm^2
Poisson ratio:		ν = 0.3
Shear modulus:	$G = E\,[2\,(1 + \nu)]^{-1}$	G = 80769 N/mm^2
Nominal yield strength (S280GD + Z275):		f_{yb} = 280 N/mm^2
Elastic strain:	$\varepsilon = (235 / f_{yb})^{1/2}$	ε = 0.9161

➢ **Elastic buckling moments:**

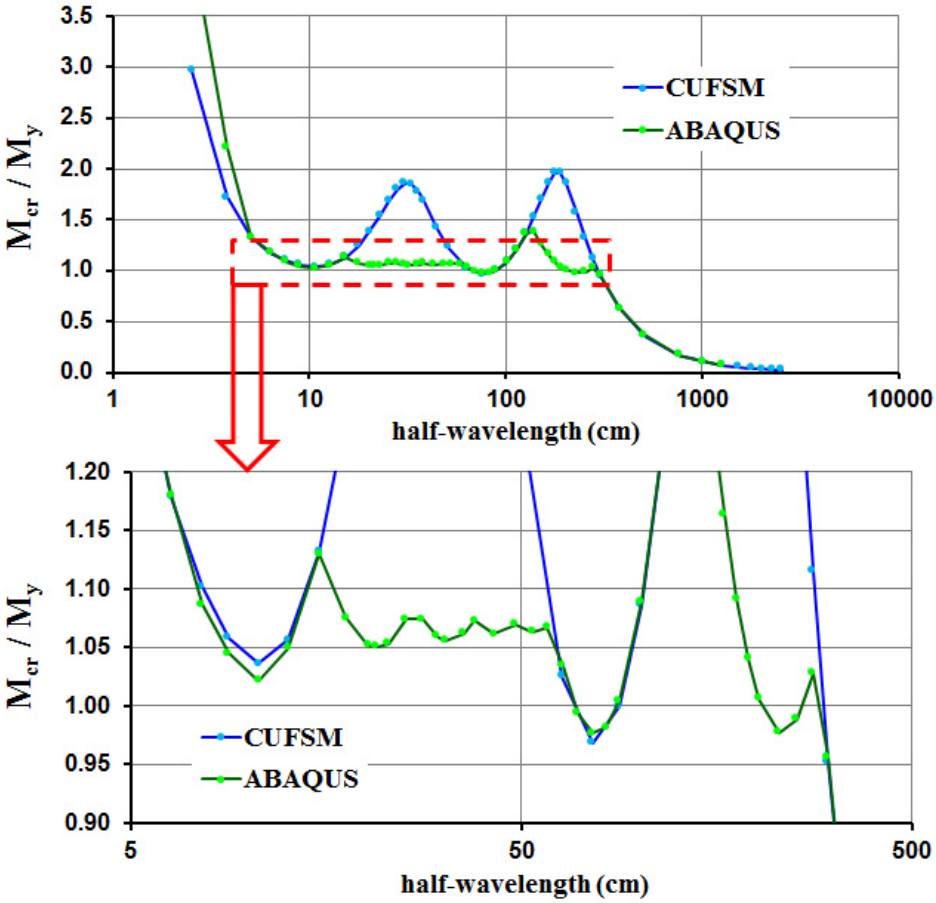

Figure D.3 – Relative buckling moment as a function of the buckling half-wavelength provided by CUFSM and ABAQUS

Second moment of area with respect to u-axis:	I_u = 3662834 mm^4
Maximum co-ordinate with respect to v-axis:	v_{max} = 99.980 mm
Section modulus of the cross-section:	W_y = 36636 mm^3
Yield moment about the strong axis:	M_y = 10.26 kN.m
Critical elastic local buckling moment:	M_{crl} = 10.633 kN.m
Critical elastic distortional buckling moment:	M_{crd} = 9.935 kN.m
Critical elastic lateral-torsional buckling moment:	M_{cre} = 5.882 kN.m

- **Nominal flexural strength:**

Nominal flexural strength for lateral-torsional buckling:

$$M_{ne} = \begin{cases} M_{cre} & \text{if } M_{cre} < 0.56M_y \\ \frac{10}{9}M_y\left(1-\left(\frac{10M_y}{36M_{cre}}\right)\right) & \text{if } 2.78M_y \geq M_{cre} \geq 0.56M_y \\ M_y & \text{if } M_{cre} > 2.78M_y \end{cases} \qquad M_{ne} = 5.88 \text{ kN.m}$$

Nominal flexural strength for local buckling:

$$M_{nl} = \begin{cases} M_{ne} & \text{if } \sqrt{M_{ne}/M_{crl}} \leq 0.776 \\ \left(1-0.15\left(\frac{M_{crl}}{M_{ne}}\right)^{0.4}\right)\left(\frac{M_{crl}}{M_{ne}}\right)^{0.4} M_{ne} & \text{if } \sqrt{M_{ne}/M_{crl}} > 0.776 \end{cases} \qquad M_{nl} = 5.88 \text{ kN.m}$$

Nominal flexural strength for distortional buckling:

$$M_{nd} = \begin{cases} M_y & \text{if } \sqrt{M_y/M_{crd}} \leq 0.673 \\ \left(1-0.22\left(\frac{M_{crd}}{M_y}\right)^{0.5}\right)\left(\frac{M_{crd}}{M_y}\right)^{0.5} M_y & \text{if } \sqrt{M_y/M_{crd}} > 0.673 \end{cases} \qquad M_{nd} = 7.91 \text{ kN.m}$$

Nominal flexural strength: $M_n = 5.88$ kN.m

- **Flexural strength:**

Flexural allowable strength (section 1.1.1.2 of the AISI S100-2004): $M_a = \frac{M_n}{\Omega}$ **M_a = 3.52 kN.m**

Flexural design strength (section 1.1.1.2 of the AISI S100-2004): $M_d = \phi \cdot M_n$ **M_d = 5.29 kN.m**

APPENDIX E Experimental Data from Tests on Cold-Formed Steel Beams under Fire Conditions

E1 Simply supported beams

E1.1 C beams

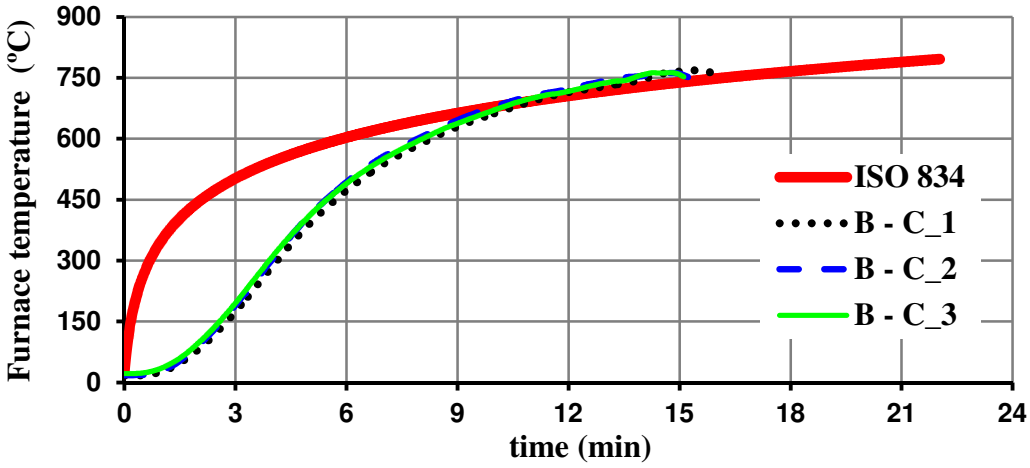

Figure E.1 – Furnace temperatures in tests on simply supported C beams

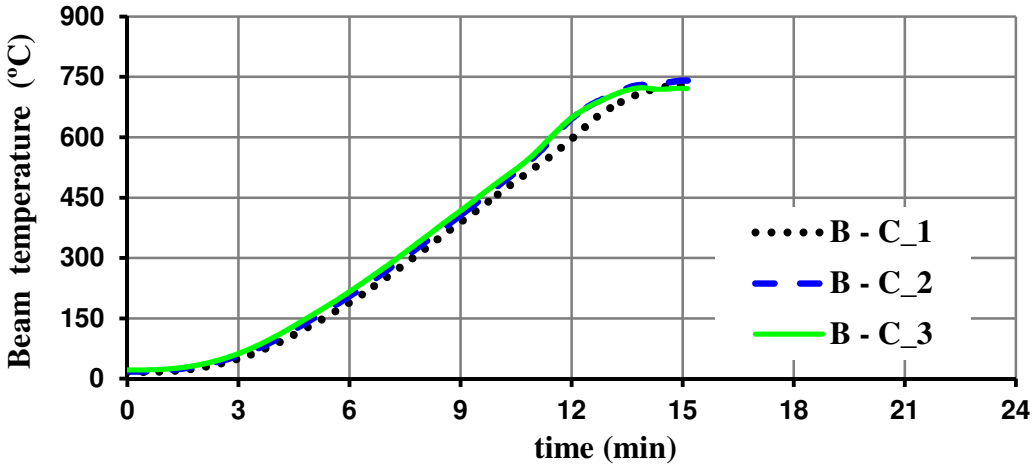

Figure E.2 – Evolution of mean temperature in simply supported C beams as a function of time

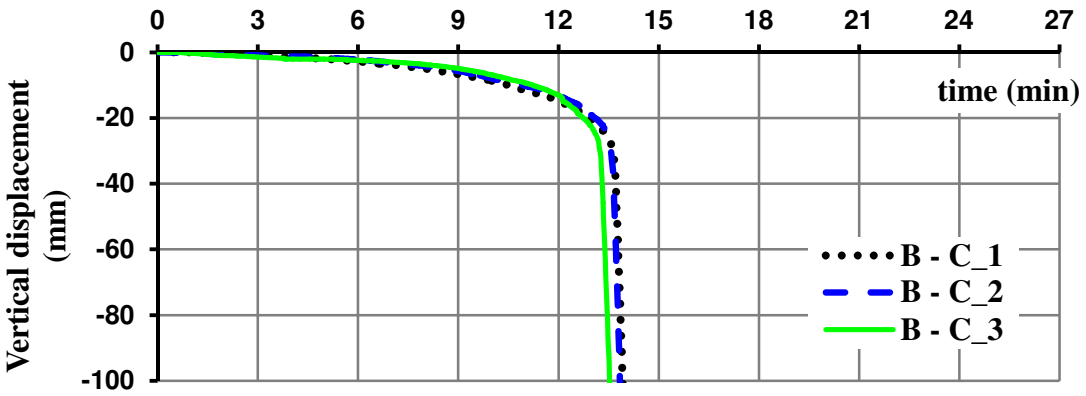

Figure E.3 – Evolution of vertical displacement at mid-span of simply supported C beams as a function of time

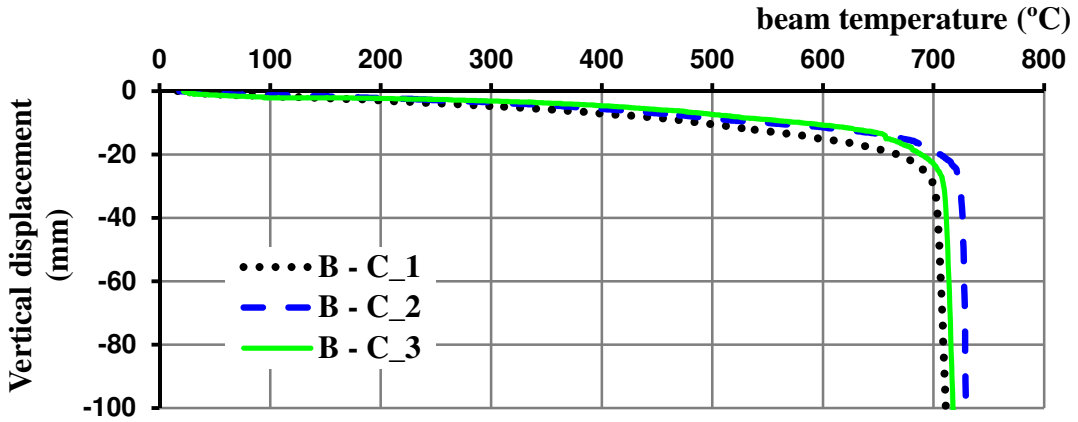

Figure E.4 – Evolution of vertical displacement at mid-span of simply supported C beams as a function of its mean temperature

E1.2 Lipped I beams

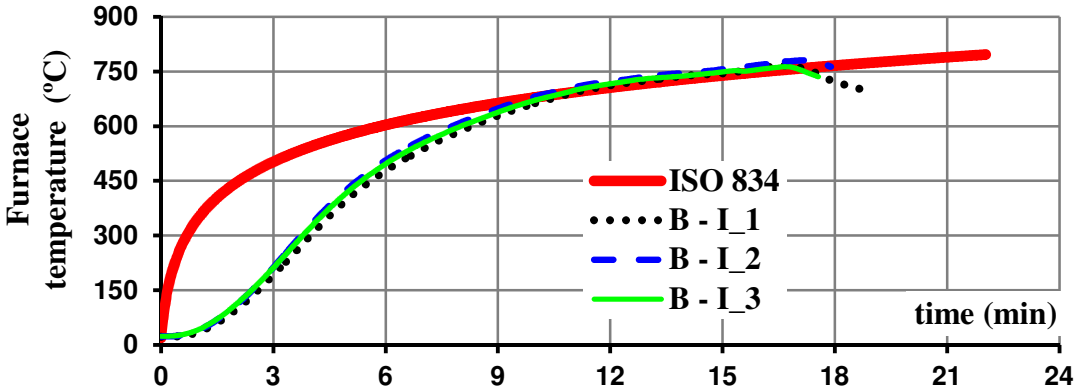

Figure E.5 – Furnace temperatures in tests on simply supported lipped I beams

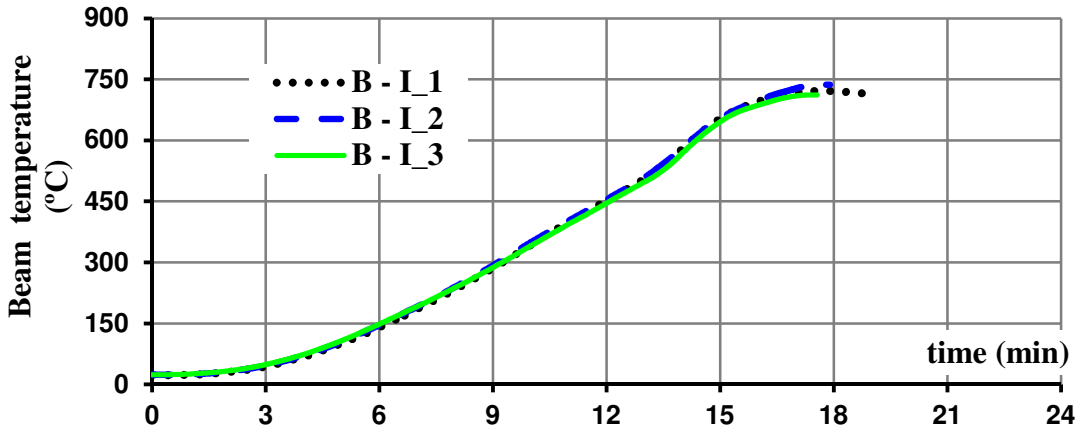

Figure E.6 – Evolution of mean temperature in simply supported lipped I beams as a function of time

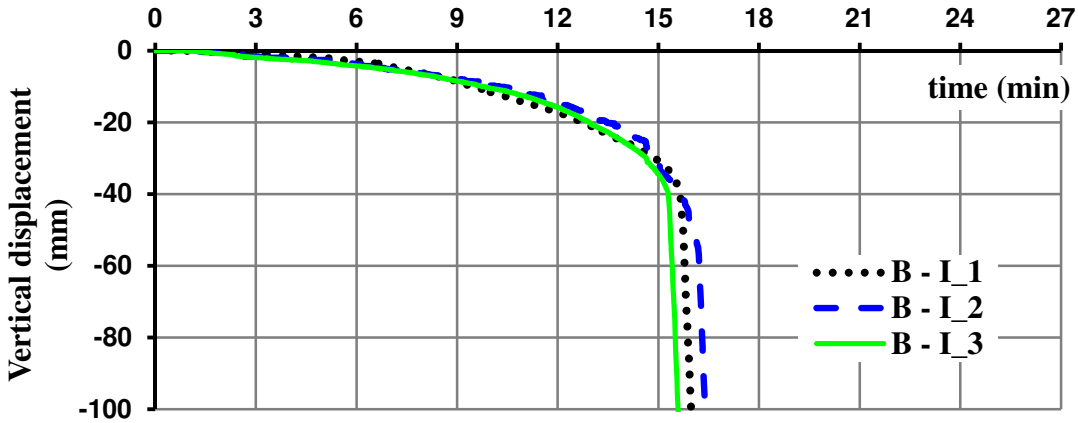

Figure E.7 – Evolution of vertical displacement at mid-span of simply supported lipped I beams as a function of time

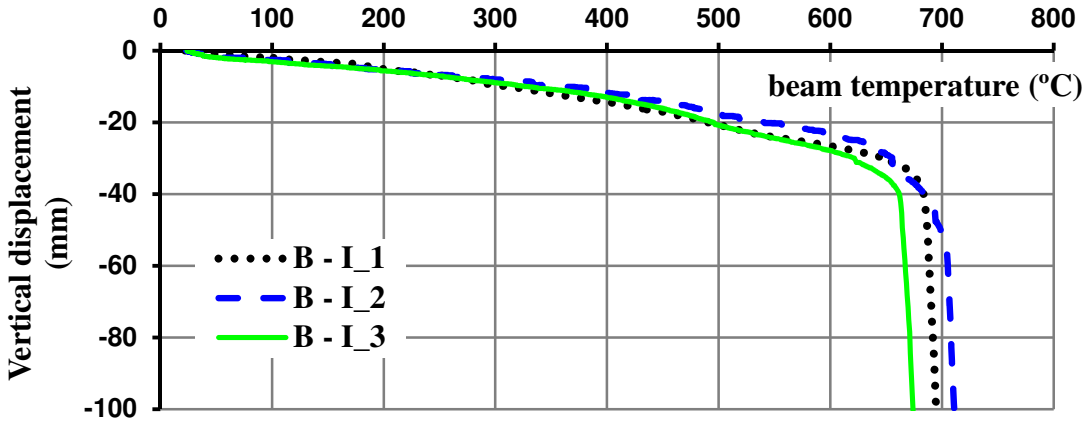

Figure E.8 – Evolution of vertical displacement at mid-span of simply supported lipped I beams as a function of its mean temperature

E1.3 R beams

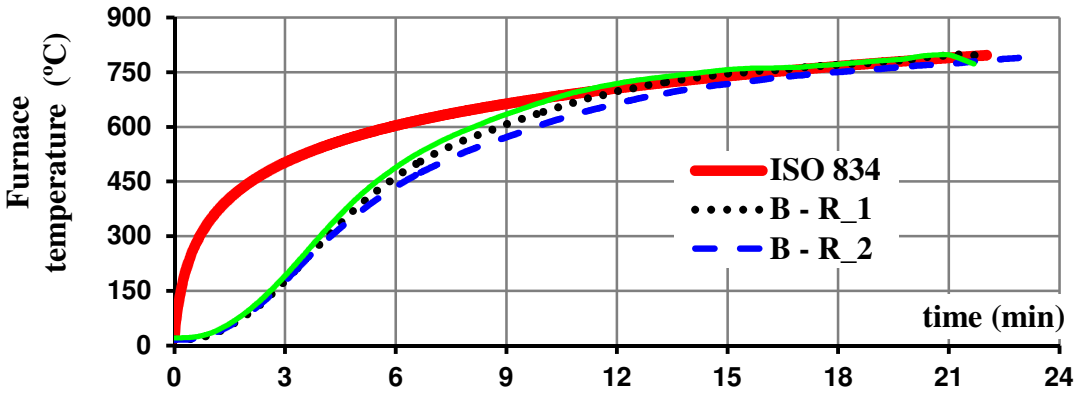

Figure E.9 – Furnace temperatures in tests on simply supported R beams

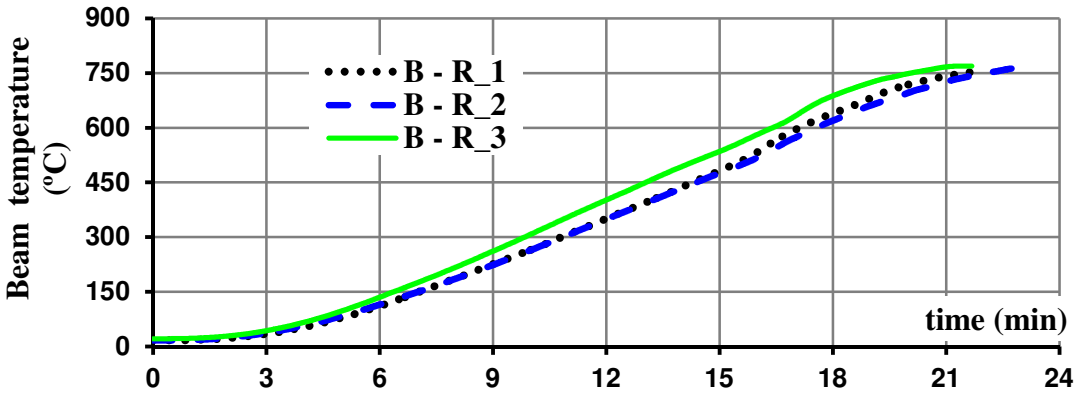

Figure E.10 – Evolution of mean temperature in simply supported R beams as a function of time

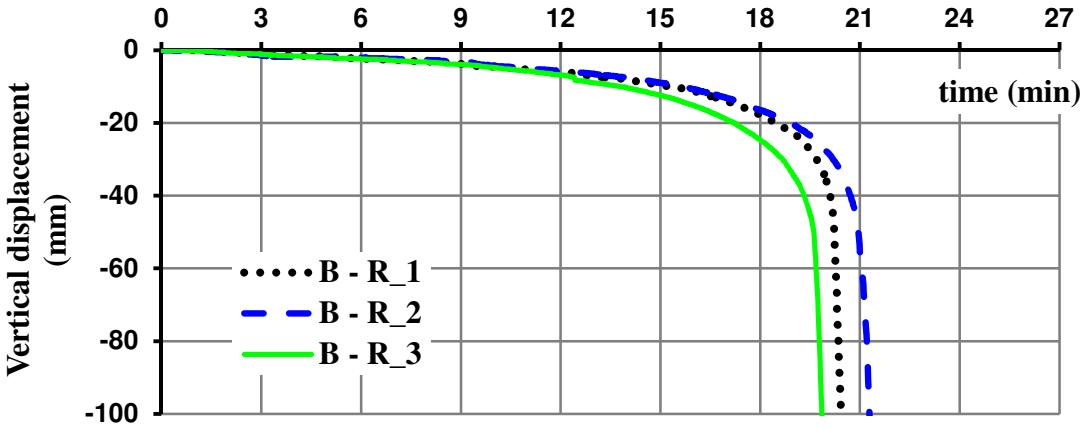

Figure E.11 – Evolution of vertical displacement at mid-span of simply supported R beams as a function of time

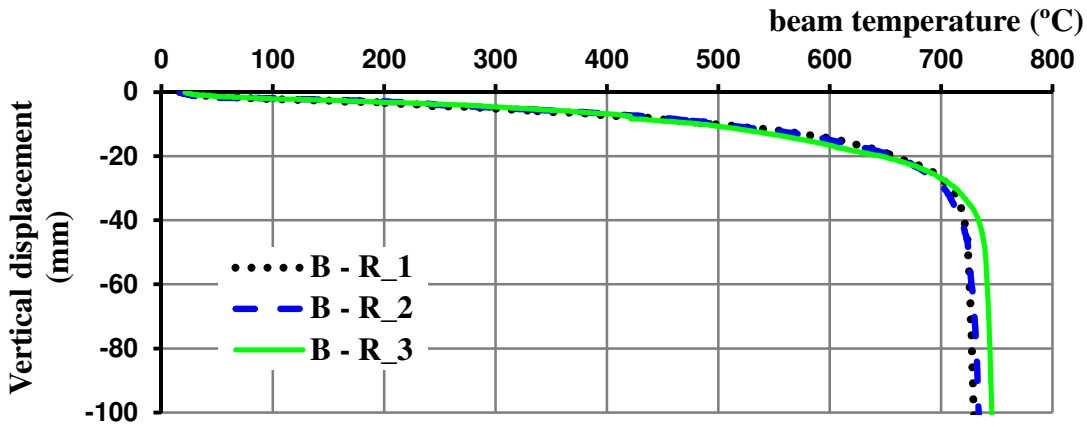

Figure E.12 – Evolution of vertical displacement at mid-span of simply supported R beams as a function of its mean temperature

E1.4 2R beams

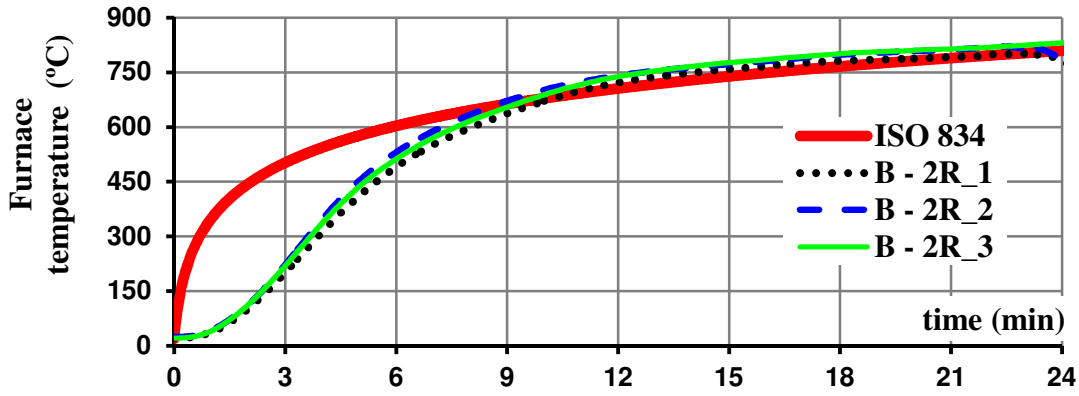

Figure E.13 – Furnace temperatures in tests on simply supported 2R beams

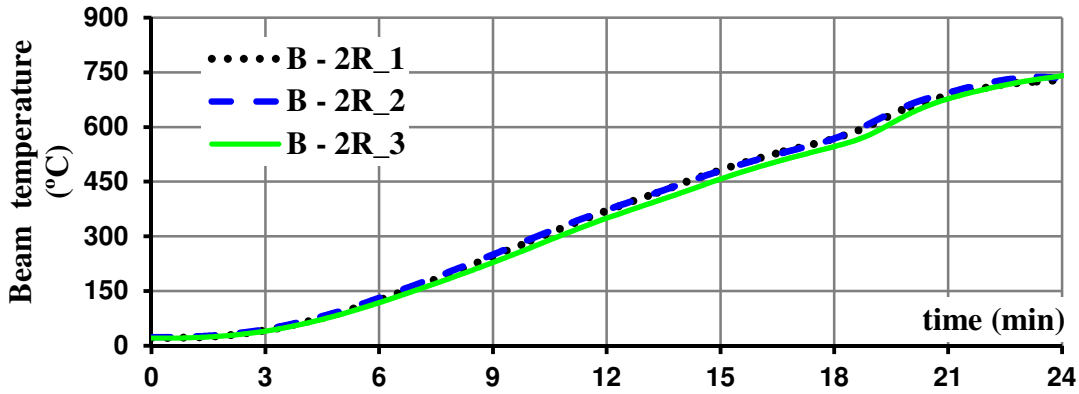

Figure E.14 – Evolution of mean temperature in simply supported 2R beams as a function of time

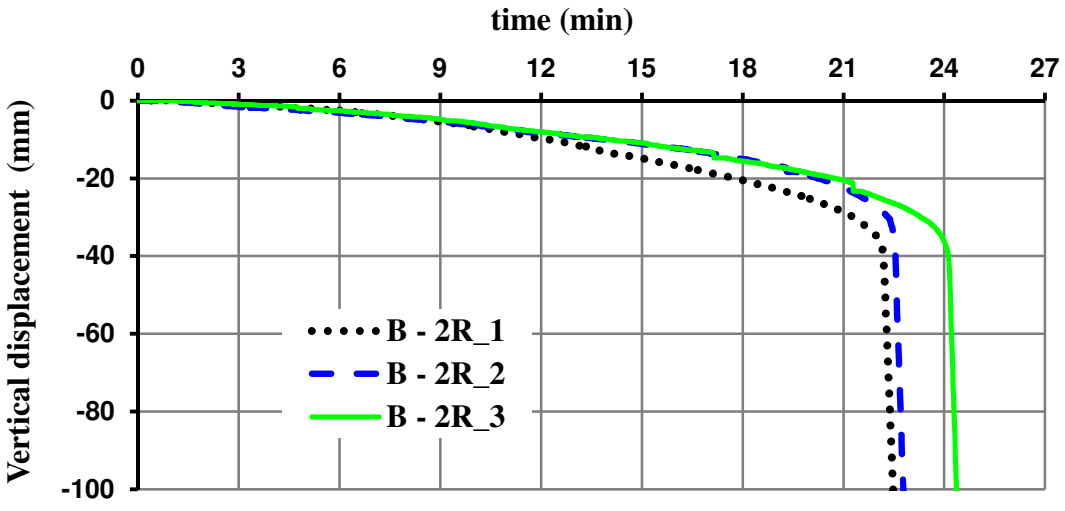

Figure E.15 – Evolution of vertical displacement at mid-span of simply supported 2R beams as a function of time

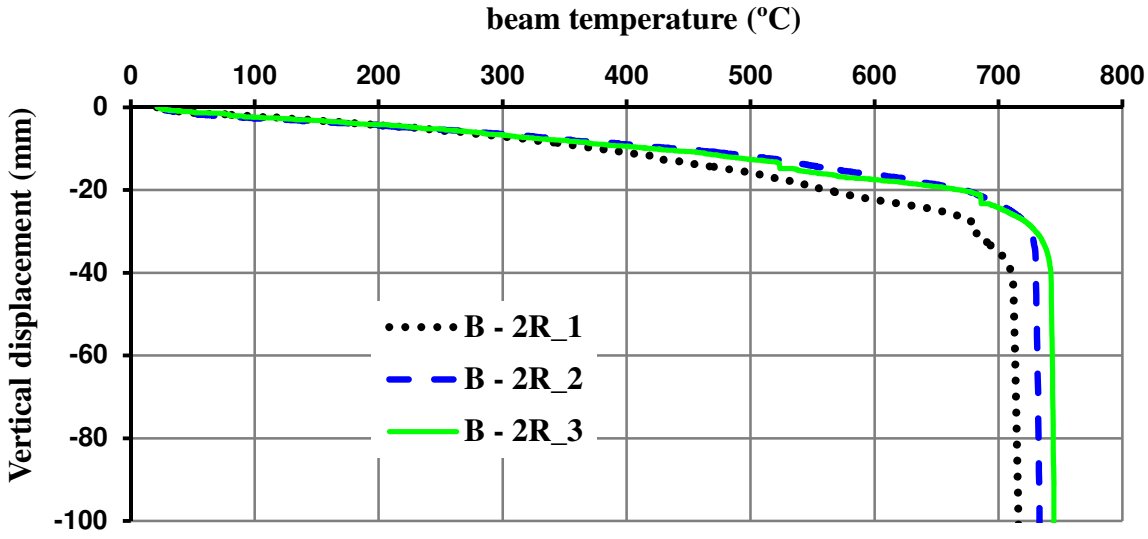

Figure E.16 – Evolution of vertical displacement at mid-span of simply supported 2R beams as a function of its mean temperature

E2 Axially restrained beams

E2.1 C beams

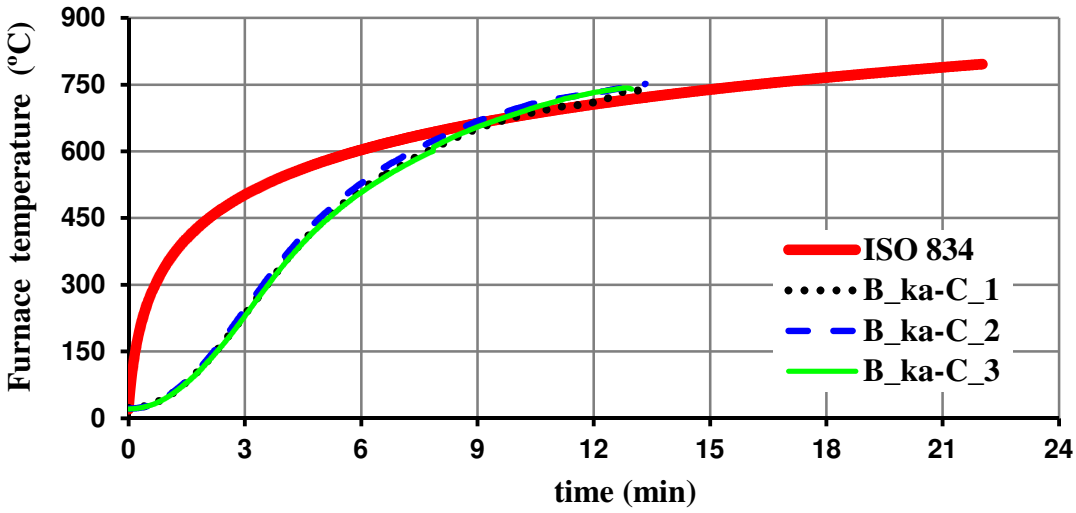

Figure E.17 – Furnace temperatures in tests of axially restrained C beams

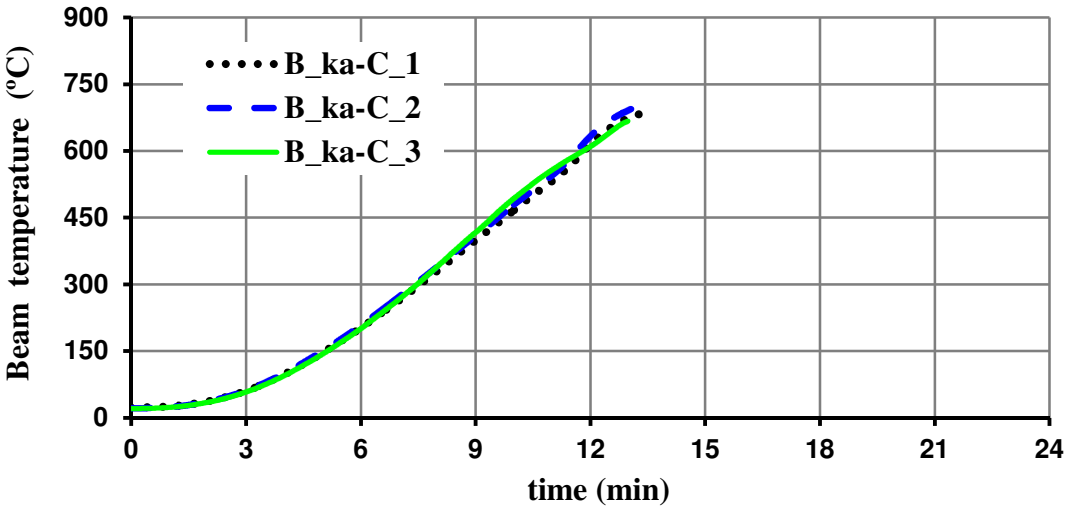

Figure E.18 – Evolution of mean temperature in axially restrained C beams as a function of time

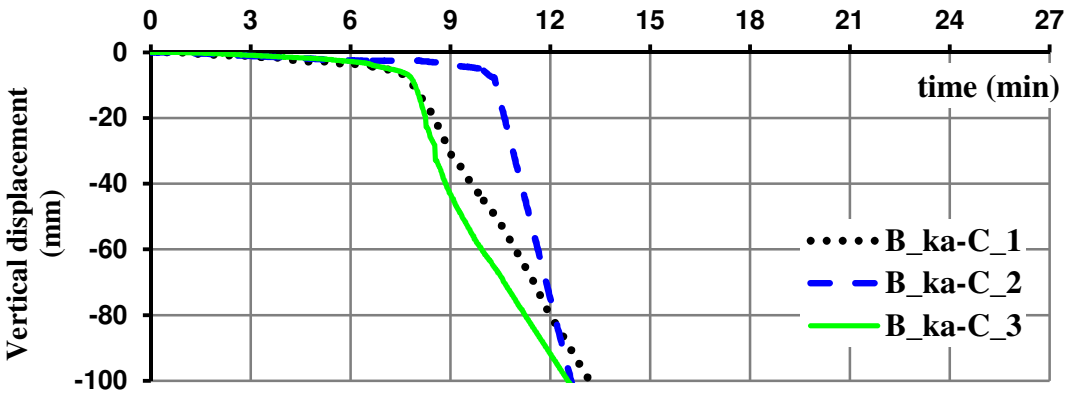

Figure E.19 – Evolution of vertical displacement at mid-span of axially restrained C beams as a function of time

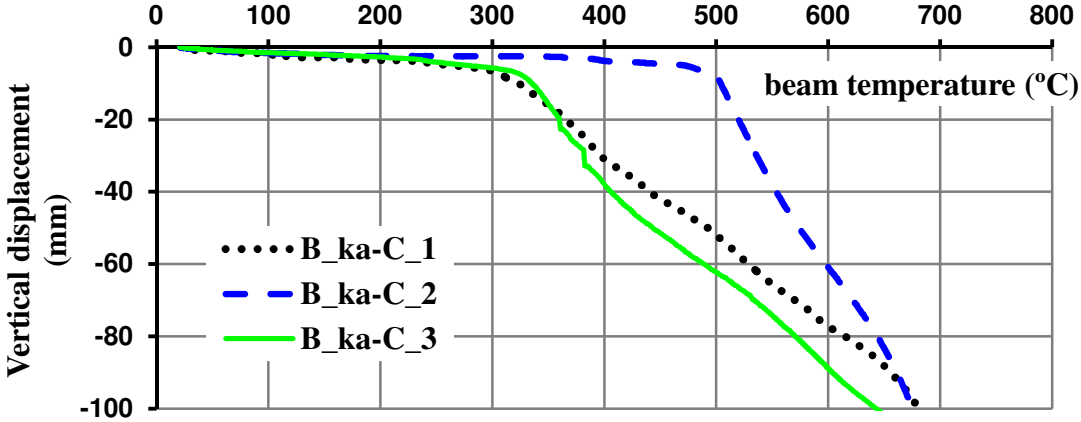

Figure E.20 – Evolution of vertical displacement at mid-span of axially restrained C beams as a function of its mean temperature

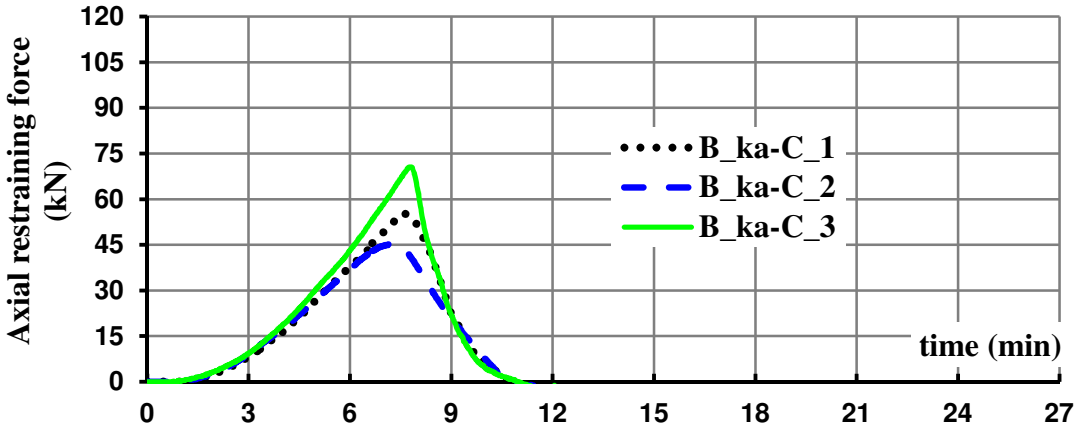

Figure E.21 – Evolution of axial restraining forces in axially restrained C beams as a function of time

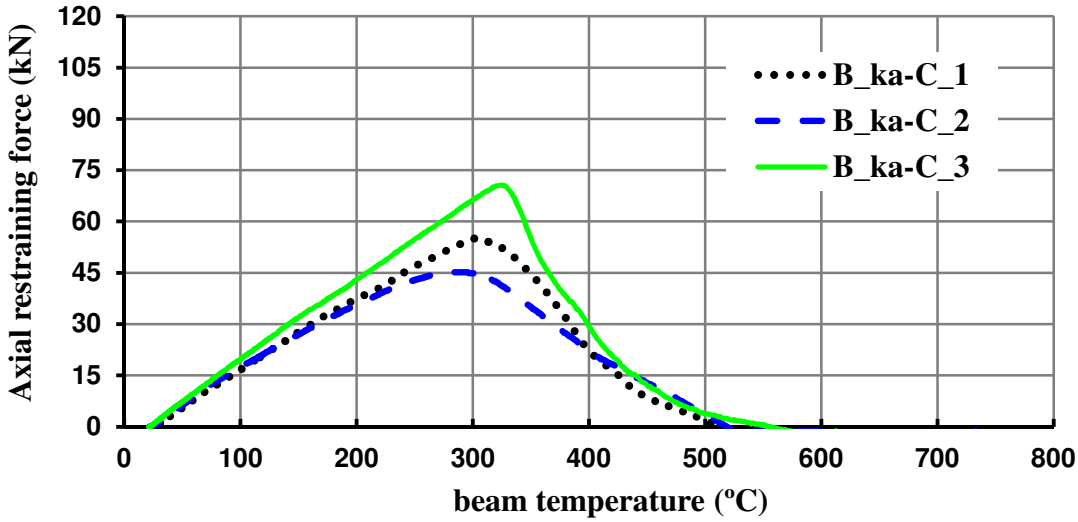

Figure E.22 – Evolution of axial restraining forces in axially restrained C beams as a function of its mean temperature

E2.2 Lipped I beams

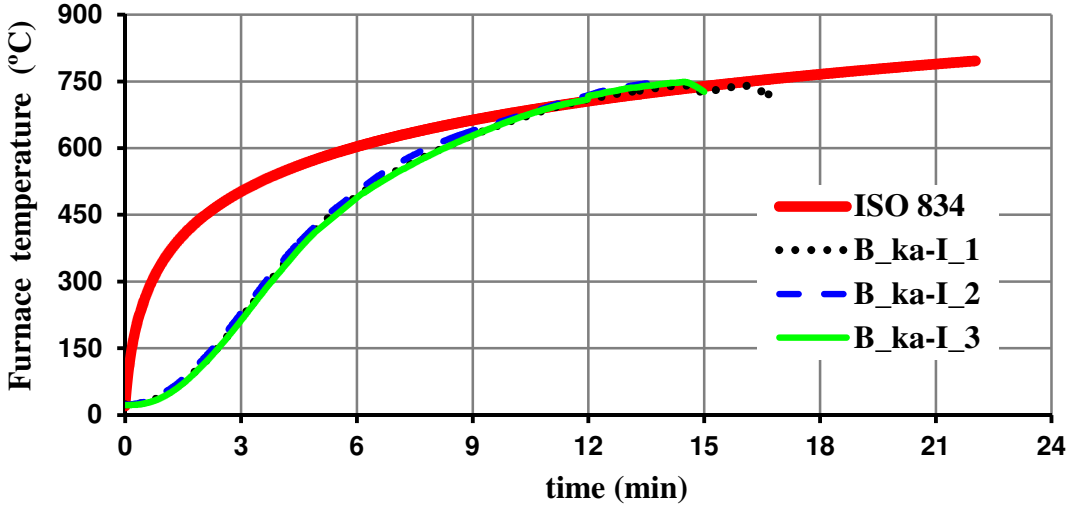

Figure E.23 – Furnace temperatures in tests of axially restrained lipped I beams

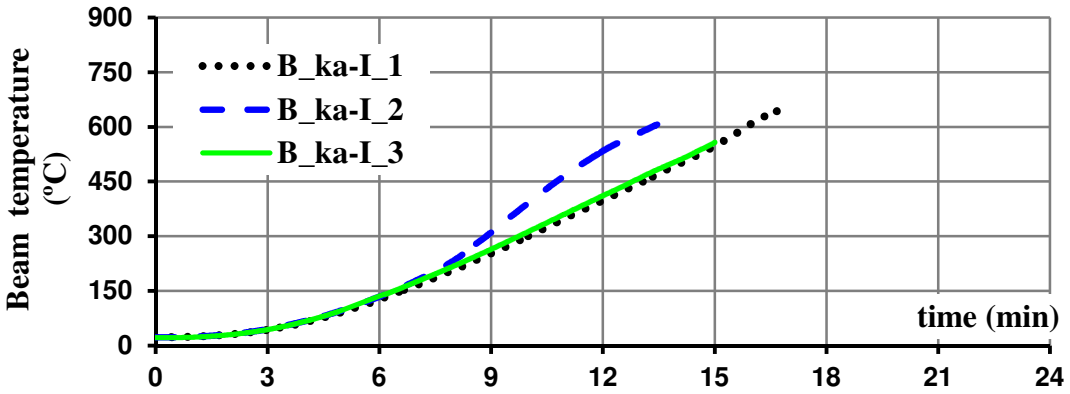

Figure E.24 – Evolution of mean temperature in axially restrained lipped I beams as a function of time

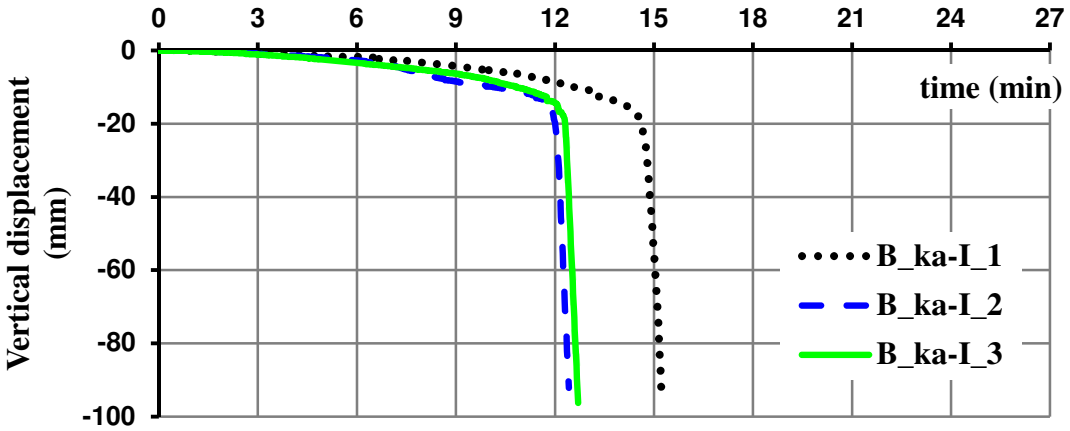

Figure E.25 – Evolution of vertical displacement at mid-span of axially restrained lipped I beams as a function of time

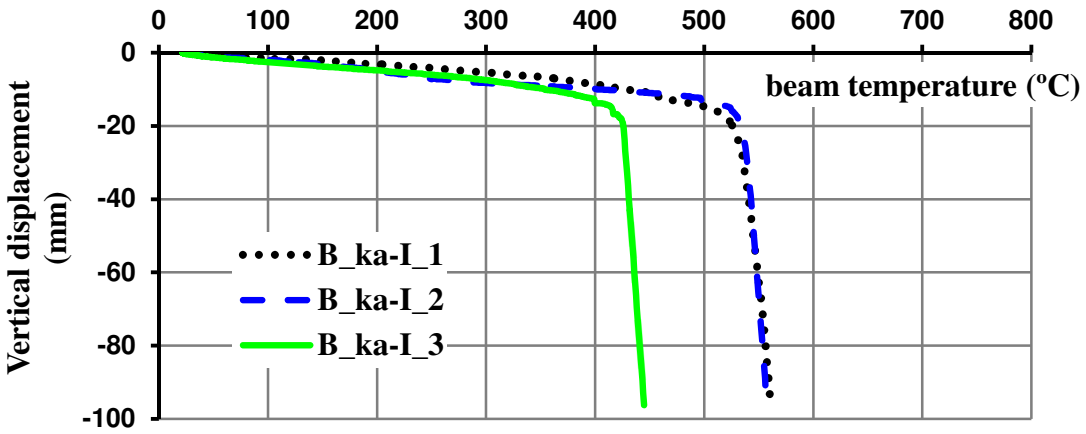

Figure E.26 – Evolution of vertical displacement at mid-span of axially restrained lipped I beams as a function of its mean temperature

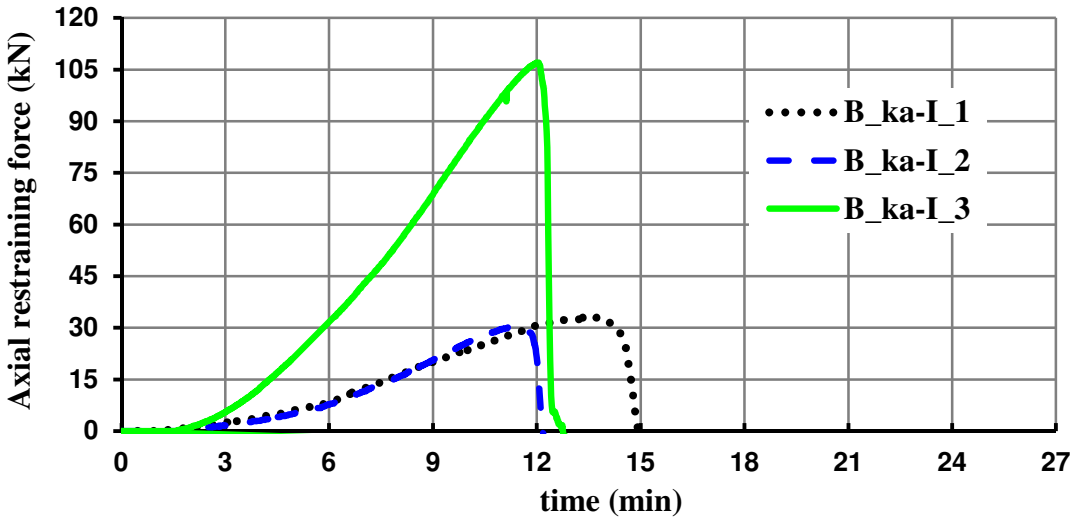

Figure E.27 – Evolution of axial restraining forces in axially restrained lipped I beams as a function of time

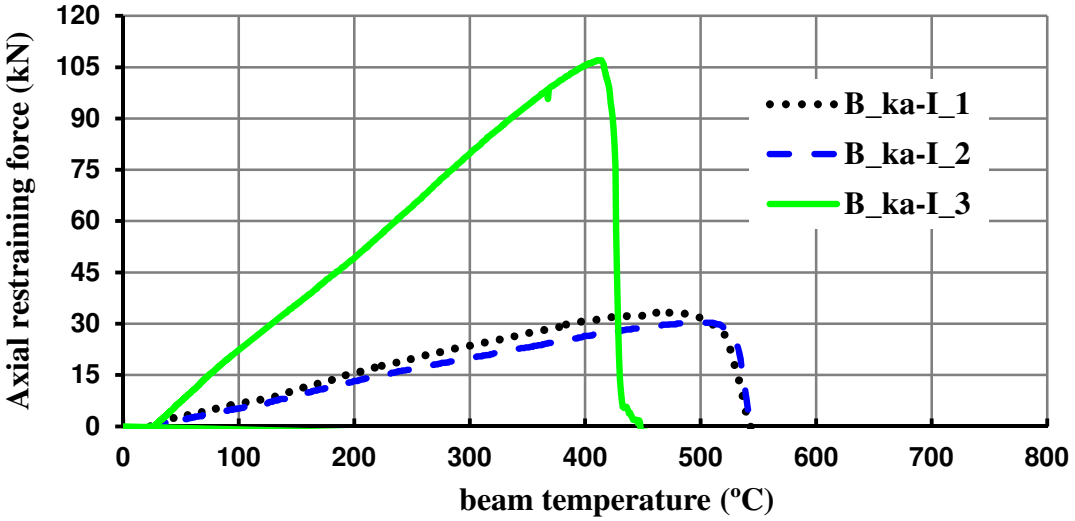

Figure E.28 – Evolution of axial restraining forces in axially restrained lipped I beams as a function of its mean temperature

E2.3 R beams

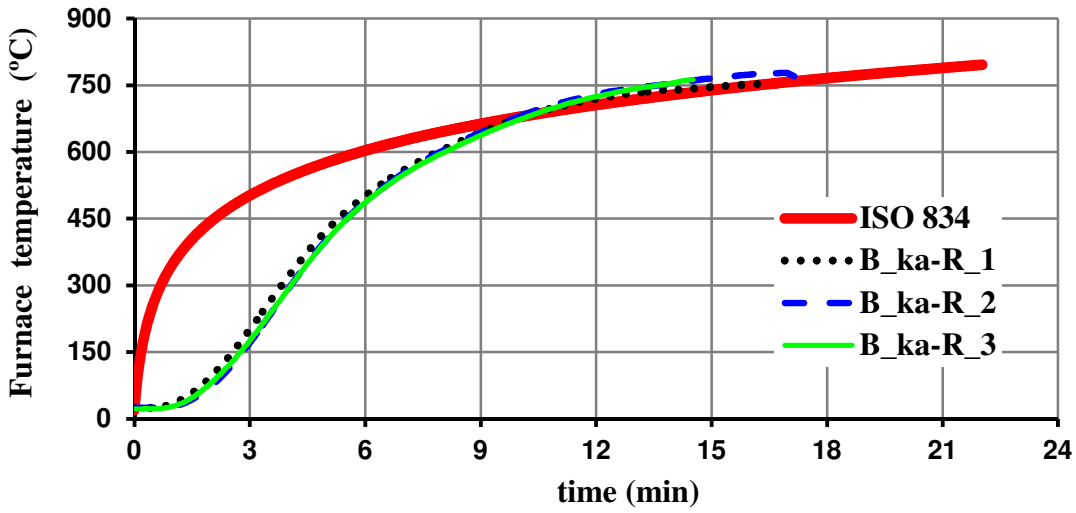

Figure E.29 – Furnace temperatures in tests of axially restrained R beams

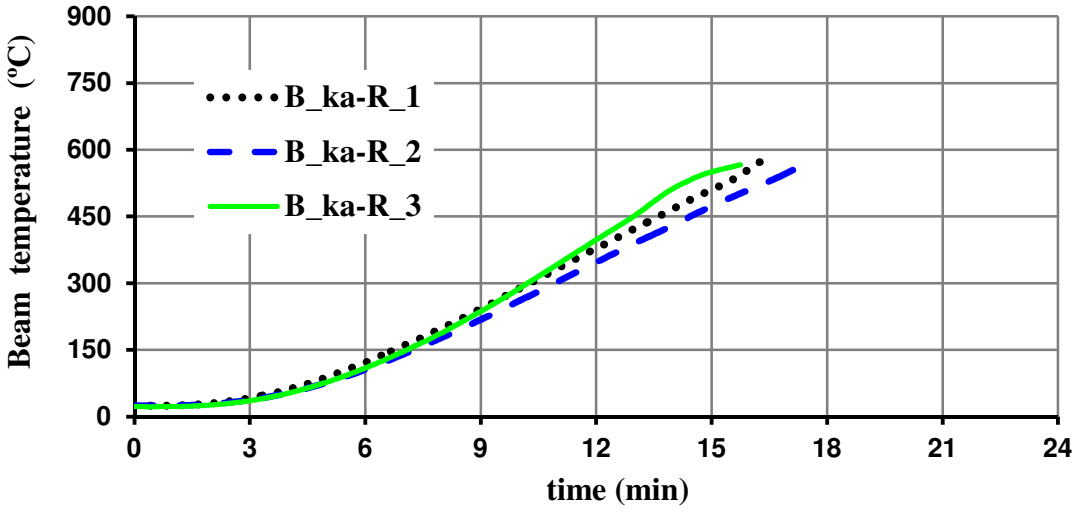

Figure E.30 – Evolution of mean temperature in axially restrained R beams as a function of time

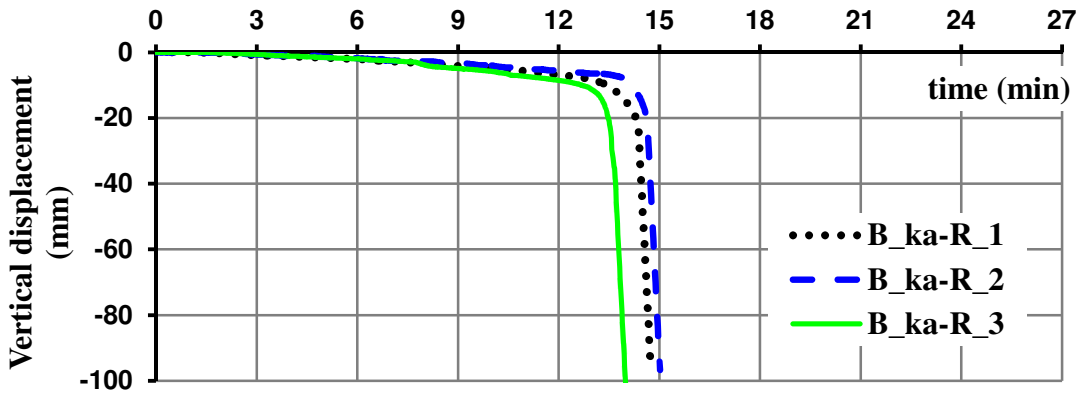

Figure E.31 – Evolution of vertical displacement at mid-span of axially restrained R beams as a function of time

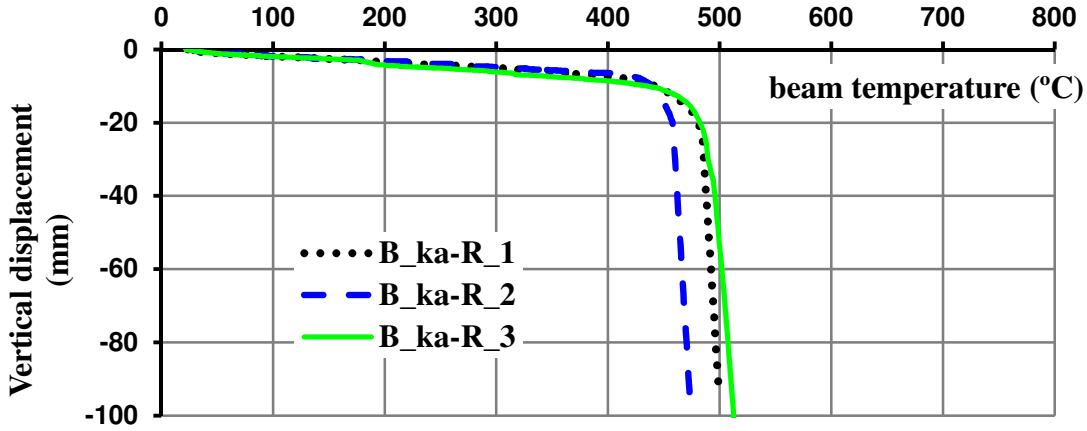

Figure E.32 – Evolution of vertical displacement at mid-span of axially restrained R beams as a function of its mean temperature

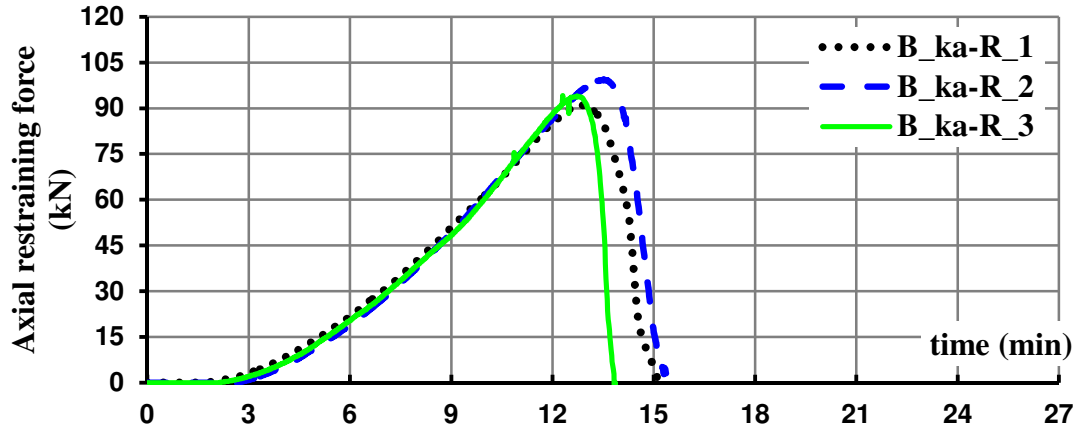

Figure E.33 – Evolution of axial restraining forces in axially restrained R beams as a function of time

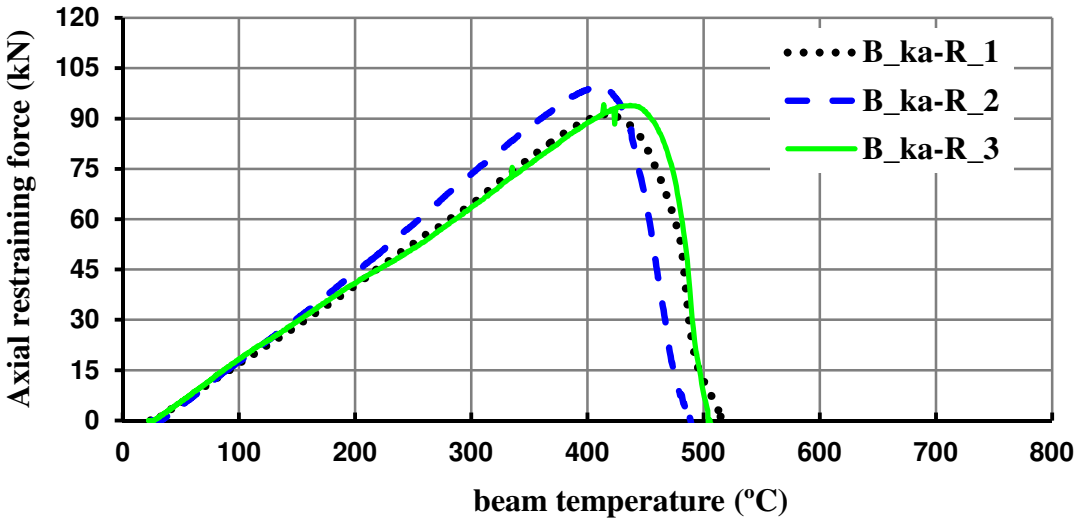

Figure E.34 – Evolution of axial restraining forces in axially restrained R beams as a function of its mean temperature

E2.4 2R beams

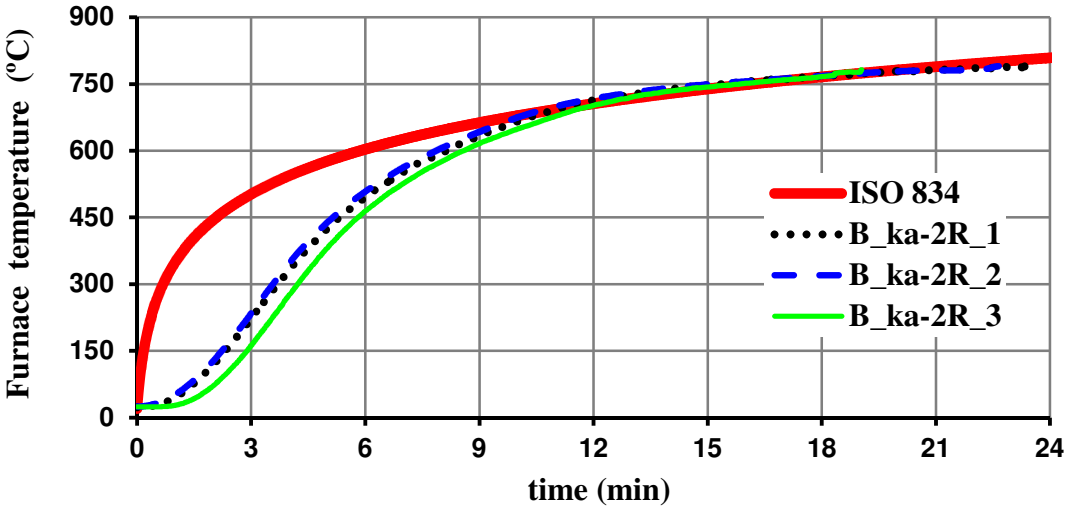

Figure E.35 – Furnace temperatures in tests of axially restrained 2R beams

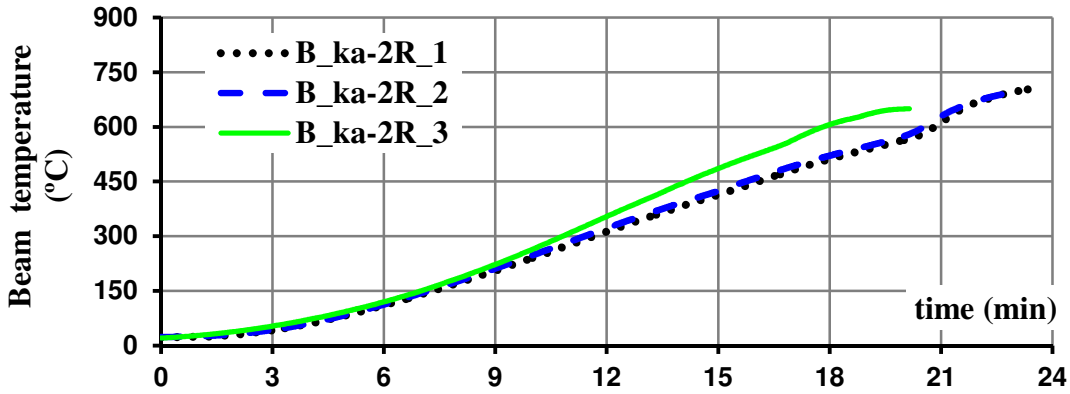

Figure E.36 – Evolution of mean temperature in axially restrained 2R beams as a function of time

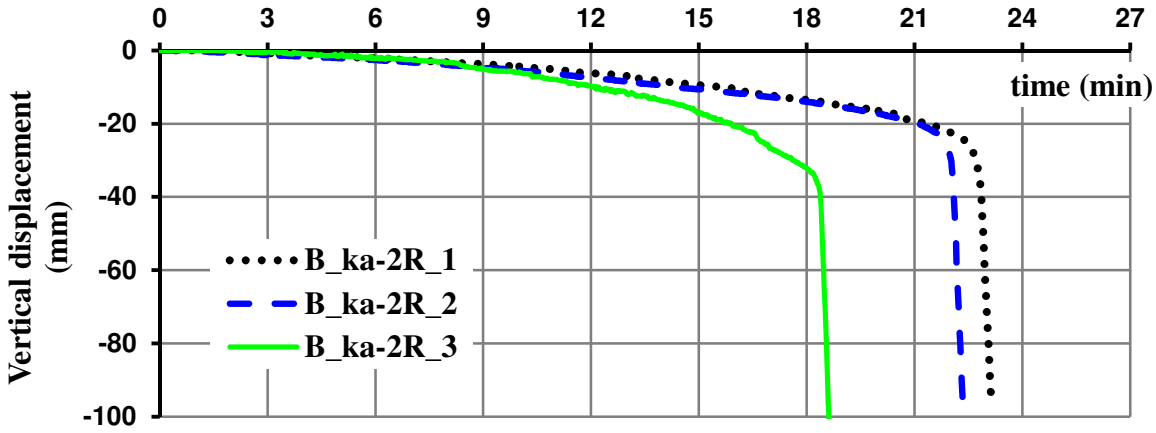

Figure E.37 – Evolution of vertical displacement at mid-span of axially restrained 2R beams as a function of time

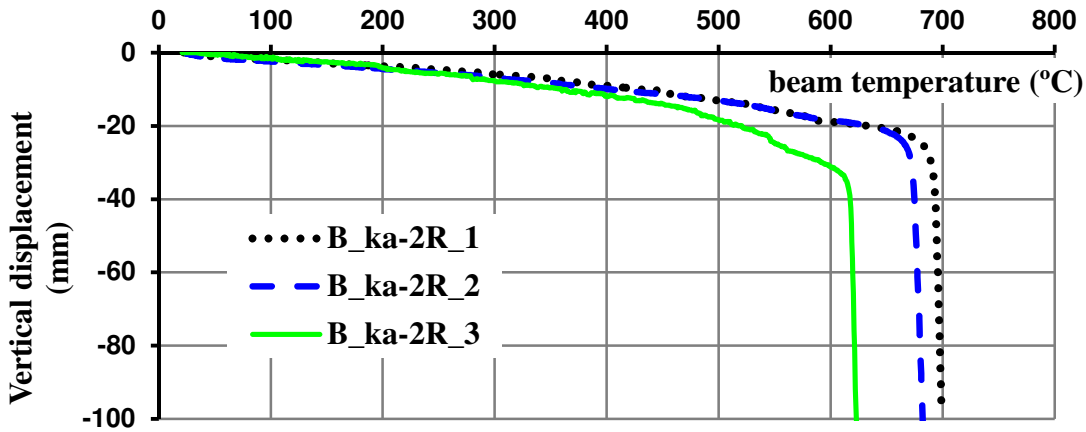

Figure E.38 – Evolution of vertical displacement at mid-span of axially restrained 2R beams as a function of its mean temperature

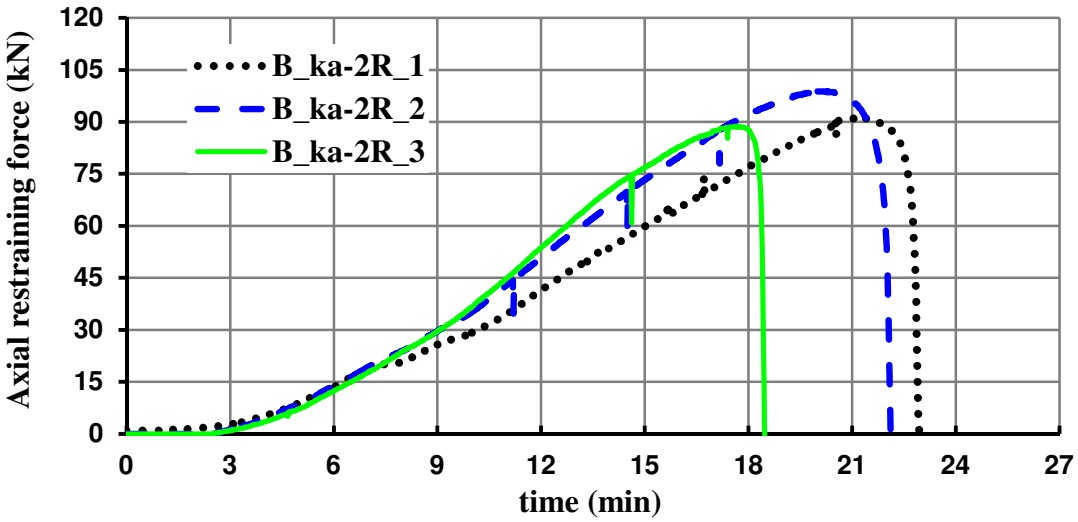

Figure E.39 – Evolution of axial restraining forces in axially restrained 2R beams as a function of time

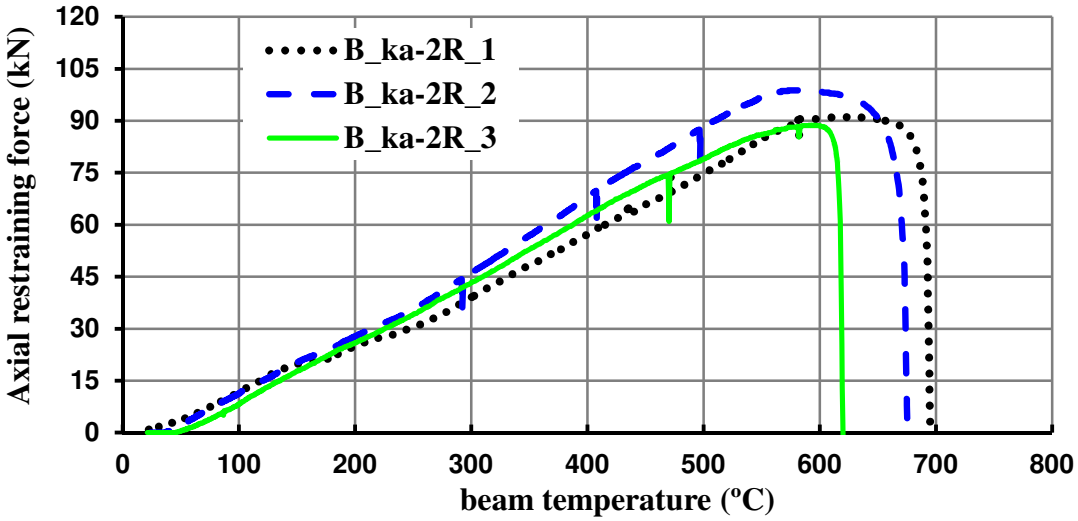

Figure E.40 – Evolution of axial restraining forces in axially restrained 2R beams as a function of its mean temperature

E3 Axially and rotationally restrained beams

E3.1 C beams

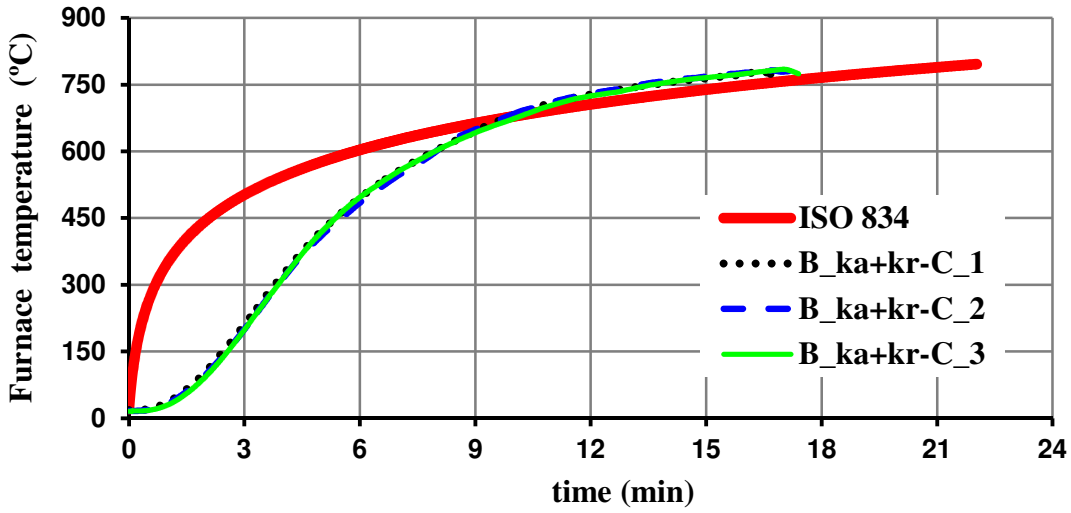

Figure E.41 – Furnace temperatures in tests of axially and rotationally restrained C beams

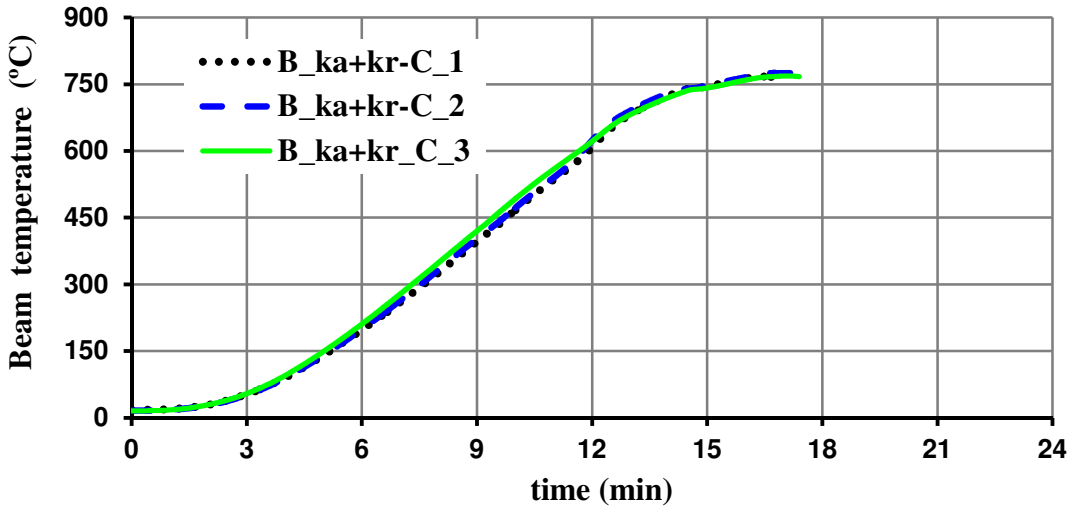

Figure E.42 – Evolution of mean temperature in axially and rotationally restrained C beams as a function of time

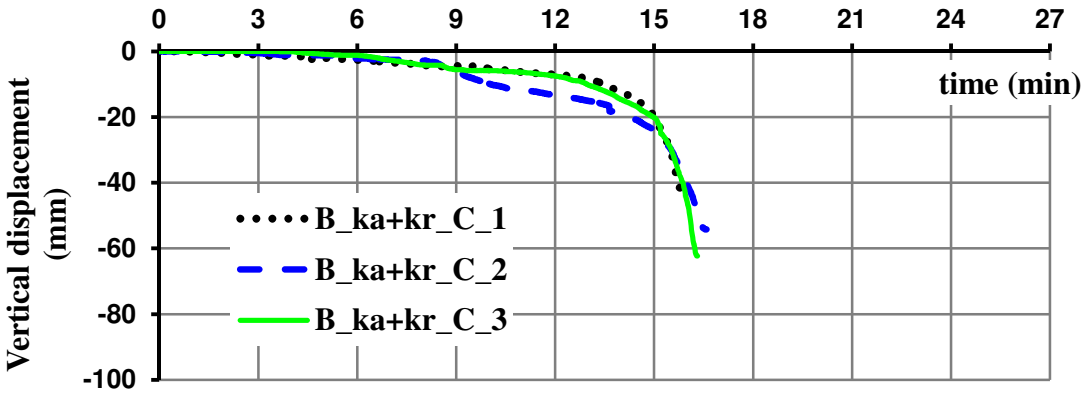

Figure E.43 – Evolution of vertical displacement at mid-span of axially and rotationally restrained C beams as a function of time

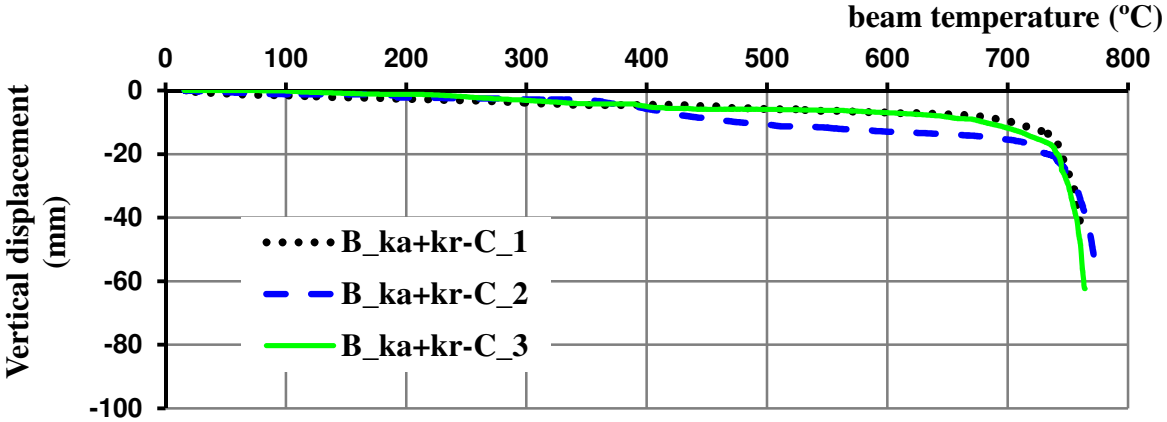

Figure E.44 – Evolution of vertical displacement at mid-span of axially and rotationally restrained C beams as a function of its mean temperature

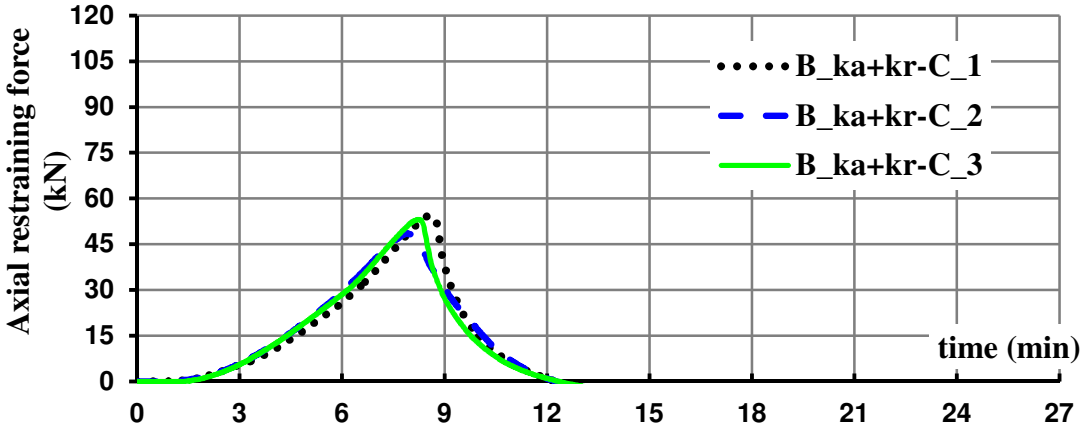

Figure E.45 – Evolution of axial restraining forces in axially and rotationally restrained C beams as a function of time

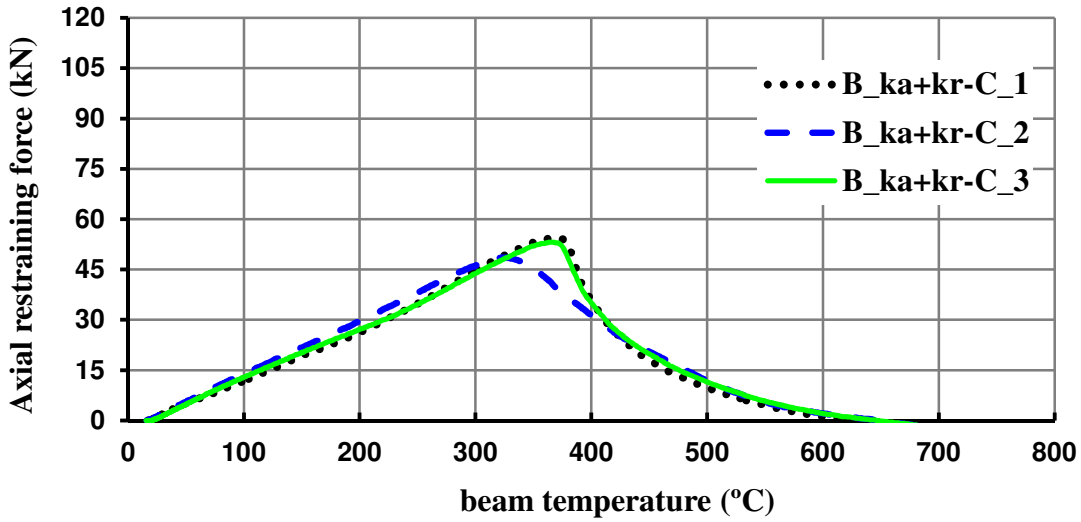

Figure E.46 – Evolution of axial restraining forces in axially and rotationally restrained C beams as a function of its mean temperature

E3.2 Lipped I beams

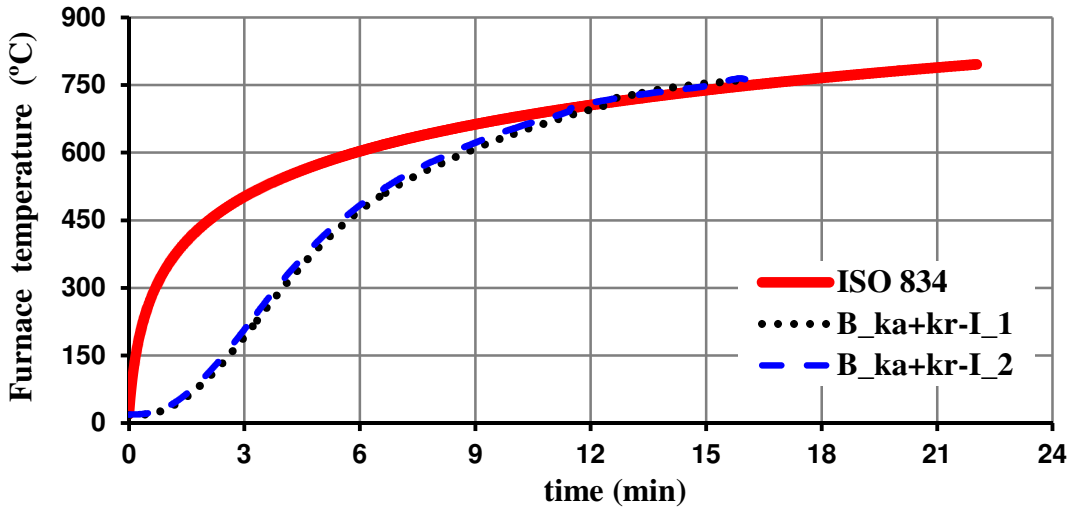

Figure E.47 – Furnace temperatures in tests of axially and rotationally restrained lipped I beams

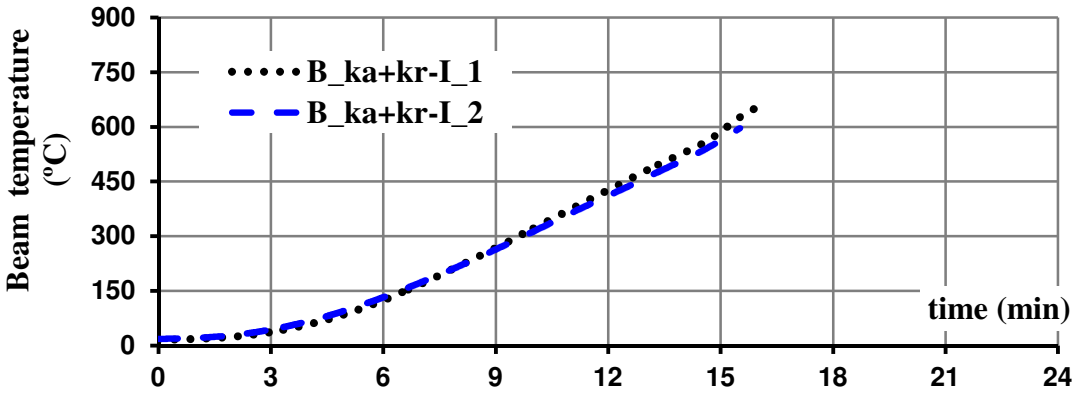

Figure E.48 – Evolution of mean temperature in axially and rotationally restrained lipped I beams as a function of time

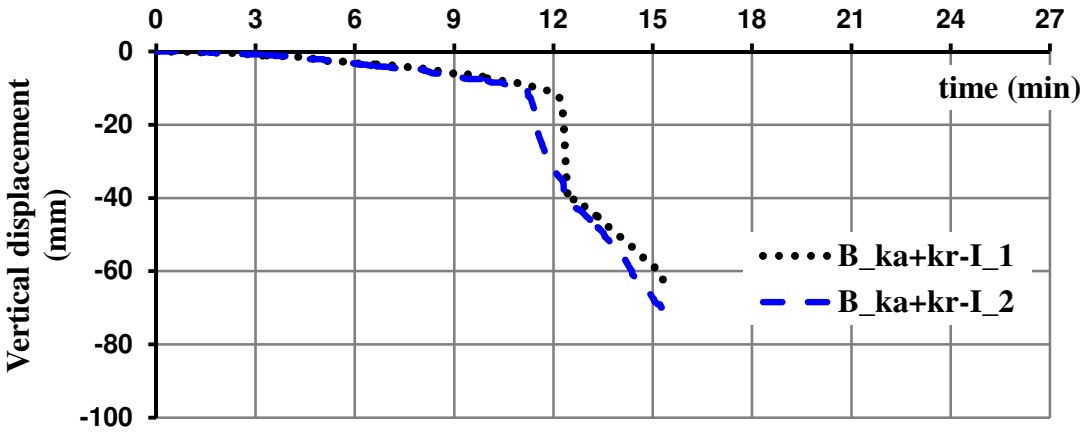

Figure E.49 – Evolution of vertical displacement at mid-span of axially and rotationally restrained lipped I beams as a function of time

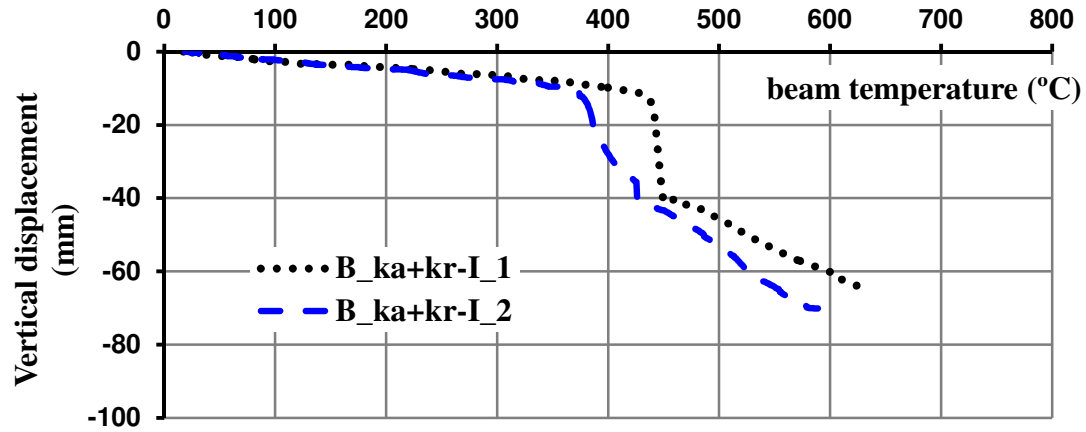

Figure E.50 – Evolution of vertical displacement at mid-span of axially and rotationally restrained lipped I beams as a function of its mean temperature

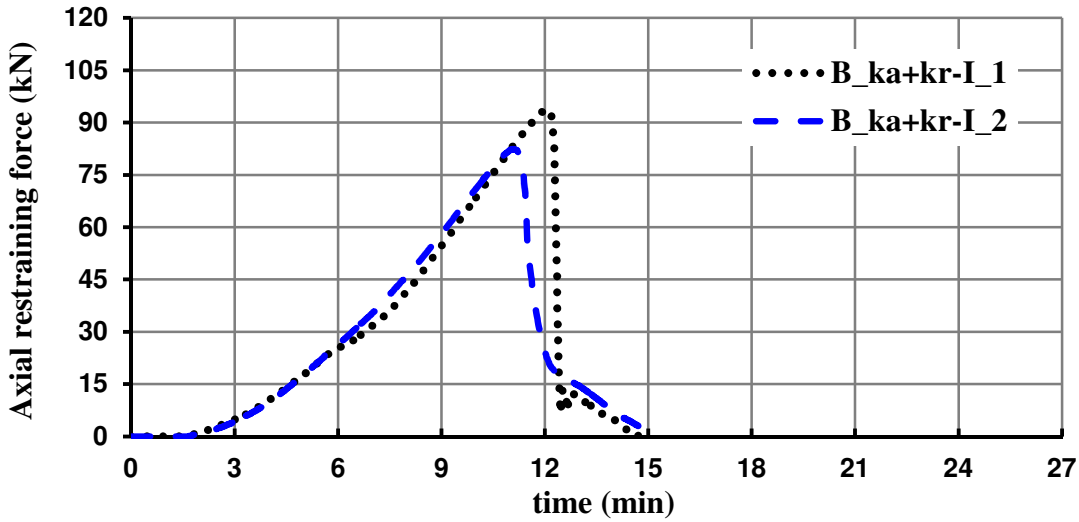

Figure E.51 – Evolution of axial restraining forces in axially and rotationally restrained lipped I beams as a function of time

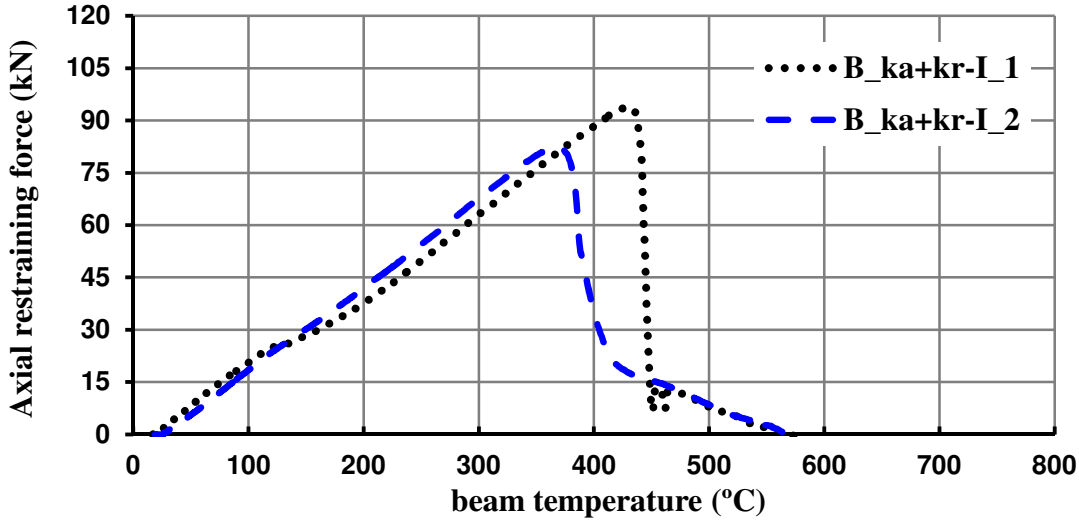

Figure E.52 – Evolution of axial restraining forces in axially and rotationally restrained lipped I beams as a function of its mean temperature

E3.3 R beams

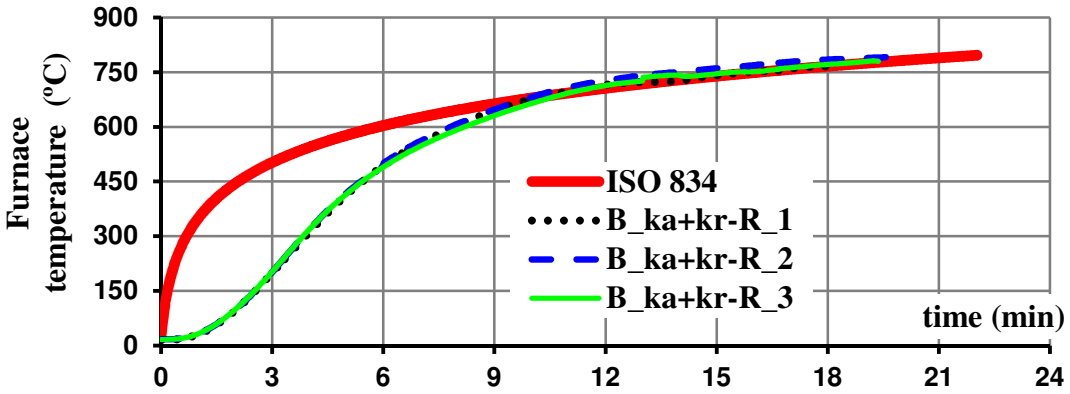

Figure E.53 – Furnace temperatures in tests of axially and rotationally restrained R beams

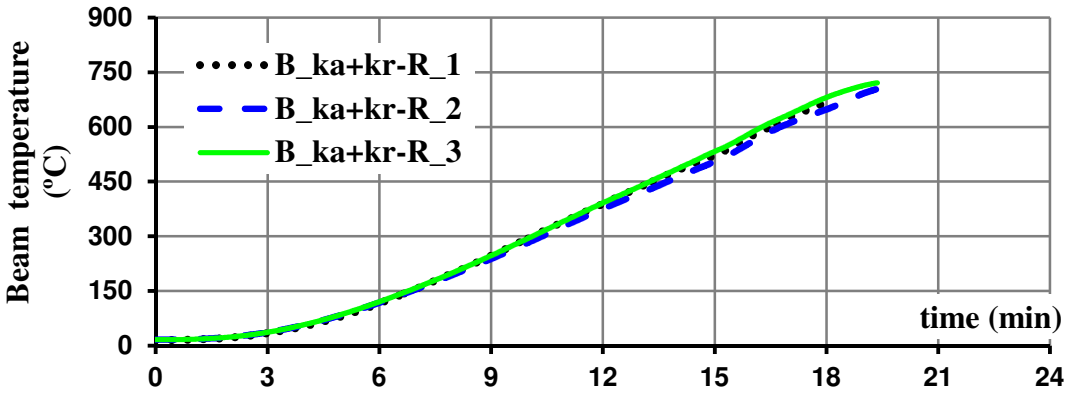

Figure E.54 – Evolution of mean temperature in axially and rotationally restrained R beams as a function of time

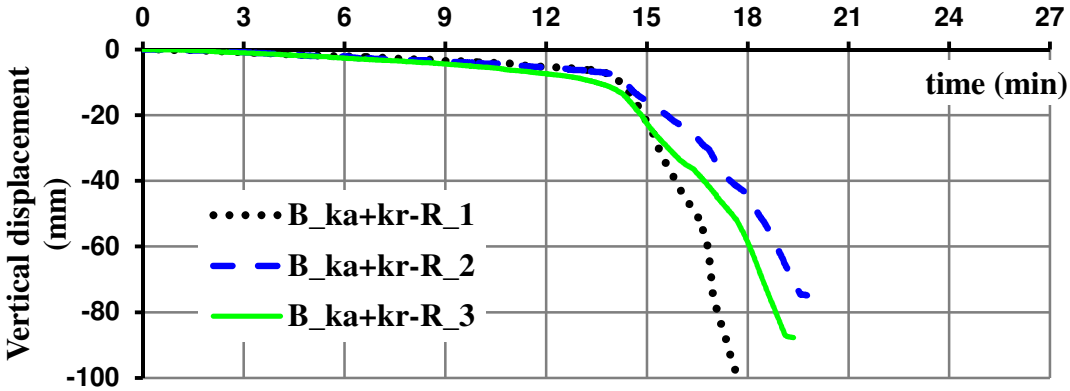

Figure E.55 – Evolution of vertical displacement at mid-span of axially and rotationally restrained R beams as a function of time

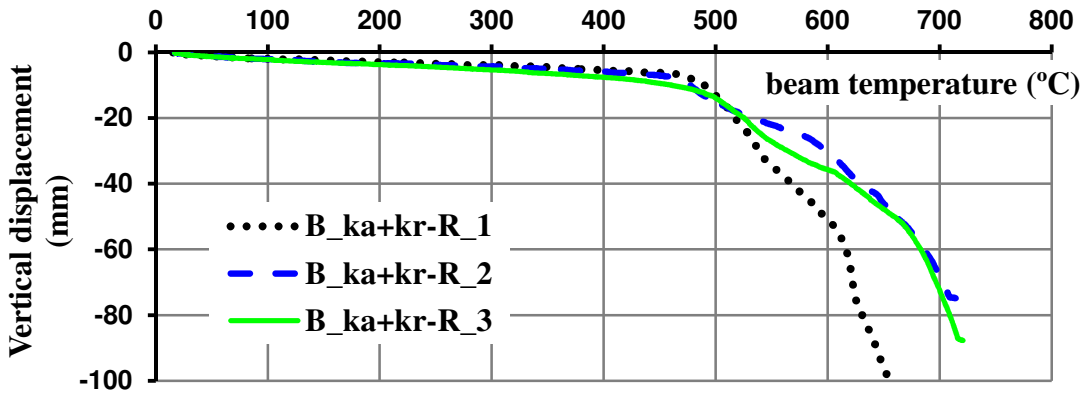

Figure E.56 – Evolution of vertical displacement at mid-span of axially and rotationally restrained R beams as a function of its mean temperature

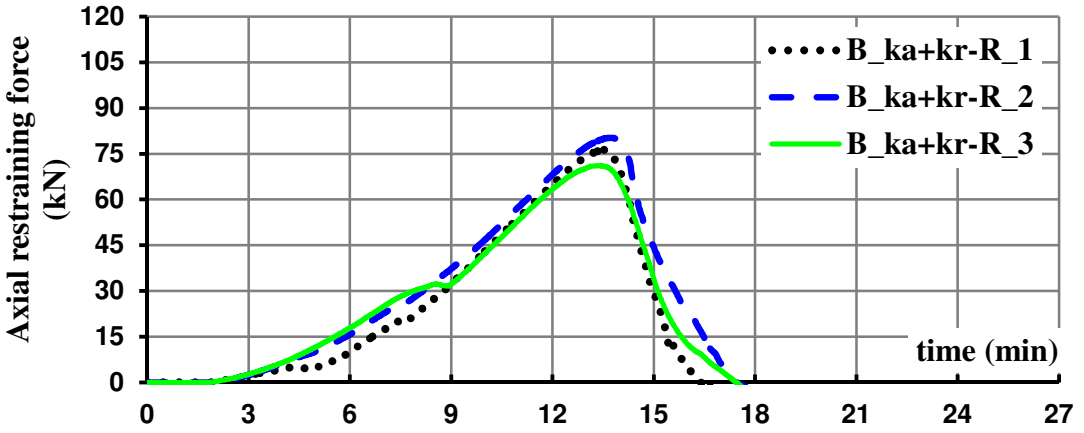

Figure E.57 – Evolution of axial restraining forces in axially and rotationally restrained R beams as a function of time

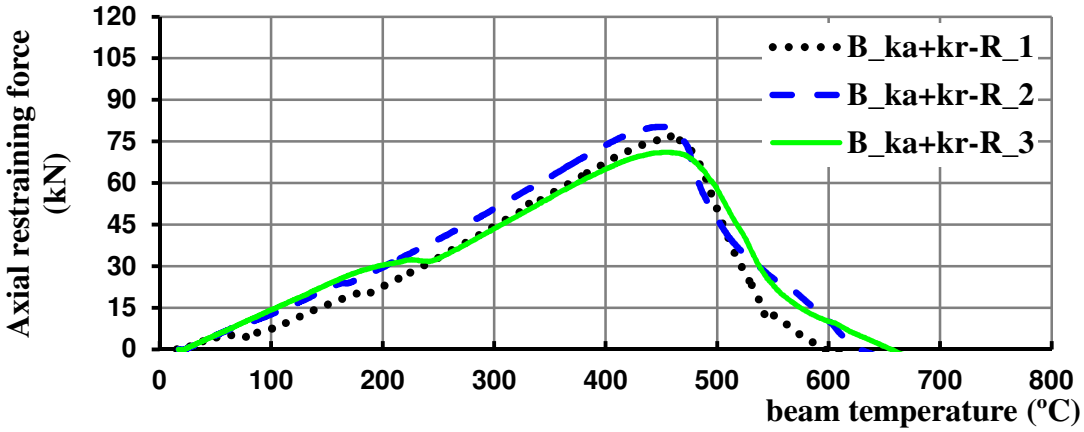

Figure E.58 – Evolution of axial restraining forces in axially and rotationally restrained R beams as a function of its mean temperature

E3.4 2R beams

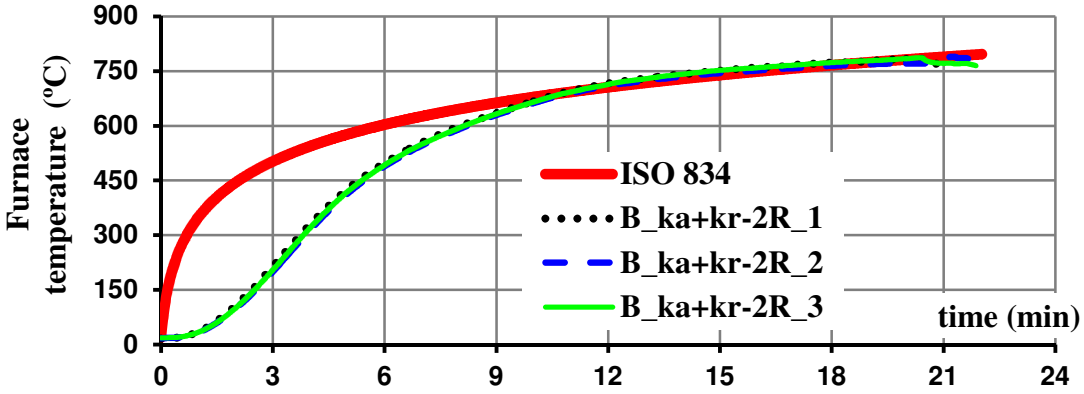

Figure E.59 – Furnace temperatures in tests of axially and rotationally restrained 2R beams

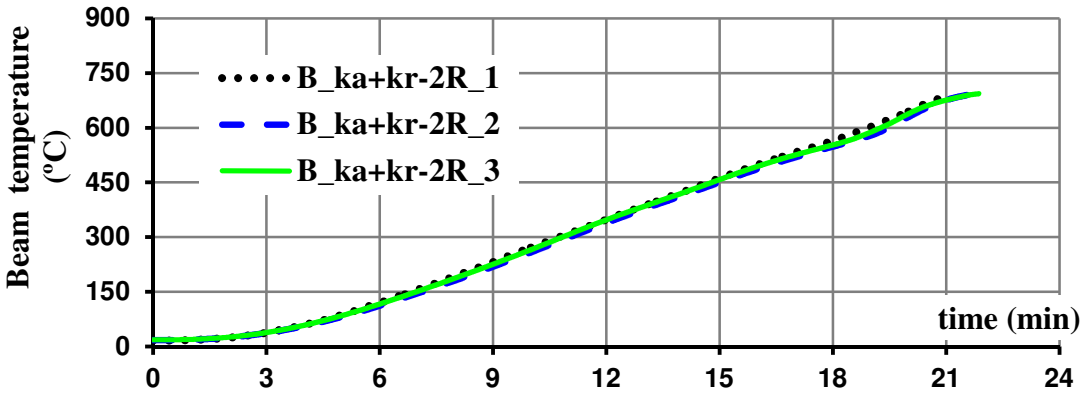

Figure E.60 – Evolution of mean temperature in axially and rotationally restrained 2R beams as a function of time

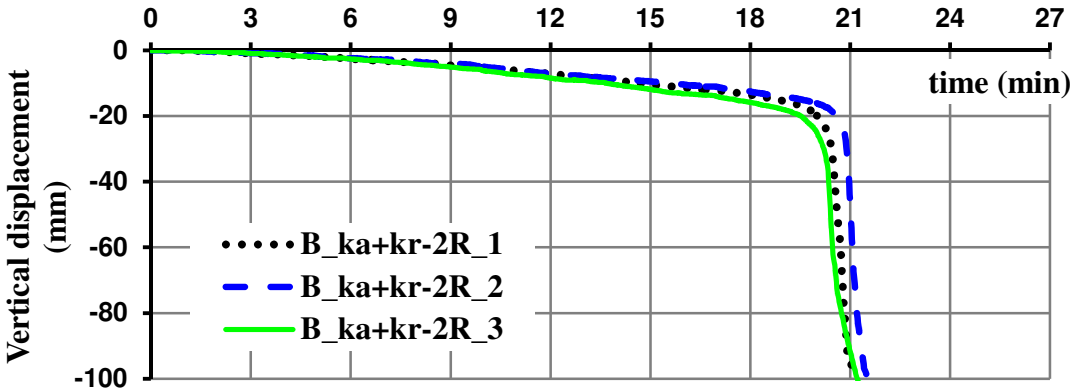

Figure E.61 – Evolution of vertical displacement at mid-span of axially and rotationally restrained 2R beams as a function of time

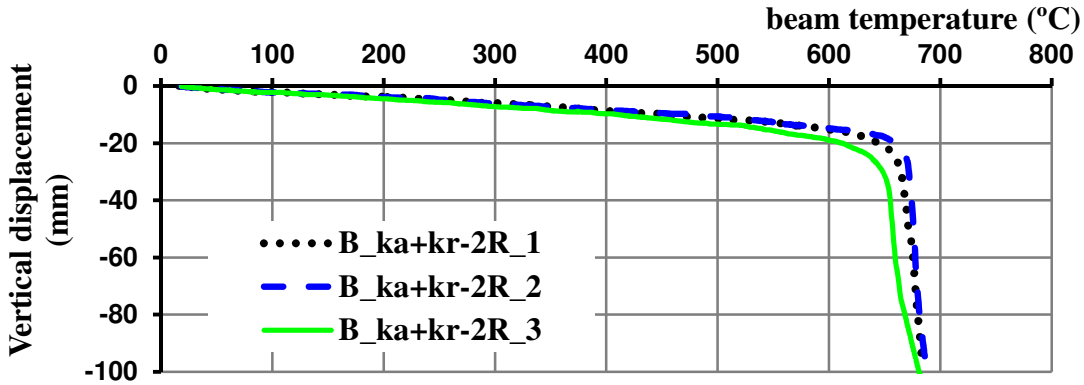

Figure E.62 – Evolution of vertical displacement at mid-span of axially and rotationally restrained 2R beams as a function of its mean temperature

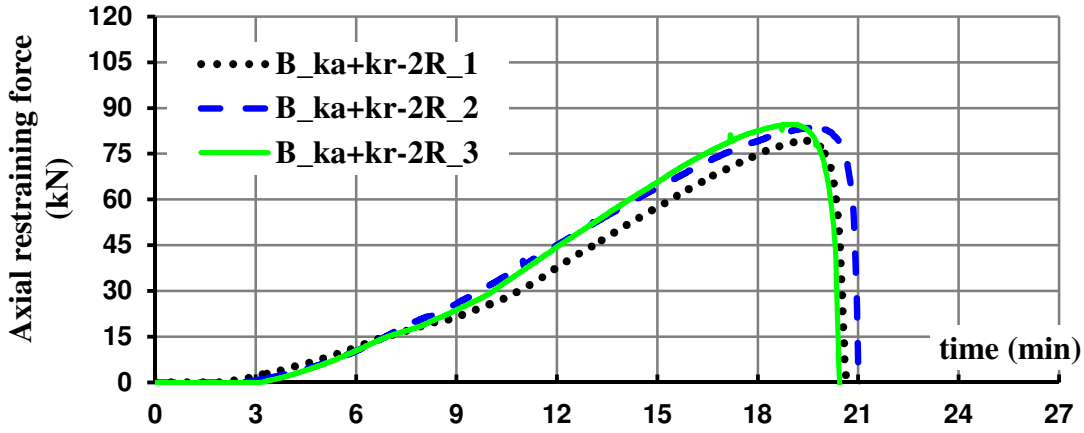

Figure E.63 – Evolution of axial restraining forces in axially and rotationally restrained 2R beams as a function of time

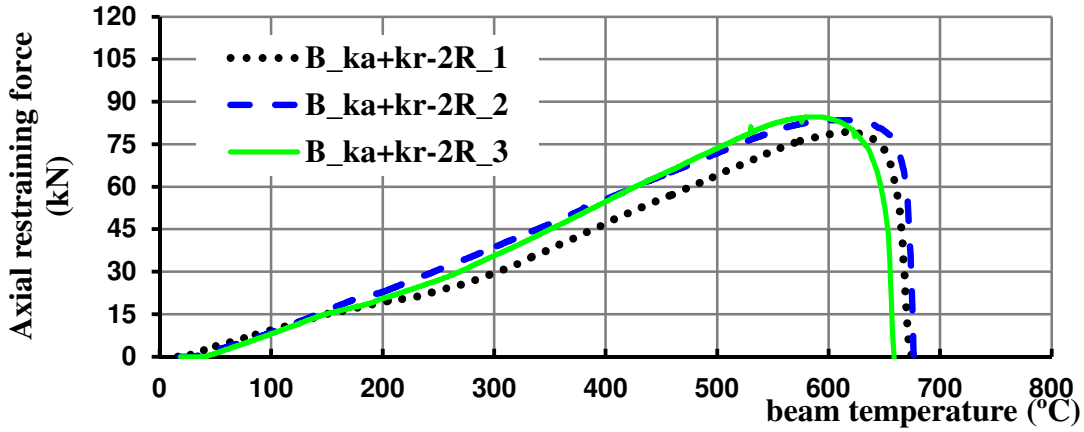

Figure E.64 – Evolution of axial restraining forces in axially and rotationally restrained 2R beams as a function of its mean temperature

APPENDIX F Photos of the Experimental Tests on Cold-Formed Steel Beams under Fire Conditions

F1 Simply supported beams

F1.1 C beams

Figure F.1 – Front views of the failure mode of the specimen B-C_1

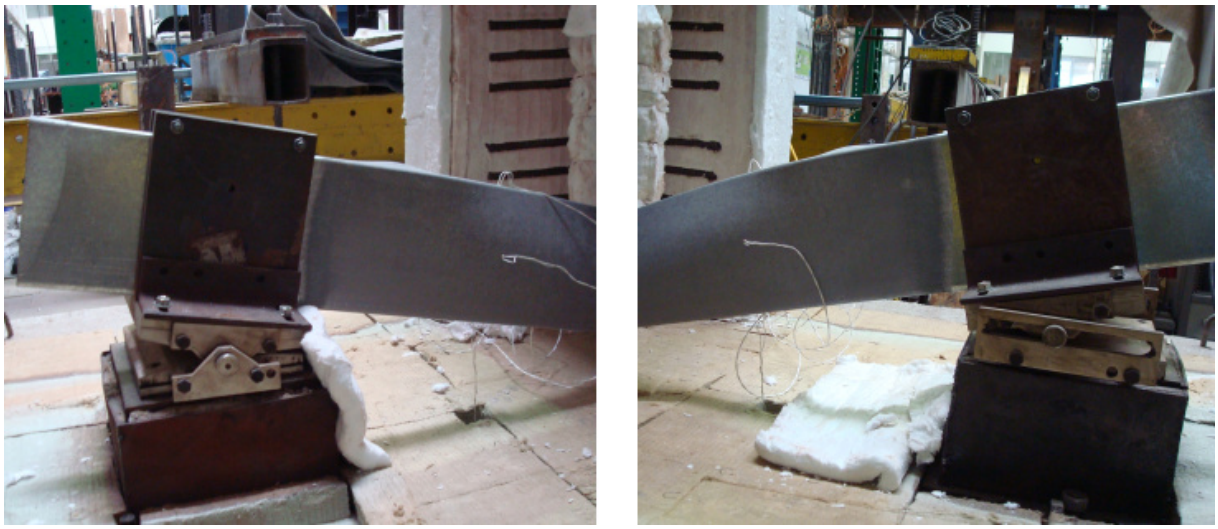

Figure F.2 – Back views of the failure mode of the specimen B-C_1

Figure F.3 – Lateral views of the failure mode of the specimen B-C_1

Figure F.4 – Detail view of the failure mode of the specimen B-C_1

Figure F.5 – Front views of the failure mode of the specimen B-C_2

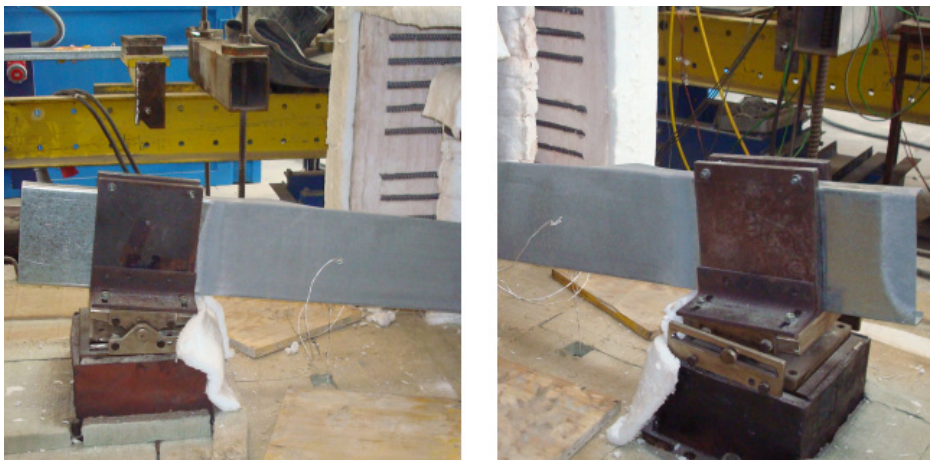

Figure F.6 – Back views of the failure mode of the specimen B-C_2

Figure F.7 – Lateral views of the failure mode of the specimen B-C_2

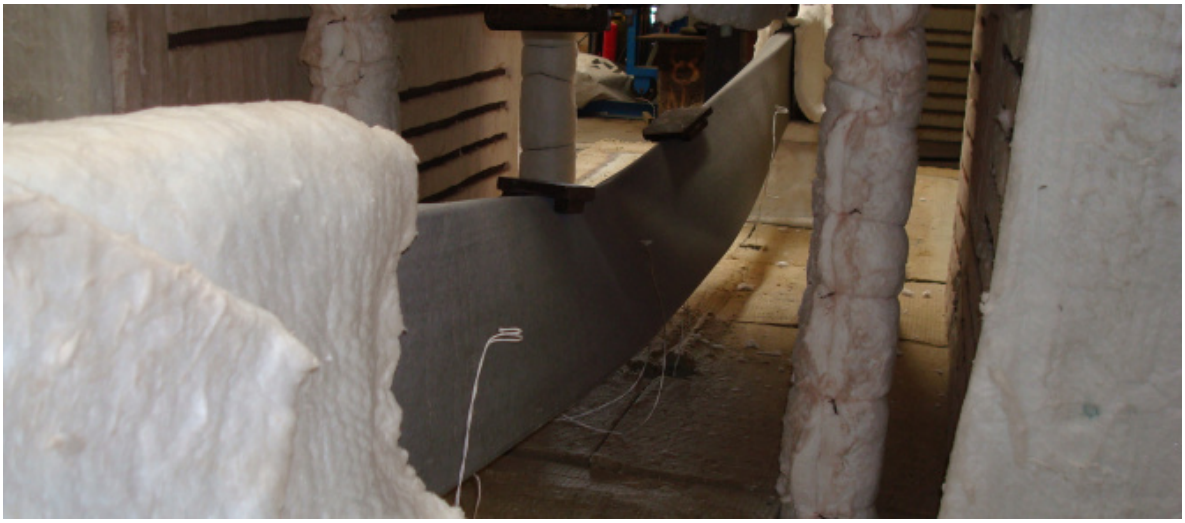

Figure F.8 – Detail view of the failure mode of the specimen B-C_2

Figure F.9 – Front views of the failure mode of the specimen B-C_3

Figure F.10 – Back views of the failure mode of the specimen B-C_3

Figure F.11 – Lateral views of the failure mode of the specimen B-C_3

Figure F.12 – Detail view of the failure mode of the specimen B-C_3

F1.2 Lipped I beams

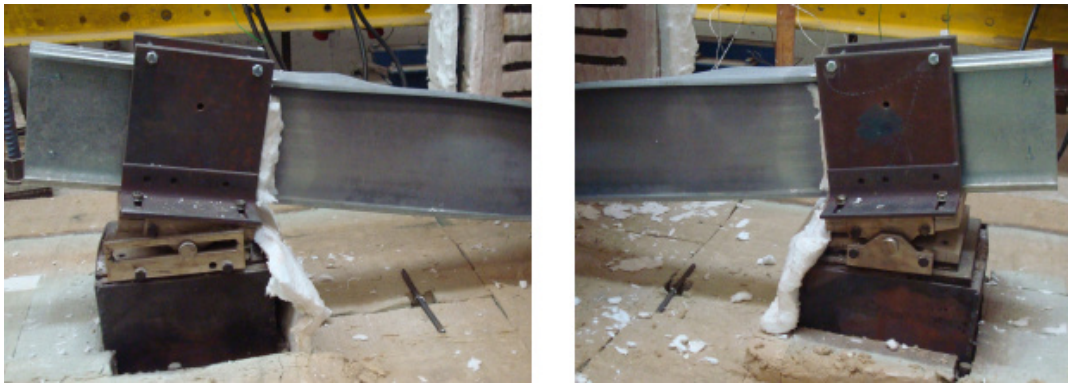

Figure F.13 – Front views of the failure mode of the specimen B-I_1

Figure F.14 – Back views of the failure mode of the specimen B-I_1

Figure F.15 – Lateral views of the failure mode of the specimen B-I_1

Figure F.16 – Detail view of the failure mode of the specimen B-I_1

Figure F.17 – Front views of the failure mode of the specimen B-I_2

Figure F.18 – Back views of the failure mode of the specimen B-I_2

Figure F.19 – Lateral views of the failure mode of the specimen B-I_2

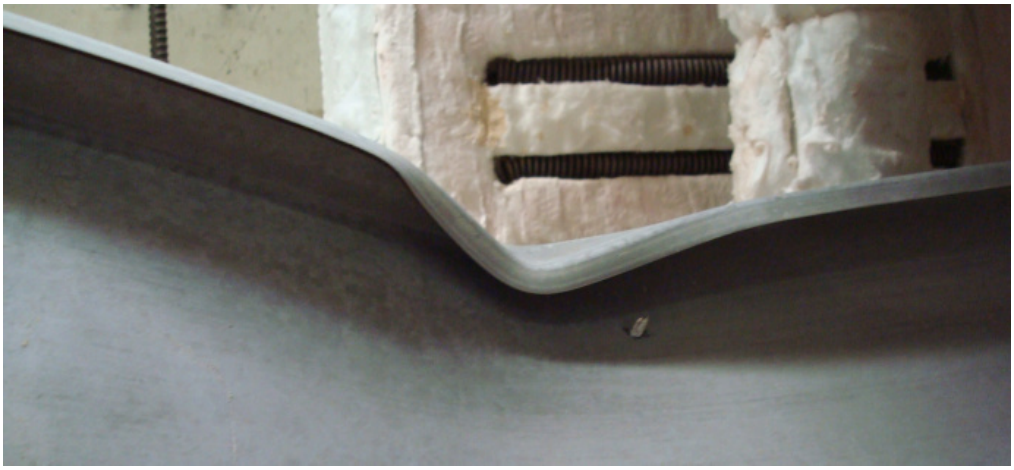

Figure F.20 – Detail view of the failure mode of the specimen B-I_2

Figure F.21 – Front views of the failure mode of the specimen B-I_3


Figure F.22 – Back views of the failure mode of the specimen B-I_3



Figure F.23 – Lateral views of the failure mode of the specimen B-I_3

Figure F.24 – Detail view of the failure mode of the specimen B-I_3

F1.3 R beams

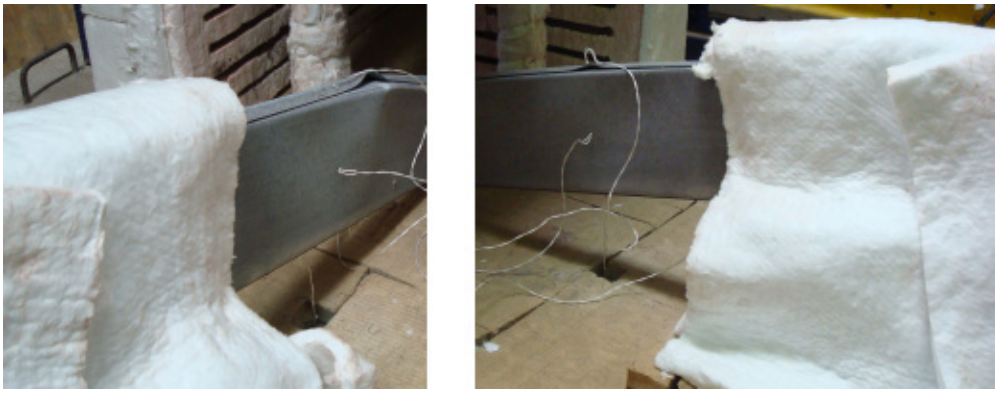

Figure F.25 – Front views of the failure mode of the specimen B-R_1

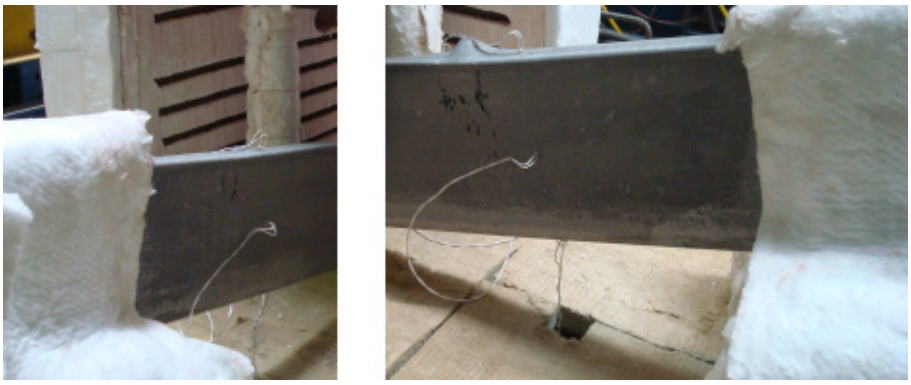

Figure F.26 – Back views of the failure mode of the specimen B-R_1

Figure F.27 – Lateral views of the failure mode of the specimen B-R_1

Figure F.28 – Detail view of the failure mode of the specimen B-R_1

Figure F.29 – Lateral views of the failure mode of the specimen B-R_2

Figure F.30 – Detail view of the failure mode of the specimen B-R_2

Figure F.31 – Front views of the failure mode of the specimen B-R_3

Figure F.32 – Back views of the failure mode of the specimen B-R_3

Figure F.33 – Lateral views of the failure mode of the specimen B-R_3

Figure F.34 – Detail view of the failure mode of the specimen B-R_3

F1.4 2R beams

Figure F.35 – Front views of the failure mode of the specimen B-2R_1

Figure F.36 – Back views of the failure mode of the specimen B-2R_1

Figure F.37 – Lateral views of the failure mode of the specimen B-2R_1

Figure F.38 – Detail view of the failure mode of the specimen B-2R_1

Figure F.39 – Front views of the failure mode of the specimen B-2R_2

Figure F.40 – Back views of the failure mode of the specimen B-2R_2

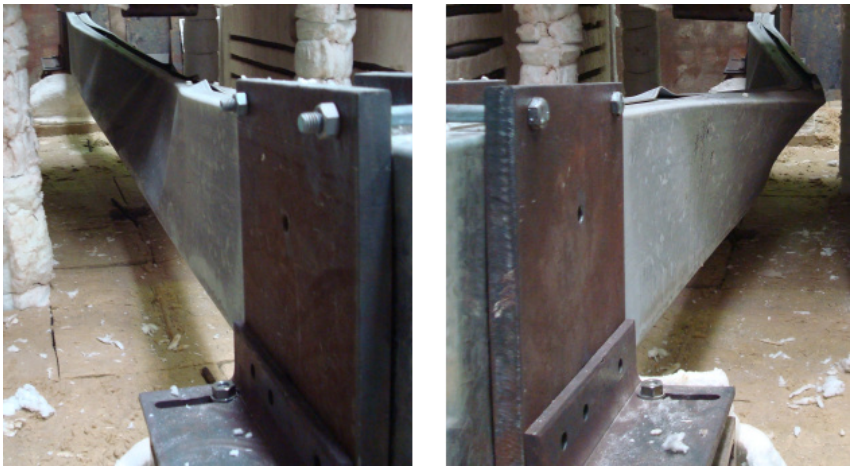

Figure F.41 – Lateral views of the failure mode of the specimen B-2R_2

Figure F.42 – Detail view of the failure mode of the specimen B-2R_2

Figure F.43 – Front views of the failure mode of the specimen B-2R_3

Figure F.44 – Back views of the failure mode of the specimen B-2R_3

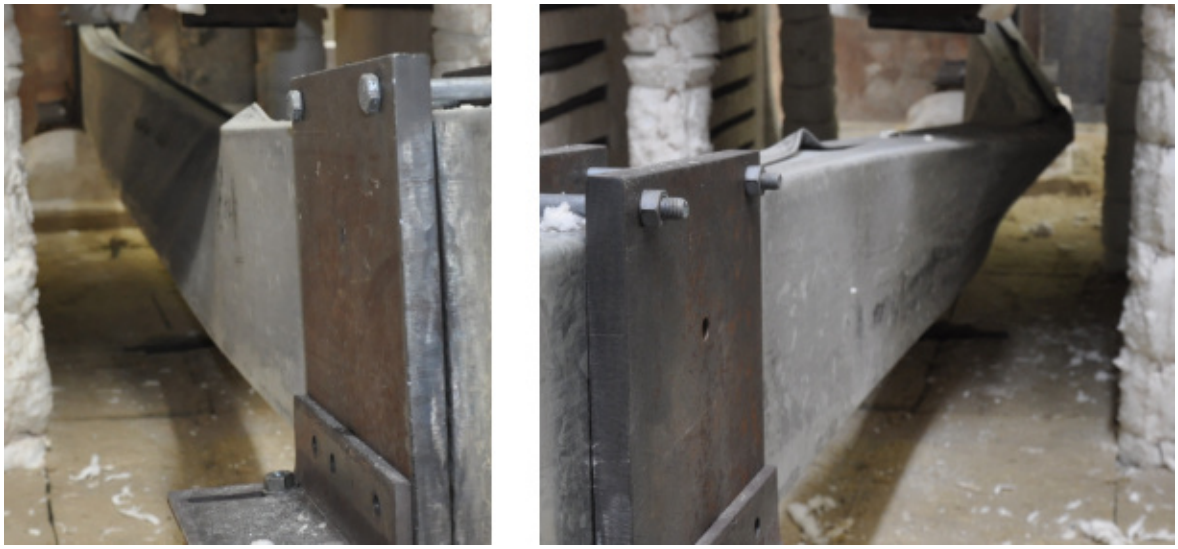

Figure F.45 – Lateral views of the failure mode of the specimen B-2R_3

Figure F.46 – Detail view of the failure mode of the specimen B-2R_3

F2 Axially restrained beams

F2.1 C beams

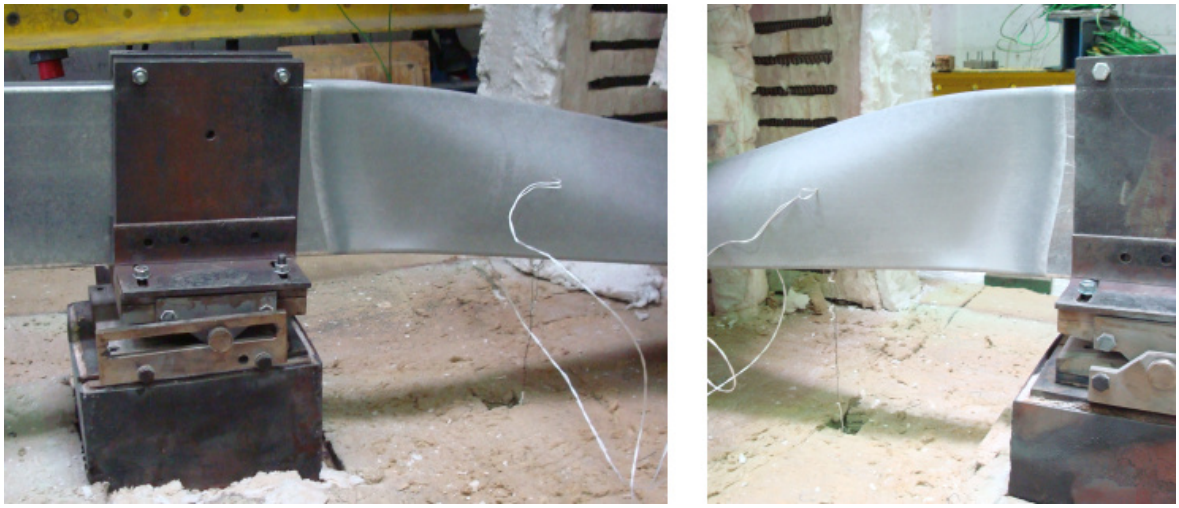

Figure F.47 – Back views of the failure mode of the specimen B_ka-C_1

Figure F.48 – Front views of the failure mode of the specimen B_ka-C_1

Figure F.49 – Lateral views of the failure mode of the specimen B_ka-C_1

Figure F.50 – Detail view of the failure mode of the specimen B_ka-C_1

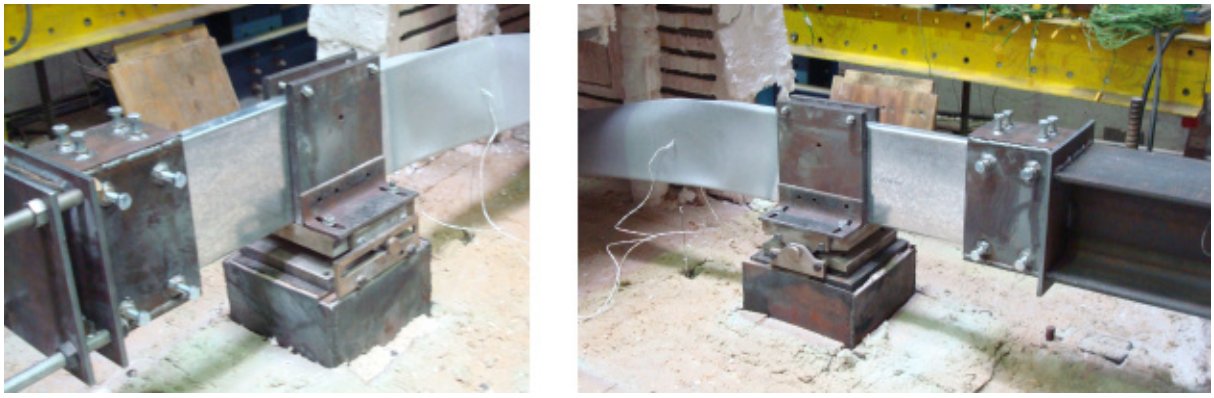

Figure F.51 – Back views of the failure mode of the specimen B_ka-C_2

Figure F.52 – Front views of the failure mode of the specimen B_ka-C_2

Figure F.53 – Lateral views of the failure mode of the specimen B_ka-C_2

Figure F.54 – Detail view of the failure mode of the specimen B_ka-C_2

Figure F.55 – Front views of the failure mode of the specimen B_ka-C_3

Figure F.56 – Lateral views of the failure mode of the specimen B_ka-C_3

F2.2 Lipped I beams

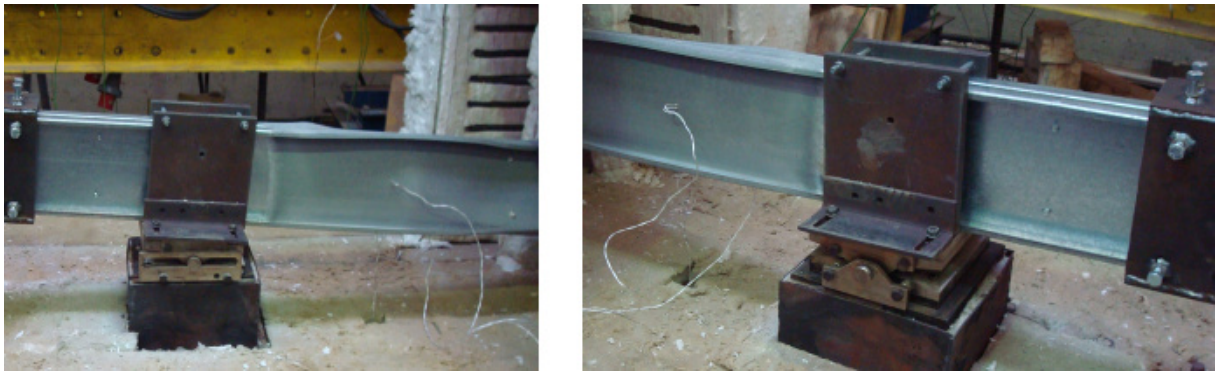

Figure F.57 – Front views of the failure mode of the specimen B_ka-I_1

Figure F.58 – Lateral views of the failure mode of the specimen B_ka-I_1

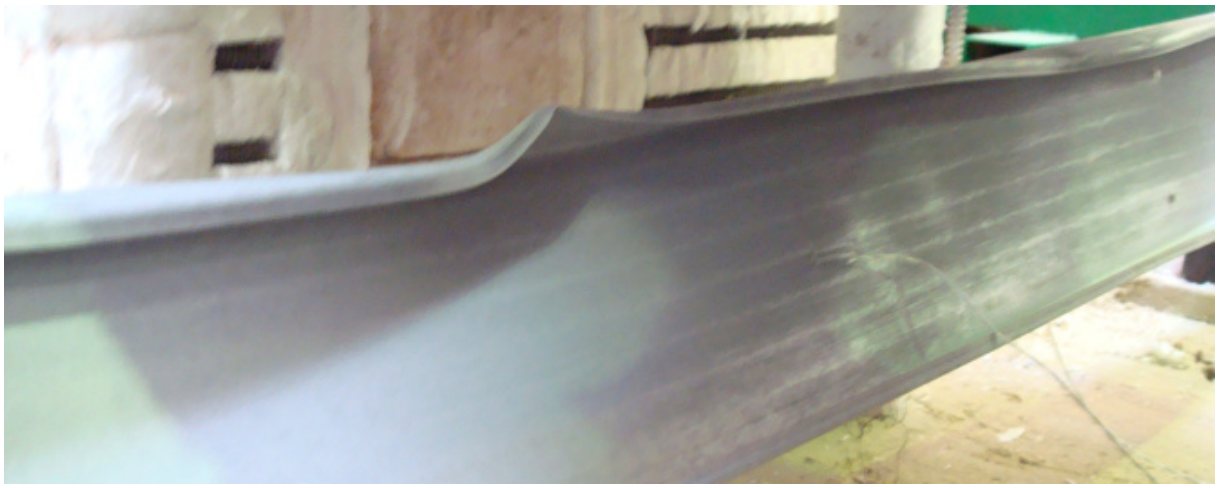

Figure F.59 – Detail view of the failure mode of the specimen B_ka-I_1

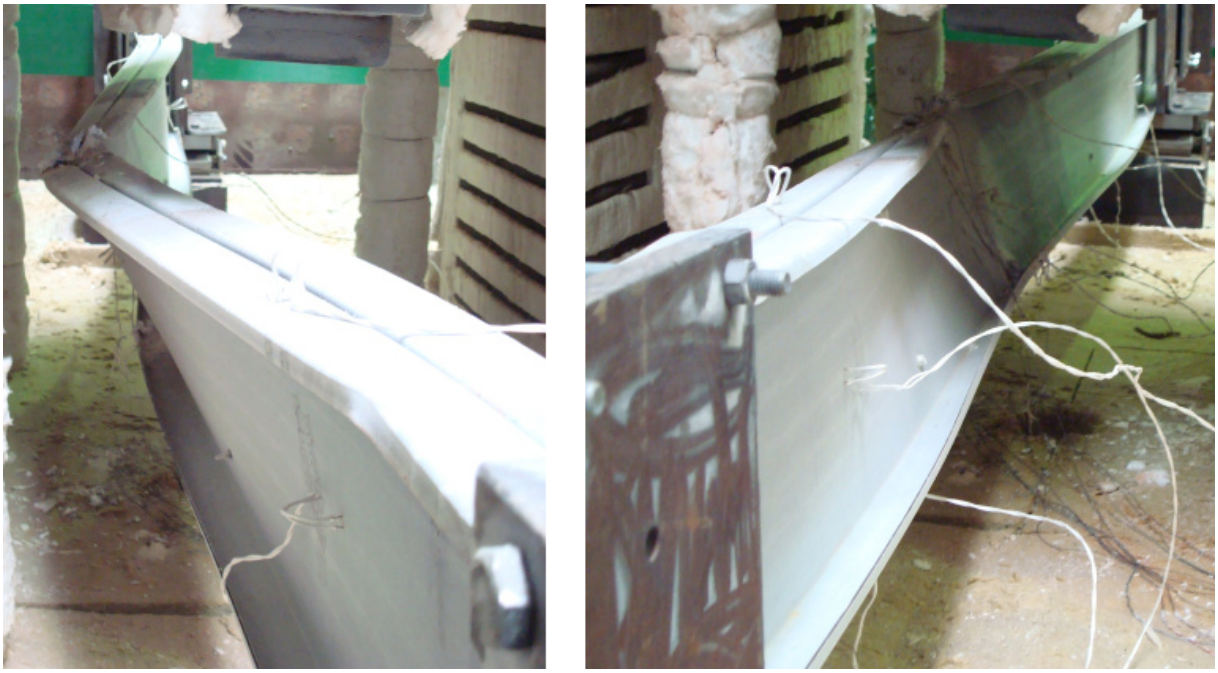

Figure F.60 – Lateral views of the failure mode of the specimen B_ka-I_2

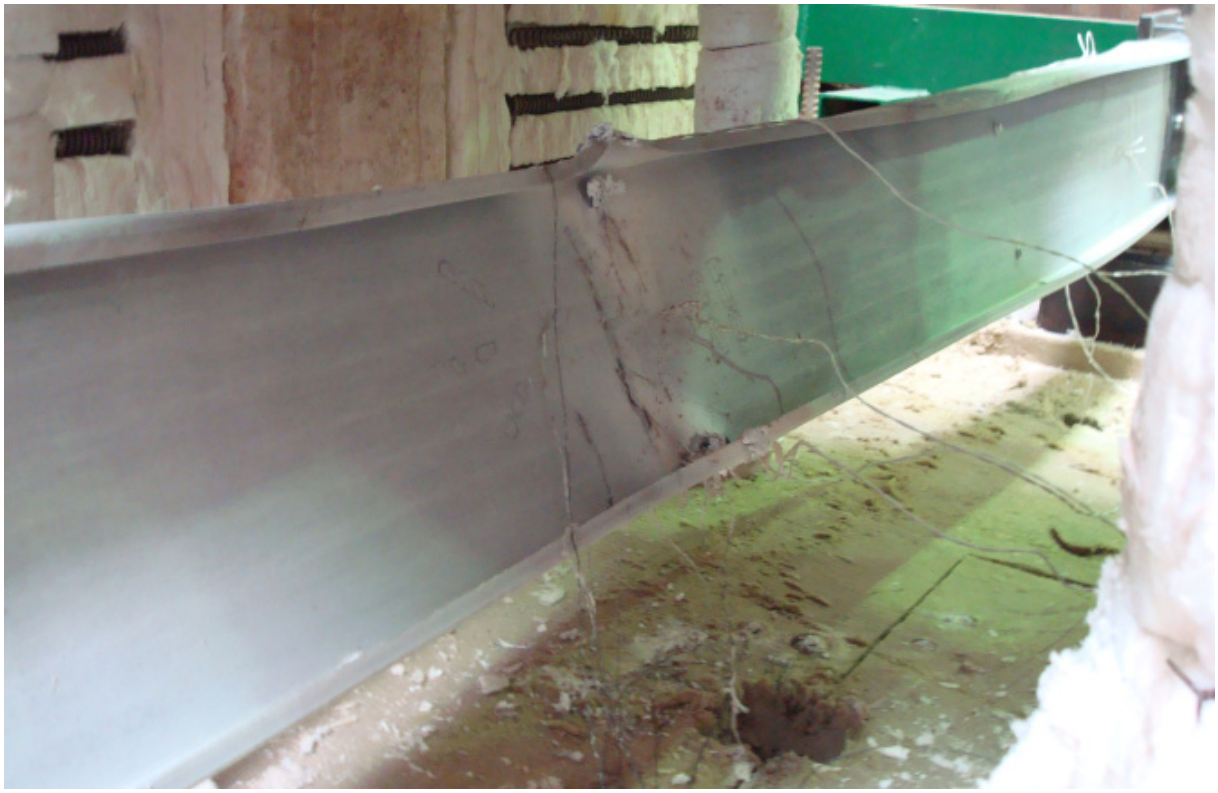

Figure F.61 – Detail view of the failure mode of the specimen B_ka-I_2

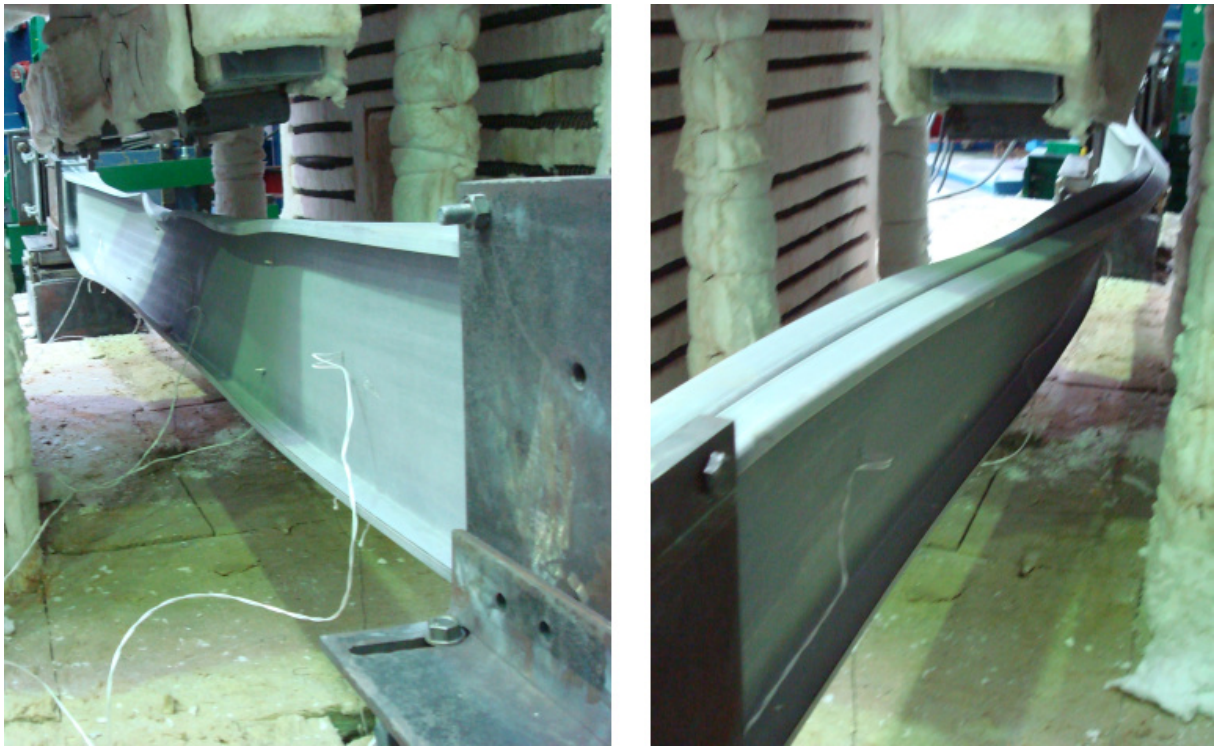

Figure F.62 – Lateral views of the failure mode of the specimen B_ka-I_3

Figure F.63 – Detail view of the failure mode of the specimen B_ka-I_3

F2.3 R beams

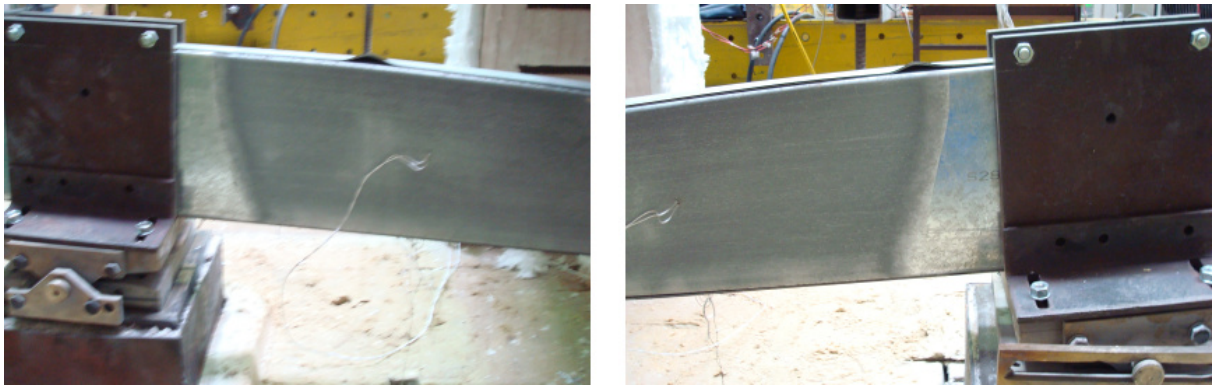

Figure F.64 – Front views of the failure mode of the specimen B_ka-R_1

Figure F.65 – Lateral views of the failure mode of the specimen B_ka-R_1

Figure F.66 – Lateral views of the failure mode of the specimen B_ka-R_2

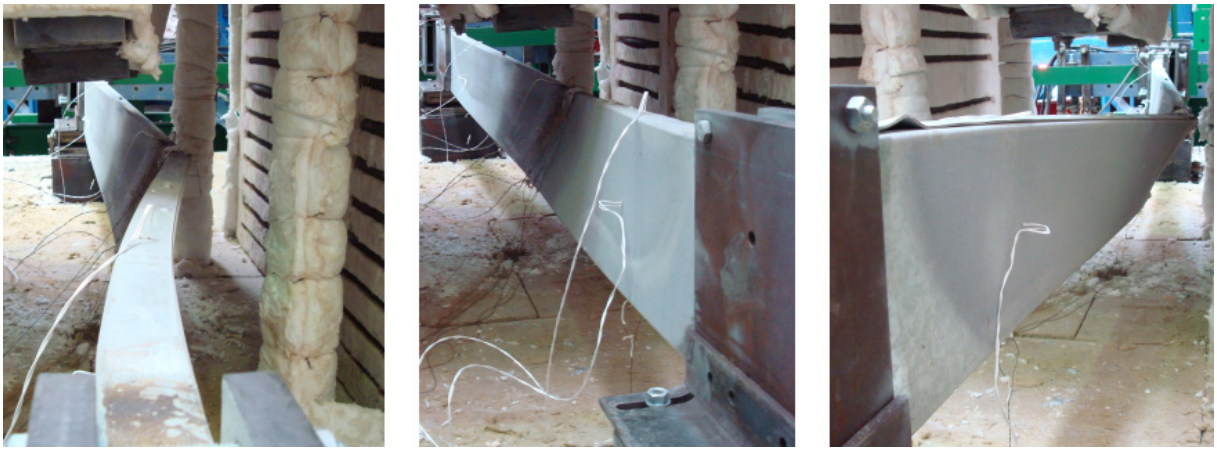

Figure F.67 – Lateral views of the failure mode of the specimen B_ka-R_3

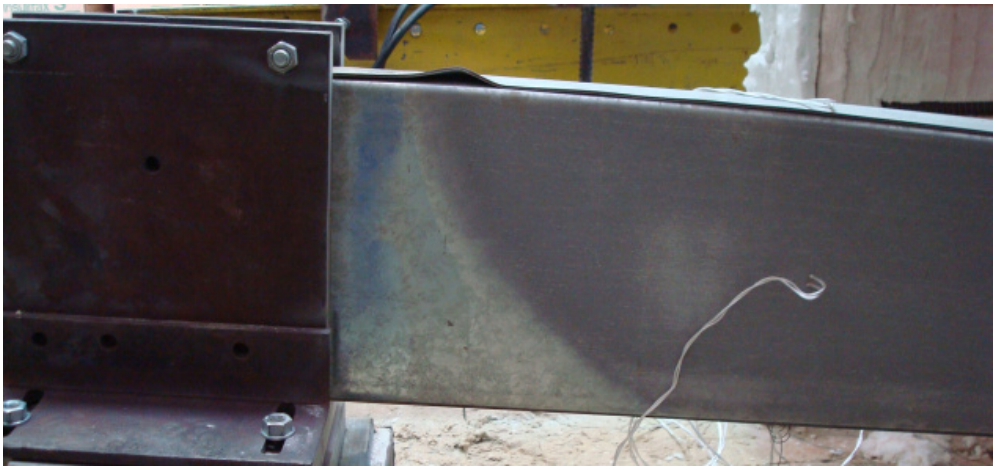

Figure F.68 – Detail view of the failure mode of the specimen B_ka-R_3

F2.4 2R beams

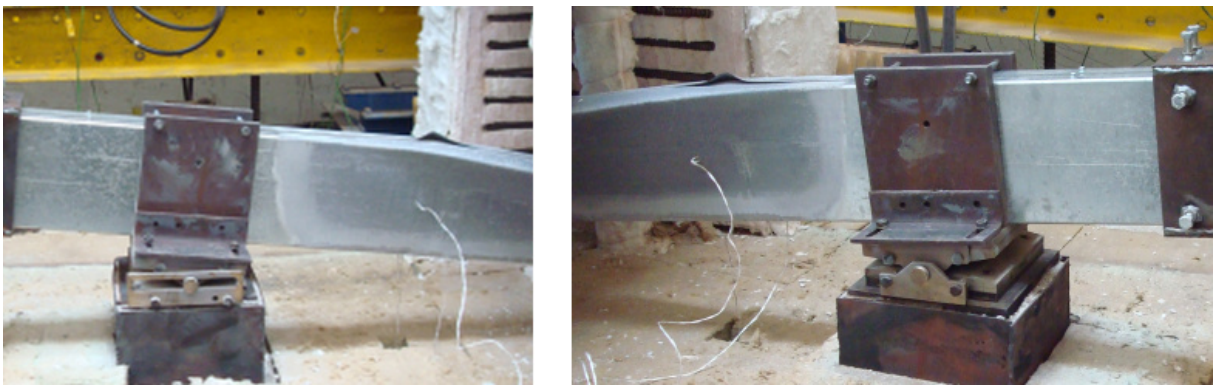

Figure F.69 – Front views of the failure mode of the specimen B_ka-2R_1

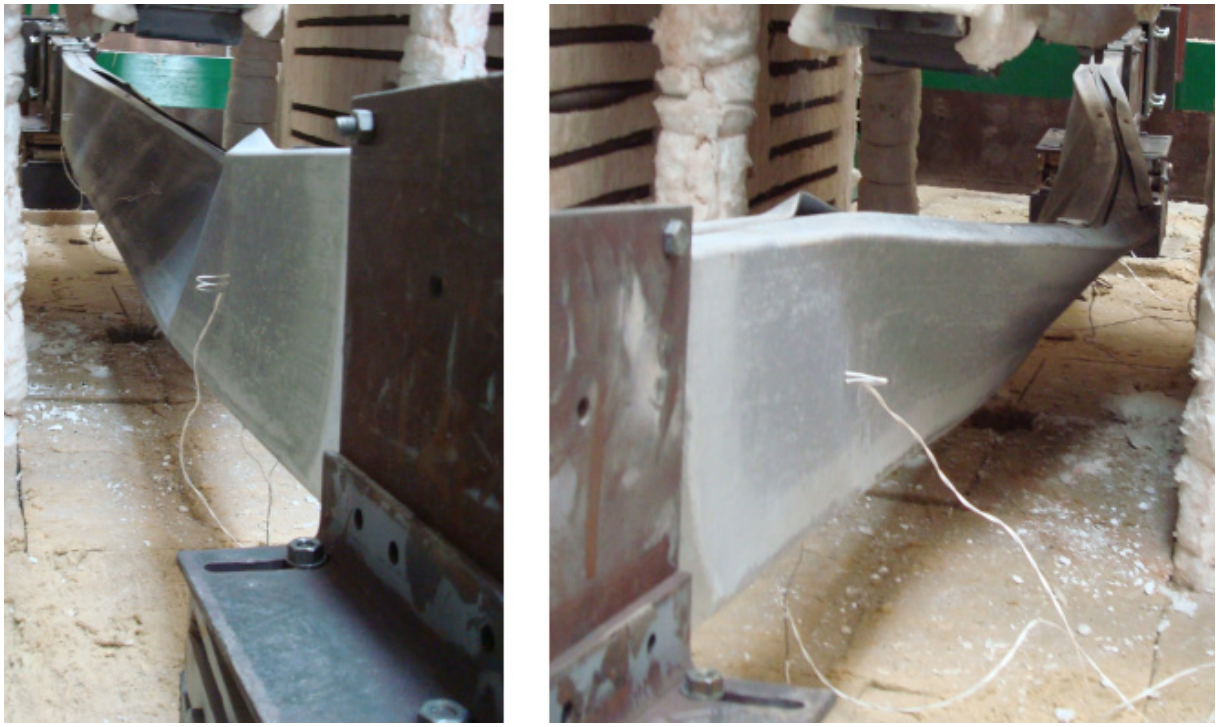

Figure F.70 – Lateral views of the failure mode of the specimen B_ka-2R_1

Figure F.71 – Detail view of the failure mode of the specimen B_ka-2R_1

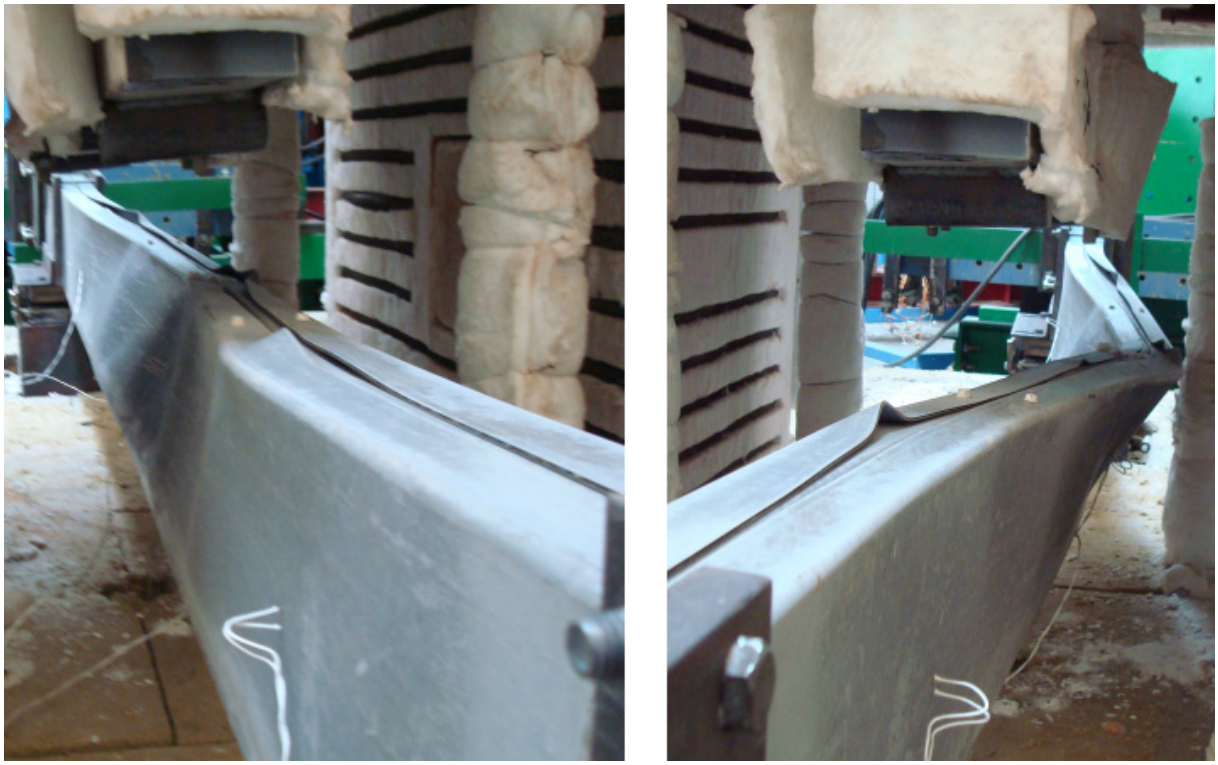

Figure F.72 – Lateral views of the failure mode of the specimen B_ka-2R_2

Figure F.73 – Detail view of the failure mode of the specimen B_ka-2R_2

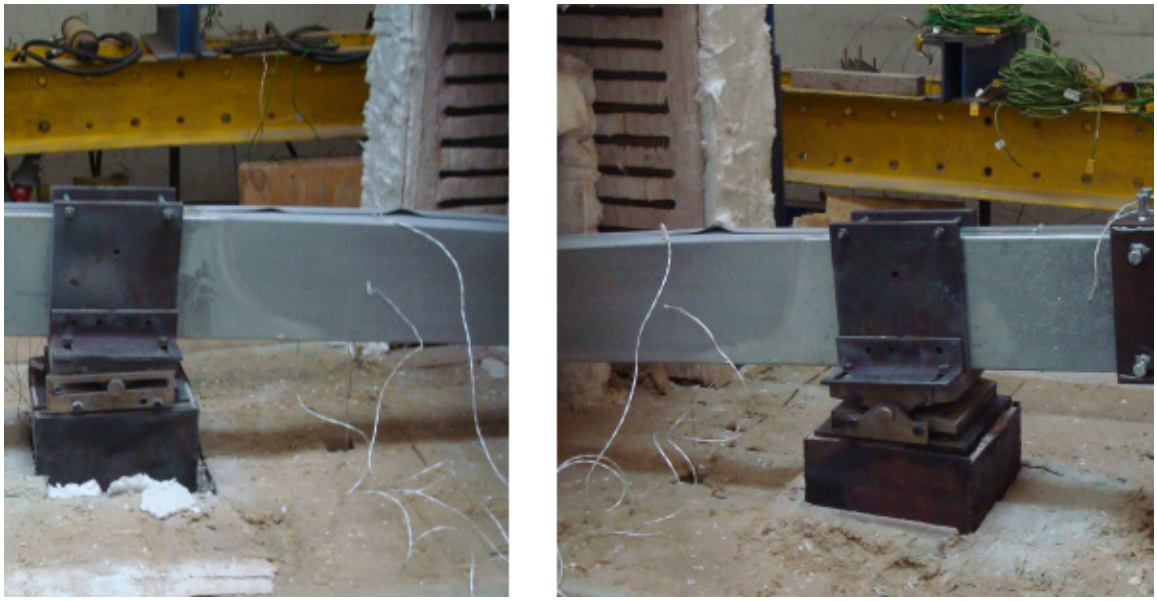

Figure F.74 – Front views of the failure mode of the specimen B_ka-2R_3

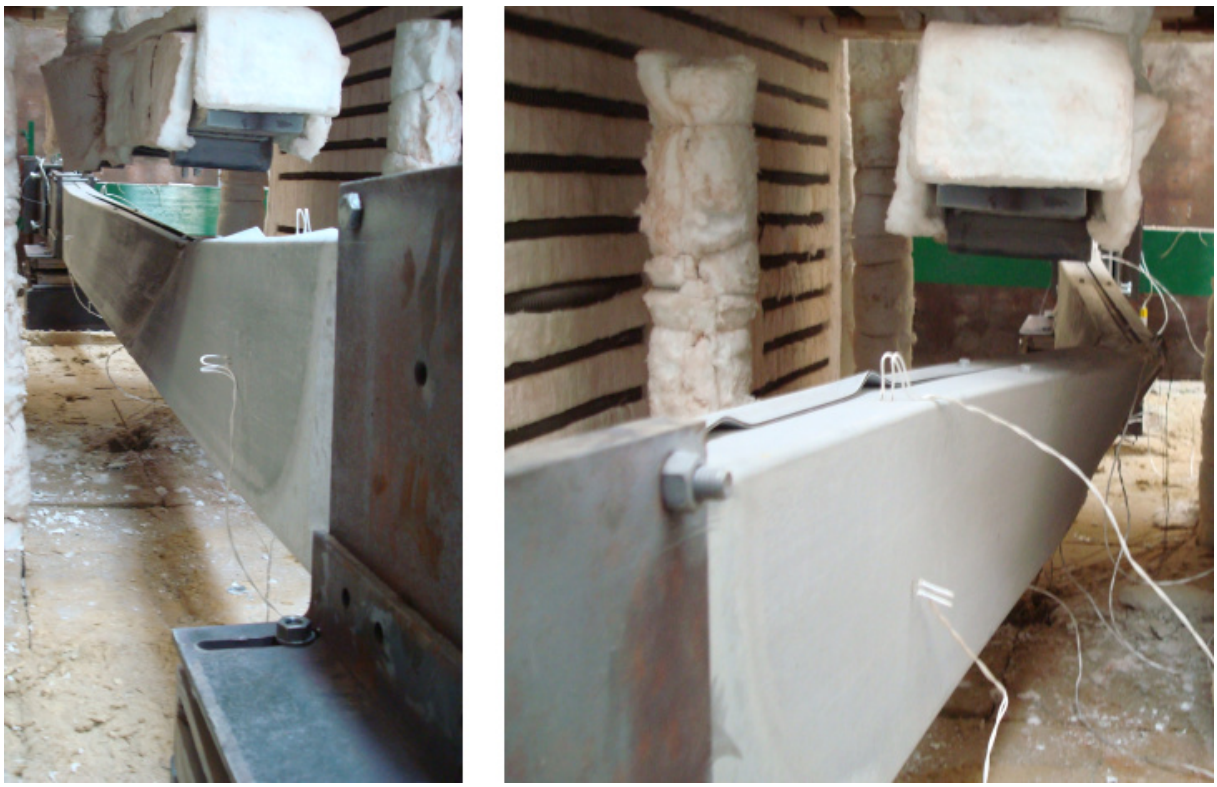

Figure F.75 – Lateral views of the failure mode of the specimen B_ka-2R_3

F3 Axially and rotationally restrained beams

F3.1 C beams

Figure F.76 – Front views of the failure mode of the specimen B_ka+kr-C_1

Figure F.77 – Lateral views of the failure mode of the specimen B_ka+kr-C_1

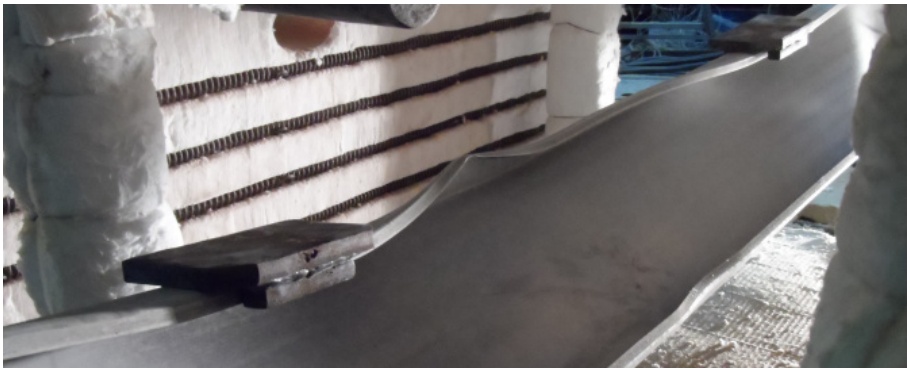

Figure F.78 – Detail view of the failure mode of the specimen B_ka+kr-C_1

Figure F.79 – Front views of the failure mode of the specimen B_ka+kr-C_2

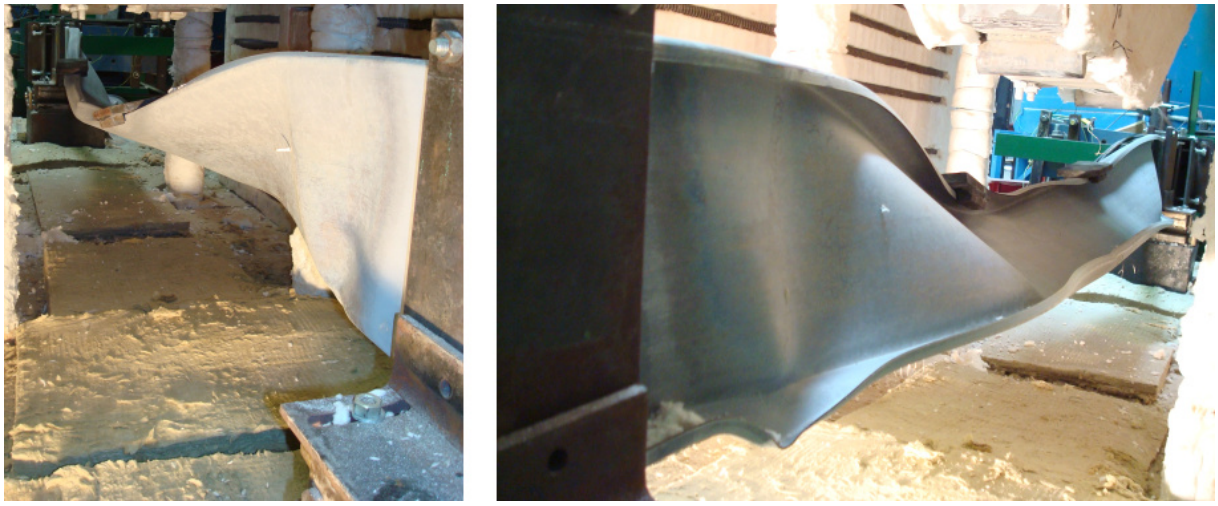

Figure F.80 – Lateral views of the failure mode of the specimen B_ka+kr-C_2

Figure F.81 – Detail view of the failure mode of the specimen B_ka+kr-C_2

Figure F.82 – Front views of the failure mode of the specimen B_ka+kr-C_3

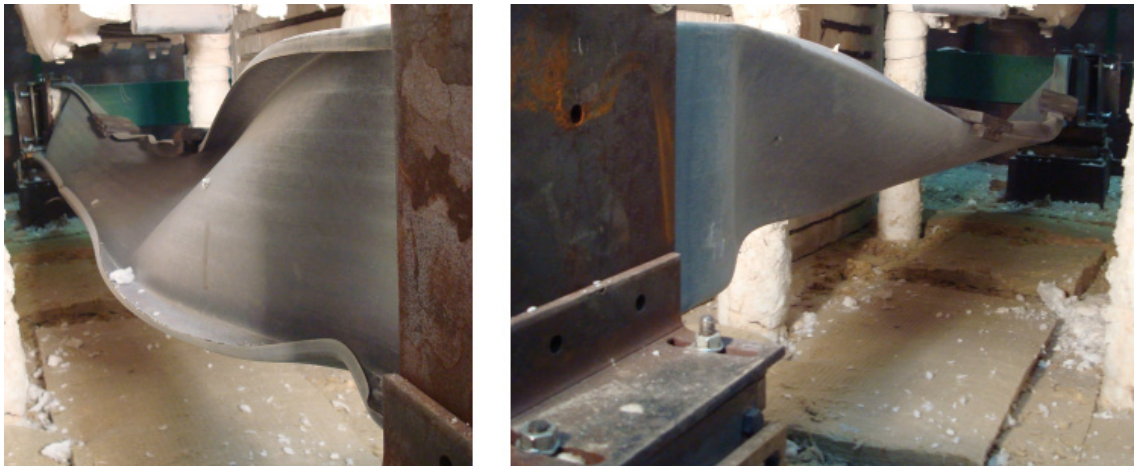

Figure F.83 – Lateral views of the failure mode of the specimen B_ka+kr-C_3

Figure F.84 – Detail view of the failure mode of the specimen B_ka+kr-C_3

F3.2 Lipped I beams

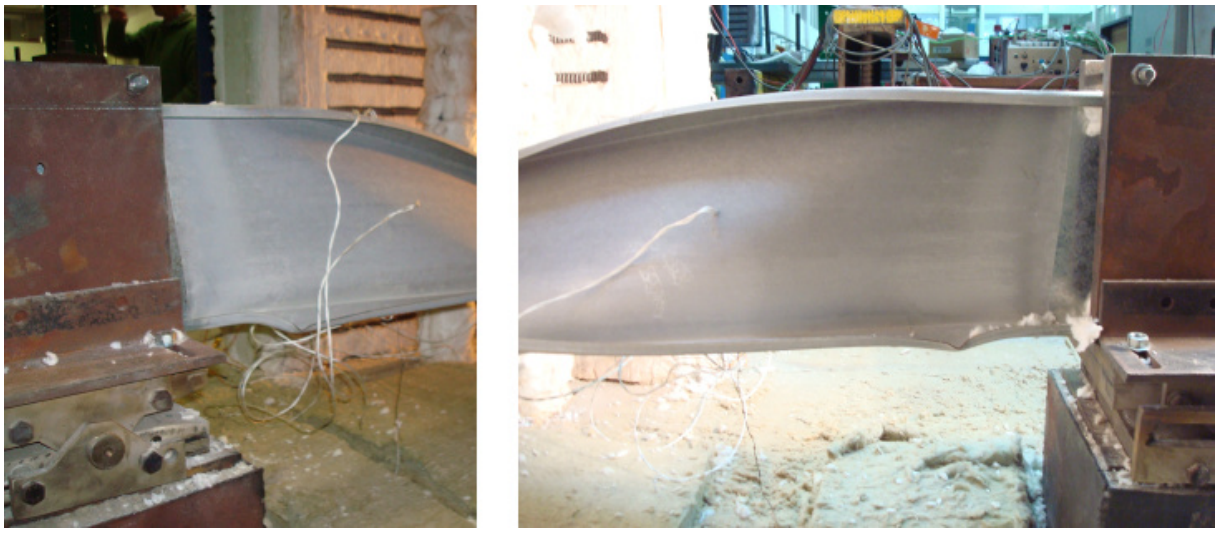

Figure F.85 – Front views of the failure mode of the specimen B_ka+kr-I_1

Figure F.86 – Lateral views of the failure mode of the specimen B_ka+kr-I_1

Figure F.87 – Front views of the failure mode of the specimen B_ka+kr-I_2

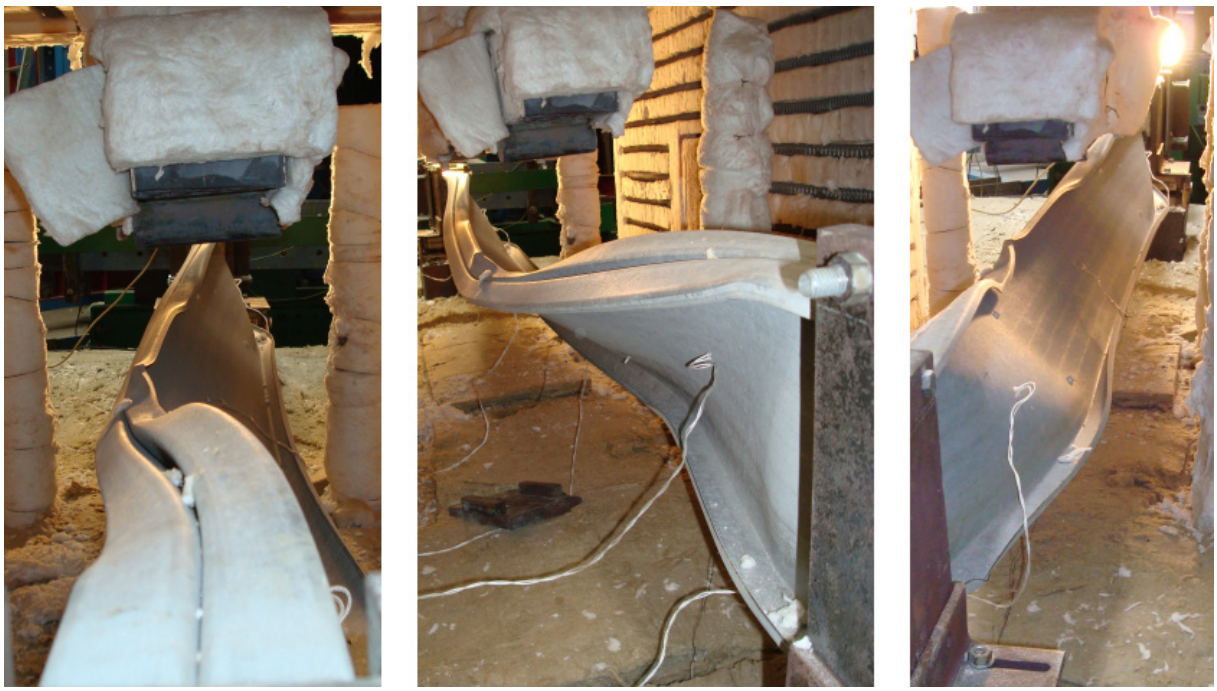

Figure F.88 – Lateral views of the failure mode of the specimen B_ka+kr-I_2

Figure F.89 – Detail view of the failure mode of the specimen B_ka+kr-I_2

F3.3 R beams

Figure F.90 – Lateral views of the failure mode of the specimen B_ka+kr-R_1

Figure F.91 – Detail view of the failure mode of the specimen B_ka+kr-R_1

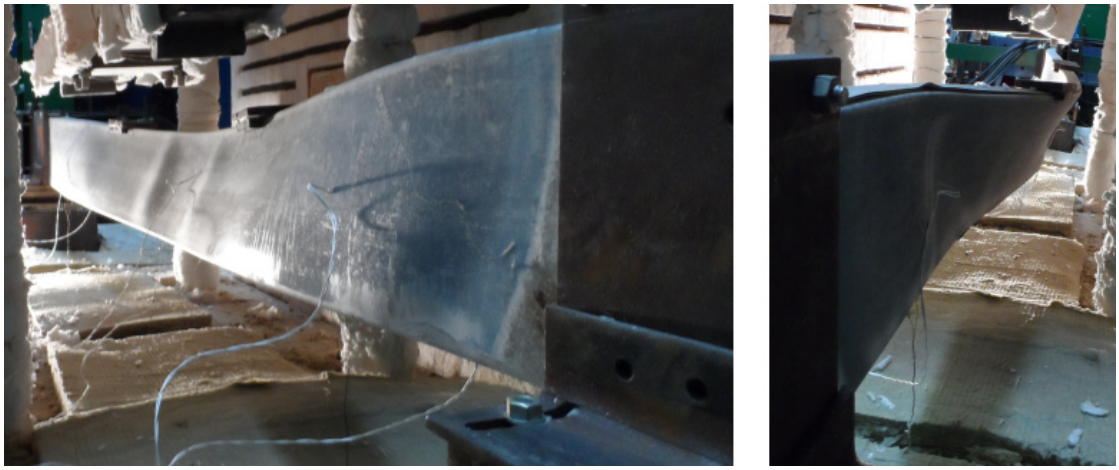

Figure F.92 – Lateral views of the failure mode of the specimen B_ka+kr-R_2

Figure F.93 – Front views of the failure mode of the specimen B_ka+kr-R_3

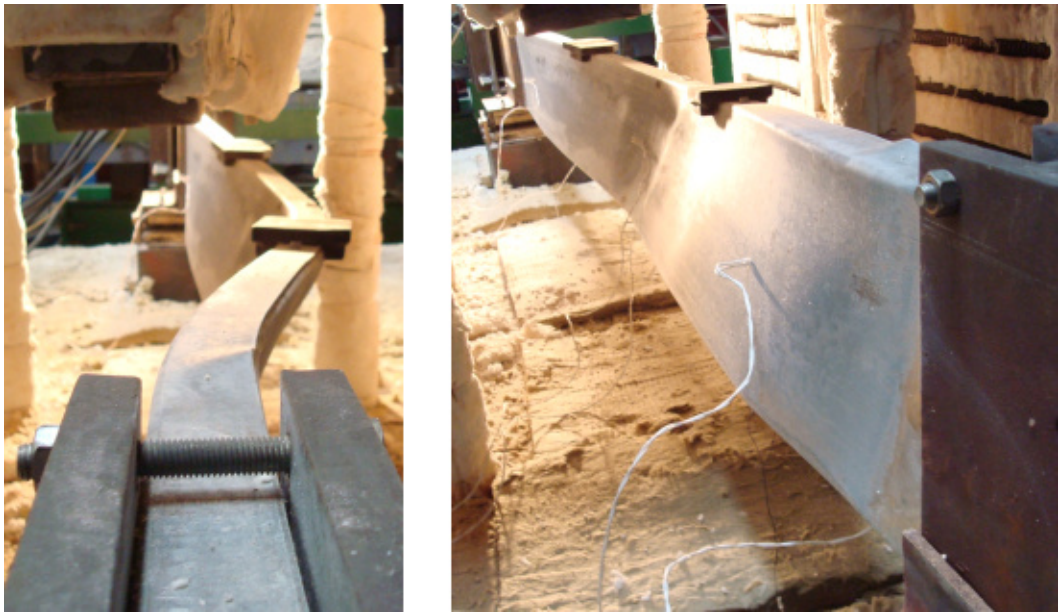

Figure F.94 – Lateral views of the failure mode of the specimen B_ka+kr-R_3

F3.4 2R beams

Figure F.95 – Front views of the failure mode of the specimen B_ka+kr-2R_1

Figure F.96 – Lateral views of the failure mode of the specimen B_ka+kr-2R_1

Figure F.97 – Detail view of the failure mode of the specimen B_ka+kr-2R_1

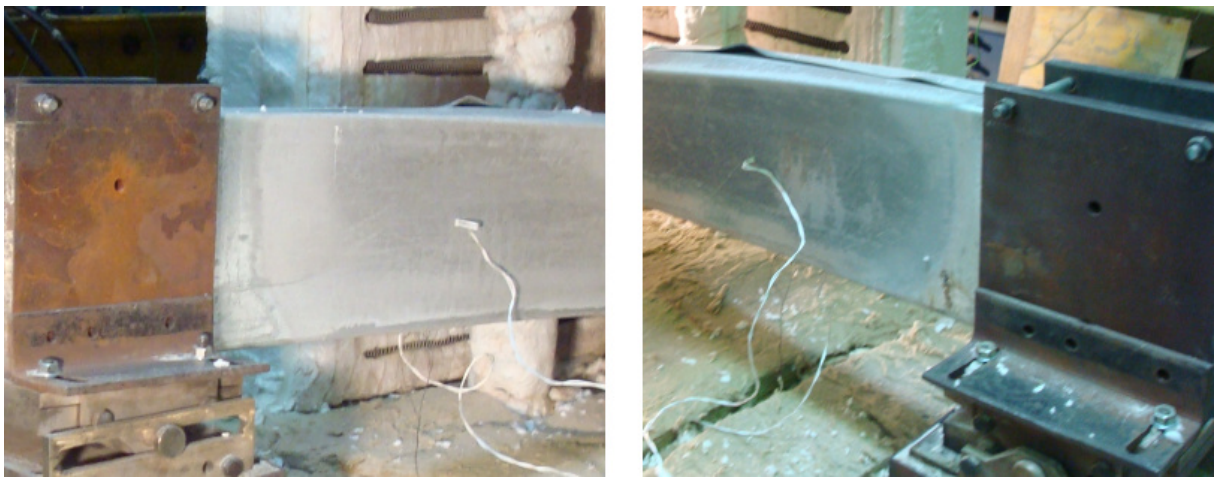

Figure F.98 – Front views of the failure mode of the specimen B_ka+kr-2R_2

Figure F.99 – Lateral views of the failure mode of the specimen B_ka+kr-2R_2

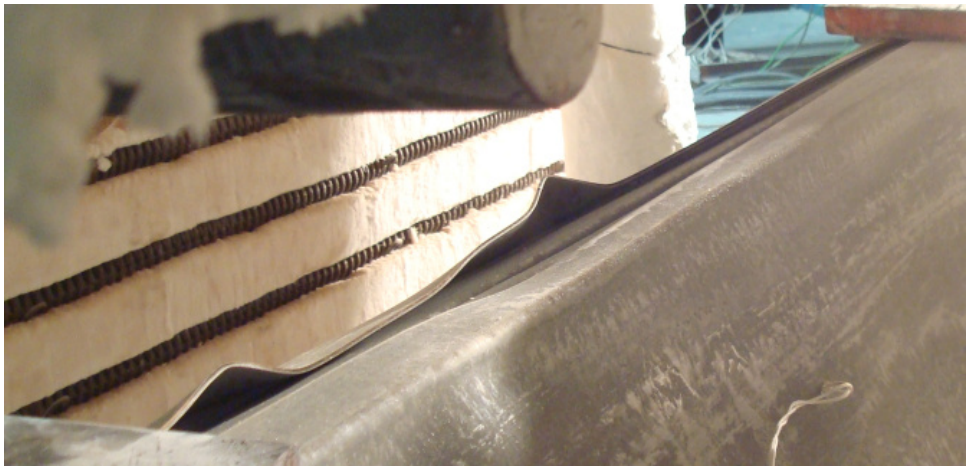

Figure F.100 – Detail view of the failure mode of the specimen B_ka+kr-2R_2

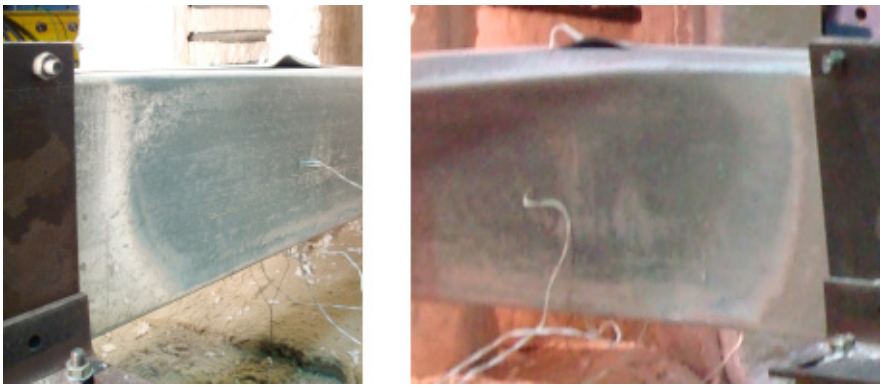

Figure F.101 – Front views of the failure mode of the specimen B_ka+kr-2R_3

Figure F.102 – Lateral views of the failure mode of the specimen B_ka+kr-2R_3

Figure F.103 – Detail view of the failure mode of the specimen B_ka+kr-2R_3

APPENDIX G Tensile Coupon Tests for Structural Steel S280GD+Z at Ambient Temperature

Figure G.1 – Tensile testing device

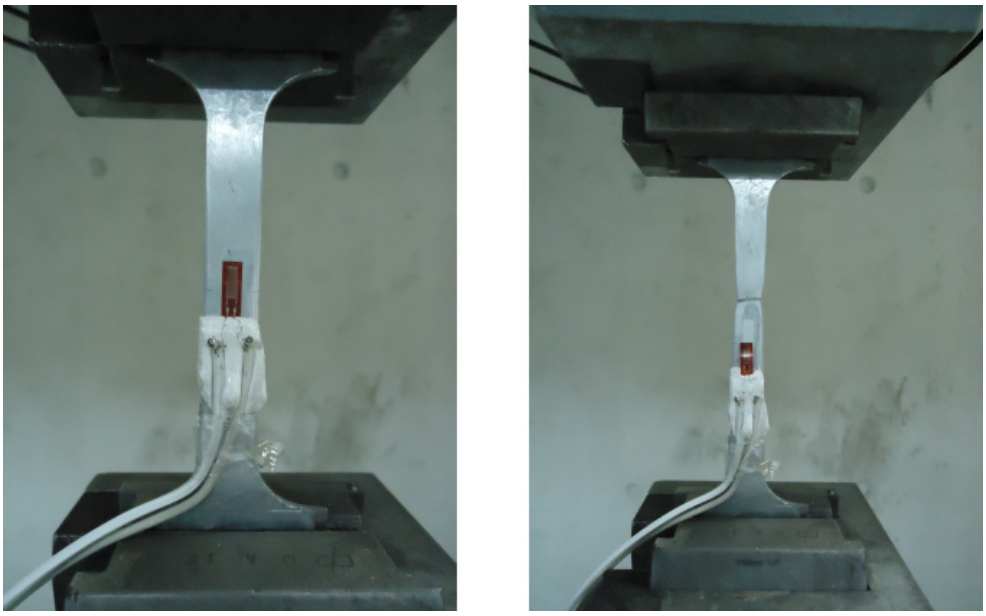

Figure G.2 – Coupon specimen

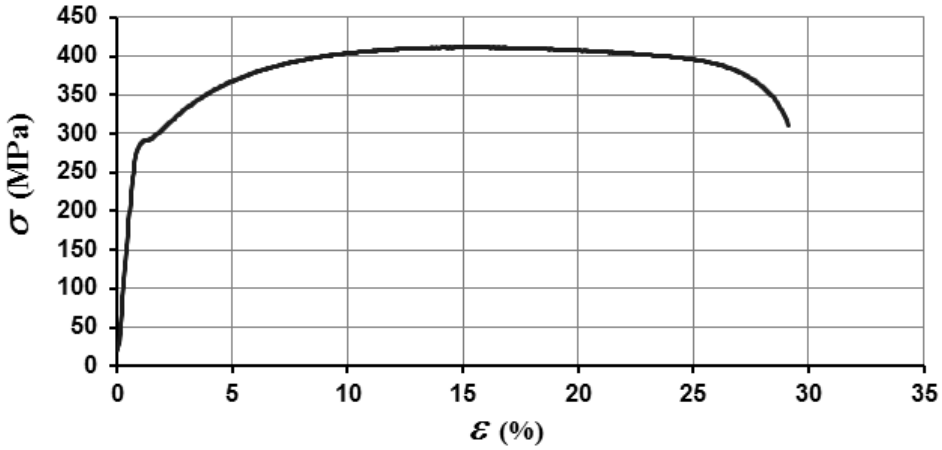

Figure G.3 – Stress-strain relationship of the specimen A up to rupture

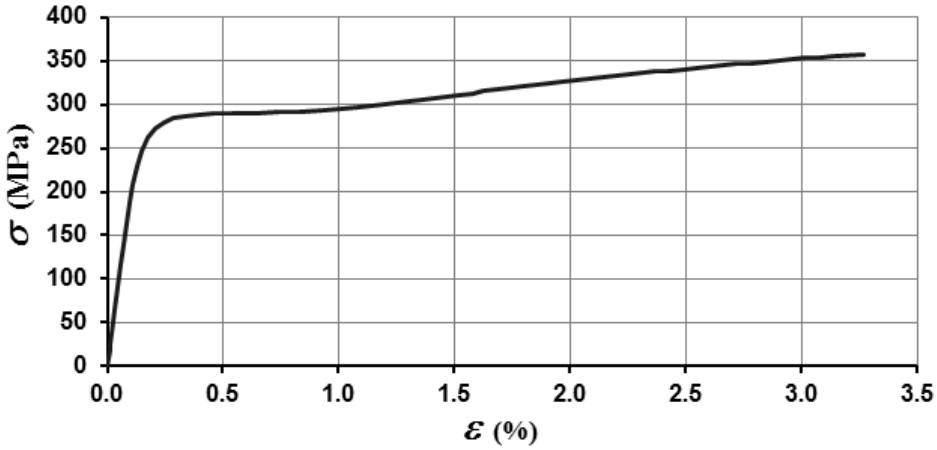

Figure G.4 – Stress-strain relationship of the specimen A up to yield plateau

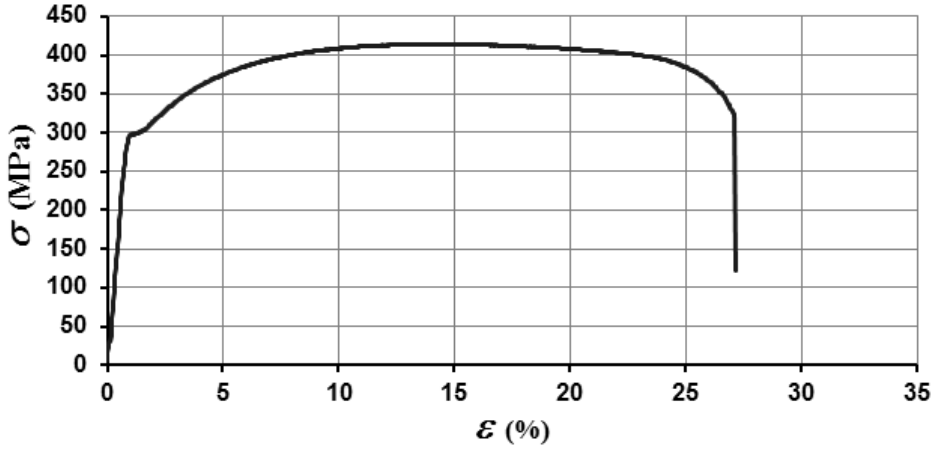

Figure G.5 – Stress-strain relationship of the specimen B up to rupture

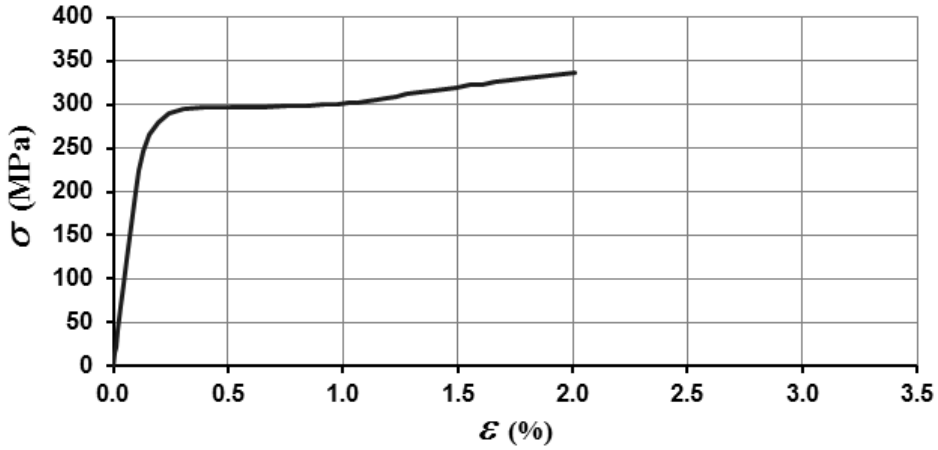

Figure G.6 – Stress-strain relationship of the specimen B up to yield plateau

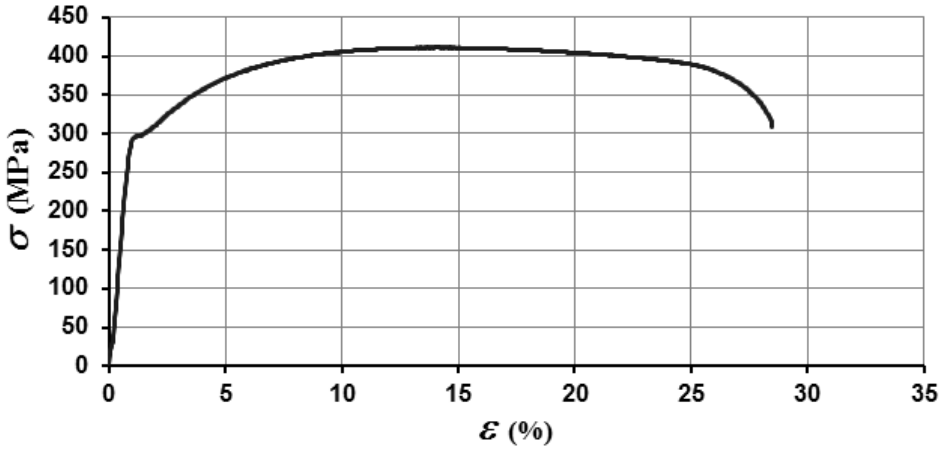

Figure G.7 – Stress-strain relationship of the specimen C up to rupture

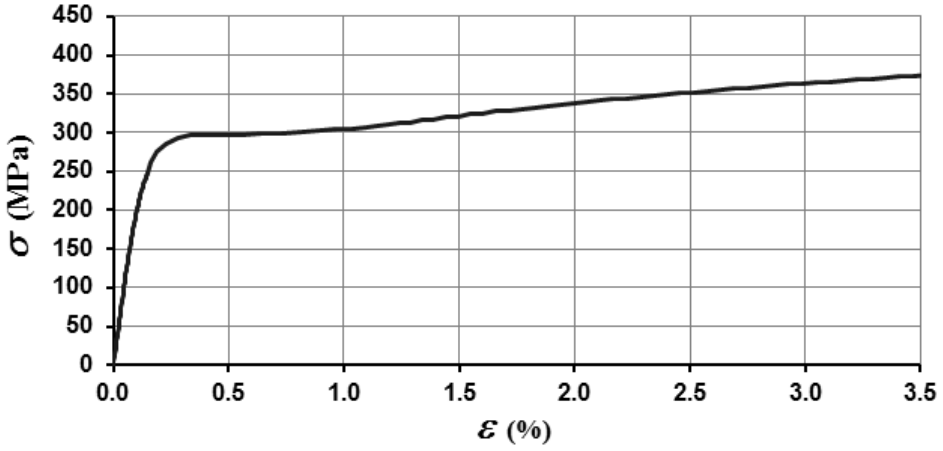

Figure G.8 – Stress-strain relationship of the specimen C up to yield plateau

APPENDIX H Comparison of Numerical Results with the Proposed Simplified Equations for the Fire Design of Cold-Formed Steel Beams

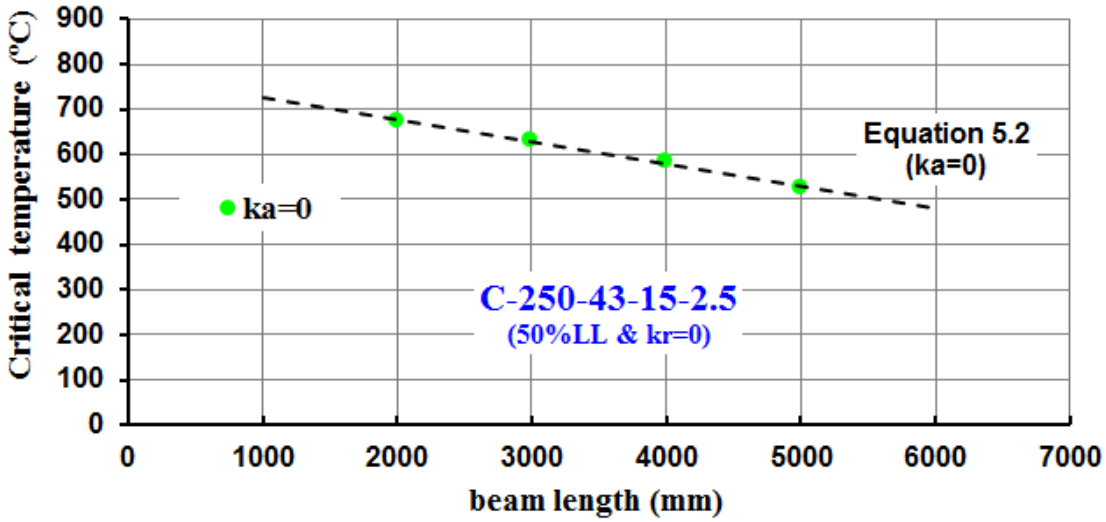

Figure H.1 – Comparison between FEA results and the proposed Equation 5.12 when the load level is 50% and the axial restrained to the thermal elongation of C-250-43-15-2.5 beam is zero as well as the rotational restraint of beam supports

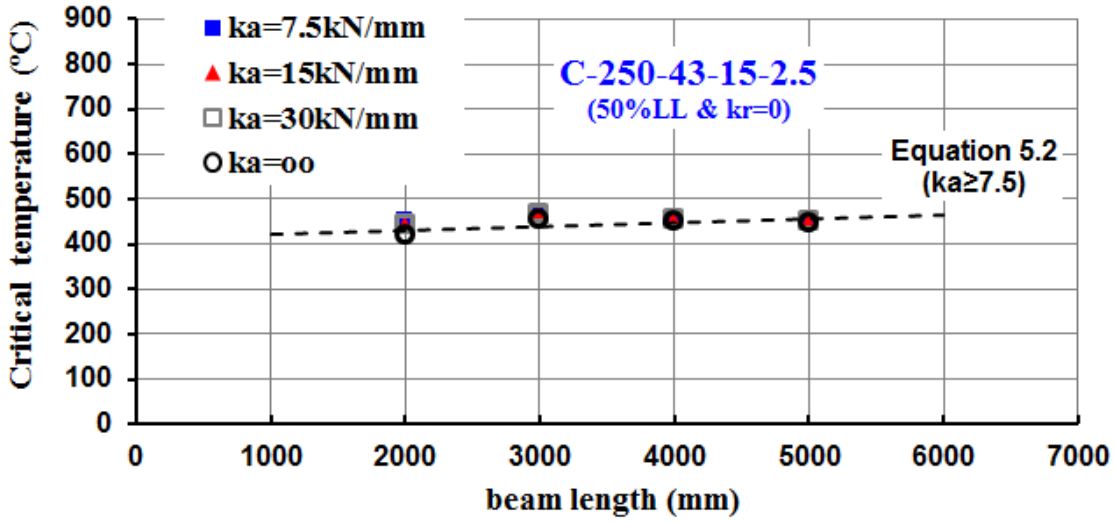

Figure H.2 – Comparison between FEA results and the proposed Equation 5.12 when the load level is 50%, the axial restrained to the thermal elongation of C-250-43-15-2.5 beam is higher than 7.5 kN/mm and the rotational restraint of beam supports is zero

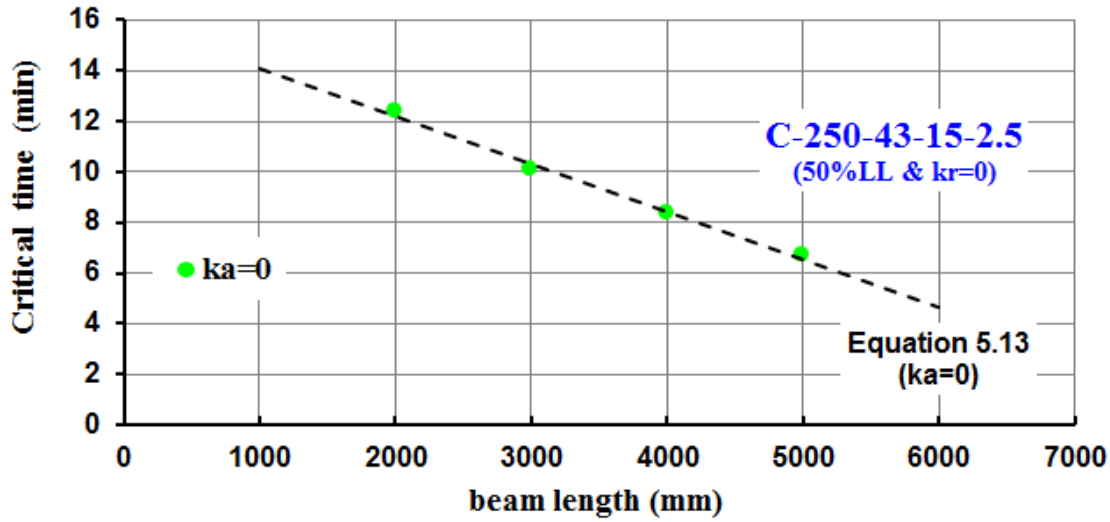

Figure H.3 – Comparison between FEA results and the proposed Equation 5.13 when the load level is 50% and the axial restrained to the thermal elongation of C-250-43-15-2.5 beam is zero as well as the rotational restraint of beam supports

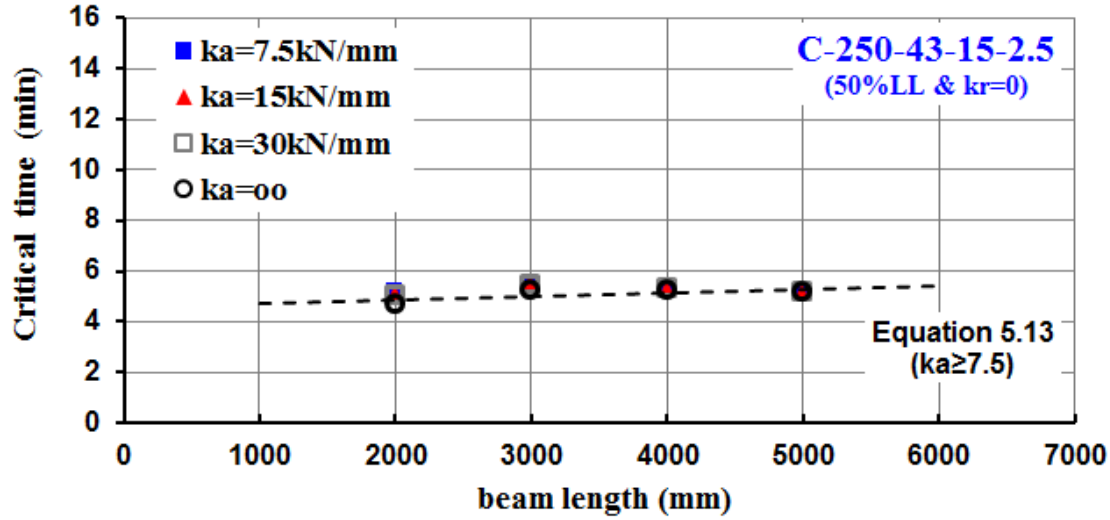

Figure H.4 – Comparison between FEA results and the proposed Equation 5.13 when the load level is 50%, the axial restrained to the thermal elongation of C-250-43-15-2.5 beam is higher than 7.5 kN/mm and the rotational restraint of beam supports is zero

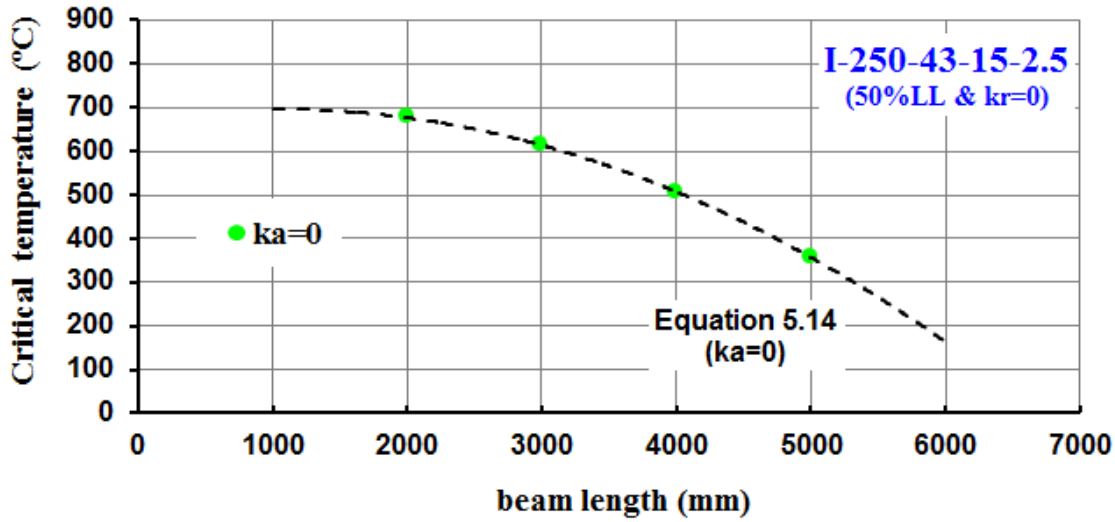

Figure H.5 – Comparison between FEA results and the proposed Equation 5.14 when the load level is 50% and the axial restrained to the thermal elongation of I-250-43-15-2.5 beam is zero as well as the rotational restraint of beam supports

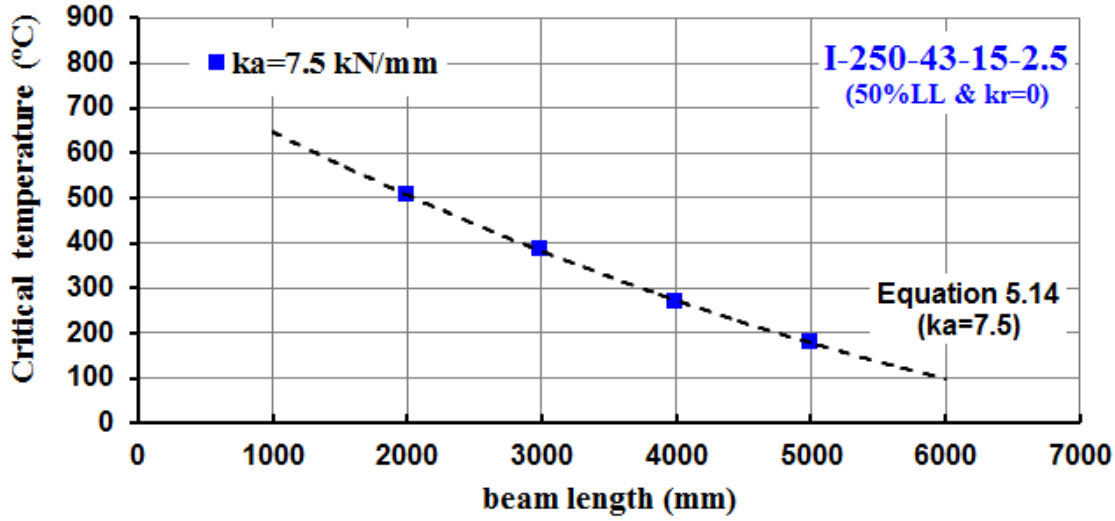

Figure H.6 – Comparison between FEA results and the proposed Equation 5.14 when the load level is 50%, the axial restrained to the thermal elongation of I-250-43-15-2.5 beam is equal to 7.5 kN/mm and the rotational restraint of beam supports is zero

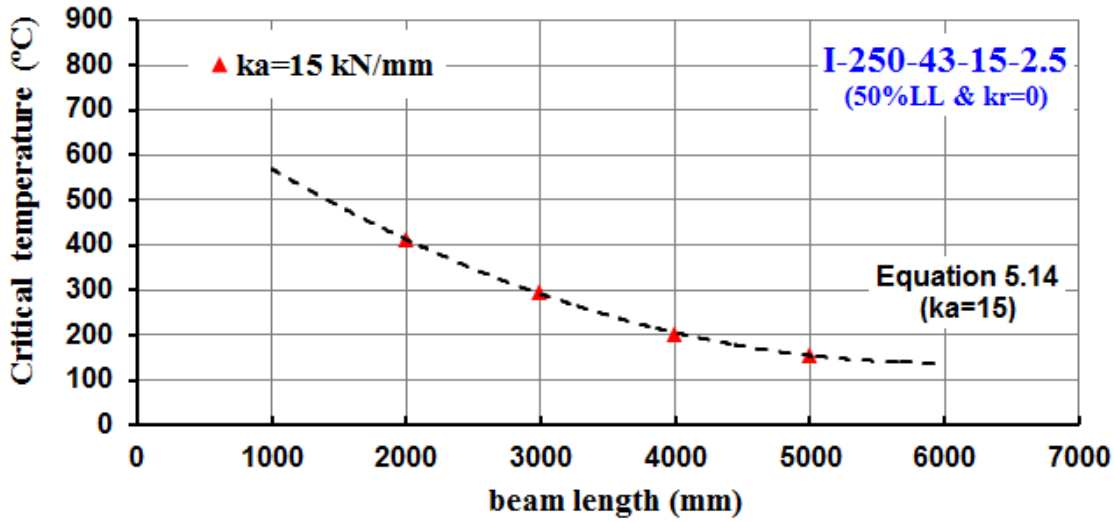

Figure H.7 – Comparison between FEA results and the proposed Equation 5.14 when the load level is 50%, the axial restrained to the thermal elongation of I-250-43-15-2.5 beam is equal to 15 kN/mm and the rotational restraint of beam supports is zero

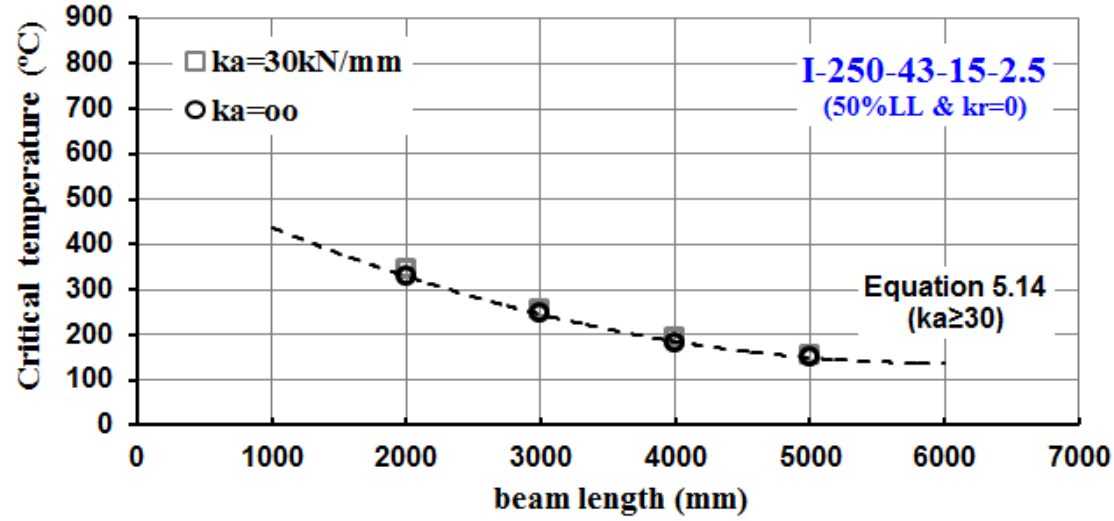

Figure H.8 – Comparison between FEA results and the proposed Equation 5.14 when the load level is 50%, the axial restrained to the thermal elongation of I-250-43-15-2.5 beam is higher than 30 kN/mm and the rotational restraint of beam supports is zero

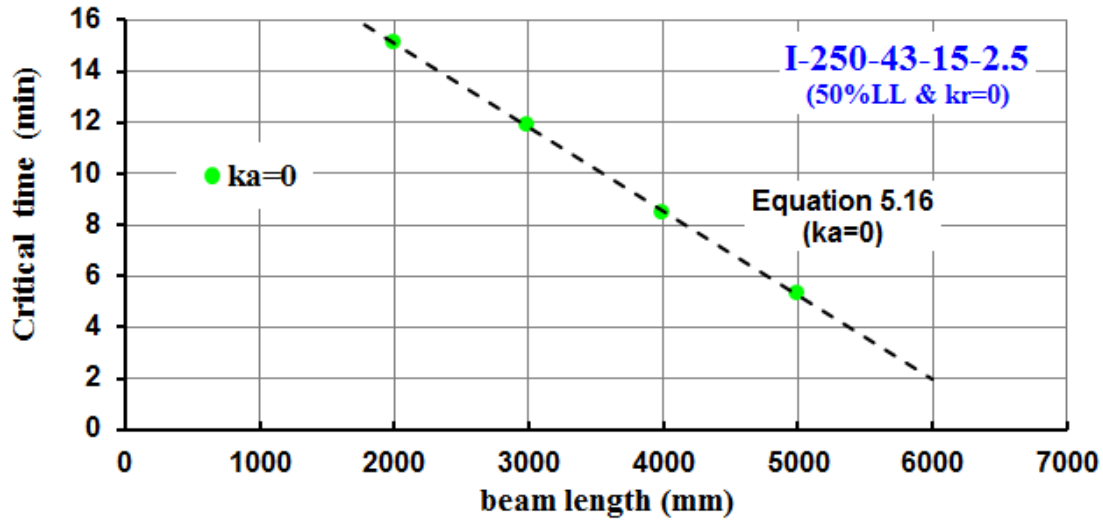

Figure H.9 – Comparison between FEA results and the proposed Equation 5.16 when the load level is 50% and the axial restrained to the thermal elongation of I-250-43-15-2.5 beam is zero as well as the rotational restraint of beam supports

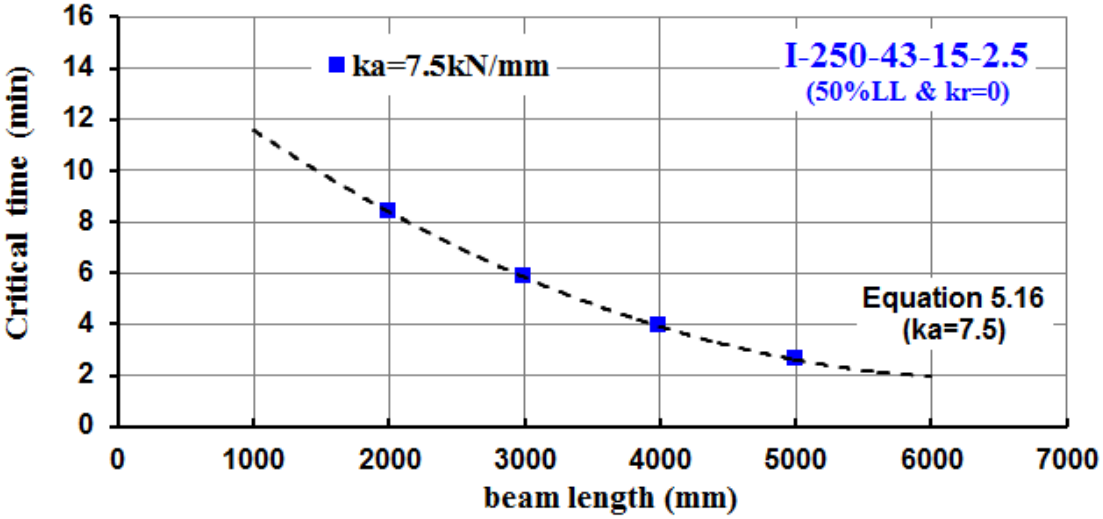

Figure H.10 – Comparison between FEA results and the proposed Equation 5.16 when the load level is 50%, the axial restrained to the thermal elongation of I-250-43-15-2.5 beam is equal to 7.5 kN/mm and the rotational restraint of beam supports is zero

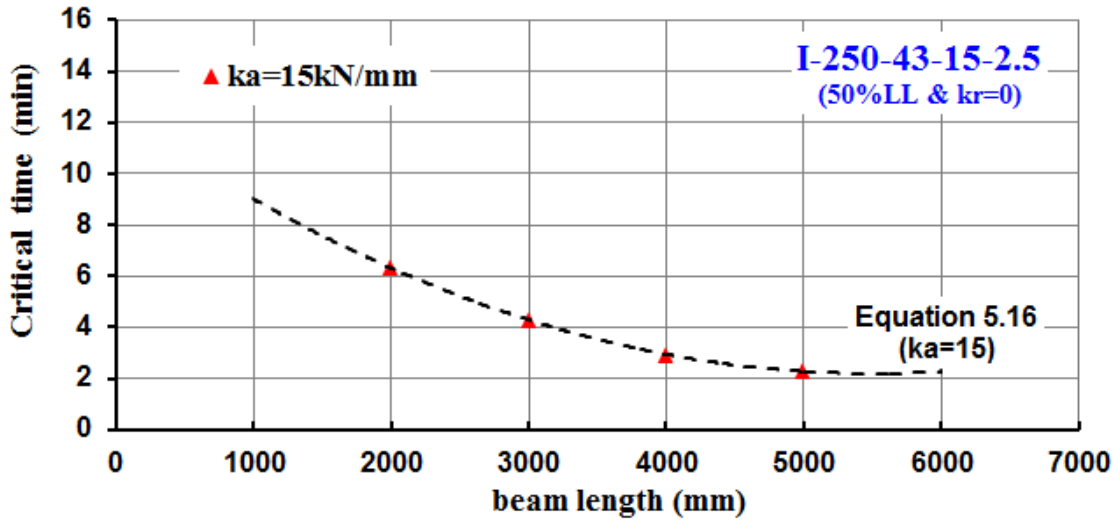

Figure H.11 – Comparison between FEA results and the proposed Equation 5.16 when the load level is 50%, the axial restrained to the thermal elongation of I-250-43-15-2.5 beam is equal to 15 kN/mm and the rotational restraint of beam supports is zero

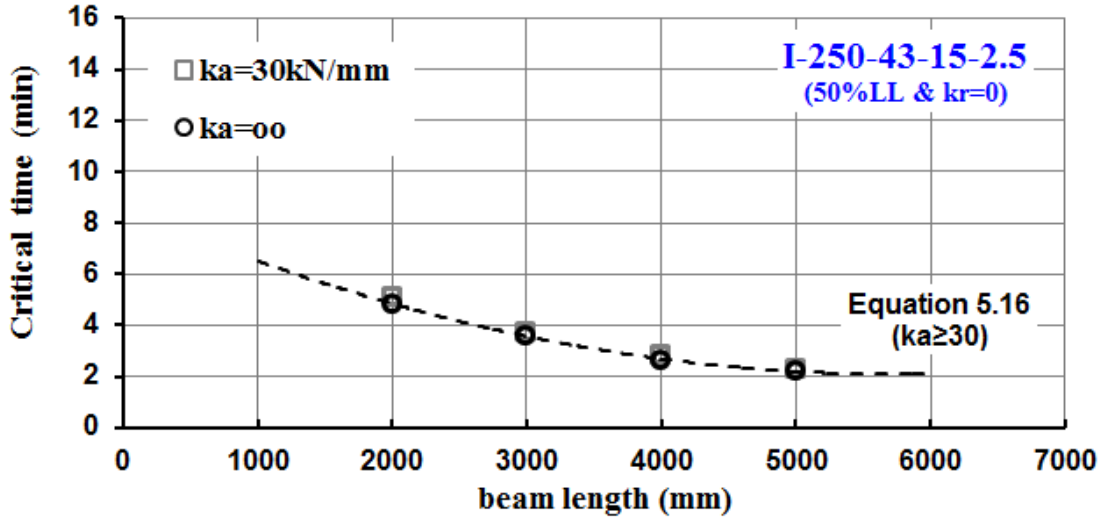

Figure H.12 – Comparison between FEA results and the proposed Equation 5.16 when the load level is 50%, the axial restrained to the thermal elongation of I-250-43-15-2.5 beam is higher than 30 kN/mm and the rotational restraint of beam supports is zero

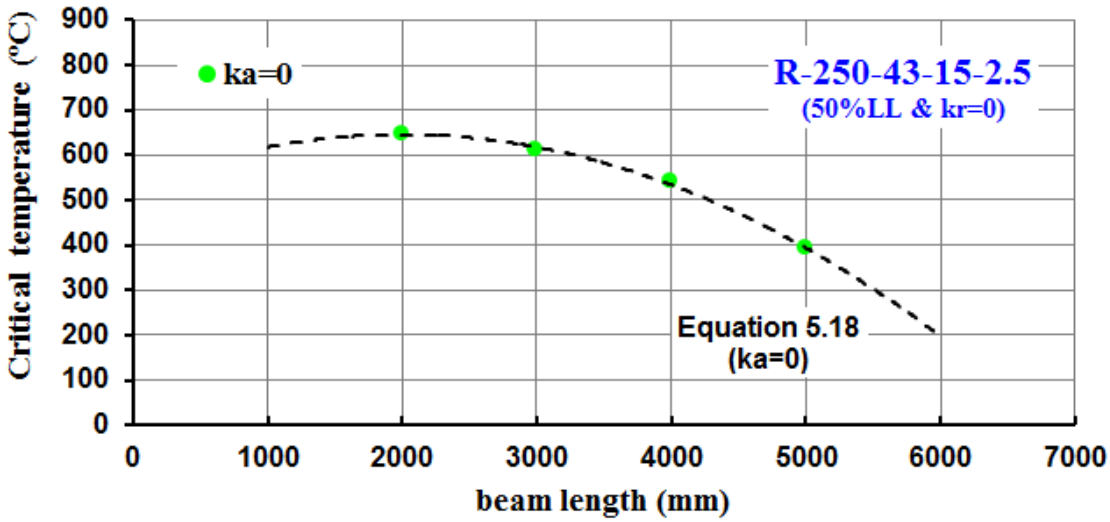

Figure H.13 – Comparison between FEA results and the proposed Equation 5.18 when the load level is 50% and the axial restrained to the thermal elongation of R-250-43-15-2.5 beam is zero as well as the rotational restraint of beam supports

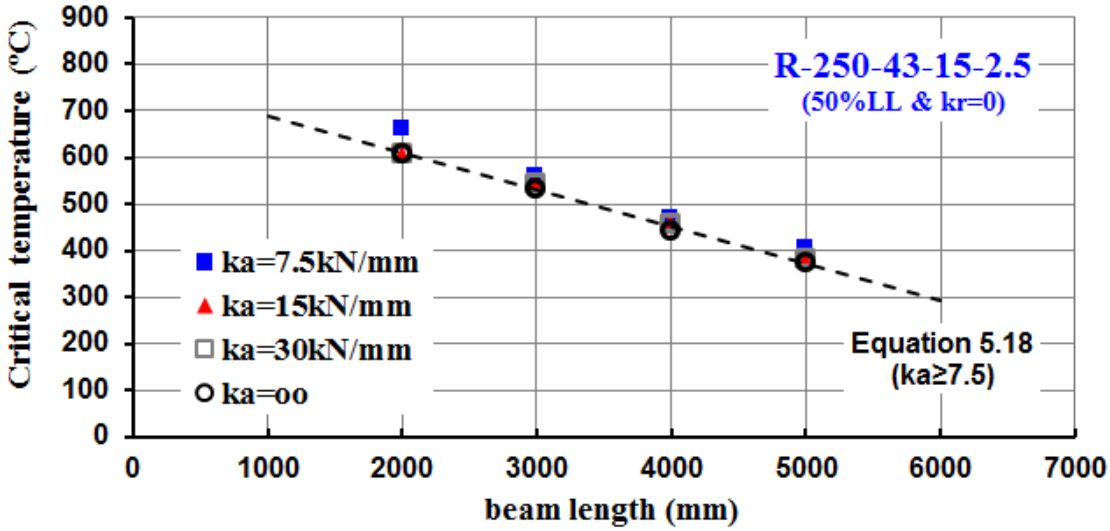

Figure H.14 – Comparison between FEA results and the proposed Equation 5.18 when the load level is 50%, the axial restrained to the thermal elongation of R-250-43-15-2.5 beam is higher than 7.5 kN/mm and the rotational restraint of beam supports is zero

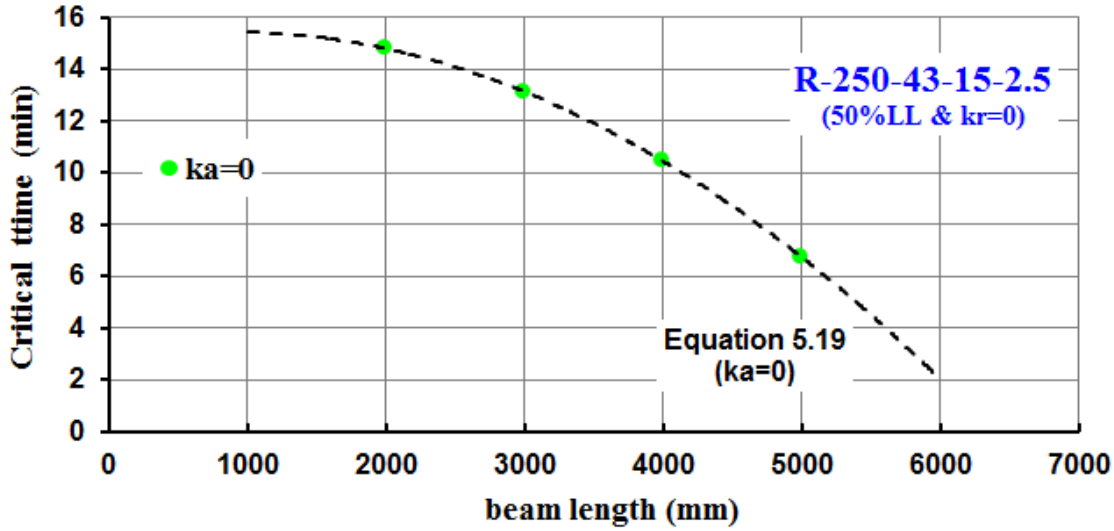

Figure H.15 – Comparison between FEA results and the proposed Equation 5.19 when the load level is 50% and the axial restrained to the thermal elongation of R-250-43-15-2.5 beam is zero as well as the rotational restraint of beam supports

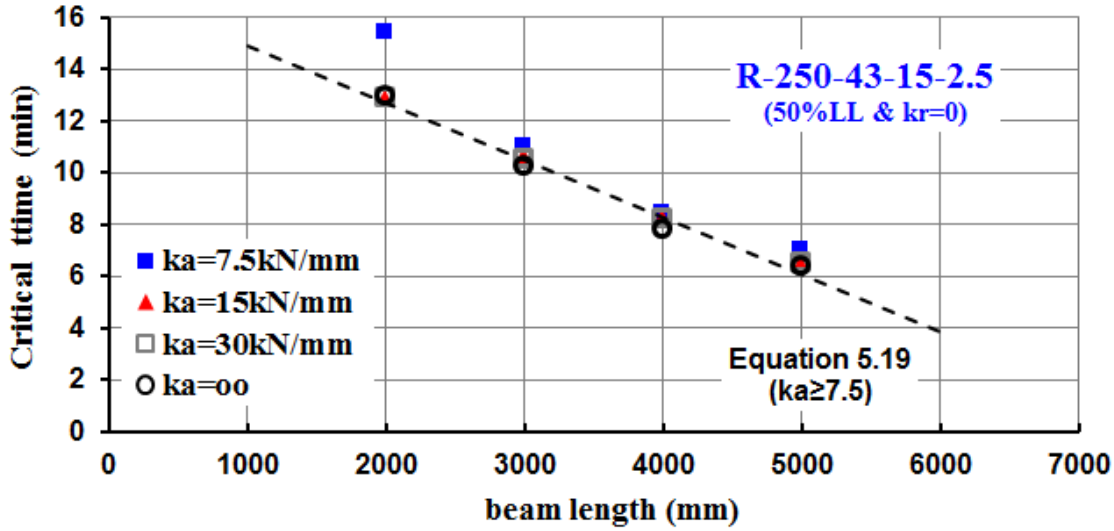

Figure H.16 – Comparison between FEA results and the proposed Equation 5.19 when the load level is 50%, the axial restrained to the thermal elongation of R-250-43-15-2.5 beam is higher than 7.5 kN/mm and the rotational restraint of beam supports is zero

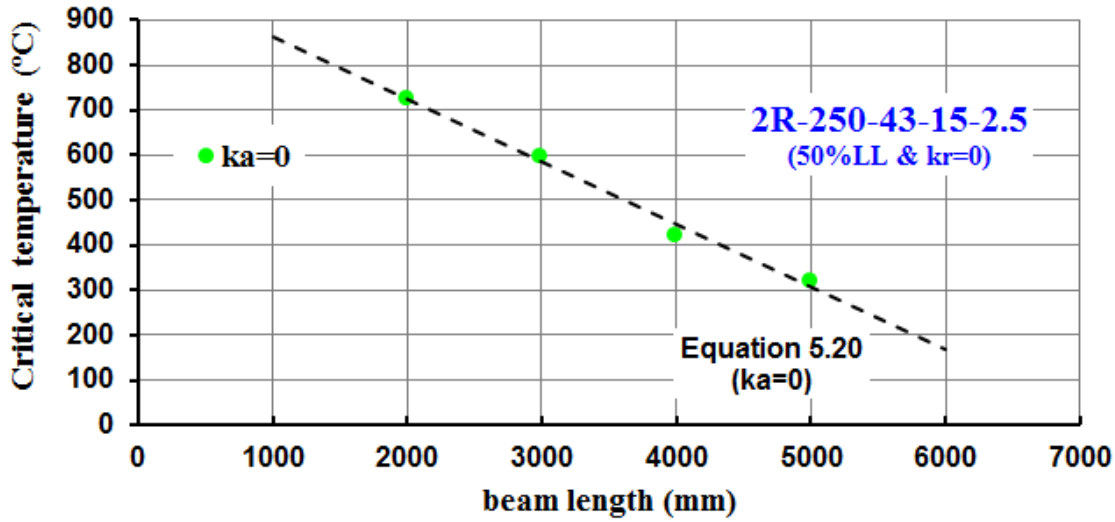

Figure H.17 – Comparison between FEA results and the proposed Equation 5.20 when the load level is 50% and the axial restrained to the thermal elongation of 2R-250-43-15-2.5 beam is zero as well as the rotational restraint of beam supports

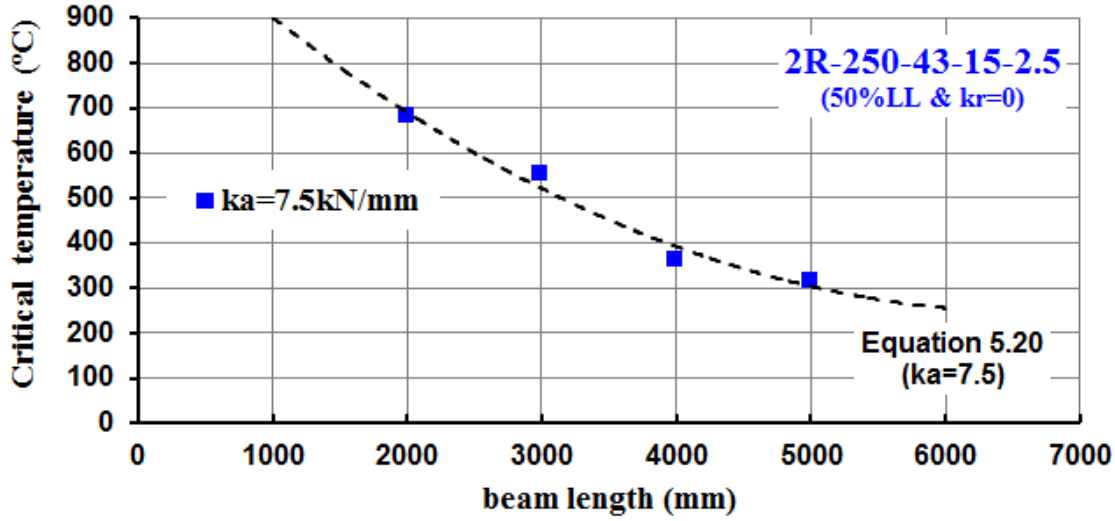

Figure H.18 – Comparison between FEA results and the proposed Equation 5.20 when the load level is 50%, the axial restrained to the thermal elongation of 2R-250-43-15-2.5 beam is equal to 7.5 kN/mm and the rotational restraint of beam supports is zero

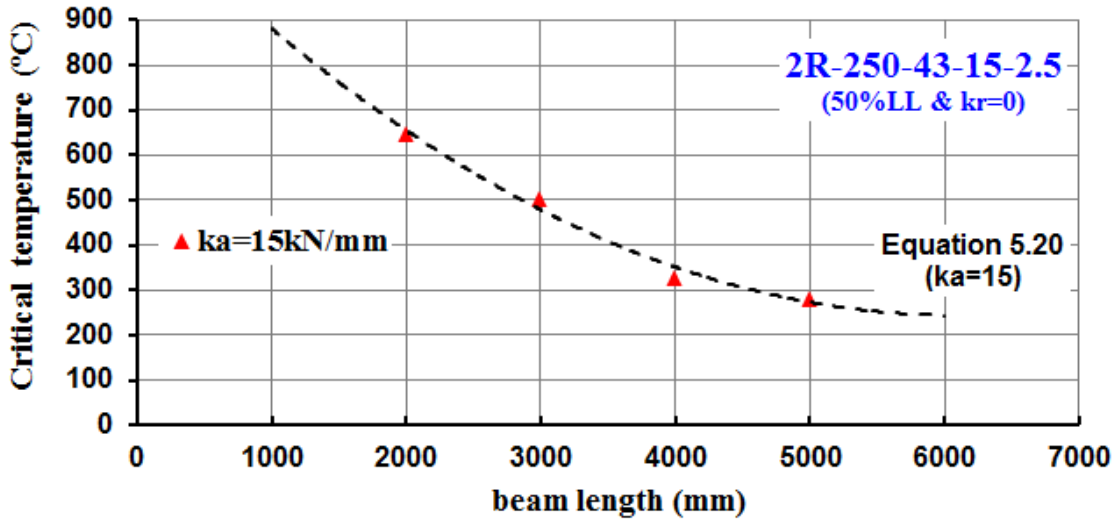

Figure H.19 – Comparison between FEA results and the proposed Equation 5.20 when the load level is 50%, the axial restrained to the thermal elongation of 2R-250-43-15-2.5 beam is equal to 15 kN/mm and the rotational restraint of beam supports is zero

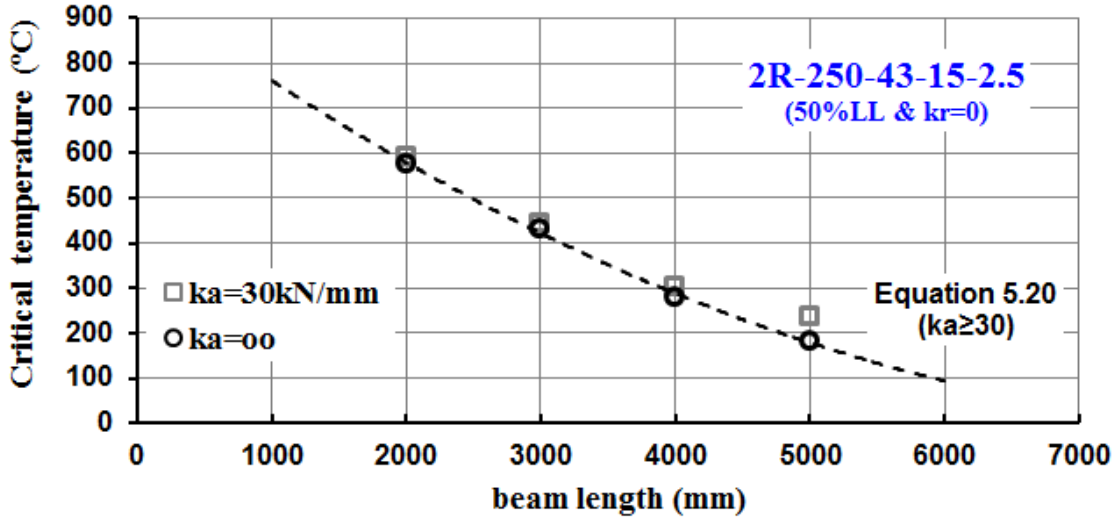

Figure H.20 – Comparison between FEA results and the proposed Equation 5.20 when the load level is 50%, the axial restrained to the thermal elongation of 2R-250-43-15-2.5 beam is higher than 30 kN/mm and the rotational restraint of beam supports is zero

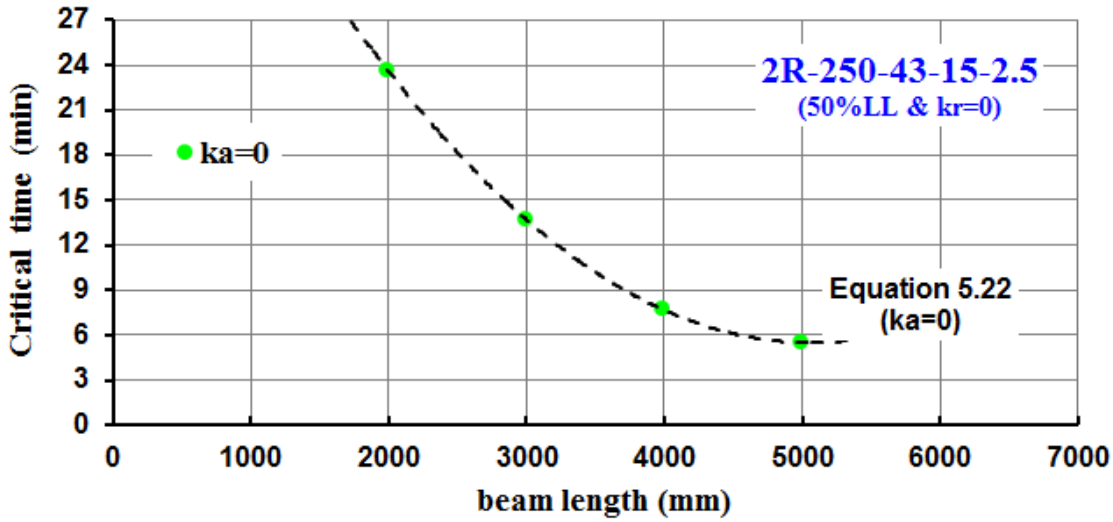

Figure H.21 – Comparison between FEA results and the proposed Equation 5.22 when the load level is 50% and the axial restrained to the thermal elongation of 2R-250-43-15-2.5 beam is zero as well as the rotational restraint of beam supports

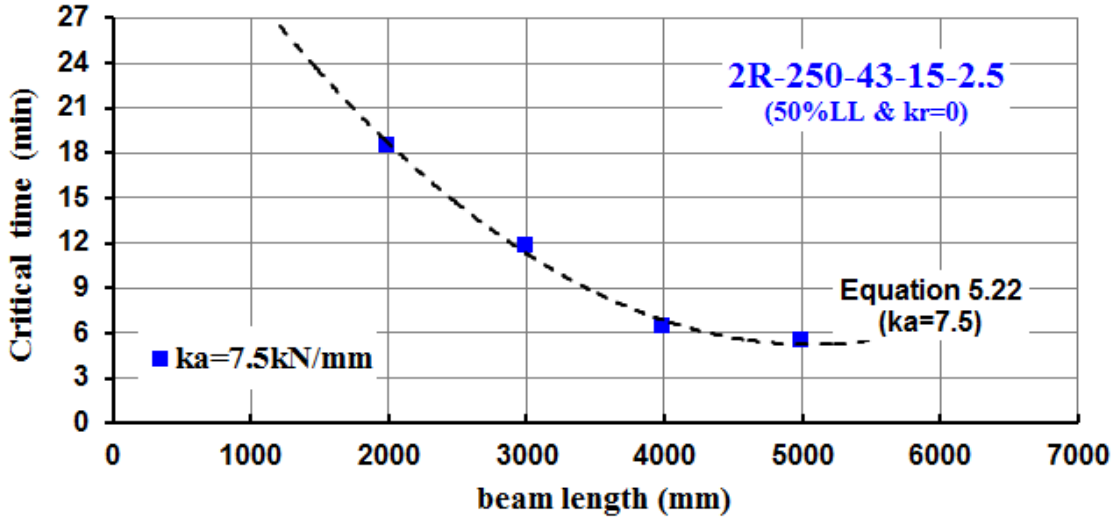

Figure H.22 – Comparison between FEA results and the proposed Equation 5.22 when the load level is 50%, the axial restrained to the thermal elongation of 2R-250-43-15-2.5 beam is equal to 7.5 kN/mm and the rotational restraint of beam supports is zero

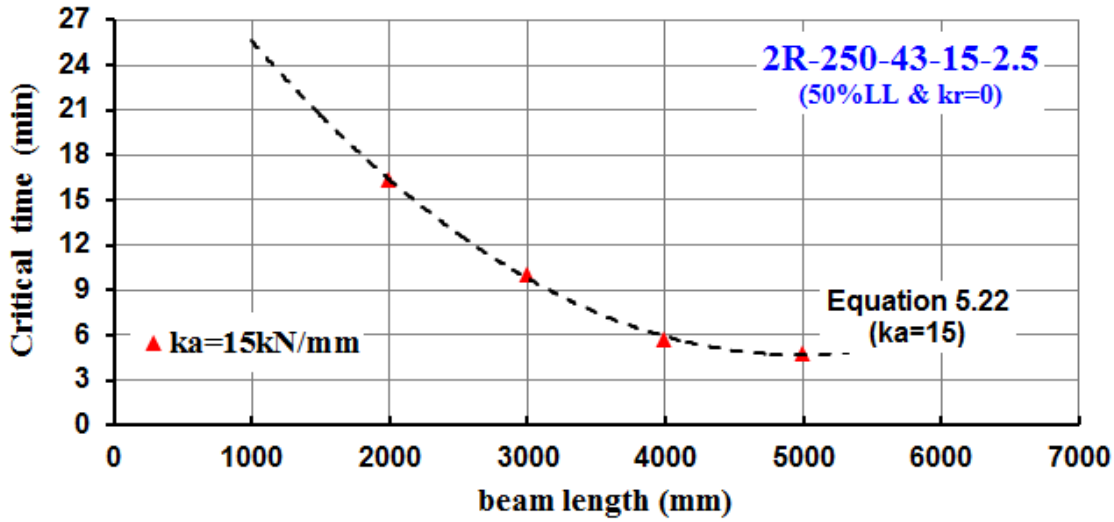

Figure H.23 – Comparison between FEA results and the proposed Equation 5.22 when the load level is 50%, the axial restrained to the thermal elongation of 2R-250-43-15-2.5 beam is equal to 15 kN/mm and the rotational restraint of beam supports is zero

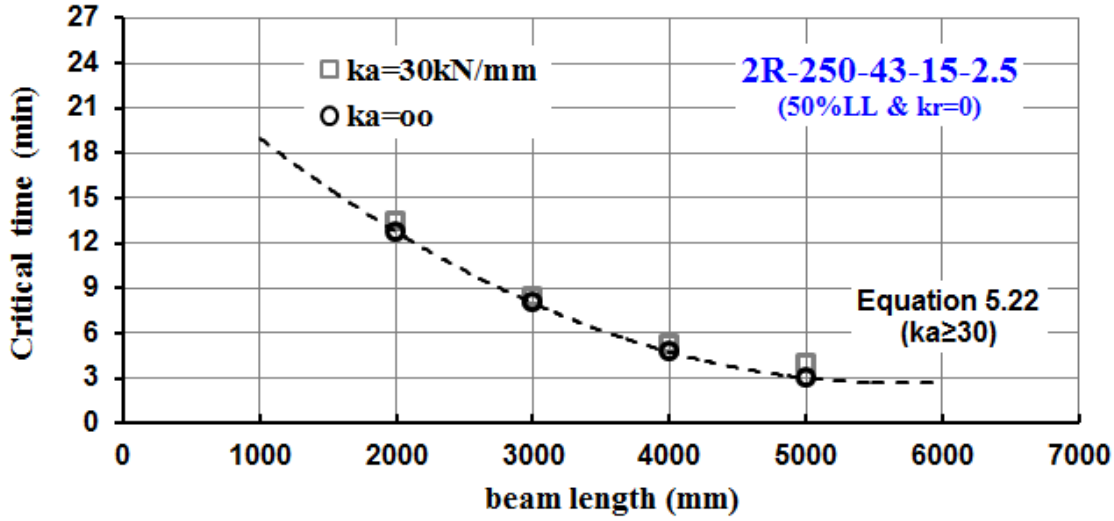

Figure H.24 – Comparison between FEA results and the proposed Equation 5.22 when the load level is 50%, the axial restrained to the thermal elongation of 2R-250-43-15-2.5 beam is higher than 30 kN/mm and the rotational restraint of beam supports is zero

APPENDIX I Axial and Rotational Restraint of Cold-Formed Steel Beams Inserted in Real Buildings

I1 Axial restraint

	(m)
Length of the square building	14.4
Column length	3.0
Beam length	4.8
Spacing between elements	0.6

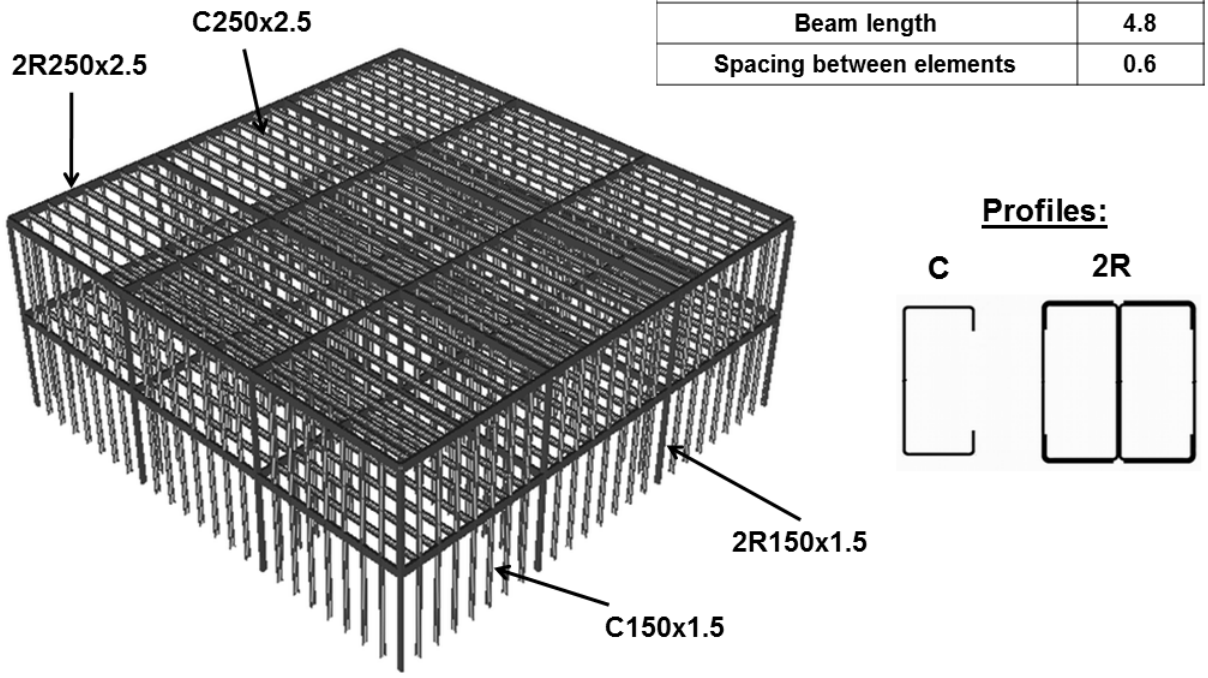

Figure I.1 – Building selected for assessing the axial restraint of a beam

- **Assumptions:**
  - truss elements (T3D2);
  - simply supported boundary conditions;
  - linear static analysis.

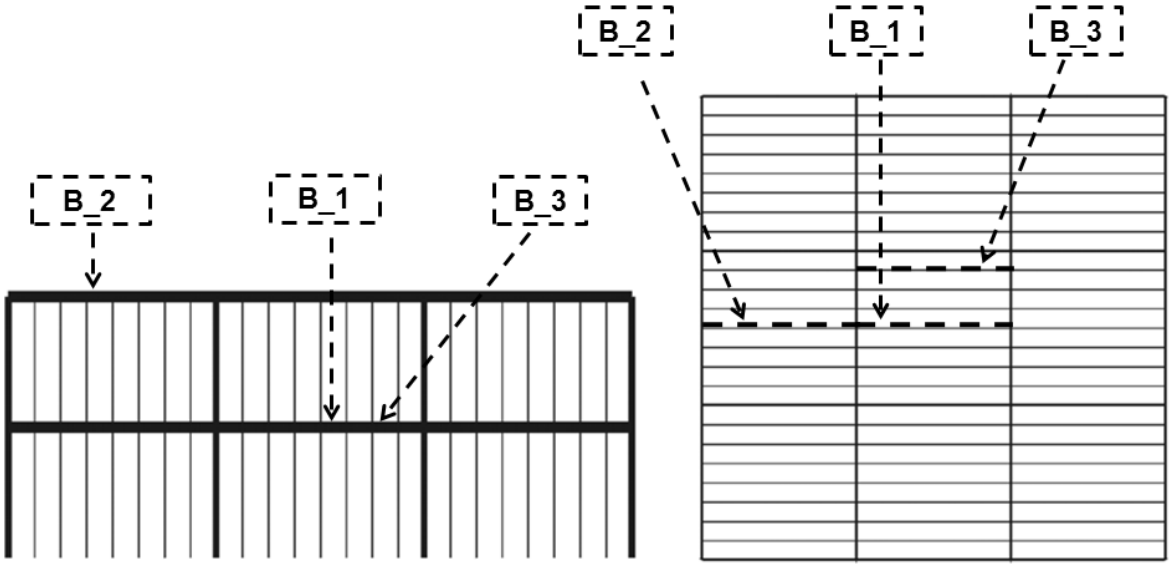

Figure I.2 – Beams selected for assessing their axial restraint

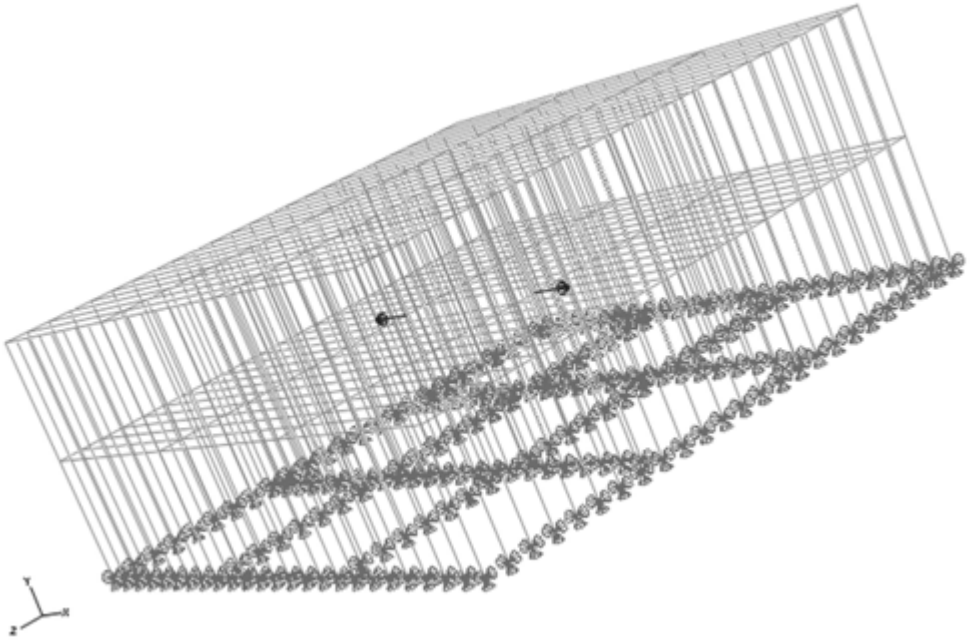

Figure I.3 – Axial forces imposed by the elongation of beam B_1

- **<u>Axial restraints obtained from the simulations:</u>**

Beam	Stiffness (kN/mm)
B_1	14.77
B_2	12.93
B_3	17.85

I2 Rotational restraint

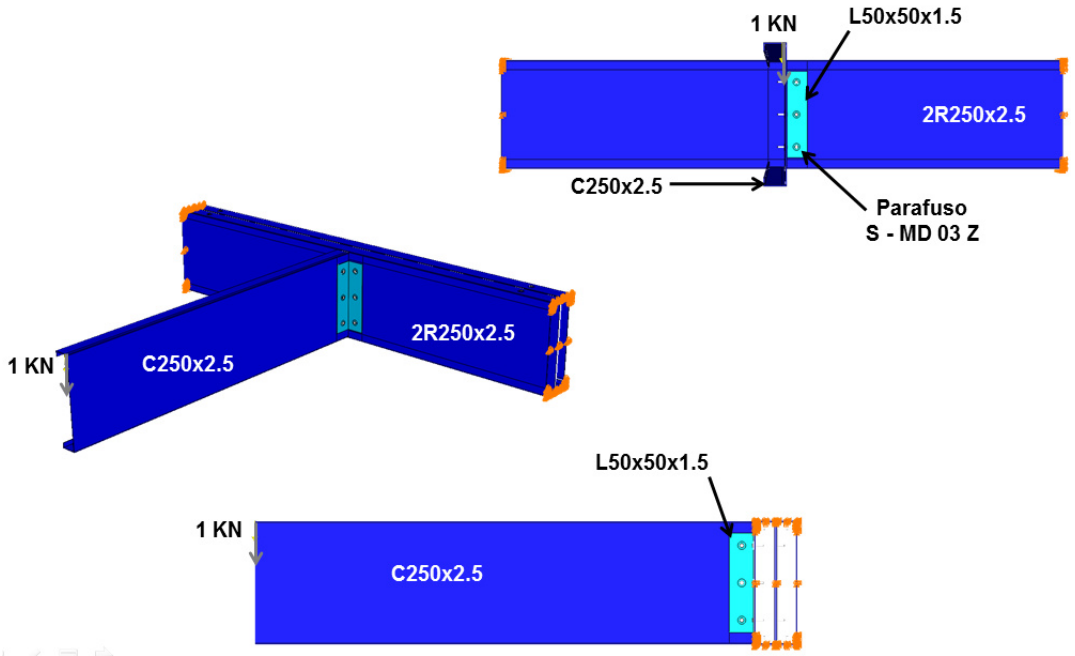

Figure I.4 – Views of a connection between a C beam and a 2R beam (connection C_1)

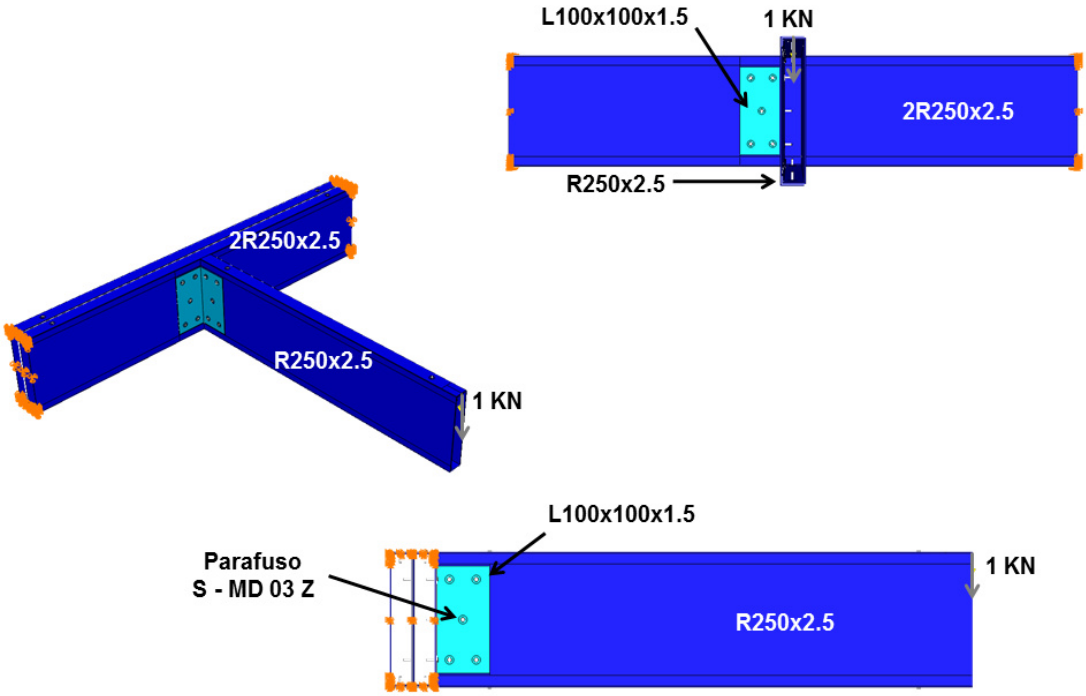

Figure I.5 – Views of a connection between an R beam and a 2R beam (connection C_2)

- **Assumptions:**
  - shell elements (S4R);
  - simply supported boundary conditions;
  - linear static analysis.

- **Rotational restraints obtained from the simulations:**

Connection	Stiffness (kN.m/rad)
C_1	188.82
C_2	232.45